



Editor, **YOGESH JALURIA** (2010)
Assistant to the Editor, **S. PATEL**

Associate Editors

Yutaka Asako, Tokyo Metropolitan University, Japan (2010)
Gautam Biswas, Indian Inst. of Tech., Kanpur (2009)
Cho Lik Chan, The University of Arizona (2010)
Louis C. Chow, University of Central Florida (2010)
Minking Chyu, Univ. of Pittsburgh (2009)
Frank J. Cunha, Pratt & Whitney (2011)
Ali Ebadian, Florida International Univ. (2011)
Ofofidi A. Ezekoye, Univ. of Texas-Austin (2011)
Satish G. Kandlikar, Rochester Inst. of Tech. (2010)
Sung Jin Kim, KAIST, Korea (2010)
Sai C. Lau, Texas A&M Univ. (2009)
Ben Q. Li, Univ. of Michigan, Dearborn (2009)
Raj M. Manglik, Univ. of Cincinnati (2009)
Jayanthi Y. Murthy, Purdue University (2010)
Pamela M. Norris, Univ. of Virginia (2011)
Patrick E. Phelan, Arizona State Univ. (2011)
Donald C. Price, Raytheon Co. (2011)
Roger R. Schmidt, IBM Corporation (2010)
S. A. Sherif, University of Florida (2010)
Peter Vadasz, Northern Arizona University (2010)
Jamal Yagoobi, Illinois Inst. of Tech. (2009)
Walter W. Yuen, Univ. of California—Santa Barbara (2011)

Past Editors

V. DHIR
J. R. HOWELL
R. VISKANTA
G. M. FAETH
K. T. YANG
E. M. SPARROW

HEAT TRANSFER DIVISION
Chair, **T. W. TONG**
Vice Chair, **C. H. OH**
Past Chair, **R. W. DOUGLASS**

PUBLICATIONS COMMITTEE
Chair, **BAHRAM RAVANI**

OFFICERS OF THE ASME
President,
THOMAS M. BARLOW
Executive Director,
THOMAS G. LOUGHLIN
Treasurer,
THOMAS D. PESTORIUS

PUBLISHING STAFF

Managing Director, Publishing
PHILIP DI VIETRO
Manager, Journals
COLIN McATEER
Production Coordinator
JUDITH SIERANT

Transactions of the ASME, Journal of Heat Transfer (ISSN 0022-1481) is published monthly by The American Society of Mechanical Engineers, Three Park Avenue, New York, NY 10016. Periodicals postage paid at New York, NY and additional mailing offices.
POSTMASTER: Send address changes to Transactions of the ASME, Journal of Heat Transfer, c/o THE AMERICAN SOCIETY OF MECHANICAL ENGINEERS, 22 Law Drive, Box 2300, Fairfield, NJ 07007-2300.
CHANGES OF ADDRESS must be received at Society headquarters seven weeks before they are to be effective. Please send old label and new address.

STATEMENT from By-Laws. The Society shall not be responsible for statements or opinions advanced in papers or ... printed in its publications (B7.1, Para. 3).
COPYRIGHT © 2008 by The American Society of Mechanical Engineers. For authorization to photocopy material for internal or personal use under those circumstances not falling within the fair use provisions of the Copyright Act, contact the Copyright Clearance Center (CCC), 222 Rosewood Drive, Danvers, MA 01923, tel: 978-750-8400, www.copyright.com.
Request for special permission or bulk copying should be addressed to Reprints/Permission Department.
Canadian Goods & Services Tax Registration #126148048

Journal of Heat Transfer

Published Monthly by ASME

VOLUME 130 • NUMBER 7 • JULY 2008

RESEARCH PAPERS

Combustion and Reactive Flows

- 071201 **A Numerical and Analytical Study of Thermally Driven Combustion Oscillations in a Perfectly Stirred Reactor**
Maria V. Petrova, Matthew McGarry, and Hai Wang

Evaporation, Boiling, and Condensation

- 071501 **Modeling of Thermophysical Processes in Liquid Ceramic Precursor Droplets Heated by Monochromatic Irradiation**
Saptarshi Basu and Baki M. Cetegen
- 071502 **Laminar Filmwise Condensation on Horizontal Disk Embedded in Porous Medium With Suction at Wall**
Tong-Bou Chang

Forced Convection

- 071701 **Heat Transfer in Trailing Edge, Wedge-Shaped Cooling Channels Under High Rotation Numbers**
Lesley M. Wright, Yao-Hsien Liu, Je-Chin Han, and Sanjay Chopra
- 071702 **Film Cooling Effectiveness Distribution on a Gas Turbine Blade Platform With Inclined Slot Leakage and Discrete Film Hole Flows**
Lesley M. Wright, Zhihong Gao, Huitao Yang, and Je-Chin Han
- 071703 **A Numerical Study of Flow and Heat Transfer Between Two Rotating Spheres With Time-Dependent Angular Velocities**
Ali Jabari Moghadam and Asghar Baradaran Rahimi
- 071704 **Effect of Pin Tip Clearance on Flow and Heat Transfer at Low Reynolds Numbers**
Ali Rozati, Danesh K. Tafti, and Neal E. Blackwell

Jets, Wakes, and Impingement Cooling

- 072201 **Computational Study of Heat Transfer in a Conjugate Turbulent Wall Jet Flow at High Reynolds Number**
E. Vishnuvardhanarao and Manab Kumar Das
- 072202 **Application of Electrohydrodynamic Atomization to Two-Phase Impingement Heat Transfer**
Xin Feng and James E. Bryan

Micro/Nanoscale Heat Transfer

- 072401 **Instability of Nanofluids in Natural Convection**
D. Y. Tzou
- 072402 **Flow Boiling Instabilities in Microchannels and Means for Mitigation by Reentrant Cavities**
C.-J. Kuo and Y. Peles
- 072403 **Critical Heat Flux of Water at Subatmospheric Pressures in Microchannels**
C.-J. Kuo and Y. Peles
- 072404 **Monte Carlo Simulation of Steady-State Microscale Phonon Heat Transport**
Jaona Randrianalisoa and Dominique Baillis

(Contents continued on inside back cover)

This journal is printed on acid-free paper, which exceeds the ANSI Z39.48-1992 specification for permanence of paper and library materials. ©™
♻️ 85% recycled content, including 10% post-consumer fibers.

Natural and Mixed Convection

- 072501 Numerical Experiments in Turbulent Natural Convection Using Two-Equation Eddy-Viscosity Models
X. Albets-Chico, A. Oliva, and C. D. Pérez-Segarra

Radiative Heat Transfer

- 072701 Performance of the Various S_n Approximations of DOM in a 3D Combustion Chamber
Manosh C. Paul

Two-Phase Flow and Heat Transfer

- 072901 Experimental and Analytical Studies of Reciprocating-Mechanism Driven Heat Loops (RMDHLs)
Yiding Cao and Mingcong Gao

TECHNICAL BRIEFS

- 074501 Analysis of the Thermal Behavior of a Multilayer Slab With Imperfect Contact Using the Dual-Phase-Lag Heat Conduction Model
K. Ramadan and M. A. Al-Nimr
- 074502 Two-Phase Convective Heat Transfer in Miniature Pipes Under Normal and Microgravity Conditions
Chidambaram Narayanan and Djamel Lakehal
- 074503 Heat Transfer Analysis Through Solar and Rooted Fins
A.-R. A. Khaled

The ASME Journal of Heat Transfer is abstracted and indexed in the following:

Applied Science and Technology Index, Chemical Abstracts, Chemical Engineering and Biotechnology Abstracts (Electronic equivalent of Process and Chemical Engineering), Civil Engineering Abstracts, Compendex (The electronic equivalent of Engineering Index), Corrosion Abstracts, Current Contents, E & P Health, Safety, and Environment, Ei EncompassLit, Engineered Materials Abstracts, Engineering Index, Enviroline (The electronic equivalent of Environment Abstracts), Environment Abstracts, Environmental Engineering Abstracts, Environmental Science and Pollution Management, Fluidex, Fuel and Energy Abstracts, Index to Scientific Reviews, INSPEC, International Building Services Abstracts, Mechanical & Transportation Engineering Abstracts, Mechanical Engineering Abstracts, METADEX (The electronic equivalent of Metals Abstracts and Alloys Index), Petroleum Abstracts, Process and Chemical Engineering, Referativnyi Zhurnal, Science Citation Index, SciSearch (The electronic equivalent of Science Citation Index), Theoretical Chemical Engineering

A Numerical and Analytical Study of Thermally Driven Combustion Oscillations in a Perfectly Stirred Reactor

Maria V. Petrova

Reaction Design,
6440 Lusk Boulevard, Suite D205,
San Diego, CA 92121
e-mail: mpetrova@reactiondesign.com

Matthew McGarry¹

Department of Engineering,
University of San Diego,
5998 Alcalá Park, Loma Hall,
San Diego, CA 92110
e-mail: mmcgarry@sandiego.edu

Hai Wang

Department of Aerospace and Mechanical
Engineering,
University of Southern California,
Los Angeles, CA 90089
e-mail: haiw@usc.edu

The oscillatory behaviors of methane and hydrogen oxidation in a perfectly stirred reactor (PSR) are examined. The work explores the parameter spaces in which oscillatory combustion and ignition take place using heat transfer coefficient, mean residence time, and reactor wall temperatures as variables. An analytic model was developed using an eigenvalue analysis to determine the nature and stability of these oscillations. Both numerical and analytical studies suggest that combustion oscillations occur at the extinction turning point of the hysteresis curve or the boundary of combustion extinction. These oscillations are found to be driven by the coupling of the heat released from the reaction and the heat dissipation through the reactor wall, and these are unstable, which perhaps explains why they were never or rarely observed experimentally. In the case of hydrogen oxidation, we demonstrate the existence of two additional types of oscillations, namely, hybrid oscillation and oscillatory ignition, both of which occur at or near the turning point of ignition. These oscillations are stable and driven by detailed reaction kinetics. The numerical results for hydrogen oxidation were compared with previous experiments and found to be within 5 K of the observed wall temperature where oscillations were observed. [DOI: 10.1115/1.2897926]

Keywords: oscillatory ignition, PSR, hydrogen oxidation, reactor

Introduction

Despite its simplicity of operation, a well-stirred reactor can produce a variety of combustion modes ranging from steady burning to extinction. Combustion in a well-stirred reactor can also be spontaneously oscillatory. Griffiths and co-workers [1–4] showed that periodic ignition and Hopf bifurcations exist for hydrogen oxidation near the second explosion limit [5]. Isothermal kinetic and thermokinetic analyses showed that the origin of the oscillations was the large third-body efficiency of water and the resulting periodic variations in the rate of chain termination reaction $H + O_2 + M \rightarrow HO_2 + M$ [2,3,6]. Specifically, as water was produced from the combustion reaction, the rate of chain terminating reaction increased, and a decrease in the combustion intensity followed. A decrease in combustion intensity reduced water production, thereby decreasing the rate of radical chain termination, increasing the oxidation intensity and leading to reignition. A nonisothermal analysis [7] showed that complex ignition oscillations and bifurcations require the thermal effects of heat release and heat loss to be included in the analysis, whereas simple periodic ignition could arise even under isothermal conditions. The amplitudes and frequencies of oscillations were found to be extremely sensitive to heat transfer rates through the reactor wall [8].

Vlachos and co-workers [9–11] performed a detailed bifurcation analysis for oscillations in isothermal well-stirred reactors. Oscillatory ignition, combustion, and bifurcation were identified near or at the ignition and extinction turning points of hysteresis curves. Multiplicity of solutions in the form of birhythmicity was

also found under certain reactor conditions [10]. Chain branching and radical losses were found to be a sufficient cause of oscillations [9].

In addition to hydrogen oxidation, combustion oscillations were also observed for fuels or fuel blends other than pure hydrogen (e.g., Refs. [12–14]). In all cases, oscillations occurred at relatively low temperatures. Like the oxidation of hydrogen, reaction chemistry specific to a given fuel appeared to have a dominant influence on the nature of the oscillations and parameter space in which oscillations occurred.

The initial motivation behind this work was to apply the previous knowledge of oscillatory combustion to efficient and clean fuel conversion. Our interest was to convert petroleum fuels to hydrogen and other forms of hydrocarbon materials by fuel-rich combustion. We reasoned that by operating a well-stirred reactor with the time period of each oscillatory cycle shorter than the induction time of pollutant formation, it might be possible to achieve sufficient fuel conversion with minimal soot and other pollutant emissions. Very quickly, however, it became clear to us that the knowledge from previous studies was insufficient to address a range of basic questions concerning combustion oscillations in a well-stirred reactor. For example, very little is known about the cause and nature of nonisothermal combustion oscillations other than those of ignition oscillations observed previously. It is also not clear whether among different types of oscillations, there could be a type of oscillations generic for all fuels. That is, the cause for oscillation is independent of reaction kinetics.

The major objective of the present work was to examine a type of combustion oscillations driven entirely by the thermal effects of heat generation and convective heat loss. The nature and cause of these oscillations will be shown to be completely different from previously studied ignition oscillations, but such oscillations may be easily misunderstood as ignition oscillation. In doing so, we

¹Corresponding author.

Contributed by the Heat Transfer Division of ASME for publication in the JOURNAL OF HEAT TRANSFER. Manuscript received February 13, 2007; final manuscript received October 17, 2007; published online May 16, 2008. Review conducted by Bengt Sunden.

hope to provide a theoretical guidance in locating the parameter space within which these oscillations may occur irrespective of the nature of the reactant fuel.

Numerical simulations of hydrogen and methane oxidation in a perfectly stirred reactor (PSR) were carried out to characterize the combustion responses as a function of relevant reactor variables. These simulations were made by using detailed reaction kinetics and by solving the transient mass and energy equations in a well-stirred reactor. An analytical eigenvalue analysis was then performed to examine the solution stability and oscillations of the underlying governing equations. We identified the principal cause of combustion oscillations to be the coupling of heat release and convective heat loss through the reactor wall, which is independent of fuel type and stoichiometry. In addition, relationships between previously studied ignition oscillations and present combustion oscillations are presented. Responses of amplitude and frequency to the variation of reactor operating parameters are also discussed. These specific properties of combustion oscillation were found to be highly dependent on the operation conditions, fuel type, and stoichiometry.

Methodologies

Numerical Computations. The PSR code [15] from the Chemkin suite of codes was employed to simulate reactions in a well-stirred reactor. The PSR code was initially written for steady-state PSR problems and was modified in this work to allow computations for a transient problem. Specifically, the integration of time-dependent governing equations of species and energy conservation was performed by a time-marching procedure employing the two-point boundary value problem solver [16]. Since oscillations and bifurcation are extremely sensitive to numerical accuracy in each time step, stringent tolerances were assigned to ensure that numerical errors during time integration have little effects on PSR solution.

A convective heat loss term was added to the energy conservation equation to account for heat loss through the reactor wall. This term takes the form of $hA/(\rho V)(T-T_w)$, where h is the heat transfer coefficient, A and V are, respectively, the wall area and the volume of the reactor, ρ is the mixture density, T is the temperature, and T_w is the wall temperature of the reactor. An effective heat transfer coefficient was defined as $\chi=hA$. Combustion responses and oscillations were examined within either the $\dot{m}\chi-T_w-T_{in}$ or the $\tau\chi-T_w$ parameter space, where \dot{m} is the mass flow rate, τ is the mean residence time, and T_{in} is the inlet reactant temperature. These parameters were varied, while other variables including reactor volume and pressure were held fixed for each fuel of interest.

For hydrogen combustion, we used the reaction model of Kim et al. [17]. The use of more recently published models of hydrogen combustion [18–21] did not affect our conclusions. The methane combustion mechanism consists of 59 species and 331 elementary reactions and is based on GRI-MECH 1.2 [22] supplemented by the combustion chemistry of acetylene and ethylene [23,24]. The modified mechanism also included the reactions leading to the formation of soot precursors [22].

Analytical Eigenvalue Analysis. To simplify this analysis, we adopted a global reaction given by



where Δh^0 is the enthalpy released during the reaction and the reaction rate constant is given by the simple Arrhenius equation $k=A \exp(-E/RT)$. The governing equations are given by

$$\frac{dC_R}{dt} = - \left[\frac{C_R - C}{\tau} + A \exp\left(-\frac{E}{RT}\right) C_R \right] \quad (1)$$

$$c_p \frac{dT}{dt} = \frac{c_p^* T^* - c_p T}{\tau} - \frac{\chi(T - T_w)}{\rho V} - \Delta h^0 A \exp\left(-\frac{E}{RT}\right) \frac{C_R}{C} \quad (2)$$

where C_R is the molar concentration of the reactant, $C=C_R+C_P$ the total molar concentration, C_P the molar concentration of the product, and c_p the mixture specific heat. The asterisk refers to reactor inlet conditions.

Following the approach of Gray and Griffiths [25], Eqs. (1) and (2) were nondimensionalized by defining the Newton cooling time [26],

$$t_N = \frac{\rho c_p V}{\chi} \quad (3)$$

The real time and mean residence time were then nondimensionalized by t_N as $t_1 = \tau/t_N$ and $t_2 = \tau/t_N$, respectively. The nondimensional temperature takes the form [26] of

$$\theta = \frac{E(T - T_w)}{RT_w^2} \quad (4)$$

The resulting nondimensionalized governing equations are given by

$$\frac{dx_R}{dt} = \frac{1 - x_R}{t_2} - t_N A \exp\left(-\frac{1}{\varepsilon}\right) \exp\left(\frac{\theta}{1 + \varepsilon\theta}\right) x_R \quad (5)$$

$$\frac{d\theta}{dt} = \frac{\theta_0 - \theta}{t_2} - \zeta A \exp\left(-\frac{1}{\varepsilon}\right) \exp\left(\frac{\theta}{1 + \varepsilon\theta}\right) x_R - \theta \quad (6)$$

where x_R is the mole fraction of the reactant, ε is a small parameter given by $\varepsilon=RT_w/E$, and $\zeta=\rho V \Delta h^0/(\varepsilon \chi)$.

Linearizing Eqs. (5) and (6) and neglecting higher-order terms, we obtained

$$\dot{\mathbf{y}} = \mathbf{J} \mathbf{y} \quad (7)$$

where $\mathbf{y}=\mathbf{x}-\mathbf{x}^*$ (\mathbf{x}^* is a steady-state point) and \mathbf{J} is the Jacobian matrix. The solution was assumed to take the form of

$$\mathbf{y}(t) = e^{\lambda t} \mathbf{v} \quad (8)$$

where λ is the growth rate and \mathbf{v} a nonzero fixed vector to be determined. Combining Eqs. (7) and (8) yielded the classic eigenvalue problem, $\mathbf{J}\mathbf{v}=\lambda\mathbf{v}$, where \mathbf{v} is now an eigenvector of \mathbf{J} with a corresponding eigenvalue λ . Solving the typical characteristic equation that accompanies an eigenvalue problem yields the quadratic equation for the eigenvalues,

$$\lambda^2 - \text{Tr} \lambda + \Delta = 0 \quad (9)$$

where Tr and Δ are, respectively, the trace and determinant of the Jacobian \mathbf{J} [27]. Solving Eq. (9), one obtains eigenvalues $\lambda_{1/2} = \alpha \pm i\omega$ and $\alpha=\text{Tr}/2$, with $\omega=[\Delta-(\text{Tr}/2)^2]^{1/2}$. The general solution for $\mathbf{y}(t)$ is given by

$$\mathbf{y}(t) = \beta_1 e^{\lambda_1 t} \mathbf{v}_1 + \beta_2 e^{\lambda_2 t} \mathbf{v}_2 \quad (10)$$

where β 's are coefficients.

Examining Eq. (10) yields several important conclusions regarding the stability of the solution. Specifically, $\mathbf{y}(t)$ is a linear combination of $e^{(\alpha \pm i\omega)t}$, which by Euler's formula, is a linear combination of $e^{\alpha t} \cos(\omega t)$ and $e^{\alpha t} \sin(\omega t)$. Depending on the value of α (and therefore Tr) and ω (assuming it is real), unstable ($\text{Tr}>0$), oscillatory ($\text{Tr}=0$), and stable ($\text{Tr}<0$) solutions can be obtained. When $\text{Tr}=0$, the solution becomes imaginary, therefore persistently oscillatory. Observing that when ω is imaginary, the solution involves only the exponential dependence of real numbers. These solutions are called nodes and can be either stable or unstable depending on whether α is positive or negative [27].

Results and Discussion

Figure 1 presents the numerically determined boundaries separating the reactive solution from the frozen solution for methane

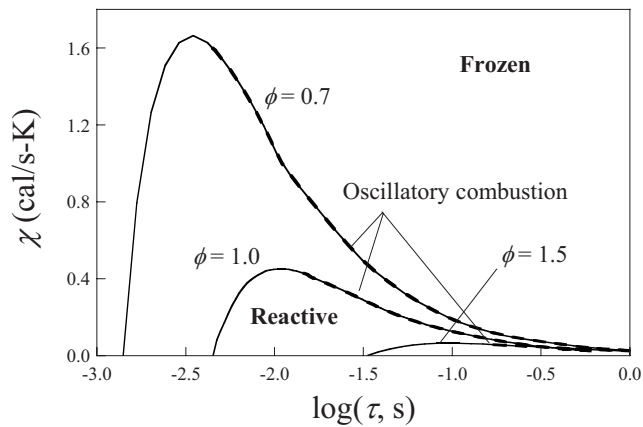


Fig. 1 Numerical characterization of PSR solution types in the parameter space of effective heat transfer coefficient versus residence time for methane in 11% O₂-89% (N₂+Ar) mixtures. The parameter space beneath each solid curve represents the condition where combustion is possible. The dashed lines indicate the conditions where combustion oscillations are observed. Argon was used to substitute N₂ for $\phi=0.7$ and 1.5 to achieve identical adiabatic flame temperature for the three equivalence ratios. Other conditions employed in the computation include $V=100\text{ cm}^3$, $p=1\text{ atm}$, and $T_{in}=T_w=300\text{ K}$.

oxidation in a PSR in a diluted air consisting of 11% O₂ and 89% (N₂+Ar) at three equivalence ratios. Argon was used to substitute a part of the nitrogen to achieve the same adiabatic flame temperature for the three mixtures. Therefore, the difference seen in

Fig. 1 is entirely the consequence of the fuel to oxygen ratio in the unburned mixture. Here, the boundaries separating the reactive solutions from nonreactive solutions are defined by the heat transfer coefficient χ and the residence time τ . Other reactor conditions are volume=100 cm³, pressure=1 atm, and wall and inlet temperatures at 300 K. Above the bell-shaped curves, a reacting solution is not possible because of excessive heat loss at a given mean residence time. The small residence time boundary is determined by the critical time needed for the unburned mixture to undergo reaction. The large residence time boundary represents the condition of sufficient reaction time, but with excessive heat loss through the reactor wall. It is seen that the variation of equivalence ratio does not affect the qualitative feature of the χ - τ boundaries. Quantitatively, however, the lower critical residence time increases markedly with an increase in equivalence ratio.

An exhaustive numerical search within the combustng domain led to observations of oscillatory combustion only on the large critical residence time boundary. Taking the $\phi=1.5$ mixture as an example, Fig. 2 illustrates that inside the combustng domain (point 1), a transient decaying oscillatory solution can be obtained. On the critical residence time boundary, we obtained sustained oscillation, whereas outside the combustng domain, the amplitude of oscillation increases with time, until the system relaxes to the frozen state.

The discussion above suggests that combustion oscillation during methane oxidation in a PSR is governed by the heat release and convective heat loss through the reactor wall. It is thus reasonable to speculate that the sustained oscillation seen in Fig. 2 must occur in a PSR as long as heat release and convective heat loss are of similar magnitudes and are tightly coupled. Considering that it is numerically more robust to obtain a solution for the

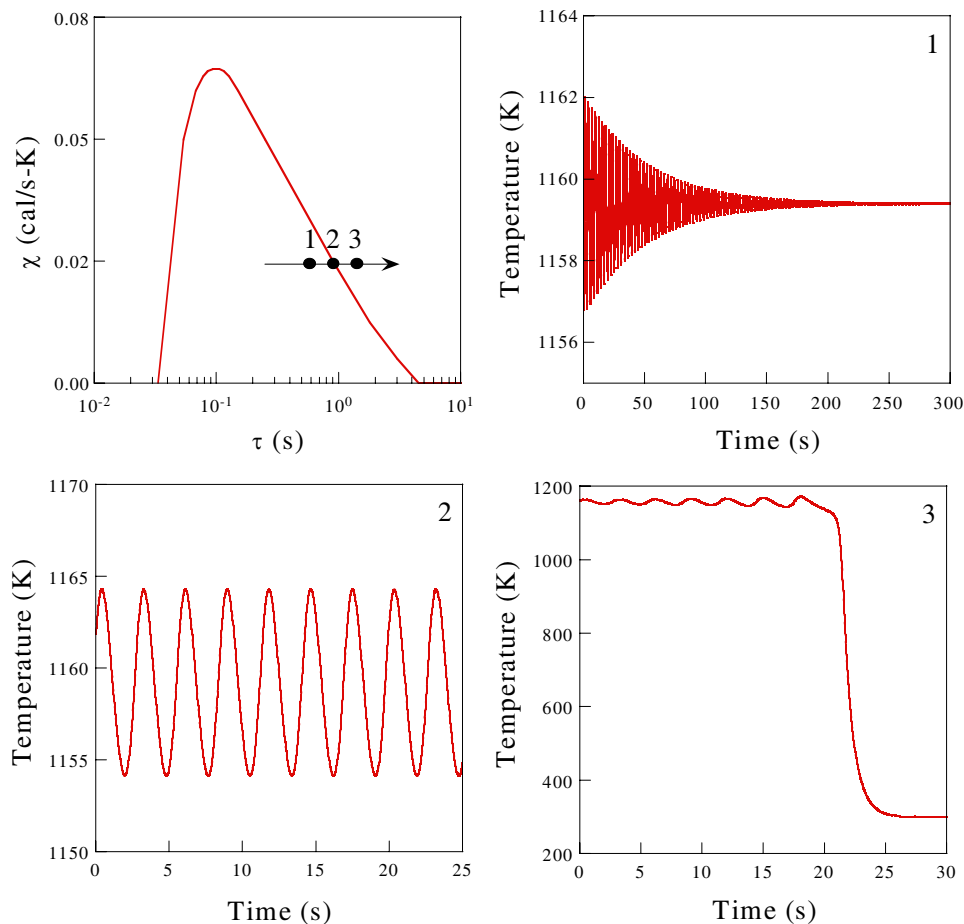


Fig. 2 Oscillatory solutions obtained from numerical simulation for the $\phi=1.5$ mixture. The PSR conditions are identical to those in Fig. 1.

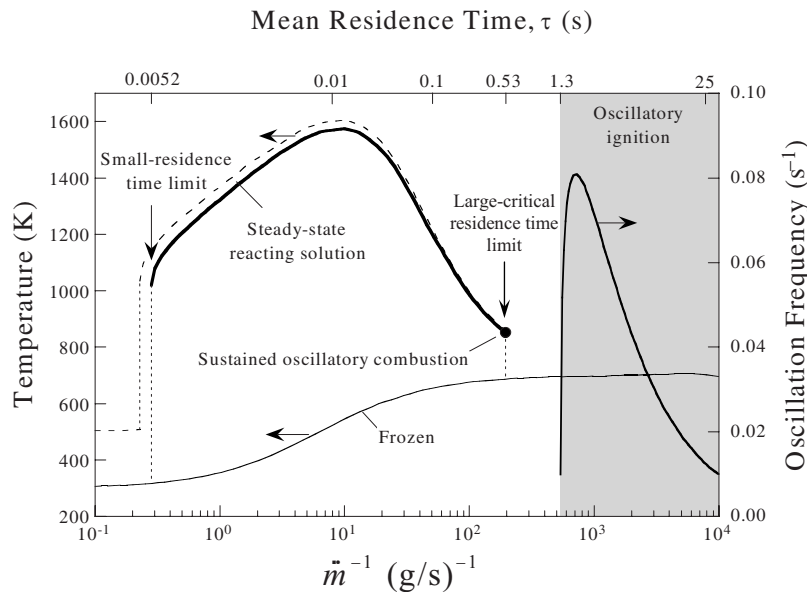


Fig. 3 Variation of the steady-state burning and frozen temperature solutions as a function of reciprocal mass flow rate (\dot{m}^{-1}) and mean residence time (τ), computed for the reaction of $2\text{H}_2 + \text{O}_2$ in a PSR ($T_w = 700$ K, $\chi = 0.093$ cal/K s, and $p = 16$ Torr). The solid lines are obtained with inlet temperature $T_{in} = 300$ K, and dashed lines with $T_{in} = 500$ K. The plot identifies the sustained oscillatory combustion point (filled circle) and the oscillatory ignition region (shaded area). The frequency of oscillatory ignition is also shown as a function of mass flow rate or mean residence time. Values on the residence time axis are those of the steady burning solution and pseudoquenched state during oscillatory ignition.

oxidation of hydrogen as opposed to a hydrocarbon, we decided to examine the oxidation of hydrogen in pure oxygen under the stoichiometric condition. The use of hydrogen oxidation in our analysis also stemmed from the fact that experimental data [15] are available for a model comparison, as will be discussed later.

Figure 3 presents a complete spectrum of temperature solutions computed as a function of mass flow rate or mean residence time for the reaction of $2\text{H}_2 + \text{O}_2$ in a PSR with a wall temperature of 700 K, effective heat transfer coefficient of 0.093 cal/s K, pressure of 16 Torr, reactor volume of 550 cm^3 , and two inlet temperatures of $T_{in} = 500$ K and 700 K. These reactor conditions are similar to those employed in the experiment of Baulch et al. [3]. The reactive solution is represented by a reaction temperature substantially larger than the wall temperature, whereas the frozen solution is characterized by the reactor condition of zero heat release. It is seen that a reactive solution is obtained within a range of residence time. The small residence time limit shown in the figure characterizes a critical kinetic limit below which no reaction is possible. As the residence time increases, the reaction temperature also increases because of a longer reaction time available for the reaction to reach completion. A further increase in the residence time brings down the reaction temperature because of heat loss. Eventually, the heat loss becomes so severe that it quenches the reaction as the residence time further increases. The point immediately before reaction quenches represents the only condition where sustained combustion oscillation is observed. This point will be referred to as the large critical residence time limit. Figure 3 also identifies the region where oscillatory ignition is detected. We shall, however, defer the discussion of this type of oscillation to a later part of this paper.

The results shown in Fig. 4 were obtained by varying the effective heat transfer coefficient and mass flow rate for three different wall temperatures at the critical point shown in Fig. 3. In this figure, a small mass flow rate corresponds to a large residence

time, and the nature of the limiting curves is similar to those of Fig. 1. The variation of wall temperature was found to affect the solution domain only quantitatively, but not qualitatively. Oscilla-

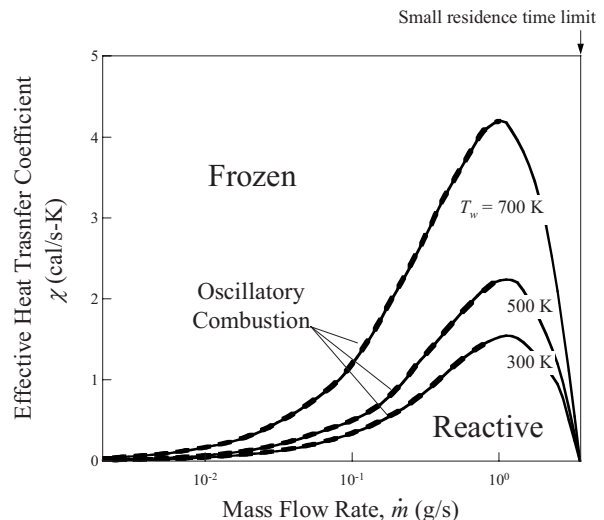


Fig. 4 Numerical characterization of PSR solution types in the parameter space of effective heat transfer coefficient versus mass flow rate, computed for the $2\text{H}_2 + \text{O}_2$ mixture. Reactive solutions are obtained below each dashed curves. The dashed lines indicate the conditions where combustion oscillations are observed. Oscillatory combustion occurs on the boundaries of frozen and reactive solutions. Other PSR conditions are inlet temperature $T_{in} = 300$ K, reactor pressure $p = 16$ Torr, and reactor volume $V = 550$ cm^3 .

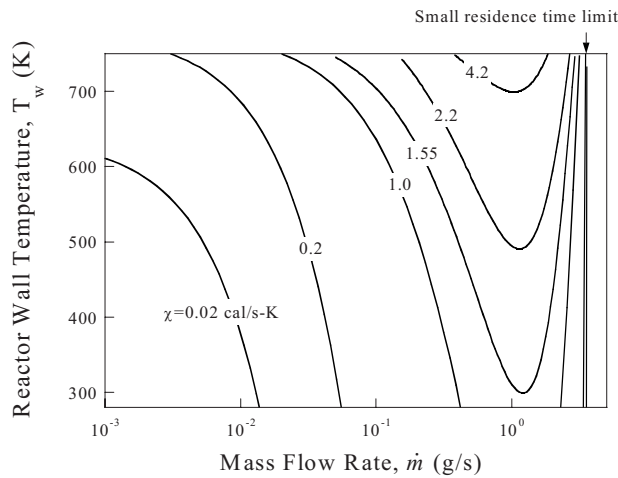


Fig. 5 Numerical characterization of solution types in the parameter space of reactor wall temperature versus mass flow rate, computed for the $2\text{H}_2 + \text{O}_2$ mixture. The mixture is reactive above each curve obtained for a specific value of effective heat transfer coefficient. Other conditions are the same as in Fig. 3.

tion conditions are represented by the dashed lines on the small critical mass flow rate boundaries or, equivalently, the large critical residence time boundaries.

To illustrate the reactive-frozen boundaries for a more complete parameter space given by the variation of T_w - \dot{m} - χ , Fig. 5 shows critical wall temperatures as a function of the mass flow rate obtained for a range of effective heat transfer coefficients from 0.02 cal/s K to 4.2 cal/s K. Again, oscillations were found only on the small critical mass flow rate/large residence time boundaries. Based on this observation as well as on the results obtained for methane combustion, we conclude that oscillatory combustion at the boundary of reactive and frozen solutions at the large critical residence time limit is independent of the combustible mixture.

To verify the conclusion reached by numerical simulations, we performed an analytical eigenvalue analysis. Figure 6 shows a representative case of the analytical solution, featuring a plot of dimensionless temperature, θ , and trace Tr versus dimensionless time t_2 . The results were obtained for parameter values of $A = 10^{12} \text{ s}^{-1}$, $E = 150 \text{ kJ/mol}$, $T_w = T^* = 300 \text{ K}$, $\Delta h^0 = -60 \text{ kJ/mol}$, $V = 1000 \text{ cm}^3$, $c_p^* = 30 \text{ J/mol K}$, $\rho c_p = 0.012 \text{ J/cm}^3 \text{ K}$, and χ

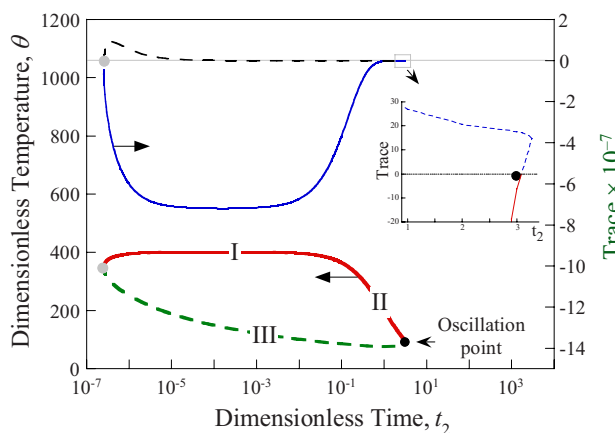


Fig. 6 Analytical solutions of dimensionless temperature (thick line) and trace (thin line) as functions of dimensionless residence time. The inset shows the variation of trace near the oscillatory point.

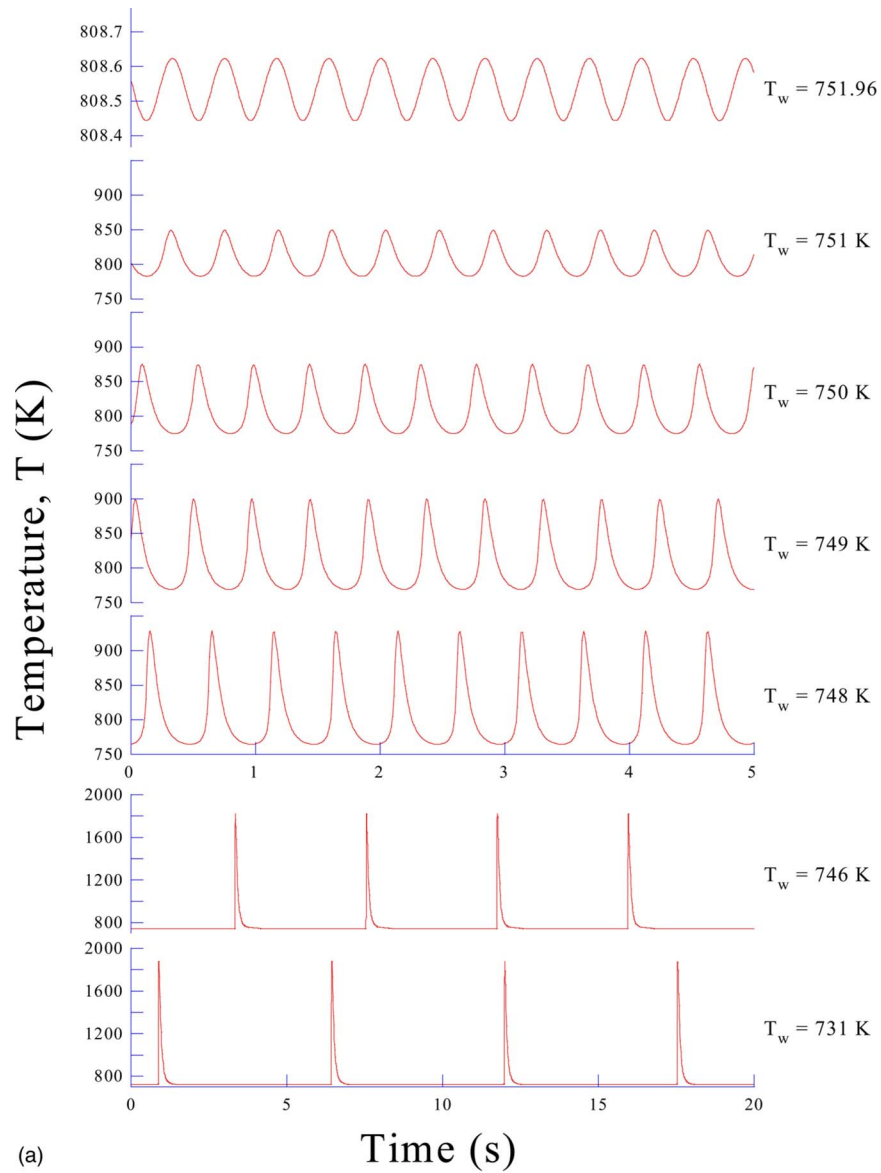
$= 0.25 \text{ cal/s K}$. It is seen that the temperature solution can be divided into three branches. Branch I corresponds to steady burning without a notable influence from the residence time or heat dissipation through the reactor wall. In branch II, temperature decreases as t_2 increases because of a gradual increase in the heat loss rate. Both branch I and II solutions are stable, whereas the solution in branch III is unstable since the trace is positive. The oscillatory solution is obtained where the trace value is equal to zero. Two such points exist, as shown by the filled circles in Fig. 6. The oscillatory solution at the small t_2 value is not important in a practical sense. The oscillatory point at the large t_2 value, however, is numerically observable.

Further analytical tests show that, again, the oscillatory solution is entirely a consequence of coupled heat release, which is governed by exponential reaction kinetics and convective heat loss through the reactor wall. Thus, this combustion oscillation is applicable to all fuels. Here, we found no evidence of detailed reaction kinetics being the cause of combustion oscillation, although this does not rule out the possibility that oscillation may be purely driven by kinetic effects, as in the case of oscillatory ignition to be discussed later.

Now that the parameter space for the oscillations has been established, Fig. 7(a) is presented to demonstrate the specific properties of these oscillations. In this figure, the mass flow rate was fixed at 1 mg/s and the effective heat transfer coefficient was 0.05 cal/s K. Here, representative samples of oscillations are shown at various reactor wall temperatures. The first plot was obtained at $T_w = 751.96 \text{ K}$ and represents a steady small-amplitude ($< 0.2 \text{ K}$) oscillatory combustion behavior. Surprisingly, as T_w was decreased by merely 1 K or more, the amplitude of the oscillation grew enormously from 60 K at $T_w = 751 \text{ K}$ to 150 K at $T_w = 748 \text{ K}$, although the frequency does not vary drastically. This behavior is representative of what will be referred to in this paper as the hybrid of combustion and ignition oscillation. It is characterized by a longer period of low reactivity, followed by a sharp rise and fall in the temperature or the reactivity. The base temperature of this type of oscillation is higher than the wall temperature of the reactor. At just a few kelvins below, the hybrid oscillation disappears, giving way to marked oscillatory ignition at a wall temperature of $\sim 746 \text{ K}$. These oscillations are characterized by base temperatures lower than the wall temperature of the PSR, low frequency, and high amplitude ($\sim 1000 \text{ K}$). The trends displayed in Fig. 7(a) between the amplitude and frequencies of oscillations as a function of vessel wall temperature were also experimentally produced by Baulch et al. [3]. Figure 7(b) shows the results that Baulch et al. observed. Figure 7(b) shows the same trend that can be seen in Fig. 7(a), specifically that the amplitude of oscillation grows with diminishing wall temperature and that the frequency decreases with decreasing wall temperature. In addition, the oscillatory ignition region is clearly shown in Figs. 7(a) and 7(b) for relatively low wall temperatures. Both figures also display the upper and lower limits of extinction.

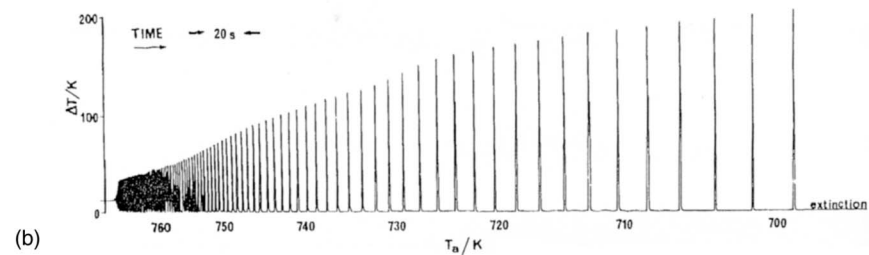
The occurrence of the three oscillatory behaviors strongly depends on reactor conditions and especially on the mass flow rate, as demonstrated in Fig. 8, where the temperature excess, defined by $T - T_w$, is plotted as a function of T_w . The results were obtained for a fixed χ value of 0.093 cal/s K. The transition from the upper $T - T_w$ branch to the lower branch occurs on the large critical residence time boundary of reactive and frozen solutions discussed previously. Thus, it is expected that the oscillations would occur near the point of transition. Here, these points will be referred to as the turning points.

Indeed, at the mass flow rate of 5 mg/s, the combustion oscillation occurs at the turning point on the upper branch ($T_w = 703 \text{ K}$). Now, as seen in the inset of the top panel of Fig. 8, the amplitude of these oscillations is relatively large ($\sim 15 \text{ K}$) when compared to that obtained for $\dot{m} = 1 \text{ mg/s}$ (Fig. 7). At wall temperatures slightly higher than 703 K, all oscillations degenerate to



(a)

COMBUSTION OF HYDROGEN



(b)

Fig. 7 (a) Representative oscillatory solutions obtained for the $2\text{H}_2 + \text{O}_2$ mixture with mass flow rate $m=1$ mg/s and effective heat transfer coefficient $\chi=0.05$ cal/s K. Other conditions are the same as in Fig. 3. (b) The temperature difference between the reactor and vessel wall temperature as a function of the vessel wall temperature (adapted from Baulch et al. [3]).

a steady-state combusting solution. The figure also shows hysteresis in the temperature excess, $T - T_w$, as a function of T_w . On the low branch of temperature excess, neither hybrid nor ignition oscillation was detected.

When the mass flow was decreased to 0.5 mg/s, a variety of

ignition and hybrid oscillation behaviors appeared (see the bottom panel of Fig. 8). Point (i) with $T_w=750$ K represents simple ignition oscillation. At the turning point (b) where $T_w=750.4$ K, however, we encountered ignition oscillation characterized by the Hopf-type bifurcation [28], which is described by a pair of igni-

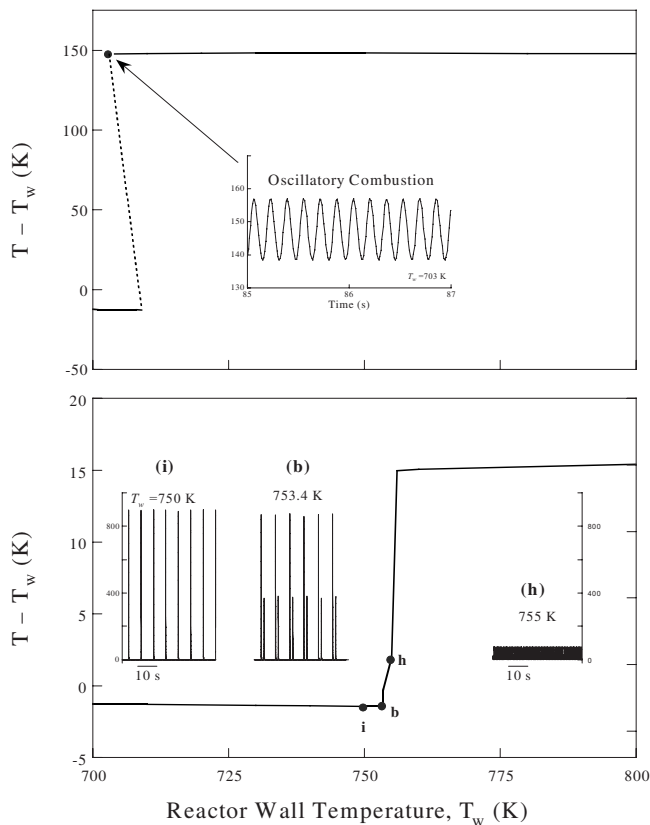


Fig. 8 Temperature excess ($T - T_w$) plotted as a function of wall temperature, computed for the reaction of $2\text{H}_2 + \text{O}_2$ in a PSR with mass flow rate $\dot{m} = 5 \text{ mg/s}$ (top panel) and $\dot{m} = 0.5 \text{ mg/s}$ (bottom panel), both with effective heat transfer coefficient $\chi = 0.093 \text{ cal/s K}$. Other conditions are the same as in Fig. 3. In the bottom panel, points (h), (b), and (i) represent hybrid, Hopf bifurcation, and ignition oscillations, respectively.

tion peaks. The first high amplitude peak is immediately followed by the second peak with a smaller amplitude. For $T_w = 755 \text{ K}$, which is slightly larger than that at the turning point, the reaction enters into the region of hybrid oscillation with base temperature being above T_w . The hybrid oscillations provide a transition from oscillatory combustion to oscillatory ignition consistent with the results demonstrated in Fig. 7(a).

We note that the reactor conditions used to obtain the computational results in the bottom panel of Fig. 8 are nearly identical to those employed in the experiment of Baulch et al. [3]. Our numerical results compare very well to the experimental data (see Fig. 8 of Ref. [3]). Specifically, the qualitative features observed in the experiment from oscillatory ignition to Hopf bifurcation and, finally, to hybrid oscillation are well captured by numerical simulation. The model also reproduces the oscillation frequencies. In addition, the numerical simulation predicts a wall temperature at the turning point being just 4.6 K lower than its experimental counterpart.

Clearly, the nature and cause of oscillatory combustion observed at the extinction turning point and oscillatory ignition at or near the ignition turning point are quite different. As stated earlier, oscillatory combustion is entirely a consequence of the coupling between reaction heat release and heat dissipation through the reactor wall. On the other hand, ignition oscillations observed in the oxidation of hydrogen are the result of kinetic competition between chain branching and chain termination, as concluded by Baulch et al. [3]. Another noted difference is that oscillatory ignition is stable as it relies entirely on the residence time being

longer than the ignition delay of the combustible mixture in the PSR. Combustion oscillation, on the other hand, is inherently unstable. A small perturbation in a reactor operating parameter could either quench the reaction or force oscillations to decay to a steady reacting condition.

The amplitude of combustion and hybrid oscillations is seen to be extremely sensitive to the variation of reactor operating conditions. Thus, while the causes for combustion and ignition oscillations may be identical among different fuels, specific oscillatory properties are dependent on the nature of the combustible mixture as well as the reactor operating conditions. The amplitude/frequency of hydrogen ignition oscillations decreases/increases, respectively, with an increase in the reactor wall temperature, whereas the frequency follows a bell-shaped dependency with respect to the residence time, as shown in Fig. 1.

Conclusions

The present study shows that combustion oscillations occur at the extinction turning point in a PSR. The cause for these oscillations is the coupling of reaction heat release and heat dissipation through the reactor wall. These oscillations are found to be unstable, which perhaps explains why they were never or rarely experimentally observed. In the case of hydrogen oxidation in a PSR, we demonstrated the existence of two other types of oscillations, namely, hybrid oscillation and oscillatory ignition, all of which could exist at or near the ignition turning point. Unlike the unstable combustion oscillations, these ignition oscillations are stable and are driven by detailed chemical kinetic effects.

Acknowledgment

The work is partially sponsored by the Air Force Office of Scientific Research (FA9550-05-1-0010).

References

- [1] Gray, P., Griffiths, J. F., and Scott, S. K., 1989, Proc. R. Soc. London, Ser. A, **394**, pp. 243–258.
- [2] Chinnick, K., Gibson, C., and Griffiths, J. F., 1986, Proc. R. Soc. London, Ser. A, **405**, pp. 117–128.
- [3] Baulch, D. L., Griffiths, J. F., Pappin, A. J., and Sykes, A. F., 1988, Combust. Flame, **73**, pp. 45–54.
- [4] Baulch, D. L. K., Griffiths, J. F., Kordylewski, W., and Richter, R., 1991, Philos. Trans. R. Soc. London, Ser. A, **337**, pp. 199–210.
- [5] Lewis, B., and von Elbe, G., 1987, *Combustion, Flames and Explosions of Gases*, 3rd ed., Academic, Orlando.
- [6] Chinnick, K., Gibson, C., and Griffiths, J. F., 1986, Proc. R. Soc. London, Ser. A, **405**, pp. 129–142.
- [7] Johnson, B. R., Scott, S. K., and Tomlin, A. S., 1991, J. Chem. Soc., Faraday Trans., **87**, pp. 2539–2548.
- [8] Vilyunov, V. N., and Ryabinin, V. K., 1991, Combust., Explos. Shock Waves, **27**, pp. 203–211.
- [9] Kalamatianos, S., and Vlachos, D. G., 1995, Combust. Sci. Technol., **109**, pp. 347–371.
- [10] Olsen, R. J., and Vlachos, D. G., 1999, J. Phys. Chem., **103**, pp. 7990–7999.
- [11] Gummalla, M., and Vlachos, D. G., 2000, Phys. Fluids, **12**, pp. 252–255.
- [12] Baulch, D. L., Griffiths, J. F., and Richter, R., 1991, Chem. Eng. Sci., **46**, pp. 2315–2322.
- [13] Griffiths, J. F., and Inomata, T., 1992, J. Chem. Soc., Faraday Trans., **88**, pp. 3153–3158.
- [14] Skrumeda, L. L., and Ross, J., 1995, J. Phys. Chem., **99**, pp. 12835–12845.
- [15] Glarborg, P., Kee, R. J., Grear, J. F., and Miller, J. A., 1992, “PSR: A Fortran Program for Modeling Well-Stirred Reactors,” Sandia National Laboratories, Sandia Report No. 1.
- [16] Grear, J. F., 1992, “Two Two-Point Problem for Boundary Value Problems,” Sandia National Laboratories, Sandia Report No. SAND91-8230.
- [17] Kim, T. J., Yetter, R. A., and Dryer, F. L., 1994, Sym. (Int.) Combust., [Proc.], **25**, pp. 759–766.
- [18] Davis, S. G., Joshi, A. V., Wang, H., and Egolfopoulos, F., 2004, Proc. Combust. Inst., **30**, pp. 1283–1292.
- [19] Li, J., Zhao, Z. W., Kazakov, A., and Dryer, F. L., 2004, Int. J. Chem. Kinet., **36**, pp. 566–575.
- [20] O’Conaire, M., Curran, H. J., Simmie, J. M., Pitz, W. J., and Westbrook, C. K., 2004, Int. J. Chem. Kinet., **36**, pp. 603–622.
- [21] Saxena, F., and Williams, F., 2005, Combust. Flame, **145**, pp. 316–323.

- [22] Frenklach, M., Wang, H., Goldenberg, M., Smith, G. P., Golden, D. M., Bowman, C. T., Hanson, R. K., Gardiner, W. C., and Lissianski, V., 1995, "GRI-Mech: An Optimized Detailed Chemical Reaction Mechanism for Methane Combustion," GRI Technical Report No. GRI-95/0058.
- [23] Wang, H., and Frenklach, M., 1997, *Combust. Flame*, **110**, pp. 173–221.
- [24] Sun, C. J., Sung, C. J., Wang, H., and Law, C. K., 1996, *Combust. Flame*, **107**, pp. 321–335.
- [25] Gray, P., and Griffiths, J., 1989, *Int. J. Wavelets, Multiresolut. Inf. Process.*, **78**, pp. 29–40.
- [26] William, F. A., 1985, *Combustion Theory*, 2nd ed., Perseus, Reading, MA.
- [27] Strogatz, S. H., 1994, *Nonlinear Dynamics and Chaos*, Addison-Wesley, Reading, MA, pp. 129–140.
- [28] Denbigh, K. G., and Turner, J. C. R., 1984, *Chemical Reactor Theory*, Cambridge University Press, New York, pp. 64–80.

Modeling of Thermophysical Processes in Liquid Ceramic Precursor Droplets Heated by Monochromatic Irradiation

Saptarshi Basu

Baki M. Cetegen¹

Fellow ASME

e-mail: cetegen@engr.uconn.edu

Mechanical Engineering Department,
University of Connecticut,
Storrs, CT 06269-3139

A transient heat and mass transfer model is formulated to describe radiative heating of ceramic precursor droplets in a nonconvective environment. Heating causes vaporization of solvent from the droplet and concentration of the solute within the droplet leading to precipitation of the solute. It is found that the temperatures within the droplets are fairly uniform, but show different spatial profiles depending on the characteristics of solute absorptivity and duration of radiative heating. Incident laser irradiance and wavelength were found to play a significant role in the temperature profiles within droplets due to the absorption characteristics of the solute and the solvent. Lower levels of incident laser irradiation allows longer times for mass diffusion within a droplet leading to a gradual increase of the solute concentration from its center to its surface. Based on an equilibrium homogeneous precipitation hypothesis, it is found that the droplets heated with low laser irradiance tend to form thick precipitate shells as compared to those exposed to higher irradiances and consequently faster rates of vaporization. Large droplets form thin shells through surface precipitation, while small droplets may precipitate into shells of varying thickness depending on the magnitude of irradiance. Comparisons with convective heating in a high temperature plasma indicate that, with proper tuning of the laser irradiance, similar internal temperatures and solute concentration distributions are achievable. These modeling results suggest that different particle morphologies can be obtained from processing of liquid ceramic precursor containing droplets by proper tailoring of radiation parameters (wavelength and irradiance level).

[DOI: 10.1115/1.2908426]

Keywords: laser heating of droplets, TBC, plasma thermal spray process, ceramic precursor

1 Introduction

High temperature processing of liquid droplets containing ceramic precursor salts has been utilized for generation of nanostructured powders [1,2] and thin ceramic coatings [3–5] utilizing high temperature oxyfuel flames and dc-arc plasmas. One of these processes involves injection of liquid ceramic precursor containing droplets in the form of a spray into a dc-arc plasma jet and deposition of ceramic coatings, such as yttria stabilized zirconia (YSZ) thermal barrier coatings (TBCs). In the plasma thermal spray process, precursor droplets undergo a series of thermophysical and chemical transformations, as schematically shown in Fig. 1. These include vaporization of solvent and increase in the concentration of the solute near the droplet surface, precipitation of the solute salts in and around the vaporizing droplets, and other thermophysical processes including precipitate shell drying, rupture, or inflation. Modeling of the thermophysical processes leading to precipitate formation has been reported earlier by Ozturk and Cetegen [6] and Basu and Cetegen [7]. In these studies, heat and mass transport within droplets heated in a flame or plasma environment were modeled to predict the evolution of temperature and solute concentration profiles within droplets. These results were then utilized in the context of a homogeneous precipitation hypothesis to predict precipitate formation. In these studies, the

weakest part of the model is the employed precipitation hypothesis. The available models assume homonucleation of precipitate upon reaching a supersaturation concentration of the solute within the droplet with precipitated regions extending throughout those zones above the equilibrium saturation concentration. However, classical nucleation theories have been found to be inadequate [8–12] for prediction of precipitation onset in liquid systems. Attempts to improve homogeneous precipitation models have included density functional approaches and considerations of heterogeneous precipitation models [10–12].

Existing practical solute precipitation models in binary materials systems assume homonucleation of the precipitate upon reaching a supersaturation concentration regardless of heating rate effects. Such models have been developed for slow heating rates and relatively low temperature processes, such as spray pyrolysis (10^2 – 10^3 K/s). Their validity is questionable at high heating rates experienced in plasmas and oxyfuel flame processes that are of the order of 10^5 – 10^6 K/s. Additionally, as a practical matter, the extremely hostile environment in a dc-arc plasma or an oxyfuel flame is not conducive to interrogating the precipitation process in situ. Because of these difficulties, simpler complementary experimental and computational studies are needed to better characterize the precipitation process in liquid precursor droplets. In this context, it is possible to perform experiments where a single stream of liquid ceramic precursor droplets is heated by infrared irradiation while being simultaneously imaged to observe their precipitation behavior. While differences in radiative and convective heating of droplets can be expected, heating rates and temperature profiles within droplets during radiative heating need to be explored to

¹Corresponding author.

Contributed by the Heat Transfer Division of ASME for publication in the JOURNAL OF HEAT TRANSFER. Manuscript received March 6, 2007; final manuscript received July 26, 2007; published online May 16, 2008. Review conducted by Louis C. Chow.

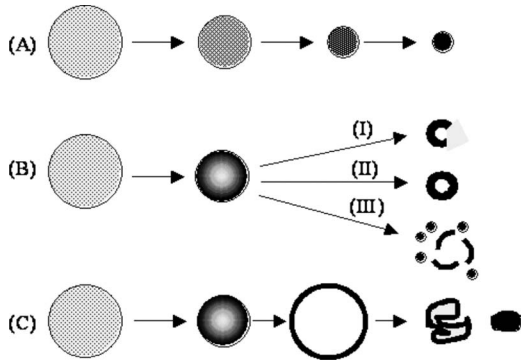


Fig. 1 Solute containing droplet vaporization and precipitation routes: (A) Uniform concentration of solute and volume precipitation leading to solid particles; (B) supersaturation near the surface followed by (I) fragmented shell formation (low permeability through the shell), (II) unfragmented shell formation (high permeability), (III) impermeable shell formation, internal heating, pressurization, and subsequent shell breakup and secondary atomization from the internal liquid; (C) elastic shell formation, inflation, and deflation by solid consolidation.

determine if such experiments can provide useful information and data for the more complicated droplet processes encountered in plasma and oxyfuel flame processing. It is therefore with this motivation that we consider modeling of the radiative heating of precursor droplets in this article.

We consider the spherically symmetric heating of zirconium acetate containing water droplets by a CO₂ laser. Parametric study of the variation of laser power, initial solute loading, and initial droplet size are presented in this article to investigate the experimental conditions to be employed in an accompanying experimental study. The absorption of laser irradiation by a liquid ceramic precursor droplet has also been parametrically varied to understand the role of droplet composition on the thermal and mass transport within the droplet. As a first step, homonuclear precipitation hypothesis was employed to determine precipitation characteristics that will be later compared to the results from the experimental study. Before we describe the developed model, a review of the literature for radiative heating of droplets is in order.

Heating of droplets by radiation has been extensively studied by Drombosky and Sazhin [13] and Lage and Rangel [14]. They mostly considered diesel fuel droplets heated by blackbody radiation. Sazhin et al. [15] calculated the absorption efficiency of these droplets and devised empirical correlations to relate this key parameter to droplet size. However, no effect of droplet composition on the absorption efficiency was considered in their work. Abramzon and Sazhin [16] reported a model of heat and mass transport in a droplet heated by blackbody radiation. In their work, they assumed homogenous absorption with a source function value of unity. Park and Armstrong [17] proposed a two dimensional directional heating model of water droplets by a CO₂ laser source. In this work, they established the fact that above a certain power threshold of the laser, droplets would undergo explosive boiling. Park and Armstrong [17] also reported the effect of non-uniform source function on the thermal history of droplets. They found that, for moderate size droplets, the differences in temperature profiles for directional and spherically symmetric irradiation are negligible for all practical purposes. Park and Armstrong's work [17] did not consider a binary composition droplet and variation of composition and thus the variable absorption characteristics within a droplet.

In the following, we first describe the monochromatic radiative heating model for a bicomponent liquid precursor droplet and subsequently present and discuss the results of this study. The article is concluded by a summary of the key findings.

2 Description of Radiative Droplet Heating Model

The binary (solute+solvent) droplets are assumed to be heated in a spherically symmetric manner by irradiation that is absorbed by the solute and/or solvent within a droplet. As heating continues, the solvent within the droplet vaporizes with simultaneous reduction in droplet size and increase in the solute concentration. The droplets are assumed to be composed of zirconium acetate (solute) dissolved in liquid water (solvent) with initial zirconium acetate mass fractions between 0.2 and 0.5. The radiation is absorbed by the water-based salt solution giving rise to volumetric heat addition within the droplet. The thermal model is based on continuum transport and equilibrium thermodynamics as it is appropriate for radiative heating conditions similar to those occurring in flame and plasma processing of droplets. Nonequilibrium conditions that may prevail under very rapid heating rates such as those encountered in pulsed laser heating of droplets need to be handled differently and the present model is not intended for such rapid heating conditions. Chemical kinetics of the binary solution studied in this article is complicated and not well understood from the evidence available in the literature [1–5], especially at high heating rates. Hence, for simplistic analysis, chemical kinetics is ignored in the model.

The conservation of solute mass and energy for a droplet subjected to radiative heating can be written as

$$\text{Le}_L \bar{r}_s^2 \frac{\partial \bar{\chi}}{\partial \tau} - 0.5 \text{Le}_L \frac{dr_s}{dt} \eta \frac{\partial \bar{\chi}}{\partial \eta} = \frac{1}{\eta^2} \frac{\partial}{\partial \eta} \left(\eta^2 \frac{\partial \bar{\chi}}{\partial \eta} \right) \quad (1)$$

$$\bar{r}_s^2 \frac{\partial \bar{T}}{\partial \tau} - 0.5 \frac{dr_s}{dt} \eta \frac{\partial \bar{T}}{\partial \eta} = \frac{1}{\eta^2} \frac{\partial}{\partial \eta} \left(\eta^2 \frac{\partial \bar{T}}{\partial \eta} \right) + \bar{r}_s^2 \dot{Q}_r(\eta) \quad (2)$$

where the following dimensionless quantities were employed: $\bar{r}_s = r/r_o$, $\tau = \alpha_L t/r_o^2$, $\eta = r/r_s$, $\bar{\chi} = (\chi - \chi_o)/\chi_o$, and $\bar{T} = (T - T_o)/T_o$, where r_o is the initial radius, α_L is the liquid thermal diffusivity, t is the time, r_s is the droplet surface radius, T is the temperature with T_o being the initial value and correspondingly χ being the solute mass fraction with χ_o being its initial value. Le_L is the liquid phase Lewis number. $\dot{Q}_r(\eta)$ or $\dot{Q}_r(r)$ is the radiation absorbed per unit volume at different radii of the droplet.

The initial and boundary conditions can be written as

$$\left\{ \begin{array}{l} \bar{\chi} \\ \bar{T} \end{array} \right\} (\tau=0) = 0 \quad \text{and} \quad \left. \frac{\partial}{\partial \eta} \left\{ \begin{array}{l} \bar{\chi} \\ \bar{T} \end{array} \right\} \right|_{\eta=0} = 0 \quad \text{and} \quad \left. \frac{\partial}{\partial \eta} \left\{ \begin{array}{l} \bar{\chi} \\ \bar{T} \end{array} \right\} \right|_{\eta=1} = \begin{cases} \frac{\dot{m}}{4\pi r_s \rho_L D_s \chi_{s,o}} \\ \frac{\dot{Q}_L}{4\pi r_s k_L T_o} \end{cases} \quad (3)$$

where k_L is the liquid conductivity, ρ_L is the liquid density, D_s is the mass diffusivity of solute in solvent, and \dot{Q}_L is the heat transferred from the droplet surface to the gas phase by conduction and convection. It also includes the latent heat of vaporization of the solvent [6]. The change in the droplet radius is given by [6]

$$\frac{dr_s}{dt} = - \frac{\dot{m}}{4\pi \rho_L r_s^2} \quad (4)$$

where \dot{m} is the mass rate of vaporization, ρ_L is the liquid density, and r_s is the radius of the droplet. The mass vaporization rate \dot{m} is obtained from the vapor and liquid phase analyses. The mass vaporization rate can be calculated from heat and mass transfer rates at the droplet surface as [6]

$$\dot{m} = 2\pi \rho_g D_{va} r_s \text{Sh}^* \ln(1 + B_M) \quad (5)$$

$$\dot{m} = 2\pi \frac{k_g}{C_{p,F}} r_s \text{Nu}^* \ln(1 + B_T) \quad (6)$$

where D_{va} is the diffusivity of the vapor in the ambient air while $C_{p,F}$ is the average heat capacity of the vapor near the droplet surface. B_M and B_T are Spalding's mass and heat transfer numbers. In Eqs. (5) and (6), the Nusselt number Nu^* and Sherwood number Sh^* are based on the nonvaporizing sphere, but modified for the vaporization effects because of the varying film thickness around the droplet [6]. The mass vaporization rate \dot{m} cannot be explicitly calculated since the Spalding heat and mass transfer numbers, B_T and B_M , include the droplet surface temperature and vapor mass fraction that are determined as a part of the coupled liquid phase solution. These equations are supplemented with the Clausius–Clapeyron equation and Raoult's law to determine the mass vaporization rate, surface temperature, and surface vapor concentration, as described in Ref. [6]. The surface temperature and mass vaporization rate are then used as boundary conditions in the solution of the conservation of energy and species equations in the liquid phase.

The heat flux \dot{Q}_L in Eq. (3) is given by

$$\dot{Q}_L = \dot{m} \left[C_{p,v} \frac{(T_\infty - T_{\text{surface}})}{B_T} - h_{lv} \right] \quad (7)$$

The modified Sherwood number and Nusselt number are the same as Ref. [6] except that the Reynolds number is zero because there is no relative motion between the droplet and the ambient.

For spherically symmetric irradiation, radiation absorption per unit volume is given by

$$\dot{Q}_r(r) = 3w(r)r_o^2 \dot{Q}_{\text{rad,total}} / (4\pi r_s^3 k_l T_o) \quad (8)$$

where $w(r)$ is the source function and $\dot{Q}_{\text{rad,total}}$ is the total radiation absorbed by the droplet. The total radiation absorbed by the droplet [15] is given by $\dot{Q}_{\text{rad,total}} = \pi r_s^2 \bar{A} \bar{I}$, where \bar{A} is the average absorption efficiency factor of the droplet fluid and \bar{I} is the average irradiance.

The absorption efficiency factor A of the droplet is given by Abramzon and Sazhin [16]

$$A = \frac{4n}{(n+1)^2} [1 - \exp(-2r_s k_\lambda)] \quad (9)$$

where n is the index of refraction and k_λ is the absorption coefficient of the droplet, which varies at different radial locations depending on the droplet composition. The average absorption efficiency used for calculating \bar{A} is given by

$$\bar{A} = \frac{\int_0^{r_s} \frac{4n}{(n+1)^2} \{1 - \exp[-2r_s k_\lambda(r)]\} 2\pi r dr}{\pi r_s^2} \quad (10)$$

For evaluation of \bar{A} , it is essential to know the variation of k_λ with composition χ as a function of the radius. At each time step, k_λ is calculated as a function of solute concentration (calculated at the previous time step) from the experimental data as a function of radial location. \bar{A} is calculated from Eq. (10) and from the known radial variation of k_λ .

In many of the studies in the literature, the source function is assumed to be homogeneous with a constant value of unity. However, in the current work, the distribution of the absorbed energy $\dot{Q}_{\text{rad,total}}$ at different radial locations within the droplet can be effectively modeled by the source function given by

$$w(r) = \frac{k_\lambda(r)}{k_{\lambda,\text{av}}} \quad (11)$$

where $k_\lambda(r)$ is the absorption coefficient at a particular radial location while $k_{\lambda,\text{av}}$ is the averaged absorption coefficient for the entire droplet at any time instant. It should be noted that both the source function and the averaged absorption coefficient are transient in nature and depend on the solute concentration as well as the instantaneous droplet size. The source function so determined is termed as “var-abs” for variable absorption in Sec. 3, since it incorporates the variable absorptivity within the droplet. In order to assess the effect of constant and variable source functions, simulations were also carried out for the constant source function given by $w(r)=1$. This case is referred to as the constant absorption source function abbreviated as “const-abs” in the rest of this article.

Park and Armstrong [17] used a different representation for $Q_r(r)$ given by

$$\dot{Q}_r(r) = \frac{4\pi I \text{Re}(n)\text{Im}(n)w(r)}{\lambda_0} \quad (12)$$

where $\text{Re}(n)$ and $\text{Im}(n)$ are the real and imaginary parts of the refractive index and λ_0 is the wavelength of the incident laser beam. A sample case is reported later in Sec. 3 for the purpose of comparison with this model for water droplets irradiated by a CO₂ laser. In all the results reported in the next section, variable absorption source function was employed unless otherwise stated.

The average incident irradiance onto a droplet is denoted by symbol \bar{I} and has units of W/m². The incident irradiance \bar{I} is nondimensionalized as

$$I^* = \frac{\bar{I} \tau_{\text{heating}} (4\pi r_o^2)}{h_{lv} \rho_l \left(\frac{4}{3} \pi r_o^3 \right)} \quad (13)$$

where τ_{heating} is the heating time scale and $4\pi r_o^2$ and $4\pi r_o^3/3$ are the surface area and volume of a spherical droplet, respectively. This quantity gives ratio of the total heat incident on a droplet to the latent heat for vaporization of that droplet. Relating the time scale of heating to the thermal diffusivity of the liquid in the droplet as $\tau_{\text{heating}} = r_o^2 / \alpha_l$, it can be written as

$$I^* = \frac{3r_o \bar{I}}{h_{lv} \alpha_l \rho_l} \quad (14)$$

The two levels of irradiance used in the calculations were $\bar{I}=5 \times 10^6$ W/m² and 10^7 W/m². The corresponding values of I^* calculated for a fixed droplet radius of $r_o=10 \mu\text{m}$ were 0.469 and 0.938. These are the values reported throughout the body of this article. It should be noted that the irradiances were fixed at these two values and did not vary with droplet diameter in the reported results with $r_o=10 \mu\text{m}$ being used as a reference value.

3 Results and Discussion

In this section, we first test the described model against the data reported in the literature and then utilize the model to predict the internal droplet temperature and solute concentration profiles for a range of droplet diameters, initial solute concentrations, and irradiances.

Figure 2 shows the comparison of the results from the developed model with those of Park and Armstrong [17] at an average value of $Q_r(r)=3.5 \times 10^{11}$ W/m³ at a wavelength of $10.6 \mu\text{m}$ for a $20 \mu\text{m}$ diameter water droplet. It is seen that the normalized temperature distributions within the droplet compare well in magnitude at three time instants during heating. Early on, the temperature within the droplet is higher near the droplet surface and at later instants the droplet center becomes hotter than the outer edge due to the surface vaporization. The differences near the droplet

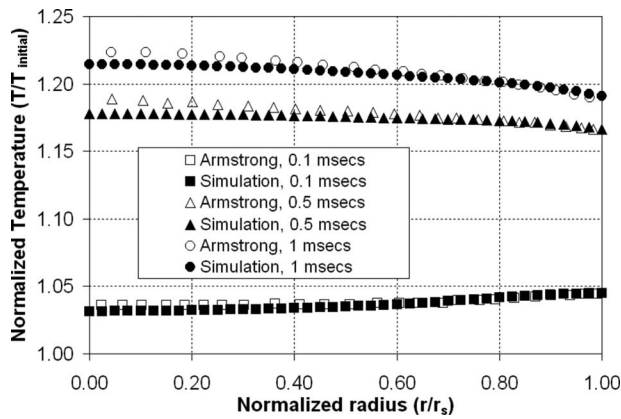


Fig. 2 Comparison of directional laser heating model of Park and Armstrong [17] with the spherically developed symmetric heating model with $Q(r)=3.5 \times 10^{11} \text{ W/m}^3$ for a $20 \mu\text{m}$ water droplet

center are principally due to the directional nature of laser heating, as modeled by Park and Armstrong [17]. This comparison clearly illustrates that, for low power laser heating, the difference between spherically symmetric and nonsymmetric heating is negligible for moderate droplet sizes.

In modeling radiative heating of liquid droplets, the absorption coefficient of the liquid plays an important role in determining the rate of volumetric heat addition. The absorption coefficient in most of the previous studies is assumed to be constant within the droplet, a suitable assumption for pure liquid droplets. However, this assumption is no longer valid for binary droplets containing two miscible fluids (solute and solvent). For example, with vaporization from the droplet surface, solute concentration progressively increases near the droplet surface, creating a radial concentration gradient. If the solute and solvent absorption coefficients are different, this would lead to a radial variation of absorptivity. For the droplet fluids of interest in this study, namely, water (solvent) and zirconium acetate (solute), the absorption coefficients were measured utilizing Fourier transform infrared (FTIR) spectroscopy. Samples of different concentration solutions were prepared and placed in narrow cuvettes and the absorption spectra were measured to determine the absorption coefficients. Figure 3 shows the absorption coefficients of zirconium acetate solutions at two wavelengths of $10.6 \mu\text{m}$ and $6.9 \mu\text{m}$ as a function of zirconium acetate mole fraction in water. The $10.6 \mu\text{m}$ wavelength corresponds to that of the CO_2 laser, which has a high absorptivity

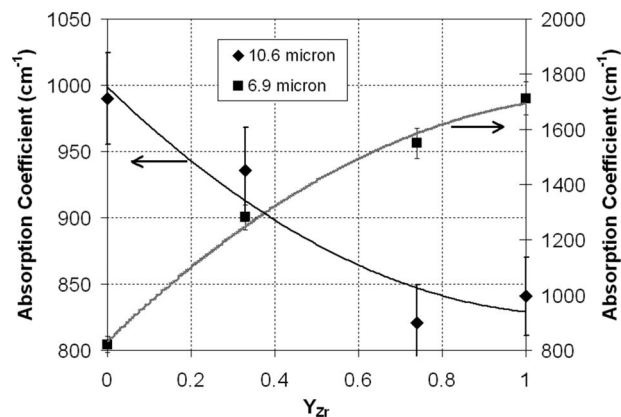


Fig. 3 Variation of absorption coefficient of zirconium acetate solution at 942 cm^{-1} ($10.6 \mu\text{m}$) and at 1446 cm^{-1} ($6.9 \mu\text{m}$) as a function of the mole fraction of zirconium acetate

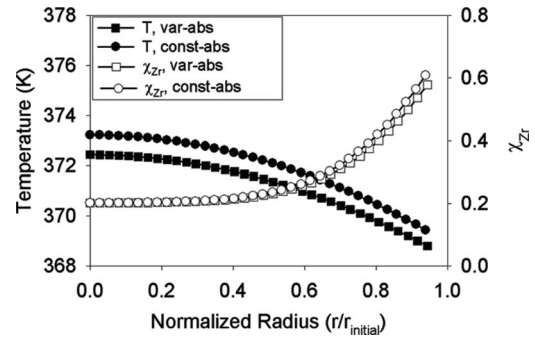


Fig. 4 Effect of source function on the radial distribution of temperature and solute concentration of a $10 \mu\text{m}$ diameter droplet after 0.5 ms of heating at an irradiance of $I^*=0.469$ at $10.6 \mu\text{m}$ wavelength

for water. At $6.9 \mu\text{m}$ wavelength, zirconium acetate shows a significant absorption peak, which is absent for water. The absorption coefficient increases by a factor of 2 from pure water to pure zirconium acetate. The reverse trend is observed for $10.6 \mu\text{m}$ wavelength where the absorption coefficient decreases by only 20% from pure water to pure zirconium acetate.

Two different source functions and absorption coefficient variations were used to study the dependence of thermal and species concentration histories of the droplets. The const-abs refers to a source function value of unity with constant absorption coefficient of $9.9 \times 10^2 \text{ cm}^{-1}$ throughout the droplet. The var-abs refers to a varying absorption coefficient throughout the droplet based on the local concentration of solute in the radial direction. The source function incorporates this variation by the ratio of absorption coefficient at any radius to the average concentration of solute throughout the droplet. The absorption efficiency factor is calculated based on the averaged absorption coefficient at each time step. In both the const-abs and the var-abs cases, there is no geometric effect on the source function. It is seen from Fig. 4 that, after identical time of 0.5 ms , the var-abs and the const-abs cases are similar with respect to the solute concentration and temperature profiles for a laser power of $I^*=0.469$ at a wavelength of $10.6 \mu\text{m}$. The const-abs case shows a slightly higher solute concentration near the surface. The temperature in the const-abs case is also marginally higher than the var-abs case. This is because the surface absorption is hindered by variable absorption due to the abundance of solute near the droplet surface. This leads to less amount of radiation being absorbed near the droplet periphery resulting in a lower temperature rise and lower vaporization rate. Because of the slower rise of the solute concentration near the droplet surface, the droplet surface will reach the supersaturation concentration at longer times. This along with more uniform solute concentrations within the droplet due to the mass diffusion will lead to precipitation of larger regions in the droplet for the case of variable absorption (var-abs). All of the following results presented are based on the variable absorption within droplets.

It is important to compare the solute concentration and temperature profiles for radiative heating at two different wavelengths from the perspective of the different absorption behaviors of the solute and the solvent. While one of the considered wavelengths is the $10.6 \mu\text{m}$ corresponding to CO_2 laser irradiation, the other is $6.9 \mu\text{m}$ corresponding to a strong absorption peak for the solute (zirconium acetate). It is known from Fig. 3 that the absorption coefficient of the droplet at $6.9 \mu\text{m}$ is significantly greater than the absorption coefficient at $10.6 \mu\text{m}$. Higher absorption coefficient leads to higher heat absorption rate for identical laser power leading to enhanced heating. This is clearly seen in Fig. 5(a) by the higher droplet temperatures recorded for the $6.9 \mu\text{m}$ irradiation compared to the $10.6 \mu\text{m}$ for an irradiance level of I^*

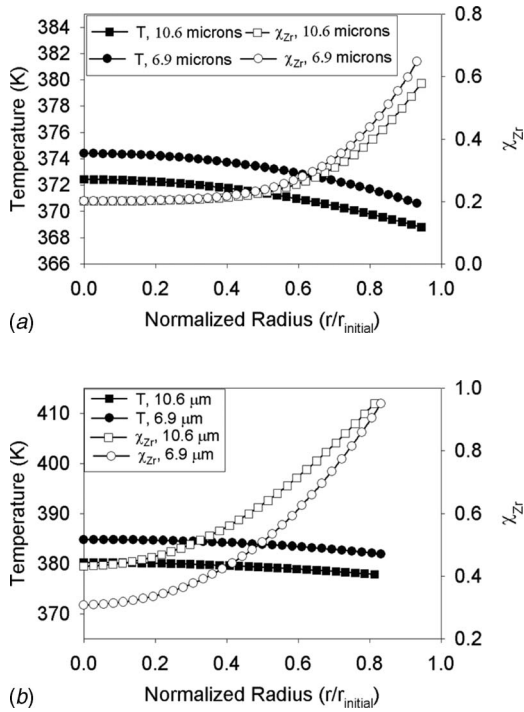


Fig. 5 Comparison of radial distributions of temperature and species concentration of 10 μm diameter droplets at wavelengths of 10.6 μm and 6.9 μm after (a) 0.5 ms and (b) prior to precipitation for $I^* = 0.469$. $\tau_{\text{precipitation}} = 1.2$ ms ($I^* = 0.469$, 10.6 μm) and 0.95 ms ($I^* = 0.469$, 6.9 μm).

$= 0.469$ for a 20 μm droplet after 0.5 ms. Similarly, faster heating rate implies faster evaporation and lower heating time prior to precipitation. This is seen by the higher solute concentration gradients at 6.9 μm radiation. At 10.6 μm , the slope of the solute concentration profile after identical heating period is slightly lower.

Figure 5(b) shows that just prior to precipitation, which is taken as the time it takes for the solute mass fraction to reach a value of 0.95, the droplets heated at 6.9 μm wavelength exhibit higher temperatures compared to the 10.6 μm irradiation case. The droplets irradiated at 10.6 μm , however, show more uniform solute concentration due to the larger time available for the mass diffusion to take place. Thus, the heating at 6.9 μm is accompanied by higher temperature rise and sharper solute concentration variations. It suggests a higher propensity toward surface precipitation with formation of thinner shells as compared to the results for the 10.6 μm irradiation.

The magnitude of laser irradiance incident on a droplet has a direct influence on the heating rate of that droplet. Adjustment of the laser irradiance offers the flexibility to study solute precipitation over a wide range of heating rates. Figure 6(a) shows the distributions of droplet temperature and solute concentration for two levels of irradiation, $I^* = 0.469$ and 0.938 at a wavelength of 10.6 μm for a 10 μm droplet. After 0.5 ms of heating, higher irradiance exhibits a temperature rise to 391 K, which is 20 K higher than the temperature of the droplet irradiated at half of that irradiance. It is seen that doubling the irradiance leads to a greater temperature rise in the same time interval. The species concentration profiles show that higher irradiance leads to precipitation in less than 0.5 ms, assuming that precipitation is triggered at a value of $\chi_{Zr, \text{sup-sat}} = 0.95$. The surface concentration of the droplet heated at low irradiance of $I^* = 0.469$ reaches only a mass fraction level of 0.59. However, at $I^* = 0.469$, the droplets have longer residence time to reach the supersaturation limit at the surface and attain a

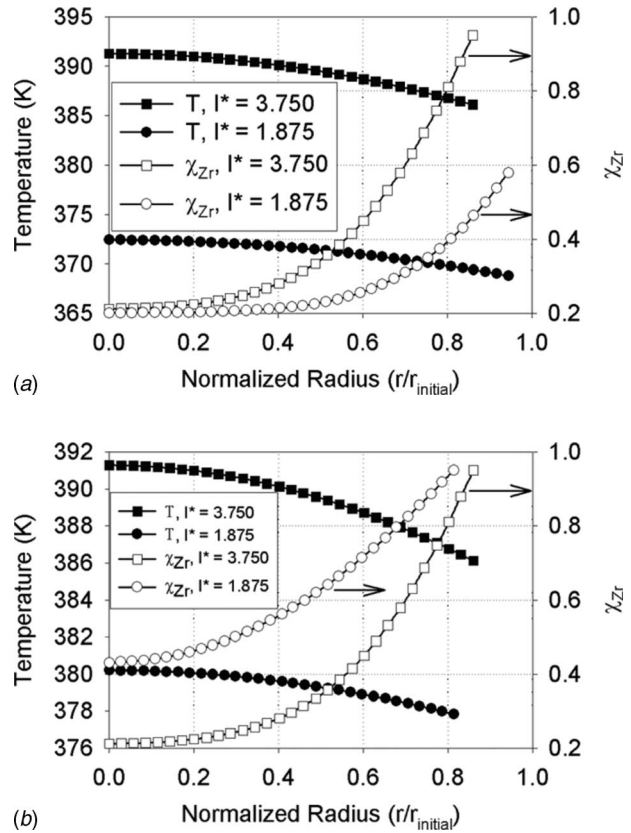


Fig. 6 Effect of irradiance on the radial distribution of temperature and solute concentration of a 10 μm droplet after (a) 0.5 ms of heating and (b) prior to precipitation at 10.6 μm wavelength. $\tau_{\text{precipitation}} = 0.5$ ms ($I^* = 0.938$) and 1.2 ms ($I^* = 0.469$).

more uniform solute concentration distribution, as shown in Fig. 6(b), where the simulation was continued until supersaturation limit was reached at the droplet surface. The center of the droplet for $I^* = 0.938$ practically remains unaffected at the initial solute mass fraction value of 0.2 as the droplet surface reaches the supersaturation concentration.

One of the motivations for this study was to investigate the similarity between the radiative and the convective heating of droplets to determine if the solute precipitation characteristics can be studied for radiative heating and be extrapolated to the convective heating in a plasma. For 10 μm droplets, it is observed in Fig. 7 that the solute concentration profiles for plasma and laser heating after 1.2 ms of heating time are almost identical. For the plasma heating, droplets were assumed to be axially injected into a high temperature plasma jet with an exit temperature of 10^4 K, as reported earlier [6,7]. In this case, the droplets experience rapid convective heating due to the large velocity difference between the droplets and the plasma gases. The temperature profile in the case of radiative heating is different than the plasma heating due to the volumetric nature of radiative heating. However, it is observed that the maximum temperature differences between the two heating modes are within 5 K and this suggests that, with careful choice of irradiance levels, almost identical temperature and solute concentration profiles can be attained.

Figure 8 shows the solute mass fraction and temperature distributions for a 5 μm diameter droplet at two different levels of irradiation. It is found that the solute concentrations rise to higher values in small droplets and tend to exhibit volumetric precipitation as found in the plasma and oxyfuel flame simulations. At low irradiances, slower heating leads to higher mass diffusion and

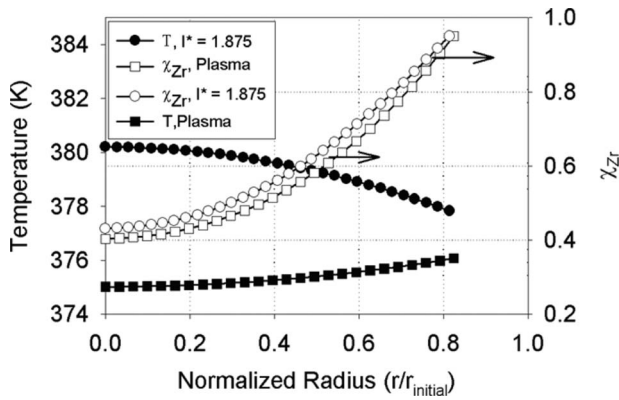


Fig. 7 Comparison of radial distributions of temperature and species concentration of 10 μm droplets prior to precipitation plasma heating and radiative heating at 1.2 ms

more uniform solute concentration distributions within the droplet. For small droplets, mass diffusion length scales is comparable to the droplet radius and as such the solute concentration increases relatively uniformly throughout the droplet. The temperature profiles show similar shapes but exhibit a temperature difference of about 10 K. This is expected because of the twofold increase in volumetric heat addition.

The results presented so far suggest that small droplets (5 μm diameter or smaller) exhibit more uniform increase of solute concentration and temperature within droplets regardless of the irradiation levels. However, for comparatively larger droplets, such as 10 μm diameter, the lower heating rate leads to delayed precipitation time but a more uniform solute concentration profile. This suggests that the precipitate morphology will depend not only on the heating rate but also on the droplet size.

For larger droplets around 20 μm in diameter, the solute concentration rises in a thin region near the droplet surface, as shown in Fig. 9(a). The rise is much greater for the higher irradiance and this type of concentration profile is expected to lead to a thin precipitate shell formation. For an irradiance of 0.938, the droplet would precipitate after 0.3 ms based on homogeneous precipitation hypothesis. For these droplets, a temperature difference of 40 K is found between the low and high irradiances after 0.3 ms of heating. Figure 9(b) compares the high and the low power radiative heating just prior to precipitation. It is seen that the higher power induces 8–10 K temperature increase in comparison to the low power, but the solute concentration profiles look very similar for both the cases, particularly when compared with those

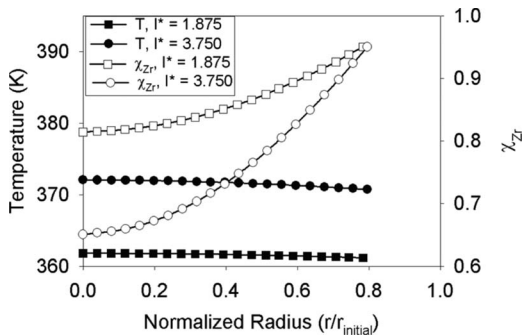


Fig. 8 Radial distribution of temperature and species concentration of 5 μm droplets prior to precipitation for variable absorption coefficient for two different irradiances of $I^*=0.469$ and 0.938. $\tau_{\text{precipitation}}=0.56$ ms ($I^*=0.938$) and 1.23 ms ($I^*=0.469$).

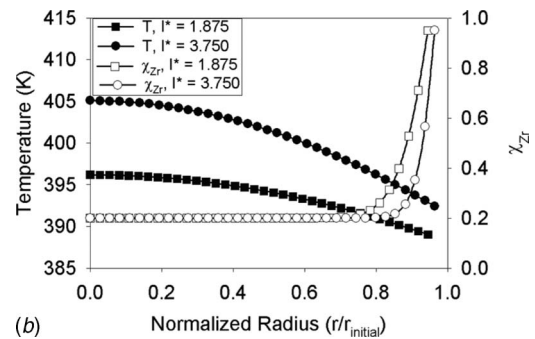
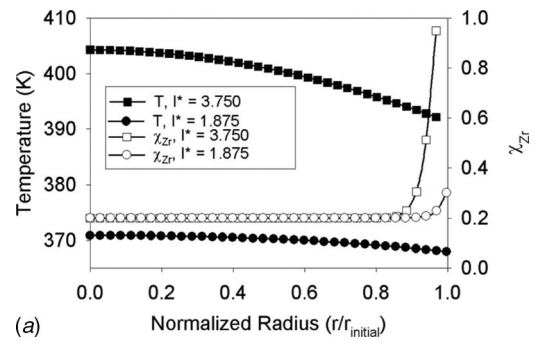


Fig. 9 Radial distribution of temperature and species concentration of 20 μm droplets after (a) 0.4 ms and (b) 1.1 ms prior to precipitation for variable absorption coefficient for irradiances of $I^*=0.469$ and 0.938. $\tau_{\text{precipitation}}=0.43$ ms ($I^*=0.938$) and 1.1 ms ($I^*=0.469$).

for a 10 μm diameter droplet shown in Fig. 6. Figure 9 shows that, for large droplets, the time needed for solute to diffuse greater distances into the droplet center is much larger than the time for the surface concentration to reach supersaturation limit. Therefore, a decrease of heating rate by a factor of 2 does not still allow sufficient time for the solute to diffuse any appreciable distance into the droplet core at the time of precipitation.

Another important parameter in droplet heating is the influence of the initial solute concentration level on the evolution of concentration profile during heating. Figure 10 shows the results for a 10 μm droplet heated at $I^*=0.469$ for three different initial solute mass fractions of 0.2, 0.4, and 0.5. It is readily seen that all the solute concentration profiles are similar except that they are offset from one another due to the difference in initial solute mass fraction. Temperature profiles are very similar with maximum deviations of only 5 K. These results indicate that the initial solute concentration level influences the onset of precipitation by pre-

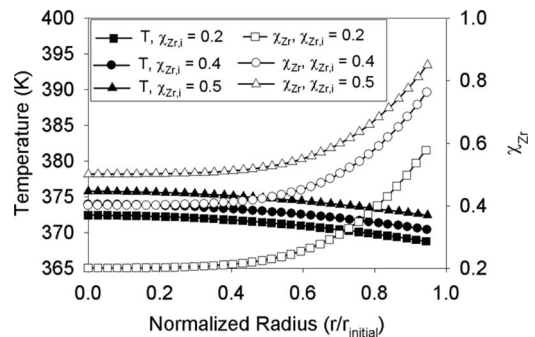


Fig. 10 Radial distributions of temperature and species concentration of 10 μm diameter droplet for different initial solute levels at irradiance of $I^*=0.469$ after 0.5 ms

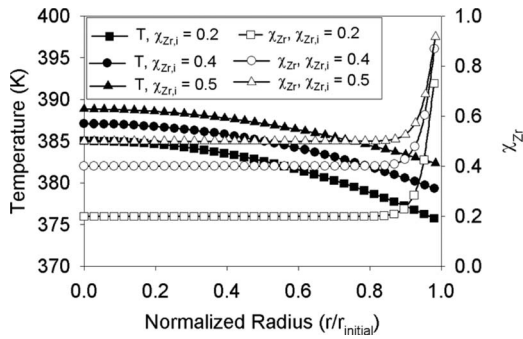


Fig. 11 Radial distributions of temperature and species concentration of 20 μm diameter droplet for different initial solute levels at an irradiance of $I^* = 0.469$ after 0.5 ms

dominantly offsetting the solute concentrations throughout the droplet in proportion to their initial values. Similar results are found for 20 μm droplets in Fig. 11 for different initial solute loadings. The temperatures for all the solute loading levels exhibit a difference of only 7 K. The solute concentration variation is confined to a surface layer of about 10% of the radius for this larger droplet size. It is anticipated that the thickness of the precipitate shell will increase with increasing initial solute mass fraction.

A 100 μm diameter droplet was studied to determine the behavior at large diameter limit. It was found that precipitation in such a droplet is extremely hard to achieve at these heating rates used, as shown in Fig. 12. The temperature at the droplet center rises to 430 K for irradiance level of $I^* = 0.938$ due to the higher volumetric absorption of radiation by the droplet. The solute concentration shows a sharp rise very near the surface with the droplet core remaining at the initial solute level. It is expected that prolonged heating of the 100 μm droplets may lead to temperatures in the droplet core exceeding the superheat limit of 600 K. This phenomenon will lead to bubble formation and explosive breakup of the droplet. Precipitation in such droplets is predicted to only happen for low levels of irradiation with prolonged heating time.

The normalized shell thickness for all values of initial solute loading shows a monotonic decay with increasing droplet radius, as shown in Fig. 13. In fact, for droplets of size greater than 20 μm , all the initial solute loadings are likely to produce similar shell thicknesses relative to the droplet diameter. Figure 14 shows the effect of irradiance on the predicted shell thickness. It is seen that decreasing the laser power facilitates formation of thicker shells for moderate droplet sizes.

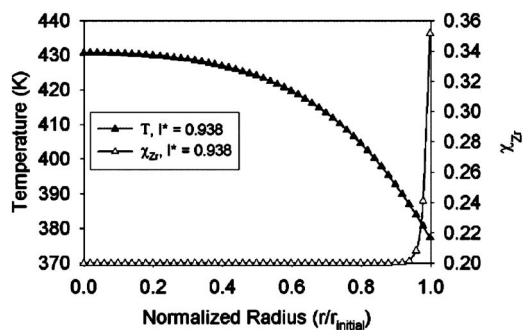


Fig. 12 Radial distributions of temperature and species concentration of 100 μm diameter droplet after 0.125 ms

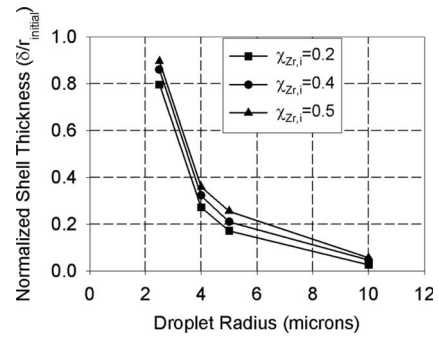


Fig. 13 Variation of shell thicknesses for different droplet diameters and initial solute concentrations for an irradiance of $I^* = 0.938$

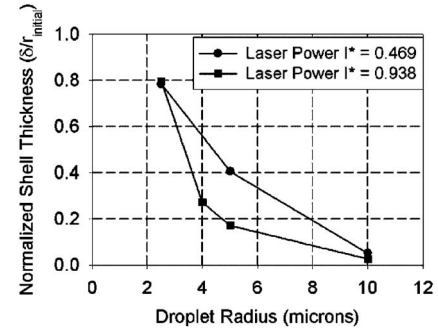


Fig. 14 Variation of shell thicknesses for different droplet diameters for two values of irradiance, for $\chi_{Zr,i} = 0.2$

4 Conclusions

A computational study is presented for the radiative heating of individual precursor droplets and prediction of their precipitation behavior. In spite of the differences in radiative and convective heating of droplets, heating rates and temperature profiles within the droplet during radiative heating have sufficient similarities to those convectively heated droplets in plasmas and flames. This study hence serves as a proof-of-concept for experiments to study the precipitation kinetics and morphology of different size droplets with different solute levels under rapid heating conditions. The work presented in this article highlights the fact that with careful choice of radiation intensity, similar time scales of heating are achievable with similar solute concentration profiles within droplets. It is found that lower irradiances combined with longer heating times promote formation of thicker precipitate shells. Small droplets less than 5 μm tend to volumetrically precipitate even for high irradiances, while the larger droplets are expected to undergo surface precipitation. Droplets around 10 μm in size show propensity to precipitate into shell sizes of varying thicknesses that is dependent on the irradiation level. Droplets of 20 μm in size form thin shells and do not exhibit much dependence on irradiance levels.

Acknowledgment

The work presented in this article was funded by the Office of Naval Research Grant No. N00014-02-1-0171, under the direction of Dr. Larry Kabakoff.

Nomenclature

- A = absorption efficiency factor
- \bar{A} = average absorption efficiency factor
- B_M = Spalding mass transfer number, $B_M = (\chi_{v,\infty} - \chi_{v,s}) / (1 - \chi_{v,s})$

B_T = Spalding heat transfer number, $B_T = C_{p,v}(T_\infty - T_s)/(h_{lv} - Q_L/\dot{m})$
 C_p = specific heat
 D_s = mass diffusivity of zirconium acetate into water
 D_{va} = mass diffusivity of solvent into ambient
 h_{lv} = latent heat of vaporization for liquid
 \bar{I} = average intensity of radiation (W/m^2)
 I^* = nondimensional intensity of radiation
 $\text{Im}(n)$ = imaginary part of refractive index
 k = thermal conductivity
 k_λ = absorption coefficient of the droplet
 $k_{\lambda,av}$ = average absorption coefficient for the entire droplet at any time instant
 Le = Lewis number, $Le = \alpha/D_s$
 \dot{m} = mass flow rate at the droplet surface due to vaporization
 n = index of refraction
 Nu^* = Nusselt number corrected for surface blowing
 Pr = Prandtl number, $\text{Pr} = \nu/\alpha$
 $\dot{Q}_r(r)$ = radiative heat absorbed in the droplet
 \dot{Q}_L = heat transfer from the droplet surface due to vaporization (no irradiance)
 $\dot{Q}_{rad,total}$ = total absorption of radiation per unit volume
 r_s = instantaneous outer radius of the droplet
 \bar{r}_s = nondimensional radius of the droplet, $\bar{r}_s = r_s/r_0$
 $\text{Re}(n)$ = real part of refractive index
 Sh^* = Sherwood number corrected for surface blowing
 t = time
 T = temperature
 \bar{T} = nondimensional temperature, $\bar{T} = (T - T_0)/T_0$
 χ = mass fraction in the before precipitation regime
 χ_s = mass fraction in the liquid core after precipitation regime
 $\bar{\chi}$ = nondimensional mass fraction, $\bar{\chi} = (\chi - \chi_0)/\chi_0$
 $w(r)$ = source function
 η = nondimensional radial coordinate, $\eta = r/r_s$
 ν = kinematic viscosity
 ρ = density
 τ = nondimensional time, $\tau = \alpha_L t / r_0^2$

Subscripts

0 = initial value
 l = liquid phase
 v = vapor phase
 ∞ = far field

References

- [1] Masters, K., 1985, *Spray Drying Handbook*, 4th ed., Wiley, New York.
- [2] Pawlowski, L., *The Science and Engineering of Thermal Spray Coatings*, Wiley, Chichester.
- [3] Padture, N. P., Schlichting, K. W., Bhatia, T., Ozturk, A., Cetegen, B. M., Jordan, E. H., and Gell, M., 2001, "Towards Durable Thermal Barrier Coatings With Novel Microstructures Deposited by Solution-Precursor Plasma Spray," *Acta Mater.*, **49**, pp. 2251–2257.
- [4] Jordan, E. H., Xie, L., Ma, X., Gell, M., Padture, N. P., Cetegen, B. M., Ozturk, A., Roth, J., Xiao, T. D., and Bryant, P. E., 2004, "Superior Thermal Barrier Coatings Using Solution Precursor Plasma Spray," *J. Therm. Spray Technol.*, **13**(1), pp. 57–65.
- [5] Bhatia, T., Ozturk, A., Xie, L., Jordan, E. H., Cetegen, B. M., Gell, M., Ma, X., and Padture, N. P., 2002, "Mechanisms of Ceramic Coating Deposition in Solution-Precursor Plasma Spray," *J. Mater. Res.*, **17**(9), pp. 2363–2372.
- [6] Ozturk, A., and Cetegen, B. M., 2004, "Modeling of Plasma Assisted Formation of Ytria Stabilized Zirconia From Liquid Precursors," *Mater. Sci. Eng., A*, **384**, pp. 331–351.
- [7] Basu, S., and Cetegen, B. M., 2007, "Modeling of Thermo-Physical Processes in Liquid Ceramic Precursor Droplets Injected into a Plasma Jet," *Int. J. Heat Mass Transfer*, **50**(17–18), pp. 3278–3290.
- [8] Cohen, M. D., Flagan, R. C., and Seinfeld, J. H., 1987, "Studies of Concentrated Electrolyte Solutions Using the Electrodynamic Balance: Solution Nucleation," *J. Phys. Chem.*, **91**, pp. 4583–4590.
- [9] Leong, K. H., 1987, "Morphological Control of Particles Generated From the Evaporation of Solution Droplets: Theoretical Considerations," *J. Aerosol Sci.*, **18**(5), pp. 511–524.
- [10] Borra, J. P., 2006, "Topical Review: Nucleation and Aerosol Processing in Atmospheric Pressure Electrical Discharges: Powders Production, Coatings and Filtration," *J. Phys. D*, **39**, pp. R19–R54.
- [11] Oxtoby, D. W., 1992, "Homogeneous Nucleation: Theory and Experiment," *J. Phys.: Condens. Matter*, **4**, pp. 7627–7650.
- [12] Palermo, J. A., 1968, "Crystallization," *Ind. Eng. Chem.*, **60**(4), pp. 65–93.
- [13] Dombrovsky, L., and Sazhin, S., 2003, "Absorption of Thermal Radiation in a Semi-Transparent Spherical Droplet: A Simplified Model," *Int. J. Heat Fluid Flow*, **24**, pp. 919–927.
- [14] Lage, P. L. C., and Rangel, R. H., 1993, "Single Droplet Vaporization Including Thermal Radiation Absorption," *J. Thermophys. Heat Transfer*, **7**(3), pp. 502–509.
- [15] Sazhin, S. S., Abdelghaffar, W. A., Sazhina, E. M., Mikhalovsky, S. V., Meikle, S. T., and Bai, C., 2004, "Radiative Heating of Semi Transparent Diesel Fuel Droplets," *ASME J. Heat Transfer*, **126**, pp. 105–109.
- [16] Abramzon, B., and Sazhin, S. S., 2005, "Droplet Vaporization Model in the Presence of Thermal Radiation," *Int. J. Heat Mass Transfer*, **48**, pp. 1868–1873.
- [17] Park, B. H., and Armstrong, R. L., 1989, "Laser Droplet Heating: Fast and Slow Heating Regimes," *Appl. Opt.*, **28**(17), pp. 3671–3680.

Laminar Filmwise Condensation on Horizontal Disk Embedded in Porous Medium With Suction at Wall

Tong-Bou Chang

Department of Mechanical Engineering,
Southern Taiwan University,
Tainan County, Taiwan 710
e-mail: tbchang@mail.stut.edu.tw

This study performs a theoretical investigation into the problem of two-dimensional steady filmwise condensation flow on a horizontal disk embedded in a porous medium layer with suction at the disk surface. The analysis considers the case of a water-vapor system and is based on typical values of the relevant dimensional and dimensionless parameters. Due to the effects of capillary forces, a two-phase zone is formed between the liquid film and the vapor zone. The minimum mechanical energy concept is employed to establish the boundary condition at the edge of the horizontal disk and the Runge–Kutta shooting method is used to solve the second-order nonlinear ordinary differential equation of the liquid film. It is found that the capillary force and wall suction effects have a significant influence on the heat transfer performance. Specifically, the results show that the dimensionless heat transfer coefficient depend on the Darcy number Da , the Jacob number Ja , the effective Rayleigh number Ra_e , the effective Prandtl number Pr_e , the suction parameter Sw , and the capillary parameter Bo_c . [DOI: 10.1115/1.2909075]

Keywords: wall suction, filmwise condensation, porous medium

Introduction

The problem of laminar film condensation on a vertical or nearly vertical wall was first analyzed by Nusselt [1] under the assumptions that the condensate film was thin, the convective and inertial effects were negligible, and the temperature profile within the liquid film was linear. Following the publication of Nusselt's original analysis in 1916, many researchers, including Rohsenow [2], Sparrow and Gregg [3], Chen [4], Koh [5], and Merte [6], improved the accuracy of the laminar film condensation solutions by removing the original overly restrictive assumptions. Recently, the effects of condensation parameters, such as surface roughness and condensation pressure, were investigated by Mohamed [7] and Jiang et al. [8], respectively. The problem of condensation on the upper surface of a horizontal plate was first studied by Nimmo and Leppert [9,10]. However, in their studies, the thickness of the film condensate layer at the plate edge was either assigned an assumed value or was specified by a particular boundary condition. Chiou and Chang [11] considered laminar film condensation on a horizontal disk and employed the minimum mechanical energy concept [12] to establish the boundary condition at the disk edge. For the cases with suction at the wall, Jain and Bankoff [13] solved the problem of condensation along a vertical tube with a uniform suction velocity. Similarly, Yang [14] investigated the effects of uniform suction on laminar film condensation along a vertical porous wall. Yang and Chen [15] and Chiou and Chang [16] examined the influence of a uniform wall suction velocity on laminar film condensation on a finite-size horizontal plate and horizontal disk, respectively. The results of Refs. [13–16] indicated that wall suction effects significantly enhance the condensation heat transfer performance.

The problem of heat and mass transfer in a porous medium has received extensive attention due to its wide range of potential applications. For example, condensation in a porous medium finds

many important applications in the fields of waste disposal, heat pipe design, geothermal energy utilization, and thermally enhanced oil recovery processes. Cheng et al. [17,18] used the Darcy model to analyze the problem of a downward condensate flow along a cool inclined surface in a porous medium. Liu et al. [19] supplied a similarity solution for film condensation in a porous medium with a lateral mass flux. Char et al. [20] investigated the problem of a mixed convection condensate flowing along a vertical wall in a porous medium. Recently, Wang et al. [21] investigated film condensation on a horizontal wavy plate in a porous medium. The results showed that the condensation heat transfer coefficient was enhanced at higher values of the wave number and amplitude of the wavy surface.

In general, the theoretical investigations described above neglected the effects of capillary forces in the porous medium. However, in practical problems concerning condensation in a porous medium, the effective pore radii are very small. Consequently, the capillary forces have a significant influence on the heat transfer performance, and must therefore be taken into consideration. Udell [22,23] performed a series of theoretical and experimental investigations of a sand-water system to examine the effect of capillary forces on heat transfer in porous media saturated with both vapor and liquid phases. Majumdar and Tien [24] studied the effect of capillary forces on film condensation on a vertical wall. Bridge et al. [25] investigated one-dimensional steady-state condensation heat and mass transfer in a two-phase zone by adding an energy equation to the system considered by Udell [22]. More recently, Chang [26,27] investigated the effects of surface tension on laminar film condensation on the different horizontal surfaces embedded in a porous medium.

Chiou and Chang [11] and Yang et al. [28] demonstrated that the heat transfer performance of a horizontal disk is better than that of a horizontal plate because the condensed liquid spreads over a wider area and therefore has a reduced thickness. Furthermore, as stated above, previous studies [13–16] reported that wall suction effects significantly enhance the condensation heat transfer performance. Accordingly, the present study investigates laminar film condensation on a horizontal disk embedded in a porous

Contributed by the Heat Transfer Division of ASME for publication in the JOURNAL OF HEAT TRANSFER. Manuscript received March 29, 2007; final manuscript received September 26, 2007; published online May 19, 2008. Review conducted by S. A. Sherif.

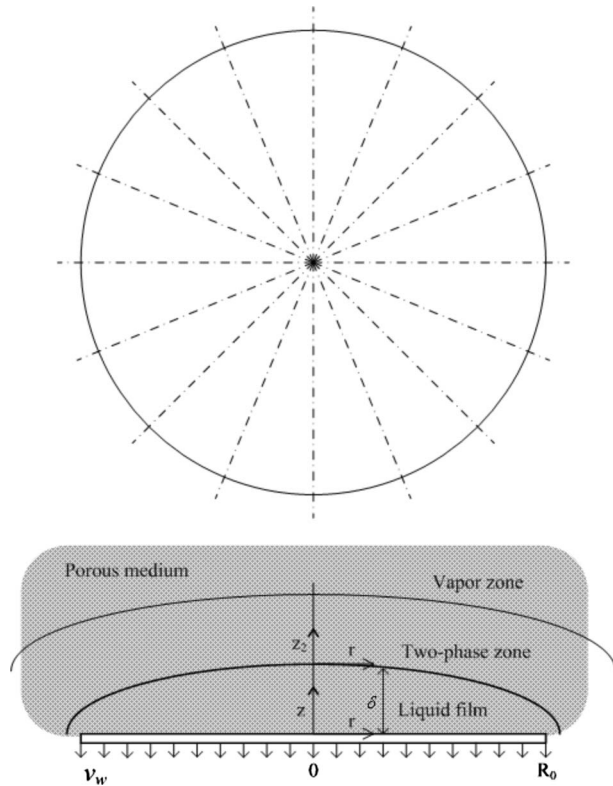


Fig. 1 Condensate film flow on horizontal disk in porous medium with suction at wall

medium with suction at the wall. To examine the effects of the capillary forces induced by the porous medium, this study employs the principles of capillary pressure and two-phase zones in the liquid flow analysis. In addition, the minimum mechanical energy concept is employed to establish the film thickness at the disk edge. Taking the case of a water-vapor system for illustration purposes, the dimensionless heat transfer coefficient is then solved for various values of the Darcy number Da , Jacob number Ja , effective Rayleigh number Ra_e , effective Prandtl number Pr_e , capillary parameter Bo_c , and suction parameter Sw .

Analysis

This study considers a horizontal disk with wall temperature T_w embedded in a porous medium filled with a dry vapor, as shown in Fig. 1. The vapor is assumed to be pure and to be at a uniform temperature T_{sat} . If the wall temperature T_w is lower than the saturation temperature T_{sat} , and the liquid ideally wets the disk surface, a film of condensate will be formed on the surface of the disk. Moreover, capillary forces result in the formation of a two-phase zone between the condensate film and the pure vapor zone. To enhance the condensation heat transfer performance, a uniform suction is applied to the disk surface to remove the condensate at a constant suction velocity v_w .

Under steady-state conditions, the thickness of the liquid film boundary layer will be greatest at the center of the disk and will gradually taper toward its minimum thickness at the disk edge. The current analysis makes the following assumptions:

1. The condensate flow is steady and laminar.
2. The inertia within the film is negligible (i.e., a creeping film flow is assumed).
3. The wall temperature and vapor temperature are uniform and remain constant.
4. The kinetic energy of the film flow is negligible.

5. The liquid film in the porous medium is governed by Darcy's law.
6. The properties of the porous medium, dry vapor, and condensate remain constant.

Under these assumptions, the governing equations of the liquid film with boundary layer simplifications can be expressed as follows.

In continuity equation,

$$\frac{1}{r} \frac{\partial(ru)}{\partial r} + \frac{\partial v}{\partial z} = 0 \quad (1)$$

where u and v are the Darcian velocity components in the r - and z -directions (see Fig. 1), respectively.

Based on the Darcy model, the momentum equation along the r -direction is given by

$$0 = -\frac{\partial P}{\partial r} - \frac{\mu_e}{K} u \quad (2)$$

where P is the static pressure within the liquid film, and μ_e and K are the effective dynamic viscosity and the intrinsic permeability of the porous medium saturated with liquid, respectively.

Meanwhile, the momentum equation along the z -direction has the form

$$0 = -\frac{\partial P}{\partial z} - \rho g \quad (3)$$

The energy equation is given by

$$\frac{u}{r} \frac{\partial(rT)}{\partial r} + v \frac{\partial T}{\partial z} = \alpha_e \frac{\partial^2 T}{\partial z^2} \quad (4)$$

where α_e is the effective thermal diffusivity of the porous medium saturated with liquid.

Integrating Eq. (3), and imposing the boundary condition $P = P_{sat}$ at $z = \delta$, the static pressure equation in the liquid film is shown to be

$$P = P_{sat} + \rho g(\delta - z) \quad (5)$$

where δ is the thickness of the liquid film and P_{sat} is the saturated pressure of the dry vapor.

Substituting Eq. (5) into Eq. (2), the velocity profile in the r -direction can be derived as

$$u = -\frac{\rho g K d \delta}{\mu_e dr} \quad (6)$$

The first law of thermodynamics and the mass conservation equation are considered to be coupled in the governing equations. Therefore, the overall energy balance in the liquid film can be written as

$$\frac{d}{dr} \left\{ \int_0^\delta \rho u (h_{fg} + Cp(T_{sat} - T)) 2\pi r dz \right\} dr + \rho h_{fg} 2\pi r dv|_{z=\delta} + \rho (h_{fg} + Cp\Delta T) v_w 2\pi r dr = \frac{k_e \Delta T}{\delta} 2\pi r dr \quad (7)$$

where Cp is the specific heat at constant pressure, h_{fg} is the latent heat of the condensate, ΔT is the reference temperature difference between the saturation temperature of the dry vapor T_{sat} and the disk surface temperature T_w , and k_e is the effective thermal conductivity of the porous medium saturated with liquid.

The right hand side of Eq. (7) represents the total energy transfer from the liquid film to the solid disk. Meanwhile, the first term on the left hand side gives the net energy flux across the liquid film (from r to $r+dr$), the second term describes the net energy transferred into the two-phase zone via capillary forces, and the

third term indicates the net energy sucked from the permeable disk. Hence, only the capillary suction velocity ($v_2|_{z_2=0}$) of the two-phase zone is unknown.

Udell [22] reported that the capillary suction velocity in the z_2 direction in the two-phase zone increases with an increasing capillary pressure gradient and is given by

$$v_2 = \frac{KK_{rl}}{\mu_e} \left(\frac{\partial P_c}{\partial z_2} - \rho g \right) \quad (8a)$$

where

$$K_{rl} = s^3 \quad (8b)$$

$$P_c = \frac{\sigma}{\sqrt{K/\epsilon}} f(s) \quad (8c)$$

$$f(s) = 1.417(1-s) - 2.120(1-s)^2 + 1.263(1-s)^3 \quad (8d)$$

where s is the dimensionless saturation parameter and has a value of

$$s = 1 \quad \text{at } z_2 = 0 \quad (8e)$$

At the interface between the two-phase zone and the liquid film, the mass continuity equation has the form

$$\frac{1}{r} \frac{\partial(ru_2)}{\partial r} \Big|_{z_2=0} + \frac{\partial v_2}{\partial z_2} \Big|_{z_2=0} = 0 \quad (9)$$

where subscript 2 indicates properties of the two-phase zone. Note that u_2 and v_2 are the velocity components in the r - and z -directions, respectively, and $z_2=0$ corresponds to the interface between the two-phase zone and the liquid film.

At this interface, the no slip condition can be written as

$$u_2|_{z_2=0} = u|_{z=\delta} \quad (10a)$$

or

$$\frac{1}{r} \frac{\partial(ru_2)}{\partial r} \Big|_{z_2=0} = \frac{1}{r} \frac{\partial(ru)}{\partial r} \Big|_{z=\delta} \quad (10b)$$

Substituting Eq. (6) into Eq. (10b) yields

$$\frac{1}{r} \frac{\partial(ru_2)}{\partial r} \Big|_{z_2=0} = - \frac{1}{r} \frac{\rho g K}{\mu_e} \frac{d}{dr} \left(r \frac{d\delta}{dr} \right) \quad (10c)$$

Substituting Eqs. (8b)–(8e) into Eq. (8a), the capillary suction velocity of the two-phase zone, v_2 , can be expressed as

$$v_2 = \frac{K}{\mu_e} s^3 \left(\frac{\sigma}{\sqrt{K/\epsilon}} f' \frac{\partial s}{\partial z_2} - \rho g \right) \quad (11)$$

Substituting Eqs. (10c) and (11) into Eq. (9), the mass continuity equation can be rewritten as

$$- \frac{1}{r} \frac{\rho g K}{\mu_e} \frac{d}{dr} \left(r \frac{d\delta}{dr} \right) + \frac{K}{\mu_e} \left\{ \frac{\sigma}{\sqrt{K/\epsilon}} \left[s^3 f'' \left(\frac{\partial s}{\partial z_2} \right)^2 + 3s^2 f' \left(\frac{\partial s}{\partial z_2} \right)^2 + f' s^3 \frac{\partial^2 s}{\partial z_2^2} \right] - 3\rho g s^2 \left(\frac{\partial s}{\partial z_2} \right) \right\} \Big|_{z_2=0} = 0 \quad (12)$$

According to the results of Majumdar and Tien [24] and Bridge et al. [25], the saturation profiles near the interface of the two-phase zone and the liquid film are approximately linear and can be expressed as

$$\frac{\partial^2 s}{\partial z_2^2} = 0 \quad \text{at } z_2 = 0 \quad (13)$$

Substituting Eq. (13) into Eq. (12), the saturation gradient at the interface of the two-phase zone can be written as

$$\frac{\partial s}{\partial z_2} \Big|_{z_2=0} = \frac{3\rho g s^2 + \sqrt{(3\rho g s^2)^2 + 4(s^3 f'' + 3s^2 f')}}{2 \frac{\sigma}{\sqrt{K/\epsilon}} (s^3 f'' + 3s^2 f')} \frac{\rho g \sigma}{\sqrt{K/\epsilon}} \frac{1}{r} \frac{d}{dr} \left(r \frac{d\delta}{dr} \right) \Big|_{z_2=0} \quad (14)$$

Substituting Eq. (14) into Eq. (11), the velocity of the liquid leaving the liquid film and entering the two-phase zone via capillary effects can be expressed as

$$v_2|_{z_2=0} = \frac{K}{\mu_e} s^3 \left(f' \frac{3\rho g s^2 + \sqrt{(3\rho g s^2)^2 + 4(s^3 f'' + 3s^2 f')}}{2(s^3 f'' + 3s^2 f')} \frac{\rho g \sigma}{\sqrt{K/\epsilon}} \frac{1}{r} \frac{d}{dr} \left(r \frac{d\delta}{dr} \right) - \rho g \right) \Big|_{z_2=0} \quad (15)$$

From the velocity profile in the r -direction (Eq. (6)) and the velocity of the liquid entering the two-phase zone via capillary effects (Eq. (15)), the overall energy balance in the liquid film (Eq. (7)) can be rewritten as

$$\frac{1}{r} \delta \frac{d}{dr} \left(r \frac{d\delta}{dr} \right) - \delta \frac{h_{fg}}{h_{fg} + \frac{1}{2} C_p \Delta T} \left(\frac{3f' s^5 + s^3 f' \sqrt{9s^4 + 4(s^3 f'' + 3s^2 f')}}{2(s^3 f'' + 3s^2 f')} \frac{\sigma}{\sqrt{K/\epsilon}} \frac{1}{\rho g r} \frac{d}{dr} \left(r \frac{d\delta}{dr} \right) - s^3 \right) \Big|_{z_2=0} - \delta \left(\frac{v_w \mu_e}{\rho g K} \left(\frac{h_{fg} + C_p \Delta T}{h_{fg} + \frac{1}{2} C_p \Delta T} \right) \right) = \frac{-k_e \Delta T \mu_e}{\rho^2 g K \left(h_{fg} + \frac{1}{2} C_p \Delta T \right)} \quad (16)$$

The corresponding boundary conditions are

$$\frac{d\delta}{dr} \quad \text{at } r = 0 \quad (17a)$$

$$\delta = \delta_{\min} \quad \text{at } r = R_0 \quad (17b)$$

The following nondimensional variables are introduced to convert the preceding equations into a nondimensional form:

$$\lambda = h_{fg} + \frac{1}{2} Cp\Delta T, \quad Ja = \frac{Cp\Delta T}{\lambda}, \quad Pr_e = \frac{\mu_e Cp}{k_e} \quad \delta^* = \delta/R_0 \quad (18)$$

$$Ra_e = \frac{\rho^2 g Pr_e R_0^3}{\mu_e^2}, \quad Da = \frac{K}{R_0^2}$$

$$Re_w = \frac{\rho v_w R_0}{\mu_e}, \quad Sw = \left(1 + \frac{1}{2} Ja\right) Re_w \frac{Pr_e}{Ra_e Da}$$

$$Bo_c = \frac{\sigma \sqrt{\varepsilon}}{\rho g K} = \frac{1}{Bo}, \quad r^* = r/R_0$$

where Ja is the Jacob number; Pr_e is the effective Prandtl number; Ra_e is the effective Rayleigh number; Da is the Darcy number; R_0 is the disk radius; Re_w is the Reynolds number, which is greater than zero when suction effects are present or less than zero for blowing along the disk surface; Sw is the suction parameter; and Bo_c is the capillary parameter.

Expressed in terms of these nondimensional variables, Eq. (16) becomes

$$\frac{1}{r^*} \delta^* \frac{d}{dr^*} \left(r^* \frac{d\delta^*}{dr^*} \delta^* \right) - \left(1 - \frac{1}{2} Ja\right) \delta^* \left(\frac{3f' s^5 + f' s^3 \sqrt{9s^4 + 4(s^3 f'' + 3s^2 f')}}{2(s^3 f'' + 3s^2 f')} Bo_c (Da)^{1/2} \frac{1}{r^*} \frac{d}{dr^*} \left(r^* \frac{d\delta^*}{dr^*} \right) \right) \Bigg|_{z_2=0} - \left(Sw - 1 + \frac{1}{2} Ja \right) \delta^* = \frac{-Ja}{Ra_e Da} \quad (19)$$

while the corresponding boundary conditions (Eqs. (17a) and (17b)) become

$$\frac{d\delta^*}{dr^*} = 0 \quad \text{at } r^* = 0 \quad (20a)$$

$$\delta^* = \delta_{\min}^* \quad \text{at } r^* = 1 \quad (20b)$$

However, even with these boundary conditions, it is still impossible to solve Eq. (19) since δ_{\min}^* is unknown.

In practice, the film thickness at the disk edge cannot be zero. According to the minimum mechanical energy principle presented by Bakhmeteff [12], a fluid flowing across the hydrostatic pressure gradient and off the plate will adjust itself such that the rate of mechanical energy within the fluid is minimized with respect to the boundary layer at the plate edge. The minimum film thickness can therefore be determined by setting the derivative of the mechanical energy with respect to δ equal to zero for the steady flow rate, i.e.,

$$\frac{\partial}{\partial \delta} \left(\int_0^\delta \left(\frac{u^2}{2} + gz + \frac{P}{\rho} \right) \rho u dz \right) \Bigg|_{\dot{m}=\dot{m}_c} = 0 \quad (21)$$

where \dot{m}_c is the critical value of the mass flow over the disk edge. The condensate mass flow rate at any section can be expressed as:

$$\dot{m} = \int_0^\delta \rho u dz \quad (22)$$

Substituting Eq. (6) into Eq. (22) yields

$$\dot{m} = - \frac{\rho^2 g K}{\mu_e} \delta \frac{d\delta}{dr} \quad (23)$$

The critical value of the mass flow rate, \dot{m}_c , at $r=R_0$ is given by

$$\dot{m}_c = - \frac{\rho^2 g K}{\mu_e} \delta_{\min} \frac{d\delta}{dr} \Bigg|_{r=R_0} \quad (24)$$

Solving Eq. (21) subject to the boundary conditions in Eqs. (20b) and (24) yields the following relationship:

$$\dot{m}_c = \rho^2 g \delta_{\min}^3 \quad (25)$$

Substituting Eq. (24) into Eq. (25), the new boundary condition is found to be

$$\frac{d\delta}{dr} \Bigg|_{r=R_0} = - \left(\frac{\mu_e^2}{\rho^2 g K^2} \delta_{\min} \right)^{1/2} \quad (26)$$

Using Eqs. (8c) and (8d), the values of s , f' and f'' at $z_2=0$ are calculated to be 1, -1.417, and -4.24, respectively. Equation (19) can then be rewritten as:

$$\frac{1}{r^*} \delta^* \frac{d}{dr^*} \left(r^* \frac{d\delta^*}{dr^*} \delta^* \right) - \left(1 - \frac{1}{2} Ja\right) \delta^* \left(\frac{4.251 + 1.417 \sqrt{9 - 33.964 Bo_c (Da)^{1/2}}}{16.982} \frac{1}{r^*} \frac{d}{dr^*} \left(r^* \frac{d\delta^*}{dr^*} \right) \right) - \left(Sw - 1 + \frac{1}{2} Ja \right) \delta^* = \frac{-Ja}{Ra_e Da} \quad (27)$$

The corresponding boundary conditions (Eqs. (20a) and (26)) therefore become

$$\frac{d\delta^*}{dr^*} = 0 \quad \text{at } r^* = 0 \quad (28a)$$

$$\frac{d\delta^*}{dr^*} \Bigg|_{r^*=1} = - \left(\frac{Pr_e}{Ra_e Da^2} \delta_{\min}^* \right)^{1/2} \quad \text{at } r^* = 1 \quad (28b)$$

From Eq. (27) and the corresponding boundary conditions, the dimensionless film thickness, δ^* , can be obtained in terms of Ja, Ra_e , Pr_e , Bo_c , Sw, and Da.

According to Fourier's law of heat conduction, the local heat flux $q_w(r)$ supplied to the disk can be calculated by

$$q_w(r) = k_e \left. \frac{\partial T}{\partial z} \right|_{z=0} = k_e \frac{\Delta T}{\delta} \quad (29)$$

From Eq. (18), the dimensionless local heat flux $q_w^*(r^*)$ can be expressed as

$$q_w^*(r^*) = \frac{q_w(r)R_0}{k_e \Delta T} = \frac{1}{\delta^*} \quad (30)$$

The local Nusselt number Nu_r is defined as

$$Nu_r = \frac{h_r R_0}{k_e} \quad (31)$$

where h_r is the local heat transfer coefficient, given by $h_r = k_e / \delta$.

The mean Nusselt number is expressed by

$$\overline{Nu} = \frac{\overline{h} R_0}{k_e} \quad (32)$$

where

$$\overline{h} = \frac{1}{\pi R_0^2} \int_0^{R_0} h(r) 2\pi r dr = \frac{1}{\pi R_0^2} \int_0^{R_0} \frac{k_e}{\delta} 2\pi r dr \quad (33)$$

In this study, Eq. (27) is numerically solved using the Runge–Kutta shooting method to obtain the dimensionless liquid film thickness. In the solution procedure, an initial estimate is made of the liquid film thickness at the disk center ($\delta^*|_{r^*=0}$) and this estimate is then substituted into Eq. (27). The δ^* value along the r^* direction is then calculated using Eq. (28a). Once all of the δ^* values (i.e., the value at every grid point) have been calculated, the resulting thickness gradient at the disk edge is checked with Eq. (28b) and a modified initial value for $\delta^*|_{r^*=0}$ obtained. This process is iteratively repeated until the solution of Eq. (28b) satisfies the convergence criterion, i.e.,

$$\left| \frac{\left. \frac{d\delta^*}{dr^*} \right|_{r^*=1} + \left(\frac{Pr_e}{Ra_e Da^2} \delta_{\min}^* \right)^{1/2}}{\left. \frac{d\delta^*}{dr^*} \right|_{r^*=1}} \right| \leq 10^{-6}$$

Note that since the gradient of the film thickness is not flat at the disk edge, the calculations apply a progressively finer grid size as the disk edge is approached.

Results and Discussion

For the particular case where the effects of capillary forces are neglected, i.e., the capillary suction velocity v_2 in the two-phase zone (Eq. (11)) is set to zero, then from the velocity profile in the r -direction (Eq. (6)) and the nondimensional variables (Eq. (18)) the overall energy balance in the liquid film (Eq. (7)) can be rewritten as

$$\frac{1}{r^*} \delta^* \frac{d}{dr^*} \left(r^* \frac{d\delta^*}{dr^*} \delta^* \right) - Sw \delta^* = \frac{-Ja}{Ra_e Da} \quad (34)$$

Note that the corresponding boundary conditions are the same as those given in Eqs. (28a) and (28b).

Wang et al. [21] used a novel transformation method to investigate film condensation on a horizontal wavy plate in a porous medium under the assumptions of no capillary force effects and no suction at the wall. Table 1 compares the results reported by Wang et al. for a plate with a wave number of $n=0$ (i.e., condensation on a flat plate) with the present results for a horizontal disk calculated using Eq. (34). It is observed that the values of \overline{Nu} for the horizontal disk are approximately 75% higher than those of Wang et al. [21].

Table 1 Comparison of solutions of Wang et al. [21] with those of present study

Parameters	\overline{Nu} (Ref. [21])	\overline{Nu} (present study)
Ja=0.01, Ra _e =10 ⁵ , Da=0.01, Pr _e =7, Sw=0	55.7	97.5
Ja=0.1, Ra _e =10 ⁵ , Da=0.01, Pr _e =7, Sw=0	25.5	45.2

One explanation for the discrepancy between the two sets of results is that the solid plate considered in the present study has the form of a circular disk, while that considered by Wang et al. [21] was a flat plate. Therefore, in the present case, the condensate film spreads over a wider area and has a thinner thickness, with the result that the Nusselt number is increased.

In simulating practical engineering problems, the values of the physical parameters used in Eq. (27) and the corresponding boundary conditions in Eqs. (28a) and (28b) (i.e., Ja, Pr_e, Da, Ra_e, Bo_c, and Sw) must be assigned reasonable values. The following analyses take water vapor as the working liquid and use the dimensional and dimensionless parameter values cited in Udell [22] and Bridge et al. [25], as summarized in Table 2.

Figure 2 shows the effect of the suction parameter, Sw, on the distribution of the dimensionless film thickness, δ^* ($\delta^* = \delta/R_0$), along the radial direction of the disk, r^* . Note that the remaining parameters are assigned the typical values shown in Table 2, i.e., Ja=0.02, Ra_e=2×10¹¹, Da=6.4×10⁻¹⁰, Pr_e=1.76, and Bo_c=6.1×10⁵. It is observed that the liquid film thickness decreases with increasing Sw. Using the relationship given in Eq. (31), Fig. 3 plots the distribution of the local Nusselt number, Nu_r , along the radial direction for the cases shown in Fig. 2. In general, it can be

Table 2 List of physical parameters used in present study

Symbol	Interpretation	Typical value
K	Permeability	6.4×10 ⁻¹² m ²
ρ	Liquid density	957.9 kg/m ³
R_0	Radius of disk	0.1 m
C_p	Specific heat at constant pressure	4217 J/kg °C
μ_e	Liquid viscosity	2.79×10 ⁻⁴ kg/m s
σ	Surface tension	5.94×10 ⁻² N/m
h_{fg}	Heat of vaporization	2257 kJ/kg
ΔT	Saturation temperature minus wall temperature ($T_{\text{sat}} - T_w$)	10 °C
ε	Porosity	0.38
Ja	$\frac{C_p \Delta T}{h_{fg} + \frac{1}{2} C_p \Delta T}$	0.02
Pr _e	$\frac{\mu_e C_p}{k_e}$	1.76
Da	$\frac{K}{R_0^2}$	6.4×10 ⁻¹⁰
Ra _e	$\frac{\rho^2 g Pr_e R_0^3}{\mu_e^2}$	2×10 ¹¹
Bo _c	$\frac{\sigma \sqrt{\varepsilon}}{\rho g K}$	6.1×10 ⁵

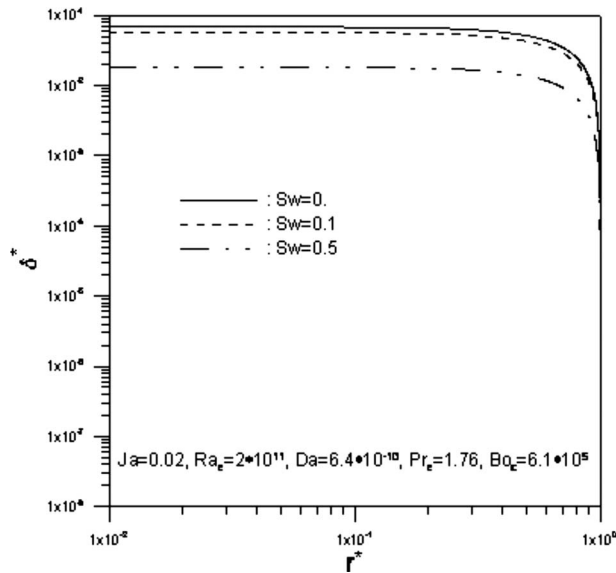


Fig. 2 Variation of dimensionless film thickness in radial direction

seen that the heat transfer performance increases with increasing Sw . Furthermore, for constant Sw , the value of Nu_r increases toward the edge of the disk.

Equation (27) and the corresponding boundary condition equations (Eqs. (28a) and (28b)) indicate that the mean Nusselt number \bar{Nu} is a function of $Ja, Pr_e, Da, Ra_e, Bo_c,$ and Sw . Figures 4–9 show the relationships between \bar{Nu} and $Ja, Pr_e, Da, Ra_e, Sw,$ and $Bo_c,$ respectively. To investigate the influence of particular parameters on the heat transfer performance, at least three of the parameters are fixed at their typical values in each figure while the other parameters are varied around their typical values. Figure 4 reveals that the mean Nusselt number \bar{Nu} decreases with increasing Jacob number Ja at different values of Sw and Da . As explained above, the other parameters remain constant at their typical values, i.e., $Ra_e=2 \times 10^{11}, Pr_e=1.76,$ and $Bo_c=6.1 \times 10^5$. From a closer inspection of Fig. 4, it is found that \bar{Nu} and Ja are related by $\bar{Nu} \propto Ja^{-1/7}$. Figure 5 shows that \bar{Nu} is apparently insensitive to the

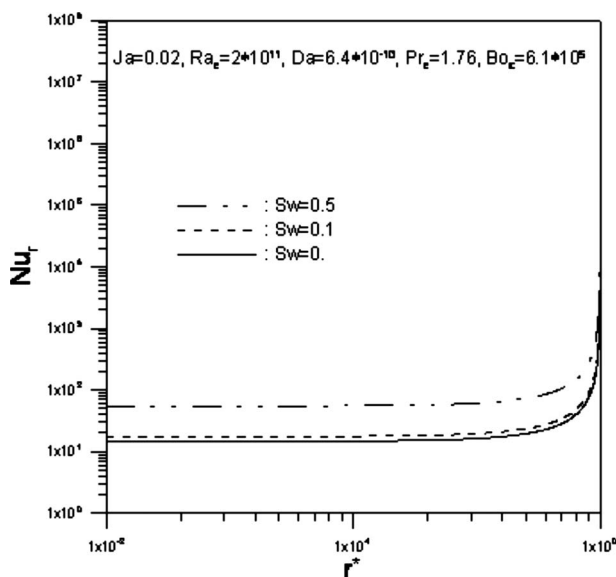


Fig. 3 Variation of local Nusselt number in radial direction as function of Sw

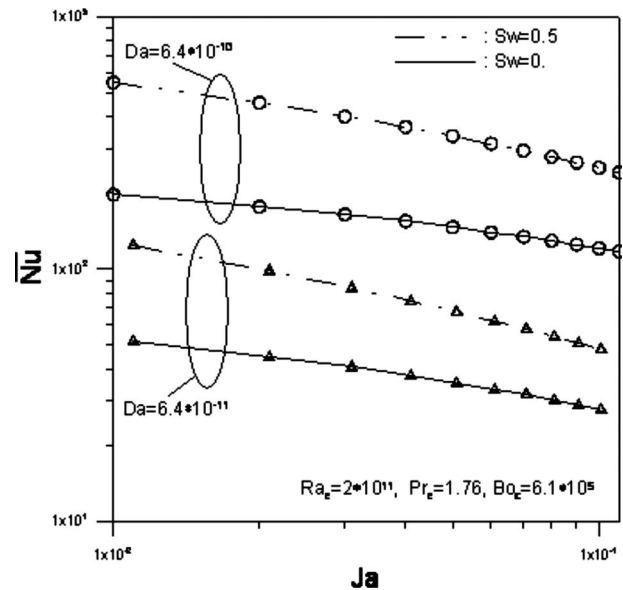


Fig. 4 Variation of \bar{Nu} with Ja as function of Sw and Da for constant $Ra_e=2 \times 10^{11}, Pr_e=1.76,$ and $Bo_c=6.1 \times 10^5$

effective Prandtl number Pr_e at different values of Ja and Sw . (Again, the other parameters, i.e., $Ra_e, Da,$ and $Bo_c,$ remain constant at their typical values.)

Figures 6 and 7 show that the mean Nusselt number \bar{Nu} increases with an increasing Darcy number Da and an increasing effective Rayleigh number Ra_e respectively. The relationship between \bar{Nu} and Da is found to be approximately $\bar{Nu} \propto Da^{2/3}$, while that between \bar{Nu} and Ra_e is approximately $\bar{Nu} \propto Ra_e^{1/2}$. However, Fig. 7 reveals that the relationship between \bar{Nu} and $Ra_e, \bar{Nu} \propto Ra_e^{1/2}$, is subject to a certain degree of error for $Ra_e > 10^{10}$. Meanwhile, Fig. 8 shows that the mean Nusselt number, \bar{Nu} increases with increasing suction at the wall Sw . It is also observed that the effect of Sw becomes more pronounced as the value of Ja

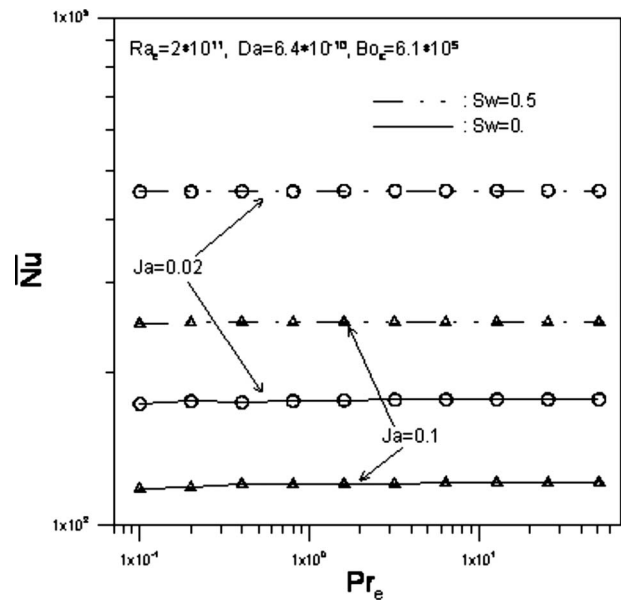


Fig. 5 Variation of \bar{Nu} with Pr_e as function of Ja and Sw for constant $Ra_e=2 \times 10^{11}, Da=6.4 \times 10^{-10},$ and $Bo_c=6.1 \times 10^5$

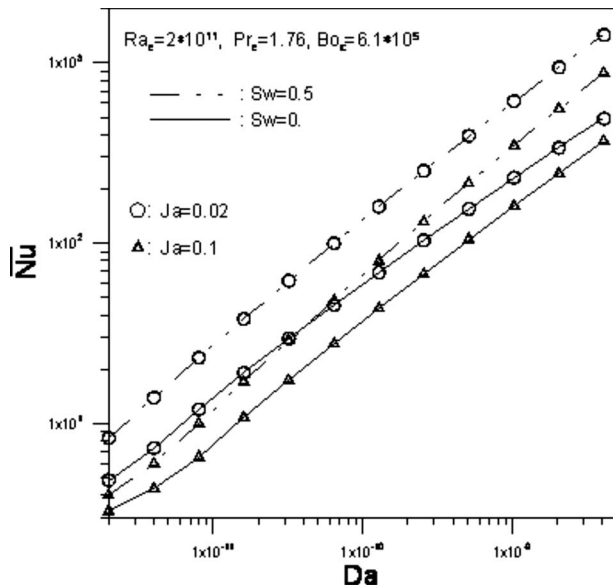


Fig. 6 Variation of \overline{Nu} with Da as function of Ja and Sw for constant $Ra_e=2 \times 10^{11}$, $Pr_e=1.76$, and $Bo_c=6.1 \times 10^5$

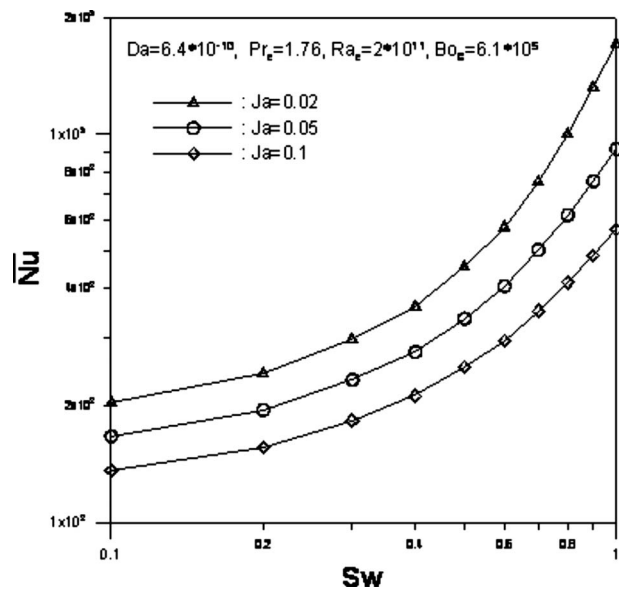


Fig. 8 Variation of \overline{Nu} with Sw as function of Ja for $Da=6.4 \times 10^{-10}$, $Pr_e=1.76$, $Ra_e=2 \times 10^{11}$, and $Bo_c=6.1 \times 10^5$

reduces. This result is reasonable because a lower value of Ja corresponds to a thinner liquid film, then the effects of wall suction parameter Sw will become relatively larger.

Figure 9 shows that the mean Nusselt number \overline{Nu} increases with an increasing value of the capillary parameter Bo_c for different Ja and Sw and constant parameter values of $Da=6.4 \times 10^{-10}$, $Pr_e=1.76$, and $Ra_e=2 \times 10^{11}$. It can be seen that when $Bo_c < 10^3$, the capillary force has a negligible effect on the heat transfer performance and can be neglected. In other words, the value of \overline{Nu} will be close to that calculated for \overline{Nu} using $Bo_c=0$ in Eq. (27). However, \overline{Nu} significantly increases with increasing Bo_c when $Bo_c > 10^3$. In other words, the results suggest that $Bo_c = 10^3$ represents a threshold value above, which the effects of capillary forces should be taken into consideration. The physical reason for this is that higher values of Bo_c imply stronger capillary forces, which result in more liquid being sucked into the

two-phase zone. This creates a thinner liquid film and a steeper temperature gradient, which both enhance the heat transfer rate. For the porous materials used in typical heat and mass transfer applications, the permeability K is of the order of 10^{-10} – 10^{-16} m^2 (see Table 1.1 in Ref. [29] or Table 2.3 in Ref. [30]). For the current problem of water vapor condensing on a horizontal disk, the value of $Bo_c (= \sigma \sqrt{\epsilon / \rho g K})$ is 6.1×10^5 , which is clearly far higher than 10^3 . Therefore, the effects of capillary forces must be taken into account.

Conclusion

This study has analyzed the problem of two-dimensional laminar film condensation on a horizontal disk embedded in a porous medium with suction at the disk surface. The present analyses have taken water vapor as the working liquid and have considered typical values of the corresponding dimensional and dimension-

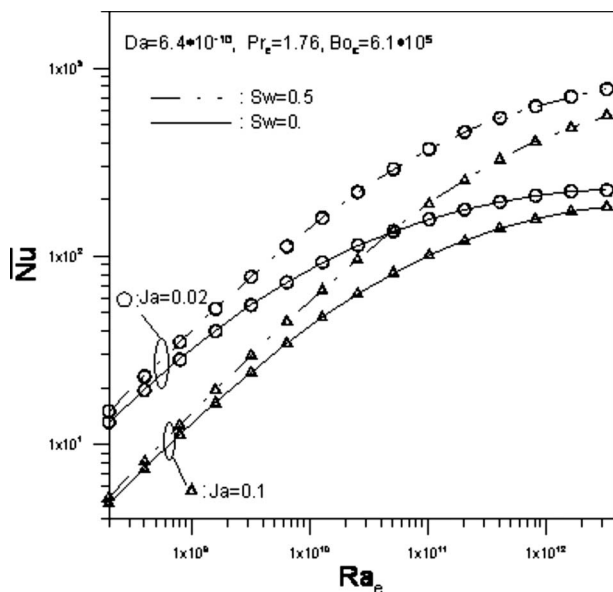


Fig. 7 Variation of \overline{Nu} with Ra_e as function of Ja and Sw for constant $Da=6.4 \times 10^{-10}$, $Pr_e=1.76$, and $Bo_c=6.1 \times 10^5$

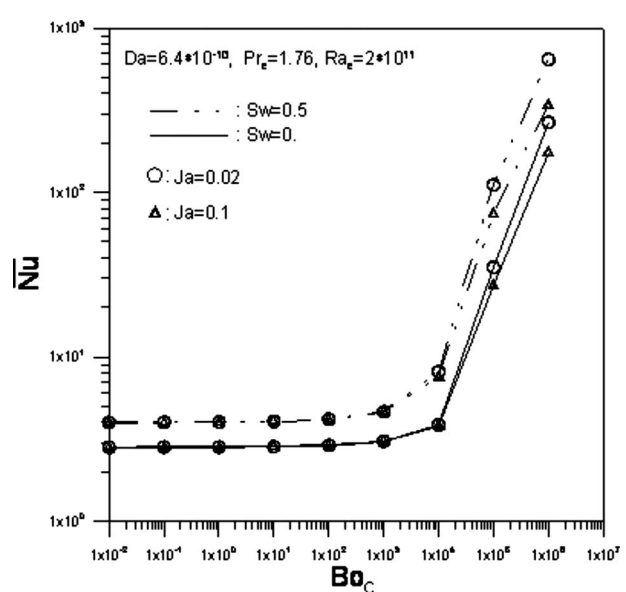


Fig. 9 Variation of \overline{Nu} with Bo_c as function of Ja and Sw for constant $Da=6.4 \times 10^{-10}$, $Pr_e=1.76$, and $Ra_e=2 \times 10^{11}$

less parameters. In problems of condensation in a porous medium, the effective pore radii are small, and therefore the present analyses have taken the effects of capillary forces on the heat and mass transfer into consideration. The presence of capillary effects leads to the formation of a two-phase zone immediately above the liquid film. The capillary forces reduce the thickness of the liquid film and increase the heat transfer coefficient. In the current water-vapor condensation problem, the results have indicated a threshold value of $Bo_c = 10^3$ for the capillary parameter above, which capillary force effects must be taken into consideration. The results have also shown that suction at the wall enhances the heat transfer performance, particularly as the value of Ja is reduced. Finally, it has been determined that when the effects of capillary forces and wall suction are neglected, the mean Nusselt number for condensation on a horizontal disk is approximately 75% higher than that for condensation on a horizontal flat plate.

Acknowledgment

This work was supported by the National Science Council of Taiwan: NSC 94-2212-E-218-017.

Nomenclature

Bo_c	= ratio of capillary force and gravity force defined in Eq. (18)
Cp	= specific heat at constant pressure
Da	= Darcy number defined in Eq. (18)
g	= acceleration of gravity
h	= heat transfer coefficient
h_{fg}	= heat of vaporization
Ja	= Jacob number defined in Eq. (18)
k	= thermal conductivity
K	= permeability of porous medium
R_o	= radius of disk
\dot{m}	= condensate mass flux
Nu	= Nusselt number defined in Eq. (32)
P	= pressure
Pr_e	= effective Prandtl number
Ra_e	= effective Rayleigh number
Sw	= suction parameter
s	= dimensionless saturation
T	= temperature
ΔT	= saturation temperature minus wall temperature
r, z	= radial and vertical coordinates
u, v	= radial and vertical velocity components

Greek Symbols

δ	= condensate film thickness
δ_0	= condensate film thickness at disk center
μ	= liquid viscosity
ρ	= liquid density
α	= thermal diffusivity
σ	= surface tension
ε	= porosity

Superscripts

—	= average quantity
*	= dimensionless variable

Subscripts

2	= properties in two-phase zone
o	= quantity at disk center
c	= capillary
min	= minimum quantity or quantity at disk edge
sat	= saturation property

w	= quantity at wall
e	= effective property

References

- [1] Nusselt, W., 1916, "Die oberflächen Kondensation des Wasserdampfes," *Zeitschrift des Vereines Deutscher Ingenieure*, **60**, pp. 541–546.
- [2] Rohsenow, W. M., 1956, "Heat Transfer and Temperature Distribution in Laminar Film Condensation," *ASME J. Heat Transfer*, **78**, pp. 1645–1648.
- [3] Sparrow, E. M., and Gregg, J. L., 1959, "Laminar Condensation Heat Transfer on a Horizontal Cylinder," *ASME J. Heat Transfer*, **81**, pp. 291–296.
- [4] Chen, M. M., 1961, "An Analytical Study of Laminar Film Condensation: Part 1—Flat Plates," *ASME J. Heat Transfer*, **83**, pp. 48–54.
- [5] Koh, J. C. Y., 1961, "On Integral of Treatment of Two Phase Boundary Layer in Film Condensation," *ASME J. Heat Transfer*, **83**, pp. 359–362.
- [6] Merte, Jr., H., 1973, "Condensation Heat Transfer," *Adv. Heat Transfer*, **9**, p. 181.
- [7] Mohamed, H. A., 2006, "Effect of Rotation and Surface Roughness on Heat Transfer Rate to Flow through Vertical Cylinders in Steam Condensation Process," *ASME J. Heat Transfer*, **128**(3), pp. 318–323.
- [8] Jiang, Y., Mitra, B., Garimella, S., and Andresen, U. C., 2007, "Measurement of Condensation Heat Transfer Coefficients at Near-Critical Pressures in Refrigerant Blends," *ASME J. Heat Transfer*, **129**(8), pp. 958–965.
- [9] Leppert, G., and Nimmo, B., 1968, "Laminar Film Condensation on Surface Normal to Body or Inertial Forces," *J. Heat Transfer*, **80**, pp. 178–179.
- [10] Nimmo, B., and Leppert, G., 1970, "Laminar Film Condensation on a Finite Horizontal Surface," *Fourth International Heat Transfer Conference*, pp. 402–403.
- [11] Chiou, J. S., and Chang, T. B., 1994, "Laminar Film Condensation on a Horizontal Disk," *Wärme- und Stoffübertragung*, **29**, pp. 141–144.
- [12] Bakhmeteff, B. K., 1966, *Hydraulics of Open Channel*, McGraw-Hill, New York, pp. 39–41.
- [13] Jain, K. C., and Bankoff, S. G., 1964, "Laminar Film Condensation on a Porous Vertical With Uniform Suction Velocity," *ASME J. Heat Transfer*, **89**, pp. 95–102.
- [14] Yang, J. W., 1970, "Effect of Uniform Suction on Laminar Film Condensation on a Porous Vertical Wall," *ASME J. Heat Transfer*, **92**, pp. 252–256.
- [15] Yang, S. A., and Chen, C. K., 1992, "Laminar Film Condensation on a Finite-Size Horizontal Plate With Suction at the Wall," *Appl. Math. Model.*, **16**, pp. 325–329.
- [16] Chiou, J. S., and Chang, T. B., 1994, "Laminar Film Condensation on a Horizontal Disk With Suction at The Wall," *Comput. Math. Appl.*, **27**(12), pp. 61–68.
- [17] Cheng, P., 1981, "Film Condensation Along an Inclined Surface in a Porous Medium," *Int. J. Heat Mass Transfer*, **24**, pp. 983–990.
- [18] Cheng, P., and Chui, D. K., 1984, "Transient Film Condensation on a Vertical Surface in a Porous Medium," *Int. J. Heat Mass Transfer*, **27**, pp. 795–798.
- [19] Liu, C. Y., Ismail, K. A. R., and Ebinuma, C. D., 1984, "Film Condensation With Lateral Mass Flux About a Body of Arbitrary Shape in a Homogeneous Porous Medium," *Int. Commun. Heat Mass Transfer*, **11**, pp. 377–384.
- [20] Char, M. L., Lin, J. D., and Chen, H. T., 2001, "Conjugate Mixed Convection Laminar Non-Darcy Film Condensation Along a Vertical Plate in a Homogeneous Porous Medium," *Int. J. Eng. Sci.*, **39**, pp. 897–912.
- [21] Wang, S. C., Chen, C. K., and Yang, Y. T., 2005, "Film Condensation on a Finite-Size Horizontal Plate Bounded by a Homogeneous Porous Layer," *Appl. Therm. Eng.*, **25**, pp. 577–590.
- [22] Udell, K. S., 1983, "Heat Transfer in Porous Media Heated From Above With Evaporation, Condensation, and Capillary Effects," *ASME J. Heat Transfer*, **105**, pp. 485–492.
- [23] Udell, K. S., 1985, "Heat Transfer in Porous Media Considering Phase Change and Capillarity—The Heat Pipe Effect," *Int. J. Heat Mass Transfer*, **28**, pp. 485–495.
- [24] Majumdar, A., and Tien, C. L., 1990, "Effects of Surface Tension on Film Condensation in a Porous Medium," *ASME J. Heat Transfer*, **112**, pp. 751–757.
- [25] Bridge, L., Bradean, R., Ward, M. J., and Wetton, B. R., 2003, "The Analysis of a Two-Phase Zone With Condensation in a Porous Medium," *J. Eng. Math.*, **45**, pp. 247–268.
- [26] Chang, T. B., 2006, "Effects of Capillary Force on Laminar Filmwise Condensation on a Horizontal Disk in a Porous Medium," *Appl. Therm. Eng.*, **26**, pp. 2308–2315.
- [27] Chang, T. B., 2008, "Laminar Film Condensation on a Horizontal Wavy Plate Embedded in a Porous Medium," *Int. J. Therm. Sci.*, **47**, pp. 35–42.
- [28] Yang, Y. T., Chen, C. K., and Hsu, P. T., 1997, "Laminar Film Condensation on a Finite-Size Horizontal Wavy Disk," *Appl. Math. Model.*, **21**, pp. 139–144.
- [29] Kaviany, M., 1991, *Principles of Heat Transfer in Porous Media*, Springer-Verlag, New York, p. 6.
- [30] Nield, D. A., and Bejan, A., 1992, *Convection in Porous Media*, Springer-Verlag, New York, p. 4.

Lesley M. Wright
Department of Aerospace and Mechanical
Engineering,
The University of Arizona,
Tucson, AZ 85721-0119

Yao-Hsien Liu

Je-Chin Han
Distinguished Professor and Marcus Easterling
Endowed Chair
e-mail: jc-han@tamu.edu

Turbine Heat Transfer Laboratory,
Department of Mechanical Engineering,
Texas A&M University,
College Station, TX 77843-3123

Sanjay Chopra
Siemens Power Company,
4400 Alafaya Trail,
Orlando, FL 32826

Heat Transfer in Trailing Edge, Wedge-Shaped Cooling Channels Under High Rotation Numbers

Heat transfer coefficients are experimentally measured in a rotating cooling channel used to model an internal cooling passage near the trailing edge of a gas turbine blade. The regionally averaged heat transfer coefficients are measured in a wedge-shaped cooling channel ($D_h = 2.22$ cm, $A_c = 7.62$ cm²). The Reynolds number of the coolant varies from 10,000 to 40,000. By varying the rotational speed of the channel, the rotation number and buoyancy parameter range from 0 to 1.0 and 0 to 3.5, respectively. Significant variation of the heat transfer coefficients in both the spanwise and streamwise directions is apparent. Spanwise variation is the result of the wedge-shaped design, and streamwise variation is the result of the sharp entrance into the channel and the 180 deg turn at the outlet of the channel. With the channel rotating at 135° with respect to the direction of rotation, the heat transfer coefficients are enhanced on every surface of the channel. Both the nondimensional rotation number and buoyancy parameter have proven to be excellent parameters to quantify the effect of rotation over the extended ranges achieved in this study. [DOI: 10.1115/1.2907437]

Keywords: rotation, turbine cooling, internal forced convection

Introduction

Advanced gas turbines operate at high temperatures to improve thermal efficiency. The high inlet temperature creates thermal stresses on the blades, which can be detrimental to the operation of the engine. In order to achieve reasonable durability goals, improved cooling techniques, such as film cooling and internal cooling, are applied to turbine blades. Internal cooling is achieved by circulating compressed air in multipass flow channels inside the blade structure. The cross section of the internal cooling channels varies depending on their location in the blade; cooling channels near the leading edge could be tall and narrow, and channels closer to the trailing edge are typically wide and short. The cooling channels are either singlepass (with radial outward flow) or multipass (both radial outward and radial inward flow) passages. To enhance the heat transfer from the walls of the channels, they are typically lined with ribs or other turbulence promoters.

The coolant flow through these internal cooling passages is complex and influenced by multiple parameters. The aspect ratio of the channels, 180 deg turns in the multipass channels, and the rib configurations all affect the level of heat transfer enhancement in nonrotating channels. However, the cooling channels in actual turbine blades are rotating. Rotation introduces the added complexities of Coriolis and buoyancy forces, which also alter the coolant flow through the passages. Many studies are available, which report the combined effect of selected parameters. The interested reader is referred to *Gas Turbine Heat Transfer and Cooling Technology* [1] for many published studies investigating internal cooling techniques.

Because the heat transfer distribution within the cooling channels is influenced by many factors, it is necessary to parametrically study these factors. Therefore, it is necessary to understand the behavior of the coolant through smooth, rotating channels (without turbulence promoters) before the more complicated behavior can be fully realized. Turbulent flow through nonrotating,

circular tubes has been thoroughly investigated; Kays and Crawford [2] summarized this work that considers the heat transfer in tubes with various entrance conditions. The Nusselt number in tubes with fully developed turbulent flow is also given by Kays and Crawford [2]. The widely accepted Dittus-Boelter correlation for fully developed turbulent flow was developed in circular tubes, but this correlation has also been applied to flow through channels with noncircular cross sections.

Although straightforward expressions have been developed for turbulent flow through nonrotating, smooth passages, coolant flow in rotating passages with smooth walls lacks closure. Wagner et al. [3,4] were the first to show that heat transfers from the leading and trailing walls of a rotating channel are not symmetrical. In other words, in their square ($AR=1 \times 1$) cooling channel with radially outward flow, the heat transfer from the trailing surface increases with rotation, while the heat transfer from the leading surface decreases. Johnson et al. [5] extended this study of a square channel to investigate the effect of channel orientation with respect to the direction of rotation. When the channel is oriented nonorthogonally to the direction of rotation, the effect of rotation decreases; in other words, the difference between the heat transfer coefficients on the leading and trailing surfaces is reduced. Dutta and Han [6] confirmed this result in a rotating, square channel.

When the impact of rotation was realized, researchers sought more detailed heat transfer measurements. Park and Lau [7] used naphthalene sublimation to obtain detailed heat/mass transfer distributions in a rotating, two-pass, square channel. The detailed distributions indicated that Coriolis forces create large spanwise variations on both the leading and trailing surfaces. Bons and Kerrebrock [8] gathered detailed heat transfer coefficient distributions using infrared thermography, and they complemented these heat transfer measurements with flow field measurements (particle image velocimetry). In this rotating, single-pass, square channel, they concluded that the reduced heat transfer from the leading wall is the result of the Coriolis force transporting the hot, low momentum wall fluid from the trailing wall to the leading wall. They also showed that the Nusselt number on the trailing surface can be twice as great as that on the leading surface due to the combined effect of the Coriolis and buoyancy forces.

These studies aided designers to create more efficient cooling

Contributed by the Heat Transfer Division of ASME for publication in the *JOURNAL OF HEAT TRANSFER*. Manuscript received February 23, 2007; final manuscript received October 31, 2007; published online May 16, 2008. Review conducted by Minking Chyu.

channels, but these studies do not include the aspect ratio effect. The cooling channels can consist of a variety of cross sections, and this must be considered. In recent years, several studies have emerged which investigate the effect of rotation in rectangular channels. Azad et al. [9] studied the combined effect of channel aspect ratio and channel orientation. Their findings for a 2×1 (width \times height), two-pass channel were similar to a 1×1 channel: In the first pass with radially outward flow, the heat transfer from the leading surface decreased while the trailing surface increased, and the opposite occurs in the second pass. Also, the effect of rotation is reduced when the channel is skewed to the direction of rotation.

Channels located near the trailing edge of the blade have an even greater aspect ratio to fit into this narrow region of the blade. Several studies have focused on the effect of rotation in a 4×1 channel. Griffith et al. [10] observed significant spanwise variation in the heat transfer distributions due to rotation. Their results also showed that the channel orientation of the 4×1 channel has a small effect on the trailing and a large effect on the leading surface in this one-pass cooling channel. In the 4×1 channel oriented at 135 deg to the direction of rotation, the heat transfer from all surfaces in the channel is enhanced with rotation. Wright et al. [11] studied the effect of entrance geometry on the heat transfer enhancement in rotating rectangular channels (4×1). They showed that with the simultaneous development of both the hydrodynamic and thermal boundary layers the Nusselt number ratios may not reach the fully developed values predicted by the Dittus/Boelter–McAdams correlation. Acharya et al. [12] used mass transfer to obtain detailed distributions in a two-pass 4×1 channel, and their findings were consistent with Griffith et al. [10]. Zhou et al. [13] considered the effect of rotation in a 4×1 channel with high rotation numbers. They concluded that there is a critical Reynolds number, beyond which the expected heat transfer trends reverse. They also showed that increasing the density ratio increases the heat transfer enhancement. Willett and Bergles [14] studied the effect of rotation in a very narrow 10×1 channel. They independently controlled the rotation number and buoyancy parameter, and they showed that heat transfer coefficients increase on the trailing surface with increasing rotation and buoyancy while the heat transfer coefficients on the leading surface increase with increasing buoyancy.

Because the secondary flow patterns in rotating channels are strongly influenced by the cross section of the channel, it is imperative to investigate the effect of rotation in low aspect ratio channels ($W/H < 1$). Cho et al. [15] used a mass transfer method to study the effect of rotation in a rotating two-pass rectangular channel ($AR=1 \times 2$). An experimental result for a 1×4 rotating two-pass channel was reported by Agarwal et al. [16] using the mass transfer method. For a smooth surface, they found that the 1×4 channel has lower heat/mass transfer compared to square channel. Fu et al. [17,18] showed how the heat transfer enhancement varied in smooth channels depending on the channel cross section, rotation number, and buoyancy parameter.

The study of turbine blade internal heat transfer should not be limited to square and rectangular channels. The cooling channels may have cross sections, which are not square or rectangular; the channels near the leading edge may have a triangular cross section, while channels near the trailing edge may also be triangular or trapezoidal.

Because channel flow has a wide variety of applications, many groups have experimentally investigated the heat transfer enhancement in a wide variety of cooling channels. Square and rectangular channels have been considered extensively, and additional work has been completed on other cross sections (i.e., triangular and trapezoidal). Contradictory results have been reported for triangular and trapezoidal cooling channels. The trends in equilateral triangles are similar to those in square and circular tubes [19–22]. However, the trends in triangular channels with small apex angles vary dramatically from circular tubes [23–25], while the trends in

trapezoidal channels can be predicted from smooth tube correlations [26,27]. The effect of rotation has been considered by many groups for square, rectangular, and triangular cooling channels; however, the effect of rotation has not been considered in the trapezoidal cooling channels.

Based on the data available in open literature, there is a clear need to investigate the effect of rotation in shaped, trailing edge cooling channels. Results have been obtained for square and rectangular channels, and limited results are available for triangular channels, which might appear near the leading edge of the channel. However, results are needed to fundamentally understand the effect of rotation in trailing edge cooling channels. To further the understanding of heat transfer in a trailing edge (wedge-shaped) cooling passage, it is necessary to know how the heat transfer enhancement changes from the wide side to the narrow side of the channel. Furthermore, it is necessary to extend the range of rotating data currently available in open literature. It is vital to validate the coupling of Reynolds number and rotational speed into the rotation number and buoyancy parameter. In an effort to validate the use of these parameters, it is necessary to extend the range of each beyond what is currently available to the engine designer. The present experimental investigation will parametrically study the effect of rotation in a wedge-shaped cooling passage over a wide range of rotation numbers (0–1.0) and buoyancy parameters (0–3.5).

Experimental Facility

Rotating Facility. The rotating facility previously used by Wright et al. [28] has recently undergone significant modification. Although the past decade has seen a number of studies focused on the effect of rotation in cooling passages, only a small portion of these studies include conditions, which are typically seen gas turbines, specifically aircraft engines. In other words, in an engine typically used for propulsion, the coolant may flow through the internal passages with a Reynolds number of approximately 50,000. With the blades rotating in the engine, the rotation number associated with the coolant is in the range of 0.2–0.3. Previous studies have attempted to replicate these rotation numbers by decreasing the Reynolds number and increasing the hydraulic diameter of the channel. Although this approach does allow researchers to replicate the nondimensional rotation number, this comes at the expense of decreased Reynolds numbers.

One method of obtaining the desired range of rotation numbers with the applicable Reynolds numbers is to run the laboratory experiments at increased pressures. With the coolant pressurized above atmospheric pressure, at a given mass flow rate (Reynolds number), the density increases while the coolant velocity decreases. The decreased velocity yields increased rotation numbers. Therefore, the existing facility was modified to incorporate a pressurized cooling loop.

As shown in Fig. 1, coolant is supplied to the rotating rig via a two-pass rotary union located at the base of the rig. Upstream of the rotary union, the coolant mass flow rate is measured with a square-edge ASME orifice meter. The coolant travels upward through insulated hose placed inside the existing, hollow shaft. The air is then ducted through the support head of the rotating arm, and an insulated hose transports the air to the test section contained within a pressure vessel located at the end of the rotating arm. The coolant passes through the test section, and the air travels through a second hose as it leaves the pressure vessel. The air travels through the support head, and downward through the hollow shaft (annularly outside the hose used to supply the coolant). The return air then passes through the rotary union and a ball valve is used to maintain the desired pressure of the cooling air.

As in the previous studies, a motor is used to drive the rotating arm. The motor is connected to a variable frequency drive, so the rotational speed of the arm can be varied. For the present study, the rotational speed varies from 0 rpm to 500 rpm. A 100-channel slip ring is located above the rotating arm to transfer thermo-

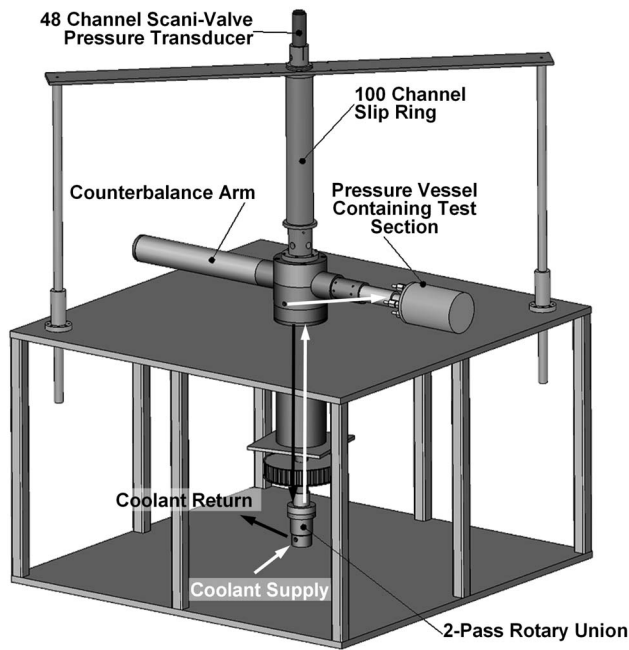


Fig. 1 Rotating test facility for internal turbine blade heat transfer studies

couple signals, pressure transducer signals, and resistance heater signals to the rotating arm. Mounted above the slip ring is a 48-channel Scani-Valve pressure transducer. The pressure transducer is used to monitor the pressure at the inlet of the test section (P_i).

Trailing Edge Test Section. As described previously, the objectives of this study are to investigate the effect of rotation within trailing edge cooling channels. As the objective of this study is to gain a fundamental understanding of flow in a wedge-shaped cooling passage, the use of turbulators is not investigated. Trailing edge cooling passages typically implore pin fins to enhance heat transfer while adding structural rigidity to the narrow passage. Investigators have shown that the effect of rotation is reduced in rotating, pin-fin channels [29]; in addition, it has been shown that spanwise variation in rotating channels is significantly reduced with the addition of pin fins in rectangular, trailing edge passages [30]. Modern gas turbine blades typically utilize trailing edge ejection or pressure side cutback cooling to protect the trailing edge of the blade. However, with this fundamental experimental investigation, the effect of ejection is not investigated. However, ejection should not be ignored completely. Previous investigators have shown how lateral injection affects the heat transfer coefficient distributions in the cooling channels [26,27]. The effect of bleed flow will also take on a second dimension in the rotating channel. As the coolant flow rate reduces due to the coolant ejection, the rotation number will increase; thus, the effect of rotation will increase from the root to the tip of the blade.

In order to fundamentally study the effect of rotation in a wedge-shaped passage, a new test section has been constructed to model a trailing edge cooling channel. Figure 2 shows the design of the present test section. The cross section of the channel is a wedge (or trapezoid). The sidewall (closer to the midspan of the blade) is 2.54 cm tall, and the cross section narrows to 0.32 cm near the trailing edge of the blade. The distance from the innermost side to the outermost side is 5.28 cm. If the channel were extended to form an isosceles triangle, the apex angle of the triangle would be 23.5 deg.

The heated length of the channel is 15.56 cm, and with a hydraulic diameter of 2.25 cm, this gives an overall heated length-to-hydraulic diameter ratio (L/D_h) of 6.30. The distance from the

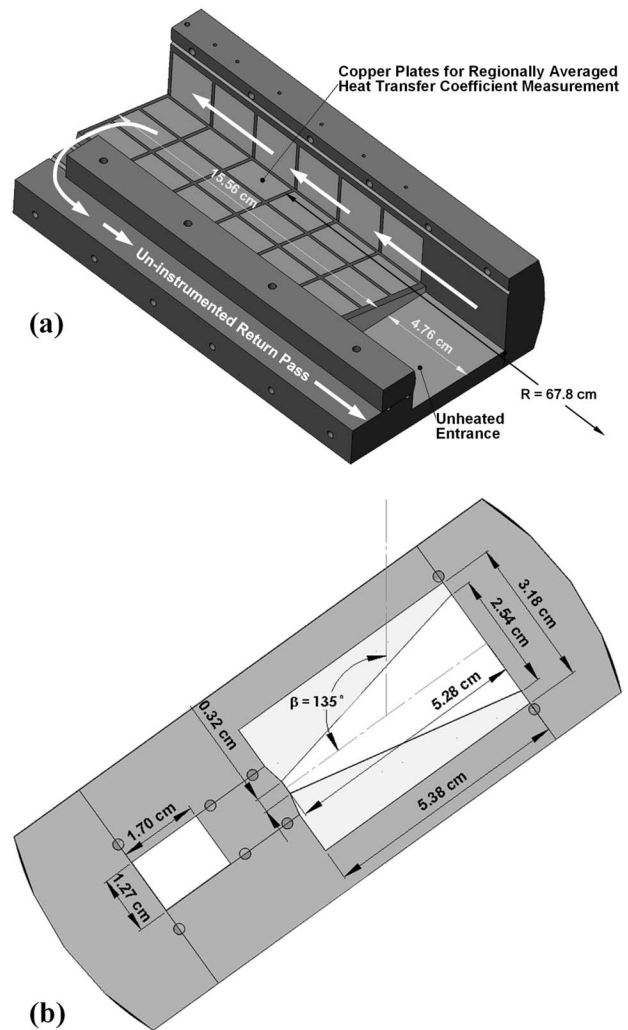


Fig. 2 Details of the wedge-shaped trailing edge test section

center of rotation to the center of the heated channel is 67.8 cm. To limit the complexities associated with the cooling channel, this study only considers the cooling passage with smooth walls (no turbulence promoters are used to enhance heat transfer). Prior to entering the heated length of the test section, the cooling air first enters the test section through the inlet plate of the pressure vessel. The air enters an unheated entrance with a rectangular cross section of 5.38 cm wide by 3.18 cm tall (as shaded in blue in Fig. 2(b)). Two mesh screens are positioned in this entrance region to help us spread the flow before it reaches the heated portion of the test section. With this entrance configuration, the air is forced through a sudden contraction as it enters the heated test section. Obviously, with the wedge-shaped cross section, the contraction ratio is much greater near the outer wall (9.9:1) of the test section than the inner wall (1.25:1). The length of entrance region is 4.76 cm.

Although only the first (radially outward) pass of the test section is instrumented for heat transfer coefficient measurements, a second pass is needed to return the flow, and maintain the desired pressure within the test section. This return pass has a rectangular cross section of 1.70 cm wide by 1.27 cm high. The flow turns 180 deg at the end of the first pass to travel into the return pass.

To measure the variation across the width (or span) of the channel, both the leading and trailing surfaces are divided into three regions. Figure 3 shows how these six regions combined with the inner sidewall give a total of seven regionally averaged heat trans-

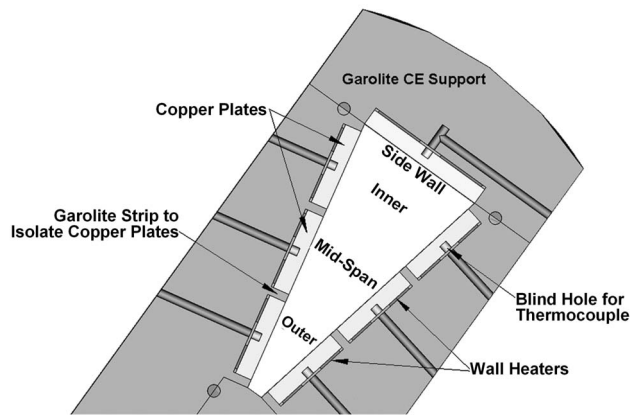


Fig. 3 Cross-sectional view of the trailing edge test section with experimental details

fer coefficient measurements. Each region consists of a single copper plate 0.318 cm thick. Each copper plate has a 0.159 cm blind hole in the back side with thermocouple mounted in the hole with high conductivity thermal epoxy. Six regions are used in the streamwise (flow) direction, so a total of 42 regions comprise the test section. The outermost wall (near the trailing edge) is left uninstrumented for the current study.

Electric resistance heaters are fixed beneath the copper plates. One heater services six copper plates; each spanwise region has an individual heater. In other words, one heater is used to heat all six copper plates of the sidewall, one heater is used for the six plates of the trailing inner surface, and so on. High conductivity paste is applied to each heater to minimize the contact resistance between the heater and the copper plates. The copper plates are mounted in the test section support structure, which is fabricated from grade CE garolite. The insulating material reduces the heat loss from the heaters to the support material. The test section is assembled and placed in the pressure vessel. Additional insulating material is used to fill the air gaps between the test section and the wall of the pressure vessel.

The coolant air enters the test section at six times the atmospheric pressure; this pressure is maintained for all cases, both stationary and rotating. The mass flow rate is varied, so the Reynolds number varies from 10,000 to 40,000. The channel is oriented similar to what is expected within the actual turbine blade; therefore, the channel is skewed 135 deg from the direction of rotation. The rotational speed of the channel is varied from 0 rpm to 500 rpm.

Data Reduction

As described with the experimental setup, regionally averaged heat transfer coefficients are measured in the current study. The regionally averaged heat transfer coefficients can be determined from Newton's law of cooling as follows:

$$h = \frac{\dot{Q}_{\text{net}}}{A(T_{w,x} - T_{b,x})} = \frac{\dot{Q}_{\text{in}} - \dot{Q}_{\text{loss}}}{A(T_{w,x} - T_{b,x})} \quad (1)$$

The net rate of heat transfer is determined from the difference of the power supplied to each resistance heater and the heat lost from the test section. The heat losses are determined from a calibration where insulation is inserted into the channel. Power is supplied to the heaters, and the power required to reach a series of given temperatures is recorded. With the insulating material placed inside the channel, the power supplied to the heaters during this calibration is equivalent to the heat lost during the actual cooling trials. Separate heat loss calibrations are required for each

rotational speed. At the lowest Reynolds number of 10,000, heat losses account for approximately 21% of the power supplied to each heater in the stationary channel and 23% in channel rotating at 500 rpm. However, when the Reynolds number increases to the maximum value of 40,000, the heat losses range from 8% in the stationary channel to 10% in the rotating channel (500 rpm).

The regional wall temperature ($T_{w,x}$) is measured using the thermocouple fixed in each copper plate. The coolant bulk temperature at a specific location ($T_{b,x}$) in the channel is determined based on the measured inlet and outlet temperatures. With thermocouples placed in the flow in the inlet section and downstream of the heated section, the inlet and outlet bulk temperatures are known. Therefore, the temperature of the coolant at any location within the channel can be calculated using linear interpolation. The outlet temperature measured by the thermocouple is compared to the value calculated using the energy balance method. Using the measured inlet temperature and the net power supplied to the cooling air, the temperature of the coolant can be calculated at any location within the channel (including the outlet). The interpolation and energy balance methods compare very well, and the difference between the two methods is generally less than to 2°C.

The measured heat transfer coefficients can be represented by the nondimensional Nusselt number. Although the Nusselt number is useful to extend the results from the laboratory to actual engine, it is often more useful to normalize the Nusselt number in order to quantify the heat transfer enhancement (or declination) due to either the specific channel geometry or rotation. The Nusselt number ratio is used to show the heat transfer enhancement relative to fully developed, turbulent heat transfer in a circular tube. This fully developed, turbulent heat transfer can be expressed with the Dittus-Boelter/McAdams correlation for heating. Equation (2) shows this Nusselt number ratio.

$$\frac{Nu}{Nu_0} = \left(\frac{hD_h}{k} \right) \left(\frac{1}{0.023 Re^{0.8} Pr^{0.4}} \right) \quad (2)$$

The experimental uncertainty for the presented results was calculated using the method developed and published by Kline and McClintock [31]. At the Reynolds number of 10,000, where the most uncertainty exists in the measured quantities, the overall uncertainty in the Nusselt number ratio is approximately 9.3% of the presented values. However, at the higher Reynolds numbers, the percent uncertainty of the individual measurements decreases, and the overall uncertainty in the Nusselt number ratio decreases to approximately 5% of the calculated value at the highest Reynolds number of 40,000.

Results and Discussion

The heat transfer in both stationary and rotating trailing edge cooling channels is considered. The stationary channel provides base line results before considering the effect of rotation. The heat transfer coefficients are measured at four different Reynolds numbers for each rotational speed. Figure 4 represents a matrix of the test conditions for the present study. In addition to depicting the Reynolds numbers and rotational speeds, this figure shows how these two quantities combine to form the rotation number. With the current experimental setup, rotation numbers up to 0.25 are achievable at the highest Reynolds number of 40,000.

As the discussion of the results progresses, it is important for the reader to bear in mind that the cross section of the channel is divided into seven regions. As shown in Fig. 5, these regions are the sidewall, leading inner, leading midspan, leading outer, trailing inner, trailing midspan, and trailing outer surfaces. As previously noted, the channel is oriented 135 deg from the direction of rotation. The orientation is applicable to cooling channels typically encountered near the trailing edge of the turbine blades. It should be noted that this orientation is defined with respect to the centerline of the channel.

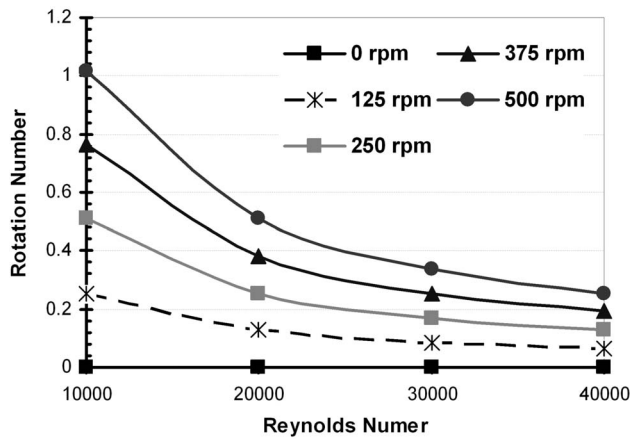


Fig. 4 Test case combinations with the resulting rotation numbers

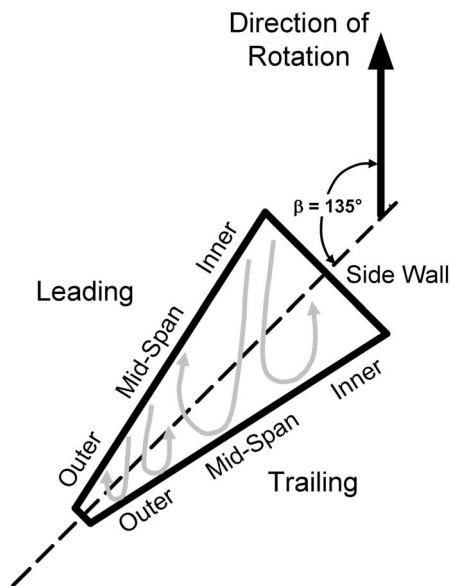


Fig. 5 Surface identification with a conceptual view of the rotation induced secondary flow

Heat Transfer in Stationary Channels. The current wedge-shaped channel used to model a typical trailing edge cooling channel combines several features, each of which has significant impacts on both the flow through the channel and the heat transfer within the channel. Therefore, it is beneficial to first consider stationary channels prior to rotating channels. In the nonrotating channel, the level of heat transfer is influenced by the channel shape. Deviating from a circular, square, or even rectangular channel results additional temperature variations across the channel cross section. With a much smaller cross section, the flow encounters more resistance near the outer surfaces than the inner surfaces of the channel. The coolant flow enters the heated portion of the test section without being hydrodynamically developed. Increased heat transfer coefficients are expected due to the simultaneous development of both the hydrodynamic and thermal boundary layers. Due to the relatively short length of the channel ($L/D_h = 6.30$), the flow likely never reaches a fully developed flow condition. An additional factor, which cannot be ignored, is the 180 deg turn used to return the flow out from the test section. Elevated heat transfer coefficients can be expected in the latter half of the channel due to the strong turn effect. The turn occurs on the outer edge of the channel.

The Nusselt number ratios for the stationary channel are shown in Fig. 6 to highlight the spanwise variation within the channel at a given Reynolds number. At any given Reynolds number, the greatest heat transfer enhancement at the inlet of the channel occurs on the inner surface, and the Nusselt number ratios are the least on the outer surface. Moving streamwise through the channel, the sidewall approaches the fully developed Nusselt number ratio of unity. Similar trends are present for the inner surface, but the level of enhancement is elevated above that of the sidewall. The Nusselt number ratios on the midspan and outer surfaces follow different trends. The strong effect of the 180 deg turn is very obvious when directly compared to the side and inner surfaces.

Additional comparisons can be made by averaging the Nusselt number ratios for each surface in the streamwise direction. The average heat transfer enhancement for each surface is compared over the range of Reynolds numbers in Fig. 7. In addition, the average Nusselt numbers in rectangular channels (4×1) with various entrance conditions are shown [11]. The fully developed Nusselt number ratios in the rectangular channel are approximately 1.25; these values are elevated above the fully developed value of one due to the thermal boundary layer development at the

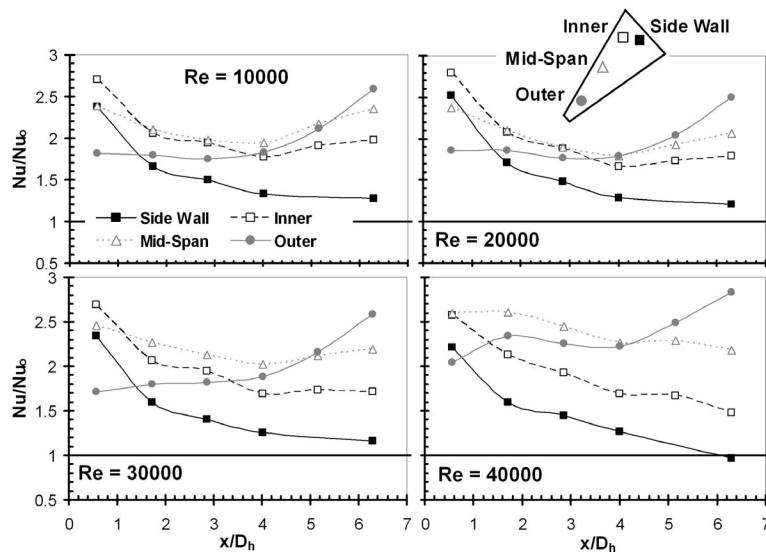


Fig. 6 Spanwise variation of the Nusselt number ratios in stationary channels

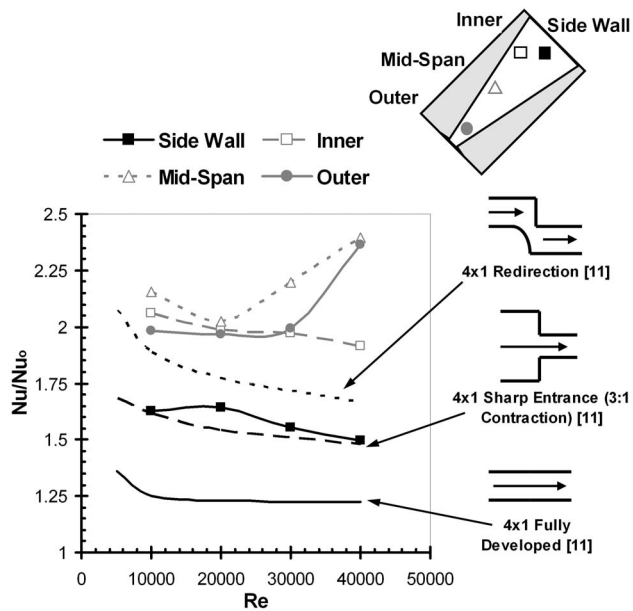


Fig. 7 Streamwise averaged Nusselt number ratios in stationary channels

entrance of the channel. With a sudden contraction, the heat transfer within the rectangular channel is clearly enhanced above that of the fully developed channel, and the heat transfer coefficients further increase with the redirected entrance. The heat transfer coefficients on the sidewall of the present, wedge-shaped channel are comparable to those in the rectangular channel with the sharp entrance. Although the contraction ratio in the present case is less than that for the rectangular channel, the flows are similar, yielding similar results. The average heat transfer coefficients on the midspan and outer surfaces decrease with increasing Reynolds number, up to a Reynolds number of 30,000. Beyond $Re = 30,000$, the Nusselt number ratios increase; this is a result of the increased enhancement through the entire length of the channel with the increased Reynolds number.

Heat Transfer in Rotating Channels. Before an in depth discussion of the effect of rotation in the trailing edge cooling passage is pursued, it is necessary to briefly discuss the general trends, which have been observed in rotating channels. For a rotating channel with radially outward flow, it has been well documented that the rotation induced Coriolis force combines with the rotation induced buoyancy force, so heat transfer enhancement is observed on the trailing surface of the channel. This enhancement comes at the expense of reduced heat transfer coefficients on the leading surface [3–5]. Depending on how the channel is oriented within the channel (with respect to the direction of rotation) and the cross section of the channel, the rotation induced secondary flow might be altered. In other words, studies have shown that the most significant declination of the heat transfer coefficients on the leading surface occur in square channels rotating orthogonal to the direction of rotation [3]. However, if the channel is skewed to the direction of rotation, the difference between the heat transfer coefficients on the leading and trailing surfaces is reduced [5]. Moreover, when a rectangular channels rotates at 135 deg, with respect to the direction of rotation, the heat transfer coefficients are enhanced on both the leading and trailing surfaces [10].

In the present study, the wedge-shaped channel rotates with $\beta = 135$ deg. It has already been shown that this specific geometry has many features, which combine to profoundly affect the heat transfer coefficients within the channel. However, it is necessary to consider how rotation affects the heat transfer through the channel. Traditional, conceptual descriptions of the rotation induced

secondary flow involve the formation of two counter-rotating vortices. The vortices form in the cross section of the channel as the coolant is forced away from the leading surface to the trailing surface [3,10]. Due to the wedge-shaped cross section of the present study, it is anticipated that there is not a distinct formation of these counter-rotating vortices. As shown in Fig. 5, this behavior is likely to occur within the wide half (near the sidewall and inner surfaces) of the channel. In other words, the coolant is forced away from the leading inner surface toward the trailing midspan and inner surfaces. In the very narrow region of the channel, these rotation induced vortices begin to breakdown, and no clear structure exists. Figure 5 conceptually shows how the secondary flow structure deteriorates, and a second (or even more) set of counter-rotating vortices forms. This structure breakdown will result in more turbulent mixing, and thus increased heat transfer coefficients of both the leading and trailing surfaces in the narrow region of the channel.

The presentation of the measured heat transfer coefficients begins with the streamwise distributions measured at each of the four Reynolds numbers at a set rotational speed of 500 rpm. As shown in Fig. 8, the heat transfer enhancement on each surface can be compared at each Reynolds number. As previously described, the rotational speed combines with the Reynolds number of the flow to form the nondimensional rotation number. Therefore, as the Reynolds number increases from 10,000 to 40,000, the rotation number decreases from 1.02 to 0.25. The isolated effect of these two parameters (Reynolds number and rotational speed) will soon be addressed.

At the lowest Reynolds number of 10,000 ($Ro=1.02$), the expected trend of nonsymmetrical heat transfer coefficient distributions is observed. In other words, more heat transfer enhancement is present on the trailing surfaces than the leading surfaces. In addition, the greatest difference between the leading and trailing surfaces occurs on the inner surfaces. In this wider area of the channel, the rotation induced secondary flow is much stronger, and organized, than in the more narrow section of the channel. In addition to the effect of rotation, the features inherent to the channel design are also present (entry region, 180 deg turn, and channel shape). As the Reynolds number increases (rotation number decreases), the Nusselt number ratios decrease. In addition, the difference between the leading and trailing surfaces decreases. As the Reynolds number increases to 40,000, the rotation number decreases to 0.25. The variation between the leading and trailing surfaces decreases as the rotation number decreases. This is most apparent with the outer surface. In this very narrow region of the channel, the heat transfer is enhanced above that of the stationary channel on both the leading and trailing surfaces due to the rotation induced mixing. However, the difference between the leading and trailing surfaces is minimized in this narrow region.

To fundamentally understand the effect of rotation, it is necessary to uncouple the Reynolds number effect from the effect of rotation. In order to do this, a series of tests have been completed with four Reynolds numbers over a range of rotational speeds. Figure 9 shows how the Nusselt number ratios vary with both varying Reynolds number and rotational speed. The Nusselt number ratios are presented at three specific locations within the channel: $x/D_h=1.7$, 4.0, and 6.3. Trends can most clearly be observed at $x/D_h=4.0$. This is the most likely candidate for fully developed flow, or is the least influenced by the contraction at the entrance and the turn at the outlet. Along the sidewall and inner surfaces, clearly, more heat transfer enhancement occurs on the trailing surface than the inner surface. Increasing the rotational speed increases the heat transfer enhancement for all four Reynolds numbers. However, moving to the midspan and outer surfaces, the only clear trend is that both the leading and trailing surfaces have increased heat transfer coefficients with the increased effect of rotation.

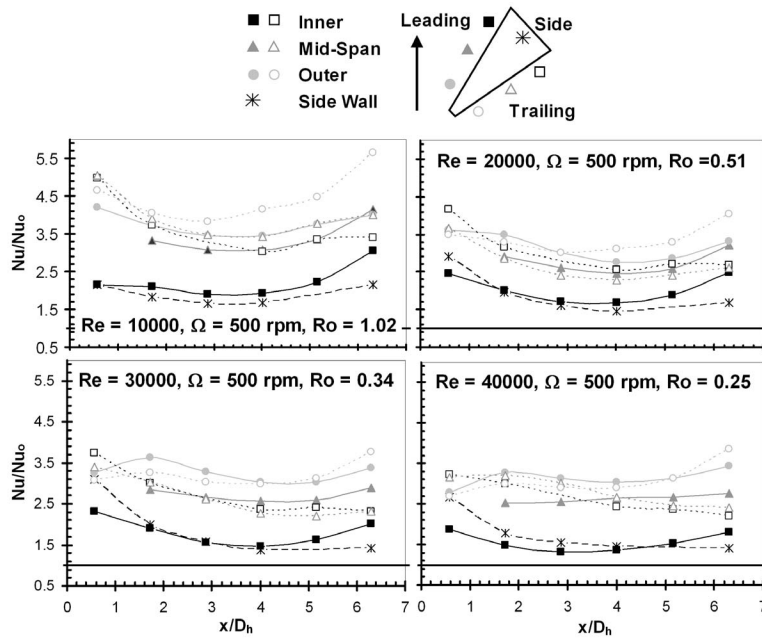


Fig. 8 Spanwise variation of the Nusselt number ratios in rotating channels (500 rpm)

Moving toward the inlet of the channel ($x/D_h=1.7$), the effect of rotation competes with the effect of the entrance condition. In the entry region of the channel, the Nusselt number ratios are elevated above those measured at a point downstream in the channel. However, the same general trend of increased heat transfer on all surfaces (both leading and trailing) is also apparent near the entrance of the channel. Near the exit of the channel ($x/D_h=6.0$), the heat transfer coefficients are influenced by the 180 deg

turn. Again, as the rotational speed increases, the heat transfer coefficients increase. However, there is no clear discernment between the leading and trailing surfaces. The Nusselt number ratios on the sidewall has a minimal impact from the 180 deg turn on the opposite side of the channel.

Presenting designers with heat transfer coefficients as a function of rotational speed has limited value, as the rotational speeds in the laboratory are not comparable with those of the actual engines. More useful information is shown in Fig. 10. These plots show the Nusselt number ratios at three locations in the channel as a function of the nondimensional rotation number. The rotation number is defined as

$$Ro = \frac{\Omega D_h}{V} \quad (3)$$

From Eq. (3), it is apparent how the rotational speed (Ω) and the Reynolds number (from the coolant velocity, V) combine to form the rotation number. In order to determine if various combinations of rotational speeds and coolant velocities result in the same Nusselt number (at the same rotation number), the rotational speed is varied from 0 rpm to 500 rpm, and the Reynolds number of the coolant varies from 10,000 to 40,000.

Again, we should first consider the location of $x/D_h=4.0$. Beginning with the sidewall and inner surfaces, the effect of Reynolds number has been eliminated. In other words, we have very distinct trends for the trailing inner surface, leading inner surface, and sidewall. Multiple points overlap where one rotation number is obtained from different combinations of Reynolds number and rotational speed. The Nusselt number ratios increase from the nonrotating channel to a maximum rotation number just greater than 1. More interesting results are observed for the sidewall and leading inner surface. Initially, the Nusselt number ratios begin decreasing with increasing rotational number. The trend continues until the rotation number reaches 0.3. Beyond the rotation number of 0.3, the heat transfer coefficients begin to increase. It is important to discuss this behavior because only a very limited number

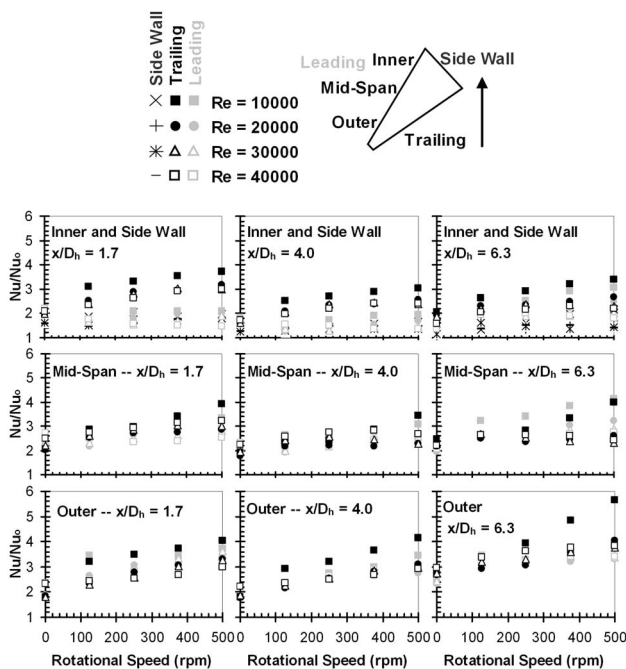


Fig. 9 Effect of rotational speed on the Nusselt number ratios in the entrance, fully developed, and exit regions of the channel

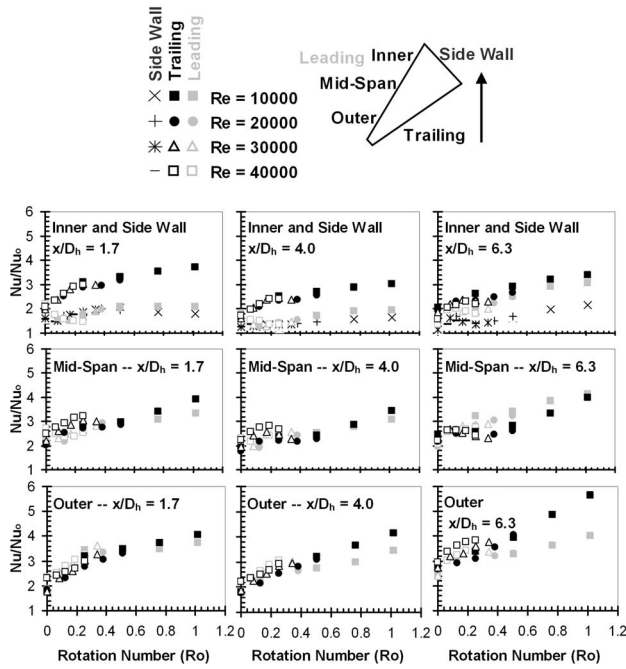


Fig. 10 Effect of rotation number on the Nusselt number ratios in the entrance, fully developed, and exit regions of the channel

of previous studies are applicable to rotation numbers greater than 0.3. It is positive information for designers to recognize that the heat transfer is enhanced on the leading surface at high rotation numbers.

The distinction between the leading and trailing surfaces diminishes in the more narrow regions of the channel. However, the leading and trailing surfaces can be distinguished on the outer surfaces, but not the midspan surface. Due to the breakdown of the rotation induced vortices, both the leading and trailing midspan surfaces benefit from rotation. With increased mixing of the coolant, both the leading and trailing surfaces experience the same level of heat transfer enhancement. In addition, for both the midspan and outer surfaces, the Nusselt number ratios increase as the rotation increases (over the entire range of rotation numbers) as a result of the channel shape and rotation angle. Similar trends are present in the entry region ($x/D_h=1.7$) and near the exit ($x/D_h=6.3$) of the channel. As noted previously, additional heat transfer enhancement occurs in these regions.

An additional way of presenting the Nusselt number ratios is as a function of the local buoyancy parameter. As shown in Eq. (4), the buoyancy parameter takes into account the rotation induced buoyancy force as well as the Coriolis force.

$$Bo_x = \left(\frac{\Delta\rho}{\rho} \right)_x Ro^2 \left(\frac{R_x}{D_h} \right) = \left(\frac{T_{w,x} - T_{b,x}}{T_{f,x}} \right) Ro^2 \left(\frac{R_x}{D_h} \right) \quad (4)$$

A similar validation is needed for the buoyancy parameter that is needed for the rotation number: Can the density ratio, rotation number, and rotating radius be varied independently, and with various combinations arrive at the same Nusselt number for the given buoyancy parameter? With the rotation number varying from 0.06 to 1.02, the local rotating radius varying from 61.5 cm to 74.2 cm, and the local density ratio varying from approximately 0.05 to 0.11, a single buoyancy parameter can be reached by several combinations of parameters. The local film temperature, $T_{f,x}$, is defined as the average of the local wall and coolant temperatures. Due to the temperature differences within the channel, the buoyancy forces act away from the center of rotation. The strength of this force is determined by the density (or temperature) difference in the fluid (from the heated wall to the

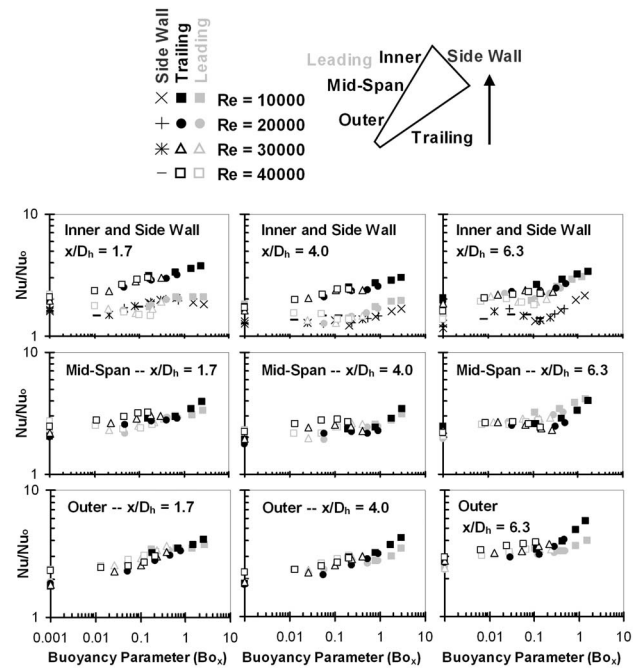


Fig. 11 Effect of buoyancy parameter on the Nusselt number ratios in the entrance, fully developed, and exit regions of the channel

cooler core). The local buoyancy parameter ranges from 0 (non-rotating channel) to 3.5. This nondimensional parameter is typically accepted as the preferred way to quantify the effect of rotation, as it includes all the parameters contributing to the effect of rotation.

Figure 11 presents the Nusselt number ratios plotted with the local buoyancy parameter. The trends, which were described in the previous figure for the different surfaces and channel locations, are again present in this figure. With the exception of the leading inner surface and sidewall, the heat transfer coefficients on all surfaces increase with the increasing buoyancy parameter. The Nusselt number ratios gradually decrease on the leading inner surface and sidewall until a critical buoyancy parameter is reached, and the Nusselt number ratios begin increasing.

The data have been presented for three specific locations within the channel. However, it is beneficial to observe the effect of rotation on the overall heat transfer enhancement. To begin this process, the Nusselt number ratios for each surface are averaged in the streamwise direction. Figure 12 shows these streamwise averages, where each data represent the average of the six streamwise regions, plotted with the rotation number. In addition to the results of this current study, the Nusselt number ratios obtained in a rotating, 4×1 rectangular channel with either a sudden contraction or redirected entrance are shown for comparison [11]. The trends observed in this figure are very similar to those observed with $x/D_h=4.0$. However, the levels of enhancement are elevated due to the increased heat transfer coefficients at the entrance and exit of the channel.

The leading inner surface of the current channel exhibits the same level of heat transfer enhancement and trends as the 4×1 rectangular channel with both a sharp entrance (contraction) and a redirected entrance. However, the level of enhancement on the trailing surface of the present wedge-shaped channel is much greater than that of the rectangular channel. This is likely due to the difference in the distance between the leading and trailing surfaces of the two channels. For this present trailing edge channel, the distance between the leading and trailing surfaces varies from 2.54 cm (at the sidewall) to 1.8 cm (adjacent to the midspan). In the rectangular channel, the distance between the leading

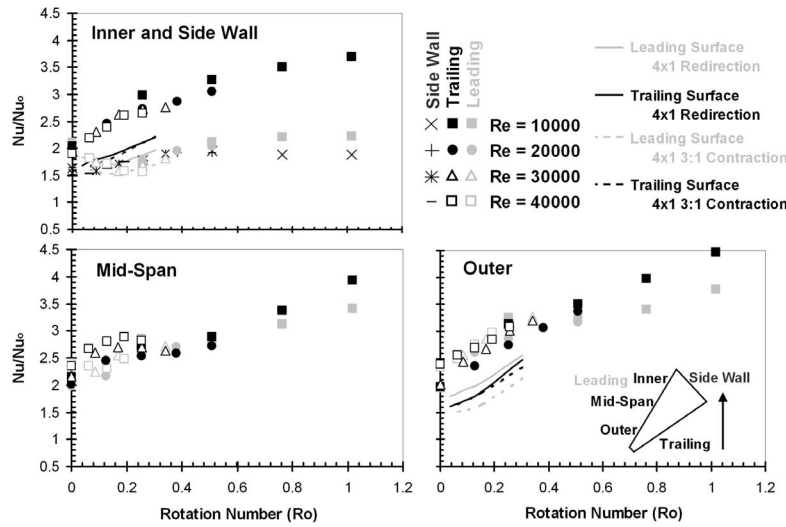


Fig. 12 Effect of rotation number on the streamwise averaged Nusselt number ratios

and trailing surfaces is 1.27 cm. With the increased distance, the rotation induced vortices possibly gain strength, and thus lead to additional heat transfer enhancement on the trailing surface. The heat transfer coefficients on the outer surfaces of the present channel are much higher than those corresponding to the rectangular channel. In the current channel, the contraction ratio for the outer surface varies from 3.0:1 up to 9.9:1; this is compared to the contraction of 3.0:1 for the rectangular channel. This large contraction ratio has a very profound effect on the heat transfer coefficients through the entire length of the channel. Figure 13 shows these streamwise averages plotted with the streamwise averaged buoyancy parameter; just as the Nusselt number ratios are averaged over six streamwise locations, the local buoyancy parameters are also averaged. As it has been shown on the previous figures, the buoyancy parameter is an excellent parameter for correlating the varying Reynolds number and rotational speed.

It has been established that the heat transfer enhancement varies across the span of the channel from the sidewall to the outer surfaces. Up until now, each surface maintained its individual identity. However, the inner, midspan, and outer surfaces can be averaged to yield an average value for both the leading and trail-

ing surfaces. The spanwise and streamwise averaged Nusselt number ratios are shown in Fig. 14. Each data point (on the leading and trailing surfaces) is now the average of 18 measured heat transfer coefficients shown as a function of the rotation number. Over the range of Reynolds numbers and rotational speeds, each of the three surfaces follows very distinct trends with the data for each surface collapsing to a common curve. Most notably is that for all three surfaces, the Nusselt number ratios increase as the rotation number increases. These results are also present in Fig. 15 with the averaged buoyancy parameters. With the very distinct trends present for each surface, correlations have been generated for the Nusselt number ratios as a function of the buoyancy parameter. The data can be represented by Eq. (5), and Table 1 shows the constants for each surface.

$$\frac{Nu}{Nu_0} = ABo^m + BBo^n \quad (5)$$

Even with the nonsymmetrical wedge-shaped channel, the skewed direction of rotation number, the variable Reynolds num-

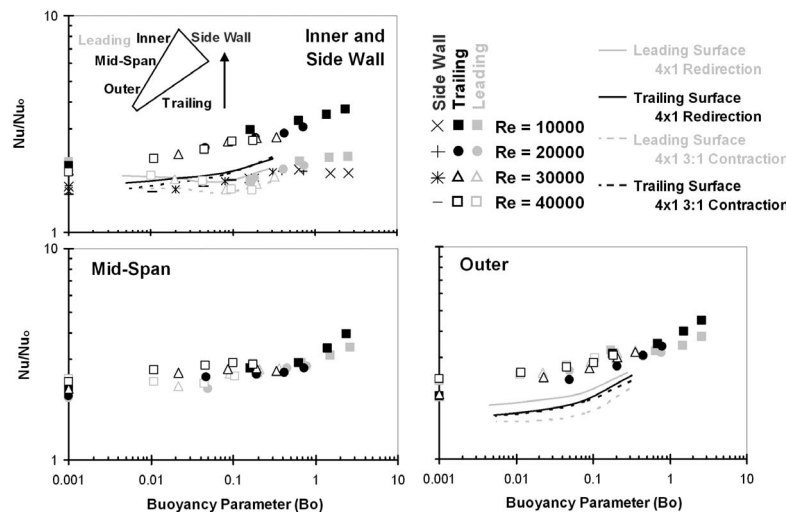


Fig. 13 Effect of buoyancy parameter on the streamwise averaged Nusselt number ratios

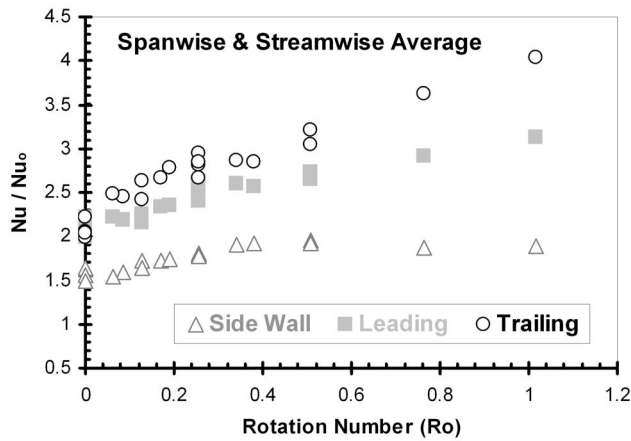


Fig. 14 Effect of rotation number on the streamwise and spanwise averaged Nusselt number ratios

ber, and the changing rotational speed, the data can be expressed with a simple correlation expressing the heat transfer enhancement as a function of the buoyancy parameter.

Conclusions

This study was initiated to extend the study of heat transfer in rotating channels. It is necessary for designers to have access to heat transfer results, which represent engine-like flow conditions (i.e. high rotation numbers obtained at high Reynolds numbers). In addition to extending the range of available data, this study also incorporates a realistic cooling passage located near the trailing edge of the turbine blade. The regional heat transfer coefficients have been measured in a wedge-shaped trailing edge cooling passage with the Reynolds number varying from 10,000 to 40,000, and the rotational speed varying from 0 rpm to 500 rpm. The following conclusions have been drawn from the current study.

- (1) In the stationary, wedge-shaped channel, the heat transfer

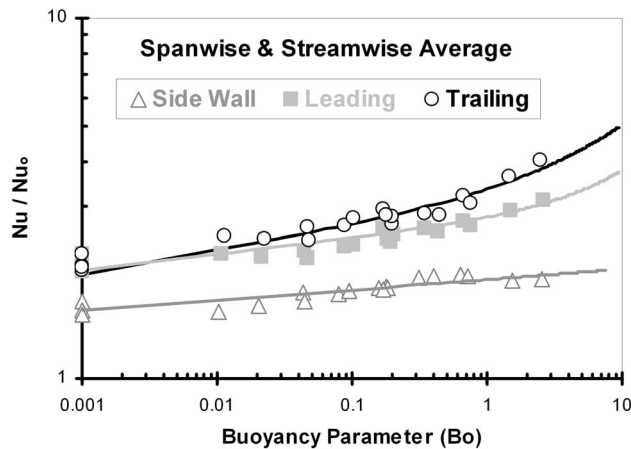


Fig. 15 Effect of buoyancy parameter on the streamwise and spanwise averaged Nusselt number ratios

Table 1 Correlation constants for average heat transfer enhancement

	A	m	B	n
Leading surface	2.7	0.043	0.1	0.9
Trailing surface	3.05	0.065	0.3	0.7
Sidewall	1.88	0.029	0	—

coefficients vary in both the streamwise and spanwise directions. The contraction entrance (with a varying contraction ratio) enhances the heat transfer in the entry region of the channel, while near the exit of the channel, the heat transfer coefficients increase due to the 180 deg turn. Very different trends are observed from the sidewall to the outer surface as the channel becomes narrower, and the heat transfer coefficients are dependent on both the spanwise position and the Reynolds number.

- (2) Both the rotation number and buoyancy parameter can be used to quantify the effect of rotation. The current parameter variation shows that the Reynolds number or rotational speed can be varied to achieve a specific rotation number, and both scenarios result in the same heat transfer coefficients.
- (3) The inner surfaces of the rotating channel are most significantly affected by rotation. In this wide section of the channel, the rotation induced secondary flow is most clearly defined.
- Although the heat transfer coefficients on the leading surface initially decrease with the increasing buoyancy parameter, beyond a critical value, the heat transfer coefficients begin to increase with rotation.
- (4) Due to the skewed angle of rotation ($\beta=135$ deg), the heat transfer coefficients on all surfaces are enhanced with rotation.

Although this study has covered a wide range of flow and rotating conditions in a shaped, trailing edge cooling passage, additional effort is needed to more completely understand trailing edge cooling passages. This study measured the heat transfer coefficients in a smooth channel. However, turbine cooling passages are typically lined with turbulence promoters to enhance heat transfer. In addition, the coolant through trailing edge cooling passages is likely to be extracted for trailing edge ejection, either through discrete hole or slots, to further protect the trailing edge of the blade. These factors are likely to have a profound effect on heat transfer in shaped, trailing edge cooling channels and are the focus of future studies.

Acknowledgment

This work has been funded through the Marcus Easterling Endowment Fund.

Nomenclature

- A = area of smooth wall
- AR = aspect ratio of square and rectangular channels
- Bo_x = local buoyancy parameter, $(\Delta\rho/\rho)_x Ro^2 (R_x/D_h)$
- D_h = hydraulic diameter
- H = channel height
- h = heat transfer coefficient
- k = thermal conductivity of coolant
- Nu = local Nusselt number, hD_h/k
- Nu_0 = Nusselt number for fully developed turbulent flow in a smooth pipe
- P_i = pressure at the inlet of the test section
- Pr = Prandtl number
- Q = heat transfer rate at wall
- R = mean rotating radius (from center of rotation to center of heated channel)
- R_x = local rotating radius (from center of rotation to local region within heated channel)
- Re = Reynolds number, $\rho V D_h / \mu$
- Ro = rotation number, $\Omega D_h / V$
- $T_{b,x}$ = local coolant temperature
- $T_{f,x}$ = local film temperature ($T_{f,x} = (T_{b,x} + T_{w,x}) / 2$)
- $T_{w,x}$ = local wall temperature
- V = bulk velocity in streamwise direction

- W = channel width
 β = angle of channel orientation with respect to the axis of rotation
 μ = dynamic viscosity of coolant
 ρ = density of coolant
 $(\Delta\rho/\rho)_x$ = local coolant-to-wall density ratio
 Ω = rotational speed

References

- [1] Han, J. C., Dutta, S., and Ekkad, S. V., 2000, *Gas Turbine Heat Transfer and Cooling Technology*, Taylor and Francis, New York.
- [2] Kays, W. M., and Crawford, M. E., 1993, *Convective Heat and Mass Transfer*, 3rd ed., McGraw-Hill, New York, pp. 311–349.
- [3] Wagner, J. H., Johnson, B. V., and Hajek, T. J., 1991, “Heat Transfer in Rotating Passage With Smooth Walls and Radial Outward Flow,” *ASME J. Turbomach.*, **113**, pp. 42–51.
- [4] Wagner, J. H., Johnson, B. V., and Kopper, F. C., 1991, “Heat Transfer in Rotating Passage With Smooth Walls,” *ASME J. Turbomach.*, **113**, pp. 321–330.
- [5] Johnson, B. V., Wagner, J. H., Steuber, G. D., and Yeh, F. C., 1994, “Heat Transfer in Rotating Serpentine Passage With Selected Model Orientations for Smooth or Skewed Trip Walls,” *ASME J. Turbomach.*, **116**, pp. 738–744.
- [6] Dutta, S., and Han, J. C., 1996, “Local Heat Transfer in Rotating Smooth and Ribbed Two-Pass Square Channels With Three Channel Orientations,” *ASME J. Heat Transfer*, **118**, pp. 578–584.
- [7] Park, C. W., and Lau, S. C., 1998, “Effect of Channel Orientation of Local Heat (Mass) Distributions in Rotating Two-Pass Square Channel With Smooth Walls,” *ASME J. Heat Transfer*, **120**, pp. 624–632.
- [8] Bons, J. P., and Kerrebrock, J. L., 1999, “Complementary Velocity and Heat Transfer Measurements in a Rotating Cooling Passage With Smooth Walls,” *ASME J. Turbomach.*, **121**, pp. 651–662.
- [9] Azad, G. S., Uddin, M. J., Han, J. C., Moon, H. K., and Glezer, B., 2002, “Heat Transfer in a Two-Pass Rectangular Rotating Channel With 45-Deg Angled Rib Turbulators,” *ASME J. Turbomach.*, **124**, pp. 251–259.
- [10] Griffith, T. S., Al-Hadhrani, L., and Han, J. C., 2002, “Heat Transfer in Rotating Rectangular Cooling Channels ($AR=4$) With Angled Ribs,” *ASME J. Heat Transfer*, **124**, pp. 617–625.
- [11] Wright, L. M., Lee, E., and Han, J. C., 2005, “Influence of Entrance Geometry on Heat Transfer in Rotating Rectangular Cooling Channels ($AR=4:1$) With Angled Ribs,” *ASME J. Heat Transfer*, **127**(4), pp. 378–387.
- [12] Acharya, S., Agarwal, P., and Nikitopoulos, D. E., 2004, “Heat/Mass Transfer in a 4:1 AR Smooth and Ribbed Coolant Passage With Rotation in 90-Degree and 45-Degree Orientations,” ASME Paper No. GT2004-53928.
- [13] Zhou, F., Lagrone, J., and Acharya, S., 2004, “Internal Cooling in 4:1 AR Passages at High Rotation Numbers,” ASME Paper No. GT2004-53501.
- [14] Willett, F. T., and Bergles, A. E., 2001, “Heat Transfer in Rotating Narrow Rectangular Ducts With Heated Sides Orientated at 60° to the R-Z Plane,” *ASME J. Turbomach.*, **123**, pp. 288–295.
- [15] Cho, H. H., Kim, Y. Y., Kim, K. M., and Rhee, D. H., 2003, “Effects of Rib Arrangements and Rotation Speed on Heat Transfer in a Two-Pass Duct,” ASME Paper No. 2003-GT-38609.
- [16] Agarwal, P., Acharya, S., and Nikitopoulos, D. E., 2003, “Heat/Mass Transfer in 1:4 Rectangular Passages With Rotation,” ASME Paper No. 2003-GT-38615.
- [17] Fu, W. L., Wright, L. M., and Han, J. C., 2005, “Heat Transfer in Two-Pass Rotating Rectangular Channels ($AR=1:2$ and $AR=1:4$) With Smooth Walls,” *ASME J. Heat Transfer*, **127**(3), pp. 265–277.
- [18] Fu, W. L., Wright, L. M., and Han, J. C., 2005, “Buoyancy Effects on Heat Transfer in Five Different Aspect-Ratio Rectangular Channels With Smooth Walls and 45-Degree Ribbed Walls,” ASME Paper No. GT 2005-68493.
- [19] Lowdermilk, W. H., Weiland, W. F., and Livingood, J. N. B., 1954, “Measurement of Heat Transfer and Friction Coefficients for Flow of Air in Noncircular Ducts at High Surface Temperatures,” NACA RM E53J07.
- [20] Ahn, S. W., and Son, K. P., 2002, “Heat Transfer and Pressure Drop in the Roughened Equilateral Triangular Duct,” *Int. Commun. Heat Mass Transfer*, **29**, pp. 479–488.
- [21] Obot, N. T., 1985, “Heat Transfer in a Smooth Scalene Triangular Duct With Two Rounded Corners,” *Int. Commun. Heat Mass Transfer*, **12**, pp. 251–258.
- [22] Zhang, Y. M., Gu, W. Z., and Han, J. C., 1994, “Augmented Heat Transfer in Triangular Ducts With Full and Partial Ribbed Walls,” *J. Thermophys. Heat Transfer*, **8**, pp. 574–579.
- [23] Eckert, E. R. G., and Irvine, T. F., 1960, “Pressure Drop and Heat Transfer in a Duct With Triangular Cross Section,” *ASME J. Heat Transfer*, **82**, pp. 125–138.
- [24] Ainsworth, R. W., and Jones, T. V., 1979, “Measurements of Heat Transfer in Circular, Rectangular, and Triangular Ducts, Representing Typical Turbine Blade Cooling Passages Using Transient Techniques,” ASME Paper No. 79-GT-40.
- [25] Rohsenow, W. M., Hartnett, J. P., and Cho, Y. I., 1998, *Handbook of Heat Transfer*, 3rd ed., McGraw Hill, Boston, MA.
- [26] Taslim, M. E., Li, T., and Spring, S. D., 1995, “Experimental Study of the Effects of Bleed Holes on Heat Transfer and Pressure Drop in Trapezoidal Passages With Tapered Turbulators,” *ASME J. Turbomach.*, **117**, pp. 281–289.
- [27] Hwang, J. J., and Lu, C. C., 2001, “Lateral-Flow Effect on Endwall Heat Transfer and Pressure Drop in a Pin Fin Trapezoidal Duct With Various Pin Shapes,” *ASME J. Turbomach.*, **123**, pp. 133–139.
- [28] Wright, L. M., Fu, W. L., and Han, J. C., 2004, “Thermal Performance of Angled, V-Shaped, and W-Shaped Rib Turbulators in Rotating Rectangular Cooling Channels ($AR=4:1$),” ASME Paper No. GT 2004-54073.
- [29] Willet, F. T., and Bergles, A. E., 2002, “Heat Transfer in Rotating Narrow Rectangular Pin-Fin Ducts,” *Exp. Therm. Fluid Sci.*, **25**, pp. 573–582.
- [30] Wright, L. M., Lee, E., and Han, J. C., 2004, “Effect of Rotation on Heat Transfer in Rectangular Channels With Pin-Fins,” *J. Thermophys. Heat Transfer*, **18**, pp. 263–272.
- [31] Kline, S. J., and McClintock, F. A., 1953, “Describing Uncertainty in Single-Sample Experiments,” *Mech. Eng. (Am. Soc. Mech. Eng.)*, **75**, pp. 3–8.

Lesley M. Wright
Department of Aerospace and Mechanical
Engineering,
The University of Arizona,
Tucson, AZ 85721-0119

Zhihong Gao

Huitao Yang

Je-Chin Han

Distinguished Professor and Marcus Easterling
Endowed Chair
e-mail: jc-han@tamu.edu

Turbine Heat Transfer Laboratory,
Department of Mechanical Engineering,
Texas A&M University,
College Station, TX 77843-3123

Film Cooling Effectiveness Distribution on a Gas Turbine Blade Platform With Inclined Slot Leakage and Discrete Film Hole Flows

A five-blade, linear cascade is used to experimentally investigate turbine blade platform cooling. A 30 deg inclined slot upstream of the blades is used to model the seal between the stator and rotor, and 12 discrete film holes are located on the downstream half of the platform for additional cooling. The film cooling effectiveness is measured on the platform using pressure sensitive paint (PSP). Using PSP, it is clear that the film cooling effectiveness on the blade platform is strongly influenced by the platform secondary flow through the passage. Increasing the slot injection rate weakens the secondary flow and provides more uniform film coverage. Increasing the freestream turbulence level was shown to increase film cooling effectiveness on the endwall, as the increased turbulence also weakens the passage vortex. However, downstream, near the discrete film cooling holes, the increased turbulence decreases the film cooling effectiveness. Finally, combining upstream slot flow with downstream discrete film holes should be cautiously done to ensure coolant is not wasted by overcooling regions on the platform.

[DOI: 10.1115/1.2907440]

Keywords: forced convection, film cooling, gas turbine heat transfer

Introduction

As economies across the world continue to grow, the demand for power also continues to increase. Commercial, industrial, and residential customers have come to expect uninterrupted electrical service required to meet a variety of needs; however, the demand for power is growing faster than the power supply. Meanwhile, the commercial airline industry is facing numerous hurdles while the military is facing new challenges. The common bond between land based power generation and aircraft propulsion is gas turbine engines. With gas turbines also being used for marine propulsion and scores of other specific industrial applications, it is vital that these engines efficiently operate. The efficiency of a gas turbine engine can be increased by raising the temperature of the hot gases at the inlet of the turbine. However, increasing the temperature of the mainstream gas must be cautiously done, as additional problems can develop. The metallic turbine components must be protected in order to survive prolonged exposure to the hot gases. The life of the turbine airfoils can be increased by implementing any of a variety of cooling techniques. As presented by Han et al. [1], air is extracted from the compressor, and used to cool the airfoils. This coolant air is injected into the hollow airfoils, and circulates through internal cooling passage of the blades and vanes. The coolant is discharged through discrete holes, where it forms a protective film on the outer surface of the airfoil. Many investigations have focused on increasing the heat transfer enhancement within the blades via rib turbulators, jet impingement, and pin fins. Also, film cooling has been studied for many years to determine the optimal hole configuration and flow conditions to maximize the protection of the coolant.

With the increasing temperature of the mainstream gases exiting the combustor, the stator vanes and rotor blades must be protected, so that they can survive the extreme temperatures. Recently, the blade platform has received renewed attention for an adequate cooling scheme. The vane endwall and the blade platforms comprise a large percentage of the area exposed to the hot mainstream gases. There is a strong potential for "hot spots" to form on the endwalls and platforms. Over this large area, it is vital to have accurate heat transfer distributions, so that efficient cooling schemes can be developed. The cooling schemes should adequately protect the platforms while minimizing the amount of coolant.

A general review of platform (endwall) flow, heat transfer, and film cooling has been completed by Han et al. [1] and Chyu [2]. Several of the papers reviewed by these sources will be considered along with other papers to develop a foundation for platform flow and heat transfer. The secondary flow in a turbine passage is very complex and varies based on the blade profile being considered. Langston et al. [3,4] performed flow measurements to gain insight into this complex secondary flow. They showed at the inlet of the passage, the boundary splits at the leading edge of the blade. A horseshoe vortex forms with one leg on the pressure side of the blade, and the other leg on the suction side of the blade (in the adjacent passage). The pressure side leg of the horseshoe vortex travels from the pressure side of the passage to the suction side; this pressure side leg of the horseshoe vortex becomes known as the passage vortex. This passage vortex will eventually meet the suction side leg of the horseshoe vortex that has remained near the junction of the suction surface and endwall. Spores and Goldstein [5] also studied the flow through a blade passage. They identified multiple "corner" vortices that developed throughout the passage. A pressure side corner vortex develops just downstream of the leading edge, and the vortex carries about one-third of the chord length. Two suction side corner vortices develop along the suction surface in the latter half of the passage.

Contributed by the Heat Transfer Division of ASME for publication in the JOURNAL OF HEAT TRANSFER. Manuscript received February 22, 2007; final manuscript received June 11, 2007; published online May 19, 2008. Review conducted by Gautam Biswas.

After the passage vortex carries to the suction side of the passage, it lifts from the endwall surface. Below the passage vortex, along the junction where the suction surface meets the endwall, suction side, counter rotating, corner vortices form.

The highly complex, three-dimensional flow has a strong influence on the heat transferred from the mainstream flow to the blade platform. Blair [6] pioneered the study of endwall heat transfer. He found significant variation of the heat transfer coefficient across the passage and downstream to the trailing edge of the vane due to the secondary flow along the endwall. Graziani et al. [7] also reported large variations in the endwall heat transfer coefficients. They showed that the heat transfer coefficients on the suction surface of the blade are also influenced by the secondary flow through the passage; however, the heat transfer coefficients on the pressure surface are not affected by the strong secondary flows. Using a mass transfer technique, Goldstein and Spores [5] showed that as the boundary layer splits to form the two legs of the horseshoe vortex near the leading edge of the blades, the heat transfer coefficients increase, and the greatest heat transfer enhancement on the endwall occurs near the leading edge. Other variations are present on the endwall due to the path of the passage and corner vortices. In addition near the trailing edge of the blade, the heat transfer coefficients are elevated as the two flows from the two passages meet at the trailing edge. The heat transfer coefficients were also measured on the endwall of a vane passage [8–10]. Similar variations were found, as the heat transfer continues to be dominated by the secondary flow. When the effect of freestream turbulence was considered [9,10], it was found that increasing the turbulence intensity increases the heat transfer coefficients on the passage endwall. However, the effect of the freestream turbulence intensity was minimal near the leading edge and near the suction surface, where the horseshoe and passage vortices dominate the heat transfer behavior.

With the local areas of high heat transfer identified, film cooling can be implemented on the blade platform to reduce the heat load in these areas. Takieshi et al. [11] obtained heat transfer and film effectiveness distributions on a vane endwall with discrete film cooling holes placed at three locations in the passage. They found that the effectiveness is very low near the leading edge on the suction side; with the rollup of the horseshoe vortex, the film coolant lifted from the surface, and offered little or no protection. The path of the coolant was also influenced by the passage vortex transporting the coolant from the pressure to the suction side of the passage. Harasgama and Burton [12] used film cooling near the leading edge, just inside the passage, with the film cooling holes located along an iso-Mach line. Although the row of film cooling holes was evenly distributed to span the passage, no coolant reached the pressure side of the passage. The film cooling configuration used by Jabbari et al. [13] consisted of discrete holes placed on the downstream half of the passage. Similar to the upstream design [12], the film cooling effectiveness significantly varied through the passage, with the coolant moving to the suction side of the passage.

Friedrichs et al. [14–16] studied the film cooling effectiveness using the ammonia and diazo technique. They found that a simple layout of the film cooling holes throughout the passage can result in areas being overcooled (or undercooled) due to the secondary flow. With their proposed “improved design,” the film holes were placed, so the strong secondary flow could be advantageously used. Using the same amount of coolant, they were able to provide improved coolant coverage. Recently, Barizozzi et al. [17] compared the film cooling effectiveness on a passage endwall with cylindrical or fan-shaped film cooling holes. With their cooling designs, they showed that by increasing the blowing ratios, the passage vortex is weakened, and the passage cross flow is reduced; therefore, coolant coverage is more uniform across the passage. Similar to flat plate film cooling, shaped film cooling holes offer better protection than cylindrical holes.

A similarity between the vane endwall and the blade platform is

the existence of slot (or gap) upstream of the airfoil leading edge. A gap is commonly in place in the transition from the combustion chamber to the turbine vane (stator). Similarly, a gap exists between the stator and rotor, so the turbine disk can freely rotate. To prevent ingestion of the hot mainstream gases, it is a common practice to inject coolant air through these slots. If this preventive measure is utilized properly, unnecessary discrete film holes can be eliminated, so coolant is not wasted by overcooling areas on the rotating platform. Blair [6] also measured the film cooling effectiveness with upstream injection in his pioneering study; he showed large variations in the film cooling effectiveness over the entire passage due to the strong secondary flow. Roy et al. [18] placed coolant slots upstream of their vane. They showed that the heat transfer near the leading edge was reduced due to the secondary air injection. Because the slots were directly placed upstream of the blades, a large area in the center of the passage did not receive adequate film cooling coverage. Slot injection has been the focus of many studies performed at the University of Minnesota [19–21]. They found that using slots, which span the majority of the passage upstream of their vanes, can provide film coverage over most of the passage to the trailing edge of the vane [19,20]. They also found that increasing the amount of coolant through the slot can reduce the effect of the secondary flow. In addition, strategically blocking the slot, so the coolant does not exit the slot that uniformly provides thermal advantages (and disadvantages) [21].

The heat transfer coefficients and the film cooling effectiveness were measured on the endwall of a vane passage with film cooling combined with upstream slot injection by Nicklas [22]. They found that in the upstream region, the film cooling effectiveness was elevated due to the large amount of cooling flow from the slot. However, the effectiveness near the discrete holes located near the center of the passages suffered due to the passage vortex. Liu et al. [23] used a high volume of discrete holes upstream of their vanes to emulate the effect of upstream slot injection. They determined that the film cooling effectiveness was primarily affected by the blowing ratio of the injection; in addition, as the blowing ratio increases, the uniformity of the coverage increases.

The film cooling effectiveness has been measured using the pressure sensitive paint by Zhang and Jaiswal [24] and Zhang and Moon [25]. They first measured the effectiveness with two upstream injection geometries: two rows of discrete holes and a single row slot. The effect of a backward facing step was also considered with the discrete hole configuration. They confirmed that increasing the coolant flow can significantly increase the effectiveness, and they reported that the use of a backward step significantly decreases the effectiveness within the passage. Knost and Thole [26] showed that with increased slot flow, the critical areas of the leading edge and pressure side junction can be adequately cooled. Cardwell et al. [27] extended this work to include midpassage misalignment. With the misalignment that may occur between the two adjacent vanes, the film cooling effectiveness is dramatically reduced.

With the secondary flow strongly influencing both the heat transfer coefficients and the film cooling effectiveness on the platform surface, recently, efforts have been directed at mitigating this destructive secondary flow. One method that is gaining popularity is endwall contouring [28,29]. Han and Goldstein [30] observed that with a fillet around the leading edge of the blade, the horseshoe vortex disappears, and the formation of the passage vortex is delayed with elevated turbulence intensity. However, with low freestream turbulence, the strength of the passage vortex is comparable to that in a passage without the fillet. The drawback of the fillet is the increased heat transfer near the leading edge on the pressure side due to the intensified corner vortices.

In recent years, the blade platform has received renewed attention. Efforts have involved providing adequate protection on the passage between two adjacent blades or vanes. This involves investigating a wide range of discrete film hole configurations while

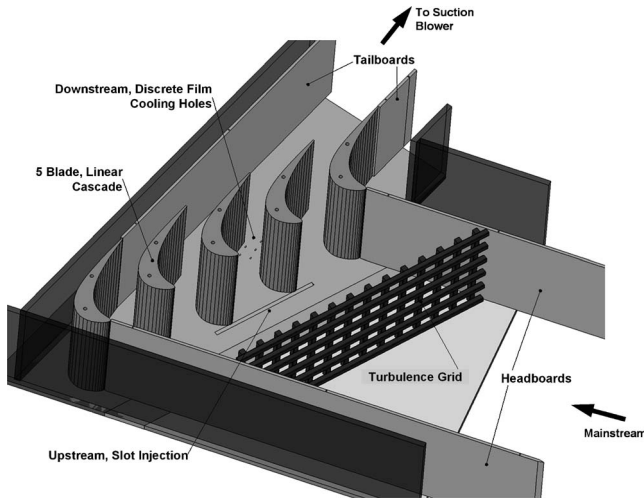


Fig. 1 Overview of the low speed wind tunnel used to study platform cooling

making use of inherent engine construction, such as gaps between the combustor and inlet guide vane or between the stator and rotor. With new measurement techniques that can more accurately obtain detailed film cooling effectiveness distributions, it is vital to further extend the study of endwall film cooling effectiveness. The majority of studies are performed in a linear vane cascade. Although the general flow behavior around the vanes and blades is similar, the detailed film cooling effectiveness measurements on the endwall of a linear blade cascade are limited. Therefore, the current study will utilize a range of flow conditions to gain valuable insight into the secondary flow behavior around a high pressure blade. With a more complete understanding of the secondary flow coupled with the detailed film cooling effectiveness measurements, problem areas can easily be pinpointed, and areas, which are overcooled, can be identified, so that coolant flow is not wasted, and the blade life can be extended.

Experimental Facility

Low Speed Wind Tunnel. An existing low speed wind tunnel facility was used to study the platform film cooling effectiveness, and the schematic of the facility is shown in Fig. 1. Modifications were made to the endwall of the wind tunnel that was previously used by Zhang and Han [31]. The open-loop wind tunnel operates in suction with two mesh screens located at the inlet of the wind tunnel. To produce uniform flow entering the cascade, a 4.5:1 contraction nozzle guides the flow to the linear cascade. The test area is 25.4 cm high by 75.0 cm wide, and has a 107.49 deg turning angle to match the turning of the five-blade cascade. Head- and tailboards were added to the leading and trailing edges of the inner and outer airfoils to further guide the flow into the cascade. The cascade inlet velocity was maintained at 20 m/s and was set using a variable frequency controller attached to the 15 hp (11.2 kW) blower. The inlet velocity was measured (and continuously monitored) using a pitot tube placed inside the wind tunnel. The mainstream accelerates through the cascade, so the mainstream velocity at the cascade exit is 50 m/s.

The freestream turbulence through the cascade was varied by placing a turbulence grid 30 cm upstream of the cascade. The grid is made of square bars that are 1.3 cm wide, and they are spaced 4.8 cm in both the horizontal and vertical directions. Zhang and Han [31] used hot wire anemometry and showed that the inlet turbulence intensity increases from 0.75% (without the grid) to 13.4% with a length scale of 1.4 cm. The turbulence intensity decreases with the flow acceleration through the passage to a level of 5% at the cascade exit.

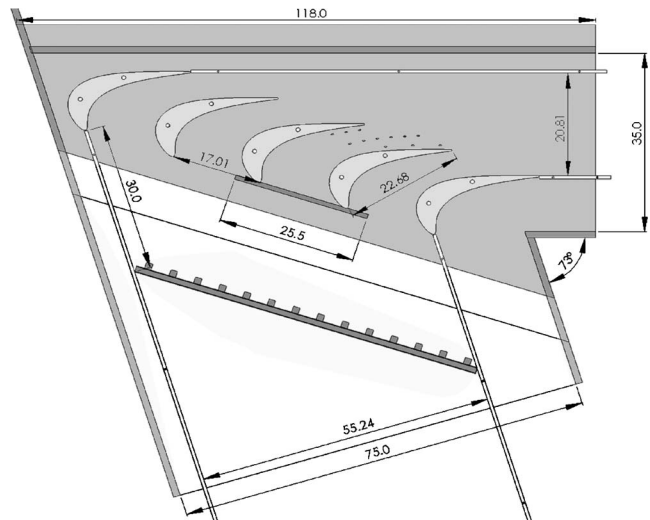


Fig. 2 Low speed wind tunnel and turbine blade details

Linear Cascade Design. Figure 2 shows the typical, advanced, high pressure turbine blade used for this study. The blade, which was scaled up five times, has a 107.49 deg turning angle with an inlet flow angle of 35 deg and an outlet flow angle of -72.49 deg. The chord length of the blade is 22.68 cm and the height of the blade is 25.4 cm. The blade-to-blade spacing at the inlet is 17.01 cm with a throat-to-span ratio of 0.2. The mainstream flow accelerates from 20 m/s at the inlet to 50 m/s at the outlet of the cascade. The inlet flow periodicity and uniformity for the blade design have been measured and reported by Zhang and Han [31]. In addition, the velocity (pressure) distributions along the pressure and suction surfaces of the blades have also been measured. The mainstream Reynolds number (based on the inlet velocity and blade chord) is 3.1×10^5 .

Platform Cooling Design. To study the film cooling effectiveness on the blade platform, the original smooth platform was altered to include both upstream slot injection and downstream discrete film cooling holes. The upstream slot, shown in Fig. 3, covers 1.5 passages. The width of the slot is 0.44 cm wide and is at a 30 deg angle to the mainstream flow. The length of the slot is

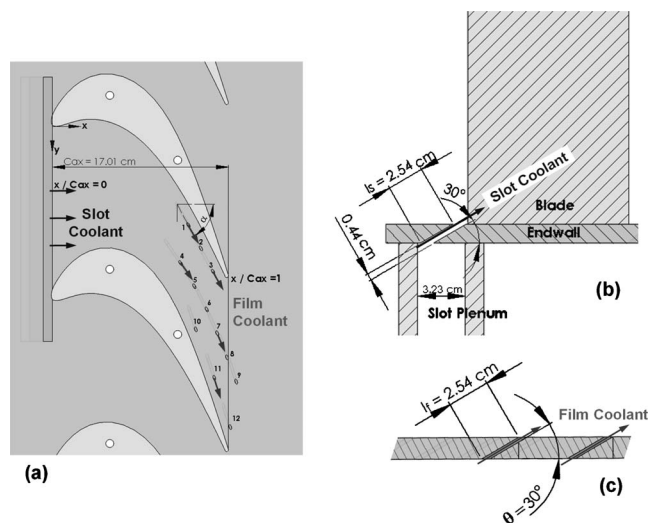


Fig. 3 Platform film cooling configurations: (a) detailed view of cooled passage; (b) upstream slot injection details; (c) cross-sectional view of two discrete film holes

Table 1 Discrete film hole location and orientation

Film hole number	x (cm)	y (cm)	d (cm)	α (deg)	θ (deg)
1	13.3	9.8	0.25	61	30
2	14.5	12.1	0.25	61	30
3	15.7	14.4	0.25	61	30
4	12.6	13.5	0.25	55.5	30
5	13.9	15.8	0.25	61	30
6	15.1	18.0	0.25	64	30
7	16.1	20.4	0.25	67	30
8	17.1	22.7	0.25	72	30
9	18.0	25.1	0.25	72	30
10	14.0	20.0	0.25	72	30
11	15.9	24.7	0.25	72	30
12	17.4	29.6	0.25	72	30

2.54 cm, so the length-to-width ratio (l_s/w) is 5.7. The downstream edge of the slot is aligned with the leading edge of the cascade. Considering the angled, downstream half of the slot as part of the blade platform, this geometry allows for a fundamental study of the coolant flow from the stator-rotor gap. Because the seal geometry was not taken from a specific engine, actual designs may consist of a longer slot length, so the platform extends further upstream of the blade leading edge. Coolant (air or nitrogen) is metered through a square edge, ASME orifice flow meter and piped to a plenum directly located beneath the slot. The plenum is sufficiently large enough to ensure the coolant is uniformly distributed at the exit of the slot. The flow rate of the slot coolant can be varied, so the film cooling effectiveness can be measured over a range of flow rates varying from 0.5% to 2.0% of the mainstream flow.

With the slot expected to provide adequate film coverage over the upstream half of the passage, discrete film cooling holes are only used on the downstream half of the passage. As shown in Fig. 3, the 12 film cooling holes are positioned to approximately follow the blade profile. The holes were spaced on the downstream half of the passage to provide adequate film coverage to this area of the platform. The holes have a diameter of 0.25 cm, a streamwise angle θ of 30 deg (as with the slot), and the lateral (compound) angle varies to match the blade profile. With a hole length of 2.54 cm, the length-to-diameter ratio (l/d) is 10. Table 1 shows the relative location and angle of the film cooling holes. The coolant (air or nitrogen) is supplied to the film cooling holes via a second plenum directly located beneath the film cooling holes. The coolant flow rate is measured using a volumetric flow meter, and the flow is varied to achieve average blowing ratios varying from 0.5 to 2.0. Because these discrete film cooling holes are located near the exit of the passage, this blowing ratio is based on the velocity of the mainstream at the exit of the cascade.

Pressure Sensitive Paint (PSP) Measurement Technique

The film cooling effectiveness has been measured using an array of measurement techniques over several decades. Thermocouples, thermochromatic liquid crystals, infrared thermography, and recently temperature sensitive paint have been used for surface temperature measurements, which can be converted to the film cooling effectiveness with knowledge of the mainstream and coolant flows. Although these techniques can be used to obtain the film cooling effectiveness, the accuracy near the film cooling holes is questioned. Near the holes, the test material can be very thin, and therefore, heat conduction through the test surface can give false representations of the film cooling effectiveness. This is a problem, which is an inherent to heat transfer experiments.

Numerical correction of the film cooling data is one alternative for producing more accurate film cooling data. Another alternative is to avoid heat transfer experiments. This approach was used by

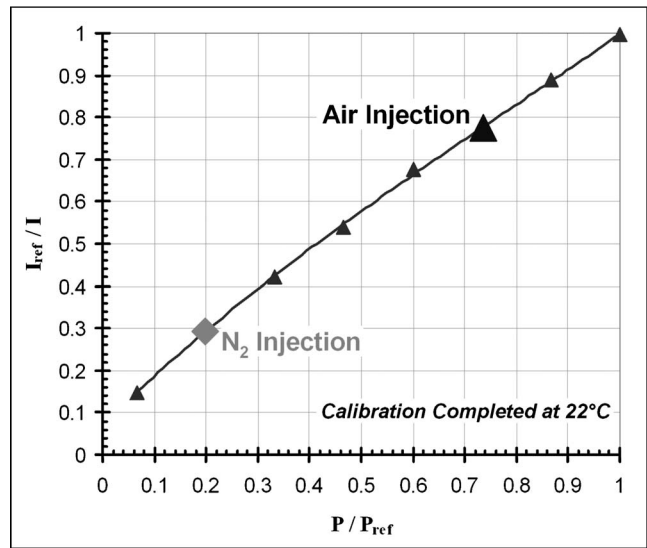


Fig. 4 PSP calibration curve

Zhang et al. [24,25] as they used PSP to measure the film cooling effectiveness on a cascade endwall. Wright et al. [32] used PSP to film the cooling effectiveness on a flat plate with compound angle film cooling holes, and they provide a detailed review of the PSP theory and application. In addition, PSP has also been used to measure the effectiveness on a cylinder placed in a low speed wind tunnel [33]. Both of these studies demonstrate the superiority of PSP measurements compared to other traditional measurement techniques, including steady state liquid crystal thermography, steady state infrared thermography, and transient infrared thermography. The PSP technique has also been applied by Ahn et al. [34,35] to measure the film cooling effectiveness on the leading edge of a rotating blade placed in a three stage research turbine. Additional film cooling effectiveness distributions have been obtained in a blow-down facility on the blade tip [36,37].

The premise behind PSP is an oxygen quenching effect. As the oxygen partial pressure of the gas in direct contact with the surface increases, the intensity of light emitted by the PSP decreases (hence, oxygen quenched). The PSP can be calibrated to determine the relationship between the emission intensity of the paint and the surrounding pressure. A test plate is sprayed with the Uni-FIB PSP (UF470-750) supplied by Innovative Scientific Solutions, Inc. (ISSI) and placed inside a vacuum chamber. At each measurement point, the PSP sample was excited using a strobe light equipped with a 500 nm broadband pass filter. A charge-coupled device (CCD) camera with a 630 nm filter records the intensity emitted by the PSP. Figure 4 shows a typical calibration curve relating a known pressure ratio to a measured intensity ratio (where the reference conditions are taken at atmospheric pressure).

After the PSP has been properly calibrated, the film cooling effectiveness can be measured on the desired test surface. Due to the size of the endwall passage, two sets of images are required to capture the entire passage. The procedures to measure the effectiveness on both the upstream and downstream halves of the passage are identical, and the results are combined to give a complete picture of the film cooling effectiveness on the platform. The film cooling effectiveness is measured based on a mass transfer technique. Two similar tests are required to calculate the film cooling effectiveness: one with air as the coolant and one with nitrogen as the coolant. The film cooling effectiveness can be calculated based on the concentration of oxygen, which is related to the partial pressure of oxygen. Therefore, the film cooling effectiveness can be calculated using Eq. (1), where the present definition is compared to the traditional film cooling effectiveness definition.

$$\eta = \frac{T_f - T_m}{T_c - T_m} = \frac{C_\infty - C_{\text{mix}}}{C_\infty} = \frac{(P_{\text{O}_2})_{\text{air}} - (P_{\text{O}_2})_{\text{N}_2}}{(P_{\text{O}_2})_{\text{air}}} \approx 1 - \frac{I_{\text{air}}}{I_{\text{N}_2}} \quad (1)$$

To accurately determine the film cooling effectiveness, a total of four images are required: (1) a black image to remove any background noise from the optical components (no mainstream flow, no coolant flow, no excitation light), (2) a reference image to establish the intensity at the reference atmospheric pressure (no mainstream flow, no coolant flow, PSP is excited with the strobe light), (3) an air image to measure the partial pressure of oxygen with air as the coolant (mainstream flow, air as coolant flow, excitation by strobe light), and (4) a nitrogen image to measure the partial pressure of oxygen with nitrogen as the coolant (mainstream flow, nitrogen as coolant flow, excitation by strobe light). As shown in Fig. 4, in the presence of oxygen, the emission intensity falls, so the intensity ratio (I_{ref}/I) increases, as shown by representative point for film cooling with air injection. When nitrogen is injected as the coolant, the emission intensity increases (due to the lack of oxygen), and the intensity ratio decreases, as shown by the point for nitrogen injection. The partial pressure of oxygen with air or nitrogen injection is determined based on the calibration of the emission intensity and pressure. The film cooling effectiveness can be determined at every pixel, giving a detailed film cooling effectiveness distribution on the passage end-wall.

Experimental uncertainty was considered using a 95% confidence level, as presented by Coleman and Steele [38]. The uncertainty of the film effectiveness measurements varies depending on the intensity level measured by the CCD camera. The experimental uncertainty is less than 2% for film effectiveness measurements greater than 0.5. However, as the effectiveness begins to approach zero (where the measured light intensities are relatively low), the uncertainty rises. For a film cooling effectiveness of 0.07, the uncertainty is approximately 10%, and continues to rise as the effectiveness approaches zero. All experimental results were repeated multiple times to confirm the repeatability of the data. The data proved to be repeatable for the entire range of film effectiveness that was measured.

Results and Discussion

The presentation of the results begins with the film cooling effectiveness obtained on the passage endwall with slot injection upstream of the cascade. This includes experimental results obtained over a wide range of slot flow rates. The effect of turbulence on this film cooling effectiveness is also experimentally considered. This discussion is followed by the presentation of the film cooling effectiveness measured downstream with coolant only from the downstream discrete holes, including the effects of various blowing ratios and turbulence intensities. The detailed film cooling effectiveness is then obtained for upstream slot injection combined with downstream discrete film cooling. After comparing the detailed film effectiveness distributions for all of these cases, final comparisons will be made using the spanwise averages of the film cooling effectiveness. Table 2 shows a summary of the 24 experimental cases considered. The slot injection rate is commonly considered as a percentage of the mainstream. However, the blowing ratio (velocity ratio, as coolant and mainstream densities are equal) is also presented as a reference. The slot blowing ratio is based on the mainstream velocity at the inlet of the cascade (20 m/s). The blowing ratio for the downstream film holes is also shown, but because the film cooling holes are located on the downstream half of the passage, the blowing ratio for the discrete holes is based on the exit velocity of the mainstream flow (50 m/s).

Upstream Slot Injection. The detailed film cooling effectiveness was obtained on a single passage with various slot injection rates. Figure 5 shows the detailed effectiveness distribution on the platform with a freestream turbulence intensity of 0.75%. The

Table 2 Experimental conditions considered in the present study

Upstream slot injection				
Slot injection rate (m_s)	M_s	I_s	DR	Tu
0.5%	0.29	0.084	1.0	0.75%, 13.4%
1.0%	0.57	0.325	1.0	0.75%, 13.4%
1.5%	0.86	0.740	1.0	0.75%, 13.4%
2.0%	1.14	1.30	1.0	0.75%, 13.4%
Downstream discrete film holes				
	M_f	I_f	DR	Tu
	0.5	0.25	1.0	0.75%, 13.4%
	1.0	1.00	1.0	0.75%, 13.4%
	1.5	2.25	1.0	0.75%, 13.4%
	2.0	4.00	1.0	0.75%, 13.4%
Combined upstream slot and downstream film				
Slot injection rate (m_s)	M_s	M_f	MFR _{total}	Tu
1.0%	0.57	0.5	1.11%	0.75%
1.0%	0.57	1.0	1.22%	0.75%
1.0%	0.57	1.5	1.34%	0.75%
1.0%	0.57	2.0	1.46%	0.75%
2.0%	1.14	0.5	2.11%	0.75%
2.0%	1.14	1.0	2.22%	0.75%
2.0%	1.14	1.5	2.34%	0.75%
2.0%	1.14	2.0	2.46%	0.75%

effect of the blowing ratio is clearly seen comparing Figs. 5(a)–5(d). At the lowest flow rate of 0.5%, the coolant ejection does not cover the entire slot. The coolant is quickly swept from the pressure side of the passage to the suction side. Although the effectiveness approaches the ideal value of unity at the exit of the slot, the effectiveness quickly diminishes, and a large area of the passage is left unprotected. This nonuniform flow and distribution of the coolant on the platform was also observed on the endwall of multiple vane studies [20,24,26]. If the injection rate is increased to 1%, the flow from the slot is more uniform. However, the general trend for the effectiveness is the same as with 0.5%: The coolant is carried from the pressure side of the passage to the suction side. The area of protection extends further downstream; however, the downstream half of the passage still does not receive adequate protection. Increasing the injection rate to 1.5% results in more uniform film coverage on the upstream half of the passage. The area of coverage increases, but coverage remains inadequate near the trailing edge of the pressure side. At the maximum flow rate of 2.0%, the effectiveness bands are more uniformly distributed through the entire passage, with the entire passage receiving protection. Zhang and Jaiswal [24] showed similar results for slot injection upstream of a vane. They concluded that at low injection rates (0.5%–1.5%), the coolant did not reach the pressure side of the passage, and the effectiveness quickly diminished downstream of the slot. However, at high injection rates (2%–3%), uniform film coverage was measured in the downstream half of the passage with the coverage extending to the trailing edge of the passage [24].

It was noted in previous studies [20,21] that upstream slot injection is an effective tool for weakening the passage vortex. The finding is observed in the present results. At the highest injection rate of 2.0%, the effectiveness distribution is much more uniform than at the lower injection rates of 0.5% and 1.0%. The high momentum coolant disrupts the secondary flow behavior including the horseshoe and passage vortices. However, with the lower momentum coolant flows, the coolant flow is greatly affected by

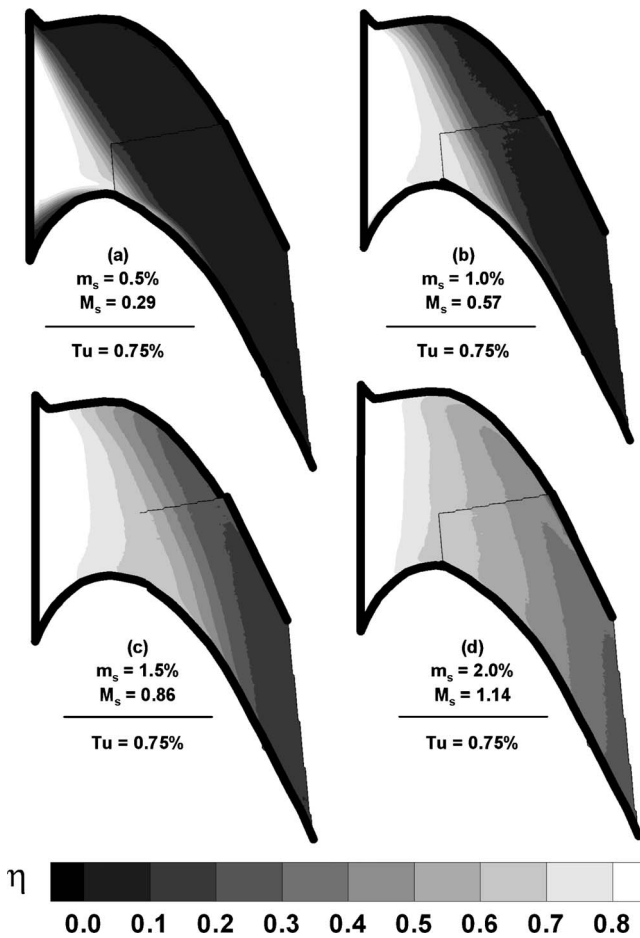


Fig. 5 Measured film cooling effectiveness with various slot injection rates ($Tu=0.75\%$)

the passage secondary flows.

At this point, it is worthwhile to extend the discussion to rotating blade platforms. The pressure gradient from the pressure side to the suction side of the passage will also be present on the rotating platform. Therefore, the general trend of the skewed film cooling effectiveness from the pressure side to the suction side of the passage is expected on the rotating platform. In fact, similar trends have been observed on a rotating platform [39].

With an understanding of secondary flow on the passage end-wall, the effect of an additional complexity on the film cooling effectiveness can be considered. With a turbulence grid added upstream of the cascade, the freestream turbulence intensity at the cascade inlet is raised to 13.4% [31]. Comparing the effectiveness distributions in Fig. 6 with those for the freestream turbulence level of 0.75% in Fig. 5, the general trends are the same: Increasing the injection rate increases the coverage area and the uniformity of the coverage. For the lowest injection rate of 0.5%, the coverage area extends further downstream with the increased turbulence; although the coverage area increases, the majority of the passage remains unprotected. A significant increase is observed in the protection area with the injection rates of 1.0% and 1.5%. In addition, at 1.5% the shape of the effectiveness contours changes from the low freestream turbulence case. The contours are more uniform across the passage. At 2.0%, the uniformity of the effectiveness continues to increase. The passage vortex is weakened with the increased freestream turbulence. The mitigated secondary flow results in better coverage of the slot coolant.

Downstream Discrete Film Cooling. Figure 7 compares the film cooling effectiveness obtained from discrete film holes on the

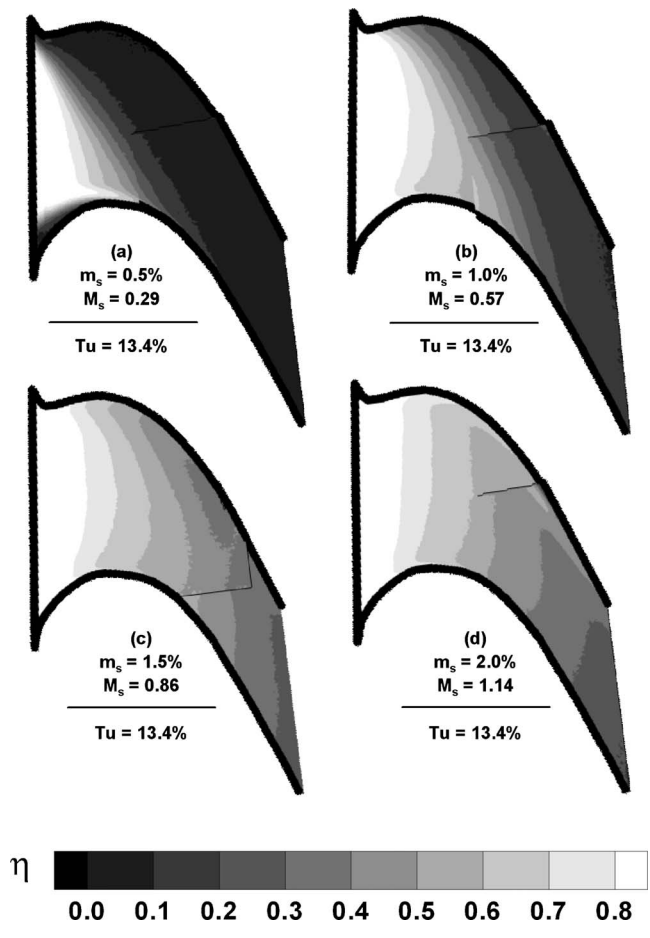


Fig. 6 Measured film cooling effectiveness with various slot injection rates ($Tu=13.4\%$)

downstream half of the passage with turbulence intensities of 0.75% and 13.4% (measured at the cascade inlet), respectively.

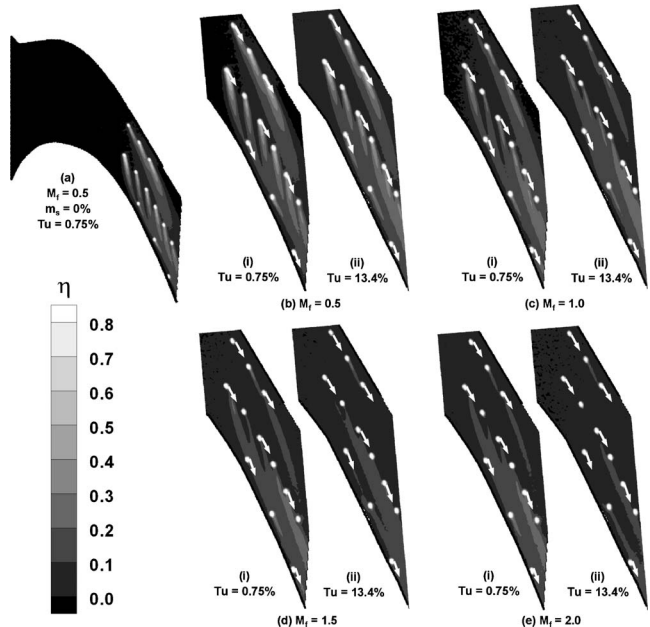


Fig. 7 Measured film cooling effectiveness with downstream discrete film cooling

The average blowing ratio varies from 0.5 to 2.0 based on the mainstream velocity at the cascade exit. As shown in this figure, increasing the blowing ratio decreases the film cooling effectiveness. At the lowest blowing ratio of 0.5, very distinct film traces are seen from each of the 12 film cooling holes. Increasing the blowing ratio increases the momentum of the jets exiting the holes, the jets blow off the endwall, and the coolant is carried away with the mainstream flow. From flat plate film cooling studies, it is accepted that the optimum blowing ratio occurs between 0.5 and 1.0; increasing the blowing ratio beyond 1.0 for the cylindrical holes results in decreased film cooling effectiveness because the coolant does not remain attached to the surface. The strong secondary flow behavior is very clear in Fig. 7(b-i); the arrows added to the figure indicate the compound angle of the film cooling hole, designed to follow the blade profile. Regarding the three holes along the pressure side of the passage, the coolant traces follow the discharge angle of the holes. Near the trailing edge of the blades, the passage vortex has already crossed the passage from the pressure side to the suction side. Therefore, the coolant from these pressure side holes does not significantly deviate from their injection angles. The migration of the passage vortex is clearer with the middle row of film cooling holes. The film traces are significantly altered from the flow direction, and the coolant is pushed to the suction side of the passage. The coolant from the suction side holes covers less area than the other holes. The passage vortex has continued to gain strength, and as shown previously with the upstream injection, the coolant along the suction surface tends to lift-off the endwall and attach to the suction surface of the blade due to the growing passage vortex.

The effect of increased turbulence intensity is opposite to the effect observed for the upstream injection. Figure 7 also shows the measured film effectiveness with the turbulence grid in the wind tunnel. The turbulence intensity at the inlet of the cascade is 13.4%, but as the mainstream continues through the passage, the turbulence intensity drops, and near the exit of the cascade, the turbulence intensity is approximately 5% [31]. The effect of blowing ratio with the increased freestream turbulence is the same as the previous case: The blowing ratio of 0.5 offers the best film cooling coverage. However, increasing the freestream turbulence decreases the film effectiveness for all blowing ratios. At $M_f = 1.0$, the peak effectiveness clearly drops, but the increased turbulence causes the jet to laterally spread, and more area is covered between the holes (while the length of the trace is reduced). At the highest blowing ratio of 2.0, the discrete holes provide coverage for a very small area, and the majority of the area is left unprotected. It is also seen in Fig. 7(b-ii) that the traces from the middle row of jets merge together as the increased turbulence spreads the cooling jets.

Combined Upstream Slot Injection and Downstream Discrete Film Cooling. The detailed film cooling effectiveness is measured on the endwall with upstream slot injection combined with discrete film cooling downstream for a freestream turbulence intensity of 0.75%. Figure 8 shows the film cooling effectiveness distribution on the platform with a slot injection rate of 1.0% and various blowing ratios for the downstream film cooling holes. From Fig. 5(b), a large area of the endwall was left uncooled where the slot coolant did not cover. The discrete film cooling holes obviously increased the effectiveness in the region near the holes, but a large area along the pressure side of the channel remains unprotected. The trends observed in this figure are the same as those observed in Fig. 5(a) and Fig. 7. Because the slot coolant is quickly carried to the suction side of the passage, there is no interaction between the slot coolant and the coolant from the film holes.

Increasing the slot injection rate to 2.0% yields protection throughout the entire passage. Now with the addition of downstream film cooling holes, the two coolants will interact. At the lowest film blowing ratio of 0.5, the peak effectiveness near the film holes is very high, as shown in Fig. 9. The peak effectiveness

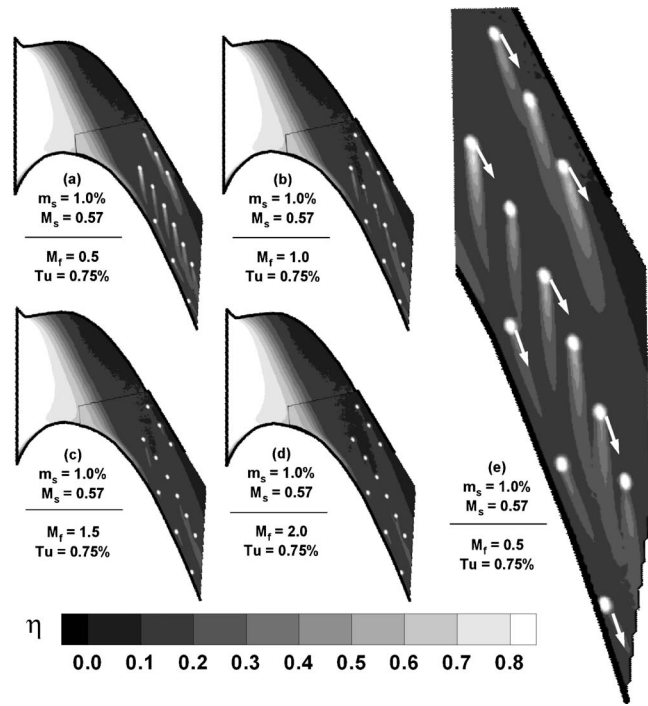


Fig. 8 Measured film cooling effectiveness with combined slot cooling (1%) and downstream film cooling ($Tu=0.75\%$)

can be as high as 0.81 immediately downstream of the first hole in the middle row. However, when there was no upstream slot injection, the corresponding effectiveness was only 0.67 (an increase of approximately 21%). The increased effectiveness is due to the film accumulation between the slot and film coolants. This effect is less obvious with the increased blowing ratios, as the jets tend to lift-off the surface. Although the peak effectiveness is not as significantly affected at the increased blowing ratios, the effective-

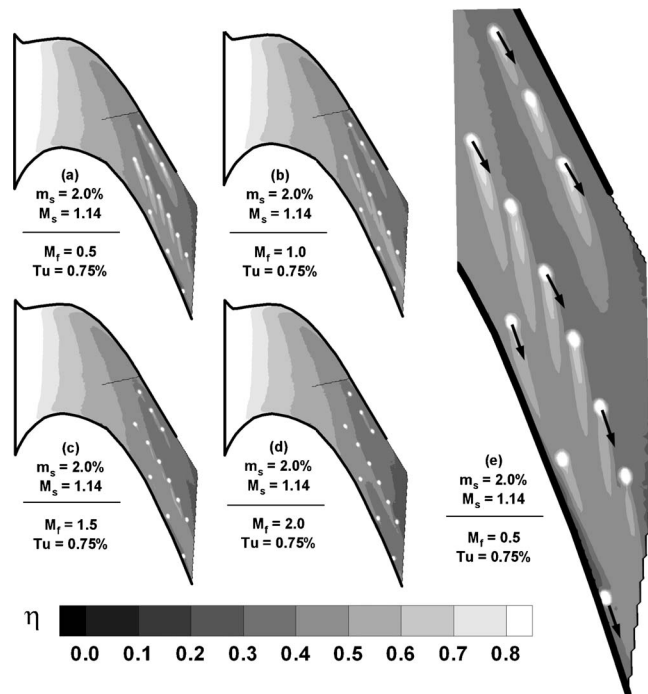


Fig. 9 Measured film cooling effectiveness with combined slot cooling (2%) and downstream film cooling ($Tu=0.75\%$)

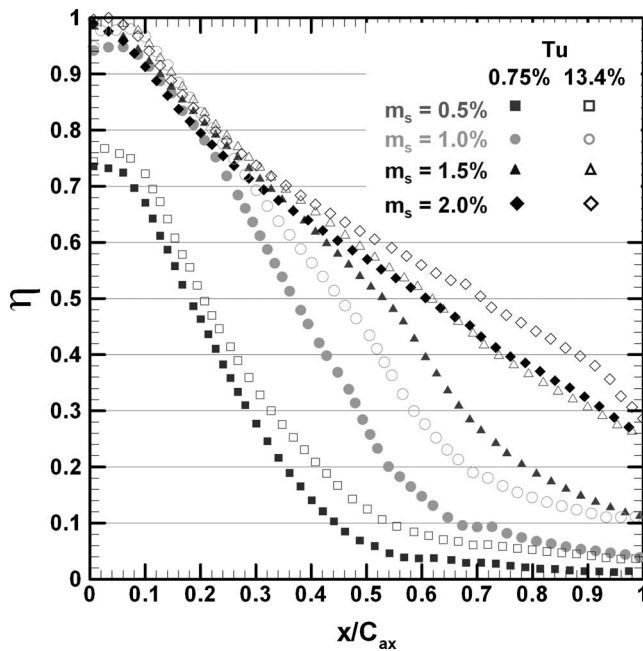


Fig. 10 Laterally averaged film cooling effectiveness on the passage endwall with upstream slot injection

ness on the downstream half of the passage does increase when compared to the measured effectiveness with only upstream injection. When the downstream film holes are combined with the upstream slot injection, the film coolant begins to cumulate. In addition, without the upstream slot injection, the high momentum

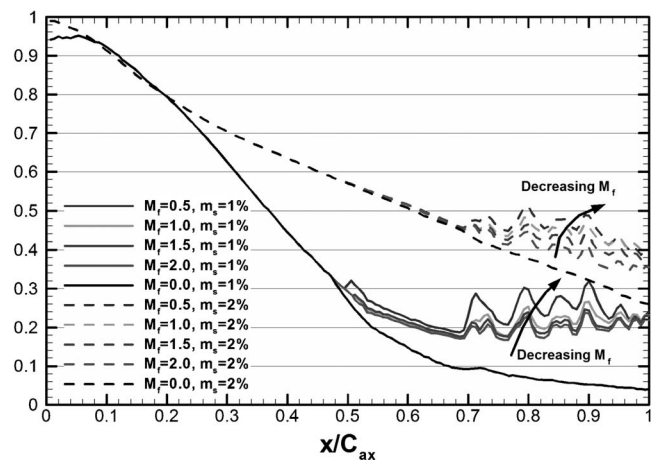


Fig. 12 Laterally averaged film cooling effectiveness on the passage endwall with combined upstream slot injection and downstream discrete film hole cooling ($Tu=0.75\%$)

downstream coolant readily blows off the surface (Fig 7). However, with the upstream injection, even the high momentum does not lift-off as readily, as it is deflected by the slot coolant and remains attached to the passage endwall.

Laterally Averaged Film Cooling Effectiveness. Although valuable insight can be obtained from the detailed distributions, many times spanwise averaged plots offer additional insight and provide clear comparisons for large amounts of data. Figures 10–13 make such comparisons of the cases previously discussed. The effectiveness is averaged from the suction side to the pressure

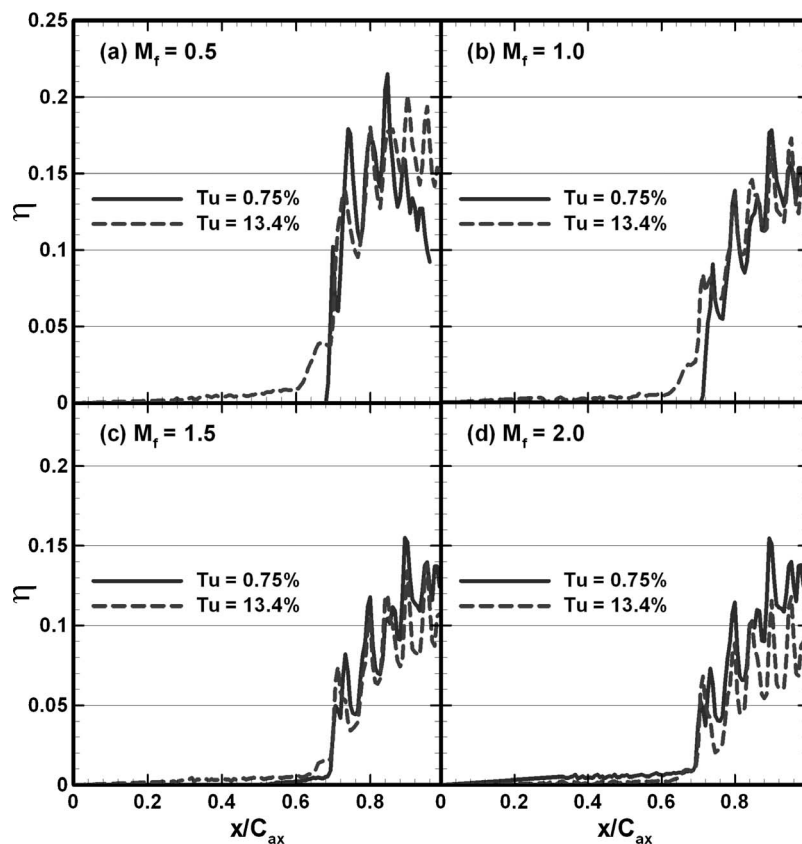


Fig. 11 Laterally averaged film cooling effectiveness on the passage end-wall downstream discrete film hole cooling

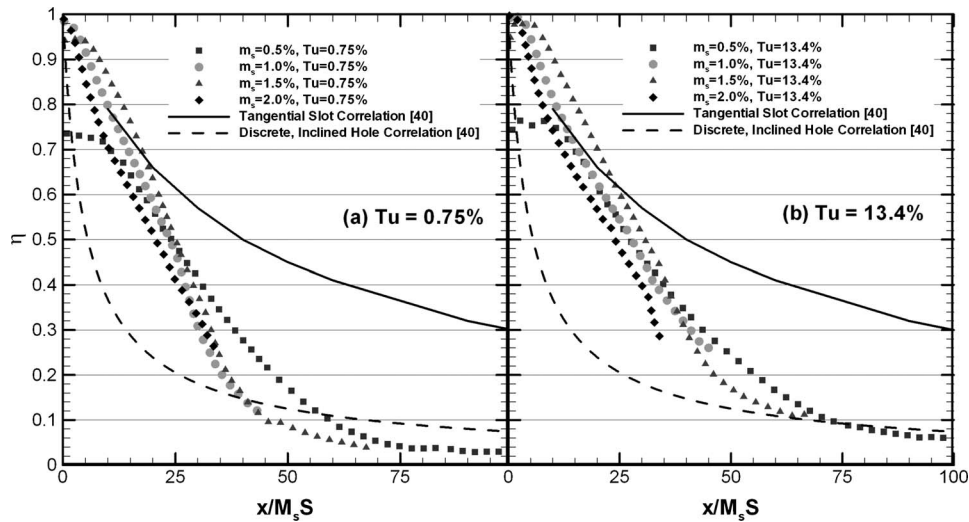


Fig. 13 Comparison of the laterally averaged film cooling effectiveness on the passage endwall with upstream slot injection with correlations for discrete, inclined film cooling holes and tangential slot injection over a flat plate

side of the passage in the x direction, as shown in Fig. 3(a). The effect of the freestream turbulence and injection rate on the effectiveness from the upstream slot injection can be seen in Fig. 10. First, increasing the injection rate increases the film cooling effectiveness. At the exit of the slot, the effectiveness of the injection rates of 1.0%, 1.5%, and 2.0% is unity, and the effectiveness gradually decreases. The maximum film cooling effectiveness is only 0.74 ($Tu=0.75\%$) for $m_s=0.5\%$. The average is significantly lower because the coolant does not cover the entire passage, as shown in Fig. 5(a). Near the slot ($x/C_{ax} < 0.4$), the level of the film cooling effectiveness for m_s ranging from 1.0 to 2.0 is the same (including $Tu=0.75\%$ and 13.4%). The blowing ratio effect is clearly seen on the downstream half of the channel ($x/C_{ax} > 0.4$), with the effectiveness being proportional to the injection rate. The effect of freestream turbulence is also shown in this figure; as discussed previously, increasing the turbulence intensity increases the film cooling effectiveness because the passage secondary flow is weakened. The combined effect of weakening the secondary flow by increased injection and increased turbulence increases the film cooling effectiveness by a maximum of 20%. The greatest combined effect is seen for $m_s=1.5\%$, where the film cooling effectiveness is increased by as much as 80%.

The lateral averages for the downstream film cooling holes are shown in Fig. 11. The effect of blowing ratio is seen by comparing Figs. 11(a)–11(d). For both turbulence intensities, the film cooling effectiveness decreases with increasing blowing ratio. The effect of freestream turbulence is more complicated. In general, increased freestream turbulence decreases the film cooling effectiveness on the platform (as also shown in Fig. 7). This finding varies from studies of film cooled flat plates. For flat plate studies, it has been shown that increasing the freestream turbulence decreases the film cooling effectiveness at low blowing ratios and increases the effectiveness at high blowing ratios. The film cooling effectiveness on the platform is influenced by both the freestream turbulence intensity and the passage induced secondary flow (passage vortex). Increasing the freestream turbulence increased the effectiveness upstream due to the slot injection. With the turbulence intensity being 13.4% at the inlet of the cascade, the passage vortex was weakened. Near the trailing edge of the passage, where the turbulence intensity is significantly lower (5%) and the passage vortex is weakened, the coolant from the discrete holes can more readily lift-off the platform (when compared to the cases without the turbulence grid). Therefore, the effectiveness de-

creases with increased freestream turbulence due to the combined effect of the freestream turbulence and the passage induced secondary flow.

Figure 12 clearly shows the combined effect of upstream slot injection and downstream discrete film cooling holes. Beginning with the slot injection rate of 1.0%, from the reference case (only upstream slot injection with $m_s=1.0\%$), the effectiveness drops quickly. However, with the addition of downstream discrete film hole cooling, the film cooling effectiveness increases more than three times the amount without the discrete film holes, with the greatest increase coming with the lowest film blowing ratio of $M_f=0.5$. With the slot injection of 2.0%, the film cooling effectiveness is greater than 1.0%. The film cooling effectiveness is elevated with the film cooling holes; however, the increase is not as significant as with the injection rate of 1.0%.

When considering the film cooling effectiveness on the passage endwall, there has been a tendency to apply data or correlations obtained from flat plate studies directly to the endwall. Figure 13 illustrates that the flat plate correlations should be cautiously applied to the endwall. Goldstein [40] gathered experimental data and correlations for the film cooling effectiveness measured downstream of both a slot and discrete film holes. Plotted with the laterally averaged data from the present study are both a correlation for the effectiveness due to discrete, inclined film cooling holes and a correlation for tangential slot injection. The film cooling effectiveness of the present study is clearly higher than the accepted correlation for discrete hole film cooling. The coolant exiting a discrete film hole is highly three dimensional with multiple pairs of vortices. These vortices increase the interaction between the coolant and the mainstream flow, and thus reduce the film cooling effectiveness. However, when the coolant exits a full coverage slot, the flow is more two dimensional, with mixing occurring at the coolant—mainstream interface. The reduced mixing results in better film coverage, and therefore, increased film cooling effectiveness.

The interesting comparison is between the present results and the correlation for tangential slot injection. Near the slot ($x/M_s S < 25$), the current experimental data for slot injection rates of 1%, 1.5%, and 2% collapse together with the established correlation. The injection rate of 0.5% is lower than the correlation because the coolant does not exit the slot uniformly (Fig. 5(a)). Therefore, the lateral average for this lowest injection rate is lower than the other experimental data and the correlation for tangential injection.

tion. However, as $x/M_s S$ increases, the current experimental data significantly deviates from the correlation. Beyond $x/M_s S=22$, the current experimental data are much lower than the established correlation. The contour plots in Fig. 5 clearly show the skewed effectiveness profiles through the passage. Unlike flow over a flat plate, the effectiveness on the passage endwall decreases due to the passage secondary flow. This variation from the tangential slot correlation is seen for both freestream turbulence levels (Figs. 13(a) and 13(b)).

Conclusions

The present study has experimentally studied the film cooling effectiveness on the blade platform within a five-blade, linear cascade. With the blade profile common to advanced gas turbines, the film cooling effectiveness is significantly affected by the complex secondary flow along the passage endwall. The PSP technique clearly demonstrates the impact of passage secondary flow on the film cooling effectiveness. The effect of the secondary flows can be weakened, if the upstream injection rate is sufficiently large (at least 1–2% of the mainstream flow). Additionally, the passage vortex can be weakened with increased freestream turbulence, so the effectiveness due to the upstream slot injection increases.

The effect of the passage secondary flow is clearly seen when the film cooling effectiveness measured on the cascade endwall is compared to the effectiveness measured on a flat plate with tangential slot injection. Near the slot, the experimental data match the correlation for the slot injection; however, downstream of the slot, the passage secondary flow strongly affects the film cooling effectiveness, and the effectiveness is significantly reduced when compared to the flat plate correlation. Therefore, the direct application of flat plate data to the blade platform should be cautiously done.

The behavior of the discrete film cooling holes is best described from traditional flat plate film cooling studies with cylindrical holes. The maximum effectiveness occurs when the blowing ratio (M_f) is 0.5. As the blowing ratio increases beyond 1.0, the coolant tends to lift-off the surface, and protection is inadequate. Unlike with slot injection, increasing the freestream turbulence (from 0.75% to 13.4% at the cascade inlet and 5% at the cascade outlet) decreases the film cooling effectiveness near the discrete film cooling holes; this is also consistent with flat plate studies.

Finally, combining upstream slot injection with downstream discrete film hole cooling has the potential to further increase the endwall film cooling effectiveness. At an injection rate of 1.0%, the film cooling effectiveness increases more than three times over the effectiveness resulting from only upstream slot injection. However, when the injection rate is increased to 2.0%, the film effectiveness increases in this downstream region, but the amount of increase is less than when film cooling is combined with the 1.0% upstream slot injection rate.

Slot injection has the potential to provide adequate film cooling protection on the platform surface and additional, limited protection on the suction surface of the blade. If the available coolant is utilized, excess discrete film hole cooling can be avoided.

Acknowledgment

This publication was prepared with the support of the U.S. Department of Energy, Office of Fossil Energy, National Energy Technology Laboratory. However, any opinions, findings, conclusions, or recommendations expressed herein are those of the authors and do not necessarily reflect the views of the DOE.

Nomenclature

C	= chord length of the blade
C_{ax}	= axial chord length of the blade
C_{mix}	= oxygen concentration of mainstream-coolant mixture
C_∞	= oxygen concentration of mainstream

d	= film hole diameter
h	= local heat transfer coefficient ($W/m^2 K$)
I_f	= discrete film hole momentum flux ratio ($=\rho_f V_f^2 / \rho_m V_{m2}^2 \cong V_f^2 / V_{m2}^2$)
I_s	= slot injection momentum flux ratio ($=\rho_s V_s^2 / \rho_m V_{m1}^2 \cong V_s^2 / V_{m1}^2$)
l_f	= discrete film hole length
l_s	= slot length
M_f	= discrete film hole blowing ratio ($=\rho_f V_f / \rho_m V_{m2} \cong V_f / V_{m2}$)
m_s	= slot injection mass flow ratio (percentage of the mainstream flow)
M_s	= slot injection blowing ratio ($=\rho_s V_s / \rho_m V_{m1} \cong V_s / V_{m1}$)
MFR _{total}	= total mass flux ratio (coolant to mainstream)
P_{O_2}	= partial pressure of oxygen
Re	= mainstream flow Reynolds number based on the inlet velocity and axial chord length
S	= slot width (m)
T_c	= coolant temperature (K)
T_f	= film temperature (K)
T_m	= local, mainstream temperature (K)
T_s	= local, coolant temperature from upstream slot (K)
Tu	= turbulence intensity
V_f	= discrete film hole velocity (m/s)
V_{m1}	= mainstream velocity at the cascade inlet (m/s)
V_{m2}	= mainstream velocity at the cascade exit (m/s)
V_s	= slot injection velocity (m/s)
w	= slot width (m)
x	= axial distance from the cascade leading edge (m)
α	= lateral injection angle
θ	= streamwise injection angle
ρ_f	= density of film coolant (kg/m^3)
ρ_m	= density of mainstream (kg/m^3)
ρ_s	= density of slot coolant (kg/m^3)
η	= film cooling effectiveness

References

- [1] Han, J. C., Dutta, S., and Ekkad, S. V., 2000, *Gas Turbine Heat Transfer and Cooling Technology*, Taylor & Francis, New York.
- [2] Chyu, M. K., 2001, "Heat Transfer Near Turbine Nozzle Endwall," *Ann. N.Y. Acad. Sci.*, **934**, pp. 27–36.
- [3] Langston, L. S., Nice, L. M., and Hooper, R. M., 1976, "Three-Dimensional Flow Within a Turbine Cascade Passage," *ASME Paper No. 76-GT-50*.
- [4] Langston, L. S., 1980, "Crossflows in a Turbine Cascade Passage," *ASME J. Eng. Power*, **102**, pp. 866–874.
- [5] Goldstein, R. J., and Spores, R. A., 1988, "Turbulent Transport on the Endwall in the Region Between Adjacent Turbine Blades," *ASME J. Heat Transfer*, **110**, pp. 862–869.
- [6] Blair, M. F., 1974, "An Experimental Study of Heat Transfer and Film Cooling on Large-Scale Turbine Endwall," *ASME J. Heat Transfer*, **96**, pp. 524–529.
- [7] Graziani, R. A., Blair, M. F., Taylor, J. R., and Mayle, R. E., 1980, "An Experimental Study of Endwall and Airfoil Surface Heat Transfer in a Large Scale Turbine Blade Cascade," *ASME J. Eng. Power*, **102**, pp. 257–267.
- [8] York, R. E., Hylton, L. D., and Mihelc, M. S., 1984, "An Experimental Investigation of Endwall Heat Transfer and Aerodynamics in a Linear Vane Cascade," *ASME J. Eng. Gas Turbines Power*, Vol. **106**, pp. 159–167.
- [9] Radomsky, R. W., and Thole, K. A., 2000, "High Free-Stream Turbulence Effects on Endwall Heat Transfer for a Gas Turbine Stator Vane," *ASME J. Turbomach.*, **122**, pp. 299–708.
- [10] Kwak, J. S., Lee, J. H., and Han, J. C., 2002, "Heat Transfer and Pressure Distributions on a Gas Turbine Vane End-Wall," *Proceedings of the 12th International Heat Transfer Conference*, pp. 693–698.
- [11] Takeishi, K., Matsuura, M., Aoki, S., and Sato, T., 1990, "An Experimental Study of Heat Transfer and Film Cooling on Low Aspect Ratio Turbine Nozzles," *ASME J. Turbomach.*, **112**, pp. 488–496.
- [12] Haragama, S. P., and Burton, C. S., 1992, "Film Cooling Research on the Endwall of a Turbine Nozzle Guide Vane in a Short Duration Annular Cascade: Part 1—Experimental Technique and Results," *ASME J. Turbomach.*, **114**, pp. 734–740.
- [13] Jabbari, M. Y., Marston, K. C., Eckert, E. R. G., and Goldstein, R. J., 1996, "Film Cooling of the Gas Turbine Endwall by Discrete-Hole Injection,"

ASME J. Turbomach., **118**, pp. 278–284.

- [14] Friedrichs, S., Hodson, H. P., and Dawes, W. N., 1996, “Distribution of Film-Cooling Effectiveness on a Turbine Endwall Measured Using the Ammonia and Diazo Technique,” ASME J. Turbomach., **118**, pp. 613–621.
- [15] Friedrichs, S., Hodson, H. P., and Dawes, W. N., 1997, “Aerodynamic Aspects of Endwall Film Cooling,” ASME J. Turbomach., **119**, pp. 786–793.
- [16] Friedrichs, S., Hodson, H. P., and Dawes, W. N., 1998, “The Design of an Improved Endwall Film Cooling Configuration,” ASME Paper No. 98-GT-483.
- [17] Barigozzi, G., Benzoni, G., Franchini, G., and Derdichizzi, A., 2005, “Fan-Shaped Hole Effects on the Aero-Thermal Performance of a Film Cooled Endwall,” ASME Paper No. GT2005-68544.
- [18] Roy, R. P., Squires, K. D., Gerendas, M., Song, S., Howe, W. J., and Ansari, A., 2000, “Flow and Heat Transfer at the Hub Endwall of Inlet Vane Passages—Experiments and Simulations,” ASME Paper No. 2000-GT-198.
- [19] Burd, S. W., Satterness, C. J., and Simon, T. J., 2000, “Effects of Slot Bleed Injection Over a Contoured End Wall on Nozzle Guide Vane Cooling Performance: Part II—Thermal Measurements,” ASME Paper No. 2000-GT-200.
- [20] Oke, R., Simon, T., Shih, T., Zhu, B., Lin, Y. L., and Chyu, M., 2001, “Measurements Over a Film-Cooled Contoured Endwall With Various Coolant Injection Rates,” ASME Paper No. 2001-GT-0140.
- [21] Oke, R. A., and Simon, T. W., 2002, “Film Cooling Experiments With Flow Introduced Upstream of a First Stage Nozzle Guide Vane Through Slots of Various Geometries,” ASME Paper No. GT-2002-30169.
- [22] Nicklas, M., 2001, “Film-Cooled Turbine Endwall in a Transonic Flow Filed: Part II—Heat Transfer and Film Cooling Effectiveness,” ASME J. Turbomach., **123**, pp. 720–729.
- [23] Liu, G., Liu, S., Zhu, H., Lapworth, B. C., and Forest, A. E., 2004, “Endwall Heat Transfer and Film Cooling Measurements in a Turbine Cascade With Injection Upstream of Leading Edge,” Heat Transfer Asian Res., **33**, pp. 141–152.
- [24] Zhang, L. J., and Jaiswal, R. S., 2001, “Turbine Nozzle Endwall Film Cooling Study Using Pressure-Sensitive Paint,” ASME J. Turbomach., **123**, pp. 730–735.
- [25] Zhang, L. J., and Moon, H. K., 2003, “Turbine Nozzle Endwall Inlet Film Cooling—The Effect of a Backward Facing Step,” ASME Paper No. GT2003-38319.
- [26] Knost, D. G., and Thole, K. A., 2004, “Adiabatic Effectiveness Measurements of Endwall Film Cooling for a First Stage Vane,” ASME Paper No. GT2004-53326.
- [27] Cardwell, N. D., Sundaram, N., and Thole, K. A., 2005, “Effects of Mid-Passage Gap, Endwall Misalignment and Roughness on Endwall Film-Cooling,” ASME Paper No. GT2005-68900.
- [28] Zess, G. A., and Thole, K. A., 2002, “Computational Design and Experimental Evaluation of Using a Leading Edge Fillet on a Gas Turbine Vane,” ASME J. Turbomach., **124**, pp. 167–175.
- [29] Shih, T. I. P., and Lin, Y. L., 2002, “Controlling Secondary-Flow Structure by Leading-Edge Airfoil Fillet and Inlet Swirl to Reduce Aerodynamic Loss and Surface Heat Transfer,” ASME Paper No. GT-2002-30529.
- [30] Han, S., and Goldstein, R. J., 2005, “Influence of Blade Leading Edge Geometry on Turbine Endwall Heat (Mass) Transfer,” ASME Paper No. GT2005-68590.
- [31] Zhang, L., and Han, J. C., 1994, “Influence of Mainstream Turbulence on Heat Transfer Coefficients From a Gas Turbine Blade,” ASME J. Heat Transfer, **116**, pp. 896–903.
- [32] Wright, L. M., Gao, Z., Varvel, T. A., and Han, J. C., 2005, “Assessment of Steady State PSP, TSP, and IR Measurement Techniques for Flat Plate Film Cooling,” ASME Paper No. HT2005-72363.
- [33] Gao, Z., Wright, L. M., and Han, J. C., 2005, “Assessment of Steady State PSP and Transient IR Measurement Techniques for Leading Edge Film Cooling,” ASME Paper No. IMECE2005-80146.
- [34] Ahn, J., Schobeiri, M. T., Han, J. C., and Moon, H. K., 2004, “Film Cooling Effectiveness on the Leading Edge of a Rotating Turbine Blade,” ASME Paper No. IMECE2004-59852.
- [35] Ahn, J., Schobeiri, M. T., Han, J. C., and Moon, H. K., 2005, “Film Cooling Effectiveness on the Leading Edge of a Rotating Film-Cooled Blade Using Pressure Sensitive Paint,” ASME Paper No. GT2005-68344.
- [36] Ahn, J., Mhetras, S., and Han, J. C., 2004, “Film-Cooling Effectiveness on a Gas Turbine Blade Tip Using Pressure Sensitive Paint,” ASME Paper No. GT2004-53249.
- [37] Mhetras, S., Yang, H., Gao, Z., and Han, J. C., 2005, “Film-Cooling Effectiveness on Squealer Rim Walls and Squealer Cavity Floor of a Gas Turbine Blade Tip Using Pressure Sensitive Paint,” ASME Paper No. GT2005-68387.
- [38] Coleman, H. W., and Steele, W. G., 1989, *Experimentation and Uncertainty Analysis for Engineers*, Wiley, New York.
- [39] Suryanarayanan, A., Mhetras, S. P., Schobeiri, M. T., and Han, J. C., 2006, “Film Cooling Effectiveness on a Rotating Blade Platform,” ASME Paper No. GT2006-90034.
- [40] Goldstein, R. G., 1971, “Film Cooling,” Adv. Heat Transfer, **7**, pp. 321–379.

A Numerical Study of Flow and Heat Transfer Between Two Rotating Spheres With Time-Dependent Angular Velocities

Ali Jabari Moghadam

Asgar Baradaran Rahimi¹

Professor
e-mail: rahimiab@yahoo.com

Faculty of Engineering,
Ferdowsi University of Mashhad,
P.O. Box 91775-1111,
Mashhad 91775, Iran

The transient motion and the heat transfer of a viscous incompressible fluid contained between two vertically eccentric spheres maintained at different temperatures and rotating about a common axis with different angular velocities are numerically considered when the angular velocities are arbitrary functions of time. The resulting flow pattern, temperature distribution, and heat transfer characteristics are presented for the various cases including exponential and sinusoidal angular velocities. Long delays in heat transfer of large portions of the fluid in the annulus are observed because of the angular velocities of the corresponding spheres. As the eccentricity increases and the gap between the spheres decreases, the Coriolis forces and convection heat transfer effect in the narrower portion increase. Special results for concentric spheres are obtained by letting eccentricity tends to zero. [DOI: 10.1115/1.2907434]

Keywords: flow and heat transfer, vertically eccentric rotating spheres, time-dependent angular velocities, numerical solution

1 Introduction

The transient motion of an incompressible viscous fluid and its heat transfer in a rotating spherical annulus are numerically considered when the spheres are vertically eccentric and their angular velocities about a common axis of rotation may be arbitrarily prescribed functions of time. Such motions may be described in terms of a pair of coupled nonlinear partial differential equations in three independent variables and the energy equation is linear when velocity field is known.

Available theoretical work concerning such problems is primarily of a boundary-layer or singular-perturbation character considered by Howarth [1], Proudman [2], Lord and Bowden [3], Fox [4], Greenspan [5], Carrier [6], and Stewartson [7]. The first numerical study of time-dependent viscous flow between two rotating spheres has been presented by Pearson [8] in which the cases of one (or both) sphere is given an impulsive change in angular velocity starting from a state of either rest or uniform rotation. Munson and Joseph [9] have considered the case of steady motion of a viscous fluid between concentric rotating spheres using perturbation techniques for small values of Reynolds number and a Legendre polynomial expansion for larger values of Reynolds numbers. Thermal convection in rotating spherical annuli has been considered by Douglass et al. [10] in which the steady forced convection of a viscous fluid contained between two concentric spheres, which are maintained at different temperatures and rotate about a common axis with different angular velocities, is studied. Approximate solutions to the governing equations are obtained in terms of a regular perturbation solution valid for small Reynolds number and a modified Galerkin solution for moderate Reynolds numbers. Viscous dissipation is neglected in their study and all

fluid properties are assumed constant. A study of viscous flow in oscillatory spherical annuli has been done by Munson and Douglass [11] in which a perturbation solution valid for slow oscillation rates is presented and compared to the experimental results. Another interesting work is the study of the axially symmetric motion of an incompressible viscous fluid between two concentric rotating spheres done by Gagliardi et al. [12]. This work involves the study of the steady state and transient motion of a system consisting of an incompressible, Newtonian fluid in an annulus between two concentric, rotating, rigid spheres. The primary purpose of their research was to study the use of an approximate analytical method for analyzing the transient motion of the fluid in the annulus between spheres, which are suddenly started and to compare the results with those of Yang et al. [13] and Ni and Negro [14]. These problems include the case where one or both spheres rotate with prescribed constant angular velocities and the case in which one sphere rotates due to the action of an applied constant or impulsive torque.

The study of transient motion and heat transfer of an incompressible viscous fluid filling the annulus of two vertically eccentric spheres rotating at angular velocities that are any prescribed function of time has not been considered in the literature. In the present study, a numerical solution of unsteady momentum and energy equations is presented for viscous flow between two vertically eccentric rotating spheres maintained at different temperatures, which are rotating with time-dependent angular velocities. Results for some example functions including exponential and sinusoidal angular velocities are presented when the outer sphere initially starts rotating with a constant angular velocity and the inner sphere starts rotating with a prescribed time-dependent function. Such containers are used in engineering designs, such as centrifuges and fluid gyroscopes, and also are important in geophysics. Special results for concentric spheres are obtained by letting eccentricity tend to zero.

¹Corresponding author.

Contributed by the Heat Transfer Division of ASME for publication in the JOURNAL OF HEAT TRANSFER. Manuscript received February 27, 2007; final manuscript received September 15, 2007; published online May 19, 2008. Review conducted by Louis C. Burmeister.

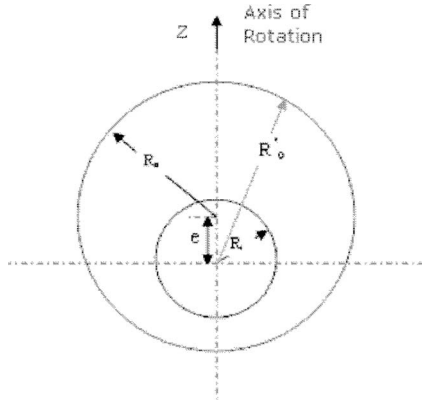


Fig. 1 Geometry of eccentric rotating spheres

2 Problem Formulation

The geometry of the spherical annulus considered is indicated in Fig. 1. The vertical eccentricity of the outer sphere is measured by the distance e . If the outer sphere is placed above the central position, e has a positive value, otherwise e is negative. The origin of the spherical coordinate system is the inner sphere center and the characteristic radius of the outer sphere, R_o' , is a function of θ . A Newtonian, viscous, incompressible fluid fills the gap between the inner and outer spheres, which are of radii R_i and R_o and with constant surface temperatures T_i and T_o and rotate about a common axis with angular velocities Ω_i and Ω_o , respectively. The components of velocity in directions r , θ , and ϕ are v_r , v_θ , and v_ϕ , respectively. These velocity components for incompressible flow and in meridian plane satisfy the continuity equation and are related to stream function ψ and angular momentum function Ω in the following manner:

$$v_r = \frac{\psi_\theta}{r^2 \sin \theta}, \quad v_\theta = \frac{-\psi_r}{r \sin \theta}, \quad v_\phi = \frac{\Omega}{r \sin \theta}, \quad (1)$$

Since the flow is assumed to be independent of the longitude, ϕ , the nondimensional Navier–Stokes equations and energy equation can be written in terms of the stream function and the angular velocity function as follows:

$$\frac{\partial \Omega}{\partial t} + \frac{\psi_\theta \Omega_r - \psi_r \Omega_\theta}{r^2 \sin \theta} = \frac{1}{\text{Re}} D^2 \Omega \quad (2)$$

$$\begin{aligned} \frac{\partial}{\partial t} (D^2 \psi) + \frac{2\Omega}{r^3 \sin^2 \theta} [\Omega_r r \cos \theta - \Omega_\theta \sin \theta] - \frac{1}{r^2 \sin \theta} [\psi_r (D^2 \psi)_\theta \\ - \psi_\theta (D^2 \psi)_r] + \frac{2D^2 \psi}{r^3 \sin^2 \theta} [\psi_r r \cos \theta - \psi_\theta \sin \theta] = \frac{1}{\text{Re}} D^4 \psi \end{aligned} \quad (3)$$

$$\begin{aligned} \frac{\partial T}{\partial t} + v_r \frac{\partial T}{\partial r} + \frac{v_\theta}{r} \frac{\partial T}{\partial \theta} = \frac{1}{(\text{Pe})} \left[\frac{\partial^2 T}{\partial r^2} + \frac{2}{r} \frac{\partial T}{\partial r} + \frac{1}{r^2} \frac{\partial^2 T}{\partial \theta^2} + \frac{\cot \theta}{r^2} \frac{\partial T}{\partial \theta} \right] \\ + (\text{Ek}) \left\{ 2 \left[\left(\frac{\partial v_r}{\partial r} \right)^2 + \left(\frac{1}{r} \frac{\partial v_\theta}{\partial \theta} + \frac{v_r}{r} \right)^2 + \left(\frac{v_r}{r} \right. \right. \right. \\ \left. \left. \left. + \frac{v_\theta}{r} \cot \theta \right)^2 \right] + \left[r \frac{\partial}{\partial r} \left(\frac{v_\theta}{r} \right) + \frac{1}{r} \frac{\partial v_r}{\partial \theta} \right]^2 \right. \\ \left. + \left[\frac{\sin \theta}{r} \frac{\partial}{\partial \theta} \left(\frac{v_\phi}{\sin \theta} \right) \right]^2 + \left[r \frac{\partial}{\partial r} \left(\frac{v_\phi}{r} \right) \right]^2 \right\} \end{aligned} \quad (4)$$

in which the nondimensional quantities Reynolds number (Re), Prandtl number (Pr), Peclet number (Pe), and Eckert number (Ek) are defined as

$$\text{Re} = \frac{\omega_o r_o^2}{\nu}, \quad \text{Pr} = \nu / \alpha, \quad \text{Pe} = \text{Re Pr} = \frac{\omega_o r_o^2}{\alpha}, \quad \text{Ek} = \frac{\nu \omega_o}{c_p (T_o - T_i)} \quad (5)$$

Here, Eq. (2) is the ϕ -momentum and Eq. (3) is obtained by omitting pressure term between r -momentum and θ -momentum equations. The following nondimensional parameters have been used in the above equations and then the asterisks have been omitted:

$$t^* = t \omega_o, \quad r^* = \frac{r}{r_o}, \quad \psi^* = \frac{\psi}{r_o^3 \omega_o}, \quad \Omega^* = \frac{\Omega}{r_o^2 \omega_o}, \quad (6)$$

$$T^* = \frac{T - T_i}{T_o - T_i}, \quad e^* = \frac{e}{R_o}$$

in which r_o and ω_o are reference values, which are selected as R_o and Ω_o , respectively. The nondimensional boundary and initial conditions for the above governing equations are as follows.

For $t < 0$,

$$\begin{aligned} \psi &= 0 \\ \Omega &= 0 \quad \text{everywhere} \\ T &= 0 \end{aligned}$$

For $t \geq 0$,

$$\begin{aligned} \theta = 0 &\rightarrow \{\psi = 0, D^2 \psi = 0, \Omega = 0\}, \quad \frac{\partial T}{\partial \theta} = 0 \\ \theta = \pi &\rightarrow \{\psi = 0, D^2 \psi = 0, \Omega = 0\}, \quad \frac{\partial T}{\partial \theta} = 0 \\ r = R_i/R_o &\rightarrow \begin{cases} \psi = 0, & \psi_r = 0, & \Omega = \frac{\Omega_i R_i^2}{\omega_o R_o^2} \sin^2 \theta \\ T = 0 \end{cases} \\ r = R_o'/R_o = e \cos \theta + \sqrt{(1 - e^2 \sin^2 \theta)} & \\ \rightarrow \begin{cases} \psi = 0, & \psi_r = 0, & \Omega = \frac{\Omega_o R_o'^2}{\omega_o R_o^2} \sin^2 \theta \\ T = 1 \end{cases} \end{aligned} \quad (7)$$

where

$$D^2 \equiv \frac{\partial^2}{\partial r^2} + \frac{1}{r^2} \frac{\partial^2}{\partial \theta^2} - \frac{\cot \theta}{r^2} \frac{\partial}{\partial \theta}$$

These governing equations along with the related boundary and initial conditions were numerically solved as described in the next section.

3 Computational Procedure

The two equations governing the fluid motion show that each is describing the behavior of one of the dependent variables Ω and ψ . On the other hand, these two equations are coupled only through nonlinear terms. To solve the problem, the momentum equations were discretized by the finite-difference method and implicit-explicit schemes. Because of the known velocity field, the energy equation is linear and is solved keeping all its terms. In each time step ($n+1$), the value of the dependent variables are guessed from their values at previous time steps (n), ($n-1$), and ($n-2$) and after using them in difference equations and repeating this, until obtaining the desired convergence, will lead to the corrected values at that time step. The same procedure is applied for the next time step.

The flow field considered is covered with a regular mesh. To solve the system of linear difference equations, a tridiagonal method algorithm is used in both directions r and θ , Press et al.

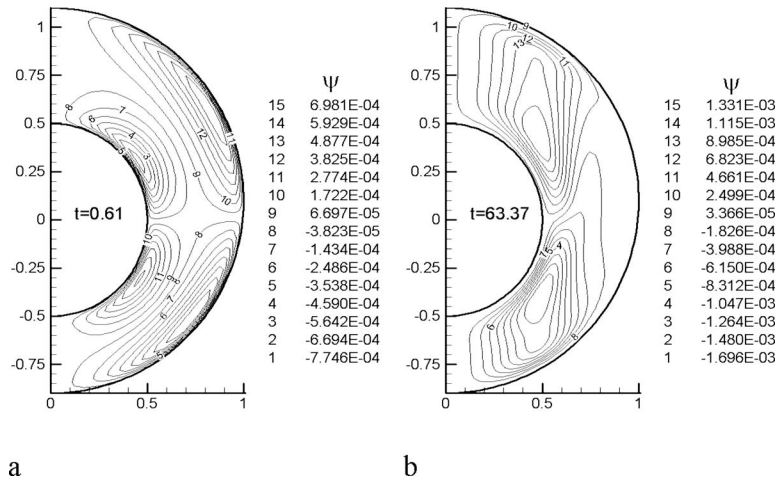


Fig. 2 Contours of ψ for $Re=1000$, $\Omega_{i0}=-\exp(1-t)$, $e=0.1$

[15]. Direct substitution of previous values of dependent variables by new calculated values can cause calculation instability, in general. To overcome this problem, a weighting procedure is used in which the optimum weighting factor depends on Reynolds number. The greater the Reynolds number, the smaller weighting factor is used to avoid instability of the results. The mesh size used in the numerical solution for equator of the circle is a uniform 40×20 or 50×25 (θ -direction $\times r$ -direction, respectively) with the ratio of $R_{out}/R_{in}=2$, which is generally a finer mesh size, though a bigger mesh size could still produce acceptable results.

In this work, the sphere angular velocity has been considered a function of time and to apply this time function to the program, an average value at the beginning of each time step has been calculated and used for the sphere angular velocity function. Therefore, for each considered time step, the sphere velocity is defined and sectionally continuous. To verify the validity of the numerical procedure used in this work, comparisons with the other research studies, such as Refs. [8–10], have been done for the case of $e=0$, which show exact agreements. The results used in these comparisons have been reproduced from these references as in Fig. 2.

4 Presentation of Results

If the bounding spherical surfaces were stationary, there would be no fluid motion and the temperature distribution would simply

be a conduction distribution. Any rotation of the bounding spheres sets up a primary flow around the axis of rotation with a fluid particle's angular velocity defined as (ω). This relative motion induces an unbalanced centrifugal force field, which drives the secondary flows (ψ) in the meridional plane. Thus, if the bounding spheres are of unequal temperatures, this secondary flow produces forced convection within the annulus, resulting in a temperature distribution, which is different from the pure conduction distribution. The relative magnitudes of the secondary flow and forced convection effects depend on the parameters involved, including those concerning the geometry of the flow such as $R_{i0}=R_i/R_o$, eccentricity and those concerning the dynamics of the flow such as $\Omega_{i0}=\Omega_i/\Omega_o$, Prandtl number, and Reynolds number. These secondary flows known as vortex have clockwise or counterclockwise motion (in first quadrant and vice versa in fourth quadrant) depending on whether or not the outer sphere or the inner sphere is dominant, as far as the secondary flow is concerned. To have a better understanding of the effect of secondary flows on temperature distribution, the contours of $(T-T_c)$ are also presented in this study, which show the difference between the actual temperature and the pure conduction case. Here, T_c is the temperature profile for pure conduction case and depends only on r . The flow and temperature fields are symmetric with respect to the rotation axis and also the equator plane if the spheres are concentric. However,

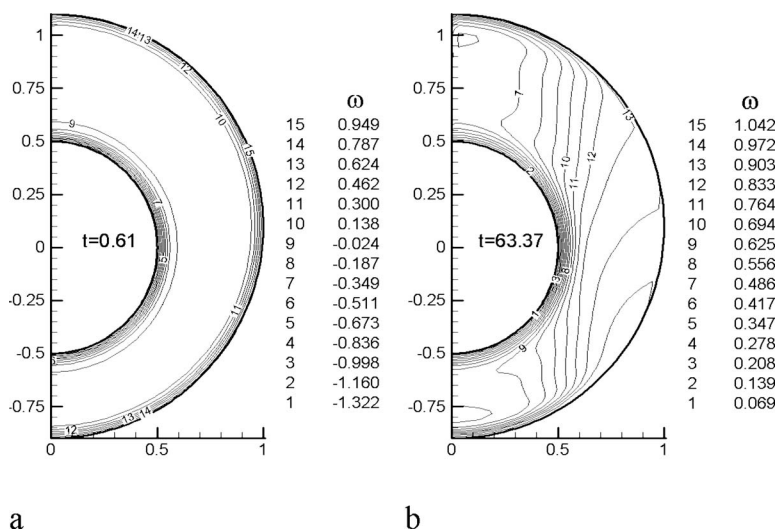


Fig. 3 Contours of ω for $Re=1000$, $\Omega_{i0}=-\exp(1-t)$, $e=0.1$

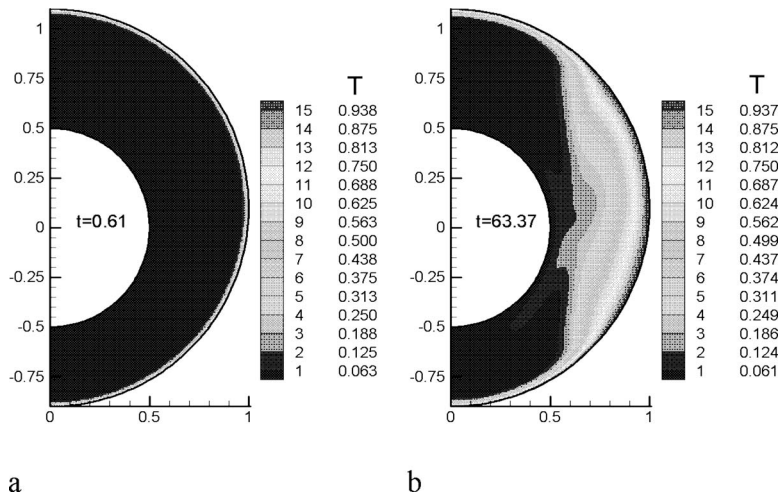


Fig. 4 Contours of T for $Re=1000$, $Pr=10$, $Ek=0$, $\Omega_{io}=-\exp(1-t)$, $e=0.1$

when the spheres are eccentric, then the flow and temperature fields are only symmetric with respect to the axis of rotation. The cases considered here include time-dependent angular velocities, which are exponential (usually encountered in start up and stopping in rotary machines) and sinusoidal (usually encountered in mixing machines). Results for the velocity and temperature fields are presented for cases when the outer sphere is rotating with a constant angular velocity and the inner sphere starts rotating with the prescribed function of time angular velocities. The viscous dissipation terms are taken into account for completeness of the problem formulation and also improvement of the results in comparison to Ref. [10], in view of the fact that a low Eckert number is used in this study.

The velocity fields for the particular case of inner sphere angular velocity, $\Omega_{io}=-\exp(1-t)$, and outer sphere rotating with constant angular velocity are presented in Figs. 2 and 3 for Reynolds number $Re=1000$ and $e=0.1$ at selected time values. At the beginning when the vortices (ψ contours) are formed, it is seen that the annulus space is under the effect of both spheres, which are dominating the flow field. A clockwise vortex close to the outer sphere and a counterclockwise vortex close to the inner sphere (both in first quadrant) are formed, Fig. 2(a). The size and the direction of these vortices are different in fourth quadrant because of the eccentricity. This factor also causes the vortices in first quadrant to penetrate into the fourth quadrant and compress the vortices in this region. As the inner angular velocity decreases

with time, its effect on the secondary flow diminishes. During this time, the clockwise vortex considerably grows and after some time there is only one big counterclockwise vortex, which indicates that the outer sphere is dominating the flow. As can be seen from the Figs. 2(b), the flow pattern tends toward the situation that the inner sphere is stationary, as one expects. Contours of ω for different time values are shown in Fig. 3. Since the Reynolds number is large, these contours get closer to the inner sphere at the equator. In fact, for large Reynolds numbers (approximately larger than $Re=300$), this secondary flow causes a considerable change in peripheral velocity (primary flow velocity profile). In general, the fluid particles in the vicinity of the equator move toward the inner sphere and return toward the axis of rotation. As a result, a secondary distribution of peripheral velocity forms, which affects the flow in meridian plane again. As time advances and if the Reynolds number is large, in the corner region between the outer sphere and equator line, the angular velocity contours move inward and those contours in the vicinity of axis of rotation move outward. This effect can be described by considering the distribution of angular momentum. The rotation of the outer sphere provides a certain amount of angular momentum for the system that is redistributed by flow in the meridian plane and by Coriolis forces and nonlinear advection. The fact that the total angular momentum of the azimuthal flow must be conserved by upward and downward moving fluid shows that the rotations of the upward moving elements of fluid (near pole) slow down and the

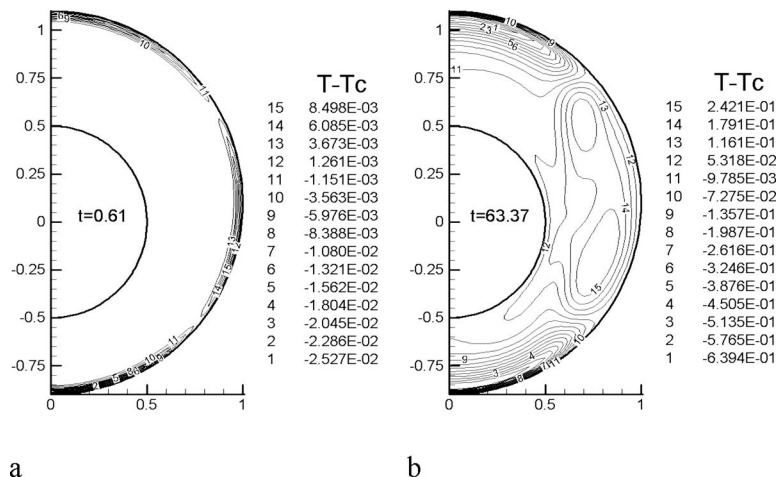


Fig. 5 Contours of $(T - T_c)$ for $Re=1000$, $Pr=10$, $Ek=0$, $\Omega_{io}=-\exp(1-t)$, $e=0.1$

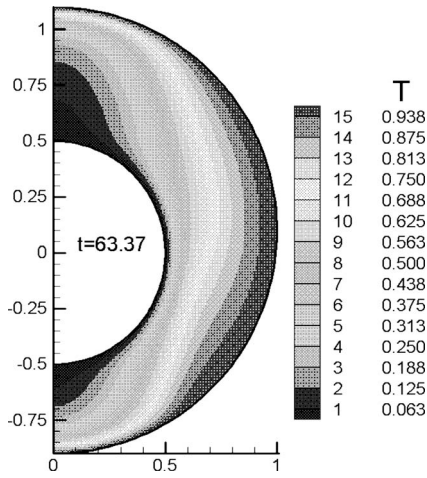


Fig. 6 Contours of T for $Re=1000$, $Pr=1$, $Ek=0$, $\Omega_{io}=-\exp(1-t)$, $e=0.1$

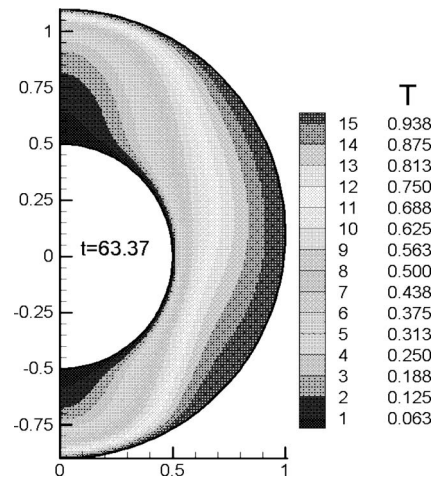


Fig. 8 Contours of T for $Re=1000$, $Pr=1$, $Ek=0.001$, $\Omega_{io}=-\exp(1-t)$, $e=0.1$

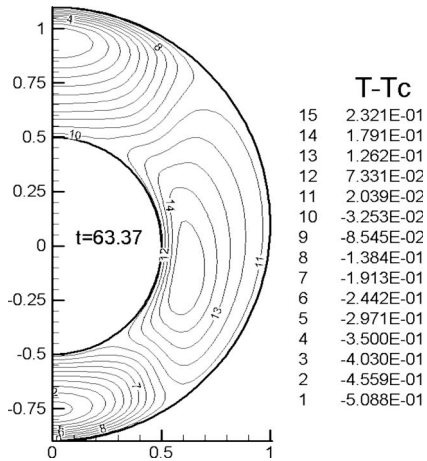


Fig. 7 Contours of $(T-T_c)$ for $Re=1000$, $Pr=1$, $Ek=0$, $\Omega_{io}=-\exp(1-t)$, $e=0.1$

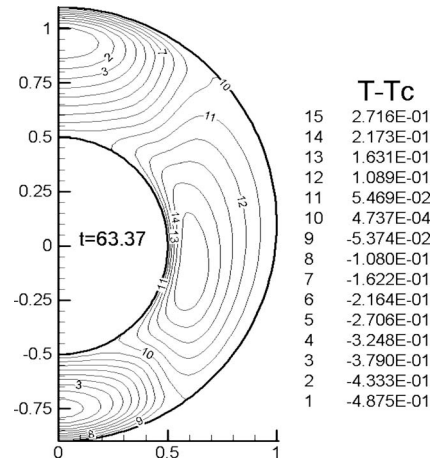


Fig. 9 Contours of $(T-T_c)$ for $Re=1000$, $Pr=1$, $Ek=0.001$, $\Omega_{io}=-\exp(1-t)$, $e=0.1$

rotations of the downward moving elements of fluid (near equator) speed up. The Coriolis forces are bigger in the lower hemisphere than in the upper hemisphere because of the eccentricity.

The contours of T and $(T-T_c)$ for the inner angular velocity of $\Omega_{io}=-\exp(1-t)$, $Re=1000$, $Pr=10$, and $Ek=0$ are shown in Figs. 4 and 5 for the case of $e=0.1$. At the outset when both spheres

dominate the flow, the diffusion of heat from the outer sphere into the field approximately takes place in a steady manner but as the rotation effect of the inner sphere becomes weak the temperature field considerably grows from the vicinity of the equator and affects the whole field. This phenomenon is more visible in the lower hemisphere. As far as $(T-T_c)$ contours, it is seen that at the

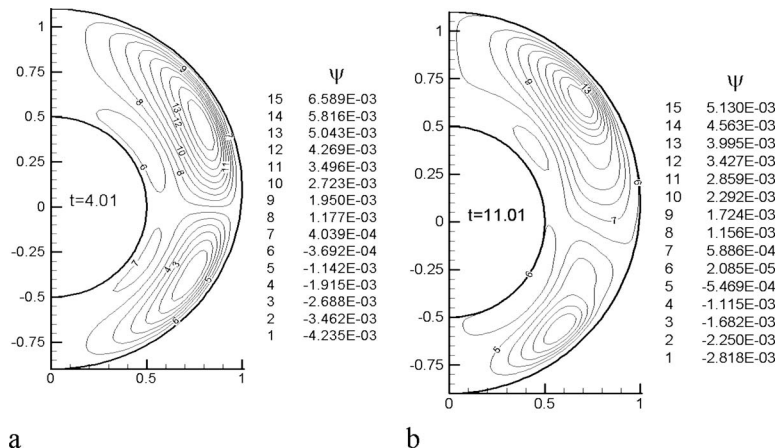


Fig. 10 Contours of ψ for $Re=1000$, $Pr=10$, $Ek=0$, $\Omega_{io}=2 \sin(\pi t/2)$, $e=0.1$

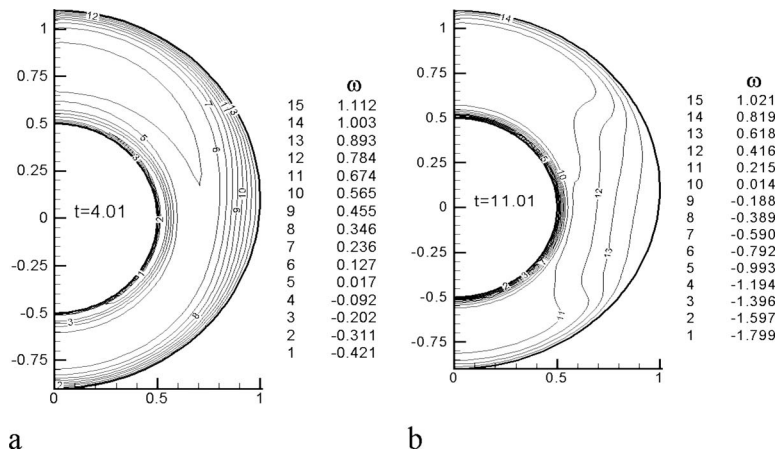


Fig. 11 Contours of ω for $Re=1000$, $Pr=10$, $Ek=0$, $\Omega_{i0}=2 \sin(\pi t/2)$, $e=0.1$

beginning the flow is forming; the difference between the actual temperature and the pure conduction temperature can be seen only in the region near the outer sphere, but as time passes this difference becomes larger because of convection. It is obvious that this difference shows itself in the form of positive and negative numbers. The contours near the pole are negative and the contours near the equator are positive. This is because the clockwise flow, which is formed by the rotation of the outer sphere, would transfer the heat of this sphere into the field and toward the equator and the inner sphere. On the contrary, as it moves along the inner sphere and rotation axis, it transfers the inner sphere coldness toward the outer sphere and the pole. As a result, in the vicinity of the pole, there are temperatures that are lower than the pure conduction case and in the vicinity of the equator there are temperatures that are higher than pure conduction case. Again, this difference is more visible in the lower hemisphere. As evidenced in Fig. 5, it is interesting to note that the angular velocities of spheres can cause long delays in heat transfer to the fluid in large areas of the annulus around the poles.

Figures 6 and 7 present the T and $(T-T_c)$ contours for the same conditions as in Figs. 4 and 5 except for $Pr=1$. As can be seen in this case, the heat diffuses faster because the heat diffusion mechanism by conduction is stronger than the diffusion of heat by convection and also as the inner sphere rotates, a counterclockwise vortex is formed, which curbs the heat convection and its transfer to the field. Therefore, when the Prandtl number is lower, the temperature field grows faster. This can be seen in Fig. 7 where the contours are steadier. Note that this diffusion of heat is more visible in lower hemisphere. The difference between Figs. 8 and 9 compared to Figs. 6 and 7 is in the Eckert number. The Eckert number is related to viscous dissipations, which are the gradients of velocity that show their effects as a source of heat in energy equation. This source, in fact, expresses the conversion of kinetic energy to heat energy, which causes the temperature of the flow field to rise. This effect (gradients of velocity) is seen in Fig. 8 in which the temperature field has more expansion compared to Fig. 6. Looking at Figs. 9 and 7, this difference is much clearer. These velocity gradients are the reason for the difference between the actual temperature and the case of pure conduction and can be seen better at the vicinity of inner sphere in Fig. 9 compared to Fig. 7. Also, as expected, the temperatures are higher when the dissipation terms are not omitted, such as in Ref. [10] and for the case of $e=0$.

Figures 10 and 11 have been drawn for inner angular velocity, $\Omega_{i0}=2 \sin(\pi/2t)$ for $Re=1000$, $Pr=10$, $Ek=0$, for the case of $e=0.1$ and in two consecutive periods (second and third) for the sine function. As known, the sine function oscillates between -1 and 1 . In these figures, the second and third periods after the sinusoidal movement have been considered. Inner sphere angular

velocity in Figs. 10(a) and 10(b) is approximately $\Omega_{i0}=0.0314$ and -1.998 , respectively. The time values selected in these figures are when the inner sphere velocity has come to an important change, meaning that it has been considered immediately after a change of acceleration. For example, for the time value between Case (a) and just before Case (b), the inner sphere acceleration is positive and the time value at (b) is the starting point of negative acceleration for this sphere. As can be seen in Fig. 11, the angular

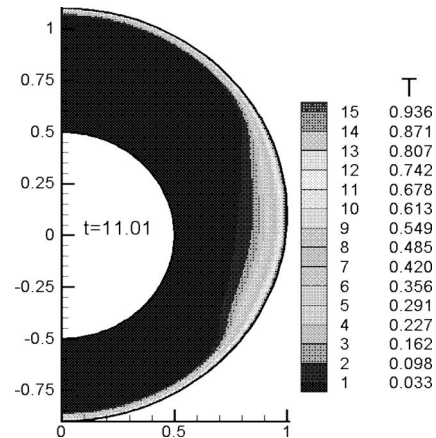


Fig. 12 Contours of T for $Re=1000$, $Pr=10$, $Ek=0$, $\Omega_{i0}=2 \sin(\pi t/2)$, $e=0.1$

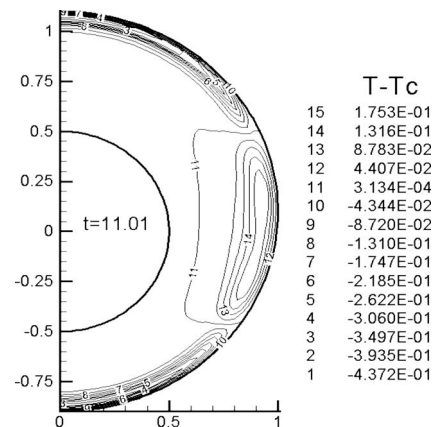


Fig. 13 Contours of $(T-T_c)$ for $Re=1000$, $Pr=10$, $Ek=0$, $\Omega_{i0}=2 \sin(\pi t/2)$, $e=0.1$

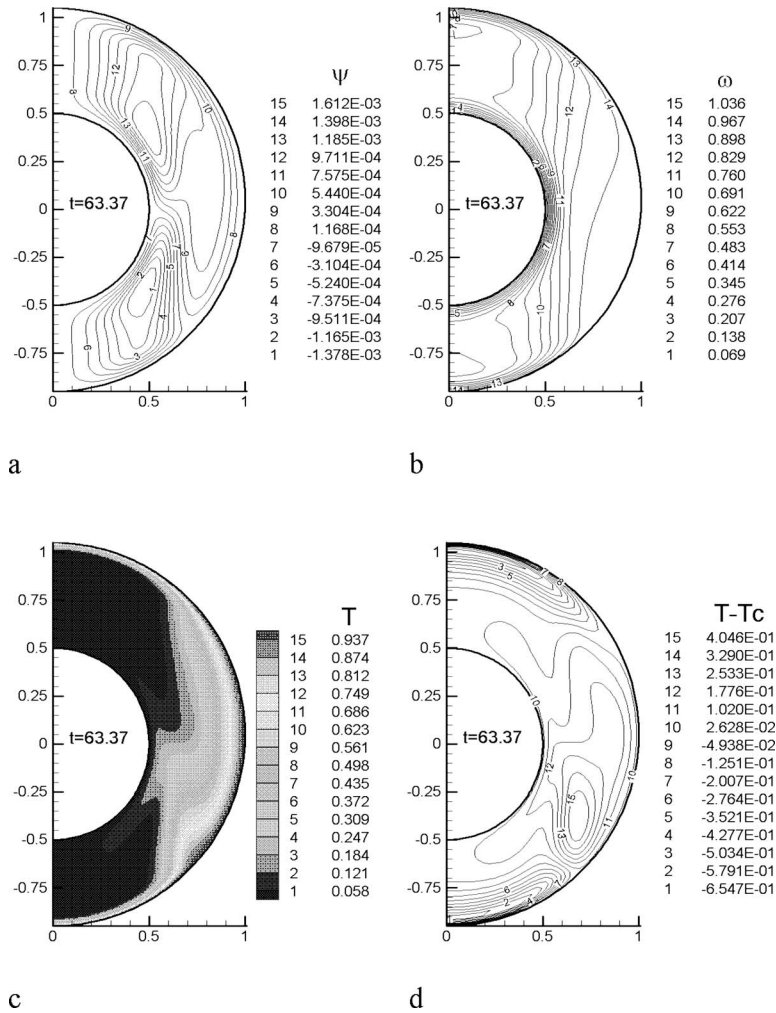


Fig. 14 Flow and heat transfer for $Re=1000$, $Pr=10$, $Ek=0$, $\Omega_{i0}=-\exp(1-t)$

velocity of a fluid element in the vicinity of the inner sphere is also dependent on the past accelerations. For example, the inner sphere has a sinusoidal oscillation with a positive velocity of 0.0314 at $t=4.01$, while nearby fluid elements have negative angular velocity. Therefore, as the outer sphere containing a constant velocity has a continuous and steady effect on the entire flow field, the inner sphere having an oscillating velocity between -2 and 2 (periodic positive and negative acceleration) induces an unsteady and oscillatory type of effect on the layers in the vicinity of the inner sphere. Also, the effect of eccentricity clearly portrays the unsymmetric situation in these figures. The vortex caused by the inner sphere is considerably smaller in the lower hemisphere compared to the upper hemisphere because eccentricity causes production of a bigger Coriolis force in lower hemisphere.

The T and $(T-T_c)$ contours for the inner angular velocity of $\Omega_{i0}=2 \sin(\pi/2t)$ are depicted in Figs. 12 and 13 for $Re=1000$, $Pr=10$, and $Ek=0$. Similar types of discussions as for Figs. 4 and 5 apply here as well. Also, the delay in heat transfer to the fluid in large portions of annulus can be seen in Fig. 12. Again, the profiles show that because of the eccentricity the Coriolis force in the lower hemisphere is bigger than in the upper hemisphere and therefore, it warms up faster.

The flow and heat transfer results for exponential inner angular velocities as before and selected values of Reynolds, Prandtl, and Eckert numbers are shown in Figs. 14 and 15 for the case when the eccentricity factor is $e=0.05$. The difference between the size and the direction of ψ contours in the fourth quadrant and also less penetration of the vortices from the first quadrant into this quad-

rant can be consistently seen from these figures by comparing with the corresponding results for the case of $e=0.1$. Here, the Coriolis forces in the lower hemisphere are not as big as for the higher eccentricity case and, therefore, the warming process is not as fast.

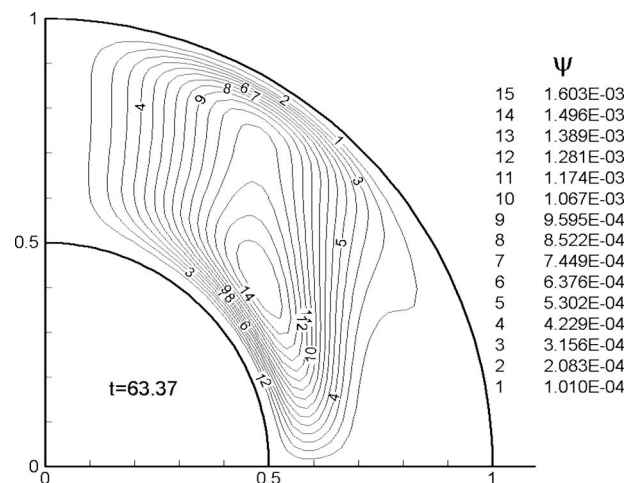


Fig. 15 Contours of ψ for $Re=1000$ and $\Omega_{i0}=-\exp(1-t)$ for $e=0$

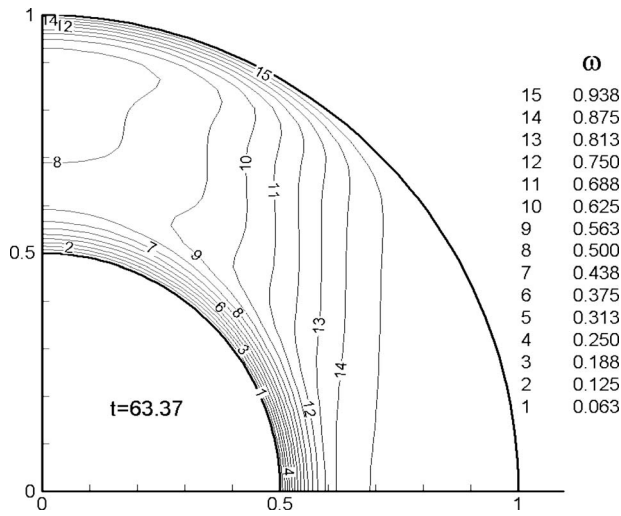


Fig. 16 Contours of ω for $Re=1000$ and $\Omega_{i0}=-\exp(1-t)$ for $e=0$

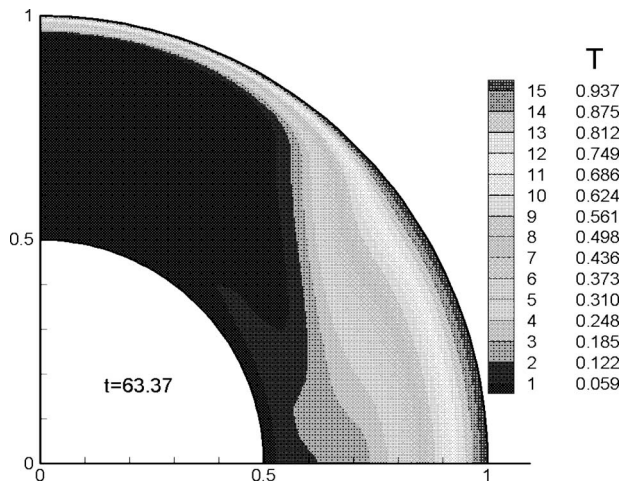
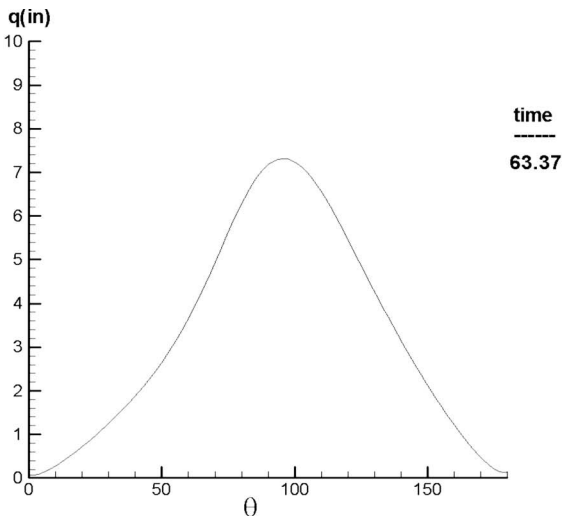


Fig. 17 Contours of T for $Re=1000$, $Pr=10$, $Ek=0$, and $\Omega_{i0}=-\exp(1-t)$ for $e=0$



a

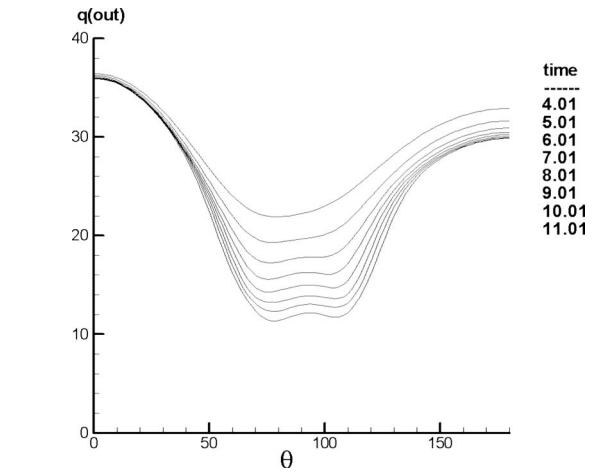
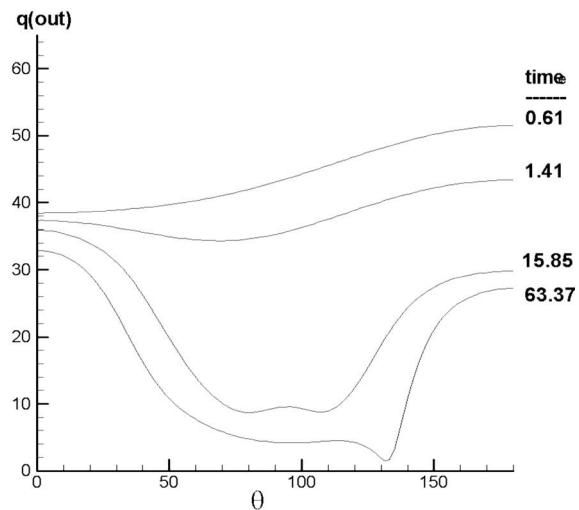


Fig. 19 Wall heat flux for $Re=1000$, $Pr=10$, $Ek=0$, $\Omega_{i0}=2 \sin(\pi t/2)$, $e=0.1$

Figures 15–17 present the velocity field and the heat transfer results for exponential and sinusoidal inner angular velocities for the case of concentric spheres where eccentricity is zero. In this case, the flow and the temperature fields are symmetric with respect to the rotation axis as well as to the equatorial plane. The consistency of the concentric spheres results with the results of the eccentric spheres cases can be seen by direct comparison.

Figures 18 and 19 present the wall heat flux for selected values of sphere rotational functions, $\Omega_{i0}=-\exp(1-t)$, $\Omega_{i0}=2 \sin(\pi t/2)$ and, for example, for $Re=1000$, $Ek=0$, $e=0.1$, $Pr=10$ and selected time values. As expected and like in the case of the temperature, the heat flux contours are not symmetric. The outer sphere wall heat flux decreases as time increases. The inner sphere wall heat flux is nonzero only when the inner sphere starts feeling the oncoming heat from the outer sphere.

The results for the nondimensional total heat transfer with respect to time according to $q_{\text{nondimensional}}=q_{\text{dimensional}}/k(T_o-T_i)/r_o$ are presented in Fig. 20 for different rotational angular velocities and selected values of flow and heat transfer parameters for the case of $e=0.1$. Time to reach steady-state situation for different rotational angular velocities and also Prandtl numbers is depicted in this presentation.



b

Fig. 18 Wall heat flux for $Re=1000$, $Pr=10$, $Ek=0$, $\Omega_{i0}=-\exp(1-t)$, $e=0.1$

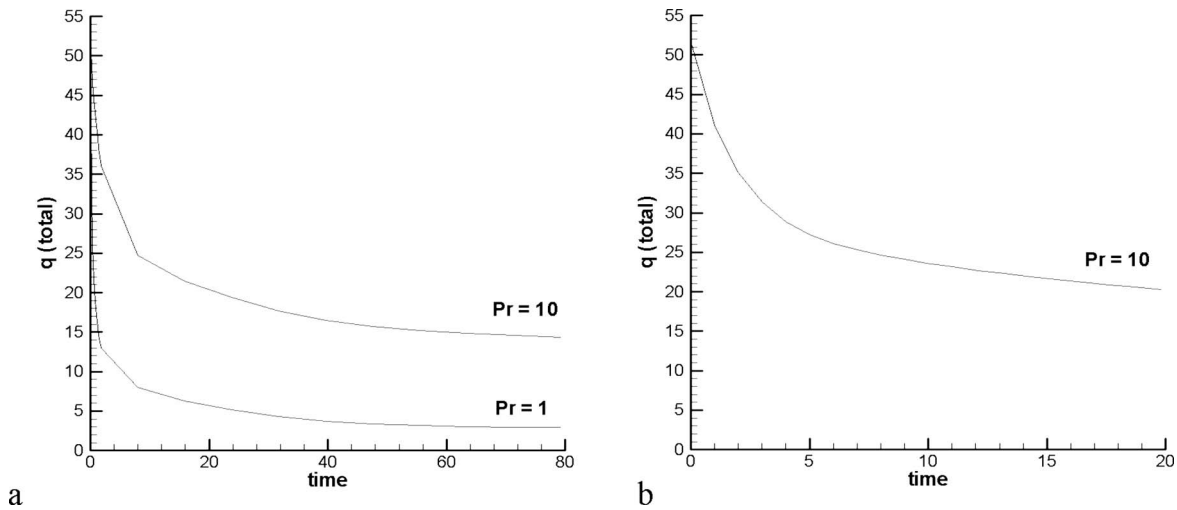


Fig. 20 Total heat transfer for $Re=1000$, $Ek=0$, selected values of Prandtl numbers, $e=0.1$ and (a) $\Omega_{i0}=-\exp(1-t)$, (b) $\Omega_{i0}=2 \sin(\pi t/2)$

5 Conclusions

A numerical study of flow and heat transfer of a viscous incompressible fluid within a rotating spherical annulus has been executed when the spheres have time-dependent prescribed values of angular velocities. The characteristics of the flow and temperature fields are strongly dependent on the values of the various dimensionless parameters considered. The characteristics of angular velocity and temperature distribution for small Reynolds numbers are similar, which is expected since it is a situation where there is a balance between convection and diffusion of momentum and heat. At small Reynolds numbers, the secondary flow or the vortices, which cause forced convection, are small and the local heat transfer is not much different from that for pure conduction. However, for large Reynolds numbers, some deviations are seen in angular velocity and temperature distributions, which is an indication of the effect of secondary flow on the primary flow. Since we have considered the case with time-dependent angular velocities, the relative velocities of the spheres are functions of time. Applying these angular velocities, shear layers are formed in the vicinity of the spheres, which get thicker because of viscous diffusion and, depending on the flow conditions, one or two circulations are formed in meridian plane. Long delays in heat transfer of the big portion of the fluid in the annulus are observed because of the angular velocities of the corresponding spheres. As the eccentricity increases and the gap between the spheres decreases, the Coriolis forces and convection heat transfer in the narrower portion increase. The results for concentric spheres are obtained by letting eccentricity tends to zero. In this case, the flow and temperature fields are symmetric with respect to the rotation axis as well as to the equatorial plane.

References

- [1] Howarth, L., 1951, "Note on Boundary Layer on a Rotating Sphere," *Philos. Mag.*, **7**(42), pp. 1308–1311.
- [2] Proudman, I., 1956, "The Almost-Rigid Rotation of Viscous Fluid Between Concentric Spheres," *J. Fluid Mech.*, **1**, pp. 505–516.
- [3] Lord, R. G., and Bowden, F. P., 1963, "Boundary Layer on a Rotating Sphere," *Proc. R. Soc. London, Ser. A*, **271**, pp. 143–146.
- [4] Fox, J., 1964, "Singular Perturbation of Viscous Fluid Between Spheres," *NASA TN D-2491*, pp. 1–50.
- [5] Greenspan, H. P., 1964, "Axially Symmetric Motion of a Rotating Fluid in a Spherical Annulus," *J. Fluid Mech.*, **21**, pp. 673–677.
- [6] Carrier, G. F., 1966, "Some Effects of Stratification and Geometry in Rotating Fluids," *J. Fluid Mech.*, **24**, pp. 641–659.
- [7] Stewartson, K., 1966, "On Almost Rigid Rotations. Part 2," *J. Fluid Mech.*, **26**, pp. 131–144.
- [8] Pearson, C., 1967, "A Numerical Study of the Time-Dependent Viscous Flow Between Two Rotating Spheres," *J. Fluid Mech.*, **28**, pp. 323–336.
- [9] Munson, B. R., and Joseph, D. D., 1971, "Viscous Incompressible Flow Between Concentric Rotating Spheres, Part I: Basic Flow," *J. Fluid Mech.*, **49**, pp. 289–303.
- [10] Douglass, R. W., Munson, B. R., and Shaughnessy, E. J., 1978, "Thermal Convection in Rotating Spherical Annuli-1. Forced Convection," *Int. J. Heat Mass Transfer*, **21**, pp. 1543–1553.
- [11] Munson, B. R., and Douglass, R. W., 1979, "Viscous Flow in Oscillatory Spherical Annuli," *Phys. Fluids*, **22**(2), pp. 205–208.
- [12] Gagliardi, J. C., Nigro, N. J., Elkouh, A. F., and Yang, J. K., 1990, "Study of the Axially Symmetric Motion of an Incompressible Viscous Fluid Between Two Concentric Rotating Spheres," *J. Eng. Math.*, **24**, pp. 1–23.
- [13] Yang, J. K., Nigro, N. J., and Elkouh, A. F., 1989, "Numerical Study of the Axially Symmetric Motion of an Incompressible Viscous Fluid in an Annulus Between Two Concentric Rotating Spheres," *Int. J. Numer. Methods Fluids*, **9**, pp. 689–712.
- [14] Ni, W., and Nigro, N. J., 1994, "Finite Element Analysis of the Axially Symmetric Motion of an Incompressible Viscous Fluid in a Spherical Annulus," *Int. J. Numer. Methods Fluids*, **19**, pp. 207–236.
- [15] Press, W. H., Flannery, B. P., Teukolsky, S. A., and Vetterling, W. T., 1997, *Numerical Recipes: The Art of Scientific Computing*, Cambridge University Press, Cambridge.

Effect of Pin Tip Clearance on Flow and Heat Transfer at Low Reynolds Numbers

Ali Rozati

Danesh K. Tafti¹

e-mail: dtafti@vt.edu

Mechanical Engineering Department,
Virginia Polytechnic Institute and State
University,
114-I Randolph Hall,
Mail Code 0238,
Blacksburg, VA 24061

Neal E. Blackwell

U.S. Army RDECOM CERDEC,
Fort Belvoir, VA 22060-5816

Cylindrical pin fins with tip clearances are investigated in the low Reynolds number range $5 < Re_D < 400$ in a plane minichannel. Five tip gaps are investigated ranging from a full pin fin ($t^ = 0.0$) to a clearance of $t^* = 0.4D^*$, where D^* is the pin diameter. It is established that unlike high Reynolds number flows, the flow and heat transfer are quite sensitive to tip clearance. A number of unique flow effects, which increase the heat transfer performance, are identified. The tip gap affects the heat transfer coefficient by eliminating viscosity dominated end wall effects on the pin, by eliminating the pin wake shadow on the end walls, by inducing accelerated flow in the clearance, by reducing or impeding the development of recirculating wakes, and by redistributing the flow along the height of the channel. In addition, tip gaps also reduce form losses and friction factor. A clearance of $t^* = 0.3D^*$ was found to provide the best performance at $Re_D < 100$; however, for $Re_D > 100$, both $t^* = 0.2D^*$ and $0.3D^*$ were comparable in performance.*

[DOI: 10.1115/1.2909184]

Keywords: heat transfer, pin fins, tip clearance, low Reynolds number, thermal performance, minichannels

Introduction

Extended surfaces, or fins, are commonly used to increase the rate of heat transfer by increasing the total heat transfer surface area, boundary layer regeneration, and inducing secondary flow structures to increase mixing. Among the various types and shapes of fins, pin fins are particularly used in internal channels such as the trailing edge of turbine blades and heat sinks. Ligrani et al. [1] showed that pin fins are capable of augmenting the heat transfer coefficient up to 500%, with penalty in friction factor up to 20 times greater than a base line plane channel. Numerous investigations have been conducted on the effect of pin fins on heat transfer in a channel. Metzger et al. [2] and Arora and Messah [3] studied the behavior of Nusselt number with the pin row number. Studies by Sparrow and co-workers [4,5], Goldstein et al. [6], Chyu et al. [7], Bilen et al. [8], Short et al. [9,10], Saha and Acharya [11], Won et al. [12], Marques and Kelly [13], Uzol and Comci [14], Kosar et al. [15], and Peles et al. [16] investigated the effect of various parameters such as Reynolds number, pin pitch, variable properties, pin density, and pin height on heat transfer augmentation and thermal performance. The majority of these studies showed that as Reynolds number increases and flow becomes unsteady and eventually turbulent, the formation of a horseshoe vortex pair at the upstream junction of pin and end wall and other three-dimensional flow structures augment the Nusselt number compared to plane channel flow. Ko et al. [17] used flow visualization techniques to show the three dimensionalities of the secondary structures, which are expected to enhance the heat transfer. However, this augmentation decreases with increase in Reynolds number. In general, staggered arrays have proven to have a better performance compared to in-line arrays of pins.

Modifications to the fin shape, such as using a diamond or cubic shaped pin, can also be potentially beneficial to the heat transfer in a pin finned channel. One modification that has been studied by a

few investigators is the introduction of a clearance on the top of the pin. Sparrow and Ramsey [18] studied the heat transfer and pressure drop in arrays of cylinder with tip clearance. Three heights for the pins were used: 30%, 60%, and 87% of the channel height, while the pin diameter was 30% of the channel height. Results showed an increase in mass/heat transfer as Reynolds number increased ($1000 < Re < 9000$, where Re was calculated based on maximum velocity and cylinder diameter). Pressure drop increased considerably with decreasing the tip clearance. Since mass/heat transfer coefficient was only measured on the coated cylinders, the effect of tip clearance was only studied on the cylinders, not the end walls. Jubran et al. [19] studied the effect of tip clearance on both staggered and in-line arrays of cylindrical fins, where the tip clearances were 50% and 100% of the pin height. They found that an in-line array is almost insensitive to the clearance, whereas a staggered array had a 7% reduction in heat transfer with tip clearance. In this study, the top wall was made of wood and a heat flux was applied only through the base wall. Chyu et al. [20] studied the effect of clearance on the top of in-line cubic pin fins at $Re = 16,000$. The results showed that for a 25% clearance of channel height, Nusselt number increased at the downstream rows where the flow was fully developed. However, as the clearance increased, Nusselt numbers on both walls and the pin decreased. They assumed that the increase in Nusselt number at a low value of tip clearance was due to an increase of turbulence level in the shear layer on the top of the pins. Moores and Joshi [21] studied the effect of tip clearance on shrouded pin fins with different height to diameter ratios for a range of $200 < Re < 7000$. In their experimental setup, only the base was heated. Results showed that a small tip clearance could increase the heat transfer coefficient. However, the overall thermal performance was found to decrease with the presence of tip clearance. To the authors' knowledge, none of the studies in the literature have investigated the effect of tip clearance in a channel with heated walls at very low Reynolds numbers (especially at $Re < 200$) in detail. In addition, there is little fundamental understanding of what flow features are responsible for the observed effect of tip clearance on heat transfer and friction. This work is motivated by the results of Rozati et al. [22], in which effects of pin shape,

¹Corresponding author.

Contributed by the Heat Transfer Division of ASME for publication in the JOURNAL OF HEAT TRANSFER. Manuscript received April 20, 2007; final manuscript received October 8, 2007; published online May 20, 2008. Review conducted by Jayathi Murthy.

pitch, and density were analyzed in a pin finned minichannel at very low Reynolds numbers. Results showed the absence of horseshoe vortices, which are responsible for heat transfer augmentation at high Reynolds numbers. Instead, it was established that the extent and size of the wake behind the cylinder and the onset of unsteadiness had a large effect on overall heat transfer augmentation.

Objective

The objective of this study is to investigate the effect of pin tip clearance on heat/mass transfer augmentation. The low Reynolds number range investigated is typical of mini-micro-channels used in electronic heat sinks and in portable fuel cell reformers. The effect of tip clearance on flow features, heat transfer coefficient, and friction is investigated in detail for Reynolds numbers ranging from 5 to 400.

Governing Equations and Numerical Method

The incompressible Navier–Stokes and energy equations are solved in a generalized coordinate system. Fully developed hydrodynamic and thermal conditions are assumed. The channel walls and pins are heated by applying a constant heat flux boundary condition (q^{*n}). The equations are nondimensionalized by pin fin diameter (D^*) as the characteristic length scale, friction velocity (u_τ^*) as the characteristic velocity scale, and $q^{*n}D^*/k$ as the characteristic temperature. Nondimensional pressure and temperature are decomposed into an inlet component, a mean gradient component, and a fluctuating periodic component [23,24],

$$\begin{aligned} P(\mathbf{x}, t) &= P_{\text{in}} - \beta x + p(\mathbf{x}, t) \\ T(\mathbf{x}, t) &= T_{\text{in}} + \gamma x + \theta(\mathbf{x}, t) \end{aligned} \quad (1)$$

The mean pressure gradient β assumes a value of unity, which drives the flow such that a mean balance exists between the flow rate and friction losses in the computational domain. The mean temperature gradient γ is calculated via a global energy balance and is used to volumetrically remove heat in the energy equation, such that there is no net energy input in the domain. The working fluid is assumed to be air with a Prandtl number, $\text{Pr}=0.7$. With these modifications, the governing equations for momentum and energy are discretized with a conservative finite-volume formulation on a multiblock body-fitted mesh using a second-order central difference scheme on a nonstaggered grid topology. The Cartesian velocities, pressure, and temperature are calculated and stored at the cell center, whereas the contravariant components of the flux vectors are stored and calculated at the cell faces. A projection method is used for time integration. Temporal advancement is performed in two steps: a predictor step, which calculates an intermediate velocity field, and a corrector step, which calculates the updated velocity at the new time step by satisfying discrete continuity. Detailed information can be found in Ref. [25].

Computational Geometry

A channel with arrays of cylindrical pins in a staggered arrangement is selected. Pin efficiency is assumed to be unity. This assumption does not affect the calculation of the heat transfer coefficient, since it is not dependent on the fin efficiency unless large property variations become important and affect the flow field. In addition, applications of the current study are in minichannels with very short pins ($O(10^{-3} \text{ m})$), in which the efficiency is close to unity. Therefore, a constant heat flux is applied on both pin and wall surfaces. With the assumption of fully developed flow, periodic boundary conditions in both streamwise and spanwise directions are applied. Five tip clearances ranging from $t=0.0$ to 0.4 are studied and analyzed for their effects on both heat transfer coefficient and friction factor. Figure 1 shows the geometry and Table 1 summarizes the geometrical parameters for all five domains. Calculations are conducted for a range of $5 < \text{Re}_D < 400$.

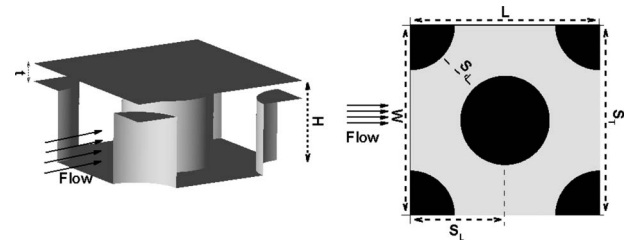


Fig. 1 Definition of pin fin channel geometry and computational domain

Performance Characterization

To calculate the friction factor for the pin finned channel, the tube bundle approach is used [26],

$$f = \frac{\Delta P}{N} \frac{1}{1/2 u_{\text{max}}^2} \quad (2)$$

where pressure and velocity are nondimensionalized by ρu_τ^{*2} and u_τ^* , respectively, and $N=2$ is the number of pin rows in the computational domain.

Using the characteristic temperature scale, the local Nusselt number can be expressed as the inverse of the difference between the surface and a reference temperature, which is calculated as the mass-flow weighted average temperature, in the computational domain

$$\theta_{\text{ref}} = \frac{\int \int \theta |u| dy dz}{\int \int |u| dy dz} \quad (3)$$

Consequently, the surface average Nusselt number is calculated as

$$\frac{1}{\text{Nu}_D} = \frac{1}{A_{\text{total}}} \int \int dA (\theta_w - \theta_{\text{ref}}) \quad (4)$$

To characterize the performance of the pin finned channel, the heat transfer coefficient and friction factor are compared to an equivalent parallel plate channel operating at the same Reynolds number (Re_H) as the pin finned channel ($\text{Re}_H = \text{Re}_D$). The following base line relationships for a plane channel (Incropera and Dewitt [27]) are used:

$$\begin{aligned} f_{\text{ch}} &= \frac{96}{\text{Re}_{D_h}} \\ \text{Nu}_{\text{ch}} &= \frac{hH}{k} = 4.115, \quad \text{Re}_H < 1000 \end{aligned} \quad (5)$$

Grid and Domain Size Independency Study

Domain I is selected to study the effect of grid density and domain size at the highest Reynolds number in the current study ($\text{Re}_D \approx 400$), which guarantees the independency of the results at lower Reynolds numbers as well. To study the grid independency, three grids are studied (coarse, intermediate, and fine), where the grid sizes are increased by factors of 8 and 16. A difference of less than 2% is observed in the computed results between the intermediate and fine grids; hence, the intermediate grid is selected to conduct the calculations. To investigate the effect of domain size, the domain in Fig. 1 is expanded by a factor of 2 in each of the streamwise and spanwise directions. Using the intermediate grid, differences of 3% and 5% in the friction and heat transfer coefficient are observed. The differences are small enough to justify the use of the smaller domain. Tables 2 and 3 show the results and

Table 1 Geometrical parameters

Domain	I	II	III	IV	V
t^*/D^*	0.0	0.1	0.2	0.3	0.4
For all domains	$S_T^*/D^*=2.121$	$S_L^*/D^*=1.061$	$S_d^*/D^*=1.5$	$L^*/D^*=W^*/D^*=2.121$	$H^*/D^*=1.0$

percentage difference for the studied grids and domain sizes. The percentage difference is obtained with fine grid in Table 2 and full domain in Table 3 as base lines.

Validation

The computer program GENIDLEST [25] has been validated extensively in studies of unsteady turbulent heat transfer augmentation using Direct Numerical Simulation (DNS) and Large Eddy Simulation (LES) (e.g., Refs. [28–30]). For the purposes of this study, predictions of friction factor are validated with the experiments of Kosar et al. [15] in Fig. 2, using stream- and spanwise pitches, $S_L=S_T=1.5$, to replicate the experiments. The comparison shows good agreement between the numerical and experimental results. Discrepancies are observed at the lower bound of Reynolds number ($Re_D=25$), which are most likely due to the increased experimental uncertainties at low Reynolds numbers (the nominal experimental uncertainty is reported as 7.2%).

To the authors’ knowledge, no suitable data of heat transfer coefficient (or Nusselt number) are available in the literature for a one-to-one comparison with the current numerical study. Therefore, to validate the accuracy of the code for flow-over-tube type geometries at low Reynolds number, heat transfer coefficient for a single tube (or cylinder) in cross flow is calculated and compared to the available correlation of Hilpert [27]. Table 4 presents the values and percentage difference for the Nusselt number.

Table 2 Grid independency study

Grid (No. of cells)	f	% diff f	Nu	% diff Nu
Coarse (16,384)	1.2530	1.6	9.53	12.0
Intermediate (131,072)	1.2547	1.5	8.43	0.9
Fine (1,048,576)	1.2739	0	8.51	0

Table 3 Domain independency study

Domain	f	% diff f	Nu	% diff Nu
Expanded domain	1.2971	3.3	8.92	4.6
Domain I	1.2547		8.51	

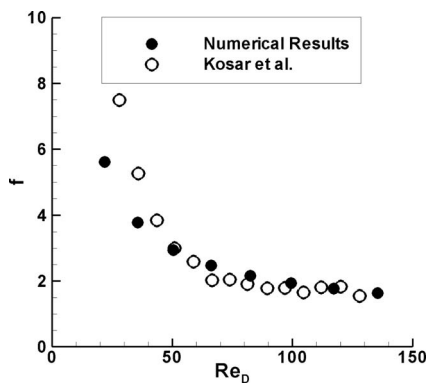


Fig. 2 Comparison of f for numerical results and experiments of Kosar et al. [15]

Results

In the first part of this section, Domain I (with no tip clearance) and Domain IV (with clearance of $t=0.3$) are compared and analyzed to show the effect of tip clearance on the flow and temperature (local Nusselt number) field. These comparisons are made at two representative Reynolds numbers at $Re_D \approx 10$ and $Re_D \approx 325$. In the second part, the augmentation in heat transfer coefficient, pressure losses, and performance of each configuration are presented for the full range of Reynolds numbers studied.

Flow and Temperature Field

Very Low Reynolds Numbers ($Re_D \approx 10$). Both domains, with and without tip clearance, show a steady flow pattern at very low Reynolds numbers. Figure 3 shows streamlines close to the pin surface. In Domain I, the flow field does not exhibit any separation in the wake of the pin and the streamlines follow the surface contour of the cylinder. Some slight streamline distortion is observed near the end walls. In the presence of tip clearance, a much stronger acceleration is observed at the upstream half of the pin tip surface, in both the streamwise and cross stream directions as the flow enters the tip gap. Flow in the tip gap decelerates as it reaches the downstream rim and gets drawn into the wake of the pin.

Although not immediately evident from the streamline plot, the tip gap alters the flow in important ways, which have an impact on heat transfer. The most subtle and difficult to identify effect is that on flow distribution along the height of the channel. The introduction of a tip gap increases the overall cross-sectional flow area near the top but can also lead to flow blockage if it is too small. The degree of flow blockage also depends on the Reynolds number. At low Reynolds number, a smaller fraction of flow would occur through a small tip gap than at higher Reynolds numbers. It was observed that for $Re_D < 50$, the smallest tip gap of $t=0.1$ reduced the amount of flow passing in the top half of the channel, effectively pushing more flow through the bottom half of the channel. This effect is identified by showing the normalized non-dimensional velocity gradient at the bottom wall in Fig. 4 at

Table 4 Comparison of Nusselt number for a single tube in cross flow

Re_D	Nusselt number		
	Numerical	Hilpert correlation	% diff Nu
4	1.33	1.38	3.6
20	2.46	2.56	3.9
100	5.10	5.18	1.5

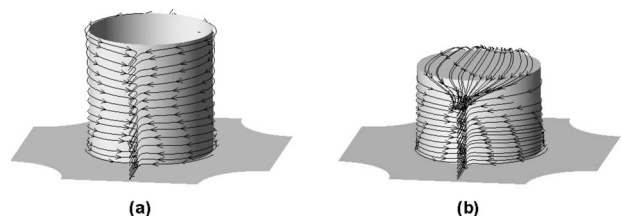


Fig. 3 Wake streamlines at $Re_D \approx 10$; (a) $t=0.0$ and (b) $t=0.3$

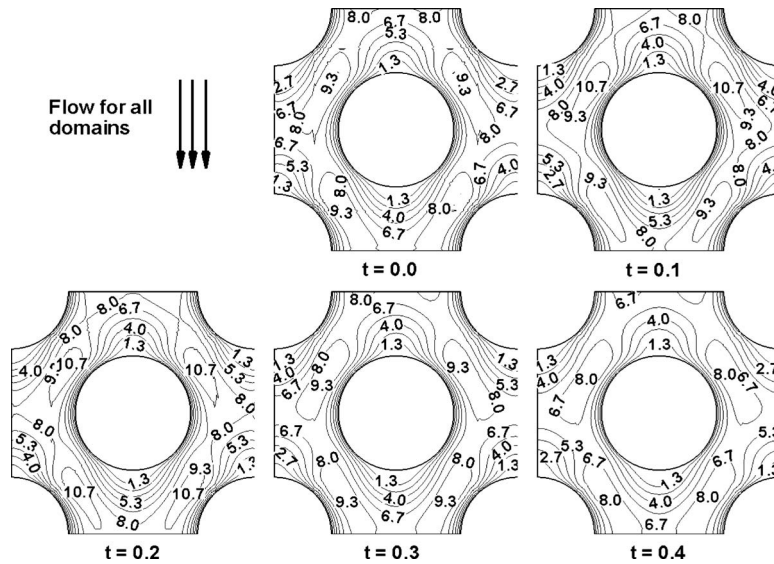


Fig. 4 Velocity gradient ($\partial u/\partial n$) on the bottom end wall at $Re_D \approx 10$ (normalized by u_{max})

$Re_D \approx 10$. This gradient ($\partial u/\partial n$) is related to the local friction coefficient by the factor of $2/Re_D$. It is clear that there is a large increase in the gradients at the bottom wall in the passage between the pins as the tip gap is introduced with $t=0.1$. As the tip gap increases to $t=0.2$, there is a slight decrease in the gradient, which decreases further at $t=0.3$ and 0.4 . While the gradient at $t=0.3$ is of the same level as that without the tip gap, $t=0.4$ falls below that of $t=0$.

Representative temperature distributions ($\theta - \theta_{ref}$) on the pin fin and end walls at $Re_D \approx 10$ are shown in Figs. 5 and 6. It is noted that in regions of high heat transfer, the surface temperature can fall below the reference temperature, which is a mass weighted average in the whole calculation domain (Eq. (3)). Hence, large negative values of ($\theta - \theta_{ref}$) signify the highest heat transfer coefficients. This is consistent with Eq. (4), in which negative local values lead to a larger surface averaged Nusselt number. As expected, the impingement at the front of the pin (stagnation) shows these small positive or negative values, which represent the high-

est rates of heat removal. The augmentation is highest at the center of the channel and decreases toward the end walls. The pattern of temperature distribution on the pin front surface for $t=0.3$ is similar to the full pin, except for the higher heat transfer at the tip due to flow acceleration. The pin surface in the wake has the lowest level of heat transfer particularly in the vicinity of the channel end walls where viscous effects are dominant. Hence, the tip clearance ($t=0.3$) does not change the pattern nor the levels substantially.

Figure 6 shows the distribution of ($\theta - \theta_{ref}$) on the bottom end wall in Domain I and top wall and pin top surface in Domain IV. The bottom end wall shows almost the same pattern of heat transfer distribution for both domains, with Domain IV having slightly lower values of heat transfer, which can be directly related to the relative velocity gradients shown in Fig. 4. A low heat transfer region is located in the immediate wake of the pin caused by the shadow of the pin wake on the wall. Without tip clearance, the ($\theta - \theta_{ref}$) pattern on the top end wall is similar to the bottom end

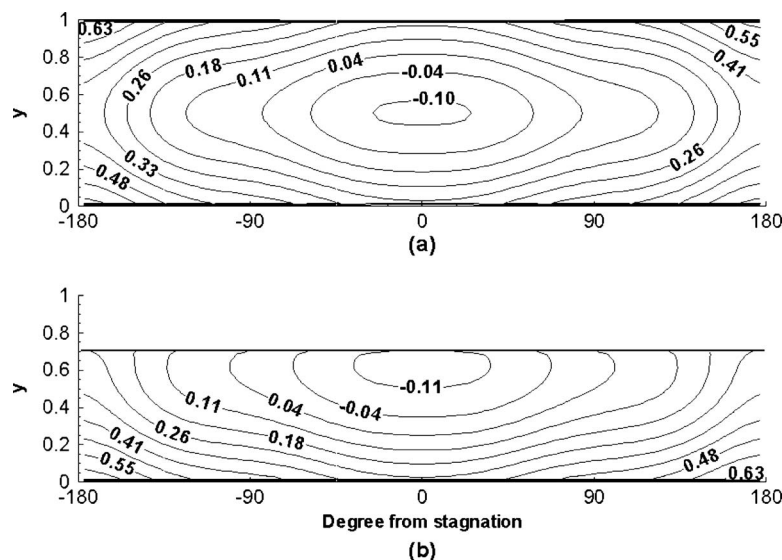


Fig. 5 Temperature ($\theta - \theta_{ref}$) on the pin surface at $Re_D \approx 10$; (a) $t=0.0$ and (b) $t=0.3$

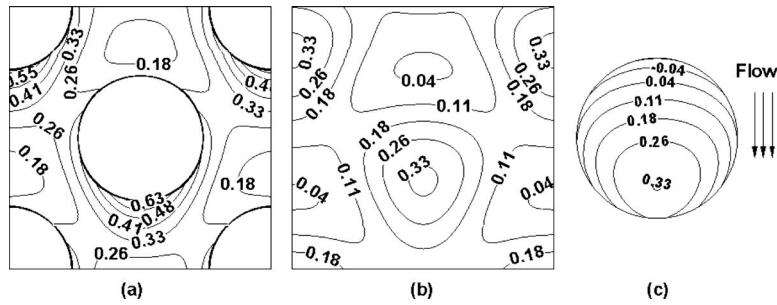


Fig. 6 Temperature ($\theta - \theta_{ref}$) on the (a) bottom end wall ($t=0.0$), (b) top wall ($t=0.3$), and (c) pin-top surface ($t=0.3$) at $Re_D \approx 10$

wall shown in Fig. 6(a). On the other hand, at $t=0.3$, the top wall is influenced significantly by the pin clearance. At the location of the upstream rim of the pin, as the flow enters the clearance, there is a region of low ($\theta - \theta_{ref}$) and high heat transfers as the flow is displaced upwards toward the end wall. This is followed by a gradual decrease in augmentation, which reaches a minimum at the location of the downstream rim of the pin. A comparison of end wall heat transfer with (Fig. 6(b)) and without (Fig. 6(a)) tip clearance shows that the introduction of tip clearance to first order reduces the negative effects of the pin wake shadow on heat transfer, which has an overall positive effect. In addition, the top surface of the pin contributes to heat transfer augmentation by regeneration of the thermal boundary layer. This is identified in Fig. 6(c), in which the leading edge region of the pin tip exhibits high heat transfer coefficients, which gradually decrease downstream.

In contrast to the clearance of $t=0.3$, which is more representative of the larger clearances, the behavior of the surface heat transfer at $t=0.1$ is very different. Unlike $t=0.3$, the heat transfer on the top wall and the pin is lower than that without any clearance, whereas the bottom wall heat transfer increases. This is shown in Fig. 7. Because of the small clearance, not much flow passes through the tip gap resulting in very low heat transfer coefficients on the top wall and the pin-top surface. Similarly, the temperature distribution on the back face of the pin exhibits higher temperatures with lower heat transfer rates.

The bottom wall exhibits much higher heat transfer when compared to $t=0.0$ and $t=0.3$ (Fig. 6(a)). In fact, for $Re_D < 50$, the

clearance of 0.1 has the largest mean Nusselt number on the bottom wall, followed by $t=0.2$, $t=0.0$, $t=0.3$, and $t=0.4$, which directly correlates with the flow distribution and the resulting velocity gradients at the bottom wall in Fig. 4.

Low Reynolds Numbers ($Re_D \approx 325$). As Reynolds number increases, steady recirculation zones develop in the wake of the pin, which eventually become unstable. The onset of the development of recirculation zones changes with different clearances. Recirculation zones are observed as early as $Re_D=70$ for Domain I with no clearance ($t=0.0$), and is delayed up to $Re_D=220$ for Domain V at $Re_D \approx 170$. Once the unsteadiness develops, the flow is characterized by a nonstationary stagnation line and oscillating wake, both of which show quasiperiodic movement in the spanwise direction. However, with the introduction of tip clearance, the onset of large-scale unsteadiness is delayed between $Re_D \approx 220$ and 380 for Domains II–V, respectively. The delay in wake formation and large-scale unsteadiness of the wake can be attributed to the momentum of the tip gap flow, which is drawn into the wake behind the pin, and which prevents or delays the formation of the characteristic recirculating wake. This attribute of the flow can be seen in Fig. 8(b). In contrast, a clear recirculating wake is observed in the time-averaged flow streamlines in Domain I without the tip clearance. It is noteworthy that as the Reynolds number increases, end wall effects become stronger and the structure of the wake has a clear variation along the height of the pin.

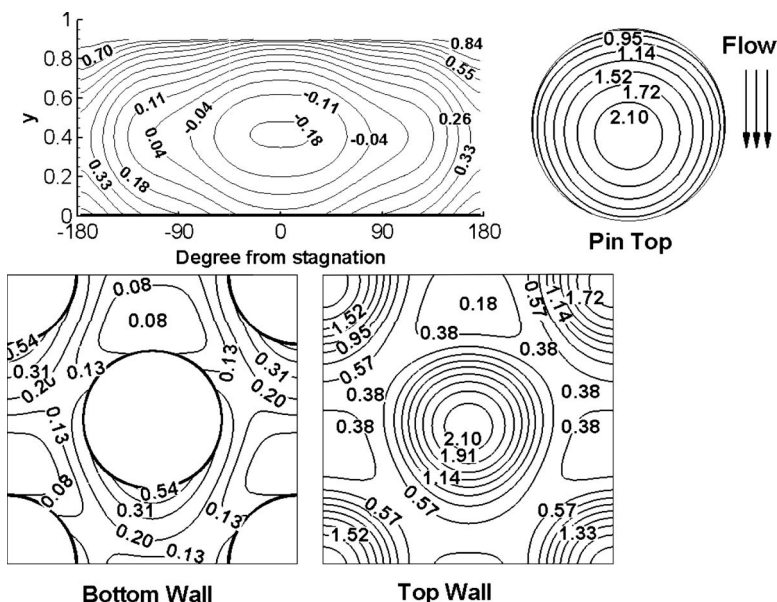


Fig. 7 Surface temperature ($\theta - \theta_{ref}$) of Domain II ($t=0.1$) at $Re_D \approx 10$

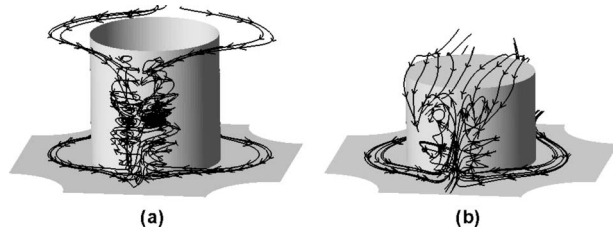


Fig. 8 Wake time-averaged streamlines at $Re_D \approx 325$; (a) $t = 0.0$ and (b) $t = 0.3$

For all unsteady cases, the averaging process is activated after the flow exhibits a stationary behavior. The averaging is then performed for between 20 and 30 nondimensional time units to obtain the time-mean results. Figure 9 shows the surface contours of $(\theta - \theta_{ref})$ at $Re_D \approx 325$ on the pin surface. Similar to what was observed at $Re_D \approx 10$, the pin front side does not show any major improvement with the presence of tip clearance. The high heat transfer region, however, now shifts to the sides due to flow acceleration in between the pins. The low heat transfer region in the wake, on the other hand, shows substantial augmentation in heat transfer coefficient in the presence of tip clearance. This improvement is chiefly a result of improved mixing between the tip gap flow and the wake, which eliminates or weakens the recirculating wake and also reduces end wall effects at the bottom. In addition to improving heat transfer in the pin wake, the tip clearance also has a large favorable effect on the top wall and the pin top as a result of the flow acceleration within the tip gap (Fig. 10).

Just as the tip gap has an effect on flow distribution in the channel at low Re_D , so does it at high Re_D . Figure 11(a) compares $(\theta - \theta_{ref})$ between $t = 0.0$ and $t = 0.3$ at $Re_D \approx 325$ at the bottom wall. First, we note that the wake shadow on the wall is somewhat smaller with tip clearance with much higher heat transfer coefficients as a result of the enhanced mixing as exemplified in Fig. 8(b). The high heat transfer regions for both domains shift to the passage between the pins due to flow acceleration in this region. Domain IV with tip clearance ($t = 0.3$) exhibits much higher heat

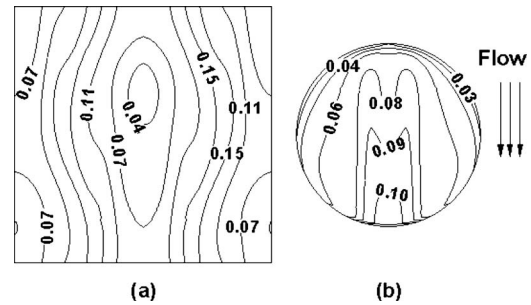


Fig. 10 Time-averaged temperature $(\theta - \theta_{ref})$ on the (a) top wall, and (b) pin-top surface ($t = 0.3$) at $Re_D \approx 325$

transfer than without tip clearance. Once again, the relative difference between the two can be directly related to the wall shear, which is shown in Fig. 11.

Friction Factor Ratio and Heat Transfer (Coefficient) Augmentation.

Friction factor and its ratio with respect to a plane channel at an equivalent Reynolds number (Re_D) are calculated and illustrated for all domains in Fig. 12 for the range of $5 < Re_D < 400$. The friction factor exhibits close to an inverse linear relationship with Reynolds number up to $Re_D \approx 50$, which agrees with laminar flow theory. Introducing tip clearance results in a decrease in form drag and an increase in shear stresses at the walls. The balance between the two determines the overall increase or decrease in friction factor. Results show a slight increase in friction factor for Domain II with $t = 0.1$ at high Reynolds numbers due to a larger increase in wall shear stresses than the corresponding decrease in form losses. However, as the clearance increases further to $t = 0.3$ and 0.4 , form drag is substantially reduced with a corresponding drop in the friction factor. Due to the dominant contribution of form drag at higher Reynolds numbers, the reduction in friction factor with increasing clearance is much more evident at higher Reynolds numbers. Overall augmentation over a plane channel ranges from 2.5 to 8 for $t = 0.0$ to a

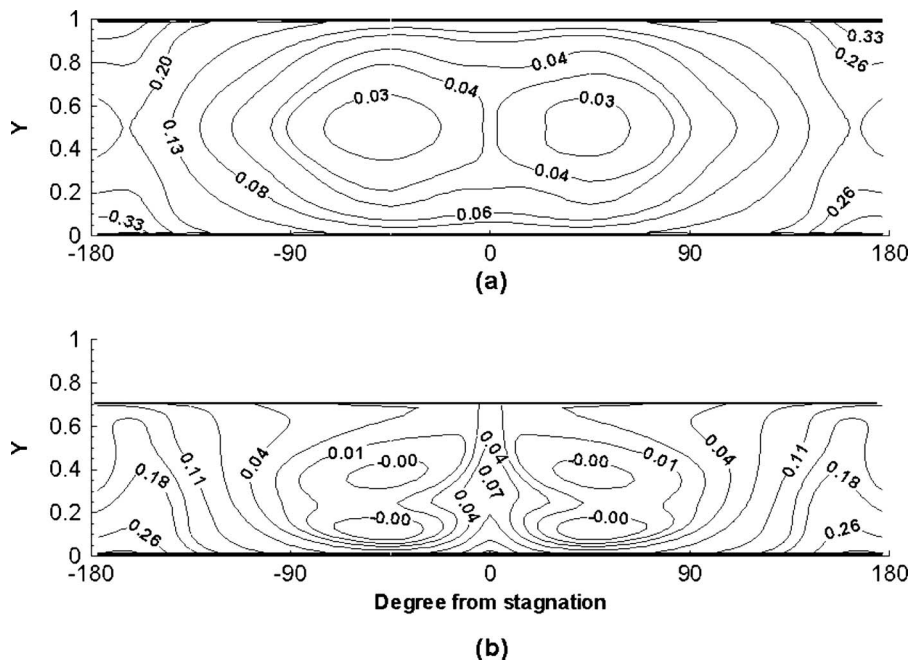


Fig. 9 Time-averaged temperature $(\theta - \theta_{ref})$ on the pin surface at $Re_D \approx 325$; (a) $t = 0.0$ and (b) $t = 0.3$

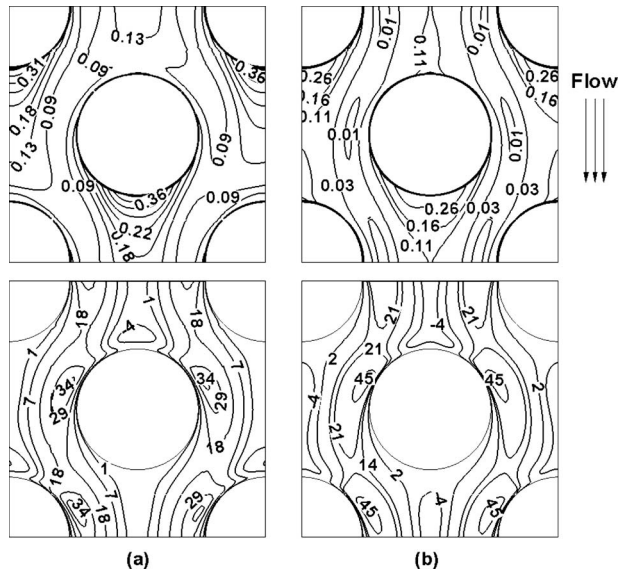
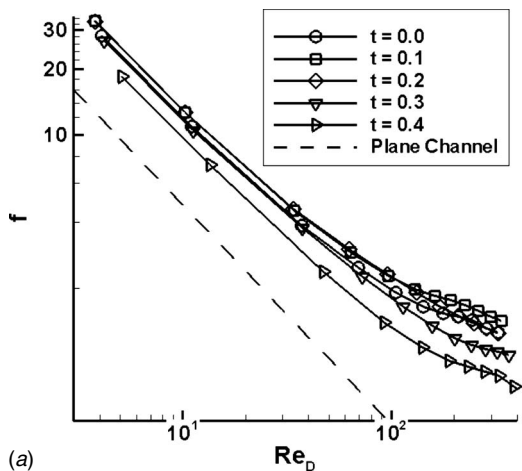
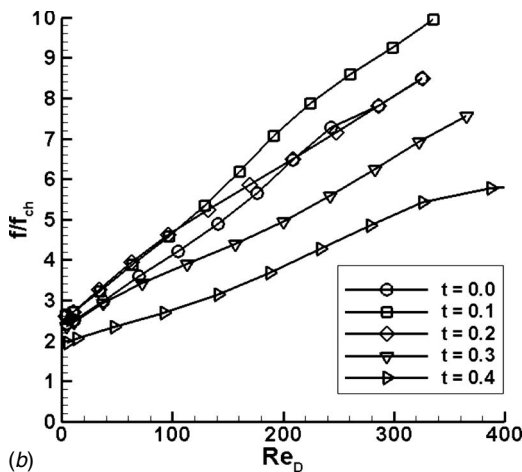


Fig. 11 Time-averaged temperature ($\theta - \theta_{ref}$) (top) and velocity gradient ($\partial u / \partial n$, bottom) on the bottom end wall at $Re_D \approx 325$ for (a) $t=0.0$ and (b) $t=0.3$



(a)



(b)

Fig. 12 (a) Friction factor and (b) friction factor ratio in pin finned channels

growth of 2–5.5 for $t=0.4$.

Figure 13 shows the calculated time- and area-averaged Nusselt numbers for each component surface broken up into top wall, bottom wall, and the pin, together with the overall Nusselt number. Similar to the trend in friction factor, it is noted that in the low Reynolds number regime ($Re_D < 50$), the Nusselt numbers exhibit a near constant value on each surface. The behavior of Nusselt number distribution can be directly related to the observations made earlier on the hydrodynamic effects of the tip gap. The tip gap affects the heat transfer coefficient by eliminating viscosity dominated end wall effects on the pin, by eliminating the pin wake shadow on the end walls, by inducing accelerated flow in the vicinity of the top wall and the pin top, by reducing or impeding the development of recirculating wakes, and by redistributing the flow along the height of the channel. For a tip gap of $t=0.1$, the Nusselt numbers decrease on all surfaces except the bottom wall. There is a sharp drop in Nusselt number on the top wall at $t=0.1$, which recovers monotonically as the tip gap increases. At $t=0.1$, very little to no flow passes through the tip gap, drastically reducing the Nusselt number on the top wall and the pin top (Fig. 7). By the same token, the bulk of the flow is pushed toward the bottom wall, which experiences increased velocity gradients and higher heat transfer coefficients. As the tip gap increases, a larger fraction of the flow passes through the gap steadily increasing the Nusselt number on the top wall and the pin top, while decreasing the Nusselt number on the bottom wall. At larger Reynolds numbers, $Re_D=200$, the Nusselt numbers show a reduced sensitivity to tip clearances for $t > 0.1$.

Figure 14(a) shows the augmentation of heat transfer coefficient with respect to a plane channel. While the tip clearance of $t=0.1$ is not very efficient in augmenting the heat transfer coefficient over the base geometry, larger clearances are more effective. At $Re_D < 50$, $t=0.3$ provides the best augmentation over a plane channel. At higher Reynolds numbers $Re_D > 50$, $t=0.2$ and 0.3 provide the best augmentation ranging from 1.7 (at $Re_D=106$) to 2.9 (at $Re_D=367$).

Pin fins not only improve the heat transfer by augmenting the heat transfer coefficient, but also by increasing the heat transfer area. The combined effect of area and heat transfer coefficient, conductance (K), is shown in Fig. 14(b). The introduction of a tip gap increases the open surface area of the top wall and the pin top while decreasing the circumferential surface area of the pin itself. For the current geometry, the neutral value (no change in surface area) of the gap is 0.5, below which there is an effective increase in surface area. At $Re_D < 50$, $t=0.3$ is the most effective in increasing the overall heat conductance, whereas at $Re_D > 50$, $t=0.2$ is the most effective, closely followed by $t=0.3$.

Performance Measure. Based on design needs and requirements, optimizing the performance of a heat exchanger may be achieved for different end objectives with certain constraints, which need to be satisfied (Gee and Webb [31]). These end objectives could be a reduction in size or weight, reduction in pumping power, an overall increase in heat or mass transfer capacity, and so on. In this study, we consider the objective of increasing the heat transfer capacity while keeping the same pumping power when compared to a base line plane channel. The base line plane channel dimensions are similar to the pin channel with the pins removed from it. To maintain the same pumping power between the two, the corresponding flow rate through the plane channel is higher because of the lower friction. Then, the question asked is whether the pin fin channel operating at the lower flow rate still provides an augmentation in conductance when compared to the plane channel operating at the augmented flow rate.

To calculate the increase in flow rate in the plane channel at the same pumping power, the following equations are used for pin finned and base line channels to calculate the power:

$$\text{Power} = \Delta P^* Q^* = \Delta P^* A_c^* u^*$$

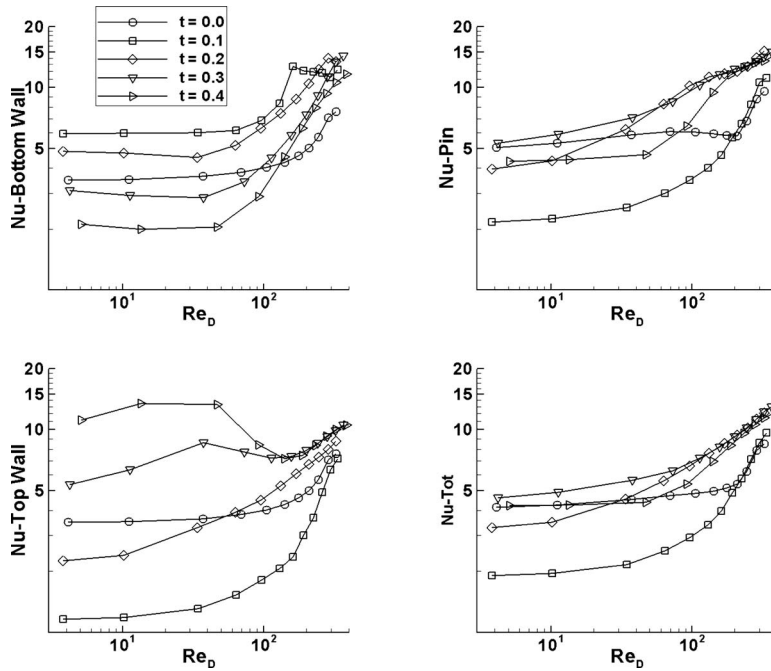


Fig. 13 Pin, end walls, and total Nusselt number versus Re_D at all clearances

for pin finned channel: $\Delta P^* = 1/2 f N \rho^* u_{max}^{*2}$

for plane channel: $\Delta P^* = f_{ch} L^* \rho^* u_{ch}^{*2} / 2 D_h^*$

Therefore, the ratio of power between a pin finned and plane channels can be expressed by

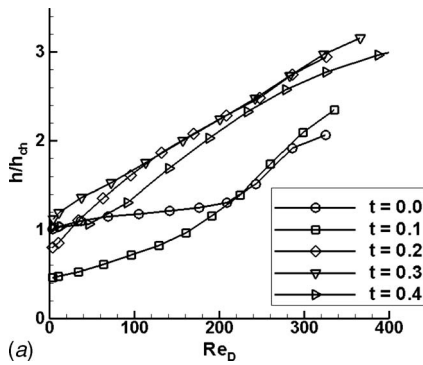
$$\frac{\text{Power}}{\text{Power}_{ch}} = \frac{ND_h}{L} \frac{A_c^*}{A_{c,ch}^*} \frac{f}{f_{ch}} \left(\frac{u_{max}^*}{u_{ch}^*} \right)^3 \quad (6)$$

The channel friction factor is obtained from Eq. (5); however, instead of using an equivalent Reynolds number (Re_D), the plane channel Reynolds number is obtained from

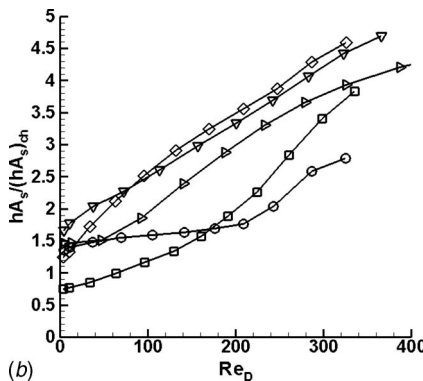
$$Re_{D_h} = Re_D \frac{u_{ch}}{u_{max}} \frac{D_h}{D} \quad (7)$$

By assuming the same pumping power ($\text{Power}/\text{Power}_{ch}=1.0$), the corresponding ratio of flow rates is calculated from Eq. (6).

In the studied range of Reynolds number and clearances, flow rate decreases between 55% and 82% when compared to a plane channel. Clearances of $t=0.4$ and 0.3 have the least reduction in flow rate. Figure 15 shows the increase in thermal conductance of the pin finned channel at the corresponding Reynolds number of a plane channel, $Re_H = 1/2 Re_{D_h}$ (not the Reynolds number of the pin



(a)



(b)

Fig. 14 (a) Heat transfer coefficient and (b) thermal conductance augmentation

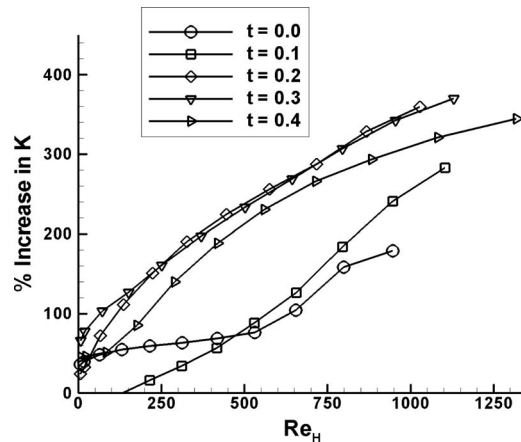


Fig. 15 Increase in thermal conductance compared to a plane channel at the same pumping power

finned channel, Re_D) at the same pumping power. Significant augmentation is observed for clearances of 0.2, 0.3, and 0.4, especially if the plane channel operates at $Re_H > 250$. The only exception is $t=0.1$ at low Reynolds number $Re_H < 100$, in which case there is a decrease in conductance (negative values are cut off from the plot). Overall, the clearance of $t=0.3$ shows the highest positive net augmentation of thermal conductance at $Re_H < 100$, and is considered the optimum clearance in this range. At higher Reynolds numbers, clearance of $t=0.2$ is comparable in performance.

Summary and Conclusion

Cylindrical pin fins with tip gap clearances are investigated in the low Reynolds number range $5 < Re_D < 400$ in a plane channel with the intention of identifying the important hydrodynamic effects, which have an impact on heat transfer. It was established that unlike high Reynolds number flows, in which tip clearances do not have a substantial effect on heat transfer (Jubran et al. [19]), the flow and heat transfer are quite sensitive to the value of the tip gap. While in the turbulent regime, heat transfer augmentation is mostly driven by the turbulent intensity and secondary junction vortices between the pins and end walls, in the low Reynolds number range the primary mechanism, which influences heat transfer, is the size and extent of the pin wake. Hence, anything which can disrupt or reduce the pin wakes has the potential of increasing heat transfer. This can be accomplished by increasing flow acceleration between pins using high density pins or by inducing unsteadiness [22]. This paper investigates the effectiveness of introducing tip clearances in the pins.

The introduction of pin tip gap or clearance has the following important effects, which influence the heat transfer: (1) the clearance eliminates viscosity dominated end wall effects on the pin; (2) it eliminates the pin wake shadow on the end wall with the clearance; (3) it induces accelerated flow in the clearance, which affects the end wall and the pin-top surfaces; (4) it reduces or impedes the development of recirculating wakes by enhanced mixing of the tip flow and the wake; and (5) it redistributes the flow along the height of the channel. These effects carry different relative imports at different Reynolds numbers and contribute to increasing the heat transfer coefficient. In addition, tip clearances reduce form losses and consequently the friction factor, as the tip clearance increases, which coupled to gains in heat transfer, increases the thermal efficiency.

Three measures of performance are investigated in relation to a plane channel: the augmentation of heat transfer coefficient, the augmentation of heat conductance, and a measure of conductance augmentation at the same pumping power as in a plane channel. While the tip clearance of $t=0.1$ is not very efficient in augmenting the heat transfer coefficient over the base geometry, larger clearances are more effective. At low Reynolds numbers $Re_D < 100$, $t=0.3$ is the most effective, whereas at higher Reynolds numbers, $t=0.2$ and $t=0.3$ are comparable in heat transfer performance.

Nomenclature

A	= area
d	= pin diameter
D_h	= plane channel hydraulic diameter
f	= friction factor
k	= thermal conductivity
K	= thermal conductance (hA)
L	= domain length
N	= number of pin rows
S_L	= streamwise pitch
S_T	= spanwise pitch
H	= channel height
\underline{n}	= surface normal vector
Nu	= spatially averaged Nusselt number

P, p	= pressure
Pr	= Prandtl number
q''	= constant heat flux on channel walls
Re_D	= Reynolds number ($u_b D / \nu$)
St	= Stanton number ($Nu / RePr$)
t	= tip clearance
u	= streamwise velocity
W	= channel width
β	= Mean pressure gradient
γ	= Mean temperature gradient
ρ	= density
θ	= modified or homogenized temperature

Subscripts

b	= bulk
c	= cross section
ch	= smooth channel
s	= heat transfer surface
w	= wall
τ	= values based on friction velocity

Superscript

*	= dimensional values
---	----------------------

References

- [1] Ligrani, P. M., Oliveira, M. M., and Blaskovich, T., 2003, "Comparison of Heat Transfer Augmentation Techniques," *AIAA J.*, **41**(3), pp. 337–362.
- [2] Metzger, D. E., Berry, R. A., and Bronson, J. P., 1982, "Developing Heat Transfer in Rectangular Ducts With Staggered Arrays of Short Pin Fins," *J. Heat Transfer*, **104**, pp. 700–706.
- [3] Arora, S. C., and Abdel Messeh, W., 1983, "Heat Transfer Experiments in High Aspect Ratio Rectangular Channel With Epoxied Short Pin Fins," *ASME Paper No. 83-GT-57*.
- [4] Sparrow, E. M., and Vemuri, S. B., 1986, "Orientation Effects on Natural Convection/Radiation Heat Transfer From Pin-Fin Arrays," *Int. J. Heat Mass Transfer*, **29**(3), pp. 359–368.
- [5] Sparrow, E. M., and Grannis, V. B., 1991, "Pressure Drop Characteristics of Heat Exchangers Consisting of Arrays of Diamond-Shape Pin Fins," *Int. J. Heat Mass Transfer*, **34**(3), pp. 589–600.
- [6] Goldstein, R. J., Jabbari, M. Y., and Chen, S. B., 1994, "Convective Mass Transfer and Pressure Loss Characteristics of Staggered Short Pin-Fin Arrays," *Int. J. Heat Mass Transfer*, **37**(1), pp. 149–160.
- [7] Chyu, M. K., Hsing, Y. C., and Natarajan, V., 1998, "Convective Heat Transfer of Cubic Fin Arrays in a Narrow Channel," *J. Turbomach.*, **120**, pp. 362–367.
- [8] Bilen, K., Akyol, U., and Yapici, S., 2001, "Heat Transfer and Friction Correlations and Thermal Performance Analysis for a Finned Surface," *Energy Convers. Manage.*, **42**, pp. 1071–1083.
- [9] Short, B. E., Jr., Raad, P. E., and Price, D. C., 2002, "Performance of Pin Fin Cast Aluminum Coldwalls, Part Friction Factor Correlations," *J. Thermophys. Heat Transfer*, **16**(3), pp. 389–396.
- [10] Short, B. E., Jr., Raad, P. E., and Price, D. C., 2002, "Performance of Pin Fin Cast Aluminum Coldwalls, Part 2: Colburn j -Factor Correlations," *J. Thermophys. Heat Transfer*, **16**(3), pp. 397–403.
- [11] Saha, A. K., and Acharya, S., 2003, "Parametric Study of Unsteady Flow and Heat Transfer in a Pin-Fin Heat Exchanger," *Int. J. Heat Mass Transfer*, **46**, pp. 3815–3830.
- [12] Won, S. Y., Mahmood, G. I., and Ligrani, P. M., 2004, "Spatially-Resolved Heat Transfer and Flow Structure in a Rectangular Channel With Pin Fins," *Int. J. Heat Mass Transfer*, **47**, pp. 1731–1743.
- [13] Marques, C., and Kelly, K. W., 2004, "Fabrication and Performance of a Pin Fin Micro Heat Exchanger," *J. Heat Transfer*, **126**, pp. 434–444.
- [14] Uzol, O., and Camci, C., 2005, "Heat Transfer, Pressure Loss and Flow Field Measurement Downstream a Staggered Two-Row Circular and Elliptical Pin Fin Arrays," *J. Heat Transfer*, **127**, pp. 458–471.
- [15] Kosar, A., Mishra, C., and Peles, Y., 2005, "Laminar Flow Across a Bank of Low Aspect Ratio Micro Pin Fins," *J. Fluids Eng.*, **127**, pp. 419–430.
- [16] Peles, Y., Kosar, A., Mishra, C., Kuo, C., and Schneider, B., 2005, "Forced Convective Heat Transfer Across a Pin Fin Micro Heat Sink," *Int. J. Heat Mass Transfer*, **48**, pp. 3615–3627.
- [17] Ko, J.-H., Ewing, M. E., Guezennec, Y. G., and Christensen, R. N., 2002, "Development of a Low Reynolds Number Enhanced Heat Transfer Surface Using Flow Visualization Techniques," *Int. J. Heat Fluid Flow*, **23**, pp. 444–454.
- [18] Sparrow, E. M., and Ramsey, J. W., 1978, "Heat Transfer and Pressure Drop for a Staggered Wall-Attached Array of Cylinders With Tip Clearance," *Int. J. Heat Mass Transfer*, **21**, pp. 1369–1377.
- [19] Jubran, B. A., Hamdan, M. A., and Abdulah, R. M., 1993, "Enhanced Heat Transfer, Missing Pin, and Optimization for Cylindrical Pin Fin Arrays," *J. Heat Transfer*, **115**, pp. 576–583.
- [20] Chyu, M. K., Yen, C. H., and Ma, W., 1999, "Effects of Flow Gap Atop Pin

- Elements on The Heat Transfer From Pin Fin Arrays,” ASME Paper No. 99-GT-47.
- [21] Moores, K. A., and Joshi, Y. K., 2003, “Effect of Tip Clearance on the Thermal and Hydrodynamic Performance of a Shrouded Pin Fin Array,” *J. Heat Transfer*, **125**, pp. 999–1006.
- [22] Rozati, A., Tafti, D. K., and Blackwell, N. E., 2007, “Thermal Performance of Pin Fins at Low Reynolds Numbers in Mini-Micro Channels,” ASME Paper No. HT2007-32158.
- [23] Zhang, L., Tafti, D., Najjar, F., and Balachander, S., 1997, “Computations of Flow and Heat Transfer in Parallel-Plate Fin Heat Exchangers on the CM-5: Effects of Flow Unsteadiness and Three-Dimensionality,” *Int. J. Heat Mass Transfer*, **40**(66), pp. 1325–1341.
- [24] Patankar, S. V., Liu, C. H., and Sparrow, E. M., 1977, “Fully-Developed Flow and Heat Transfer in Ducts Having Streamwise-Periodic Variations of Cross-Sectional Area,” *ASME J. Heat Transfer*, **99**, pp. 180–186.
- [25] Tafti, D. K., 2001, “GenIDLEST—A Scalable Parallel Computational Tool for Simulating Complex Turbulent Flows,” *Proceedings of ASME Fluids Engineering Division*, FED-Vol. 256, ASME, New York.
- [26] Zukauskas, A., 1972, “Heat Transfer From Tubes in Cross Flow,” *Advances in Heat Transfer*, J. P. Hartnett and T. F. Irvine, Jr., eds., Vol. 8, Academic, New York.
- [27] Incropera, F. P., and DeWitt, D. P., 2006, *Fundamental of Heat and Mass Transfer*, 6th ed., Wiley, New York.
- [28] Tafti, D. K., 2005, “Evaluating the Role of Subgrid Stress Modeling in a Ribbed Duct for the Internal Cooling of Turbine Blades,” *Int. J. Heat Fluid Flow*, **26**(1), pp. 92–104.
- [29] Sewall, E. A., Tafti, D. K., Thole, K. A., and Graham, A., 2006, “Experimental Validation of Large Eddy Simulations of Flow and Heat Transfer in a Stationary Ribbed Duct,” *Int. J. Heat Fluid Flow*, **27**(2), pp. 243–258.
- [30] Elyyan, M. A., Rozati, A., and Tafti, D. K., 2008, “Investigation of Dimpled Fins for Heat Transfer Enhancement in Compact Heat Exchangers,” *Int. J. Heat Mass Transfer*, **51**, pp. 2950–2966.
- [31] Gee, D. L., and Webb, R. L., 1980, “Forced Convection Heat Transfer in Helically Rib-Roughened Tubes,” *Int. J. Heat Mass Transfer*, **23**, pp. 1127–1136.

Computational Study of Heat Transfer in a Conjugate Turbulent Wall Jet Flow at High Reynolds Number

E. Vishnuvardhanarao

Research Scholar
e-mail: elaprolu@iitg.ernet.in

Manab Kumar Das¹

Former Associate Professor
e-mail: manab@mech.iitkgp.ernet.in

Department of Mechanical Engineering,
Indian Institute of Technology Guwahati,
Guwahati 781 039, India

In the present case, the conjugate heat transfer involving the cooling of a heated slab by a turbulent plane wall jet has been numerically solved. The bottom of the solid slab is maintained at a hot uniform temperature, whereas the wall jet temperature, is equal to the ambient temperature. The Reynolds number considered is 15,000 because it has already been experimentally found and reported that the flow becomes fully turbulent and is independent of the Reynolds number. The high Reynolds number two-equation model (κ - ϵ) has been used for the turbulence modeling. The parameters chosen for the study are the conductivity ratio of the solid-fluid (K), the solid slab thickness (S), and the Prandtl number (Pr). The ranges of parameters are $K=1-1000$, $S=1-10$, and $Pr=0.01-100$. Results for the solid-fluid interface temperature, local Nusselt number, local heat flux, average Nusselt number, and average heat transfer are presented and discussed. [DOI: 10.1115/1.2908429]

Keywords: wall jet, conjugate heat transfer, turbulent flow, numerical simulation

1 Introduction

A conjugate heat transfer problem occurs when the fluid regime is coupled with the conducting solid wall having a finite thickness. The temperature and the heat fluxes at the solid-fluid interface are considered to be equal. This is referred to as the fourth-kind boundary condition [1]. Conjugate heat transfer applies to a thermal system in which the multimode convection/conduction heat transfer is of particular importance to thermal design. In most instances, it arises where the external and the internal temperature fields are coupled. Conjugate heat transfer is involved in many applications such as high speed jet engines, electronics cooling, film cooling of turbine blades, extrusion of materials, and so forth.

In the present case, conjugate heat transfer occurring due to a turbulent plane wall jet is considered. Glauert [2] has defined a plane wall jet as a stream of fluid blown tangentially along a plane wall. Similarity solution for a plane wall jet as well as a radial wall jet for both the laminar and the turbulent cases are presented. Seban and Back [3] have measured and computed the turbulent velocity profile and the adiabatic wall temperature. The results agree generally with each other. Launder and Rodi [4] have given a review of the experimental literature on the turbulent wall jets. They have considered the cases of the two-dimensional wall jet on a plane surface, the two-dimensional wall jet on a curved surface, and the three-dimensional wall jet. Experiments with good accuracy and the ability to test the reliability of the new crop of calculation methods for turbulent flows are identified. Later on, Launder and Rodi [5] have reviewed the experimental data and theoretical models for expressing the computational fluid dynamics of turbulent wall jets. The wall jet is defined as a boundary layer in which, due to some initially supplied momentum, the flow velocity over some region in the shear layer exceeds the

freestream velocity. Attempts to formulate generalized expressions for the velocity profiles in a plane two-dimensional wall jet are reviewed, together with the turbulent energy balance in an equilibrium wall jet. The applications of Boussinesq viscosity models and Reynolds stress closure models to numerically express turbulent wall jets are addressed. Dakos et al. [6] have made extensive single-point turbulence measurements in a heated wall jet on a convex wall and in an equivalent plane flow. They have reported that the turbulence structure and the transfer of heat and momentum are affected by wall curvature.

In case of laminar flow, many publications are devoted to conjugate heat transfer on a flat plate, details of which may be found in Ref. [7]. However, the conjugate heat transfer study involving a turbulent flow has received little attention. Some of the conjugate heat transfer work published in literature (involving turbulent flow) are by Iaccarino et al. [8], Kassab et al. [9], and Hsieh and Lien [10]. In the conjugate heat transfer approach, the conduction and the convection equations are solved simultaneously. The near-wall treatments of turbulence models are the key factors to yield accurate wall heat transfer predictions. In the standard high Reynolds number κ - ϵ models, wall functions are commonly employed to bridge the turbulent and near-wall viscous regions.

In the present case, the conjugate heat transfer involving a turbulent plane wall jet is considered. The parameters considered are the conductivity ratio, the solid slab thickness, and the Prandtl number. The Reynolds number considered is 15,000 because the flow becomes fully turbulent and then it becomes independent of the Reynolds number, as has been experimentally observed by Holland and Liburdy [11]. The purpose of the study is to observe and describe the effect of Prandtl number (Pr), thermal conductivity ratio (K), and the thickness of solid slab (S) on the interface surface temperature, heat transfer between the solid and the fluid, local Nusselt number, distribution, average Nusselt number and the temperature distribution in the solid and the fluid. The ranges of parameters considered are 0.01–100 for Pr , 1–1000 for K , and 1–100 for S .

¹Corresponding author. Present address: Associate Professor, Department of Mechanical Engineering, Indian Institute of Technology Kharagpur, West Bengal 721302, India.

Contributed by the Heat Transfer Division of ASME for publication in the JOURNAL OF HEAT TRANSFER. Manuscript received March 7, 2007; final manuscript received October 23, 2007; published online May 16, 2008. Review conducted by Louis C. Burmeister.

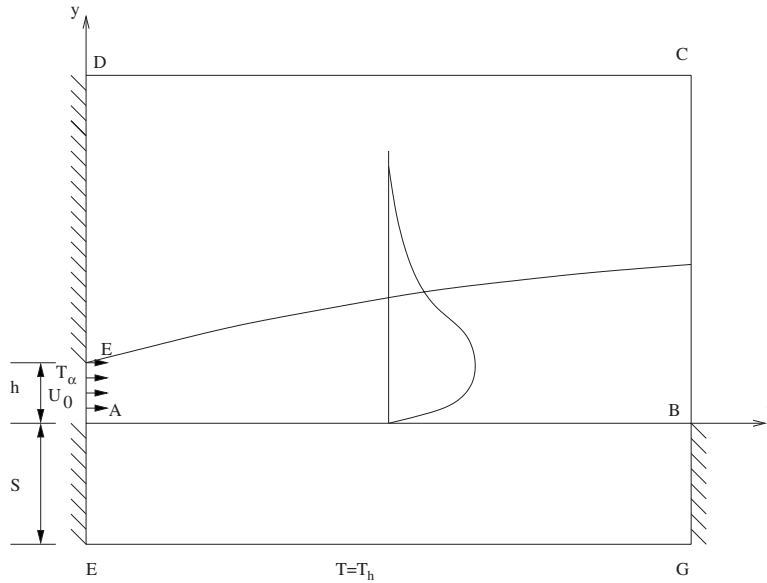


Fig. 1 Schematic and computational domain of the wall jet flow

2 Problem Description and Governing Equations

The schematic diagram of the two-dimensional wall jet with a solid slab is shown in Fig. 1. The governing equations are considered to be steady, two dimensional, and incompressible. Thermophysical properties are assumed to be constant. In the fluid region, the flow is fully turbulent and the Reynolds averaged Navier–Stokes (RANS) equations are used for predicting the turbulent flow. The Boussinesq approximation is used to link the Reynolds stresses to the velocity gradients. The standard κ - ϵ model is used for calculating the turbulent viscosity (ν_t). In the solid region, the two-dimensional heat transfer equation is solved. The dimensionless variables are defined as

$$\bar{U} = \frac{\bar{u}}{U_0}, \quad \bar{V} = \frac{\bar{v}}{U_0}, \quad X = \frac{\bar{x}}{h}, \quad Y = \frac{\bar{y}}{h}, \quad \bar{\theta} = \frac{\bar{T} - T_\infty}{T_h - T_\infty} \quad (1)$$

$$\bar{P} = \frac{\bar{p} - p_0}{\rho U_0^2}, \quad k_n = \frac{k}{U_0^2}, \quad \epsilon_n = \frac{\epsilon}{U_0^3/h}, \quad \nu_{t,n} = \frac{\nu_t}{\nu}, \quad \alpha_{t,n} = \frac{\alpha_t}{\alpha} \quad (2)$$

The non-dimensionalized equations are as follows:

In the fluid:

continuity equation,

$$\frac{\partial \bar{U}}{\partial X} + \frac{\partial \bar{V}}{\partial Y} = 0 \quad (2)$$

x-momentum equation,

$$\frac{\partial(\bar{U})^2}{\partial X} + \frac{\partial(\bar{U}\bar{V})}{\partial Y} = -\frac{\partial}{\partial X} \left(\bar{P} + \frac{2}{3}k \right) + \frac{1}{\text{Re}} \frac{\partial}{\partial X} \left[(1 + \nu_{t,n}) \frac{\partial \bar{U}}{\partial X} \right] + \frac{1}{\text{Re}} \frac{\partial}{\partial Y} \left[(1 + \nu_{t,n}) \frac{\partial \bar{U}}{\partial Y} \right] \quad (3)$$

y-momentum equation,

$$\frac{\partial(\bar{U}\bar{V})}{\partial X} + \frac{\partial(\bar{V})^2}{\partial Y} = -\frac{\partial}{\partial Y} \left(\bar{P} + \frac{2}{3}k \right) + \frac{1}{\text{Re}} \frac{\partial}{\partial X} \left[(1 + \nu_{t,n}) \frac{\partial \bar{V}}{\partial X} \right] + \frac{1}{\text{Re}} \frac{\partial}{\partial Y} \left[(1 + \nu_{t,n}) \frac{\partial \bar{V}}{\partial Y} \right] \quad (4)$$

temperature equation ($\bar{\theta}$),

$$\frac{\partial(\bar{U}\bar{\theta})}{\partial X} + \frac{\partial(\bar{V}\bar{\theta})}{\partial Y} = \frac{1}{\text{Re Pr}} \frac{\partial}{\partial X} \left[(1 + \alpha_{t,n}) \frac{\partial \bar{\theta}}{\partial X} \right] + \frac{1}{\text{Re Pr}} \frac{\partial}{\partial Y} \left[(1 + \alpha_{t,n}) \frac{\partial \bar{\theta}}{\partial Y} \right] \quad (5)$$

turbulent kinetic energy (k_n) equation,

$$\frac{\partial(\bar{U}k_n)}{\partial X} + \frac{\partial(\bar{V}k_n)}{\partial Y} = \frac{1}{\text{Re}} \frac{\partial}{\partial X} \left[\left(1 + \frac{\nu_{t,n}}{\sigma_k} \right) \frac{\partial k_n}{\partial X} \right] + \frac{1}{\text{Re}} \frac{\partial}{\partial Y} \left[\left(1 + \frac{\nu_{t,n}}{\sigma_k} \right) \frac{\partial k_n}{\partial Y} \right] + G_n - \epsilon_n \quad (6)$$

rate of dissipation (ϵ_n) equation is

$$\frac{\partial(\bar{U}\epsilon_n)}{\partial X} + \frac{\partial(\bar{V}\epsilon_n)}{\partial Y} = \frac{1}{\text{Re}} \frac{\partial}{\partial X} \left[\left(1 + \frac{\nu_{t,n}}{\sigma_\epsilon} \right) \frac{\partial \epsilon_n}{\partial X} \right] + \frac{1}{\text{Re}} \frac{\partial}{\partial Y} \left[\left(1 + \frac{\nu_{t,n}}{\sigma_\epsilon} \right) \frac{\partial \epsilon_n}{\partial Y} \right] + C_{1\epsilon} \frac{\epsilon_n}{k_n} G_n - C_{2\epsilon} \frac{\epsilon_n^2}{k_n} \quad (7)$$

production (G_n),

$$G_n = \frac{\nu_{t,n}}{\text{Re}} \left[2 \left(\frac{\partial \bar{U}}{\partial X} \right)^2 + 2 \left(\frac{\partial \bar{V}}{\partial Y} \right)^2 + \left(\frac{\partial \bar{U}}{\partial Y} + \frac{\partial \bar{V}}{\partial X} \right)^2 \right] \quad (8)$$

eddy viscosity ($\nu_{t,n}$),

$$\nu_{t,n} = C_\mu \text{Re} \frac{k_n^2}{\epsilon_n} \quad (9)$$

eddy diffusivity ($\alpha_{t,n}$),

$$\alpha_{t,n} = \nu_{t,n} / \text{Pr} \quad (10)$$

where $\sigma_k=1.0$, $\sigma_\epsilon=1.30$, $C_{1\epsilon}=1.44$, $C_{2\epsilon}=1.92$, and $C_\mu=0.09$ In the solid region, the energy equation is

$$\frac{\partial^2 \bar{\theta}}{\partial X^2} + \frac{\partial^2 \bar{\theta}}{\partial Y^2} = 0 \quad (11)$$

3 Boundary Conditions

The jet enters the quiescent ambient fluid at the surface of the wall. The nondimensionalized boundary conditions are provided as input to the solution. At the inlet (AE) of the jet, $U=1.0$, $V=0$, and $\theta=0$ are the boundary conditions for the velocities and temperature, respectively. For the turbulent kinetic energy equation, the boundary condition at the inlet is $k_n=1.5I^2$, where I is the turbulence intensity and is equal to 0.02 [12]. For the dissipation equation, the boundary condition at inlet is $\epsilon_n=k_n c_\mu^{3/4}/l$, where $l=0.07h$ [12]. At the solid wall (DE), the no-slip boundary condition for velocities and the adiabatic condition for the temperature are used. At the entrainment and exit boundaries (i.e., CD and BC, respectively), Neumann boundary conditions are provided, i.e., $\partial\phi/\partial n=0$, where $\phi=\bar{U}$, \bar{V} , $\bar{\theta}$, k_n , and ϵ_n . At the solid-fluid interface (AB), no-slip boundary conditions are applied for velocities and for the temperature, equality of temperature, and flux, i.e., $(\theta_s)_w=(\theta_f)_w$ and $(Q_w)_s=(Q_w)_f$ are applied and the details are mentioned in Appendix A. Wall functions are used to prescribe the shear stress, production, and dissipation rates at the walls. It has been ensured that the first grid falls within the logarithmic region, i.e., $20 \leq Y^+ \leq 60$, where $Y^+=y u_\tau/\nu$, u_τ being the friction velocity.

4 Numerical Scheme and Validation of the Code

In the present work, for the fluid and the solid regions, the dimensionless governing equations are discretized using the control volume method [13]. The power-law scheme of Patankar [13] is used to discretize the convective terms, which uses a polynomial expression to evaluate the flux (Versteeg and Malalasekera [14]). The central difference scheme is used for the diffusive terms, which is second order accurate. These two schemes are followed to ensure the stability of the solution. To avoid the fine mesh required to resolve the viscous sublayer near the boundary, the wall function method [15] has been used, which is appropriate for high Reynolds number flows. The SIMPLE [13] algorithm is followed to solve the finite difference equations. A pseudotransient approach [14] was used to underrelax the momentum and the turbulent equations. An under-relaxation of 0.2 is used for pressure. In the solid region, central differencing is used for discretizing the energy equation by a finite difference technique.

The code has been validated for the fluid flow and the heat transfer solution with the experimental results for an offset jet. In case of an offset jet, the fluid issues from a slot at a distance above the wall, the distance called the offset. The velocity profile at five downstream locations, viz., 3, 6, 9, 12, and 15, are compared with the experimental results of Pelfrey and Liburdy [16] for an offset ratio (offset height/slot width) of 7. An excellent agreement has been obtained. The temperature distributions at various downstream locations are computed for wall jet, and offset ratios 3, 7, and 11. In this case, the bottom wall is maintained at an adiabatic condition. The results are compared with the experimental results of Holland and Liburdy [11]. A very good agreement has been obtained. In all the Reynolds number considered is 15,000. The comparisons are presented in detail in Ref. [17]. Since the flow is incompressible, the already available fluid flow solution is used to solve the energy equation in both the solid and the fluid regions. Grid independence is shown in the solid for $S=1$ by varying the Prandtl number and thermal conductivity ratio (K). For other sizes, the grid size is correspondingly increased, which is reasonably valid in the solid block.

After the code validation, a grid independence study was carried out for all the cases and the effect of domain size was also considered and tested. After considerable numerical testing, it was found that the domain size of 75×35 is satisfactory for all the cases. It has been observed that even though a grid size of 121×101 produces a good solution, the grid size of 151×101 has been considered for all the cases.

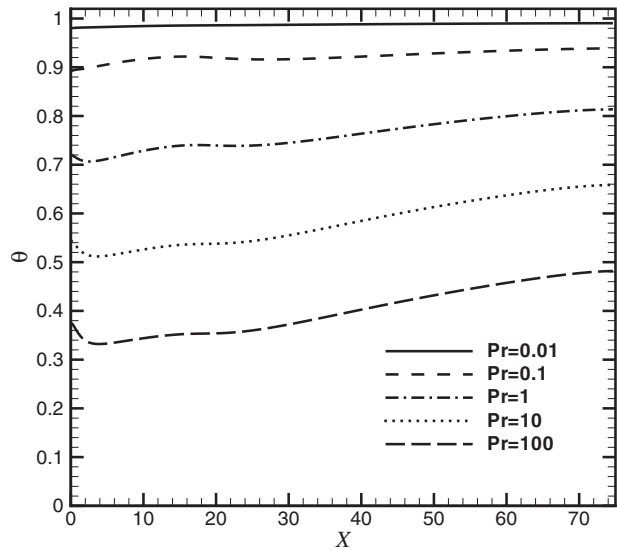


Fig. 2 Interface temperature distribution (θ_i) distribution for $S=10$ and $K=1000$ at various Prandtl numbers

5 Results and Discussion

In the present work, $Re=15,000$ is chosen for all computations. The flow then is fully turbulent and there is no discernible Reynolds number effect on the mean flow characteristics [11]. Since the uniform velocity and some turbulent intensity are given at the inlet of the jet, it takes some length for the flow to become fully turbulent and develop the self-similar region. It is observed that approximately at $X \approx 30$ the flow becomes fully turbulent and self-similarity is achieved. The effects of Pr , K , and S on the interface surface temperature (θ_i), heat transfer between the solid and the fluid (Q_i), local Nusselt number distribution (Nu_x), average Nusselt number (Nu), and the temperature distribution in the solid and the fluid have been discussed. In the present study, Pr is varied between 0.01 and 100, K is varied between 1 and 1000, and S is varied between 1 and 10. The derivation of heat flux is given in Appendix A. The definitions of Nu and Nu_x are shown in Appendix B.

5.1 Interface Temperature. Figure 2 shows the interface temperature (θ_i) distribution at various Prandtl numbers keeping the solid thickness ($S=10$) and the thermal conductivity ratio ($K=1000$) constant. It is observed that θ_i is high at low Pr . This is because at low Pr , the thermal boundary layer is thick. A large surface temperature is required to dissipate the heat to the jet fluid. Conversely, the interface temperature decreases significantly as Pr increases because the thermal boundary layer is thin and a lower surface temperature is sufficient to dissipate the heat. The surface temperature increases along the wall at high Prandtl numbers because initially the heat transfer is large, which decreases gradually along the length. The interface temperature distribution at various thermal conductivity ratios keeping the Prandtl number equal to 1.0 and solid thickness equal to 10 are given in Fig. 3. When K is small, the resistance to heat transfer is large, the drop in temperature is large, and, thus, the interface temperature is small. As K increases to 1000, the interface temperature is relatively large because of the same reason. The variation of θ_i distribution at various solid thicknesses (S) keeping the Prandtl number ($Pr=1.0$) and thermal conductivity ratio ($K=1000$) is plotted in Fig. 4. For a small slab thickness $S=1$, the thermal resistance is less leading to a higher interface temperature. As S is increased to 10, it is observed that the interface temperature has dropped down because of the same reason.

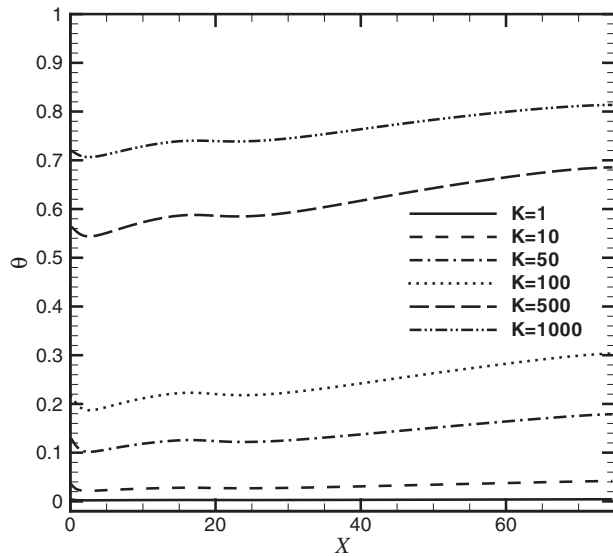


Fig. 3 Interface temperature distribution (θ) distribution for $Pr=1$ and $S=10$ at various thermal conductivity ratios (K)

5.2 Local Nusselt Number. The local Nusselt number variation is shown in Fig. 5 for various Prandtl numbers keeping the solid thickness ($S=10$) and thermal conductivity ratio ($K=1000$) constant. In general, Nu_x increases to a large value near the jet entry and then gradually decreases in the direction of flow. This is a characteristic of the jet boundary layer formation. As shown in Fig. 5, it demonstrates clearly that Nu_x increases with Pr because of the thinning of the thermal boundary layer. Figure 6 shows the Nu_x distribution at various thermal conductivity ratios keeping $Pr=1.0$ and $S=10$. It is observed that for the range of K , the Nu_x distribution is independent of K . The Nu_x distribution at various solid thicknesses (S) keeping $Pr=1.0$ and thermal conductivity ratio $K=1000$ is shown in Fig. 7. Similar to the previous case, the Nu_x distributions for the range of S superimpose with each other. From these three figures, it is concluded that Nu_x is dependent on the fluid property Pr and independent of K and S .

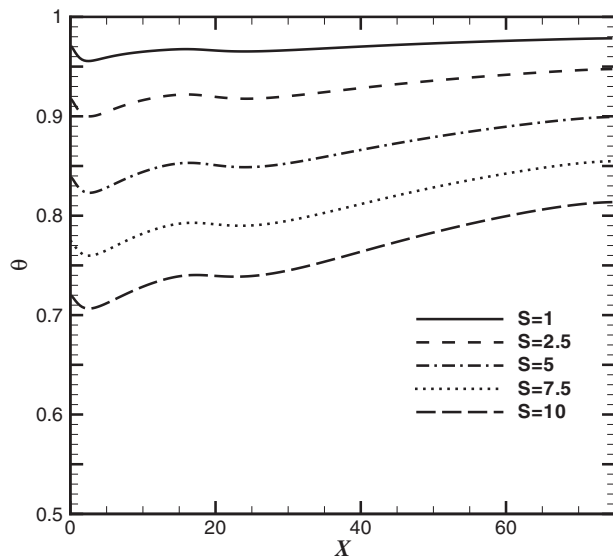


Fig. 4 Interface temperature distribution (θ) distribution for $Pr=1$ and $K=1000$ at solid thickness ratios (S)

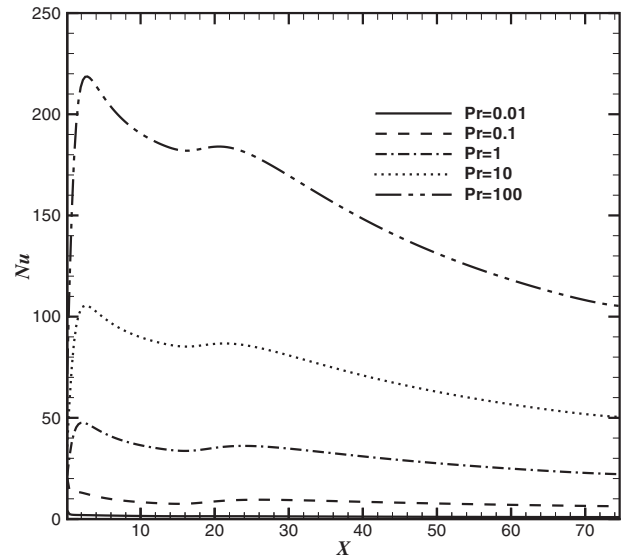


Fig. 5 Local Nusselt number (Nu_x) distribution for $S=10$ and $K=1000$ at various Prandtl numbers

5.3 Local Heat Flux. Figure 8 shows the local heat flux Q_w distribution at various Prandtl numbers keeping $S=10$ and $K=1000$. Contrary to the Nu_x behavior, heat flux (Q_w) shown in Fig. 8 decreases as Pr increases. Heat flux is almost constant along the wall and increases as Pr decreases. The rate of decrement also increases as Pr decreases. Figure 9 shows the Q_w distribution at various thermal conductivity ratios keeping $Pr=1.0$ and $S=10$. Heat flux increases as K increases and it decreases along the wall at higher thermal conductivity ratio. Figure 10 shows the Q_w distributions at various solid thicknesses (S) keeping $Pr=1.0$ and $K=1000$. As expected, the heat flux (Q_w) increases as the solid thickness decreases.

5.4 Average Nusselt Number. Extensive computations are done in their respective ranges and results of the average Nusselt number (\overline{Nu}) are presented in Table 1. It clearly shows that \overline{Nu} is a function of Prandtl number only. The effects of solid thickness

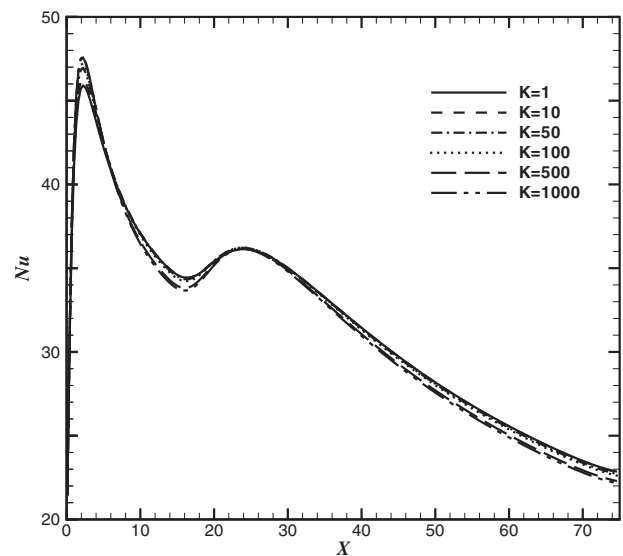


Fig. 6 Local Nusselt number (Nu_x) distribution for $Pr=1$ and $S=10$ at various thermal conductivity ratios (K)

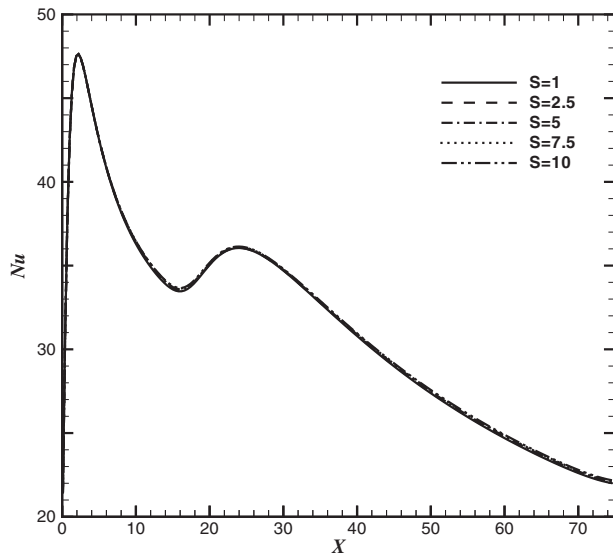


Fig. 7 Local Nusselt number (Nu_x) distribution for $Pr=1$ and $K=1000$ at various solid thickness ratios (S)

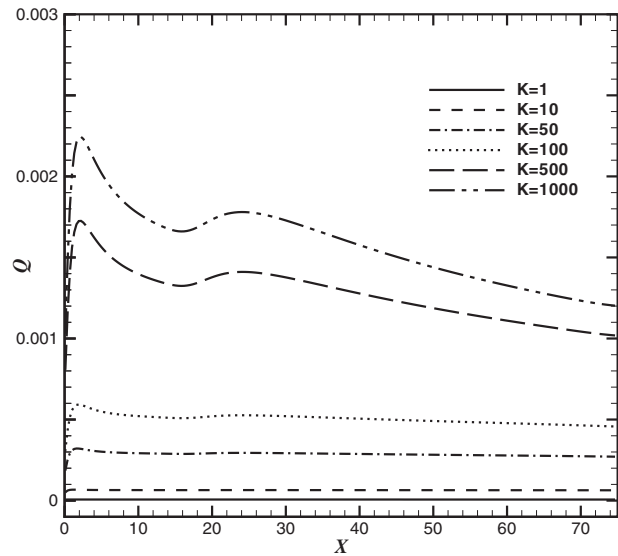


Fig. 9 Heat flux (Q_x) distribution for $Pr=1$ and $S=10$ at various various thermal conductivity ratios (K)

(S) and thermal conductivity ratio (K) are negligibly small. It is observed that \bar{Nu} increases with the increase of Pr .

5.5 Average Heat Transfer. The average heat transfers integrated over the surface for various S , K , and Pr are shown in Table 2. The heat transfer for the conjugate case is compared with the nonconjugate case ($S=0$). It is observed that as the solid thickness increases, heat transfer decreases. However, as K is increasing, Q_i increases. For $K=1000$, Q_i approaches almost equal to the nonconjugate case.

6 Concluding Remarks

The Reynolds number considered is 15,000 because the flow becomes fully turbulent and then it becomes independent of the Reynolds number. It is observed that the interface temperature is high at low Pr . Conversely, the interface temperature decreases significantly as Pr increases. When K is small, the interface temperature is small. As K increases to 1000, the interface tempera-

ture is relatively large. For a small slab thickness $S=1$, the thermal resistance is less leading to a higher interface temperature. As S is increased to 10, it is observed that the interface temperature has dropped down. It is demonstrated clearly that Nu_x increases with Pr because of the thinning of the thermal boundary layer. It is observed that for the range of K and S , the Nu_x distributions superimpose with each other. Heat flux increases as K increases and it decreases along the wall at higher thermal conductivity ratio. The heat flux increases as the solid thickness decreases. It shows clearly that average Nu is a function of Prandtl number only. As K increases, the average heat transfer increases. For $K=1000$, the average heat transfer almost equals the nonconjugate case.

Nomenclature

- $C_{1\epsilon}, C_{2\epsilon}, C_\mu$ = turbulence model constants
- h = width of the jet
- k = turbulent kinetic energy

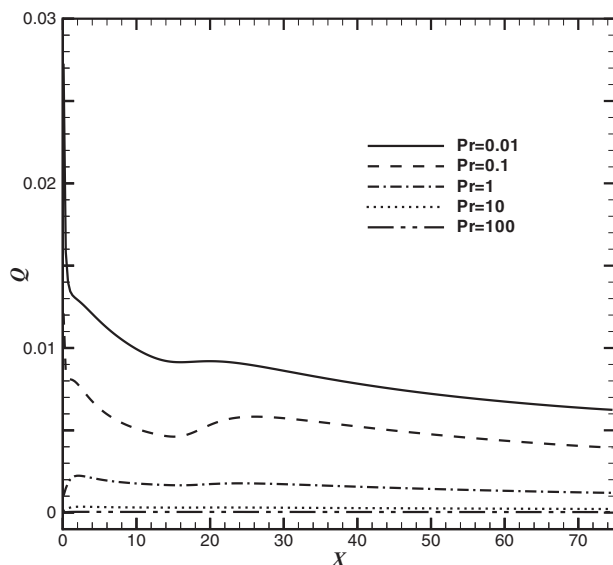


Fig. 8 Heat flux (Q_x) distribution for $S=10$ and $K=1000$ at various Prandtl numbers

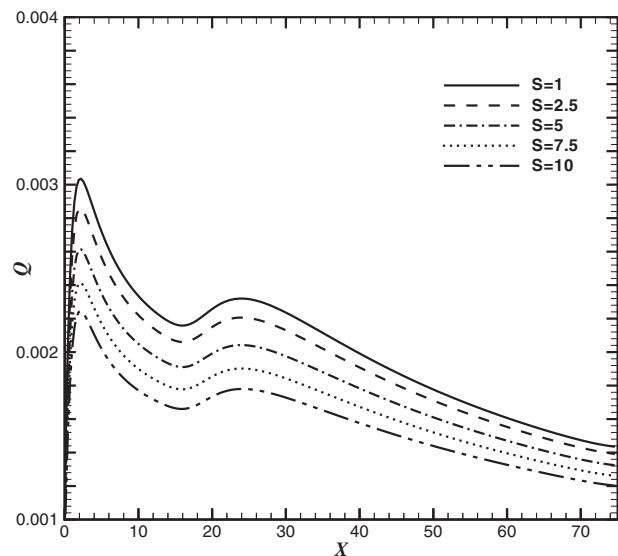


Fig. 10 Heat flux (Q_x) distribution for $Pr=1$ and $K=1000$ at various various solid thickness ratios (S)

Table 1 Average Nusselt number (\overline{Nu}) at various Prandtl numbers

S (thickness of solid slab)	Thermal conductivity ratio $K(k_s/k_f)$	\overline{Nu} (Pr=0.01)	\overline{Nu} (Pr=0.1)	\overline{Nu} (Pr=1)	\overline{Nu} (Pr=10)	\overline{Nu} (Pr=100)
0 (nonconjugate)	—	1.27179	8.30537	31.096	72.7912	152.969
1	1	1.33476	8.83939	31.6452	73.0195	153.062
1	100	1.27354	8.36272	31.2762	72.9244	153.043
1	1000	1.27197	8.31165	31.1207	72.8155	152.989
5	1	1.35813	8.8736	31.6568	73.0216	153.062
5	100	1.27916	8.48842	31.5269	73.0311	153.075
5	1000	1.27258	8.33092	31.203	72.8876	153.033
10	1	1.36203	8.8775	31.6584	73.0219	153.062
10	100	1.28428	8.55228	31.6108	73.0585	153.082
10	1000	1.27321	8.34651	31.2697	72.9384	153.056

- K = thermal conductivity ratio of solid to fluid (k_s/k_f)
- \bar{p} = static pressure
- p_0 = ambient pressure
- \bar{P} = nondimensional static pressure
- Pr = Prandtl number
- Re = Reynolds number, $U_0 h / \nu$
- S = thickness of solid slab
- \bar{T} = dimensional temperature
- T_∞ = inlet and ambient temperatures
- U_0 = average inlet jet velocity
- \bar{u}, \bar{v} = dimensional mean velocities in x and y directions, respectively
- \bar{U}, \bar{V} = nondimensional velocities in X and Y directions, respectively
- x, y = dimensional coordinates
- X, Y = nondimensional coordinates and

Greek Symbols

- α, α_t = laminar and turbulent thermal diffusivities, respectively
- ϵ = dissipation
- $\bar{\theta}$ = nondimensionalized temperature
- ν, ν_t = laminar and turbulent kinematic viscosities
- $\sigma_k, \sigma_\epsilon$ = turbulence model constants

Appendix A: Deriving the Expression for Heat Flux in the Fluid Side

At the interface between the solid and fluid, the following conditions are applied.

- $\theta_s = \theta_f$ at the interface.
- Heat transfer across the interface must be equal.

The wall heat flux on the fluid side is given by

$$Q_f = \frac{(\theta_w - \theta_{p,f}) c_\mu^{3/4} k_n^{1/2}}{\text{Pr}_t \left(\frac{1}{\kappa} \log(EY^+) + P_f \right)} \tag{A1}$$

where P_f is given by

$$P_f = 9.24 \left[\left(\frac{\text{Pr}}{\text{Pr}_t} \right)^{3/4} - 1 \right] \left[1 + 0.28 \exp \left(-0.007 \frac{\text{Pr}}{\text{Pr}_t} \right) \right] \tag{A2}$$

The heat transfer in the solid side is given by

$$Q_s = - \frac{1}{\text{Re Pr}} \left(\frac{k_s}{k_f} \right) \frac{\partial \theta}{\partial Y} = \frac{1}{\text{Re Pr}} \left(\frac{k_s}{k_f} \right) \frac{\theta_{p,s} - \theta_w}{\Delta Y} \tag{A3}$$

The interface temperature is calculated by equating Eqs. (2), (A1), and (A3) where $\theta_{p,f}$ and $\theta_{p,s}$ are neighbor temperatures in the fluid and solid regions.

Appendix B: Deriving the Expression for Nusselt Number Calculation

$$\text{Nu}_x = \frac{h_c H}{k} = h_c (\bar{T}_w - \bar{T}_\infty) \frac{\nu}{\alpha} \frac{1}{\rho C_p U_0 (\bar{T}_w - \bar{T}_\infty)} \frac{1}{\nu} \frac{U_0 H}{\nu} \tag{B1}$$

$$\text{Nu}_x = \frac{Q_w \text{Pr Re}}{\rho C_p (\bar{T}_w - \bar{T}_\infty) U_0} \tag{B2}$$

We can write the above equation as

$$\text{Nu}_x = \frac{Q_w \text{Pr Re}}{\rho C_p (\bar{T}_w - \bar{T}_\infty) U_0} \frac{(\bar{T}_h - \bar{T}_\infty)}{(\bar{T}_h - \bar{T}_\infty)} \tag{B3}$$

Finally,

Table 2 Heat transfer across the interface (Q_i) at various Prandtl numbers

S (thickness of solid slab)	Thermal conductivity ratio $K(k_s/k_f)$	Q_i (Pr=0.01)	Q_i (Pr=0.1)	Q_i (Pr=1)	Q_i (Pr=10)	Q_i (Pr=100)
0 (nonconjugate)	—	0.635897	0.415269	0.15548	0.0363956	0.00764847
1	1	0.282885	0.0448034	0.00484193	0.000492944	4.97E-05
1	100	0.628321	0.384863	0.118324	0.0208609	0.00299052
1	1000	0.635132	0.41203	0.150738	0.0338425	0.00659982
5	1	0.0868023	0.00977382	0.000993511	9.97E-05	9.99E-06
5	100	0.599475	0.296107	0.060686	0.00779314	0.00088023
5	1000	0.63207	0.399399	0.1344	0.0264942	0.00428858
10	1	0.0464729	0.00494282	0.000498372	4.99E-05	5.00E-06
10	100	0.56658	0.229028	0.0377512	0.004378	0.00046808
10	1000	0.628251	0.384457	0.118385	0.0208823	0.00299318

$$\text{Nu}_x = \frac{Q_{w,n} \text{Pr Re}}{\bar{\theta}_w} \quad (\text{B4})$$

where $Q_{w,n}$ is given by

$$Q_{w,n} = \frac{Q_w}{\rho C_p (\bar{T}_w - \bar{T}_\infty) U_0} \quad (\text{B5})$$

since $\bar{\theta}_\infty = 0$, which is used for calculating the local Nusselt number distribution. The average Nusselt number is calculated as

$$\bar{\text{Nu}} = \frac{1}{L} \int_0^L \text{Nu}_x dx \quad (\text{B6})$$

References

- [1] Luikov, A. V., Aleksashenko, V. A., and Aleksashenko, A. A., 1971, "Analytical Methods of Solution of Conjugated Problems in Convective Heat Transfer," *Int. J. Heat Mass Transfer*, **14**, pp. 1047–1056.
- [2] Glauert, M. B., 1956, "The Wall Jet," *J. Fluid Mech.*, **1**, pp. 625–643.
- [3] Seban, R. A., and Back, L. H., 1961, "Velocity and Temperature Profiles in a Wall Jet," *Int. J. Heat Mass Transfer*, **3**, pp. 255–265.
- [4] Launder, B. E., and Rodi, W., 1981, "The Turbulent Wall Jet," *Prog. Aerosp. Sci.*, **19**(2–4), pp. 81–128.
- [5] Launder, B. E., and Rodi, W., 1983, "The Turbulent Wall Jet-Measurements and Modeling," *Annu. Rev. Fluid Mech.*, **15**, pp. 429–459.
- [6] Dakos, T., Verriopoulos, C. A., and Gibson, M. M., 1984, "Turbulent Flow With Heat Transfer in Plane and Curved Wall Jets," *J. Fluid Mech.*, **145**, pp. 339–360.
- [7] Kanna, P. R., and Das, M. K., 2005, "Conjugate Forced Convection Heat Transfer From a Flat Plate by Laminar Plane Wall Jet Flow," *Int. J. Heat Mass Transfer*, **48**(14), pp. 2896–2910.
- [8] Iaccarino, G., Ooi, A., Durbin, P. A., and Behnia, M., 2002, "Conjugate Heat Transfer Predictions in Two-Dimensional Ribbed Passages," *Int. J. Heat Fluid Flow*, **23**, pp. 340–345.
- [9] Kassab, A., Divo, E., Heidmann, J., Steinhilber, E., and Rodriguez, F., 2003, "BEM/FVM Conjugate Heat Transfer Analysis of a Three-Dimensional Film Cooled Turbine Blade," *Int. J. Numer. Methods Heat Fluid Flow*, **13**, pp. 581–610.
- [10] Hsieh, K. J., and Lien, F. S., 2005, "Conjugate Turbulent Forced Convection in a Channel With an Array of Ribs," *Int. J. Numer. Methods Heat Fluid Flow*, **15**(5), pp. 462–482.
- [11] Holland, J. T., and Liburdy, J. A., 1990, "Measurements of the Thermal Characteristics of Heated Offset Jets," *Int. J. Heat Mass Transfer*, **33**(1), pp. 69–78.
- [12] Biswas, G., 2002, "The κ - ϵ Model, the RNG κ - ϵ Model and the Phase-Averaged Model," *Turbulent Flows: Fundamentals, Experiments and Modeling*, G. Biswas and V. Eswaran, eds., Narosa, New Delhi, India, Chap. 11, pp. 339–375.
- [13] Patankar, S. V., 1980, *Numerical Heat Transfer and Fluid Flow*, Hemisphere, New York.
- [14] Versteeg, H. K., and Malalasekera, W., 1996, *An Introduction to Computational Fluid Dynamics. The Finite Volume Method*, Longmans, Green, New York.
- [15] Launder, B. E., and Spalding, D. B., 1974, "The Numerical Computation of Turbulent Flows," *Comput. Methods Appl. Mech. Eng.*, **3**, pp. 269–289.
- [16] Pelfrey, J. R. R., and Liburdy, J. A., 1986, "Mean Flow Characteristics of a Turbulent Offset Jet," *ASME Trans. J. Fluids Eng.*, **108**, pp. 82–88.
- [17] Vishnuvardhanarao, E., and Das, M. K., 2008, "Computation of Mean Flow and Thermal Characteristics of Incompressible Turbulent Offset Jet Flows," *Numer. Heat Transfer, Part A*, **53**, pp. 843–869.

Application of Electrohydrodynamic Atomization to Two-Phase Impingement Heat Transfer

Xin Feng

James E. Bryan

e-mail: bryanje@missouri.edu

Department of Mechanical and Aerospace
Engineering,
University of Missouri,
Columbia, MO 65211

The effect of electric fields applied to two-phase impingement heat transfer is explored for the first time. The electric field applied between a capillary tube and heated surface enhances the heat transfer by controlling the free boundary flow modes from discrete drops to jets, to sprays. Through an experimental study, the impingement heat transfer was evaluated over a range of operating conditions and geometrical parameters with subcooled ethanol used as the working fluid. The ability to change the mode of impinging mass did change the surface heat transfer. The characteristics of the impinging mass on heat transfer were dependent on flow rate, applied voltage, capillary tube to heated surface spacing, capillary tube geometry, heat flux, heater surface geometry, and capillary tube array configuration. Enhancement occurred primarily at low heat fluxes (below 30 W/cm^2) under ramified spray conditions where the droplet momentum promoted thin films on the heated surface resulting in 1.7 times enhancement under certain conditions. Higher heat fluxes resulted in greater vapor momentum from the surface, minimizing the effect of different impingement modes. The use of capillary tube array allowed for electrohydrodynamic atomization enhancement and higher liquid flow rates, but electrostatic repulsive forces diverted the spray from the heater surface. This reduced the mass flux to the surface, leading to premature dryout under certain conditions.

[DOI: 10.1115/1.2885178]

Keywords: electric fields, jet, spray, two-phase heat transfer, electrohydrodynamics, impingement heat transfer

1 Introduction

Two-phase impingement heat transfer through the use of discrete drops, jets, or sprays is considered a viable method for cooling power electronics where high heat flux and high heat transport are required as described by Webb [1] and Mudawar [2]. The characteristics of the boiling and/or evaporation will vary depending on the form (i.e., drops, jets, or sprays) of the impinging mass on the surface. Understanding of the influence of the impinging mass form is difficult because discrete drops, jets, and sprays typically cannot be created under the same conditions. Some jet and spray comparison studies have been accomplished. However, the fluid dynamic operating conditions and geometrical structure are not the same; only the heating surface conditions are the same. Cho and Wu [3] measured the same level of critical heat flux (CHF) for both jets (0.76 mm) and sprays, but found that sprays resulted in a more uniform surface temperature distribution. Estes and Mudawar [4] compared three small orifice diameter (0.66 mm, 0.86 mm, and 1.14 mm) jets and three industrial spray nozzles with different spray angles. They found that the jet and sprays produced comparable CHF at high subcooling with FC-72. However, at low subcooling, sprays were better than jets due to the weak attachment of liquid film. Fabbri et al. [5] tested an industrial nozzle and an array of microjets ($D_i=0.14 \text{ mm}$). Their results showed that the microjet array required less pumping power per unit of power removed. However, at same flow rate, the

spray produced higher heat transfer coefficients, because the pressure required to produce the spray resulted in higher droplet momentum to the heated surface.

It is very difficult to study the effect of different impinging mass forms under the same flow rate and flow exiting area by mechanical means. Thus, the objective of this work is to explore the use of electric fields to control the impinging mass form. An application of an electric field to free boundary flow exiting a capillary tube can produce a range of modes.

Electrospraying or electrohydrodynamic atomization (EHDA) is a process in which the free boundary surface of a liquid flowing out of a capillary tube is transformed as a result of electric stress. When an electric field is applied in the vicinity of liquid flow from a capillary tube, surface charge will be induced on the liquid meniscus. The applied electric field accelerates the surface charge reshaping the meniscus. The shape and characteristic behavior of the free boundary surface will depend on the interaction of electrostatic, liquid momentum, gravity, surface tension, and viscosity forces. This interaction of forces can produce modes from dripping to jets to sprays under the same flow conditions by just changing the applied voltage. The electric field usually has an obvious effect on the free boundary flow exiting a capillary tube within the flow rate range from $10^{-12} \text{ m}^3/\text{s}$ to $10^{-7} \text{ m}^3/\text{s}$ for applied voltages up to 30 kV. Even at higher voltages the current flow is so low, ranging from $\sim 10^{-4} \text{ A}$ to 10^{-6} A , that Joule heating is negligible.

Zeleny [6] was the first to discover that the nature of liquid dripping and sprays changed under application of an electric field. It was over 45 years later when Taylor [7] provided a theoretical explanation of the well known "Taylor" cone jet mode. This mode is only one of many that have been discovered over the years since Zeleny. Using water and various organic liquids in air, Clou-

Contributed by the Heat Transfer Division of ASME for publication in the JOURNAL OF HEAT TRANSFER. Manuscript received November 30, 2006; final manuscript received July 19, 2007; published online May 20, 2008. Review conducted by Jamal Seyed-Yagoobi.

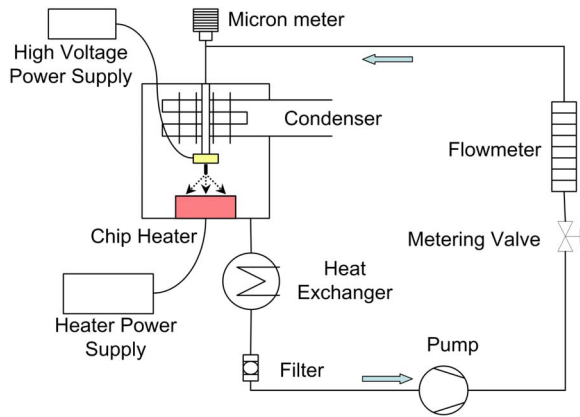


Fig. 1 Schematic of impingement cooling system

peau and Prunet-Foch [8] classified five modes not including dripping: cone jet, microdripping, spindle, simple jet, and ramified jet. From a review on EHDA, Grace and Marijnissen [9] created a flow chart identifying 12 modes created from a dripping state, with changes in modes occurring as flow rate and applied voltage increased. Furthermore, Jaworek and Krupa [10], through a qualitative study, distinguished ten modes and classified them in terms of processes occurring in the spray system. Most of these modes are similar or the same among these three groups of researchers and were all obtained using a dc applied voltage. Due to the complexity of these free boundary flows in electric fields, there has been limited progress made in establishing a complete fundamental and theoretical understanding. However, it is understood that the modes produced depend on the interaction among electrostatic, fluid dynamic, and gravitational forces.

EHD enhanced heat transfer has seen significant attention by researchers, as reviewed by Jones [11], Chang et al. [12], Castellanos [13], and Seyed-Yagoobi and Bryan [14]. However, the application of EHDA to enhancing surface heat transfer has not been studied before to the authors' knowledge. In the present study, the use of electric fields to affect two-phase impingement heat transfer will be explored for the first time. The effect of various parameters, flow rate, applied voltage, capillary tube type, capillary tube to heater surface spacing, surface structure, and capillary tube interaction is investigated by comparing the impingement heat transfer under different conditions. The study is accomplished using ethanol under a dc field, because this working fluid is affected by electric fields over a wide range of flow rates.

2 Experimental Setup and Data Reduction

The experimental system, shown in Fig. 1, is a closed loop allowing for vertical impingement on a horizontal heated surface within a visualization chamber. Liquid ethanol is pumped by a variable speed peristaltic pump through a flow meter to a capillary tube support fixture connected to the chamber. The capillary tube support fixture is attached to a micrometer to allow for precise height adjustment between the capillary tube and heated surface. The chamber has optical access via three windows, two that are $17.8 \times 15.2 \text{ cm}^2$, and one that is $8.9 \times 4.4 \text{ cm}^2$. The vapor produced is directly condensed in the chamber around the periphery of the heater mounting surface, which is 6.5 cm in diameter. The condensate is drawn out of the chamber through a subcooling heat exchanger and then pumped back through the system. In the present study, two different capillary tube geometries made of acrylic ($D_o=4 \text{ mm}$, $D_i=1 \text{ mm}$) and stainless steel ($D_o=0.47 \text{ mm}$, $D_i=0.25 \text{ mm}$) are used, as shown in Fig. 2. The heated surface, shown in Fig. 2, is made of electronic grade copper having a flat circular surface area of either 1 cm^2 or 0.5 cm^2 , which is mounted to a flat or 9 deg sloped surface made of polyetheretherketone

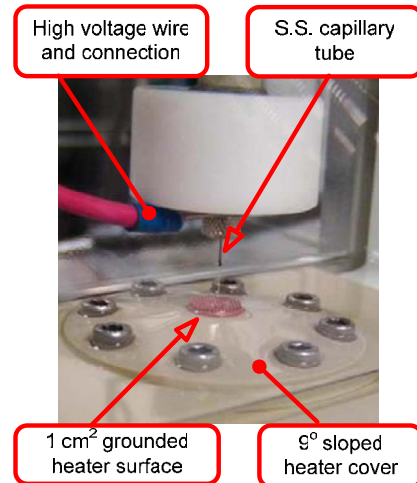
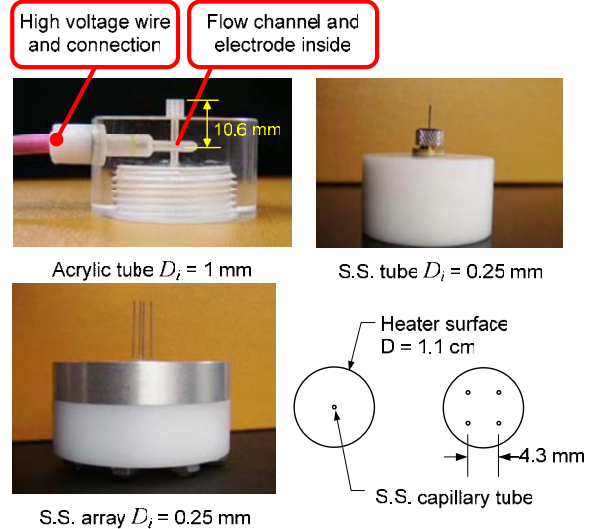
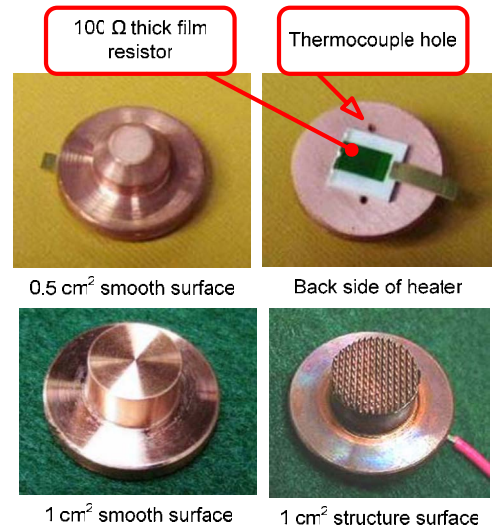


Fig. 2 Photographs showing copper heater coupon, capillary tube fixture, and mounting surface configurations

(PEEK). A 100Ω thick film resistor capable of supplying 250 W is vacuum brazed to the copper coupon using an 80%/20% Au–Sn eutectic alloy strip, which is $25 \mu\text{m}$ thick (see Fig. 2).

Two 0.5 mm, ungrounded, T-type thermocouple probes are em-

Table 1 Thermal bridge surrounding the heater

Components	Material	Area (cm ²)	Conductivity (W/m K)	Thickness (cm)	Thermal resistance (K/W)
Heater coupon	Copper	1.00	400	0.86	0.22
Heater cover	ULTEM	5.98	0.13	0.55	70.8
Heater supporter	PEEK	4.57	0.25	1.00	87.5
Test chamber	Delrin	4.57	0.36	4.00	243.1

bedded in the copper coupon on the centerline. One is 1 mm from the surface and the other is 3.7 mm beneath the first and above the thick film resistor. The response time of the thermocouple probes is on the order of 1.3 s. The inlet liquid temperature and chamber vapor temperature are measured with thermistors. The volumetric flow rate is measured using a calibrated rotameter. The power to the thick film resistor is supplied through a 150 V programmable dc power supply. A 0 to +10 kV (0–10 mA) dc power supply is connected to the capillary tube and the heater surface is grounded. A high speed digital camera was used to capture the flow structure of the impinging mass and the two-phase heat transfer characteristics.

The impingement heat transfer performance is determined using the temperature measurements, the flow rate, and the measured heater power. The heat flux to the surface is determined as

$$q'' = \frac{V_p^2}{R_f A_s} \tag{1}$$

The film resistance R_f is 100 Ω. The accuracy of the heater power was ±0.2 W. The heater power was used instead of the measured temperature difference within the copper coupon to determine the surface heat flux, because the total uncertainty in the temperature difference over the 3.7 mm was too high at low power. The copper coupon is held in place by the PEEK mounting surface and sealed with silicone o-rings.

The various thermal resistances surrounding the copper coupon (heater), shown in Table 1, were at least two orders of magnitude greater than the resistance of the copper coupon. The thermal resistance of impinging flow depended on the testing condition. Using these resistances, the heat loss was estimated to be less than 20% at 5 W/cm² and less 2% at 35 W/cm². It should be noted that the contact resistances are not included in Table 1; thus, the actual heat losses will be lower than the estimated values.

Knowing the heat flux, the heat transfer coefficient is determined from

$$\bar{h} = \frac{q''}{(\bar{T}_s - \bar{T}_i)} \tag{2}$$

The surface temperature T_s was determined from the probe temperature 1 mm beneath the surface by accounting for the thermal resistance. For all the results presented, measurements were ob-

Table 2 Uncertainty values for variables in this work

Measurement	Avg	Min	Max
T_s 0–3 kV	±0.04°C	±0.02°C	±0.12°C
T_s 4–8 kV	±0.05°C	±0.03°C	±0.11°C
T_i	±0.006°C	±0.005°C	±0.008°C
Q	NA	NA	±0.1 ml/min

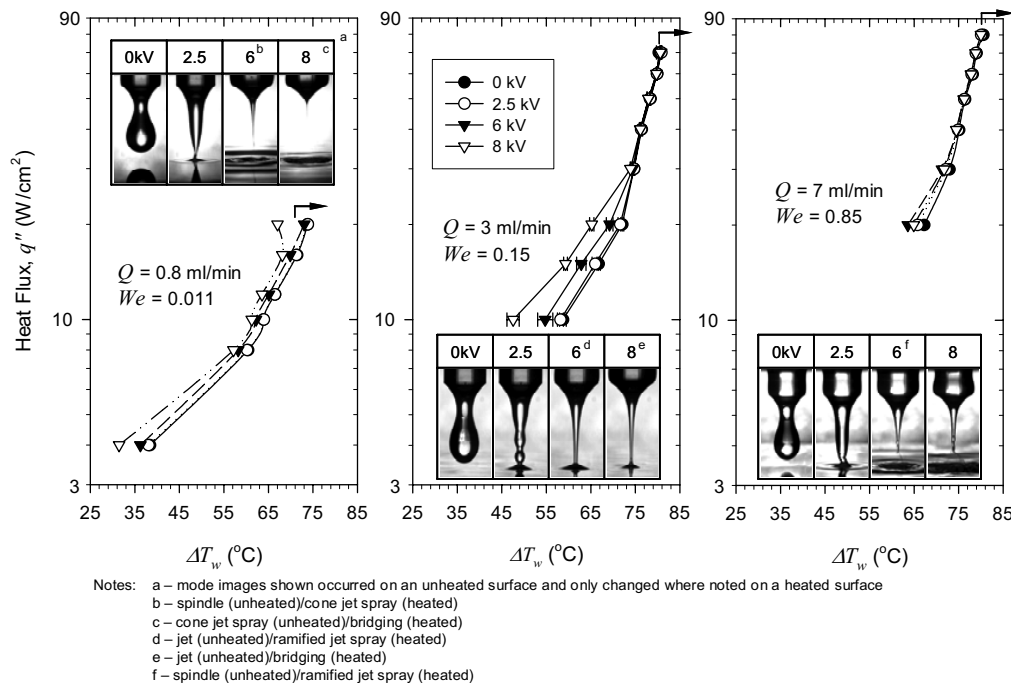


Fig. 3 EHDA effect on two-phase impingement heat transfer at different volumetric flow rates and applied voltages: $A_s=0.5$ cm² and $H=1$ cm on flat mounting surface

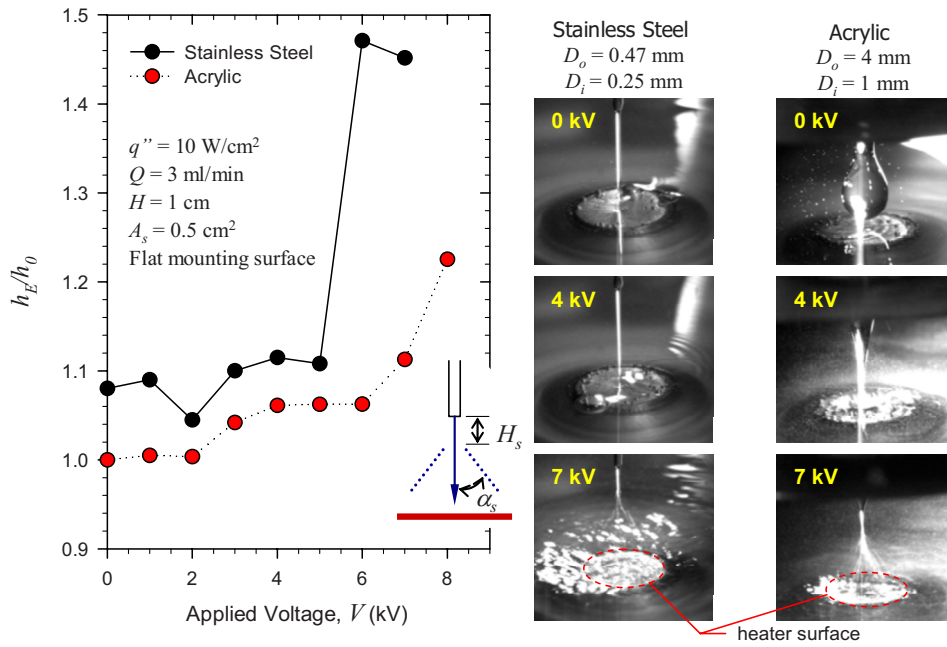


Fig. 4 Effect of applied voltage and capillary tube geometry on impingement heat transfer (h_E is the average enhanced heat transfer coefficient and h_o the average heat transfer coefficient obtained at 0 kV with the acrylic capillary tube)

tained once steady state was reached, defined as less than 0.1% temperature change over 5 min. Then 60 data points at a sampling rate of 3.3 samples/s were recorded via a data acquisition system.

All of tests were conducted at atmospheric pressure, resulting in 56°C subcooled ethanol impinging on the heated surface. Before each test, ethanol was circulated for at least 10 min and then the liquid electric conductivity was measured. The conductivity usually ranged from 2.8×10^{-5} S/m to 4.5×10^{-5} S/m; if it exceeded 4.5×10^{-5} S/m, the fluid was replaced. The system was operated at a condition close to CHF for 10 min, and then experimental data were obtained during heating cycle. For each test condition, the testing period would not exceed 8 h. When the test was completed, the liquid conductivity was rechecked. The peristaltic pump provided a stable flow rate over the range studied, with less than 3% flow oscillation at the lowest flow rate of 0.8 ml/min. The flow rate was determined with a rotameter calibrated with ethanol at room temperature. Typical total uncertainties (bias and precision) of the different variables are shown in Table 2.

3 Results and Discussion

The present study is exploratory in nature with the goal being to better understand (1) how EHDA will affect two-phase impingement heat transfer and (2) if EHDA can be used as a tool to study the effect of impinging mass form on heat transfer. The interaction among the electrostatic and hydrodynamic forces will determine the form of the impinging mass. The modes that evolve will depend on

$$\text{Mode}_E = f \left[\underbrace{(V, Q, H)}_{\text{operating parameters}}, \underbrace{(\rho, \sigma, \mu, \sigma_{el}, \varepsilon_l, \sigma_{ev}, \varepsilon_v)}_{\text{fluid properties}}, \underbrace{(D_i, D_o, M_e)}_{\text{geometrical parameters}} \right] \quad (3)$$

The effect of the operating and geometrical parameters on two-phase impingement heat transfer will be explored with ethanol as the working fluid. The ranges of operating parameters studied are applied voltage V from 0 kV to 8 kV, volumetric flow rate Q from 0.8 ml/min to 9 ml/min, and capillary tube to heated sur-

face distance H from 0.5 cm to 2 cm. Furthermore, initial results highlighting the effect of a structured surface and capillary tube array on EHDA enhanced two-phase impingement heat transfer will be presented.

3.1 Effect of Flow Rate. The impingement heat transfer was studied as a function of volumetric flow rate and applied voltage, using the acrylic capillary tube. For a given capillary tube dimension, the magnitude of the flow rate will establish the hydrodynamic nature of the flow exiting the capillary tube. The flow, whether it is surface tension or momentum dominated, can be characterized with the Weber number, defined here as

$$\text{We} = \frac{4\rho_l D_o Q^2}{(\pi D_i^2)^2 \sigma} \quad (4)$$

Results for three different flow rates are shown in Fig. 3.

The heat transfer is enhanced as applied voltage and volumetric flow rate are varied, as shown in Fig. 3. The electrostatic and liquid momentum forces, relative to surface tension force, increase with increasing voltage and flow rate, respectively, which are qualified by the Weber number (We) and electric Weber number (We_E) shown in Table 3. The electric Weber number relates the electric pressure to surface tension defined here as

$$\text{We}_E = \frac{\varepsilon E_o^2 D_o}{4\sigma} \quad (5)$$

The electric field is approximated as the field between a hyperboloid and plate [15]

$$E_o = \frac{4V}{D_o \ln(8H/D_o)} \quad (6)$$

In general, the increase in electrostatic force results in a lower wall superheat by changing the mass distribution to the surface while the increase in momentum results in a higher achievable CHF. However, the effect of the electrostatic force changes as the flow rate increases due to the increased liquid momentum. This is better understood by examining the EHDA mode images within each graph (Fig. 3) and the ratio of We_E/We shown in Table 3. For the low flow rate, 0.8 ml/min, the electrostatic force domi-

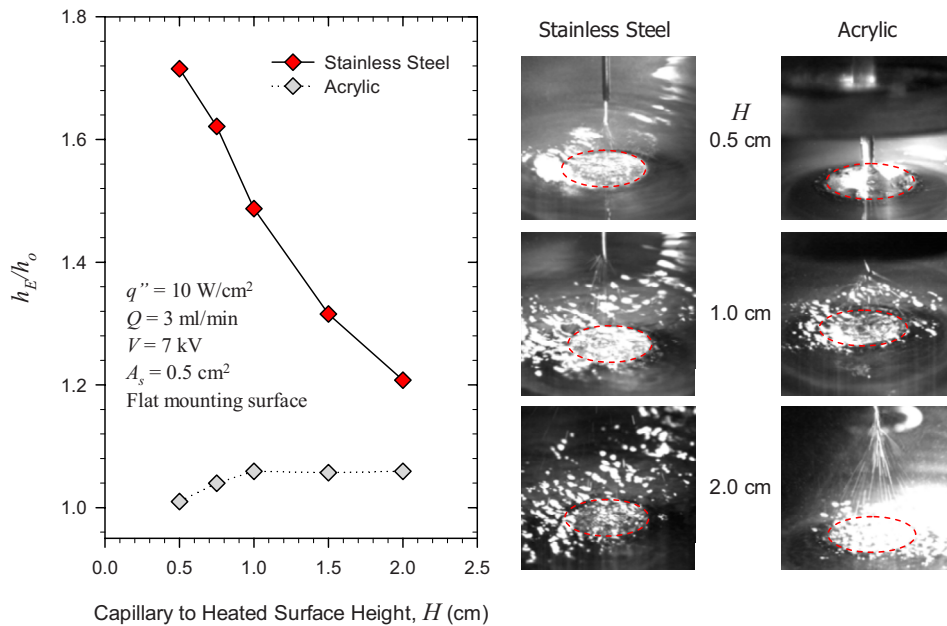


Fig. 5 Effect of height and nozzle geometry on impingement heat transfer (h_E is the average enhanced heat transfer coefficient and h_o the average heat transfer coefficient obtained at 0 kV with the acrylic capillary tube)

nates over surface tension and liquid momentum. The change in the impinging mode, i.e., mass distribution to the surface, results in a slight decrease in the wall superheat throughout the heat flux range once a spray is created ($V \geq 6$ kV). The spray mode is different at this flow as the droplets produced are more monodisperse. As the flow rate is increased, the spray produced becomes more polydisperse because the jet breakup starts from a kink-type instability, breaking the jet into a range of droplet sizes [8–10]. Both sprays produce enhancement. The effect of EHDA on the two-phase heat transfer process decreases as the heat flux and flow rate increase due to the increase in vapor momentum at the surface and liquid momentum to the surface, respectively. Beyond $q'' = 30$ W/cm², the vigorous surface boiling and increased vapor flow prevent any further enhancement with EHDA. However, once a spray is produced ($V > 6$ kV), the surface mass flux decreases because the impact diameter of the spray is larger than the heated surface. This will be discussed further in the next section. It is important to note that at voltages of 6 kV and 8 kV, the modes can change (see descriptions in Fig. 3) once the impinging surface is heated due to the vapor interaction with the impinging flow.

The variation in the EHDA effect was the greatest at $Q = 3$ ml/min, so it was decided that the effect of other parameters presented would be studied at this flow rate. The repeatability of the results at $Q = 3$ ml/min, shown as the error bars in the graph, was verified by repeating the experiments over three different days.

3.2 Effect of Applied Voltage, Capillary Tube Type, and Height. The greatest variation in heat transfer with EHDA was measured at $Q = 3$ ml/min and $q'' = 10$ W/cm². This condition was used to better understand the effect of the applied voltage (V), the type of capillary tube, and the capillary tube to heated surface spacing (H). Results are shown in Figs. 4 and 5. The results are presented as the ratio of the average enhanced heat transfer coefficient h_E to the average heat transfer coefficient h_o obtained at 0 kV with the acrylic capillary tube. The effects of momentum and electric field for the same flow rate and applied voltage are compared using the stainless steel and acrylic capillary tubes. Hydrodynamically, the momentum will increase by 16 times as the

inside diameter D_i decreases from 1 mm (acrylic) to 0.25 mm (stainless steel). This effect can be seen in the h_E/h_o data and the images shown in Fig. 4 at 0 kV. However, the increase in heat transfer is limited to less than 10% because surface tension maintains a liquid film on the heater surface. The flat mounting plate, see Fig. 2, maintains the liquid film, ~ 2 mm thick, over the entire surface.

The intensity of the electric field for a given applied voltage is significantly greater for the stainless steel capillary tube compared to the acrylic capillary tube. The voltage is directly applied to the stainless steel capillary (see Fig. 2). In the acrylic capillary tube, the high voltage is applied to a 1.6 mm electrode located in the liquid channel (see Fig. 2), 10.6 mm upstream from the exit of the capillary tube. Thus, the spacing between the high voltage source and the grounded heater surface is smaller for the stainless steel capillary tube. The combination of the smaller spacing and smaller tube diameter results in a much more intense electric field in the region around the tube tip for the stainless steel capillary tube, creating a larger Coulombic force.

As voltage is increased from 0 kV, the heat transfer enhancement for both capillaries increases differently, as seen in Fig. 4. EHDA has only a slight effect for applied voltages less than 5 kV with the stainless steel capillary tube due to the 16 times increase in momentum, even with the more intense electric field. This can be seen visually in the image at 4 kV in Fig. 4 where there is no noticeable change in the jet compared to 0 kV. However, the transition from dripping to a jet occurs between 2 and 6 kV with the acrylic capillary tube, see image at 4 kV, and this results in an increase in heat transfer. The transition to a spray for both capillary tubes is obvious but different. For the stainless steel, the increase in heat transfer is significant from 5 kV to 6 kV but drops slightly from 6 kV to 7 kV. For the acrylic, the transition from jet to spray occurs from 6 kV to 7 kV with a continued increase in heat transfer with further increase in applied voltage. The reason for the increased heat transfer and differences between the two capillary tubes is due to the momentum and spreading of the spray. When the mode transitions to a spray, the momentum of the drops increases evident by the thinning of the liquid film over the heated surface, seen to some degree in the images at 7 kV in Fig. 4. The increased droplet momentum is due to the Coulombic

Table 3 Comparison of the ratio of We_E/We for results shown in Fig. 3

Q (ml/min)	We	We_E/We		
		2.5 kV 4.6	6 kV 26.5	8 kV 47.2
0.8	0.01	460	2650	4720
3.0	0.15	31	177	315
7.0	0.85	5	31	56

force attraction of the charged drops to the heated surface. This is obviously greater with the stainless steel capillary due to the more intense electric field. Once a spray is created, further increase in applied voltage (increase in field intensity) will increase the spray angle α_s due to the increased repulsive force between the charged droplets. Additionally, once a spray is produced, further increase in field intensity will shorten the point of jet breakup, smaller H_s , increasing the height above the heated surface where the spray is created. Both of these effects, greater α_s and smaller H_s , will result in less mass flux to the heated surface as electric field intensity increases. Inspection of the images at 7 kV in Fig. 4 shows this effect. The spray impinging diameter is much greater than the heated surface diameter for the stainless steel capillary tube resulting in a measurable decrease in heat transfer enhancement for applied voltages greater than 6 kV. The spray and surface diameters are similar for the acrylic capillary tube for the voltage range studied; however, the same decay in heat transfer enhancement would occur at higher applied voltages.

Knowing that the electric field intensity will have a significant effect on the spray angle and in turn the heat transfer, the effect of capillary tube to surface height was studied for both configurations. The results for the two configurations are different, as shown in Fig. 5. As H is increased, the heat transfer enhancement decreases significantly for the stainless steel capillary tube. From inspection of the images, it is evident that the mass flux and momentum to the heater surface are highest at $H=0.5$ cm and decrease with increasing H . The behavior for the acrylic nozzle is

Table 4 Current measurements with stainless steel capillary tube for $Q=3$ ml/min and $H=1$ cm

V (kV)	Measured current (μA)	
	at 0 W/cm ²	at 10 W/cm ²
2.5	5	5
6	9	9
7	10	11

different with the heat transfer increasing with increasing H , but only slightly. The electric field intensity for the acrylic is less than the stainless steel, so the spray, if produced will have less momentum. Since the momentum is less, the liquid film on the heater surface caused by the flat mounting plate remains, which can be seen to some extent in the images in Fig. 5. At $H=0.5$ cm, the liquid film on the heater surface is drawn up to the tip of the capillary tube due to the polarization force (dielectrophoretic force, $-\frac{1}{2}E^2\nabla\epsilon$), which will draw the liquid of higher permittivity toward the region of highest electric field intensity. This bridging effect, shown in Fig. 5, prevents a spray from being produced resulting in no increase in heat transfer. As H is increased, a spray is produced, but with less momentum resulting in a slight heat transfer enhancement.

The power consumption was also evaluated by measuring the current for selected conditions from the data shown in Fig. 4; these results are listed in Table 4. The current for the stainless steel capillary tube was always the highest for a given applied voltage due to the higher field intensity. The maximum power consumption measured was 0.08 W occurring at 7 kV and 10 W/cm². The current measured in this work was generally one order of magnitude lower than the current typically measured in EHD enhanced heat transfer processes [14]. Convection of charge was measurable and increased with increasing flow rate and heat flux.

The results presented in Figs. 4 and 5 were obtained at a heat flux of only 10 W/cm². The effect of heat flux for the two capillaries tube configurations is shown in Fig. 6. There is no measur-

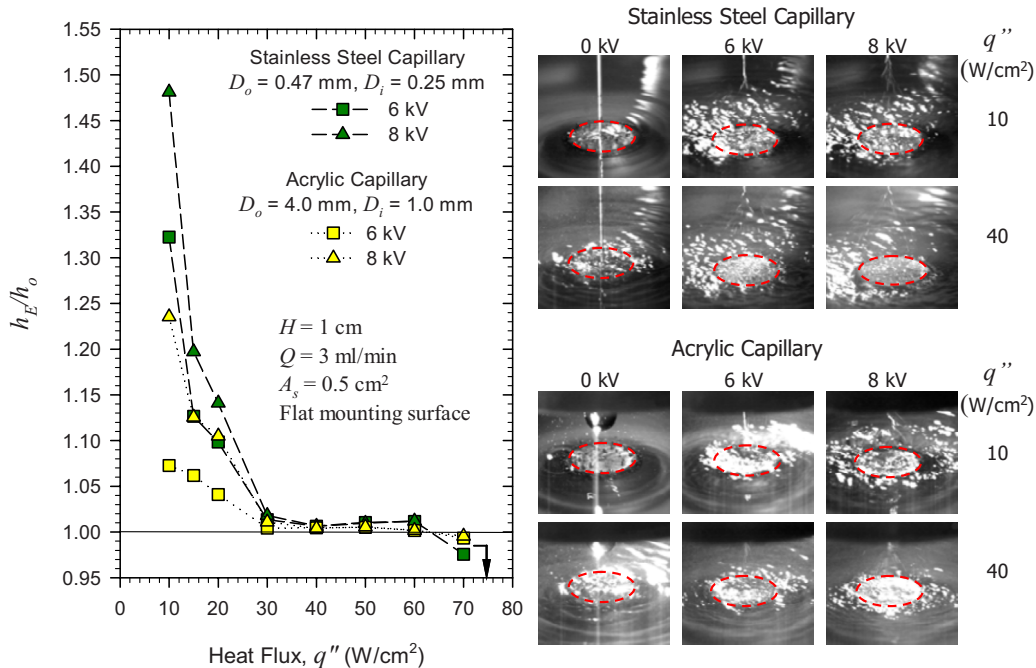


Fig. 6 Effect of heat flux on impingement heat transfer (h_E is the average enhanced heat transfer coefficient and h_o the average heat transfer coefficient obtained at 0 kV with the acrylic capillary tube)

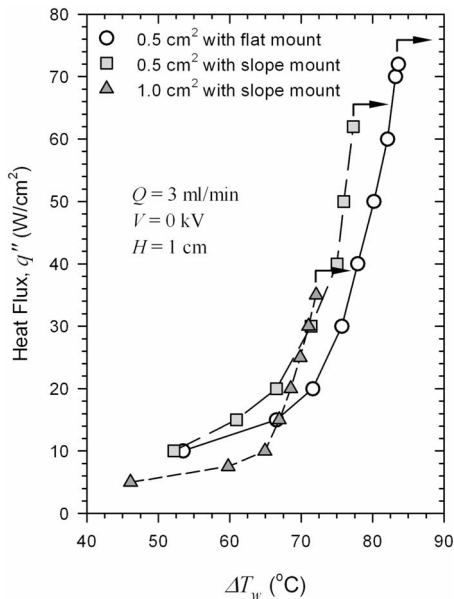


Fig. 7 Effect of surface support structure and surface area on impingement evaporation with no applied electric field through stainless capillary tube

able increase in the heat transfer above 30 W/cm^2 compared to the 0 kV case, represented as h_o . It is evident from the images that the mass flux to the heater surface has decreased at 6 kV and 8 kV , because of the repulsive forces on the charged drops. However, the heat transfer is not negatively effected until 70 W/cm^2 , just before CHF is reached. This is interesting considering less mass is impacting the heater surface, providing evidence that greater boiling efficiency can be achieved with better impinging mass distribution. It is important to note that increasing heat flux

has an effect on the EHDA modes produced. The amount of vapor flow around the capillary tube increases as the heat flux increases affecting the surface charge behavior on the jet. The change in EHDA modes with and without a heated surface is noted in Fig. 3.

3.3 Effect of Mounting and Heater Surfaces. Both the mounting surface and size of the heater surface affect the heat transfer from the surface, as shown in Fig. 7. The mounting surface affects liquid drainage from the heated surface. With a flat mounting surface (see Fig. 2), liquid is retained on the surface around the heater due to the surface tension. This has two effects: (1) A liquid film is retained over the heated surface increasing the thermal resistance, and (2) additional liquid is supplied to heater surface as impinging mass is evaporated. These two effects result in a higher wall superheat and higher CHF, respectively, compared to the sloped mounting surface. The effect of the liquid film resistance with the flat mounting surface is evident in Fig. 7, where the wall superheat is greater at all heat fluxes compared to the sloped surface. The sloped surface prevents liquid retention, so the only liquid held around the heater surface is due to its surface tension only.

An increase in the heater surface area with a sloped mounting surface further changes the heat transfer characteristics for a given impinging mass flow rate condition. At low heat fluxes, $<30 \text{ W/cm}^2$, the larger surface area allows for greater liquid retention thus greater thermal resistance resulting in a higher wall superheat. Above 30 W/cm^2 the interaction of the surface nucleation process and the convection via jet impingement result in a slightly lower thermal resistance for the larger 1 cm^2 surface compared to the 0.5 cm^2 surface. However, the larger surface area leads to local dryout occurring at the periphery at lower heat fluxes.

The application of an electric field further changes the heat transfer for the different surface conditions. These results presented as h_e/h_o versus heat flux are shown in Fig. 8. The mounting surface and surface size influenced the liquid distribution on the heater surface where the electric field influences the mass distribution coming to the surface. The mass impacting the surface

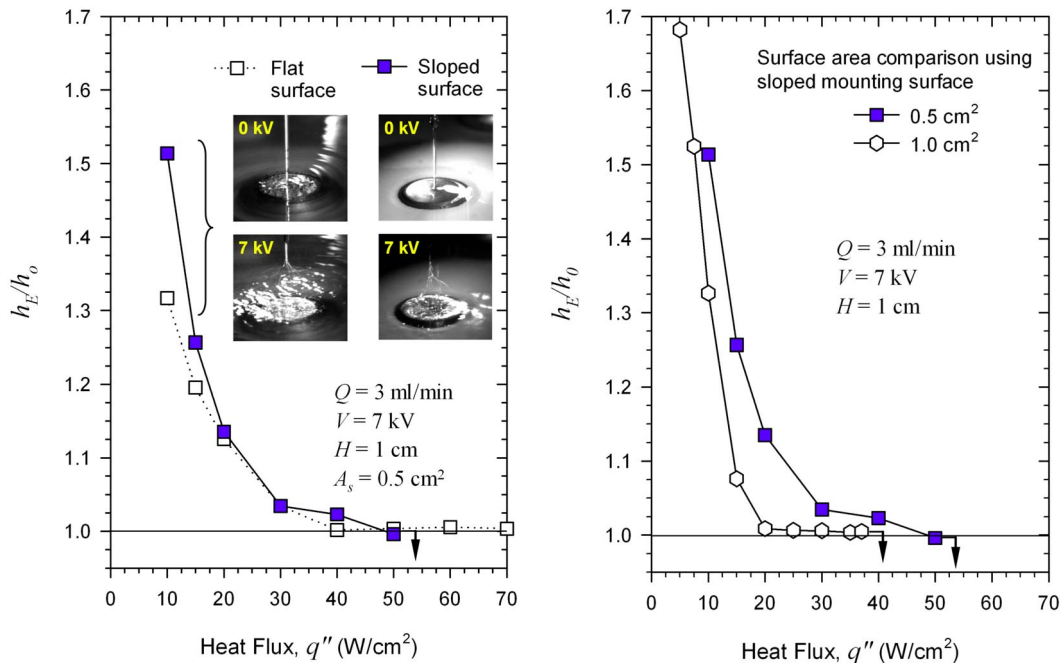


Fig. 8 Effect of EHDA, surface support structure, and surface area on impingement heat transfer with the stainless capillary tube (h_e is the average enhanced heat transfer coefficient and h_o the average heat transfer coefficient obtained at 0 kV)

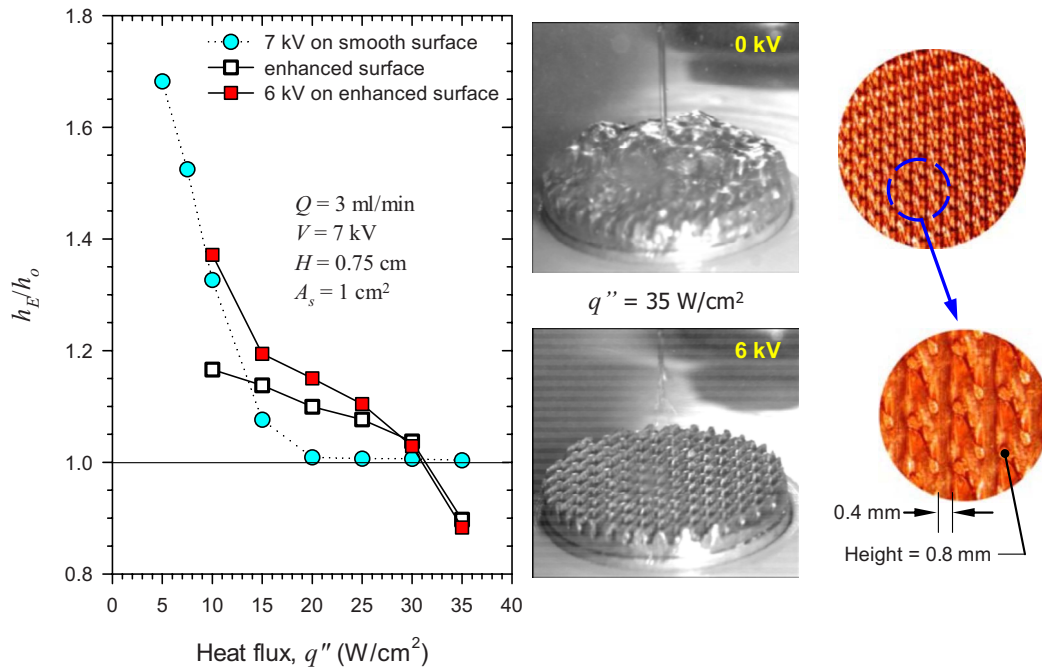


Fig. 9 Effect of surface structure and EHDA on impingement heat transfer (h_E is the average enhanced heat transfer coefficient and h_o the average heat transfer coefficient obtained at 0 kV on the smooth surface)

at an applied voltage of 7 kV is in the form of a ramified spray (polydisperse droplet distribution) compared to a jet at 0 kV. At 7 kV, the volumetric flow rate at 3 ml/min is distributed over a larger area than 1 cm². The overall momentum of the mass impacting the surface is greater and the amount of mass is less with the ramified spray resulting in a thinner liquid film and a pronounced increase in heat transfer. The heat transfer enhancement decreases rapidly as the heat flux increases due to the increase in surface nucleation, increase in vapor momentum escaping from the surface, and less than 3 ml/min impacting the heater surface.

3.4 Effect of Heater Surface Geometry. The effect on EHDA on a geometrically enhanced heater surface was explored, recognizing the influence and interaction between the impinging mass and the surface conditions. The enhanced surface structure shown in Fig. 9 was vacuum brazed to the heater surface. This surface is being investigated for microchannel convective boiling and is only tested here to obtain a preliminary understanding of the effect of enhanced surfaces on impingement heat transfer. The results are shown in Fig. 9, where the effects of the enhanced surface and EHDA are compared to the same size smooth surface. A lower thermal resistance is achieved with the enhanced surface at 0 kV compared to the smooth surface up to 30 W/cm². It is important to note that the heat transfer coefficient, determined from Eq. (2), was based on the same thermocouple location for both the smooth and enhanced surfaces. That is, the temperature measurement was not normalized to the surface, indicating that the 0.8 mm high finned surface reduced the overall liquid film resistance. Higher thermal resistance resulted at heat fluxes greater than 30 W/cm², because the channels blocked liquid supply from evenly distributing over the 1 cm² surface, resulting in premature dryout starting at the periphery. This is shown in Fig. 9 as an h_E/h_o value less than 1.0, because the smooth surface produced a lower thermal resistance than the enhanced surface above 30 W/cm². The thermal resistance was decreased further with EHDA at 6 kV for heat fluxes below 25 W/cm². The EHDA provided better liquid distribution over the enhanced surface. Above 25 W/cm², no measureable enhancement occurred due in part to some of the liquid not impacting the heated surface.

3.5 Single Capillary Tube Versus Capillary Tube Array. The impinging liquid distribution on the heated surface directly affects the nature of the two-phase heat transfer. The results presented thus far have been for free boundary flow from a single capillary tube impinging on a heated surface. An array of capillaries creates the ability to redistribute and/or increase the mass

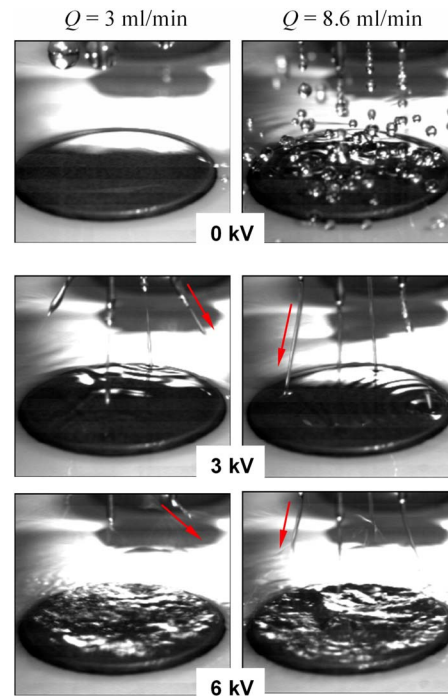


Fig. 10 Sequence of images showing effect of electric field on capillary tube array

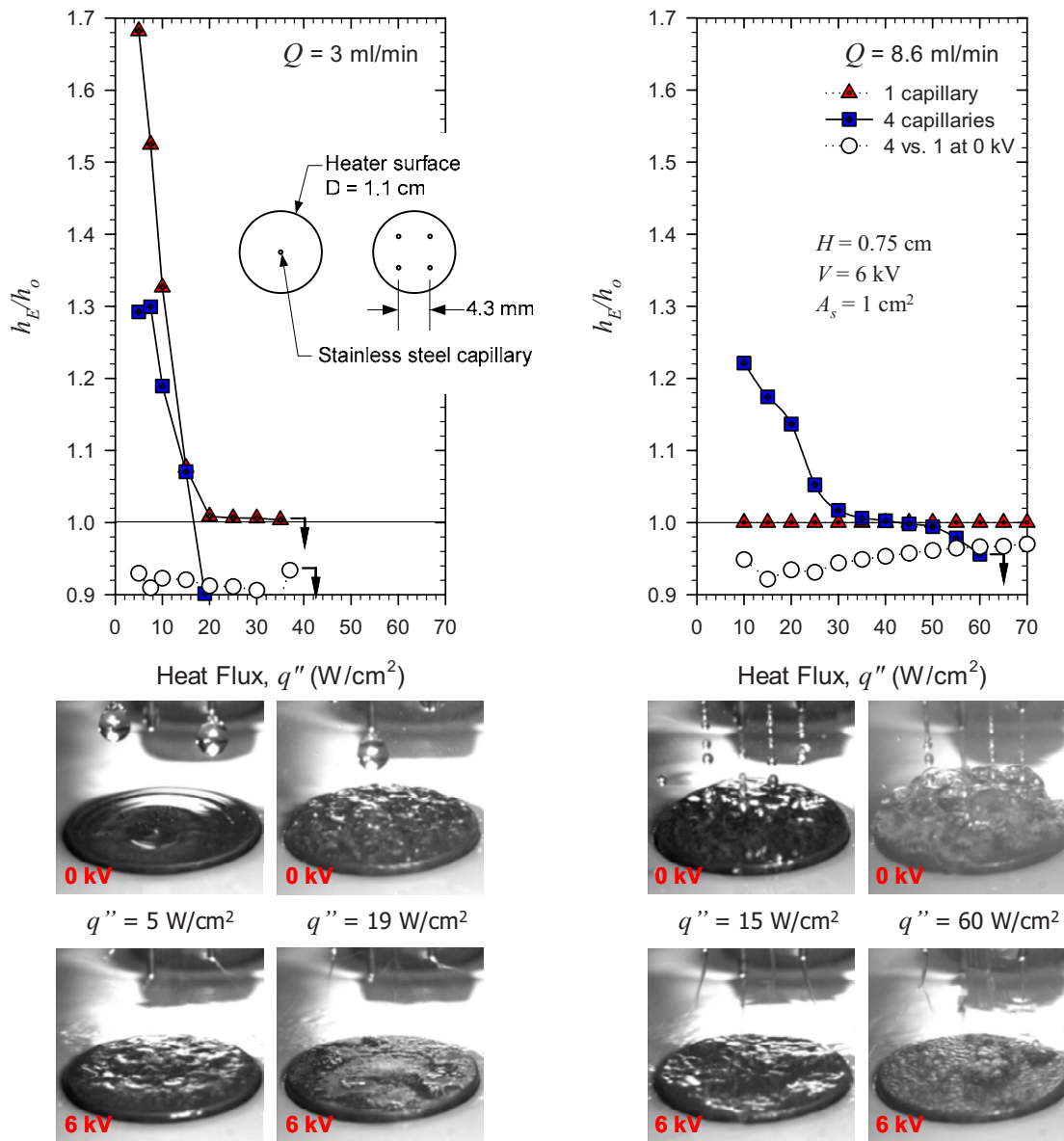


Fig. 11 Effect of capillary tube array on impingement heat transfer (h_E is the average enhanced heat transfer coefficient and h_o the average heat transfer coefficient obtained at 0 kV with a single capillary tube)

rate to the heated surface. Preliminary array experiments were performed to understand how the electric fields would affect the impinging liquid characteristics.

The application of an electric field to an array of capillary tubes compared to a single capillary tube is different. A sequence of images is presented in Fig. 10 showing that as the applied voltage is increased, surface charge distorts the jets produced. The increase in surface charging and electric field causes the jets and droplets to divert away from neighboring capillary tubes, due to the like charge repulsion. As seen in the images, the electrostatic repulsive force competes with the flow momentum. The repulsive forces are significant relative to the liquid momentum at a flow of 3 ml/min where the jets are diverted beyond the edge of the heater surface at 3 kV and above. It should be noted that without EHDA the jets would impinge on the heated surface 2 mm radially from the periphery. The increased liquid momentum at 8.6 ml/min reduces the significance of the repulsive forces.

As expected, the application of an electric field to an array will change the impinging heat transfer characteristics compared to a

single capillary tube under the same total mass flow rate. Results highlighting the difference in heat transfer enhancement between a single capillary tube and array for two different flow rates are shown in Fig. 11. At a flow rate of 3 ml/min and 6 kV applied voltage, the heat transfer is suppressed and CHF is reached just above 20 W/cm², because the electrostatic repulsive forces divert most of the liquid from impinging on the heated surface. At the higher flow rate, EHDA enhancement is created for the array up to 50 W/cm², but not for a single capillary tube. With the array, the liquid momentum is lower and EHDA enhances the liquid distribution to the heater surface through a ramified spray. In the single capillary tube, the liquid momentum is 16 times greater, so at the same applied voltage EHDA has no measurable impact on the heat transfer. Above 50 W/cm², the lower mass flux to the surface caused by the diverging sprays leads to premature dryout compared to the 0 kV condition. It is important to note that at 0 kV the array of four capillary tubes results in a lower heat transfer coefficient compared to a single capillary tube because the flow

from a single capillary tube is a jet while the flow from the array is discrete drops, which have lower momentum. Lower liquid momentum at the heated surface correlates to lower convective heat transfer enhancement.

4 Conclusion

In this work, the effect of applying an electric field to two-phase impingement heat transfer was explored. The ability to change the mode of impinging mass from discrete drops to a jet and then a spray did change the surface heat transfer. The effect of the impinging mass on enhancing heat transfer was dependent on flow rate, applied voltage, capillary tube to heated surface spacing, capillary tube geometry, heat flux, heater surface geometry, and capillary tube array configuration.

The enhancement occurred primarily at low heat fluxes (below 30 W/cm²) under ramified spray conditions where the droplet momentum promoted thin films on the heated surface. Higher heat fluxes resulted in greater vapor momentum from the surface minimizing the effect of different impingement modes. The use of capillary tube array allowed for EHDA enhancement and higher liquid flow rates, but electrostatic repulsive forces diverted the spray from the heater surface reducing the mass flux to the surface leading to premature dryout under certain conditions. Increased EHDA enhancement at higher heat fluxes will require a better understanding of electric field interaction within arrays and greater knowledge of impinging mass to surface interactions.

Based on this exploratory study, the application of electric fields to two-phase impingement heat transfer can result in the reduction and control of wall superheat. Furthermore, the results obtained provide indication of the opportunities and challenges with two-phase impingement heat transfer. It is evident that both impinging mass characteristics and surface conditions influence the surface thermal resistance and the maximum transport achievable.

Acknowledgment

This research was supported by the Office of Naval Research under Contract No. N000140410465 directed by Dr. Mark Spector.

Nomenclature

A_s	=	heater surface area (cm ²)
D_i	=	inner diameter of the nozzle (mm)
D_o	=	outside diameter of the nozzle (mm)
E	=	electric field (V/m)
h	=	heat transfer coefficient (W/m ² K)
H	=	distance from the capillary tip to heated surface (cm)
H_s	=	distance from the capillary tip to jet breakup (mm)
M_e	=	geometry parameter

Q	=	flow rate (ml/min)
q''	=	heat flux (W/cm ²)
R_h	=	thick film resistance (Ω)
\bar{T}_i	=	average impinging liquid temperature ($^{\circ}$ C)
\bar{T}_s	=	average heater surface temperature ($^{\circ}$ C)
V	=	applied voltage (kV)
V_p	=	heater voltage (V)
We	=	weber number
We_E	=	electric Weber number
α_s	=	spray angle
ΔT_w	=	temperature difference between heater surface and impinging liquid ($^{\circ}$ C)
ϵ	=	permittivity (F/m)
μ	=	viscosity
ρ	=	density (kg/m ³)
σ	=	surface tension (N/m)
σ_e	=	electric conductivity (S/m)

Subscripts

E	=	enhanced
l	=	liquid

References

- [1] Webb, R. L., 2005, "Next Generation Devices for Electronic Cooling With Heat Rejection to Air," *ASME J. Heat Transfer*, **127**(1), pp. 2–10.
- [2] Mudawar, I., 2001, "Assessment of High-Heat-Flux Thermal Management Schemes," *IEEE Trans. Compon. Packag. Technol.*, **24**(2), pp. 22–141.
- [3] Cho, C., and Wu, K., 1988, "Comparison of Burnout Characteristics in Jet Impingement Cooling and Spray Cooling," *Proceedings of National Heat Transfer Conference*, Houston TX, pp. 561–567.
- [4] Estes, K., and Mudawar, I., 1995, "Comparison of Two-Phase Electronic Cooling Using Free Jets and Spray," *ASME J. Electron. Packag.*, **117**, pp. 323–332.
- [5] Fabbri, M., Jiang, S., and Dhir, V. K., 2005, "A Comparative Study of Cooling of High Power Density Electronics Using Spray and Microjets," *ASME J. Heat Transfer*, **127**, pp. 38–48.
- [6] Zeleny, J., 1917, "Instability of Electrified Liquid Surfaces," *Phys. Rev.*, **10**, pp. 1–6.
- [7] Taylor, G. A., 1964, "Disintegration of Water Drops in an Electric Field," *Proc. R. Soc. London, Ser. A*, **280**, pp. 383–397.
- [8] Cloupeau, M., and Prunet-Foch, B., 1994, "Recipes Electrohydrodynamic Spraying Functioning Modes: A Critical Review," *J. Aerosol Sci.*, **25**(6), pp. 1021–1036.
- [9] Grace, J. M., and Marjijnissen, J. C. M., 1994, "A Review of Liquid Atomization by Electrical Means," *J. Aerosol Sci.*, **25**(6), pp. 1005–1019.
- [10] Jaworek, A., and Krupa, A., 1999, "Classification of the Modes of EHD Spraying," *J. Aerosol Sci.*, **30**(7), pp. 873–893.
- [11] Jones, T. B., 1978, "Electrohydrodynamically Enhanced Heat Transfer in Liquids—A Review," *Adv. Heat Transfer*, **14**, pp. 107–148.
- [12] Chang, J., Kelly, A., and Crowley, J., 1995, *Handbook of Electrostatic Processes*, CRC, Boca Raton, FL.
- [13] 1998, *Electrohydrodynamics*, A. Castellanos, ed., Springer Wien, New York.
- [14] Seyed-Yagoobi, J., and Bryan, J. E., 1999, "Enhancement of Heat Transfer and Mass Transport in Single-Phase and Two-Phase Flows with Electrohydrodynamics," *Adv. Heat Transfer*, **33**, pp. 95–180.
- [15] Watanabe, H., Matsuyama, T., and Yamamoto, H., 2003, "Experimental Study on Electrostatic Atomization of Highly Viscous Liquids," *J. Electrostat.*, **57**(2), pp. 183–197.

Instability of Nanofluids in Natural Convection

D. Y. Tzou

James C. Dowell Professor
Fellow ASME
Department of Mechanical and Aerospace
Engineering,
University of Missouri,
Columbia, MO 65211
e-mail: tzou@missouri.edu

Instability of natural convection in nanofluids is investigated in this work. As a result of Brownian motion and thermophoresis of nanoparticles, the critical Rayleigh number is shown to be much lower, by one to two orders of magnitude, as compared to that for regular fluids. The highly promoted turbulence, in the presence of nanoparticles for as little as 1% in volume fraction, significantly enhances heat transfer in nanofluids, which may be much more pronounced than the enhancement of the effective thermal conductivity alone. Seven dominating groups are extracted from the nondimensional analysis. By extending the method of eigenfunction expansions in conjunction with the method of weighted residuals, closed-form solutions are derived for the Rayleigh number to justify such remarkable change by the nanoparticles at the onset of instability.

[DOI: 10.1115/1.2908427]

Keywords: nanofluids, nanoparticles, instability, natural convection, critical Rayleigh number

1 Introduction

Novelty of nanofluids, regular fluids (water and ethylene glycol) mixed with a very small amount of suspended metallic or metallic oxide nanoparticles (Cu, CuO, and Al₂O₃) or nanotubes, includes the significant enhancement of the effective thermal conductivity [1–5] and the considerably higher Nusselt number [6–10] than those predicted from macroscopic models. For as little as 0.3% volume fraction (0.3 vol %) of 10 nm copper nanoparticles blended with ethylene glycol, the effective thermal conductivity of the nanofluid compound could increase by 40% [1]. Alumina nanoparticles mixed with water, as another example, results in 10–30% increase in the effective thermal conductivity when 1–4 vol % of alumina is present in the compound [5]. Single-phase convective heat transfer coefficient, in parallel, has been extended to estimate the heat removal rate by nanofluids. Even with the use of the nanofluid thermophysical properties in the single-phase correlation for turbulent flow in round tubes [6,7,10], however, Nusselt number can still be over 30% higher than predicted. Other examples for the drastic change of thermofluid properties by nanoparticles include abnormal increase in viscosity in the presence of 1–10 vol % of alumina/titania added in water [6].

Remarkable enhancements in the presence of nanoparticles/nanotubes at extremely low volume fractions have attracted a lot of attention in identifying the governing mechanisms. The surface-area-to-volume ratio inversely proportional to the diameter of the particle is believed to be responsible for the large deviations from the macroscopic model when predicting the effective thermal conductivity [1]. Since most macroscopic models do not include the particle size, the deviation would increase as the particle size becomes smaller. Various attempts have thus been made to determine the governing mechanisms in nanoscale, including a modified Maxwell model accounting for the ordered nanolayer near the particle-fluid interface [11], Brownian motion of nanoparticles in fluids [12,13], ballistic nature of heat transport within nanoparticles [14,15], thermophoretic diffusion of nanoparticles in fluids [10], and thermal lagging in nanoparticles with a large surface-area-to-volume ratio [16]. It seems that combination of some of the above, such as Brownian motion combined with

fluid mediated clustering/ballistic phonon transport or thermal lagging combined with large surface-area-to-volume ratios in nanoparticles, contribute much more than any effect alone in explaining the anomalous enhancement of the effective thermal conductivity.

This work is motivated by the recent experimental finding that as the power input increases, the temperature difference between the evaporator and the condenser in the nanofluid heat pipe was able to keep constant [17]. For 1 vol % of diamond nanoparticles of 5–50 nm, this unusual phenomenon prolongs to a power input of 336 W, which is the highest that the experimental setup could reach. While the effective thermal conductivity of nanofluids could be very well improved by the nanoparticles immersed, additional mechanisms must exist in nanofluids that enhances the overall heat transfer coefficient under such high power input. Nanoparticles will not stationarily suspend as a temperature gradient is established across the test section. In addition to Brownian motion of the nanoparticles, even though the nanofluid may appear quiescent overall, thermophoretic diffusion [10,18] is another driving force that repositions the nanoparticles in the fluid all the time. Should natural convection be found more effective than the increase in the effective thermal conductivity, in terms of earlier/easier transition from the laminar into the turbulent regimes, for example, the overall heat transfer coefficient would become higher since the heat transfer coefficient in turbulence is much higher than that in laminar flow. While heat transfer correlation for turbulent flow of nanofluids in a round tube has been established [10] and enhancement of thermal conductivity for free convection of nanofluids in a rectangular cavity has been accommodated [19], this work aims to resolve the Bénard instability of nanofluids between two plates at different temperatures and volume fractions of nanoparticles. The emphasis is placed on the significant reduction in the critical Rayleigh number, and hence the earlier/easier transition into the turbulent regime, as a result of the Brownian motion and thermophoresis of nanoparticles in a quiescent fluid. Bénard instability for regular fluids is reformulated to accommodate such effects. It is shown that in the presence of a mere 1 vol % of nanoparticles, the critical Rayleigh number governing the transition from laminar to turbulent regime is reduced by *one to two orders of magnitude*. The resulting critical Rayleigh number is of the order of several (10^0) to several tens (10^1), as compared to 657.5 (10^2) for regular fluids, justifying dominance of turbulence in nanofluids, which may improve the heat transfer rate by as much as one order of magnitude as compared to that in

Contributed by the Heat Transfer Division of ASME for publication in the JOURNAL OF HEAT TRANSFER. Manuscript received March 6, 2007; final manuscript received October 23, 2007; published online May 16, 2008. Review conducted by Jayathi Murthy.

laminar flow. To demonstrate such unusual enhancement of turbulence in nanofluids, a nondimensional analysis is performed to extract the dominating parameters, and closed-form solutions are obtained to avoid all numerical uncertainties. Their effects are illustrated along with the characteristic dimension of the Bènard cells developed in nanofluids.

2 Formulation

While viscosity, density, thermal conductivity, and specific heat of nanofluids may depend on the volume fraction of nanoparticles, for the purpose of characterization and estimates of the various effects on the order of magnitude, all thermophysical properties of nanofluid shall be assumed constant in the analytical formulation. The nanofluid is assumed incompressible, with gravity aligned with the x_3 -direction. The continuity and momentum equations are

$$\frac{\partial u_i}{\partial x_j} = 0, \quad \rho \left(\frac{\partial u_i}{\partial t} + u_j \frac{\partial u_i}{\partial x_j} \right) = - \frac{\partial p}{\partial x_i} + \mu u_{i,jj} - \rho g \delta_{i3}, \quad i, j = 1, 2, 3 \quad (1)$$

where a repeated index (j) refers to summation, $u_j(\partial/\partial x_j) \equiv u_1(\partial/\partial x_1) + u_2(\partial/\partial x_2) + u_3(\partial/\partial x_3)$, and $u_{i,jj} \equiv u_{i,11} + u_{i,22} + u_{i,33} = \nabla^2 u_i$. The nanofluid density (ρ) in Eq. (1) is

$$\rho = \phi \rho_p + (1 - \phi) \rho_f \quad \text{or} \quad \frac{\rho}{\rho_f} = \phi \left(\frac{\rho_p}{\rho_f} \right) + (1 - \phi) \quad (2)$$

Inheriting the concept of volume fraction, mixture theory (weighted mean) has been applied to estimate the nanofluid density. Such weighted means may be more suitable for more nanoparticles than a few percent, but have been adopted in the phenomenological approaches describing the nanofluid properties [10]. The density of the nanofluid can be approximated by that of the base fluid, i.e., $\rho \approx \rho_f$, since the volumetric fraction of nanoparticles is only a few percent [1]. For alumina nanoparticles in water, for example, $(\rho_p/\rho_f) \approx 4$ and a value of $\phi = 2\%$ results in $(\rho/\rho_f) \approx 1.06$. With the nanofluid density used in Eq. (1), therefore, the Boussinesq approximation is extended to the base fluid (ρ_f) in accounting for the density change due to the temperature change. The specific weight (ρg) in Eq. (1) thus becomes

$$\rho g = [\phi \rho_p + (1 - \phi) \rho_f] g \equiv [\phi \rho_p + (1 - \phi) \rho_f \{ \rho(1 - \beta(T - T_0)) \}] g \quad (3)$$

Relative to the flow velocities, nanoparticles also display Brownian motion and thermophoresis due to their size on the nanoscale. Brownian motion is proportional to the volumetric fraction of nanoparticles, in the direction from high to low concentration, whereas the thermophoresis is proportional to the temperature gradient, from hot to cold. Mass flux of the nanoparticles in base fluid (\mathbf{j}_p), therefore, is superposition of the two [10],

$$\mathbf{j}_p = - \rho_p D_B \nabla \phi - \rho_p \left(\frac{D_T}{T_b} \right) \nabla T \quad (4)$$

where D_B represents the Brownian diffusion coefficient, given by Einstein-Stokes's equation, and D_T represents the thermophoretic diffusion coefficient of the nanoparticles:

$$D_B = \frac{k_B T}{3 \pi \mu d_p}, \quad D_T = \left(\frac{\mu}{\rho} \right) \left(\frac{0.26k}{2k + k_p} \right) \phi \quad (5)$$

Note that the expression D_T shown in Eq. (5) was established for particles greater than 1 μm in diameter. In the absence of thermophoretic data, however, it has also been extended to particles of mean diameters in 1–100 nm. Vector notations are recovered in Eq. (4) to avoid coexistence of p (for nanoparticles) and j (Cartesian coordinates) in the indicial notations. Bulk temperature (T_b) in natural convection can be defined on the basis of the "fictitious" velocity, $g\beta D(\Delta T)$ [20], in preserving the rate of enthalpy advection over a cross section. In the linear theory, temperature change

in the nanofluid is assumed small in comparison to T_b . Therefore, nanofluid temperature T in the denominator of Eq. (4) has been replaced by T_b . Likewise, in approximating a constant value for D_T in Eq. (5), ϕ is replaced by ϕ_b , the nominal nanoparticle volume fraction [10]. By assuming constant coefficients in Eq. (4), the continuity equation for the nanoparticles is

$$\frac{\partial \phi}{\partial t} + u_j \frac{\partial \phi}{\partial x_j} = - \frac{1}{\rho_p} \nabla \cdot \mathbf{j}_p = D_B \phi_{,jj} + \left(\frac{D_T}{T_b} \right) T_{,jj} \quad (6)$$

Drifting of nanoparticles in fluids represented by \mathbf{j}_p , now including both Brownian motion and thermophoretic diffusion relative to the flow velocities, introduces additional flow work in the energy equation,

$$\rho c \left[\frac{\partial T}{\partial t} + u_j \frac{\partial T}{\partial x_j} \right] = - \nabla \cdot \mathbf{q} + h_p \nabla \cdot \mathbf{j}_p \quad \text{where} \quad \mathbf{q} = -k \nabla T + h_p \mathbf{j}_p \quad (7)$$

Substituting the expression for \mathbf{q} and restoring \mathbf{j}_p as shown in Eq. (4), the energy equation becomes

$$\rho c \left[\frac{\partial T}{\partial t} + u_j \frac{\partial T}{\partial x_j} \right] = k T_{,jj} + \rho_p c_p \left[D_B \left(\frac{\partial \phi}{\partial x_j} \right) \left(\frac{\partial T}{\partial x_j} \right) + \left(\frac{D_T}{T_b} \right) \left| \frac{\partial T}{\partial x_j} \right|^2 \right] \quad (8)$$

Clearly, Brownian motion and thermophoresis of nanoparticles introduce additional nonlinear effects for heat transport in nanofluids.

Equations (1), (6), and (8) provide six equations for six unknowns: three velocity components (u_i), pressure (p), volumetric fraction of nanoparticles (ϕ), and temperature (T). By introducing the following nondimensional parameters,

$$X_i = \frac{x_i}{D}, \quad \tau = \frac{t}{(D^2/\alpha)}, \quad P = \frac{p}{(\rho \alpha^2/D^2)}, \quad \Phi = \frac{\phi - \phi_1}{\phi_0 - \phi_1}, \quad (9)$$

$$\theta = \frac{T - T_1}{T_0 - T_1}, \quad U_i = \frac{u_i}{(\alpha/D)}$$

the unabridged forms of Eqs. (1), (6), and (8) become

$$\frac{\partial U_1}{\partial X_1} + \frac{\partial U_2}{\partial X_2} + \frac{\partial U_3}{\partial X_3} = 0 \quad (10)$$

$$\frac{\partial U_1}{\partial \tau} + U_1 \frac{\partial U_1}{\partial X_1} + U_2 \frac{\partial U_1}{\partial X_2} + U_3 \frac{\partial U_1}{\partial X_3} = - \frac{\partial P}{\partial X_1} + \text{Pr} \nabla^2 U_1 \quad (11)$$

$$\frac{\partial U_2}{\partial \tau} + U_1 \frac{\partial U_2}{\partial X_1} + U_2 \frac{\partial U_2}{\partial X_2} + U_3 \frac{\partial U_2}{\partial X_3} = - \frac{\partial P}{\partial X_2} + \text{Pr} \nabla^2 U_2 \quad (12)$$

$$\begin{aligned} & \frac{\partial U_3}{\partial \tau} + U_1 \frac{\partial U_3}{\partial X_1} + U_2 \frac{\partial U_3}{\partial X_2} + U_3 \frac{\partial U_3}{\partial X_3} \\ & = - \frac{\partial P}{\partial X_3} + \text{Pr} \nabla^2 U_3 - H \{ [-1 + \beta(T_1 - T_0)](\phi_1 - 1) + R_p \phi_1 \} \\ & \quad - \text{RaPr}(\phi_1 - 1)\theta - H[R_p - 1 + \beta(T_1 - T_0)](\phi_0 - \phi_1)\Phi \\ & \quad - \text{RaPr}(\phi_0 - \phi_1)\theta\Phi \quad \text{with} \quad H = \frac{\text{RaPr}}{\beta(T_0 - T_1)} \end{aligned} \quad (13)$$

$$\frac{\partial \Phi}{\partial \tau} + U_1 \frac{\partial \Phi}{\partial X_1} + U_2 \frac{\partial \Phi}{\partial X_2} + U_3 \frac{\partial \Phi}{\partial X_3} = N_{BT} \nabla^2 \Phi + N_{TT} \nabla^2 \theta \quad (14)$$

$$\begin{aligned} \frac{\partial \theta}{\partial \tau} + U_1 \frac{\partial \theta}{\partial X_1} + U_2 \frac{\partial \theta}{\partial X_2} + U_3 \frac{\partial \theta}{\partial X_3} \\ = \nabla^2 \theta + \frac{1}{Le} \left[\left(\frac{\partial \Phi}{\partial X_1} \right) \left(\frac{\partial \theta}{\partial X_1} \right) + \left(\frac{\partial \Phi}{\partial X_2} \right) \left(\frac{\partial \theta}{\partial X_2} \right) + \left(\frac{\partial \Phi}{\partial X_3} \right) \left(\frac{\partial \theta}{\partial X_3} \right) \right] \\ + \frac{R_N}{Le} \left[\left(\frac{\partial \theta}{\partial X_1} \right)^2 + \left(\frac{\partial \theta}{\partial X_2} \right)^2 + \left(\frac{\partial \theta}{\partial X_3} \right)^2 \right] \end{aligned} \quad (15)$$

The nanofluid is thus characterized by seven parameters:

$$Ra = \frac{gD^3 \beta (T_0 - T_1)}{\alpha^2} \quad (\text{Rayleigh number})$$

$$Pr = \frac{\nu}{\alpha} \quad (\text{Prandtl number})$$

$$Le = \frac{k}{\rho_p c_p D_B (\phi_0 - \phi_1)} \quad (\text{Lewis number}), \quad N_{BT} = \frac{D_B}{\alpha}, \quad R_N = \frac{\rho_p}{\rho} \quad (16)$$

$$N_{TT} = \frac{D_T}{\alpha} \left(\frac{T_0 - T_1}{\phi_0 - \phi_1} \right), \quad \text{and} \quad R_N = \frac{N_{TT}}{N_{BT}}$$

2.1 Primary Flow. Parallel to the Bénard instability for regular fluids [21], Eqs. (10)–(15) will be studied for a quiescent nanofluid between two parallel plates between $x_3=0$ and $x_3=D$, where temperature and volumetric fraction of nanoparticles are kept constant: $T=T_0$ and $\phi=\phi_0$ at $x_3=0$ and $T=T_1$ and $\phi=\phi_1$ at $x_3=D$. In terms of the nondimensional variables defined in Eq. (9), they are $\theta=1$ and $\Phi=1$ at $X_3=0$ and $\theta=0$ and $\Phi=0$ at $X_3=1$.

The primary flow is assumed to be stationary, $\bar{U}_i=0$ for $i=1,2,3$, with both temperature ($\bar{\theta}$) and nanoparticle volumetric fraction ($\bar{\Phi}$) varying in the X_3 -direction only. From Eqs. (13)–(15), the equations governing the primary flow are thus

$$\begin{aligned} \frac{d^2 \bar{\Phi}}{dX_3^2} + R_N \frac{d^2 \bar{\theta}}{dX_3^2} = 0, \quad \frac{d^2 \bar{\theta}}{dX_3^2} + \frac{1}{Le} \left(\frac{d\bar{\Phi}}{dX_3} \right) \left(\frac{d\bar{\theta}}{dX_3} \right) + \frac{R_N}{Le} \left(\frac{d\bar{\theta}}{dX_3} \right)^2 = 0 \\ - \frac{d\bar{P}}{dX_3} = H[-1 + \beta(T_1 - T_0)](\phi_1 - 1) + RaPr(\phi_1 - 1)\bar{\theta} \\ + H[R_p - 1 + \beta(T_1 - T_0)](\phi_0 - \phi_1)\bar{\Phi} + RaPr(\phi_0 - \phi_1)\bar{\theta}\bar{\Phi} \end{aligned} \quad (17)$$

The boundary conditions for $\bar{\theta}(X_3)$ and $\bar{\Phi}(X_3)$ are

$$\bar{\theta}(0) = 1, \quad \bar{\Phi}(0) = 1 \quad \text{and} \quad \bar{\theta}(1) = 0, \quad \bar{\Phi}(1) = 0 \quad (18)$$

Constant volume fraction of nanoparticles at the surface is difficult to achieve in reality, which is introduced here for the purpose of reducing the analytical results to those for regular fluids in the simplest mathematical context. The equations governing $\bar{\theta}$ and $\bar{\Phi}$ in Eq. (17) are nonlinearly coupled, with the relation

$$\bar{\Phi} = -R_N \bar{\theta} + c_1 X_3 + c_2 \quad (19)$$

resulting from integrating the first expression in Eq. (17). By substituting Eq. (19) into the second equation in Eq. (17), it results in

$$\frac{d^2 \bar{\theta}}{dX_3^2} + \frac{c_1}{Le} \left(\frac{d\bar{\theta}}{dX_3} \right) = 0 \quad (20)$$

which can easily be integrated for $\bar{\theta}$. Substituting the result of $\bar{\theta}$ into Eq. (19) and employing the boundary conditions in Eq. (18) in the process of integrations, the primary flow is determined:

$$\begin{aligned} \bar{\Phi}(X_3) = \left\{ R_N \exp \left[\frac{(1+R_N)X_3}{Le} \right] + \exp \left(\frac{1+R_N}{Le} \right) [1 - (1+R_N)X_3] \right. \\ \left. + (1+R_N)(X_3 - 1) \right\} / \left[\exp \left(\frac{1+R_N}{Le} \right) - 1 \right] \\ \bar{\theta}(X_3) = \frac{\left\{ 1 - \exp \left[-\frac{(1+R_N)(1-X_3)}{Le} \right] \right\}}{\left\{ 1 - \exp \left(-\frac{1+R_N}{Le} \right) \right\}} \end{aligned} \quad (21)$$

The pressure distribution in the primary flow \bar{P} can then be obtained by integrating the third expression in Eq. (17) with respect to X_3 , with $\bar{\theta}$ and $\bar{\Phi}$ given by Eq. (21). For most nanofluids investigated so far [10], $R_N \sim 10^0 - 10$, $Le \sim 10^5 - 10^6$, and consequently $\varepsilon = (1+R_N)/Le \sim 10^{-5} - 10^{-4}$. By expanding $\bar{\theta}$ and $\bar{\Phi}$ into the power series of ε and retaining up to the first-order terms,

$$\begin{aligned} \bar{\Phi}(X_3) = 1 - X_3 + \left[\frac{R_N X_3 (X_3 - 1)}{2} \right] \varepsilon + \dots \\ \bar{\theta}(X_3) = 1 - X_3 + \left[\frac{X_3 (1 - X_3)}{2} \right] \varepsilon + \dots \end{aligned} \quad (22)$$

With $\varepsilon \sim 10^{-4}$, as compared to $(1-X_3) \sim 10^0$, the zeroth-order terms are dominant in both $\bar{\theta}$ and $\bar{\Phi}$. Consequently, $\bar{\theta}(X_3) = \bar{\Phi}(X_3) \cong 1 - X_3$, which display *linear* distributions in X_3 . Nonlinear behaviors in Eq. (21) become pronounced for $Le \sim 10$ and smaller. For the nanofluids being explored so far, however, the value of Lewis number (Le) is about three to four orders of magnitude larger. Even though closed-form solutions for $\bar{\theta}$ and $\bar{\Phi}$ exist, therefore, the linear approximations, i.e., $\bar{\theta}(X_3) = \bar{\Phi}(X_3) \cong 1 - X_3$, are adequate and will be used in this work.

2.2 Disturbance Flow. Disturbances are now superimposed onto the primary flow,

$$U_i = U'_i, \quad P = \bar{P} + P', \quad \theta = \bar{\theta} + \theta', \quad \Phi = \bar{\Phi} + \Phi' \quad (23)$$

With $\bar{\theta} = \bar{\Phi} \cong 1 - X_3$, and consequently $d\bar{\theta}/dX_3 = d\bar{\Phi}/dX_3 = -1$, substitution of Eq. (23) into Eqs. (10)–(15) yields

$$\frac{\partial U'_1}{\partial x_1} + \frac{\partial U'_2}{\partial x_2} + \frac{\partial U'_3}{\partial x_3} = 0 \quad (24)$$

$$\frac{\partial U'_1}{\partial \tau} = -\frac{\partial P'}{\partial x_1} + Pr \nabla^2 U'_1, \quad \frac{\partial U'_2}{\partial \tau} = -\frac{\partial P'}{\partial x_2} + Pr \nabla^2 U'_2 \quad (25)$$

$$\begin{aligned} \frac{\partial U'_3}{\partial \tau} = -\frac{\partial P'}{\partial x_3} + Pr \nabla^2 U'_3 - RaPr(\phi_1 - 1)\theta' \\ - (\phi_0 - \phi_1) \{ H[R_p - 1 + \beta(T_1 - T_0)]\Phi' + RaPr(\bar{\theta}\Phi' + \bar{\Phi}\theta') \} \end{aligned} \quad (26)$$

$$\frac{\partial \Phi'}{\partial \tau} - U'_3 = N_{BT} \nabla^2 \Phi' + N_{TT} \nabla^2 \theta' \quad (27)$$

$$\frac{\partial \theta'}{\partial \tau} - U'_3 = \nabla^2 \theta' - \frac{1}{Le} \left(\frac{\partial \theta'}{\partial x_3} + \frac{\partial \Phi'}{\partial x_3} \right) - \left(\frac{2R_N}{Le} \right) \frac{\partial \theta'}{\partial x_3} \quad (28)$$

In the linear theory of instability, all nonlinear terms in Eqs. (24)–(28), such as $u'_i(\partial u'_i / \partial x_j)$ or $\theta'\Phi'$, are neglected. In the ab-

sence of nanoparticles, i.e., for regular fluids with $\phi_1 = \phi_0 = 0$, $D_B = 0$, $D_T = 0$, $d\bar{\Phi}/dX_3 = 0$, and $\text{Le} \sim 1/D_B \rightarrow \infty$, $N_{BT} = N_{TT} = 0$ the term $-U'_3$ on the left hand side of Eq. (27) vanishes due to $d\bar{\Phi}/dX_3 = 0$. Equation (27) thus becomes a zero identity, and Eqs. (24)–(26) and (28) are reduced to the momentum and energy equations for free convection in regular fluids.

Equations (24)–(28) provide six equations to be solved for six unknowns: three velocity disturbances (U'_i for $i=1, 2$, and 3), pressure disturbance (P'), temperature disturbance (θ'), and volumetric-fraction disturbance of nanoparticles (Φ'). To reduce the order of coupling among the six unknowns, U'_1 and U'_2 are eliminated from Eqs. (25) and (26). This results in the following equation for U'_3 that are coupled with Φ' (Eq. (27)) and θ' (Eq. (28)):

$$\begin{aligned} \frac{\partial}{\partial \tau} \nabla^2 U'_3 &= \text{Pr} \nabla^4 U'_3 - \text{RaPr}(\phi_1 - 1) \nabla_1^2 \theta' \\ &\quad - (\phi_0 - \phi_1) \{ H[R_\rho - 1 + \beta(T_1 - T_0)] \nabla_1^2 \Phi' \\ &\quad + \text{RaPr}(\bar{\theta} \nabla_1^2 \Phi' + \bar{\Phi} \nabla_1^2 \theta') \} \end{aligned} \quad (29)$$

where $\nabla^4 \equiv \partial^4 / \partial x_1^4 + \partial^4 / \partial x_2^4 + \partial^4 / \partial x_3^4 + 2\partial^4 / \partial x_1^2 \partial x_2^2 + 2\partial^4 / \partial x_2^2 \partial x_3^2 + 2\partial^4 / \partial x_1^2 \partial x_3^2$ is the three-dimensional biharmonic operator, $\nabla^2 \equiv \partial^2 / \partial x_1^2 + \partial^2 / \partial x_2^2 + \partial^2 / \partial x_3^2$ is the three-dimensional Laplacian operator, and $\nabla_1^2 \equiv \partial^2 / \partial x_1^2 + \partial^2 / \partial x_2^2$ is the two-dimensional Laplacian operator on the X_1 - X_2 plane. By seeking for the convective cell patterns on the X_1 - X_2 plane, with their intensities varying in the X_3 -direction,

$$\left. \begin{aligned} \Phi'(X_1, X_2, X_3) \\ \theta'(X_1, X_2, X_3) \\ U'_3(X_1, X_2, X_3) \end{aligned} \right\} = \exp(\sigma\tau) f(X_1, X_2) \left\{ \begin{aligned} F(X_3) \\ \Theta(X_3) \\ U(X_3) \end{aligned} \right\} \quad (30)$$

the in-plane cell pattern, $f(X_1, X_2)$, is governed by

$$\nabla_1^2 f + a^2 f = 0 \quad \text{or} \quad \frac{\partial^2 f}{\partial X_1^2} + \frac{\partial^2 f}{\partial X_2^2} + a^2 f = 0 \quad (31)$$

with a being the reciprocal of the side length of the convective cell, which is an unknown to be determined from the onset of instability. A closed form solution to Eq. (31) is [21]

$$f = \cos \left[\frac{a(\sqrt{3}X_1 + X_2)}{2} \right] + \cos \left[\frac{a(\sqrt{3}X_1 - X_2)}{2} \right] + \cos(aX_2) \quad (32)$$

which gives the hexagonal pattern in correspondence with the Bénard cells for regular fluids. The amplification rate of disturbances, σ in Eq. (30), is complex in nature, i.e., $\sigma = \sigma_r + i\sigma_i$ with $i = \sqrt{-1}$. The onset of instability is dictated by $\sigma_i = 0$, which separates the unstable regime ($\sigma_r > 0$) from the stable regime ($\sigma_r < 0$). The nanofluid remains to be laminar in the case of $\sigma_r < 0$, since the disturbance will eventually diminish according to Eq. (30). All disturbances will grow with time in the case of $\sigma_r > 0$, on the other hand, and the nanofluid would transit into turbulence. The possibilities for overstability and oscillatory convection near the onset of instability require nonlinear analysis on bifurcation, which will not be covered in the present framework of linear instability. We are not interested in the stable response represented by σ_i , under which the disturbances are sinusoidal and always stable. The onset of instability is thus represented by $\sigma = 0$, which is the same conditions used in studying the Bénard instability for regular fluids. By setting $\sigma = 0$ and substituting Eq. (30) into Eqs. (27)–(29), the equations governing the onset of instability are

$$F'' - a^2 F + R_N(\Theta'' - a^2 \Theta) + \frac{U}{N_{BT}} = 0 \quad (33)$$

$$\Theta'' - \left(\frac{1 + 2R_N}{\text{Le}} \right) \Theta' - a^2 \Theta - \frac{F'}{\text{Le}} = -U \quad (34)$$

and

$$\begin{aligned} U'''' - 2a^2 U'' + a^4 U + a^2 \text{Ra}[(\phi_1 - 1) + (\phi_0 - \phi_1) \bar{\Phi}] \Theta + a^2(\phi_0 - \phi_1) \\ \times \left\{ \frac{\text{Ra}}{\beta(T_1 - T_0)} [R_\rho - 1 + \beta(T_1 - T_0)] + \text{Ra} \bar{\theta} \right\} F = 0 \end{aligned} \quad (35)$$

with prime denoting differentiation with respect to X_3 . The function U can be first eliminated from Eqs. (33) and (34):

$$\begin{aligned} F'' - a^2 F + R_N(\Theta'' - a^2 \Theta) \\ = \frac{1}{N_{BT}} \left[\Theta'' - \left(\frac{1 + 2R_N}{\text{Le}} \right) \Theta' - a^2 \Theta - \frac{F'}{\text{Le}} \right] \end{aligned} \quad (36)$$

Equation (35) requires four boundary conditions for U , two at $X_3 = 0$ and two at $X_3 = 1$. For a rigid surface thereby [22], the nonslip condition and the continuity equation result in $U'_3 = 0$ and $\partial U'_3 / \partial X_3 = 0$, or $U = 0$ and $dU/dX_3 = 0$ according to Eq. (30). For a free surface where stress-free conditions apply, vanishing of the shear stresses tangent to the surface and continuity equation gives $U'_3 = 0$ and $\partial^2 U'_3 / \partial X_3^2 = 0$, or $U = 0$ and $d^2 U / dX_3^2 = 0$. Free surfaces at both $X_3 = 0$ and 1 will be assumed to examine the effect of nanoparticle drifting in the simplest possible mathematical content. With the boundary values of $\bar{\theta}$ and $\bar{\Phi}$ absorbed in the primary flow, Eq. (18), the boundary conditions for $\theta'(\Theta)$ and $\Phi'(F)$, and $U'_3(U)$ in Eqs. (33)–(36) are thus

$$F = 0, \quad \Theta = 0, \quad U = 0, \quad U'' = 0 \quad \text{at } X_3 = 0 \quad \text{and } 1 \quad (37)$$

Equations (35)–(37) display an eigenvalue problem for Ra , which is a function of a in correspondence with a specific size of the convection cells. To characterize the onset of instability, however, the smallest value of Ra , denoted by Ra_c and termed critical Rayleigh number, is targeted among all the possible values of a . Mathematically, this condition is represented by $d(\text{Ra})/d(a) = 0$ for Ra_c to exist at a_c .

3 Eigenfunction Expansions

A closed-form solution for the critical Rayleigh number will be attempted by the method of eigenfunction expansions in conjunction with the method of weighted residuals. The method has been shown highly accurate, within 0.4% as compared to the numerical solution by the use of only the first fundamental mode in the eigenfunction expansions for temperature.

3.1 Regular Fluids. In the absence of nanoparticles, i.e., $\text{Le} \rightarrow \infty$ and $\phi_0 = \phi_1 = 0$, Eqs. (34) and (35) reduce to the governing equations for regular fluids [21,22]:

$$\Theta'' - a^2 \Theta = -U, \quad \Theta = 0 \quad \text{at } X_3 = 0 \quad \text{and } 1 \quad (38)$$

$$\begin{aligned} U'''' - 2a^2 U'' + a^4 U - a^2 \text{Ra} \Theta = 0, \quad U = 0, \quad U'' = 0 \\ \text{at } X_3 = 0 \quad \text{and } 1 \end{aligned} \quad (39)$$

Reciprocal of the cell size (a) and Rayleigh number (Ra) are the only parameters remained. By expanding Θ in terms of $\sin(m\pi X_3)$, which satisfy the boundary conditions in Eq. (38) and are orthogonal in the physical domain of $X_3 \in [0, 1]$,

$$\Theta(X_3) = \sum_{m=1}^{\infty} A_m \sin(m\pi X_3) \quad (40)$$

Eq. (39) can be solved for $U(X_3)$:

$$\begin{aligned}
U(X_3) = & \sum_{m=1}^{\infty} \frac{ae^{-aX_3} \text{Ra} A_m}{2(e^{2a}-1)^2 [a^2 + (m\pi)^2]^2} \left\{ e^a \left[-2a(e^{2a}-1)(e^{2aX_3}-1) \right. \right. \\
& + [a^2 + (m\pi)^2] [1 + e^{2a(1+X_3)}(X_3-1) - X_3 \\
& + (X_3+1)(e^{2a}-e^{2aX_3})] \left. \right\} \sin(m\pi) \\
& + 2ae^{2a}(e^{2a}-1)^2 \sin(m\pi X_3) \left. \right\} \quad (41)
\end{aligned}$$

$$\sum_{m=1}^{\infty} A_m b_{mn}(\text{Ra}, a) = 0, \quad n = 1, 2, \dots, m,$$

$$\begin{aligned}
b_{mn}(\text{Ra}, a) = & \left\{ -2n(e^{2a}-1)^2 [a^2 + (m\pi)^2]^2 [a^6 + a^4(m^2 + 2n^2)\pi^2 + (mn^2\pi^3)^2 + a^2[2(mn\pi^2)^2 + (n\pi)^4 - \text{Ra}]] \cos(n\pi) \sin(m\pi) \right. \\
& + \left\{ 2m(e^{2a}-1)^2 [a^2 + (n\pi)^2]^2 [a^6 + 3(m\pi a^2)^2 + (m\pi)^6 + a^2[3(m\pi)^4 - \text{Ra}]] \cos(m\pi) - a(m^2 - n^2) \pi \text{Ra} [4a^5 e^{2a} + 3a^4(e^{4a}-1) \right. \\
& + [4a^3 e^{2a} + a^2(e^{4a}-1)](m^2 + n^2)\pi^2 + [4ae^{2a} - (e^{4a}-1)](mn\pi^2)^2 \left. \right\} \sin(m\pi) \left. \right\} \sin(n\pi) \\
& / \{ 2\pi(e^{2a}-1)^2 (n^2 - m^2) [a^2 + (m\pi)^2]^2 [a^2 + (n\pi)^2]^2 \}
\end{aligned} \quad (42)$$

where the paired brackets and braces are labeled for easier identifications. For nontrivial solutions of A_m at a prescribed value of m approximating Θ according to Eq. (40), the determinant of the coefficients must vanish, i.e., $|b_{mn}|=0$, which gives the relation between Ra (Rayleigh number) and a (cell size) as the m th order solution. With $m=1$ and $n=1$ in Eq. (42), the first-order solution can be obtained,

$$b_{11} = -\frac{a^6 + 3a^4\pi^2 + \pi^6 + a^2(3\pi^4 - \text{Ra})}{2(a^2 + \pi^2)^2} = 0 \quad \text{or} \quad \text{Ra} = \frac{(a^2 + \pi^2)^3}{a^2} \quad (43)$$

The critical cell size at the onset of instability is then determined from the condition

$$\left(\frac{d\text{Ra}}{da} \right)_{a=a_c} = 0 \quad \text{which gives} \quad 2a_c^6 + 3\pi^2 a_c^4 - \pi^6 = 0 \quad \text{or} \quad a_c = \frac{\pi}{\sqrt{2}} \quad (44)$$

Numerically, $a_c \cong 2.22144$. By substituting the value of a_c into Eq. (43), $\text{Ra}_c = 27\pi^4/4 \cong 657.511$, which is exactly identical to the well-known result for Bénard instability [22]. The closed-form solutions developed here, most desirably, facilitate the general result for the m th mode, $a_c = m\pi/\sqrt{2}$ and $\text{Ra}_c = 27(m\pi)^4/4$, which may not have been reported before. From this general result, the second mode ($m=2$) occurs at $a_c = \sqrt{2}\pi \cong 4.44288$ with $\text{Ra}_c = 108\pi^4 \cong 10,520.2$ and the third mode ($m=3$) occurs at $a_c = 3\pi/\sqrt{2} \cong 6.66432$ with $\text{Ra}_c = 2187\pi^4/4 \cong 53,258.4$. The method of eigenfunction expansions employed in Eqs. (40)–(42) lies within the general framework of Trefftz's variational boundary method [23]. With all the boundary conditions satisfied in the eigenfunction expansions for the unknowns, the method is capable of capturing the fundamental mode, particularly the eigenvalue, governing the onset of linear instability.

3.2 Nanofluids. In the presence of Brownian motion and thermophoretic diffusion of nanoparticles in the fluid, the eigenfunction expansion for temperature, Eq. (40), remains the same. The modal response for the volume fraction of the nanoparticles, $F(X_3)$, results from solving Eq. (36) subject to the boundary conditions in Eq. (37). The result is

Substituting Eq. (40) (for Θ) and Eq. (41) (for U) into Eq. (38) to form the residual, weighing the residual to zero by multiplying $\sin(n\pi X_3)$ on the residual, in turn, with $n=1, 2, \dots, m$, and integrating the results with respect to X_3 from 0 to 1, the results can be expressed in the following form:

$$\begin{aligned}
F(X_3) = & \sum_{m=1}^{\infty} [f_{1m} \cos(m\pi) + f_{2m} \sin(m\pi) + f_{3m} \sin(m\pi X_3) \\
& + f_{4m} \cos(m\pi X_3) + f_{5m}]
\end{aligned}$$

where

$$\begin{aligned}
f_{1m} = & -4(g_1^{X_3} - 1) \exp \left[(1 - X_3) \left(\frac{1}{2\text{Le}N_{\text{BT}}} + \sqrt{g_1} \right) \right] \\
& \times \text{Le}^3 N_{\text{BT}}^2 m\pi (a^2 + m^2\pi^2) [1 + N_{\text{BT}}(1 + R_N)] / [g_2(g_1 - 1)] \\
f_{2m} = & -4(g_1^{X_3} - 1) \exp \left[(1 - X_3) \left(\frac{1}{2\text{Le}N_{\text{BT}}} + \sqrt{g_1} \right) \right] \\
& \times (\text{Le}N_{\text{BT}})^2 [\text{Le}^2 N_{\text{BT}}(a^2 + m^2\pi^2)^2 - [\text{Le}N_{\text{BT}}(a^2 + m^2\pi^2)]^2 R_N \\
& - m^2\pi^2(1 + 2R_N)] / [g_2(g_1 - 1)] \\
f_{3m} = & \{ [\text{Le}(a^2 + m^2\pi^2)]^2 N_{\text{BT}} - [\text{Le}N_{\text{BT}}(a^2 + m^2\pi^2)]^2 R_N \\
& - (m\pi)^2(1 + 2R_N) \} / \{ (m\pi)^2 + [\text{Le}N_{\text{BT}}(a^2 + m^2\pi^2)]^2 \} \\
f_{4m} = & \frac{\text{Le}(a^2 + m^2\pi^2)m\pi - [1 + N_{\text{BT}}(1 + R_N)]}{(m\pi)^2 + [\text{Le}N_{\text{BT}}(a^2 + m^2\pi^2)]^2} \\
f_{5m} = & 4(g_1^{X_3} - g_1) \exp \left[-X_3 \left(\frac{1}{2\text{Le}N_{\text{BT}}} + \sqrt{g_1} \right) \right] \\
& \times \text{Le}^3 N_{\text{BT}}^2 m\pi (a^2 + m^2\pi^2) [1 + N_{\text{BT}}(1 + R_N)] / [g_2(g_1 - 1)]
\end{aligned}$$

with

$$g_1 = \exp \left[\frac{\sqrt{1 + (2a\text{Le}N_{\text{BT}})^2}}{\text{Le}N_{\text{BT}}} \right] \quad (45)$$

$$g_2 = [1 + 2\text{Le}^2(a^2 + m^2\pi^2)N_{\text{BT}}^2] - (2a\text{Le}N_{\text{BT}})^2 - 1$$

Equation (45) needs to be simplified to obtain a closed-form solution for the critical Rayleigh number. Noting that Le is of the order of 10^5 and $(\text{Le}N_{\text{BT}})$ is of the order of $10^5 - 10^6$ [10], the long expression in Eq. (45) can be first expanded in terms of $1/\text{Le}$ and then the result in terms of $1/(\text{Le}N_{\text{BT}})$ to yield

$$F(X_3) = \left(R_N - \frac{1}{N_{BT}} \right) \left(\frac{e^{-aX_3}}{e^{2a} - 1} \right) \sum_{m=1}^{\infty} A_m [e^a (e^{2aX_3} - 1) \sin(m\pi) - e^{aX_3} (e^{2a} - 1) \sin(m\pi X_3)] + O\left(\frac{1}{Le N_{BT}} \right) \quad (46)$$

Equation (40) (for $\Theta(X_3)$) and Eq. (46) (for $F(X_3)$) can now be substituted into Eqs. (35) and (37) to solve for $U(X_3)$. With $\Theta(X_3)$, $F(X_3)$, and $U(X_3)$ thus obtained, Eq. (34) is used to derive the residual. Following the same procedure for the case of regular fluids, multiplying the residual, in turn, by $\sin(n\pi X_3)$ with $n = 1, 2, \dots, m$, and integrating the result with respect to X_3 from 0 to 1, a similar expression to Eq. (42) can be obtained. The general expressions in this case, even with a greatly simplified expression for $F(X_3)$, become much more involved due to the tangling behaviors of Brownian motion and thermophoresis of nanoparticles.

4 First-Order Approximation

The first-order approximation with $m=1$ in Eq. (40), evidenced by the case of regular fluids in Eq. (43), is expected to yield a close approximation to the critical Rayleigh number for the case of nanofluids. With $\Theta = A_1 \sin[\pi X_3]$, $F(X_3)$ in Eq. (46) becomes

$$F(X_3) = A_1 \left(\frac{1}{N_{BT}} - R_N \right) \sin[\pi X_3]$$

and consequently,

$$F'(X_3) \cong A_1 \left(\frac{1}{N_{BT}} - R_N \right) \pi \cos[\pi X_3] \quad (47)$$

With $(Le N_{BT}) \sim 10^5$ accuracy of Eq. (47) is on the order of 10^{-5} as compared to the full expression shown in Eq. (45). With practical properties of nanofluids, Eq. (47) will be shown indistinguishable from the general solution in the numerical examples, as presented later in Fig. 2. The residual of Eq. (34) can now be calculated by integrating Eq. (35) for $U(X_3)$, with the boundary conditions in Eq. (37). By weighing the residual by $\sin[\pi X_3]$ in integrating the result from 0 to 1, diminution of the coefficient of A_1 , $b_{11} = 0$ in correspondence with Eq. (43) results in

$$Ra = -2(a^2 + \pi^2)^3 N_{BT} \beta (T_0 - T_1) / \left\{ a^2 \left[[2(R_\rho - 1) - \beta(T_0 - T_1)] \times (\phi_0 - \phi_1) + N_{BT} \{-2R_N(R_\rho - 1)(\phi_0 - \phi_1) + \beta(T_0 - T_1)[(1 + R_N)(\phi_0 - \phi_1) + 2(\phi_1 - 1)]\} \right] \right\} \quad (48)$$

To preserve the novelty observed in nanofluids, the value of ϕ_1 needs to be less than a few percent [1]. With ϕ_1 on the order of 10^{-2} , the factor $[2(\phi_1 - 1)]$ in the denominator of Eq. (48) can be replaced by -2 without causing too much error. The Rayleigh number, therefore, is a function of the cell-size parameter (a), the temperature difference ($T_1 - T_0$), the volume-fraction difference nanoparticles ($\phi_0 - \phi_1$), the thermal expansion coefficient (β) of the nanofluids, the density ratio (R_ρ), and the two nondimensional parameters N_{BT} and R_N . Note that the Rayleigh number is no longer a function of Lewis number (Le), which was dropped in the first-order approximation for $F(X_3)$, Eq. (47).

The critical Rayleigh number is the minimum value of Ra that occurs at a particular value of $a = a_c$, resulting from the condition $d(Ra)/d(a) = 0$. Note that Eq. (48) possesses the same functional structure in a , $(a^2 + \pi^2)^3/a^2$, as that in Eq. (43) for the regular fluid. Consequently, the critical value for a_c will be the same as that shown in Eq. (44) for the regular fluid, $a_c = \pi/\sqrt{2} \cong 2.22144$. The interweaving behaviors of Brownian motion and thermophoresis of nanoparticles, evidently, does not change the critical size of the Bénard cell at the onset of instability. As such, the

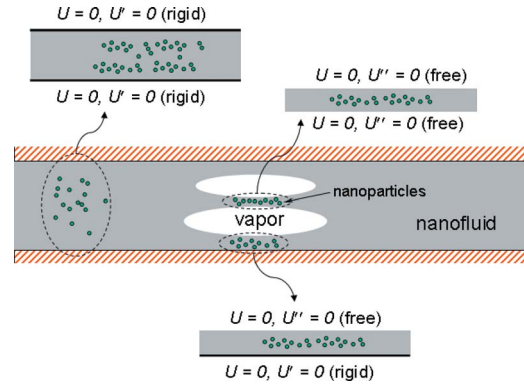


Fig. 1 The various surfaces bounding the nanofluids

critical size is not a function of any thermophysical property of the nanofluid. The critical Rayleigh number (Ra_c) can now be calculated from Eq. (48). With a replaced by a_c ,

$$Ra_c = -27\pi^4 N_{BT} \beta (T_0 - T_1) / \left\{ 2 \left[[2(R_\rho - 1) - \beta(T_0 - T_1)] (\phi_0 - \phi_1) + N_{BT} \{-2R_N(R_\rho - 1)(\phi_0 - \phi_1) + \beta(T_0 - T_1)[(1 + R_N)(\phi_0 - \phi_1) - 2]\} \right] \right\} \quad (49)$$

Whereas a_c is independent of the properties of nanofluids, the value of Ra_c depends on $(T_1 - T_0)$, $(\phi_0 - \phi_1)$, β , R_ρ , N_{BT} , and R_N .

4.1 Other Boundary Conditions. Equations (48) and (49) were derived based on free surfaces bounding the nanofluid, $U = 0$ and $U'' = 0$ at $X_3 = 0$ and 1 shown in Eq. (37). This condition simulates the nanofluid segment between adjacent bubbles in a heat pipe, as illustrated in the upper right in Fig. 1. Possible combinations are rigid surfaces, upper left in Fig. 1, where the nonslip conditions apply, $U = 0$ and $U' = 0$ at $X_3 = 0$ and 1 in place of the correspondence in Eq. (37), and rigid-free surfaces, bottom in Fig. 1, where the nonslip condition ($U = 0$ and $U' = 0$) applies at $X_3 = 0$ and the stress-free condition ($U = 0$ and $U'' = 0$) applies at $X_3 = 1$.

The critical Rayleigh number under the various surface conditions can be determined in exactly the same way. The first-order ($m=1$) solutions are as follow.

Rigid-rigid surfaces: $a_c \cong 3.11421$ and

$$Ra_c = -3430.16 N_{BT} \beta (T_0 - T_1) / \left\{ [2(R_\rho - 1) - \beta(T_0 - T_1)] (\phi_0 - \phi_1) + N_{BT} \{-2R_N(R_\rho - 1)(\phi_0 - \phi_1) + \beta(T_0 - T_1)[R_N(\phi_0 - \phi_1) - 2]\} \right\} \quad (50)$$

Rigid-free surfaces: $a_c \cong 2.6824$ and

$$Ra_c = -2100.05 N_{BT} \beta (T_0 - T_1) / \left\{ [1.887(R_\rho - 1) - \beta(T_0 - T_1)] (\phi_0 - \phi_1) + N_{BT} \{-1.887R_N(R_\rho - 1)(\phi_0 - \phi_1) + \beta(T_0 - T_1)[(0.887 + R_N)(\phi_0 - \phi_1) - 1.887]\} \right\} \quad (51)$$

More complicated coefficients, particularly for the case with rigid-free surfaces (Eq. (51)) where even and odd boundary conditions are mixed, result from the substitutions of numerical values of a_c into the analytical expression of Ra .

5 Results and Discussion

Validity of Eq. (47) is a key to obtain the closed-form solution of the Rayleigh number. For the fundamental mode with $m=1$, based on which the closed-form solutions are derived in Eqs. (48) and (49), Fig. 2 compares the full expression of $F(z)$ shown by

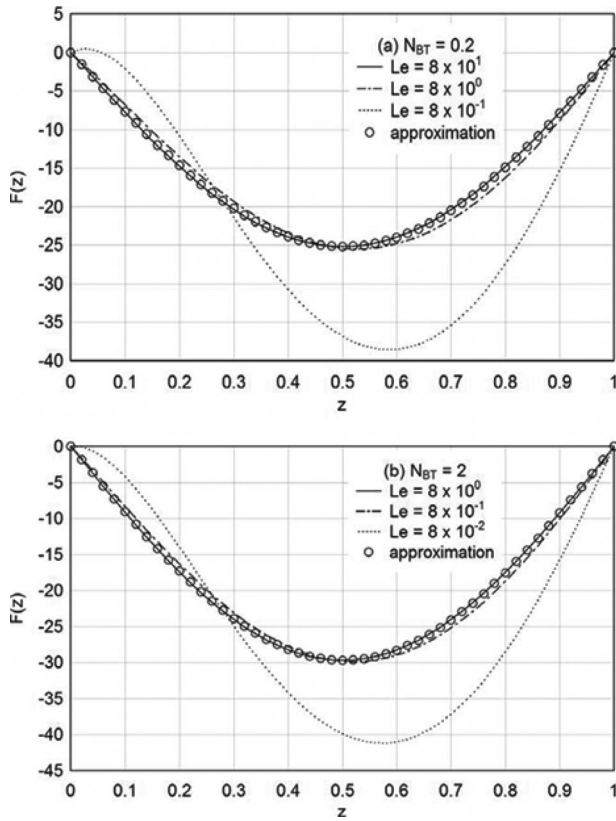


Fig. 2 Comparisons of the fundamental mode ($m=1$) for $F(z)$: full expression shown by Eq. (45) and approximate expression shown by Eq. (47)

Eq. (45) and the approximate solution shown by Eq. (47). For $N_{BT}=0.2$, a typical value for alumina/water nanofluids as shown in Fig. 2(a), the full expression becomes indistinguishable from the approximate solution as the value of Le increases beyond 8×10^1 . For $Le \approx 8 \times 10^5$ in alumina/water nanofluids, which is four orders of magnitude greater, the approximate expression becomes exact. The same behavior is observed for copper/water nanofluids with $N_{BT}=2$, Fig. 2(b). No sensible difference between the full and approximate expressions can be observed beyond $Le \sim 8 \times 10^0$, as compared to $Le \approx 7 \times 10^5$ for copper/water nanofluids. Equation (47), therefore, is indeed a very close approximation to the full solution shown by Eq. (45).

Figure 3 compares the stability curves for water-based nanofluids with alumina and copper nanoparticles. Thermofluid properties are calculated based on 10 nm nanoparticles, which are summarized in the figure caption. The numerical results are prepared for nanofluids bounded between two surfaces, Eqs. (48) and (49). The critical value of Rayleigh number (Ra_c) occurs at $a_c = \pi/\sqrt{2} \approx 2.22144$, as analytically proven above. The value of Ra_c is lowered by one order of magnitude, 48.8526 for the alumina/water nanofluid and 19.0276 for the copper/water fluid, as compared to $Ra_c \approx 657.5$ for the regular fluid without nanoparticle. In terms of the higher value of Ra_c at the onset of instability, alumina/water nanofluid is more stable than the copper/water nanofluid.

The closed-form solution of the Rayleigh number obtained in Eq. (48) makes it convenient to illustrate the various effects involved. Threshold values for water nanofluids with metallic/metallic oxide nanoparticles of 1–100 nm are used in the numerical examples: $R_N=30.18$, $N_{BT}=0.2$, $Le=8 \times 10^5$, and $\beta=5.32 \times 10^{-4}$ 1/K. The value of $R_p=6$ is taken from the mean between 4 (aluminum nanoparticles) and 9 (copper nanoparticles). The values of ΔT and $\Delta\phi$ are taken as 80 K and 1 vol %, respectively,

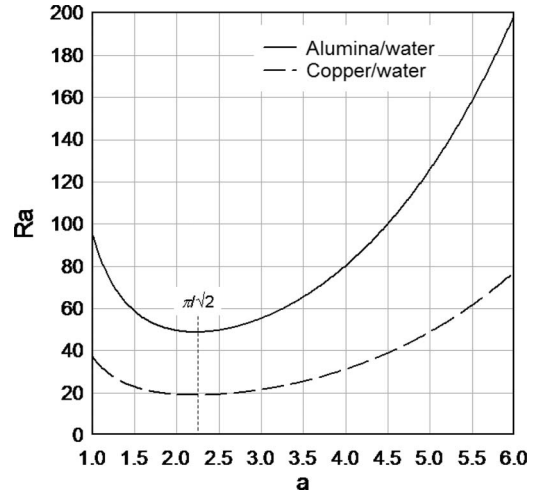


Fig. 3 Water-based nanofluids with alumina and copper nanoparticles with $\Delta T=10$ K and $\Delta\phi=1$ vol %. Al_2O_3 : $\beta=6 \times 10^{-3}$ 1/K, $Le=8 \times 10^5$, $N_{BT}=0.2$, $R_p=4$, $R_N=30.18$; Cu: $\beta=6 \times 10^{-4}$ 1/K, $Le=7 \times 10^5$, $N_{BT}=2$, $R_p=9$, $R_N=3.018$. Critical Rayleigh number occurs at $a_c = \pi/\sqrt{2} \approx 2.22144$.

unless otherwise stated. A stabilizing/destabilizing effect is reflected by a larger/smaller critical Rayleigh number as certain parameters vary. Figure 4 shows the stabilizing (destabilizing) effect as (a) the temperature difference $\Delta T=T_0-T_1$ increases (decreases), (b) the volume-fraction difference of nanoparticles, $\Delta\phi = \phi_0 - \phi_1$, decreases (increases), (c) the density ratio R_p (ρ_p/ρ) decreases (increases), (d) the ratio R_N (N_{TT}/N_{BT}) decreases (increases), and (e) the value of N_{BT} (D_B/α) decreases (increases). The critical value of Rayleigh number (Ra_c) remains to occur at $a_c=2.22144$ in all cases and, depending on the thermophysical properties of the nanofluids, the critical Rayleigh number can be lowered than that of the regular fluid by two orders of magnitude. A larger temperature difference (ΔT) produces a larger buoyancy force, which effectively suppresses the temporal growth of the disturbances and consequently results in a more stable behavior, as shown in Fig. 4(a). Brownian motion of the nanoparticles is promoted as the difference of the volume fraction of nanoparticles ($\Delta\phi$) increases. This is a destabilizing effect, as shown by Fig. 4(b), in terms of a much lower value of Ra_c now only of the order of 10^0-10^1 . With other conditions remained the same, effect of R_p shown by Fig. 4(c), heavier nanoparticles moving through the base fluid produce stronger disturbances. It thus facilitates development of turbulence, resulting in a lower critical Rayleigh number at a larger value of R_p . Figure 4(d) shows that the critical value of Ra_c decreases as the ratio of R_N increases. While both thermophoresis and Brownian motion are driving forces in support of the motion of nanoparticles, thermophoresis at a higher value of thermophoretic diffusivity is more favorable to the initiation of turbulence in nanofluids. Although not as strong as thermophoresis, Brownian motion also promotes turbulence in nanofluids, as shown in Fig. 4(e). The critical Rayleigh number is lower for nanofluids with a larger value of the Brownian diffusion coefficient. Note that the case of $N_{BT}=2$ (the case of copper/water nanofluids) shown in Fig. 4(e) has already approached the lower bound of $N_{BT} \rightarrow \infty$. From Eq. (48),

$$\lim_{N_{BT} \rightarrow \infty} Ra = -\frac{[2(a^2 + \pi^2)^3 \beta(T_0 - T_1)]}{\{a^2[-2R_N(R_p - 1)(\phi_0 - \phi_1) + \beta(T_0 - T_1)][(1 + R_N)(\phi_0 - \phi_1) - 2]\}} \quad (52)$$

With the same parameters used in Fig. 4, $Ra_c \approx 18.1133$ as $N_{BT} \rightarrow \infty$, which is the value of Ra_c at $a_c = \pi/\sqrt{2}$ shown in Fig. 4(e).

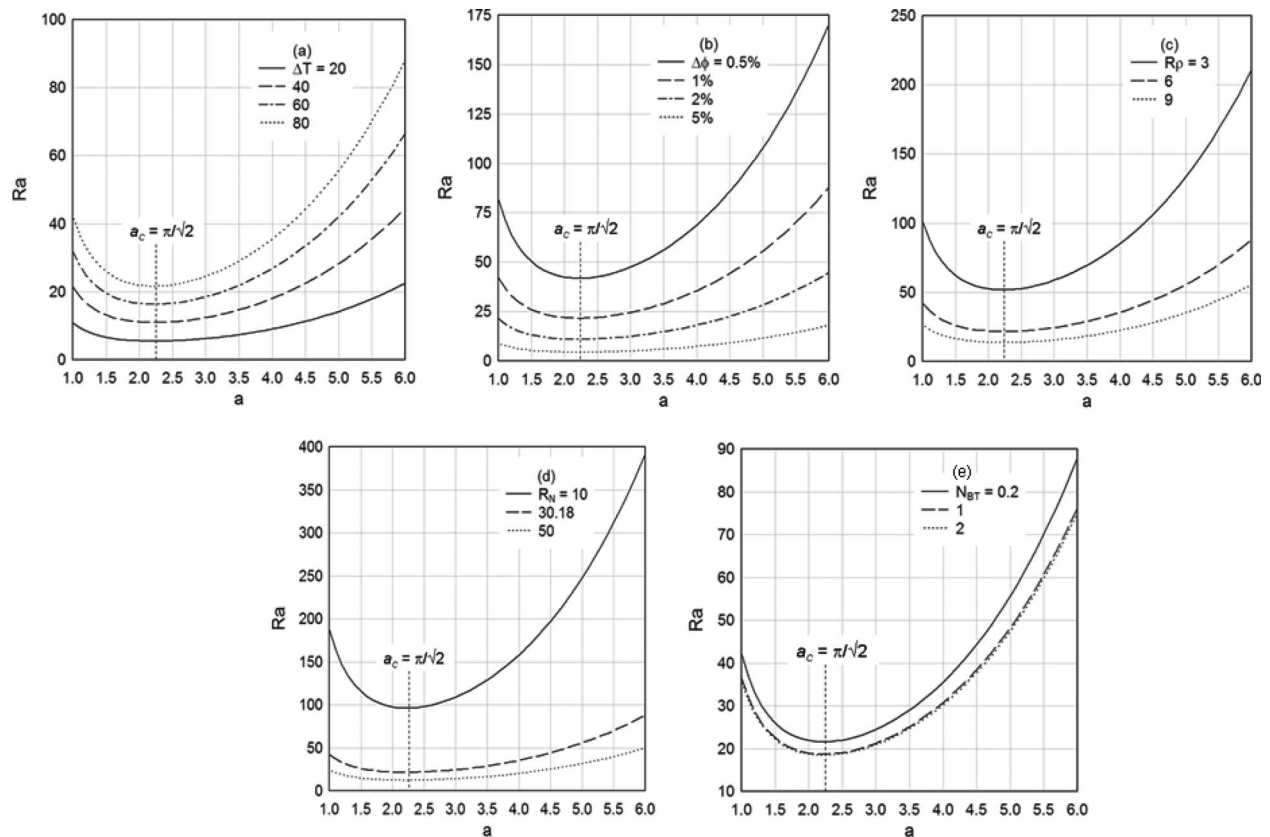


Fig. 4 Effects of (a) $\Delta T = T_0 - T_1$, (b) $\Delta\phi = \phi_0 - \phi_1$, (c) R_ρ , and (d) R_N on the Rayleigh number (Ra): $a = \pi/\sqrt{2} \cong 2.22144$ in all cases; (e) effects of N_{BT} on the Rayleigh number (Ra): $a = \pi/\sqrt{2} \cong 2.22144$.

The critical Rayleigh number for the case of $\Delta T = 80$ K in Fig. 4(a) is 21.5925, which is the base for comparison as other parameters are varied in Fig. 4. The second and third harmonics in correspondence are $Ra_c \cong 583$ for $m=2$ in Eqs. (40) and (46) and $Ra_c \cong 5485.32$ for $m=3$. In the present case with even boundary conditions in U , Eq. (37), the critical Rayleigh number resulting from the first-order solution ($m=1$) is not at all affected by the higher modes. The first-order solution for Ra_c would be affected by as little as 0.4% by the higher modes for problems involving odd/nonsymmetrical boundary conditions in U , showing that the combined use of the eigenfunction expansion method and the weighted residual method in this work does provide a highly accurate approach as far as the critical Rayleigh number (eigenvalues) is concerned.

In correspondence with $a_c = \pi/\sqrt{2} \cong 2.22144$ and $Ra_c \cong 21.5925$, under the same conditions, the critical conditions for the case of rigid-rigid surfaces are $a_c \cong 3.11421$ and $Ra_c \cong 56.3136$ (Eq. (50)) and those for the case of rigid-free surfaces are $a_c \cong 2.6824$ and $Ra_c \cong 36.5496$ (Eq. (51)). Compared to the corresponding cases for regular fluids [22], $a_c \cong 3.117$ and $Ra_c \cong 1707.762$ (rigid-rigid) and $a_c \cong 2.682$ and $Ra_c \cong 1100.65$ (rigid-free), the length parameter at the onset of instability (a_c) stays the same while the critical Rayleigh number is again lowered by one order of magnitude due to the combined behavior of Brownian motion and thermophoresis of nanoparticles.

6 Conclusion

Natural convection for nanofluids between two plates, heated from below, is studied in this work. The combined behavior of Brownian motion and thermophoresis of nanoparticles is shown to provide destabilizing effects, which can reduce the critical Rayleigh number by as much as two orders of magnitude as compared to that of the regular fluids without nanoparticles. The much lower

critical Rayleigh number suggests that turbulence may be the dominating mode for natural convection in most nanofluids. The critical Rayleigh number depends on the differences of temperature ($T_0 - T_1$) and volume concentration ($\phi_0 - \phi_1$) between the two plates, as well as the thermal expansion coefficient of the nanofluids (β), the density ratio of the nanoparticle to the base fluid (R_ρ), the Brownian-to-thermal-diffusivity ratio (N_{BT}), and the Brownian-motion-to-thermophoretic diffusivity ratio (R_N). Lewis number (Le) has been confirmed to be a high-order effect, which does not enter the critical Rayleigh number. Closed-form solutions for the Rayleigh number have been established to resolve the nanoparticle effect. For nanofluids between two free surfaces, Brownian motion and thermophoresis of nanoparticles do not change the geometrical configuration of the convective cell. At the onset of instability, the critical value of a_c , which is inversely proportional to the length of the side of the hexagon, stays at $\pi/\sqrt{2} \cong 2.22144$. Such a critical value for a_c is independent of the nanofluid properties. The presence of nanoparticles does not affect the critical cell size at the onset of instability, regardless of the surface conditions involved. The case of free-free surfaces results in the lowest value of Ra_c , as compared to the cases of rigid-free and rigid-rigid surfaces, and hence displays the most unstable pattern. Due to less constraints imposed on the disturbances in nanofluids bounded by two free surfaces, turbulence may be the easiest to produce among the three cases examined. Constant volume fractions of nanoparticles assumed at the plates are idealized and highly mathematical, for the sake of illustrating the tangling effects of Brownian and thermophoretic diffusion of nanoparticles in the simplest manner. More realistic conditions in terms of specified fluxes of nanoparticles are favorable, which will change the boundary conditions from the Dirichlet to the Neumann type. Reduction in the critical Rayleigh number, however, should stay on the same order of magnitude as that reported in this work since

the mathematical structure is well posed in the linear theory of instability and the change of the type of boundary conditions will not expect to result in a drastic change in the solutions.

Heat transfer enhancement by nanoparticles involves more than a sole increase in the effective thermal conductivity. Dominance of turbulence shown by this work, in terms of the much lower critical Rayleigh number by one to two orders of magnitude, may be a key to explain the recent experimental finding on the temperature uniformity across the nanofluid heat pipes in the presence of an uprising heat input. Reduction in the critical Rayleigh number by one to two orders of magnitude, however, does warrant a direct experimental verification for natural convection in nanofluids. This work is in progress.

Nomenclature

A	= size parameter of Bénard cell
A, B	= coefficient
B	= determinant
c	= specific heat (J/kg K)
$c_{1,2}$	= coefficient
d	= diameter of nanoparticles
D	= distance (m)
$D_{B,T}$	= diffusion coefficient (m^2/s)
f	= in-plane distribution of Bénard cell
F	= amplitude of volume fraction
g	= gravitation (m/s^2)
h	= enthalpy (J/kg)
H	= parameter
\mathbf{j}	= mass flux ($kg/m^2 s$)
k	= thermal conductivity (W/m K)
k_B	= Boltzmann constant (J/K)
Le	= Lewis number
N	= ratio
p	= pressure (Pa)
P	= pressure
Pr	= Prandtl number
R_N	= N_{TT}/N_{BT}
Ra	= Rayleigh number
t	= time (s)
T	= temperature (K)
u_i	= velocity (m/s), $i=1,2,3$
U_i	= velocity, $i=1,2,3$
x_i	= space (m), $i=1,2,3$
X_i	= coordinate, $i=1,2,3$

Greek

α	= thermal diffusivity (m^2/s)
β	= thermal expansion coefficient (1/K)
δ	= Kronecker delta
Δ	= changes
ϕ	= volume fraction of nanoparticles
Φ	= volume fraction
θ	= temperature
Θ	= temperature amplitude
μ	= viscosity ($N s/m^2$)
ρ	= mass density (kg/m^3)
σ	= amplification rate of disturbance
τ	= time

Subscripts and Superscripts

0	= reference state, bottom plate
---	---------------------------------

1	= top plate
b	= bulk
c	= critical value
B	= Brownian motion
BT	= Brownian-to-thermal-diffusivity ratio
f	= base fluid
i	= imaginary
p	= nanoparticle
r	= real
T	= thermophoresis
TT	= thermophoresis-to-thermal-diffusivity ratio
\bar{z}	= primary flow of z
z'	= disturbance of z or dz/dX_3

References

- [1] Eastman, J. A., Choi, S. U. S., Li, S., Yu, W., and Thompson, L. J., 2001, "Anomalous Increased Effective Thermal Conductivities of Ethylene Glycol-Based Nanofluids Containing Copper Nanoparticles," *Appl. Phys. Lett.*, **78**, pp. 718–720.
- [2] Lee, S., Choi, S. U. S., Li, S., and Eastman, J. A., 1999, "Measuring Thermal Conductivity of Fluids Containing Oxide Nanoparticles," *ASME J. Heat Transfer*, **121**, pp. 280–289.
- [3] Xuan, Y., and Li, Q., 2000, "Heat Transfer Enhancement of Nanofluids," *Int. J. Heat Mass Transfer*, **21**, pp. 58–64.
- [4] Choi, S. U. S., Zhang, Z. G., Yu, W., Lockwood, F. E., and Grulke, E. A., 2001, "Anomalous Thermal Conductivity Enhancement in Nanotube Suspensions," *Appl. Phys. Lett.*, **79**, pp. 2252–2254.
- [5] Das, S. K., Putra, N., Thiesen, P., and Roetzel, W., 2003, "Temperature Dependence of Thermal Conductivity Enhancement for Nanofluids," *ASME J. Heat Transfer*, **125**, pp. 567–574.
- [6] Pak, B. C., and Cho, Y., 1998, "Hydrodynamics and Heat Transfer Study of Dispersed Fluids With Submicron Metallic Oxide Particles," *Exp. Heat Transfer*, **11**, pp. 151–170.
- [7] Xuan, Y., and Li, Q., 2003, "Investigation of Convective Heat Transfer and Flow Features of Nanofluids," *ASME J. Heat Transfer*, **125**, pp. 151–155.
- [8] Xuan, Y., and Roetzel, W., 2000, "Conceptions for Heat Transfer Correlation of Nanofluids," *Int. J. Heat Mass Transfer*, **43**, pp. 3701–3707.
- [9] Maïga, S., Nguyen, C. T., Galanis, N., and Roy, G., 2004, "Heat Transfer Behaviors of Nanofluids Under in a Uniformly Heated Tube," *Superlattices Microstruct.*, **35**, pp. 543–557.
- [10] Buongiorno, J., 2006, "Convective Transport in Nanofluids," *ASME J. Heat Transfer*, **128**, pp. 240–250.
- [11] Yu, W., and Choi, S. U. S., 2003, "The Role of Interfacial Layers in the Enhanced Thermal Conductivity: A Renovated Maxwell Model," *J. Nanopart. Res.*, **5**, pp. 167–171.
- [12] Jang, S. P., and Choi, S. U. S., 2004, "Role of Brownian Motion in the Enhanced Thermal Conductivity of Nanofluids," *Appl. Phys. Lett.*, **84**(21), pp. 4316–4318.
- [13] Kumar, D. H., Patel, H. E., Rajeev Kumar, V. R., Sundararajan, J., Pradeep, T., and Das, S. K., 2004, "Model for Heat Conduction in Nanofluids," *Phys. Rev. Lett.*, **93**, p. 144301.
- [14] Keblinski, P., Phillpot, S. R., Choi, S. U. S., and Eastman, J. A., 2002, "Mechanisms of Heat Flow in Suspensions of Nano-Sized Particles (Nanofluids)," *Int. J. Heat Mass Transfer*, **45**, pp. 855–863.
- [15] Chen, G., 2001, "Ballistic-Diffusive Heat-Conduction Equation," *Phys. Rev. Lett.*, **86**(11), pp. 2297–2300.
- [16] Vadasz, P., 2006, "Heat Conduction in Nanofluid Suspensions," *ASME J. Heat Transfer*, **128**, pp. 465–477.
- [17] Ma, H. B., Wilson, C., Yu, Q., Choi, U. S., and Tirumala, M., 2006, "An Experimental Investigation of Heat Transport Capability in a Nanofluid Oscillating Heat Pipe," *ASME J. Heat Transfer*, **128**, pp. 1213–1216.
- [18] McNab, G. S., and Meisen, A., 1973, "Thermophoresis in Liquids," *J. Colloid Interface Sci.*, **44**(2), p. 339.
- [19] Jang, S. P., and Choi, U. S. U., 2004, "Free Convection in a Rectangular Cavity (Bénard Convection) With Nanofluids," *Proceedings of the 2004 IMECE*, Anaheim, CA, Nov. 13–20.
- [20] Incropera, F. P., Dewitt, D. P., Bergman, T. L., and Lavine, A. S., 2007, *Introduction to Heat Transfer*, 5th ed., Wiley, Hoboken, NJ.
- [21] Yih, C. S., 1977, *Fluid Mechanics: A Concise Introduction to the Theory*, West River Press, Ann Arbor, MI, Chap. 9.
- [22] Chandrasekhar, S., 1961, *Hydrodynamic and Hydromagnetic Stability*, Oxford University Press, Oxford.
- [23] Finlayson, B. A., 1972, *The Method of Weighted Residuals and Variational Principles*, Academic, New York.

Flow Boiling Instabilities in Microchannels and Means for Mitigation by Reentrant Cavities

C.-J. Kuo

Y. Peles¹

e-mail: pelesy@rpi.edu

Department of Mechanical, Aerospace and
Nuclear Engineering,
Rensselaer Polytechnic Institute,
Troy, NY 12180

The ability of reentrant cavities to suppress flow boiling oscillations and instabilities in microchannels was experimentally studied. Suppression mechanisms were proposed and discussed with respect to various instability modes previously identified in microchannels. It was found that structured surfaces formed inside channel walls can assist mitigating the rapid bubble growth instability, which dominates many systems utilizing flow boiling in microchannels. This, in turn, delayed the parallel channel instability and the critical heat flux (CHF) condition. Experiments were conducted using three types of $200 \times 253 \mu\text{m}^2$ parallel microchannel devices: with reentrant cavity surface, with interconnected reentrant cavity surface, and with plain surface. The onset of nucleate boiling, CHF condition, and local temperature measurements were obtained and compared in order to study and identify flow boiling instability. [DOI: 10.1115/1.2908431]

Keywords: flow instability, boiling, microchannel, CHF

1 Introduction

Flow boiling instabilities can seriously hinder the thermal performance of many cooling systems utilizing liquid-vapor phase change in channels. As a result, numerous studies have been dedicated to obtain fundamental knowledge and engineering data of various instability modes [1–8] in an attempt to eliminate their occurrences or at least better predict them.

Driven by the rapid advancement in microelectromechanical systems (MEMS) and the need for new cooling systems to dissipate the ever increasing demand for power density/heat generation in electronic systems, two-phase flow in microchannels has received increasing interest since it is perceived as an enabling cooling method as well as a rich field of scientific inquisitiveness. It appears that flow boiling instability in microchannels is a very notable problem if improperly addressed [8–22]. In fact, many studies on microchannel flow boiling report results for relatively low mass quality, in which, perhaps, some sort of flow instability can be contained; at higher qualities, flow instabilities (especially at low and moderate mass fluxes) can bring into question the physical meaning and relevance of the results. Bergles and Kandlikar [8] argued that *all* of the critical heat flux (CHF) studies in microchannels discussed in their paper [9–12] were affected by flow oscillation. Furthermore, the large discrepancies between various heat transfer coefficient data at the microscale might be attributed to flow oscillations. Thus, properly considering flow instabilities and developing means to suppress them are key issues, which hinder advancement of knowledge about flow boiling in microchannels.

Several endeavors aimed at unraveling key processes controlling flow instabilities in microchannels and means to suppress their occurrence have been recently reported [17,18]. With the maturity of the field, new concepts and methods to enhance the performance of flow boiling in microchannels are being developed [18–21]. As a part of this effort, Kuo et al. [20] and Pate et al. [21] proposed to form reentrant cavities on microchannel walls to pro-

mote bubble nucleation. As will be discussed in Sec. 2, there are reasons to believe that the enhancement of bubble ebullition can be exploited to mitigate flow oscillations.

In this study, the use of structured reentrant cavity surfaces is explored as a mean to suppress (or at least delay) flow oscillations. Various instabilities modes detailed in previous microchannel studies are discussed in Sec. 2. Also, possible means to contain their occurrence are presented. Following, new experimental results on flow boiling in microchannels with reentrant cavity surfaces are presented and possible mechanisms controlling the phenomena are discussed (Sec. 5).

2 Background and Hypothesis

Bergles and Kandlikar in their insightful article on the nature of CHF in microchannels [8] stated that the two major instabilities that affect microchannel heat exchangers are *upstream compressible volume/pressure drop* and *excursive instabilities*. For the purpose of the discussion presented in this paper, two additional modes are included: *rapid bubble growth* and the CHF. While any flow boiling system is susceptible to the CHF instability, when opposite thermal and/or hydrodynamic conditions develop, be it through conventional dryout or departure from nucleate boiling (DNB) mechanisms, the rapid bubble growth instability is distinct to the microscale. These four instabilities are extensively discussed in numerous papers and here they are briefly outlined in relation to a structured surface.

2.1 Rapid Bubble Growth. This instability refers to the often reported rapid growth of bubbles in microchannel systems [20] and is characterized by high frequencies ($f \geq 100$ Hz). In the initial stage of the nucleation cycle, i.e., during the rapid bubble growth, a spherical bubble grows until it attains a size comparable to the channel hydraulic diameter. The bubble then grows rapidly in the longitudinal direction (downstream as well as upstream), which causes flow reversal. The oscillations caused by this rapid bubble growth can be linked to two distinct mechanisms: the high liquid superheated temperature required to initiate bubble growth in MEMS-based microchannel systems (Mechanism A), and the elevated pressures generated during bubble growth (Mechanism B).

2.1.1 Mechanism A: Liquid Superheat. MEMS-based microchannels are typically microfabricated by the use of deep reactive

¹Corresponding author.

Contributed by the Heat Transfer Division of ASME for publication in the JOURNAL OF HEAT TRANSFER. Manuscript received March 8, 2007; final manuscript received July 6, 2007; published online May 16, 2008. Review conducted by Satish G. Kandlikar.

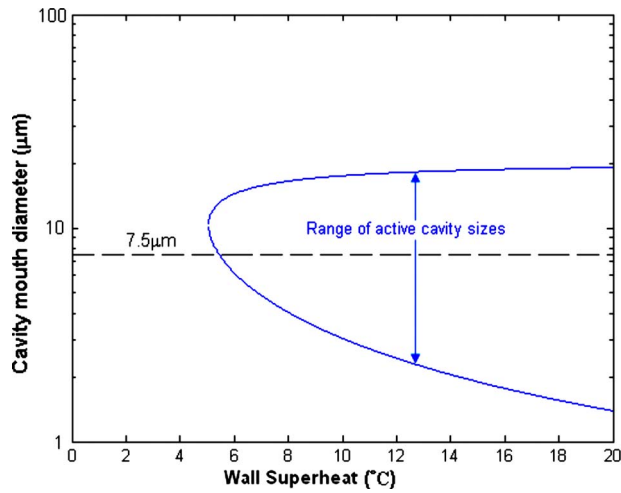


Fig. 1 Range of active cavity size as a function of wall superheat for flow boiling of water for the current microchannels based on Hsu's criteria [23]

ion etching (DRIE) process, which form deep trenches with a characteristic sidewall peak-to-peak roughness of $\sim 0.3 \mu\text{m}$. Using Hsu's [23] well known model, it can be shown (Fig. 1) that 300 nm nucleus triggers phase change at relatively high surface temperatures for water, and, as a result, the liquid adjacent to the wall, as well as the bulk liquid, will attain high superheated temperatures before nucleation occurs. Once boiling is triggered, the superheated liquid will readily (and rapidly) change phase causing an explosivelike vapor growth.

2.1.2 Mechanism B: Bubble Dynamics and Elevated Pressures. The Rayleigh–Plesset equation [24,25] predicts a large temporary pressure increase in a liquid field, which surrounds a rapidly growing bubble. In large scale boiling systems, the local high pressure generated by a single bubble is confined to a very small region of the channel and can hardly affect the global pressure distribution and the bulk flow dynamics. As the paradigm size diminishes, the bubble-to-channel diameter ratio increases. Moreover, when the bubble departure diameter is comparable to the channel hydraulic diameter, any change to the pressure in the vicinity of the bubble will be felt throughout the channel. Thus, the high pressures associated with the growth of a bubble can cause transient flow reversal upstream the growing bubble.

2.1.3 Means to Suppress Rapid Bubble Growth Instability. Different means to suppress the above two distinct mechanisms are required. The prime prerequisite to suppress Mechanism A is to reduce the liquid superheated temperature. This can be achieved by providing effective surface nuclei in the form of reentrant cavities on the channel wall. On the other hand, to suppress Mechanism B, the inlet pressure must be abruptly increased in response to the rapid pressure rise as the bubble nucleation begins. This can be done, for instance, by placing a one-way valve in the channel inlet. It should be noted that such solution can considerably complicate the microfabrication process. A simpler solution is to place an orifice in the channel inlet [17,18], which, undesirably, comes with the penalty of higher pressure drops. The flow oscillations instigated by Mechanism B can also be abated by decelerating the bubble growth rate through reducing the liquid tendency to rapidly change phase, i.e., reducing the liquid superheat. As discussed earlier, this can be achieved by forming reentrant cavities on the channel walls.

2.2 Parallel Channel Instability. *Parallel channel instability* is closely related to the *excursive instability*—both are well documented in numerous reports (e.g., Ref. [1]). The excursive instability can only occur at the negative slope portion of pressure

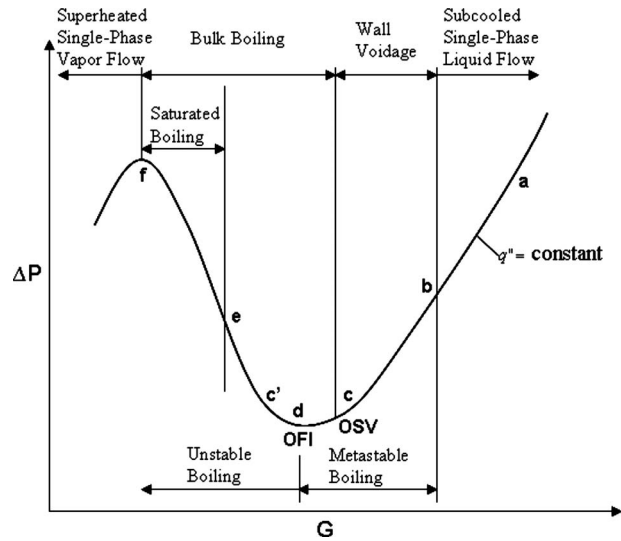


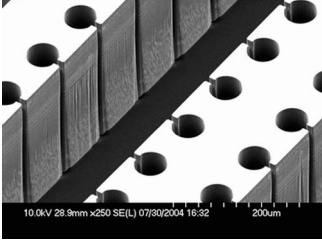
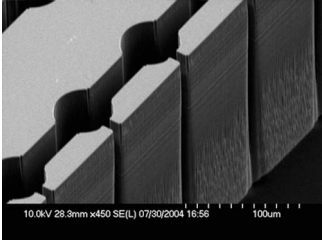
Fig. 2 Pressure drop–mass flux curve for a uniformly heated channel [7]

drop–mass flow rate curve—Segment d-f in Fig. 2. As discussed by Bergles and Kandlikar [8] and experimentally shown by Koşar et al. [18], inlet orifices in each channel can completely eradicate these two instabilities. However, reentrant cavities can provide some means (although limited) to delay or moderate excursive instability. This can be better understood by considering Fig. 2, which is adopted from Stoddard et al. [7]. As the mass flux decreases, for a fixed heat flux at the single-phase liquid branch of the curve (from Points a to b), the flow is stable. However, with the inception of boiling, the system gradually loses its stability and Segment b-d is in a metastable state. In large systems, the perturbation generated by the ebullition of a single bubble is relatively small, and a transition from the metastable branch to the unstable branch (Segment d-f) is unlikely to occur. In microchannels, the perturbation generated by a single bubble can be relatively large and an abrupt transition from Point c to Point c' is more probable. Thus, by reducing the explosivelike characteristic of the bubble nucleation through the use of structured reentrant cavity surface, the system can gradually approach the local minima of the curve (also defined as the onset of flow instability (OFI) in some reports [7]).

2.3 Compressible Volume Instability. Compressible volume/pressure drop instability is a density wave oscillation that can be triggered by excursive instability [1,6]. It is often associated with pressure drop oscillations, having a characteristic frequency of $\sim 0.1 \text{ Hz}$, combined with density wave oscillations, having a characteristic frequency of $\sim 1 \text{ Hz}$. Compressible volume instability occurs in systems that have a significant compressible volume upstream, or within, the heated section. In microchannel, a small volume of subcooled liquid is sufficient to cause the compressible volume instability and lead to premature CHF [8].

2.4 Critical Heat Flux Instability. It has been suggested by various researchers [5–8] that flow oscillations, such as compressible volume instability or parallel channel instabilities, are closely connected with premature CHF conditions. A more uniform and gradual bubble formation process in boiling system can moderate the local void fraction/density change, mitigate the compressible volume instability, and delay the parallel channel instability. The reduction in flow oscillation, in turn, can suppress early onset of the CHF conditions.

Table 1 Microchannels with different wall configurations

Device	Description	SEM images
1NR	Nonconnected reentrant cavity microchannel	
2IR	Interconnected reentrant cavity microchannel	
3PW	Plain wall microchannel	

3 Device Overview

The MEMS devices consist of five parallel, 10,000 μm long, 200 μm wide, and 253 μm deep microchannels, each spaced 200 μm apart. Table 1 outlines the three types of devices used in

the current investigation along with scanning electron microscope (SEM) images of the channel sidewall. In Device 1NR, the microchannel sidewall encompasses an array of 100 reentrant cavities spaced 100 μm apart. An acute angle connects the 7.5 μm mouth to the 25 μm inside diameter reentrant body. Device 2IR is similar to Device 1NR, except a 20 μm wide interconnection is formed on each sidewall to connect the reentrant cavities. A plain wall microchannel device (Device 3PW) is also fabricated. For all microdevices, an air gap is formed on the two ends of the sidewalls in order to minimize ambient heat losses, and inlet and exit plenums are etched on the thin silicon substrate ($\sim 150 \mu\text{m}$). On the top of the device, a Pyrex cover seals the device and allows flow visualization. Figure 3(a) depicts a computer aided design (CAD) model of the back side of the device. Three thermistors, 10 μm wide and 300 μm long, are located 3400 μm , 6700 μm , and 10,000 μm downstream the channel inlet together with electrical connecting vias, as shown in Fig. 3(b). On top of the thermistors, a 1 μm silicon oxide layer is deposited for electrical insulation. A heater is then formed on top of the oxide layer to deliver the heating power, and it also serves as an additional thermistor to measure the average temperature of the entire heated area.

4 Device Fabrication, Experimental Apparatus, and Procedures

4.1 Microchannel Fabrication Method. The MEMS device was micromachined on a polished double-sided *n*-type (100) single crystal silicon wafer, which employs techniques adapted from integrated circuit (IC) manufacturing. A 1 μm thick high-

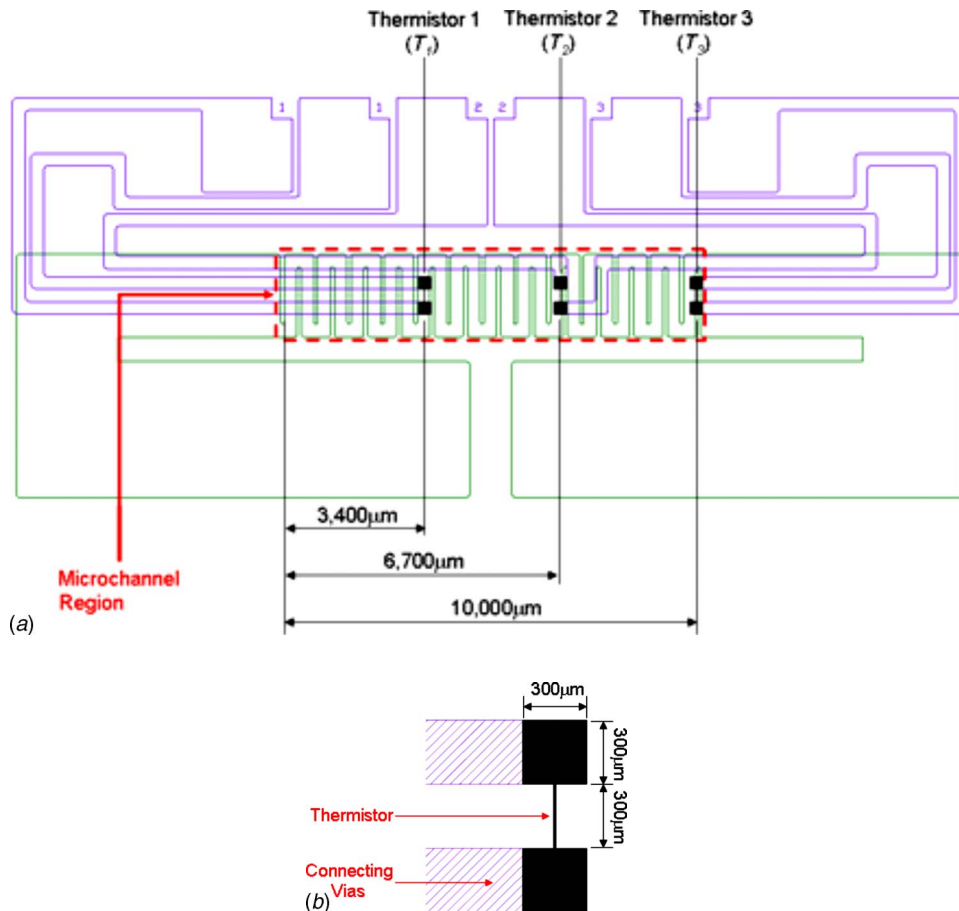


Fig. 3 CAD models of (a) the heater and the thermistors on the back side of the microdevice, and (b) a single thermistor

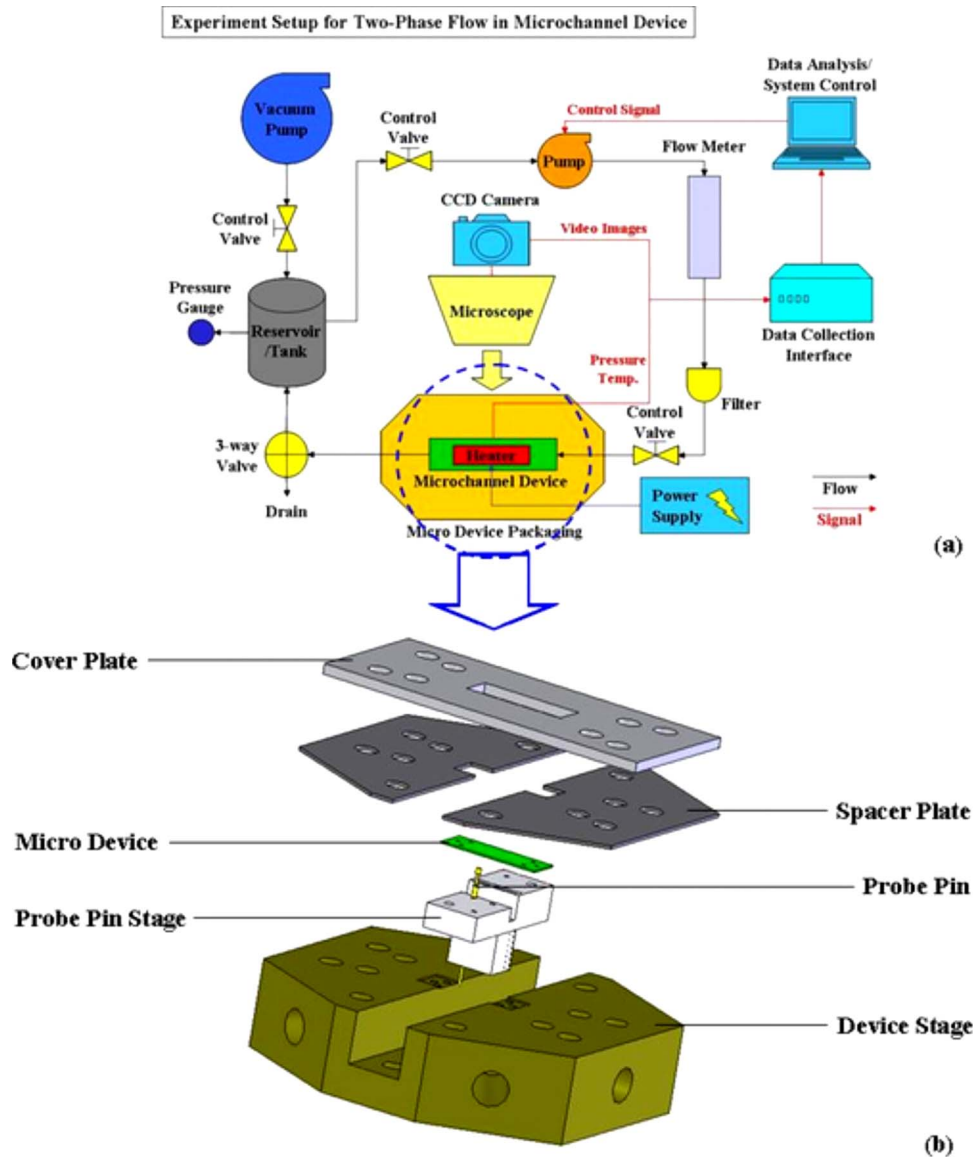


Fig. 4 (a) Experimental setup and (b) microdevice package

quality oxide film was deposited on both sides of the silicon wafer to shield the bare wafer surface during processing and to serve as an electrical insulator. A layer of 150 Å thick titanium was deposited by a cryopumped CVC 601 sputter deposition system and patterned on the back side of the wafer to form the thermistors. Vias of 0.2 μm aluminum containing 1% silicon and 4% copper was subsequently formed in order to create electrical connections to the thermistors. Following, a 1 μm thick plasma enhanced chemical vapor deposition (PECVD) oxide was deposited to insulate the thermistors and the vias from the lower layer. The heater was then formed on top of the oxide layer by CVC sputtering deposition. A 70 Å thick layer of titanium was initially deposited to enhance adhesion characteristics and was followed by sputtering a 1 μm thick layer of Al-1%Si-4%Cu. Subsequent photolithography and concomitant wet bench processing created the heater on the back side of the wafer. Another 1 μm thick PECVD oxide was deposited to protect the back side features during further processing.

Next, the microchannels were formed on the top side of the wafer. The wafer was taken through a photolithography step and a reactive ion etching (RIE) oxide removal process to mask certain areas on the wafer, which were not to be etched during the DRIE

process. The wafer was consequently etched in the DRIE process, and silicon was removed from places not protected by the photoresist/oxide mask. A profilometer and SEM were employed to measure and record various dimensions of the device.

The wafer was flipped, and the back side was then processed to create an inlet, outlet, side air gap, and pressure port taps for the transducers. A photolithography step followed by a buffered oxide etch (BOE) (6:1) oxide removal process was carried out to create a pattern mask. The wafer was then etched through in a DRIE process to create the fluidic ports. Thereafter, electrical contacts/pads were opened on the back side of the wafer by performing another round of photolithography and RIE processing. Finally, the processed wafer was stripped of any remaining resist or oxide layers and anodically bonded to a 1 mm thick polished Pyrex (glass) wafer to form a sealed device. After successful completion of the bonding process, the processed stack was die sawed to separate the devices from the parent wafer.

4.2 Experimental Test Rig. The setup, shown in Fig. 4(a), consists of three primary subsystems: the flow loop section, instrumentation, and a data acquisition system. The test section houses the MEMS microchannel devices and its fluidic and ther-

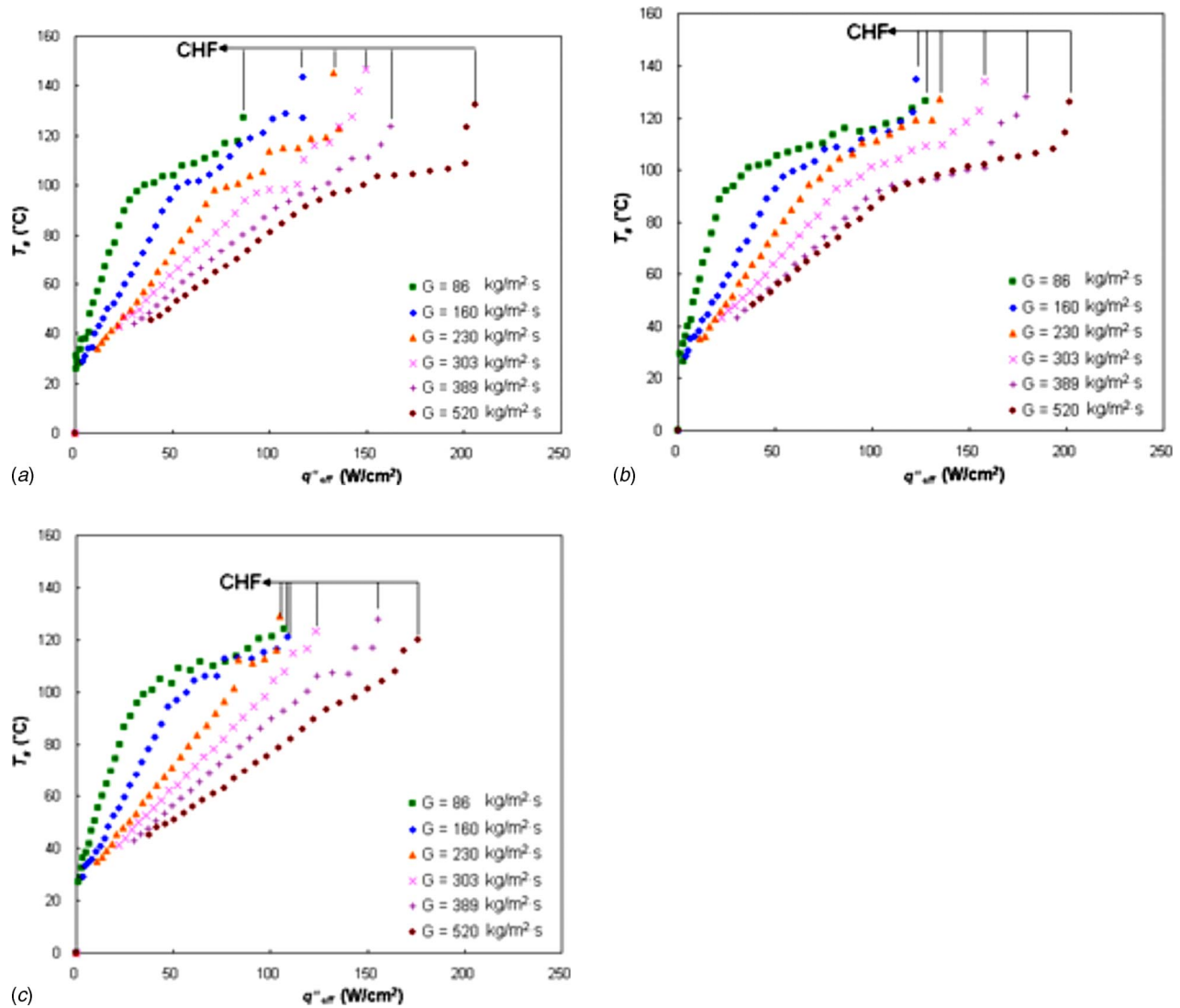


Fig. 5 Substrate temperature as a function of effective heat flux for (a) Device 1NR, (b) Device 2IR, and (c) Device 3PW

mal packaging module (Fig. 4(b)). The microchannel device is mounted on the fluidic packaging module through miniature “o-rings” to ensure a complete leak-free system. The fluidic packaging delivers the working fluid and access to the pressure transducers. The external electrical connections to the thermistors and the heater were achieved from beneath through spring-loaded probe pins, which connected the thermistors and the heater to electrical pads, which reside away from the main microchannel body.

The main flow loop includes the microchannel device, a pulseless gear pump, a reservoir that consists of a deaerator unit and a heating element to control the inlet temperature, a flow meter, and a dissolved oxygen meter. The test section heater is connected to a power supply with an adjustable dc to provide power to the device. The thermistor output signals are recorded by the National Instrument data acquisition system. Simultaneously, the inlet pressure and test section pressure drop are collected, and the boiling process in the microchannels is recorded by a Phantom V4.2 high-speed camera (maximum frame rate of 90,000 frames/s and 2 μ s exposure time) mounted over a Leica DMLM microscope. Calibration of the heater and the thermistors is performed prior to the experiment by placing the device in an oven and establishing the resistance-temperature curve for each individual sensor.

4.3 Experimental Procedures and Data Reduction. The deionized water was first degassed until the oxide concentration

level dropped below 3 ppm. Then, the water flow rate was fixed at the desired value, and experiments were conducted after steady conditions were reached with an exit atmospheric pressure and ambient room temperature ($\sim 22^\circ\text{C}$). The electrical resistances of the thermistors were also measured at room temperature. During the experiment, voltage was applied in 0.5 V increments to the test section heater, and the resistance data for the heater and the thermistors were recorded once steady state was reached. The procedure was repeated for different flow rates.

To estimate heat losses, electrical power was applied to the test section after evacuating the water from the test loop. Once the temperature of the test section became steady, the temperature difference between the ambient and test section was recorded with the corresponding power. The plot of power versus temperature difference was used to calculate the heat loss (\dot{Q}_{loss}) associated with each experimental data point.

Data obtained from the voltage, current, and pressure measurements were used to calculate the average single- and two-phase temperatures, heat transfer coefficients, and CHF conditions. The electrical input power, P , and heater resistance, R , respectively, were determined by the measured voltage, V , and current, I , with

$$P = V \times I \quad (1)$$

and

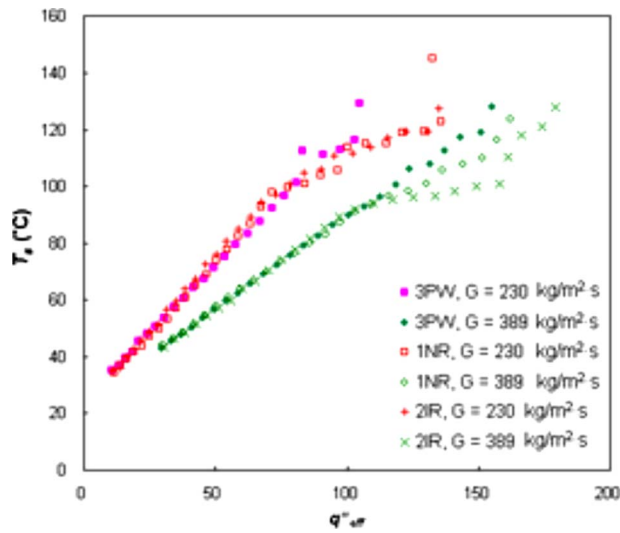


Fig. 6 Substrate temperature, T_s , as a function of effective heat flux for the three microchannel devices

$$R = V/I \quad (2)$$

The electrical resistance-temperature calibration curve of the heater and the thermistors were used for determining the average heater temperature, \bar{T}_{heater} , and the thermistor temperature for each local position, $T_{\text{thermistor}}$. The substrate temperature, T_s , and the local surface temperatures (T_1, T_2, T_3) at the base of the microchannels were then calculated as

$$T_s = \bar{T}_{\text{heater}} - \frac{(P - \dot{Q}_{\text{loss}})t_b}{k_s A_p} \quad (3)$$

$$T_1, T_2, T_3 = T_{\text{thermistor}} - \frac{(P - \dot{Q}_{\text{loss}})t_b}{k_s A_p} \quad (4)$$

where t_b , k_s , and A_p are the base thickness, thermal conductivity of silicon, and the platform area ($A_p = 0.2 \text{ cm}^2$ in the current study), respectively. The effective heat flux, q''_{eff} , is defined as

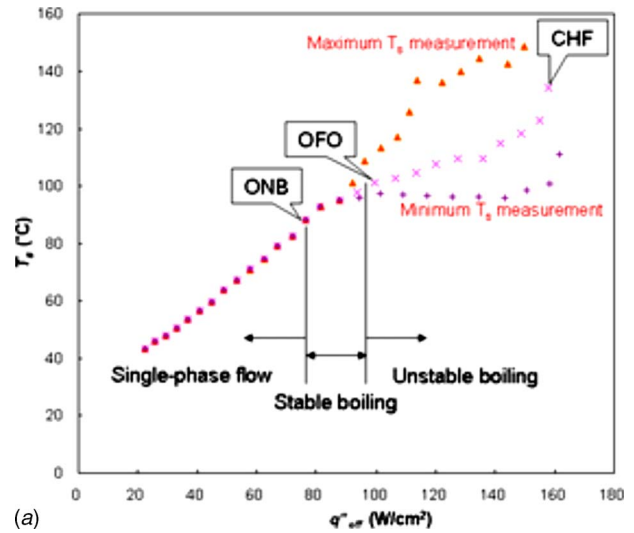
$$q''_{\text{eff}} = \frac{P - \dot{Q}_{\text{loss}}}{A_t} \quad (5)$$

where A_t is the total channel surface area. $A_t = 0.353 \text{ cm}^2$ and was unchanged for all three microdevices. The heat loss, \dot{Q} , was estimated to be 5–10% of the total power depending on the heat flux and mass flux.

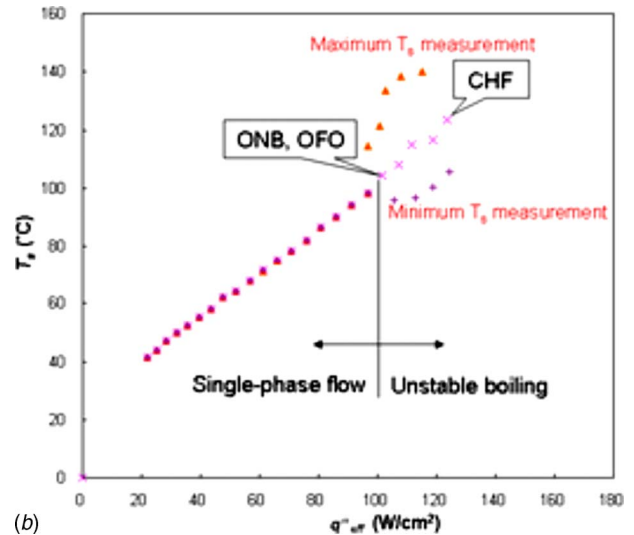
4.4 Uncertainty Analysis. The uncertainties of the measured values are obtained from the manufacturers' specification sheets, while the uncertainties of the derived parameters are calculated using the method developed by Kline and McClintock [26]. Uncertainties in the mass flux (G), heat flux (q''_{eff}), temperature (T) are estimated to be $\pm 1\%$, $\pm 1\%$, and $\pm 3\%$, respectively.

5 Results and Discussion

5.1 General Observation. The substrate temperature, T_s , as a function of the effective heat flux for all three devices is shown in Fig. 5 for mass fluxes ranging from $86 \text{ kg/m}^2 \text{ s}$ to $520 \text{ kg/m}^2 \text{ s}$. At low heat fluxes, single-phase liquid flow existed, which was represented by the linear temperature increase with heat flux. Above a certain heat flux, boiling initiated and a drastic change in the slope was apparent, indicating the ONB, which was also verified by visual inspection of bubbles forming in the channel. For the devices with reentrant cavities (Devices 1NR and 2IR), initially stable boiling was maintained until the heat flux reached a



(a)



(b)

Fig. 7 Substrate temperature as a function of effective heat flux for $G = 303 \text{ kg/m}^2 \text{ s}$. (a) Device 1NR and (b) Device 3PW.

condition, where boiling instability commenced with considerable temperature fluctuations. This condition was marked as the onset of flow oscillation (OFO) and defined as the conditions corresponding to a substrate temperature fluctuation greater than 5°C . With further increase in the heat flux, a critical state was reached, in which a meager increase in the heat flux resulted in a sharp and abrupt increase in the substrate temperature, indicating the arrival of CHF condition. Note that the substantial temperature fluctuation following OFO was characterized by a very low dominant frequency ($\sim 0.1 \text{ Hz}$)—a characteristic of upstream compressible volume instability. Unlike Devices 1NR and 2IR, Device 3PW reveals a different boiling trend (Fig. 5(c)), where the transition from ONB to CHF was much more rapid, and only for $G \leq 160 \text{ kg/m}^2 \text{ s}$ a relatively appreciable pre-CHF boiling region was maintained. This is better shown by directly comparing the boiling curves for the three micro-devices (Fig. 6) for $G = 230 \text{ kg/m}^2 \text{ s}$ and $G = 389 \text{ kg/m}^2 \text{ s}$. While all three devices had very similar single-phase $T_s - q''_{\text{eff}}$ curves, Devices 1NR and 2IR (with reentrant cavities) experienced ONB at much lower heat fluxes with significant temperature slope change followed by a more stable boiling process, and, eventually, reached higher CHF values.

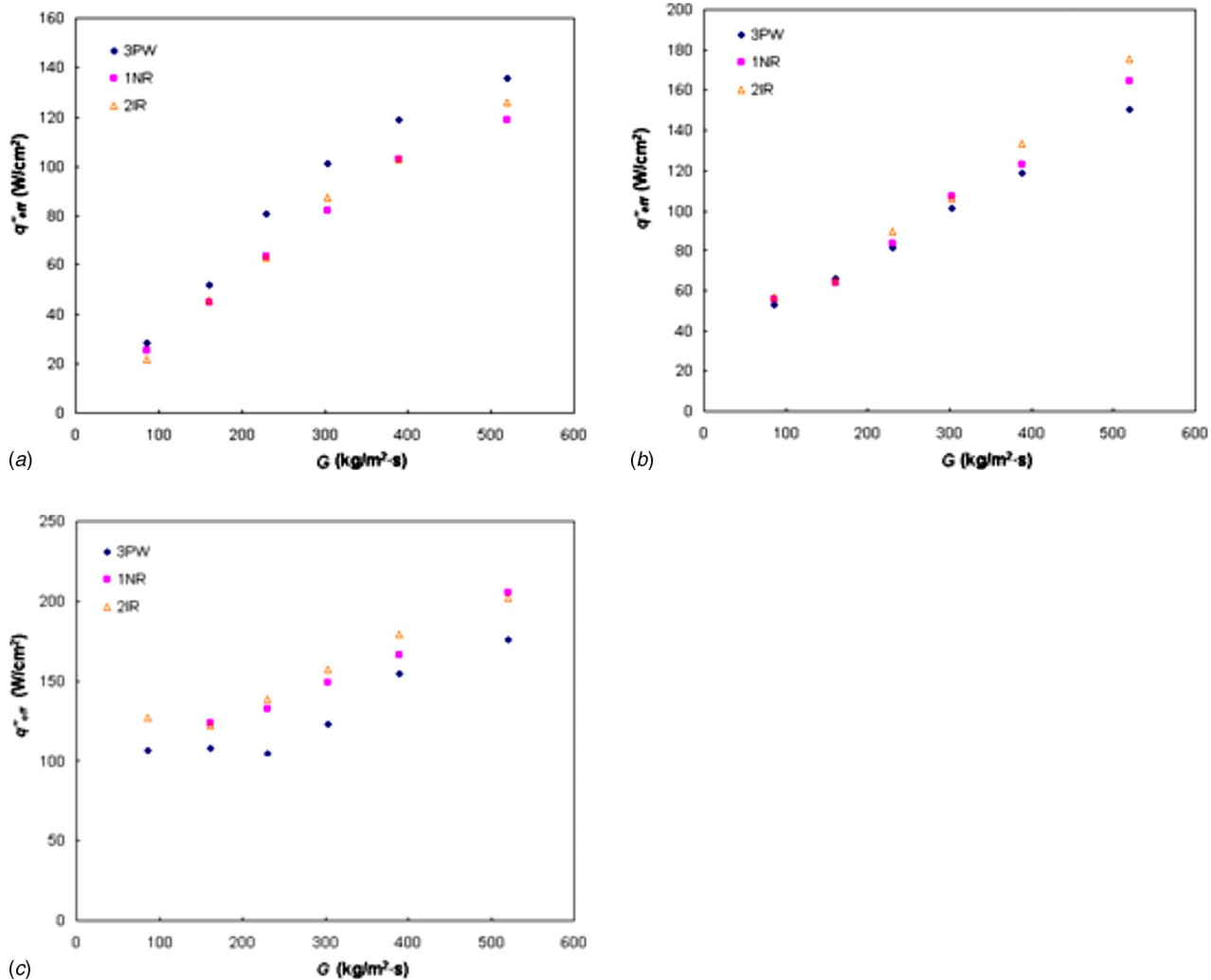


Fig. 8 Effective heat flux at (a) ONB, (b) OFO, and (c) CHF for different mass fluxes and different types of microdevices

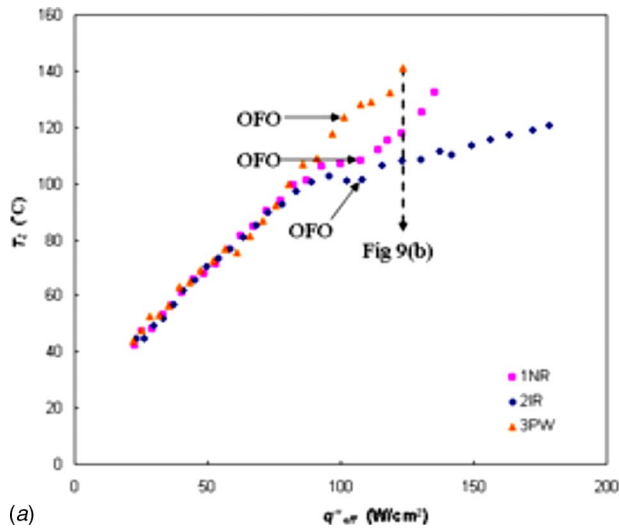
The boiling curves for Devices 1NR and 3PW for $G = 303 \text{ kg/m}^2 \text{ s}$ are shown in Fig. 7 along with the corresponding maximum/minimum surface temperatures. The ONB, OFI, and CHF are also marked. For Device 1NR (Fig. 7(a)), stable boiling existed between $q''_{eff} = 81 \text{ W/cm}^2$ and $q''_{eff} = 99 \text{ W/cm}^2$, and the temperature oscillation after OFO increased gradually from 5°C to 27°C . On the other hand, with Device 3PW (Fig. 7(b)), OFO was triggered immediately with the ONB and experienced initial temperature oscillation of 10°C that gradually increased to 22°C prior to the CHF condition. Very limited stable boiling condition was observed with Device 3PW.

Comparisons of the heat flux at ONB, OFO, and CHF as a function of mass flux are depicted in Fig. 8. A reduction in the heat flux of 13–23% at ONB and 15–33% improvement in the CHF condition were observed with Devices 1NR and 2IR in comparison to Device 3PW. Device 3PW showed greater tendency than Devices 1NR and 2IR to trigger instabilities, as evident by its lower heat flux at OFO. This is apparent especially at moderate and high mass fluxes ($G \geq 303 \text{ kg/m}^2 \text{ s}$). The reentrant cavities appeared to delay and modify the prime instability modes—the compressible volume and parallel channel instability, as will be discussed in Sec. 5.2—but not to eliminate their occurrences.

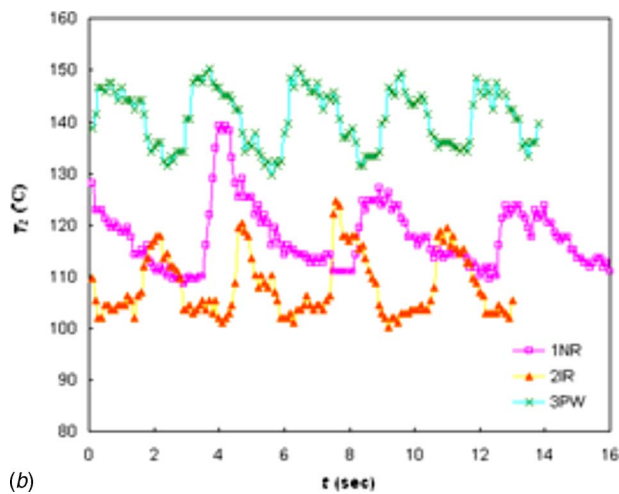
The reduction of the heat flux at ONB and the increased CHF are related to boiling instability in two ways. The delay of flow oscillation resulting from enhanced bubble nucleation can improve CHF; this is especially significant for high mass flux (G

$\geq 303 \text{ kg/m}^2 \text{ s}$). It was stated by Koşar et al. [19] and Kuo et al. [20] that reentrant cavity can reduce wall superheat required to activate bubble nucleation, and, thus, enhance the boiling process, especially for high mass fluxes. The microfabrication technique commonly used to form plain wall microchannels severely restricts the range of active cavity sizes available for heterogeneous bubble nucleation. As discussed by Collier and Thome [27], this requires the bulk liquid to be considerably superheated before vapor generation can take place at the surface. Once a vapor bubble forms in the superheated liquid it grows very rapidly. As discussed in Sec. 2.1, the explosive growth of vapor bubbles (rapid bubble growth instability) triggers large flow oscillations. In the plain microchannel device, this instigated early parallel channel instability and amplified compressible volume instability, and, in turn, caused premature CHF. For high mass fluxes, it is evident [19,20] that reentrant cavities enable a more orderly bubble nucleation process with significant lower surface temperatures, and, to an extent, suppress the rapid bubble growth. To further elaborate on this issue, it is useful to examine the local effects of the reentrant cavities. This is now discussed in the following subsection.

5.2 Transient and Local Thermal-Hydraulic Characteristic. The average local temperature T_2 as a function of heat flux for $G = 303 \text{ kg/m}^2 \text{ s}$ for the three devices is shown in Fig. 9(a). No appreciable deviation was recorded for T_2 during



(a)

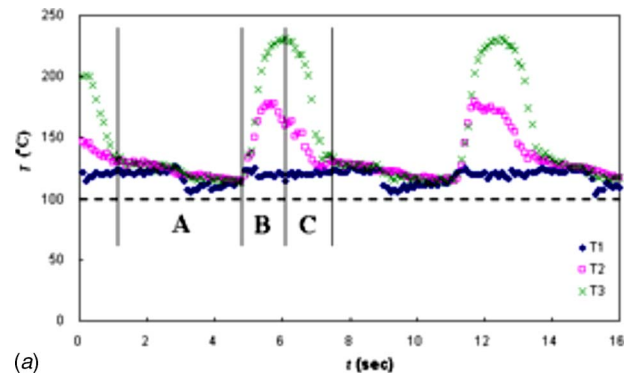


(b)

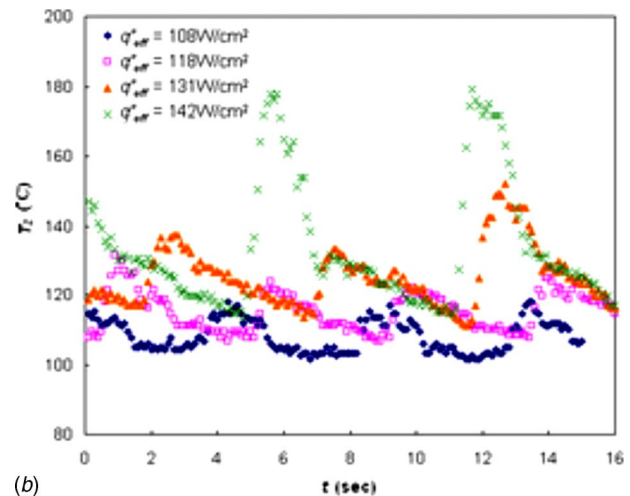
Fig. 9 (a) T_2 as a function of effective heat flux for $G = 303 \text{ kg/m}^2 \text{ s}$, and (b) Transient T_2 for $G = 303 \text{ kg/m}^2 \text{ s}$ and $q''_{\text{eff}} = 123 \text{ W/cm}^2$

single-phase flow. However, similar to the substrate temperature, T_s , the average local temperature T_2 for the structured-surface microchannel devices (Devices 1NR and 2IR) was much lower than for the plain wall channel device (Device 3PW) after ONB. To further evaluate the apparent deviation of local temperature after ONB between the test devices, the transient response of T_2 for $G = 303 \text{ kg/m}^2 \text{ s}$ and $q''_{\text{eff}} = 123 \text{ W/cm}^2$ is shown in Fig. 9(b). Besides the significant increase in T_2 , the temperature fluctuation magnitudes for all microchannel devices are comparable. However, the structured-surface microchannels seem to have longer low-temperature period between temperature peaks, which is the probable cause for the significant lower average T_2 .

Local transient surface temperature at post-OFO conditions coupled with transient pressure drop and flow visualization revealed a characteristic thermal-hydraulic cycle that can be divided into three distinct stages: (a) bubble nucleation (Stage A), (b) vapor filling/dryout (Stage B), and (c) post-dryout/upstream flooding (Stage C). A typical transient temperature curve for $G = 303 \text{ kg/m}^2 \text{ s}$, $q''_{\text{eff}} = 142 \text{ W/cm}^2$, for Device 1NR is shown in Fig. 10(a), along with the three boiling stages. Additionally, the transient T_2 at the same hydraulic condition is shown for four different heat fluxes (Fig. 10(b)), and the images captured by the microscope and the high-speed camera at different stages of the boiling process are also shown in Fig. 11. In Stage A (Fig. 11(a)),



(a)



(b)

Fig. 10 (a) Transient local temperature for Device 1NR for $G = 303 \text{ kg/m}^2 \text{ s}$, $q''_{\text{eff}} = 142 \text{ W/cm}^2$; (b) comparison of transient T_2 for different heat fluxes for $G = 303 \text{ kg/m}^2 \text{ s}$ (Device 1NR)

the bubbles generated from the channel wall maintained relatively stable flow, and the heat transfer, as well as the surface temperature, hardly changed. Depending on the heat flux, the corresponding time period and surface temperature varied, and, at low heat flux, subcooled liquid existed in the inlet region. For the plain wall microchannel, the bubble nucleation stage (Stage A) was very limited and bubbles rapidly grew and dominated the early stage of unstable boiling. This, in turn, promoted the subsequent stage (Stage B), where vapor rapidly propagated upstream, completely filled the channel, and increased the upstream pressure, as shown in Fig. 11(b). The sudden void fraction increase with temporary/local dryout at high heat flux is also evident by the rapid increase in the downstream local temperature (T_2, T_3). As can be seen from Fig. 10(b), the peak temperature raised rapidly with heat flux. As the inlet pressure builds up, following the increase in the void fraction during Stage B, unstable hydraulic condition was reached, in which the pressure drop was sufficiently large to overcome the channel demand for pressure drop. As a consequence, the mass flow rate increased and liquid rapidly filled the channel while significantly reducing the pressure drop demand (Fig. 11(c))—this was accompanied by a rapid decrease in the surface temperature (Stage C). At lower heat fluxes, the enlarged vapor bubble gradually moved downstream, which results in a more steady temperature drop slope, as shown in Fig. 10(b).

The data presented in the previous figures suggest that, without proper arrangements such as inlet restrictors [18–20], the compressible volume instability, which is triggered by excursive instability, dominates both enhanced surface and plain wall devices. However, the presence of structured wall cavities modifies the characteristics of this prime instability. Structured surfaces tend to

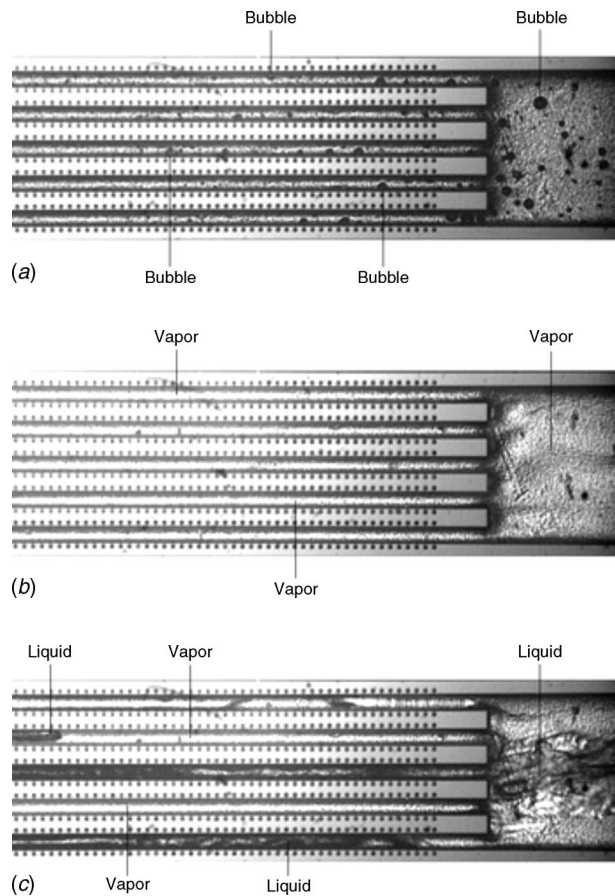


Fig. 11 Boiling stages in unstable boiling flow for $G = 303 \text{ kg/m}^2 \text{ s}$, $q''_{\text{eff}} = 142 \text{ W/cm}^2$ (Device 1NR): (a) bubble nucleation (Stage A), (b) vapor filling/dryout (Stage B), and (c) post-dryout/upstream flooding (Stage C)

moderate the oscillation caused by the rapid bubble growth, and therefore, delay the onset of parallel channel instability. In the present study, this manifested itself as an extended, stable, and effective boiling period (Stage A in Fig. 10(a)). In the plain wall channel, on the other hand, the onset of boiling is accompanied by significant rapid bubble growth oscillation, which instantaneously triggered the parallel channel instability, and, as a result, the compressible volume instability. The modification of the prime instability mode has important ramifications with respect to the average heat transfer coefficient (or the average surface temperature). The tendency of the reentrant cavities to form a more stable boiling process, with longer periods of steady nucleate boiling, facilitates a more effective two-phase heat transfer process, as evident from Fig. 9(b).

6 Conclusion

The current investigation examined the ability of reentrant cavities to suppress flow boiling oscillations and instabilities in microchannels. Various boiling instability modes previously identified in microchannel (i.e., rapid bubble growth, parallel channel, compressible volume instabilities, and CHF) were studied, and suppression mechanisms were proposed and discussed. Three types of microchannel devices were used to experimentally investigate boiling instability: microchannel with reentrant cavities, microchannel with interconnected reentrant cavities, and plain wall microchannel. ONB, CHF condition, and local temperature measurements were acquired and compared. The main conclusions drawn from this study are presented below.

1. Structured reentrant cavities in microchannel devices can assist, to an extent, to mitigate flow boiling instability.
2. For the reentrant cavity devices, the reduced superheat and pressure at the initial stages of the bubble nucleation delayed and moderated the flow oscillation, and, thus, extended the stable boiling region and increased the CHF.
3. Local transient temperature coupled with flow visualization revealed various stages of the unstable boiling cycle, which showed the effect of reentrant cavities in mitigating rapid bubble growth, parallel channel, and pressure drop/compressible volume instabilities.

Acknowledgment

This work was supported by the Office of Naval Research through the Young Investigator Program (Yoav Peles) under Contract No. N00014-05-1-0582.

Nomenclature

- A_p = platform area (heating surface area above the heater) (m^2)
 A_f = total channel surface area (m^2)
 G = mass flux ($\text{kg/m}^2 \text{ s}$)
 I = electrical current (A)
 k_s = thermal conductivity of the substrate (silicon) ($\text{W/m}^\circ\text{C}$)
 p = pressure (kPa)
 P = electrical power (W)
 q''_{eff} = effective heat flux (W/cm^2)
 Q_{loss} = heat loss (W)
 R = electrical resistance (Ω)
 t = time (s)
 t_b = base thickness (m)
 T = temperature ($^\circ\text{C}$)
 \bar{T}_{heater} = average heater temperature ($^\circ\text{C}$)
 T_s = substrate temperature ($^\circ\text{C}$)
 $T_{\text{thermistor}}$ = thermistor temperature ($^\circ\text{C}$)
 T_1, T_2, T_3 = local surface temperature ($^\circ\text{C}$)
 V = electrical voltage (V)

References

- [1] Boure, J. A., Bergles, A. E., and Tong, L. S., 1973, "Review of Two-Phase Flow Instability," *Nucl. Eng. Des.*, **25**, pp. 165–192.
- [2] Saha, P., Ishii, M., and Zuber, N., 1976, "An Experimental Investigation of the Thermally Induced Flow Oscillations in Two-Phase Systems," *J. Heat Transfer*, **98**, pp. 616–622.
- [3] Carey, V. P., 1992, *Liquid-Vapor Phase-Change Phenomena*, Taylor and Francis, New York, pp. 565–571.
- [4] Ruan, S. W., Bartsch, G., and Yang, S. M., 1993, "Characteristic of the Critical Heat Flux for Downward Flow in a Vertical Tube at Low Flow Rate and Low Pressure Conditions," *Exp. Therm. Fluid Sci.*, **7**, pp. 296–306.
- [5] Ozawa, M., Umekawa, H., Mishima, K., Hibiki, T., and Saito, Y., 2001, "CHF in Oscillatory Flow Boiling Channels," *Trans IChemE, Part A*, **79**, pp. 389–401.
- [6] Daleas, R. S., and Bergles, A. E., 1965, "Effect of Upstream Compressibility on Subcooled Critical Heat Flux," ASME Paper No. 65-HT 67.
- [7] Stoddard, R. M., Blasick, A. M., Ghiassian, S. M., Abdel-Khalik, S. I., Jeter, S. M., and Dowling, M. F., 2002, "Onset of Flow Instability and Critical Heat Flux in Thin Horizontal Annuli," *Exp. Therm. Fluid Sci.*, **26**, pp. 1–14.
- [8] Bergles, A. E., and Kandlikar, S. G., 2005, "On the Nature of Critical Heat Flux in Microchannels," *J. Heat Transfer*, **127**(10), pp. 101–107.
- [9] Bower, M. B., and Mudawar, I., 1994, "High Flux Boiling in Low Flow Rate, Low Pressure Drop Mini-Channel and Micro-Channel Heat Sinks," *Int. J. Heat Mass Transfer*, **37**, pp. 321–332.
- [10] Jiang, L., Wong, M., and Zohar, Y., 1999, "Phase Change in Microchannel Heat Sinks With Integrated Temperature Sensors," *IEEE JMEMS*, **8**, pp. 358–365.
- [11] Mukherjee, S., and Mudawar, I., 2002, "Smart, Low-Cost, Pumpless Loop for Micro-Channel Electronic Cooling Using Flat and Enhanced Surface," *Proceedings of JTherm*, IEEE, Piscataway, NJ, pp. 360–370.
- [12] Qu, W., and Mudawar, I., 2004, "Measurement and Correlation of Critical Heat Flux in Two-Phase Micro-Channel Heat Sinks," *Int. J. Heat Mass Transfer*, **47**, pp. 2045–2059.
- [13] Kennedy, J. E., Roach, G. M., Jr., Dowling, M. F., Abdel-Khalik, S. I., Ghiassian, S. M., Jeter, S. M., and Quershi, Z. H., 2000, "The Onset of Flow

- Instability in Uniform Heated Horizontal Microchannels," *J. Heat Transfer*, **122**, pp. 118–125.
- [14] Koo, J.-M., Jiang, L., Zhang, L., Zhou, P., Panerjee, S. S., Kenny, T. W., Santiago, J. G., and Goodson, K. E., 2001, "Modeling of Two-Phase Microchannel Heat Sinks for VLSI Chips," *Proceedings of the Fourth Conference on MEMS*, IEEE, Piscataway, NJ, pp. 422–426.
- [15] Wu, H. Y., and Cheng, P., 2003, "Visualization and Measurements of Periodic Boiling in Silicon Microchannels," *Int. J. Heat Mass Transfer*, **46**, pp. 2603–2614.
- [16] Qu, W., and Mudawar, I., 2003, "Measurement and Prediction of Pressure Drop in Two-Phase Micro-Channel Heat Sinks," *Int. J. Heat Mass Transfer*, **46**, pp. 2737–2753.
- [17] Kandlikar, S. G., Kuan, W. K., Willistein, D. A., and Borrelli, J., 2006, "Stabilization of Flow Boiling in Microchannels Using Pressure Drop Elements and Fabricated Nucleation Sites," *J. Heat Transfer*, **128**(4), pp. 389–396.
- [18] Koşar, A., Kuo, C. J., and Peles, Y., 2006, "Suppression of Boiling Flow Oscillations in Parallel Microchannels With Inlet Restrictors," *J. Heat Transfer*, **128**(3), pp. 251–260.
- [19] Koşar, A., Kuo, C.-J., and Peles, Y., 2005, "Boiling Heat Transfer in Rectangular Microchannels With Reentrant Cavities," *Int. J. Heat Mass Transfer*, **48**(23–24), pp. 4867–4886.
- [20] Kuo, C.-J., Koşar, A., Peles, Y., Virost, S., Mishra, C., and Jensen, M. K., 2006, "Bubble Dynamics During Boiling in Enhanced Surface Microchannels," *IEEE JMEMS*, **15**(6), pp. 1514–1527.
- [21] Pate, D. T., Jones, R. J., and Bhavnani, S. H., 2006, "Cavity-Induced Two-Phase Heat Transfer in Silicon Microchannels," *Thermomechanical Phenomena in Electronic Systems—Proceedings of the Intersociety Conference, Tenth Intersociety Conference on Thermal and Thermomechanical Phenomena and Emerging Technologies in Electronic Systems, ITherm 2006*, pp. 71–78.
- [22] Hardt, S., Schilder, B., Tiemann, D., Kolb, G., Hessel, V., and Stephan, P., 2007, "Analysis of Flow Patterns Emerging During Evaporation in Parallel Microchannels," *Int. J. Heat Mass Transfer*, **50**(1–2), pp. 226–239.
- [23] Hsu, Y. Y., 1962, "On the Size Range of Active Nucleation Cavities on a Heating Surface," *J. Heat Transfer*, **84**, pp. 207–216.
- [24] Rayleigh, L., 1917, "Pressure Developed in a Liquid During the Collapse of a Spherical Cavity," *Philos. Mag.*, **34**, pp. 94–98.
- [25] Plesset, M. S., 1949, "The Dynamics of Cavitation Bubbles," *J. Appl. Mech.*, **16**, pp. 277–282.
- [26] Kline, S., and McClintock, F. A., 1953, "Describing Uncertainties in Single-Sample Experiments," *Mech. Eng. (Am. Soc. Mech. Eng.)*, **75**(1), pp. 3–8.
- [27] Collier, J. G., and Thome, J. R., 1994, *Convective Boiling and Condensation*, 3rd ed., Oxford University Press, Oxford, pp. 193–195.

Critical Heat Flux of Water at Subatmospheric Pressures in Microchannels

C.-J. Kuo

Y. Peles¹

e-mail: pelesy@rpi.edu

Department of Mechanical, Aerospace, and
Nuclear Engineering,
Rensselaer Polytechnic Institute,
Troy, NY 12180

Critical heat flux conditions for water at subatmospheric pressures in an array of silicon-based, 227 μm hydraulic diameter, rectangular microchannels were experimentally studied. Experiments were conducted at exit pressures from 0.1 atm to 1 atm, mass fluxes from 86 $\text{kg}/\text{m}^2 \text{ s}$ to 303 $\text{kg}/\text{m}^2 \text{ s}$, and an effective heat flux up to 444 W/cm^2 . The annular flow pattern revealed during flow visualization and the high exit qualities at CHF conditions suggest dryout to be the CHF mechanism. An analysis, based on the experimental results and known CHF characteristics, on the dependency of the critical heat flux on various variables was performed. It was found that the boiling number at the CHF condition was approximately a constant. [DOI: 10.1115/1.2909077]

Keywords: microchannel, flow boiling, CHF, heat transfer

1 Introduction

The rapidly increasing use of electronics in industry and military hardware is generating unprecedented thermal management needs. The cooling requirements of many electronic systems dictate dissipation of ultrahigh heat fluxes while maintaining isothermal low surface temperatures (e.g., isothermal surfaces at $\sim 50^\circ\text{C}$ or lower). Flow boiling in microchannels is one of the most potent convective heat transfer methods and has been a topic of numerous studies in the past several years [1–18]. Water has superior thermophysical properties compared to most practical engineering fluids; it is readily available, environmental friendly, and nonhazardous. As such, water is seriously considered the fluid of choice for many flow boiling cooling systems of ultrahigh power electrical components. However, the requirement of low surface temperatures necessitates the use of flow boiling of water at subatmospheric pressures.

Any boiling system is susceptible to a condition known as the critical heat flux (CHF) condition. CHF is one of the most important thermal-hydraulic transition phenomena in flow/pool boiling and is of significant engineering importance. It sets the upper limit of heat flux for many engineering systems and marks the transition from a very effective heat transfer mode to a very ineffective one. In conventional scale, many studies have been devoted to obtaining knowledge about the conditions leading to CHF, and in-depth reviews on the phenomenon are available in textbooks [19–21] and in archival manuscripts [22]. Another limit on the maximum heat flux is given by the kinetic theory [19]. Gambill and Lienhard [23] compiled the CHF data from various studies and related the highest CHF values reported with the maximum heat flux from the kinetic theory as a function of dimensionless pressure (Fig. 1). Van Carey, in a panel discussion in the Thermal Challenges in Next Generation Electronic Systems (THERMES 2007) Conference [24], compared several sets of CHF microchannel data with Gambill and Lienhard's results. He speculated that the significantly lower CHF values reported in microchannels are a characteristic of the microscale and urged the heat transfer community to study the phenomenon in diminishing length scales to validate/invalidate his hypothesis. Conventional scale studies strongly suggest that CHF conditions are closely related to the

heat transfer mechanism prior to their appearance. However, flow boiling heat transfer mechanisms in microchannels are not fully understood even at atmospheric conditions. It is also widely accepted that flow boiling of low surface tension liquids (e.g., hydrofluorocarbon) can have considerably different thermal-hydraulic mechanisms than high surface tension fluids such as water, especially at the microscale. An experimental study on CHF in microchannel with water at subatmospheric pressures will extend current limited knowledge pertinent to microdomains.

This manuscript reports on the results of CHF study of water at subatmospheric pressures in an array of five parallel, 227 μm hydraulic diameter microchannels. The effects of system pressure, mass flux, and inlet subcooled temperature on CHF conditions are examined. The results are also compared to Gambill and Lienhard's map in an attempt to address Van Carey's hypothesis.

2 Device Overview

A computer aid design (CAD) model of the microdevice used in the current study is shown in Fig. 2. The microdevice consists of five parallel, 10,000 μm long, 200 μm wide, and 253 μm deep microchannels, each spaced 200 μm apart. A 20 μm wide and 400 μm long orifice is installed at the entrance of each channel to suppress flow instabilities [25]. To minimize ambient heat losses, air gaps are formed on the two ends of the sidewalls. Inlet and exit plenums are etched on the thin silicon substrate ($\sim 200 \mu\text{m}$). A Pyrex cover seals the device from the top and allows flow visualization. On the backside, a heater is formed underneath the microchannels to deliver the heating power, and it also serves as a thermistor to measure the average temperature of the entire microchannel area.

3 Device Fabrication, Experimental Apparatus, and Procedures

3.1 Microchannel Fabrication Method. The microdevice was micromachined on a polished double-sided *n*-type (100) single crystal silicon wafer employing techniques adapted from integrated circuit (IC) manufacturing. A 1 μm thick high-quality oxide film was deposited on both sides of the silicon wafer to shield the bare wafer surface during processing and to serve as an electrical insulator. The heater was then formed on the backside of the wafer. A 70 \AA thick layer of titanium was initially deposited by a cryopumped CVC 601 sputter deposition system to enhance adhesion characteristics and was followed by sputtering a 1 μm

¹Corresponding author.

Contributed by the Heat Transfer Division of ASME for publication in the JOURNAL OF HEAT TRANSFER. Manuscript received April 9, 2007; final manuscript received July 31, 2007; published online May 20, 2008. Review conducted by Louis C. Chow.

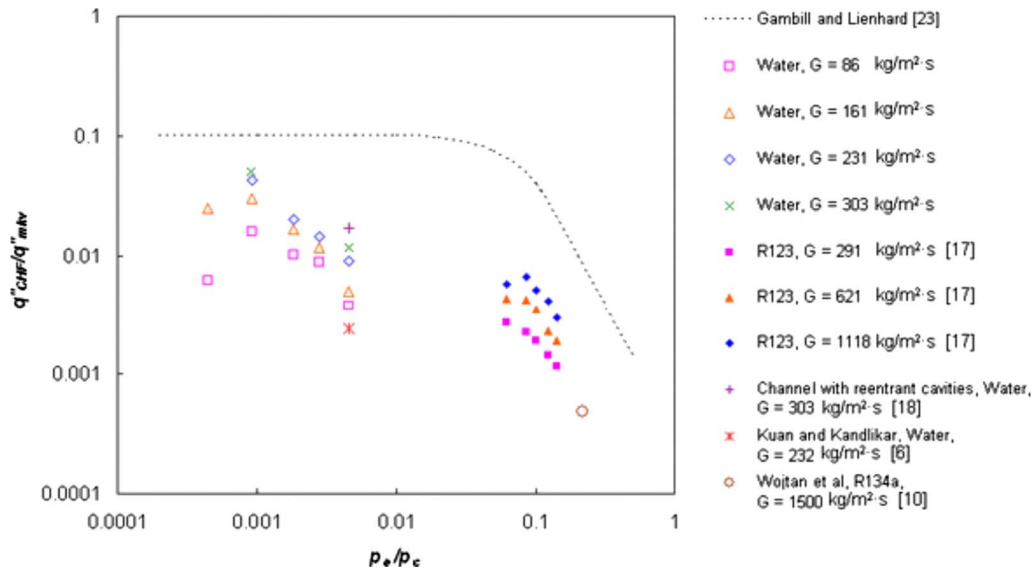


Fig. 1 The ratio of the highest measured CHF to the maximum heat flux from the kinetic theory, q''_{CHF}/q''_{mkn} , as a function of dimensionless exit pressure, p_e/p_c

thick layer of Al-1%Si-4%Cu. Subsequent photolithography and concomitant wet bench processing created the heater on the backside of the wafer. Another $1\ \mu\text{m}$ thick PECVD oxide was deposited to protect the backside features during further processing.

Next, the microchannels were formed on the top side of the

wafer. The wafer was taken through a photolithography step and a reactive ion etching (RIE) oxide removal process to mask certain areas on the wafer, which were not to be etched during the deep RIE (DRIE) process. The wafer was consequently etched in the

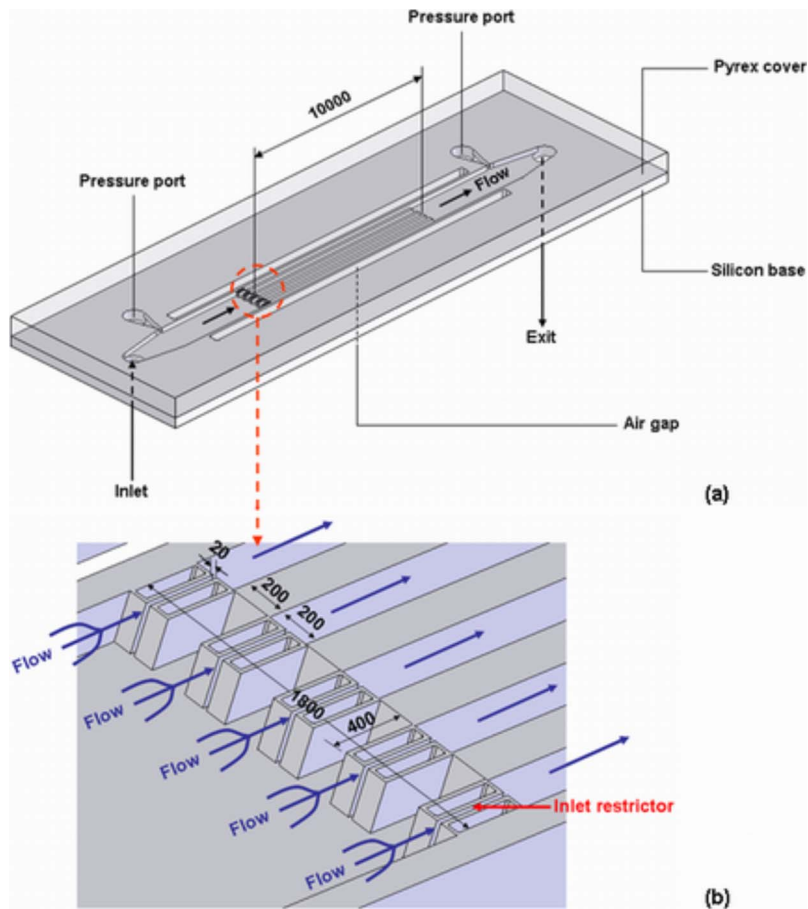


Fig. 2 (a) A CAD model of the microdevice; (b) geometry of the inlet orifice configuration (all units in μm)

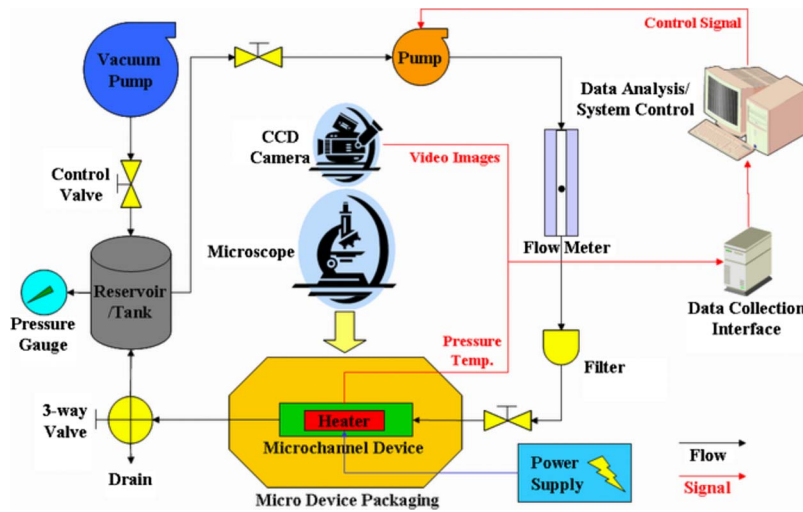


Fig. 3 Experiment setup

DRIE process, and silicon was removed from places not protected by the photoresist/oxide mask. A profilometer was employed to measure and record various dimensions of the device.

The wafer was flipped, and the backside was then processed to create an inlet, an outlet, side air gaps, and pressure port taps for the transducers. A photolithography step followed by a buffered oxide etch (BOE) (6:1) oxide removal process was carried out to create a pattern mask. The wafer was then etched through in a DRIE process to create the fluidic ports. Thereafter, electrical contacts/pads were opened on the backside of the wafer by performing another round of photolithography and RIE processing. Finally, the processed wafer was stripped of any remaining resist or oxide layers and anodically bonded to a 1 mm thick polished Pyrex (glass) wafer to form a sealed device. After a successful completion of the bonding process, the processed stack was dicesawed to separate the devices from the parent wafer.

3.2 Experimental Test Rig. The setup, shown in Fig. 3, consists of three primary subsystems: the flow loop section, instrumentations, and a data acquisition system. The test section houses the microelectromechanical system (MEMS) microchannel devices and its fluidic and thermal packaging module. The microchannel device is mounted on the fluidic packaging module through miniature “o-rings” to ensure a complete leak-free system. The fluidic packaging delivers the working fluid and access to the pressure transducers. The external electrical connections to the heater were achieved from beneath through spring-loaded probe pins, which connected the heater to electrical pads residing away from the main microchannel body.

The main flow loop includes the microchannel device, a pulseless gear pump, a reservoir, a vacuum pump, and a pressure gauge to control the system pressure, a flow meter, and a dissolved oxygen meter. The test section heater is connected to a power supply with an adjustable dc current to provide power to the device. Simultaneously, the inlet pressure and test section pressure drop are collected, and the boiling process in the microchannels is recorded by a Phantom V4.2 high-speed camera (maximum frame rate of 90,000 frames/s, and 2 μ s exposure time) mounted over a Leica DMLM microscope. Calibration of the heater is performed prior to the experiment by placing the device in an oven and establishing the resistance-temperature curve for the heater.

3.3 Experimental Procedures and Data Reduction. The deionized water was first degassed until the oxide concentration level dropped below 3 ppm. Then the system pressure was adjusted to the desired experimental value. The water flow rate was fixed at the desired value, and experiments were conducted after

steady conditions were reached with a desirable system pressure and ambient room temperature ($\sim 22^\circ\text{C}$). The electrical resistance of the heater was also measured at room temperature. During the experiment, voltage was applied in 0.5 V increments to the test section heater, and the resistance data for the heater were recorded once the steady state was reached. The procedure was repeated for different flow rates.

To estimate heat losses, electrical power was applied to the test section after evacuating the water from the test loop. Once the temperature of the test section became steady, the temperature difference between the ambient and test section was recorded with the corresponding power. The plot of power versus temperature difference was used to calculate the heat loss (\dot{Q}_{loss}) associated with each experimental data point.

Data obtained from the voltage, current, and pressure measurements were used to calculate the average surface temperatures and CHF. The electrical input power P and heater resistance R , respectively, were determined by the measured voltage V and current I with

$$P = VI \quad (1)$$

and

$$R = V/I \quad (2)$$

The electrical resistance-temperature calibration curve of the heater was used for determining the average heater temperature, \bar{T}_{heater} . The average surface temperature T_s was then calculated as

$$T_s = \bar{T}_{\text{heater}} - \frac{(P - \dot{Q}_{\text{loss}})t}{k_s A_p} \quad (3)$$

where t , k_s , and A_p are the substrate thickness, thermal conductivity of silicon, and the platform area, respectively. The effective heat flux, q''_{eff} , is defined as

$$q''_{\text{eff}} = \frac{P - \dot{Q}_{\text{loss}}}{A_p} \quad (4)$$

To compare with existing CHF data, the channel wall heat flux at the CHF condition, q''_{CHF} , is defined as

$$q''_{\text{CHF}} = \frac{P - \dot{Q}_{\text{loss}}}{A_t} \quad (5)$$

where A_t is the total channel surface area ($A_t = (W + 2H)L$). The exit mass quality is obtained by

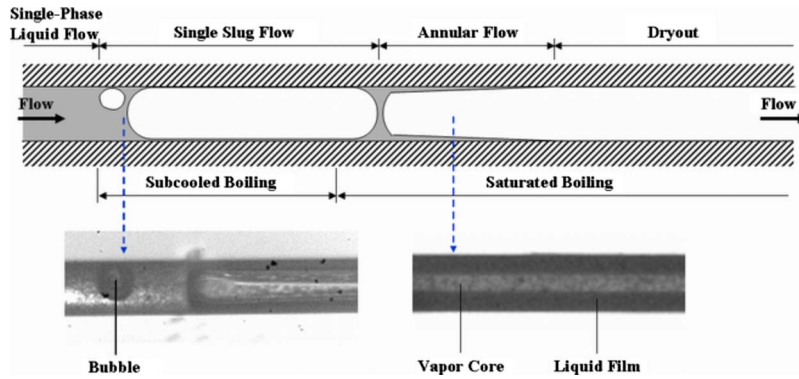


Fig. 4 Characteristic flow boiling morphologies

$$x_e = \frac{(P - \dot{Q}_{\text{loss}}) - GA_{s,\text{tot}}c_p\Delta T_{\text{sub}}}{GA_{s,\text{tot}}h_{fg}} \quad (6)$$

where G and $A_{s,\text{tot}}$ are the mass flux and the total channel cross-section area ($A_{s,\text{tot}}=5A_s$ for the current device), respectively.

The uncertainties of the measured values are obtained from the manufacturers' specification sheets, while the uncertainties of the derived parameters are calculated using the method developed by Kline and McClintock [26]. Uncertainty in the mass flux (G), heat flux (q''), temperature (T), and mass quality (x) are estimated to be $\pm 1\%$, $\pm 1\%$, $\pm 1\%$, and $\pm 3\%$, respectively.

4 Results and Discussion

4.1 Flow Morphology at Impending CHF. In conventional scale, CHF conditions are often led by two different mechanisms: departure from nucleate boiling (DNB) and dryout [19,20]. For subcooled boiling or low quality saturated boiling, where nucleate boiling is the predominant heat transfer mechanism, CHF is referred as DNB, and for saturated boiling of high exit quality, with a typical annular flow pattern, the CHF condition results from dryout of the liquid film on the channel wall.

Figure 4 depicts the characteristic flow patterns visualized at the CHF condition: single-phase liquid flow, single bubble/slug flow, annular flow, and dryout beginning at the exit of the channel. The annular flow pattern/dryout at the channel exit, coupled with the relatively high exit quality at CHF conditions (Fig. 5), suggests that CHF is triggered by liquid dryout.

Previous studies suggest that for the dryout mechanism the exit quality at CHF conditions ($x_{e,\text{CHF}}$) decreases with increased mass flux [17,19,20]. While the current observation (Fig. 5(a)) appears to concur with other data, at least trendwise, the exit quality at CHF conditions does not seem to be strongly affected by the mass flux. In fact, the CHF exists over a relatively narrow range of mass qualities (Fig. 5(b)). It is frequently argued that the reduction in $x_{e,\text{CHF}}$ at high mass fluxes for dryout mechanism is a result of increased droplet entrainment in the vapor core depleting liquid from the wall [19] or interfacial wave instabilities induced by shear or surface tension forces [27]. If these reasoning are adopted here, it can be concluded that the droplet entrainment varies little with mass flux and the interfacial wave instabilities are not strongly dependent on the mass flux, at least under the current experiment conditions. This, in some respect, contradicts the results of Koşar and Peles [17], which showed significant reduction in exit qualities with increasing mass flux. Considering the surface tension to be an important variable dictating the entrainment and the interfacial waves, it is very likely that the hydrodynamics of the droplet and interface wave formation for R123 is considerably different than for water.

4.2 Comparison With the Maximum Heat Flux Limitation. The practical limitation given by Gambill and Lienhard (Fig. 1) suggests that the maximum achievable CHF for $p_e/p_c < 0.01$ ($p_e=221$ kPa) is 10% of the maximum heat flux ob-

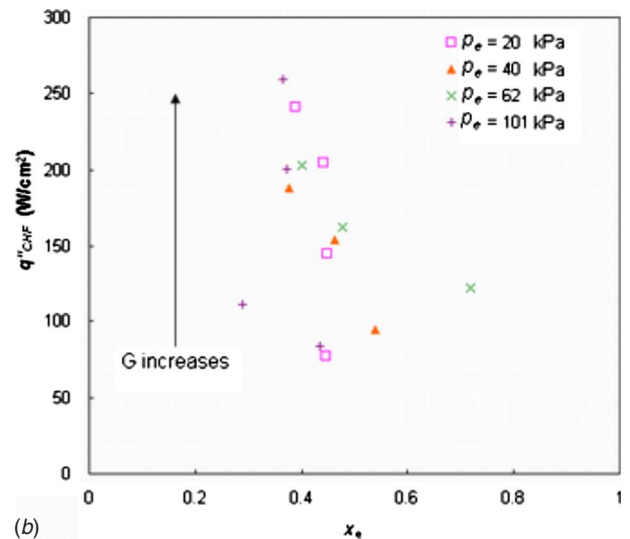
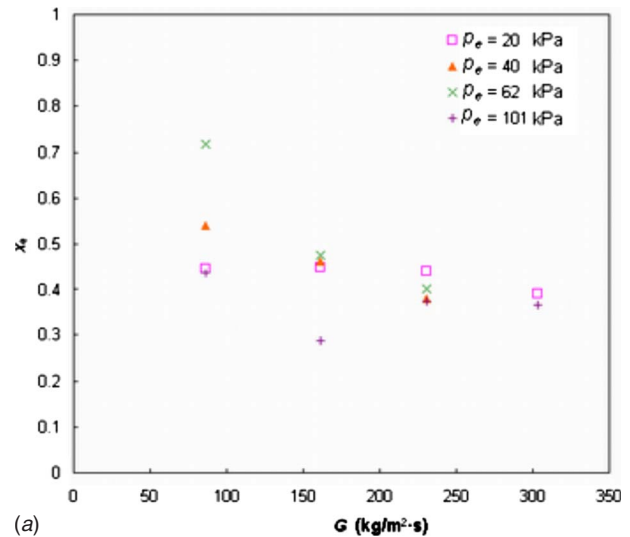


Fig. 5 (a) The exit mass quality at CHF conditions as a function of mass flux; (b) CHF as a function of mass quality

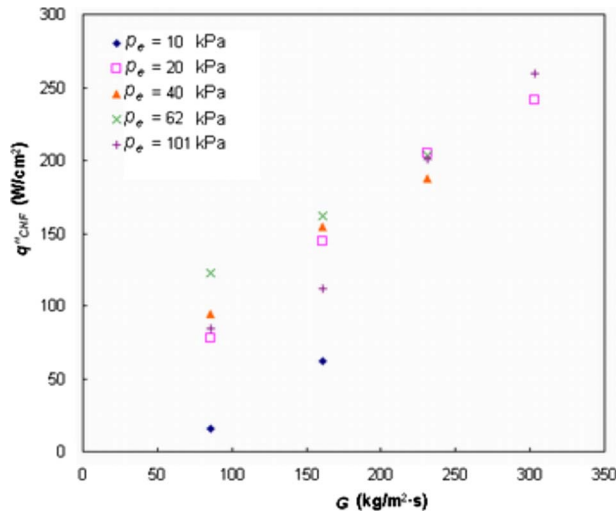


Fig. 6 CHF as a function of mass flux

tained from the kinetic theory. In the current microchannel study, a maximum $q''_{\text{CHF}}/q''_{\text{mkv}}$ value of 0.05 was obtained for $p_e/p_c \cong 0.001$ ($p_e=20$ kPa) and $G=303$ kg/m²·s. The CHF data for water and coolants seem to follow the general trend of Gambill and Lienhard's curve, but the values are at least 50% below the curve. However, the high exit qualities at CHF conditions, in this and in Koşar and Peles's studies, do not indicate that the CHF at the microscale is fundamentally lower than in the conventional scale. Regardless, an exit quality of 1 will trigger CHF in the present experiment (due to complete dryout), resulting in $q''_{\text{CHF}}/q''_{\text{mkv}} < 0.1$. It is important to note that the dashed curve in the figure was obtained from the highest measured CHF value ever recorded, and it might very well be that higher values than the available data at the microscale can be achieved in microchannels for enhanced configurations or at higher mass fluxes.

4.3 CHF and the Independent Variables. In conventional scale, the CHF in channels is often a strong function of mass flux G , exit quality, x_e , channel exit pressure, p_e , channel hydraulic diameter, d_h , channel length, L , and fluid properties [20]. For flow boiling of water in a given channel (i.e., fixed length and diameter), q''_{CHF} is a function of three primary independent variables:

$$q''_{\text{CHF}} = f(G, x_e, p_e) \quad (7)$$

Assuming the CHF can be expressed as a product of two functions, one of which depends only on the mass flux, while the other depends on the exit quality and channel exit pressure, q''_{CHF} can be expressed as

$$q''_{\text{CHF}} = f_1(G)f_2(x_e, p_e) \quad (8)$$

where f_1 is a function of G only, and f_2 is a function of x_e and p_e only. Such assumption has been implicitly made while developing CHF correlations for macro- and microscale systems [3,28,29]. As discussed in the previous section, in the current study, the CHF varies over a small range of exit qualities, and the effect of x_e can be viewed similar to the channel length and hydraulic diameter (i.e., $x_e = \text{constant}$). Therefore, the functional dependency of f_2 can be reduced to p_e only (i.e., $f_2(p_e)$). Furthermore, it is often assumed that the functional dependency of q''_{CHF} on G is polynomial:

$$q''_{\text{CHF}} \propto G^m \quad (9)$$

where m is a constant. Inspection of the CHF as a function of mass flux for five exit pressures (Fig. 6) suggests that the CHF is approximately a linear function of mass flux (i.e., $m \cong 1$), which is in agreement with some macroscale channel studies [20]. From Eqs. (8) and (9), it follows (for $m=1$):

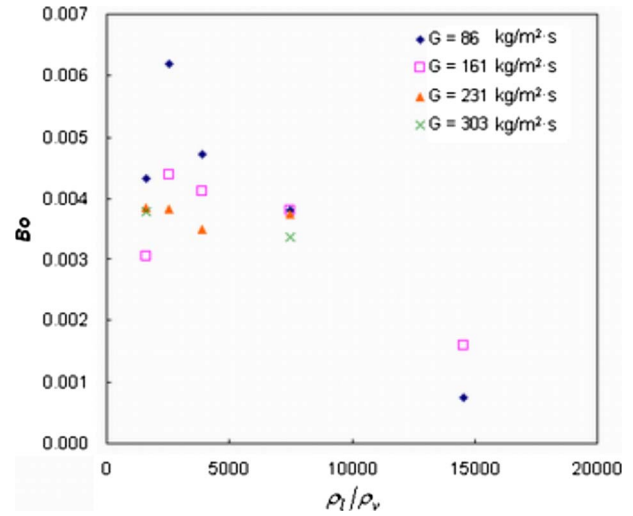


Fig. 7 The boiling number at CHF conditions as a function of liquid-to-vapor density ratio, ρ_l/ρ_v

$$\frac{q''_{\text{CHF}}}{G} = f_2(p_e) \quad (10)$$

Expressing Eq. (10) in dimensionless form:

$$\text{Bo}_{\text{CHF}} = \frac{q''_{\text{CHF}}}{Gh_{fg}} = f\left(\frac{p_e}{p_c}\right) \quad (11)$$

where Bo_{CHF} is the boiling number at CHF condition, h_{fg} is the latent heat of vaporization, and p_c is the critical pressure.

The system pressure (exit pressure) in a boiling system can have a complex effect on CHF conditions, since it can modify several important independent variables: the liquid-to-vapor density ratio (ρ_l/ρ_v), the surface tension (σ), and the latent heat of vaporization (h_{fg}). The surface tension and the latent heat of vaporization can vary somewhat with the saturation pressure (or temperature), but the liquid-to-vapor density ratio vary by an order of magnitude when the system pressure changes from 0.1 atm to 1 atm. Therefore, for a first order analysis, it can be concluded that the effect of exit pressure is merely the effect of ρ_l/ρ_v . Thus, Eq. (11) can be expressed as

$$\text{Bo}_{\text{CHF}} = f\left(\frac{\rho_l}{\rho_v}\right) \quad (12)$$

Figure 7 shows the boiling number as a function of liquid-to-vapor density ratio. It appears that the dependency of boiling number on the density ratio is not significant, except for the highest ρ_l/ρ_v data points ($p_e=10$ kPa). Therefore, the boiling number at the CHF condition can be expressed as

$$\text{Bo}_{\text{CHF}} \cong 3.7 \times 10^{-3} \quad (13)$$

For annular flow at subatmospheric pressure, the condition leading to CHF is dictated by the presence of liquid film adjacent to the channel wall. While the density ratio can affect the droplet entrainment in the vapor core, which can indirectly control the conditions leading to the liquid dryout on the wall, it does not appear to significantly modify it, as apparent by the narrow range of the exit quality at CHF conditions (Fig. 5). Better knowledge of the mechanism controlling the thin liquid layer through interfacial wave instabilities or the formation of droplet entrainment in the vapor core will provide clues to the conditions leading to CHF under the thermal-hydraulic conditions studied here and elsewhere. The significant reduction in the boiling number at CHF conditions for the very high density ratio (i.e., $p_e=10$ kPa) is not

completely clear. Other effects such as compressibility, sonic limit, and rarefaction may become significant at such low pressure.

5 Conclusion

In the current study, experiments were conducted to obtain CHF data for flow boiling of water at subatmospheric pressures in microchannels. Flow visualization was performed to aid the identification of CHF mechanism. The effects of independent variables, which are important in macroscale, were evaluated. The main conclusions drawn from the study are as follows:

1. Dryout is the primary CHF mechanism for flow boiling of water in microchannels at subatmospheric pressure, at low to moderate mass fluxes.
2. The CHF values obtained were lower than the limits suggested by Gambill and Lienhard. Further studies on flow boiling in boiling enhanced configurations or flow conditions may result in CHF values that approach their limit.
3. Performing first order analysis, it was found that the mass quality at CHF conditions did not vary significantly, and the system pressure did not strongly affect CHF. The CHF data were reduced to a simple correlation, which related the critical boiling number to a constant.

Acknowledgment

This work was supported by the Office of Naval Research through the Young Investigator Program under Contract No. N00014-05-1-0582.

Nomenclature

A_p	= platform area (heating surface area above the heater), m^2
A_s	= single channel cross-section area, m^2
$A_{s,tot}$	= total channels cross-section area, m^2
A_f	= total channel surface area, m^2
Bo	= the boiling number,
c_p	= specific heat, $J/kg\ K$
d_h	= channel hydraulic diameter, m
G	= mass flux, $kg/m^2\ s$
H	= channel height, m
h_{fg}	= latent heat of vaporization, J/kg
I	= electrical current, A
k_s	= thermal conductivity of the substrate (silicon), $W/m\ ^\circ C$
L	= channel length, m
\dot{m}	= mass flow rate, kg/s
N	= number of channel
p_c	= critical pressure, kPa
p_e	= exit pressure, kPa
P	= electrical power, W
q	= heat transfer rate, W
q''	= heat flux, W/cm^2
q''_{CHF}	= channel wall heat flux at the CHF condition, W/cm^2
q''_{eff}	= effective heat flux, W/cm^2
\dot{Q}_{loss}	= heat loss, W
R	= electrical resistance, Ω
t	= thickness of the silicon substrate, m
\bar{T}_{heater}	= average heater temperature, $^\circ C$
T_s	= average surface temperature, $^\circ C$
ΔT_{sub}	= inlet subcooled temperature, $^\circ C$
V	= electrical voltage, V
W	= channel width, m
x_e	= exit mass quality
$x_{e,CHF}$	= exit mass quality at the CHF condition

Greek

ρ_l	= liquid density, m^3/s
ρ_v	= vapor density, m^3/s
σ	= surface tension, N/m

References

- [1] Bergles, A. E., and Kandlikar, S. G., 2005, "On the Nature of Critical Heat Flux in Microchannels," *ASME J. Heat Transfer*, **127**(10), pp. 101–107.
- [2] Thome, J. R., 2004, "Boiling in Microchannels: A Review of Experiment and Theory," *Int. J. Heat Fluid Flow*, **25**, pp. 128–139.
- [3] Qu, W., and Mudawar, I., 2004, "Measurement and Correlation of Critical Heat Flux in Two-Phase Micro-Channel Heat Sinks," *Int. J. Heat Mass Transfer*, **47**, pp. 2045–2059.
- [4] Bowers, M. B., and Mudawar, I., 1994, "High Flux Boiling in Low Flow Rate, Low Pressure Drop Mini-Channel and Micro-Channel Heat Sinks," *Int. J. Heat Mass Transfer*, **37**(2), pp. 321–334.
- [5] Kandlikar, S. G., Kuan, W. K., Willistien, D. A., and Borrelli, J., 2006, "Stabilization of Flow Boiling in Microchannels Using Pressure Drop Elements and Fabricated Nucleation Sites," *ASME J. Heat Transfer*, **128**(4), pp. 389–396.
- [6] Kuan, W. K., and Kandlikar, S. G., 2006, "Experimental Study on Saturated Flow Boiling Critical Heat Flux in Microchannels," *Proceedings of the Fourth International Conference on Nanochannels, Microchannels and Minichannels*, pp. 45–52.
- [7] Jiang, L., Wong, M., and Zohar, Y., 2001, "Forced Convection Boiling in a Microchannel Heat Sinks," *J. Microelectromech. Syst.*, **10**(1), pp. 80–87.
- [8] Zhang, L., Koo, J., Jiang, L., Asheghi, M., Goodson, K. E., Santiago, J. G., and Kenny, T. W., 2002, "Measurements and Modeling of Two-Phase Flow in Microchannels With Nearly Constant Heat Flux Boundary Conditions," *J. Microelectromech. Syst.*, **11**(1), pp. 12–19.
- [9] Flynn, R. D., Kramer, T. A., Koo, J. M., Cheng, C. H., Fogg, D. W., Wang, E. N., and Goodson, K. E., 2005, "Convective Boiling in Silicon Microchannels With Localized Heating and Thermometry," *ASME Paper No. ICMM2005-75209*.
- [10] Wojtan, L., Revellin, R., and Thome, J. R., 2006, "Investigation of Saturated Critical Heat Flux in a Single, Uniformly Heated Microchannel," *Exp. Therm. Fluid Sci.*, **30**(8), pp. 765–774.
- [11] Pate, D. T., Jones, R. J., and Bhavnani, S. H., 2006, "Cavity-Induced Two-Phase Heat Transfer in Silicon Microchannels," *Thermomechanical Phenomena in Electronic Systems—Proceedings of the Intersociety Conference*, Tenth Intersociety Conference on Thermal and Thermomechanical Phenomena and Emerging Technologies in Electronic Systems, ITherm, pp. 71–78.
- [12] Hardt, S., Schilder, B., Tiemann, D., Kolb, G., Hessel, V., and Stephan, P., 2007, "Analysis of Flow Patterns Emerging During Evaporation in Parallel Microchannels," *Int. J. Heat Mass Transfer*, **50**(1–2), pp. 226–239.
- [13] Chang, K. H., and Pan, C., 2007, "Two-Phase Flow Instability for Boiling in a Microchannel Heat Sink," *Int. J. Heat Mass Transfer*, **50**(11–12), pp. 2078–2088.
- [14] Chen, T., and Garimella, S. V., 2006, "Measurements and High-Speed Visualizations of Flow Boiling of a Dielectric Fluid in a Silicon Microchannel Heat Sink," *Int. J. Multiphase Flow*, **32**(8), pp. 957–971.
- [15] Koşar, A., Kuo, C.-J., and Peles, Y., 2005, "Boiling Heat Transfer in Rectangular Microchannels With Reentrant Cavities," *Int. J. Heat Mass Transfer*, **48**(23–24), pp. 4867–4886.
- [16] Koşar, A., Kuo, C.-J., and Peles, Y., 2005, "Reduced Pressure Boiling Heat Transfer in Rectangular Microchannels With Interconnected Reentrant Cavities," *ASME J. Heat Transfer*, **127**, pp. 1106–1114.
- [17] Koşar, A., and Peles, Y., 2007, "Critical Heat Flux of R-123 in Silicon-Based Microchannels," *ASME J. Heat Transfer*, **129**(7), pp. 844–851.
- [18] Kuo, C.-J., and Peles, Y., 2007, "Local Measurement of Flow Boiling in Structured Surface Microchannels," *Int. J. Heat Mass Transfer*, **50**(23–24), pp. 4513–4526.
- [19] Carey, V. P., 1992, *Liquid-Vapor Phase-Change Phenomena*, Taylor & Francis, London.
- [20] Collier, J. G., and Thome, J. R., 1994, *Convective Boiling and Condensation*, 3rd ed., Oxford University Press, New York.
- [21] Celata, G. P., and Mariani, A., 1999, "CHF and Post-CHF (Post-Dryout) Heat Transfer," *Handbook of Phase Change: Boiling and Condensation*, Taylor & Francis, Philadelphia, pp. 443–493.
- [22] Katto, Y., 1994, "Critical Heat Flux," *Int. J. Multiphase Flow*, **20**, pp. 563–590.
- [23] Gambill, W. R., and Lienhard, J. H., 1987, "An Upper Bound for the Critical Boiling Heat Flux," *Proceedings of ASME-JSME Thermal Engineering Joint Conference*, 3, pp. 621–626.
- [24] Carey, V. P., 2007, *Thermal Challenges in Next Generation Electronic Systems*

(*THERMES 2007*) Conference, S. V. Garimella and A. S. Fleisher, eds., Santa Fe, NM, Jan. 7–10.

- [25] Koşar, A., Kuo, C. J., and Peles, Y., 2006, “Suppression of Boiling Flow Oscillations in Parallel Microchannels With Inlet Restrictors,” *ASME J. Heat Transfer*, **128**(3), pp. 251–260.
- [26] Kline, S., and McClintock, F. A., 1953, “Describing Uncertainties in Single-Sample Experiments,” *Mech. Eng. (Am. Soc. Mech. Eng.)*, **75**(1), pp. 3–8.
- [27] Revellin, R., and Thome, J. R., 2008, “A Theoretical Model for the Prediction of the Critical Heat Flux in Heated Microchannels,” *Int. J. Heat Mass Transfer*, **51**(5-6), pp. 1216–1225.
- [28] Katto, Y., and Ohne, H., 1984, “An Improved Version of the Generalized Correlation of Critical Heat Flux for Convection Boiling in Uniformly Heated Vertical Tubes,” *Int. J. Heat Mass Transfer*, **27**(9), pp. 1641–1648.
- [29] Shah, M. M., 1987, “Improved General Correlation for Critical Heat Flux During Upflow in Uniformly Heated Vertical Tubes,” *Int. J. Heat Mass Transfer*, **8**(4), pp. 326–335.

Monte Carlo Simulation of Steady-State Microscale Phonon Heat Transport

Jaona Randrianalisoa¹

Dominique Baillis

CETHIL UMR5008,
CNRS,
INSA-Lyon,
Université Lyon 1,
F-69621 Villeurbanne, France

Heat conduction in submicron crystalline materials can be well modeled by the Boltzmann transport equation (BTE). The Monte Carlo method is effective in computing the solution of the BTE. These past years, transient Monte Carlo simulations have been developed, but they are generally memory demanding. This paper presents an alternative Monte Carlo method for analyzing heat conduction in such materials. The numerical scheme is derived from past Monte Carlo algorithms for steady-state radiative heat transfer and enables us to understand well the steady-state nature of phonon transport. Moreover, this algorithm is not memory demanding and uses very few iteration to achieve convergence. It could be computationally more advantageous than transient Monte Carlo approaches in certain cases. Similar to the famous Mazumder and Majumdar's transient algorithm (2001, "Monte Carlo Study of Phonon Transport in Solid Thin Films Including Dispersion and Polarization," ASME J. Heat Transfer, 123, pp. 749–759), the dual polarizations of phonon propagation, the nonlinear dispersion relationships, the transition between the two polarization branches, and the nongray treatment of phonon relaxation times are accounted for. Scatterings by different mechanisms are treated individually, and the creation and/or destruction of phonons due to scattering is implicitly taken into account. The proposed method successfully predicts exact solutions of phonon transport across a gallium arsenide film in the ballistic regime and that across a silicon film in the diffusion regime. Its capability to model the phonon scattering by boundaries and impurities on the phonon transport has been verified. The current simulations agree well with the previous predictions and the measurement of thermal conductivity along silicon thin films and along silicon nanowires of widths greater than 22 nm. This study confirms that the dispersion curves and relaxation times of bulk silicon are not appropriate to model phonon propagation along silicon nanowires of 22 nm width.

[DOI: 10.1115/1.2897925]

Keywords: Monte Carlo simulation, steady-state regime, phonon transport, relaxation time, thermal conductivity, silicon nanowire, silicon thin film

1 Introduction

This past decade, energy transport in submicron materials has attracted much attention due to the rapid development of micro- and nanotechnologies. Heat conduction by phonons is one of the most important heat transfer modes in dielectric and semiconductor nanostructures. When the characteristic size of such materials is comparable to or smaller than the phonon mean free path, phonon transport can be significantly influenced by size effects; therefore, the macroscopic heat conduction model, known as Fourier's law, breaks down. In such a situation, a more rigorous treatment of phonon transport must be performed.

It is commonly accepted that phonon transport can be modeled well by the Boltzmann transport equation (BTE), expressed hereafter in terms of the phonon distribution function, $n(t, \mathbf{s}, \boldsymbol{\kappa}, p)$, of a polarization mode p in the wave vector state $\boldsymbol{\kappa}$ and space vector \mathbf{s} and at time t . In the absence of external fields, the BTE can be reduced to [1,2]

$$\frac{\partial n}{\partial t} + \mathbf{v}_g \cdot \nabla n = (\partial n / \partial t)_{\text{coll}} \quad (1)$$

where \mathbf{v}_g is the phonon group velocity vector. The terms in the left-hand side of Eq. (1) correspond to the total time rate of

change of n and the diffusion in geometric space due to the phonon group velocity \mathbf{v}_g , while the right-hand side represents the rate of change of n due to scattering to other wave vectors and polarizations [2,3].

In a three-dimensional space, Eq. (1) is a function of several independent variables, such as the time, the three space variables, the three wave vector variables, and the polarization modes. In addition, the collision (or scattering) term, $(\partial n / \partial t)_{\text{coll}}$, is a nonlinear function of wave vectors. Therefore, the resolution of Eq. (1) is a very complicated task and is not convenient for engineering problems. To overcome this difficulty, the relaxation time approximation (RTA), which consists of linearizing the scattering term $(\partial n / \partial t)_{\text{coll}}$, has been commonly used [2]. In literature, different resolution methods of the BTE under the RTA have been suggested. Among these are the discrete ordinate method [4–6], the (unstructured modified) finite-volume method [7,8], the method of characteristics [9], and the Monte Carlo method [10–12]. A review concerning the advantages and the drawbacks of each method is recently reported by Pilon and Katika [9]. To our knowledge, the Monte Carlo simulations can be identified as the most powerful technique that enables us to better describe most of the physics of phonons and to handle complex problems in terms of geometrical, spatial, and directional dependency without significantly increasing the complexity of the formulation. In the past, the Monte Carlo method has attracted less attention due to the cost of computation time. However, thanks to the rapid development of high speed computers, such simulation can be performed nowadays with reasonable computation time and satisfactory accuracy.

¹Corresponding author.

Contributed by the Heat Transfer Division of ASME for publication in the JOURNAL OF HEAT TRANSFER. Manuscript received February 12, 2007; final manuscript received June 4, 2007; published online May 20, 2008. Review conducted by Suresh V. Garimella.

The current study aims at proposing a new Monte Carlo algorithm for modeling the steady-state phonon transport regime in submicron semiconductors. This alternative approach does not question the validity of the conventional transient Monte Carlo simulations [11,12] but enriches the comprehension of the steady-state nature of phonon transport and could reduce the cost of computation according to the following reasons.

- (i) One common modeling approach is to neglect optical phonons due to their low group velocities and assumes that acoustic phonons are the main heat carriers. Concerning the thermal conductivity simulations, this assumption is generally valid. However, under certain conditions, optical phonons can influence heat conduction [3,7,13]. For example, optical phonons can alter the time scale of the simulation because they cannot be propagated but can be divided into acoustic phonons. Therefore, the time accuracy of previous transient methods that do not account for optical modes could be questionable [3,7,13,14]. As the current method is based on a timeless algorithm, it therefore allows us to properly acknowledge the steady-state nature of phonon transport through nanostructured materials.
- (ii) In transient Monte Carlo methods, the characteristics (e.g., frequencies, wave vectors, polarization modes, and locations) of every phonon are stored while they are not absorbed. This data storage can last several time steps; therefore, the transient algorithms become very memory demanding and require computers with high capacity storage. In this work, the algorithm consisting in tracking phonons one by one is developed, as will be detailed later, so that there is no storage limitation. In addition, as we will show later, the proposed scheme requires few iterations on the temperature field to achieve convergence. Thus, we think that the current algorithm can run faster compared to transient Monte Carlo simulations in some cases.

The first part of this paper focuses on the theoretical background. The second part describes the Monte Carlo algorithm for steady-state phonon transport. The third part concerns the numerical scheme verification in both ballistic and diffusive transport regimes, followed by an examination of its capability to model the boundary and impurity scattering on the phonon transport. The fourth part focuses on the prediction of thermal conductivity along silicon thin films and nanowires over the temperature range of 40–300 K. The simulation results are compared with previous predictions and experimental data [12,15–17].

2 Theoretical Background

2.1 Phonons and Crystal Energies. Under the influence of temperature, crystal atoms oscillate around their equilibrium positions. The oscillation of atoms results in vibration waves called “phonons,” which carry energy. Similar to wavelike particles, a phonon is characterized by an angular frequency ω , polarization mode p , and group velocity v_g . A phonon energy is equal to $\hbar\omega$, where $\hbar=1.054 \times 10^{-34}$ J s/rad is the Planck constant divided by 2π . For a vibrating crystal, its energy U , excluding the zero point energy, can be expressed as [1,19]

$$U = \sum_p \int_{\omega} \langle n \rangle \hbar \omega \mathcal{D}(\omega, p) d\omega \quad (2)$$

In Eq. (2), the summation is performed over all polarization modes, while the integral is performed over the frequency space; $\mathcal{D}(\omega, p)$ is the density of states (DOS) and can be expressed as [20]

$$\mathcal{D}(\omega, p) = V \frac{\kappa^2}{2\pi^2 v_g(\omega, p)} = V \frac{\omega^2}{2\pi^2 v_g(\omega, p) v_p^2(\omega, p)} \quad (3)$$

where $v_p = \omega/\kappa$ is the phase velocity, $v_g(\omega, p) = \partial\omega/\partial\kappa$ the group velocity, and V the crystal volume. $\langle n \rangle$ is the average number of phonons that occupy the vibration state of wave vector κ . Phonons obey the Bose–Einstein statistical distribution; therefore, the average number of phonons $\langle n \rangle$ at an equilibrium temperature T is given by [2,19]

$$\langle n(\omega, T) \rangle = \frac{1}{\exp(\hbar\omega/k_B T) - 1} \quad (4)$$

where $k_B = 1.38 \times 10^{-23}$ J K⁻¹ is the Boltzmann constant.

The spectral phonon energy (per unit volume) of polarization p and frequency ω at equilibrium can be expressed as

$$u_{\omega, p} = \langle n(\omega, T) \rangle \hbar \omega \dot{\mathcal{D}}(\omega, p) \quad (5)$$

where $\dot{\mathcal{D}}(\omega, p)$ refers to the DOS per unit volume.

2.2 Energies Emitted Per Unit Time From Surface and Volume Elements. Most thermal engineers are familiar with the concept of photons, which has many conceptual similarities with phonons; therefore, it is useful to treat phonons in the same manner as photons.

The analogy with Planck’s law of blackbody radiation [21] allows us to express the equilibrium phonon intensity $I_{\omega, p}^0$ of frequency ω and polarization p at temperature T as follows:

$$I_{\omega, p}^0 = \frac{u_{\omega, p} v_g(\omega, p)}{4\pi} = \frac{1}{4\pi} v_g(\omega, p) \langle n(\omega, T) \rangle \hbar \omega \dot{\mathcal{D}}(\omega, p) \quad (6)$$

The intensity given by Eq. (6) differs from that previously defined by Majumdar [1,4] by the presence of the factor $1/(4\pi)$; here, it refers to the phonon energy emitted per unit time per unit area per unit solid angle per unit frequency interval.

- (i) Using Eq. (6), the phonon energy emitted per unit time from a surface A at temperature T_b over a hemisphere, hereafter referred to as “the emitted phonon flux,” is

$$\begin{aligned} Q^+ &= A \int_{2\pi} \left(\sum_p \int_{\omega} I_{\omega, p}^0 d\omega \right) \cos \theta d\Omega \\ &= \frac{A}{4} \sum_p \int_{\omega} v_g(\omega, p) \langle n(\omega, T_b) \rangle \hbar \omega \dot{\mathcal{D}}(\omega, p) d\omega \quad (7) \end{aligned}$$

where $d\Omega = \sin \theta d\theta d\varphi$ is the unit solid angle in which θ and φ are the polar and azimuth angles characterizing the intensity direction. The superscript “+” denotes that the phonons leave the surface element. The subscript b refers to the temperature of a surface element.

- (ii) Using Eq. (6), the phonon energy emitted per unit time from a volume V at temperature T is

$$\begin{aligned} G^+ &= V \int_{4\pi} \left(\sum_p \int_{\omega} K(\omega, p, T) I_{\omega, p}^0 d\omega \right) d\Omega \\ &= V \sum_p \int_{\omega} \tau_{3\text{ph}}^{-1}(\omega, p, T) \langle n(\omega, T) \rangle \hbar \omega \dot{\mathcal{D}}(\omega, p) d\omega \quad (8) \end{aligned}$$

with $1/K(\omega, p, T) = v_g(\omega, p) \tau_{3\text{ph}}(\omega, p, T)$, in which $\tau_{3\text{ph}}$ refers to the average time after which there is an emission or an absorption of phonon(s). $\tau_{3\text{ph}}$ is called “three-phonon relaxation time” [19], which will be detailed later.

For solid crystals containing two atoms per primitive cell, there are three optical and three acoustic polarizations [19]. Since optical phonons have low velocity, their contribution to the steady-state heat transport is very little. In our simulations, the summa-

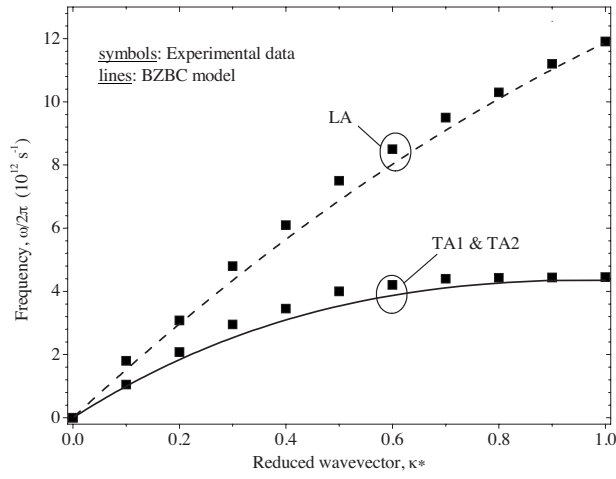


Fig. 1 Comparison between the acoustic phonon dispersion curves measured at room temperature and in the wave vector direction [001] [22] and those obtained from the BZBC relations. TA1 and TA2 means that these polarization branches are overlapping.

tions in Eqs. (7) and (8) are performed only over the acoustic modes: one longitudinal, LA, and two transverses, TA1 and TA2. The phonon wave number κ , polarization p , and frequency ω are connected by the “dispersion relations.” In this study, the dispersion relations are obtained from the “Brillouin zone boundary condition” (BZBC) model recently suggested by Chung et al. for germanium [20]. For the LA polarization mode, the dispersion relation is

$$\omega(\kappa^*, \text{LA}) = v_g(0, \text{LA})\kappa_m\kappa^* + [\omega_m(\text{LA}) - v_g(0, \text{LA})\kappa_m]\kappa^{*2} \quad (9)$$

while those corresponding to TA1 and TA2 polarization modes are

$$\omega(\kappa^*, p) = v_g(0, p)\kappa_m\kappa^* + [3\omega_m(p) - 2v_g(0, p)\kappa_m]\kappa^{*2} + [v_g(0, p) - 2\omega_m(p)]\kappa^{*3}, \quad p = \text{TA1, TA2} \quad (10)$$

where $\kappa_m = 2\pi/a$ is the wave number at the first Brillouin zone (a is the lattice parameter), $\kappa^* = \kappa/\kappa_m$ is a reduced wave number, $v_g(0, p)$ is the group velocity of polarization p at low frequency limit ($\omega \rightarrow 0$), and $\omega_m(p)$ is the cutoff frequency of polarization p corresponding to $\kappa = \kappa_m$. For each polarization mode p , $v_g(0, p)$ and $\omega_m(p)$ can be deduced from the experimental data of dispersion curves. Figure 1 shows a close match between the experimental dispersion curves of silicon in the [001] wave vector direction measured at room temperature [22] and the curves resulting from the BZBC relations (Eqs. (9) and (10)). Note that the TA1 and TA2 branches, hereafter referred to as TA, are identical for both experimental and BZBC curves.

3 Monte Carlo Algorithm for Steady-State Phonon Transport Regime

3.1 Assumptions. In this study we present the following assumptions.

- (i) Phonons are considered to be only the heat carriers. In fact, dielectric materials and semiconductors have low electron density; therefore, the contribution of electrons to the heat transport can be neglected.
- (ii) The phonon dispersion curves and relaxation rates of dense crystals are used because most of the material dimensions are greater than the critical sizes beyond which they break down due to phonon confinement. Note that previous investigations have shown that confinement is

not significant in silicon thin films of thicknesses greater than or equal to 20 nm and in silicon nanowires of sizes greater than 22 nm [12,16,18,23].

- (iii) Phonons are treated as massless particles by neglecting the interference of phonon waves. This assumption is valid as long as the smallest material dimension is greater than the phonon wavelength λ or the phonon coherence length [24]. For silicon, the dominant wavelength λ at room temperature is between 1 nm and 2 nm, while the smallest material dimension is about several nanometers [11,12,15–18,23].

3.2 Description of the Steady-State Monte Carlo Algorithm.

Solving the steady-state energy transfer problem by using the Monte Carlo algorithm implies tracing the history of a statistically meaningful random sample of heat carriers from their points of emission to their points of absorption. The steady-state Monte Carlo algorithm is a timeless algorithm that is well developed for radiative heat transfer in semitransparent media as reported in standard textbooks [21,25], whereas this is its first development for submicron scale heat conduction. Due to some differences between the physics of photons and phonons, it is not appropriate to entirely apply the Monte Carlo algorithm for steady-state radiative heat transfer to model the phonon transport. The following changes need to be addressed.

- (i) Each phonon sample contains a constant phonon number of frequency-dependent energy instead of a frequency-dependent phonon number of constant energy, as is the case in the radiative heat transfer Monte Carlo simulations [21,25].
- (ii) Polarized phonons are considered due to the transition of polarization mode during the phonon-phonon interaction process [2].
- (iii) A group velocity is assigned to each sample of phonon depending on its frequency and its polarization due to the nonlinear and polarization-dependent dispersion curves.
- (iv) A new scheme to treat the phonon-phonon scattering process is implemented to ensure the energy conservation during this process. In fact, in the Monte Carlo simulations of radiative heat transfer [21,25], when a photon packet is absorbed, a new packet of equal energy is reemitted. Since each phonon has frequency-dependent energy according to (i), this collision scheme allows us to conserve the phonon number but not the phonon energy.

First of all, the material is discretized into N_{cell} three-dimensional cells (the case of a parallelepiped bin is considered to simplify). For each cell, an arbitrary temperature T , which still has to be determined, is assigned. The size of cells is chosen to be smaller than the phonon mean free path. We will justify this choice later. We designate the sides of cells that separate the material from the surrounding medium by boundaries. Some of these boundaries (where N_{bw} is their number) have prescribed temperatures and, therefore, can emit phonons. The phonon flux emitted from each one of the N_{bw} boundaries (Eq. (7)) is divided into a very large number of samples. Then, the following three steps constituting the heart of the current Monte Carlo algorithm are performed.

- (1) For each phonon sample, random position, direction, frequency, and polarization are assigned. Then, the method consists of tracking one by one the samples emitted from N_{bw} boundaries. A phonon moves according to a drift motion, while its direction is altered when it interacts with material imperfection (e.g., defect or impurity) or is reflected by a boundary. The track of a phonon is stopped when it is absorbed at an absorbing element (boundary or cell). Each time a phonon is absorbed, the energy of the absorbing element is incremented by the phonon energy.

After tracking all samples emitted from N_{bw} boundaries, the energy absorbed (per unit time) at each element i , denoted by Q_i^- for the boundary and G_i^- for the cell, is computed. The superscript “-” indicates that the phonons arrive at the element.

- (2) From each cell i , a certain number of phonons are emitted so that the cell emitted energy, denoted by G_i^+ , is equal to the cell absorbed energy G_i^- . These newly emitted phonons are tracked again one by one until they are all absorbed according to the reasons mentioned in step (1). After this phonon tracking, the energies absorbed at cells and walls only during this step, hereafter referred to as “energies absorbed step by step” are computed.
- (3) While the energies absorbed step by step at cells and walls are greater than zero, they are added to the absorbed energies (Q^- for walls and G^- for cells), and the algorithm goes back to step (2). Since the phonons absorbed at boundaries are not reintroduced, the total phonon number in the studied system decreases step by step and becomes equal to zero after a certain number of steps. In terms of energy, the energies absorbed step by step at cells and walls change with the simulation step and decrease up to zero after a certain number of steps. The necessary information, such as the cell equivalent temperatures and the net energy fluxes crossing the material, are extracted from the absorbed and emitted energies ($Q^-, Q^+, G^-,$ and G^+).

As the initial cell temperatures are unknown, the frequency distribution of phonons in the cells is not correct. Therefore, iteration on the temperatures is required until the temperature profile is stable. This consists of repeating steps (1)–(3) using the latest computed temperatures as initial temperatures. The different simulation steps are summarized by the flowchart reported in Fig. 2. In the following sections, only some important points for the readers are detailed.

3.2.1 Initialization. In this study, the case of black and adiabatic boundary conditions is considered. Black boundaries are absorbing/emitting walls and their temperatures are prescribed, while adiabatic boundaries are reflecting walls, which are characterized by a specular probability parameter d varying between 0 and 1. The values $d=0$ and $d=1$ correspond to isotropic and specular reflections, respectively. More details concerning these types of boundary can be found in the Mazumder and Majumdar’s paper [11].

The simulation is started with false temperatures since the temperatures of cells are unknown. The choice of initial cell temperatures is arbitrary, and the simulation results are shown to be independent of it. In this study, the initial cell temperatures are taken equal to the lowest boundary temperature.

The number of phonons emitted per unit time, N^+ , from a black wall of area A at temperature T_b can be deduced from Eq. (7) by omitting the energy per phonon mode $\hbar\omega$,

$$N^+ = \frac{A}{4} \sum_p \sum_{i=1}^{m_p} v_g(\omega_i, p) \langle n(\omega_i, T_b) \rangle \dot{D}(\omega_i, p) \Delta\omega \quad (11)$$

In Eq. (11), the integral over the frequency space is substituted for a discrete sum where m_p is the spectral band number with a uniform bandwidth $\Delta\omega$. The band number for LA polarization modes is taken equal to $m_{LA}=500$, while that for TA polarization modes m_{TA} is deduced from the relation $\omega_m(TA) = m_{TA} \Delta\omega$, knowing the cutoff frequency of TA branch $\omega_m(TA)$ and the bandwidth $\Delta\omega$. These band numbers are chosen to better take into account all details of the phonon spectrum without much increasing the computation time.

From Eq. (11) the number of phonons emitted per unit time within the spectral range $[\omega_i, \omega_i + \Delta\omega]$ from the same surface can be deduced,

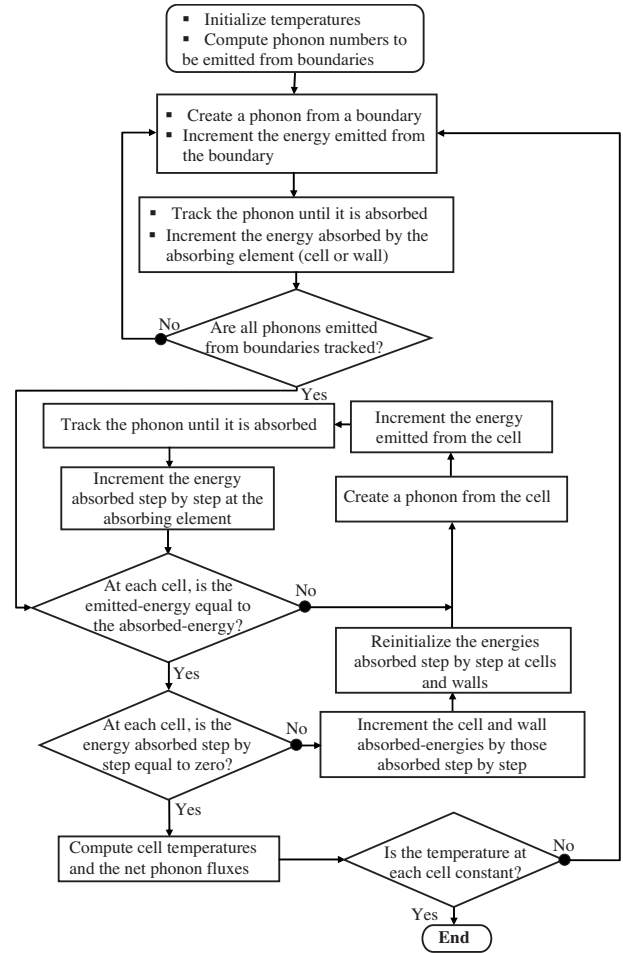


Fig. 2 Monte Carlo flowchart for steady-state microscale phonon transport

$$N^+(\omega_i) = \frac{A}{4} \sum_p v_g(\omega_i, p) \langle n(\omega_i, T_b) \rangle \dot{D}(\omega_i, p) \Delta\omega \quad (12)$$

Note that N^+ and $N^+(\omega)$ are generally very large numbers, and their simulation is time consuming. In practice, only reasonable phonon numbers N_S^+ and $N_S^+(\omega)$ are simulated. They can be connected to N^+ and $N^+(\omega)$ by a sort of time step Δt given by

$$\Delta t = N_S^+ / N^+ = N_S^+(\omega) / N^+(\omega) \quad (13)$$

Thus, by simulating the N_S^+ phonons, each phonon sample has an energy per unit time equal to $\hbar\omega / \Delta t$.

Now, let $T_{b,H}$ be the highest boundary temperature and N_S^+ be the phonon number emitted from the boundary of temperature $T_{b,H}$ (N_S^+ is fixed by the user). The phonon number emitted from the j th boundary of temperature $T_{b,j}$ is deduced from

$$N_{S,j}^+ = \Delta t N^+(T_{b,j}), \quad j = 1, N_{bw} \quad (14)$$

3.2.2 Phonon Creation

3.2.2.1 Location. Considering that the black boundaries are isothermal, the phonon location can be drawn randomly over the surface. Concerning the emission of phonons from a cell, it results from the phonon-phonon scattering; therefore, the locations of absorbed phonons at each cell should be stored and used as positions of phonons to be created. This procedure is usually adopted in the previous transient Monte Carlo algorithms. However, it is clear that when the number of phonon-phonon scattering events

within a cell and the number of cells become important, such storage procedure becomes very memory-demanding and requires a high-capacity storage computer. To overcome this difficulty, the basic idea is to reset the locations of absorbed phonons within each cell and to pick random positions within this cell. To avoid excessive approximations, the cell sizes must be smaller enough than the material dimension. A practice criterion is to choose the cell sizes smaller than the mean free path of heat carriers. The procedures to select random positions within a three-dimensional bin and over a surface element can be found in references [10,11,21,25]; therefore, they are not described here anymore.

3.2.2.2 Frequency and polarization. The procedures to select random frequency and polarization are similar as those described elsewhere [11], but the governing equations are slightly different because here they depend on where the phonon is emitted.

Emission from a boundary. The probability to find a frequency smaller than ω_j is described by the cumulative probability distribution function, denoted by $F(\omega)$, expressed in terms of $N^+(\omega)$ and N^+ ,

$$F(\omega_j) = \frac{1}{N^+} \sum_{i=1}^j N^+(\omega_i) \quad (15)$$

Thus, the actual phonon frequency ω_j is deduced from the relation $F(\omega_j) = \xi$, where ξ is a random number between 0 and 1. Knowing the frequency, the probability to find a longitudinal mode of frequency ω_j is

$$P(\text{LA}) = \frac{A v_g(\omega_j, \text{LA}) \langle n(\omega_j, T_b) \rangle \dot{D}(\omega_j, \text{LA}) \Delta \omega}{4 N^+(\omega_j)} \quad (16)$$

Now, the probability $P(\text{LA})$ is compared to a new random number ξ . If $P(\text{LA})$ is greater than ξ , the phonon polarization p is LA, else, $p = \text{TA}$. In Eq. (16), T_b refers to the boundary temperature and A is the boundary surface.

Emission from a cell. The phonon frequency ω and polarization p are determined in a similar manner as before, except that in Eqs. (15) and (16), $N^+(\omega_j)$ and N^+ are substituted for the phonon number emitted per unit time from a volume V , denoted by M^+ , and the phonon number emitted per unit time within the frequency interval $[\omega_j, \omega_j + \Delta \omega]$ from the same volume, denoted by $M^+(\omega_j)$, such as

$$M^+ = V \sum_p \sum_{j=1}^{m_p} \tau_{3\text{ph}}^{-1}(\omega_j, p, T) \langle n(\omega_j, T) \rangle \dot{D}(\omega_j, p) \Delta \omega \quad (17)$$

and

$$M^+(\omega_j) = V \sum_p \tau_{3\text{ph}}^{-1}(\omega_j, p, T) \langle n(\omega_j, T) \rangle \dot{D}(\omega_j, p) \Delta \omega \quad (18)$$

Here, T refers to the cell temperature. Instead of Eq. (16), the probability to find a longitudinal phonon of frequency ω_j is

$$P(\text{LA}) = V \frac{\tau_{3\text{ph}}^{-1}(\omega_j, \text{LA}, T) \langle n(\omega_j, T) \rangle \dot{D}(\omega_j, \text{LA}) \Delta \omega}{M^+(\omega_j)} \quad (19)$$

Note that Eqs. (17)–(19) differ from Mazumder and Majumdar's ones by the presence of the three-phonon relaxation rate $1/\tau_{3\text{ph}}$.

3.2.2.3 Wave vector. Once the frequency and polarization of the phonon are known, the wave number κ and the velocities v_p and v_g can be deduced from the dispersion relations (Eqs. (9) and (10)). The relations determining the wave vector direction can be recovered from literature [11].

3.2.3 Phonon Tracking. Each time a phonon sample is created at the j th cell, the energy emitted (per unit time) from this cell is incremented by the phonon energy, i.e.,

$$G_j^+ = G_j^+ + \hbar \omega / \Delta t \quad (20)$$

3.2.3.1 Point of interaction. When a phonon travels within a material, it can strike a boundary or undergo a volume scattering, e.g., scattering by impurities, defects, or phonons. Let us consider a phonon at the vector position \mathbf{s} , propagating along the vector direction Δ . Let λ_{bd} be the distance between the phonon and the nearest boundary and λ_{vol} be the distance between the phonon and the nearest scatterer in the volume. The distance up to the next interaction is the shortest path between λ_{bd} and λ_{vol} . Thus, the new point of interaction, denoted by \mathbf{s}_{new} , is defined by

$$\mathbf{s}_{\text{new}} = \mathbf{s} + \min(\lambda_{\text{bd}}, \lambda_{\text{vol}}) \Delta \quad (21)$$

The distance λ_{bd} is determined knowing the position of the phonon and that of boundaries, while λ_{vol} is calculated from the following conventional relation [21,25]:

$$\lambda_{\text{vol}} = \ell \ln(1/\xi) \quad (22)$$

where $\ell = v_g \tau_{\text{eff}}$ refers to the effective mean free path in which τ_{eff} is the effective relaxation time defined later. ξ is a random number chosen between 0 and 1.

3.2.3.2 Scattering. When a phonon reaches a black wall, the energy absorbed (per unit time) at this wall is incremented by the incident phonon energy. In this case, the track of the phonon is stopped. When a phonon interacts with an adiabatic wall, its energy is conserved, but its direction is altered either specularly or diffusely and the phonon continues its path. The procedures to determine the type of reflection and to select the direction after reflection can be found elsewhere [11] and are not given here anymore.

When the phonon scatters inside the volume, a test to determine the type of interaction is required. In this study, the most important sources of phonon scattering in dielectric crystals are considered. Among these are defects (or dislocations), impurities, and phonons.

- (i) The scattering by defects, dislocations, or impurities is characterized by a relaxation time according to [26]

$$\tau_l^{-1} = \beta \sigma \delta |v_g| \quad (23)$$

where β is a constant of the order of unity, δ is the impurity (or defect) density per unit volume, and σ is the scattering cross section defined by

$$\sigma = \pi r^2 \left(\frac{\chi^4}{\chi^4 + 1} \right) \quad (24)$$

in which $\chi = r|\kappa|$ is the scatterer size parameter [27] and r is the atomic radius of the impurity (or defect radius). When the parameters β , δ , and σ are not well known and the impurities (or defects) are small compared to the phonon wavelength, i.e., $\chi < 1$, the relaxation time τ_l is proportional to $1/\omega^4$ and, in practice, Eq. (23) is substituted for

$$\tau_l^{-1}(\omega, p) = B_l \omega^4, \quad p = \text{LA, TA} \quad (25)$$

where B_l is called an ‘‘impurity relaxation time parameter.’’ Usually, B_l is determined from a fit between modeling and measurement of thermal conductivity of dense materials [20,28]. In addition, Chung et al. [20] showed that the B_l parameter is sensitive to the model of dispersion curves and suggested to determine it for each model of dispersion curves. According to Eq. (23), B_l is also proportional to $v_g(\omega, p)$, but Holland [28] assumed that it is proportional to v_s (where v_s is the average group velocity of LA and TA branches at low frequencies). In this study, a more refined consideration of B_l is performed. This consists in separating the cases of longitudinal (LA) and transverse modes (TA), and the cases of low ($\omega < \omega_{1/2}$) and high frequencies ($\omega > \omega_{1/2}$). $\omega_{1/2}$ is the frequency of the

Table 1 Scattering relaxation time parameters

Parameter B_I	Impurity and defect scattering		Unit
	Frequency $\omega < \omega_{1/2}$	Frequency $\omega > \omega_{1/2}$	
Polarization mode			
LA	1.32×10^{-45}	6.22×10^{-46}	s^{-3}
TA		2.64×10^{-46}	
Parameter B_{3ph}	Three-phonon scattering		Unit
	Frequency $\omega < \omega_{1/2}$	Frequency $\omega > \omega_{1/2}$	
Polarization mode			
LA	2.0×10^{-24}	8.03×10^{-25}	$s K^3$
TA N process	9.3×10^{-13}	—	K^3
TA U process	—	7.4×10^{-19}	s

TA mode corresponding to $\kappa^* = \kappa / \kappa_m = 0.5$. In this manner, B_I is identical to Holland's parameter for low frequencies but slightly different for high frequencies LA and TA modes, as reported in Table 1.

- (ii) In dielectric or semiconductor materials, the three-phonon scattering, known as Umklapp (U) and Normal processes (N), are the main source of the scattering by phonons. These processes are well detailed in the solid physics textbooks [2,19] and not recapitulated here. The three-phonon relaxation times are commonly used to characterize the phonon-phonon scattering. Rigorous formulations about them can be found in Refs. [2,28–31], but in the following, the most useful relations are used [28].

For the N process,

$$\tau_N^{-1}(p, \omega, T) = \begin{cases} B_{3ph}(p) \omega^2 T^3, & p = \text{LA} \\ B_{3ph}(p) \omega T^4, & p = \text{TA and } \omega < \omega_{1/2} \\ 0, & p = \text{TA and } \omega \geq \omega_{1/2} \end{cases} \quad (26)$$

For the U process,

$$\tau_U^{-1}(p, \omega, T) = \begin{cases} B_{3ph}(p) \omega^2 T^3, & p = \text{LA} \\ 0, & p = \text{TA and } \omega < \omega_{1/2} \\ B_{3ph}(p) \omega^2 \sinh(\hbar \omega / k_B T), & p = \text{TA and } \omega \geq \omega_{1/2} \end{cases} \quad (27)$$

The coefficients $B_{3ph}(p)$ are “the three-phonon relaxation time parameters.” They can be determined in a similar manner as B_I , i.e., by a fitting procedure. The identified values of $B_{3ph}(p)$ parameters based on the BZBC dispersion curves of silicon are reported in Table 1.

By using Eqs. (25)–(27), the effective relaxation time τ_{eff} can be defined by

$$\frac{1}{\tau_{\text{eff}}} = \frac{1}{\tau_I} + \frac{1}{\tau_{3ph}} \quad (28)$$

where $\tau_{3ph}^{-1} = \tau_N^{-1} + \tau_U^{-1}$ refers to the inverse of the average time after which there is a three-phonon scattering. Now, the test to decide the type of the scattering is implemented as follows: First, the probability of scattering due to impurities or defects, namely, ϖ , is calculated,

$$\varpi = \frac{\tau_{\text{eff}}}{\tau_I} \quad (29)$$

Then, a new random number ξ is drawn and compared to ϖ . If $\xi < \varpi$, the phonon scatters by an impurity; therefore, a new random direction is assigned assuming an isotropic distribution [11],

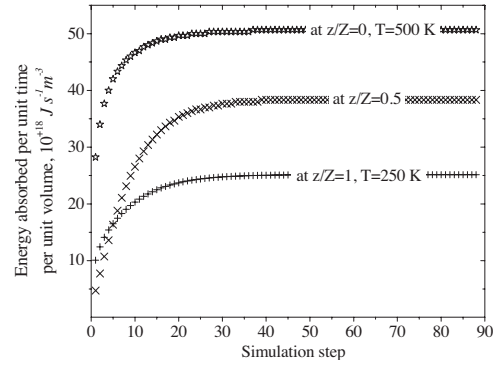


Fig. 3 Evolution of the energies absorbed per unit volume at cells at the abscissas $z/Z=0$, $z/Z=0.5$, and $z/Z=1$ as a function of the simulation step

and the phonon continues its path. Else, the phonon is absorbed due to the three-phonon scattering, and the track of its path is stopped. Each time a phonon is absorbed in a cell, the cell absorbed energy is updated.

3.2.4 Steady-State Regime. The net phonon flux at the i th absorbing/emitting wall, Q_i , is the difference between the flux absorbed Q_i^- and that emitted Q_i^+ ,

$$Q_i = Q_i^- - Q_i^+, \quad i = 1 \text{ to } N_{\text{bw}} \quad (30)$$

where N_{bw} is the number of absorbing/emitting walls. At a steady-state regime, the net fluxes are constant. In the current Monte Carlo method, this regime takes place when the energy absorbed in each cell becomes constant. In practice, we assume that the absorbed energy is constant when its step by step variation is equal to or less than a tolerance energy equal to $\hbar \omega_{m,TA} / \Delta t$ where, $\omega_{m,TA}$ is the frequency of the transverse mode at the first Brillouin zone.

To illustrate the energy propagation through the material as a function of the Monte Carlo steps, let us analyze heat conduction across a simple one-dimensional pure silicon film of thickness $Z = 60$ nm. The geometry used in all simulations is a parallelepiped box of Z length and $X \times Y$ cross section. The hot boundary at the abscissa $z=0$ is maintained at $T_{b,H}=500$ K, while the cold boundary at the abscissa $z=Z$ is maintained at $T_{b,C}=250$ K. The four other sides of the box are assumed specular ($d=1$) to mimic the one-dimensional heat transfer condition. The film thickness is subdivided into 20 juxtaposed parallel cells. The initial cell temperatures are taken equal to 250 K.

For a single temperature iteration, the variation of the energies absorbed (per unit time) per unit volume at cells at the abscissas $z/Z=0$, $z/Z=0.5$, and $z/Z=1$ as a function of the Monte Carlo step is shown in Fig. 3. It can be noted that the energies absorbed at the considered cells increase as the number of steps increases; these energies become constant after a certain number of steps. To understand why these absorbed energies become constant at large simulation steps, the variation of the normalized energies absorbed step by step at the same cells as a function of the simulation step is depicted in Fig. 4. The normalization consists in dividing the energy absorbed step by step at a cell by the sum over steps of the energy absorbed in this cell. We can see that at the beginning of the simulation, the cells at the boundaries absorb more phonons than the cell at the center of the film. During the first steps, the energies absorbed step by step at the bounding cells decrease rapidly, while that at the central cell continues to increase due to the phonons coming from the neighboring cells. As the number of steps increases, the energies absorbed step by step decrease up to the tolerance energy since every phonon reaching

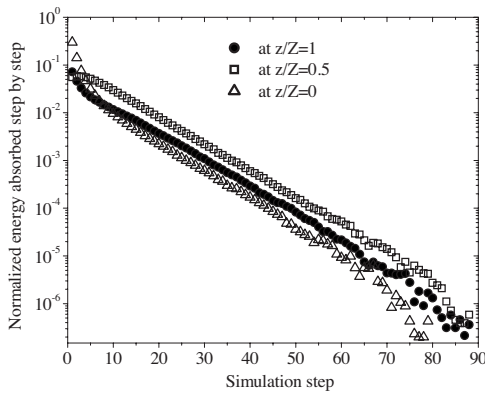


Fig. 4 Evolution of the normalized energies absorbed step by step at cells at the abscissas $z/Z=0$, $z/Z=0.5$, and $z/Z=1$ as a function of the simulation step

absorbing walls is not reintroduced. The fluctuation of the energies absorbed step by step at large simulation steps is due to the small number of samples absorbed at these cells.

The variation of the absolute net phonon fluxes per unit surface

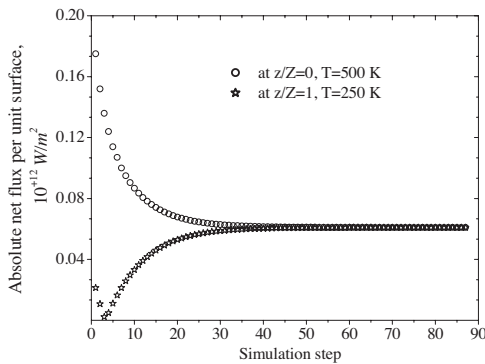


Fig. 5 Evolution of the absolute net energy fluxes per unit surface at the boundaries at $z/Z=0$ and $z/Z=1$ as a function of the simulation step

at the hot and cold boundaries as a function of the simulation step, for a single temperature iteration, is plotted in Fig. 5. It can be seen that when the number of steps increases, the net fluxes per unit surface decrease and become constant at the same simulation step at which the energies absorbed at cells are constant (see Fig. 3). In Fig. 5, the plot of absolute values explains the abrupt change of the net flux at the cold boundary when this boundary begins to absorb more phonons than it emitted.

In micro- and nanoscale systems, the nonequilibrium nature of the phonon transport prevails; therefore, the concept of temperature breaks down. However, a pseudotemperature can be introduced to represent the energy of a spatial bin [10,11]. The pseudotemperature of the j th cell, denoted as T_j , can be related to the energy emitted (per unit time) from this cell by Eq. (8). Therefore, knowing the energy absorbed at this cell at a steady-state regime, i.e., G_j^- (or the emitted energy G_j^+), the pseudotemperature T_j can be deduced from the following relation:

$$G_j^- = V_j \sum_p \sum_{i=1}^{m_p} \tau_{3\text{ph}}^{-1}(\omega_i, p, T_j) \langle n(\omega_i, T_j) \rangle \dot{D}(\omega_i, p) \hbar \omega_i \Delta \omega, \quad j = 1, N_{\text{cell}} \quad (31)$$

where V_j is the volume of the j th cell.

3.2.5 Convergence Test. Since scattering serves to bring the system back to equilibrium; new phonons are selected from the equilibrium distribution, which depends on temperature. As the temperatures of cells are unknown at the beginning of the simulation, the frequency distribution of phonons in cells is not correct. To obtain the correct cell pseudotemperatures, a common technique used in steady-state heat transfer simulations is to perform iteration on the temperature field. In our scheme, while the relative deviation between the cell pseudotemperatures issued from successive iterations are greater than 0.1%, the entire simulation (steps (1)–(3)) is repeated by taking the last computed cell temperatures as initial temperatures.

To illustrate the evolution of the temperature profiles issued from successive iterations, let us consider the studied case in Sec. 3.2.4. The results issued from the first three iterations are plotted in Fig. 6. We can see that after two or three iterations, the results become independent of the iteration number: The simulation con-

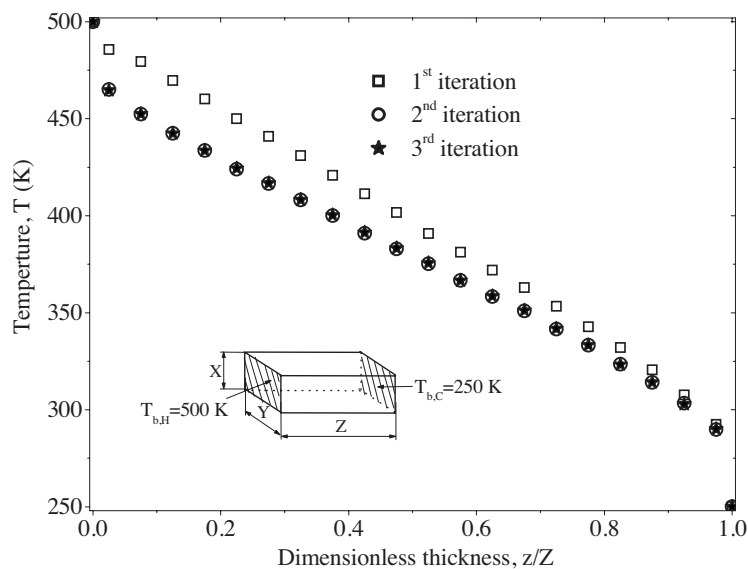


Fig. 6 Temperature profiles across silicon films of thickness 60 nm issued from the first three iterations

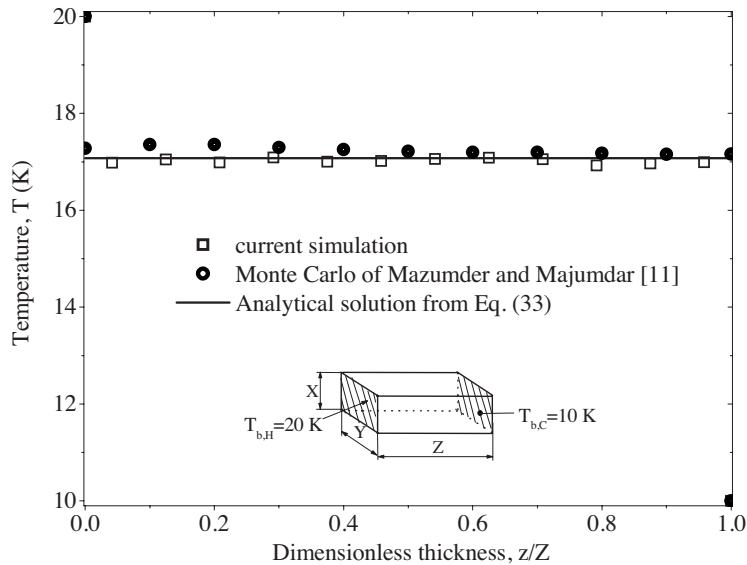


Fig. 7 Temperature profiles across gallium arsenide films of thickness 400 nm at very low temperature

vergence is reached. We have verified that this conclusion is independent of the initial cell temperatures, boundary temperatures, and film thickness, as shown in Fig. 8.

3.3 Statistical Errors and Computation Time. The statistical errors are inherent in the Monte Carlo method. They depend primarily on the simulated sample number ($N_{\bar{\sigma}}$) and the scattering events. The higher the simulated phonon number, the lower the statistical errors. The statistical errors are evaluated as follows: When the convergence on temperature is achieved, the simulation is run five times. During each one, a different random number seed is used. Thus, from the results issued from these five runs, the standard deviations of the cell temperatures, denoted as $\sigma_{T,i=1,N_{\text{cell}}}$, and the standard deviations of the net phonon fluxes, denoted as $\sigma_{Q,i=1,N_{\text{bw}}}$, were evaluated. In this study, the prescribed phonon number $N_{\bar{\sigma}}$ is chosen to ensure statistical errors on both temperatures ($\sigma_{T,i=1,N_{\text{cell}}}$) and net fluxes ($\sigma_{Q,i=1,N_{\text{bw}}}$) less than 5%. In this manner, we have found that for simulations with an average temperature less than 150 K, a number of phonons per emitting wall about 5×10^5 is sufficient to satisfy these accuracies, while a phonon number per emitting wall about 5×10^6 is required to achieve the same accuracies for simulations at higher temperatures. As these phonon numbers are evaluated for silicon films, the same analysis should be performed for other materials.

Considering that the algorithm is well implemented, the computation time depends on the desired accuracy, the Knudsen number ($\text{Kn}=\ell/Z$), and the computer. To give an idea concerning the computation time, a simulation of phonon transport across silicon film of thickness equal to 500 nm at room temperature is carried out. In this case, the value of Kn is about 0.5. A sample number about 5×10^6 per emitting boundary is considered to ensure uncertainties σ_T and σ_Q less than 5%. The simulation lasts 30 min with an Intel(R) Pentium(R) M, 1.73 GHz, 504 MO random access memory (RAM) computer. Under the same conditions but increasing the film thickness up to 10 μm ($\text{Kn} \approx 0.025$), the simulation time increased up to 10 h. We can tell that for a fixed phonon number, the computation time is approximately proportional to the inverse of the Knudsen number.

3.4 Numerical Scheme Verification. First, the current algorithm is tested to reproduce the two limiting cases of phonon

transport, such as the ballistic and diffusion regimes. Then, its capability to model the boundary and impurity scattering mechanisms is examined.

3.4.1 Ballistic Regime. The ballistic regime takes place when the mean free path of phonons is larger than the material dimensions. Thus, most phonons move from one end to the other end without being scattered. To perform this test, let us consider the famous phonon transport across a gallium arsenide film of thickness $Z=400$ nm [9,11]. The BZBC relations (Eqs. (9) and (10)) are used to model the dispersion curves where experimental data are retrieved from Waugh and Dolling [32]. The geometry (Fig. 7) has $Z=400$ nm of length and $X \times Y=100 \times 100$ nm² of cross section. The boundaries at the abscissas $z=0$ and $z=Z$ are black and are maintained at $T_{b,H}=20$ K and $T_{b,C}=10$ K, respectively. The remaining boundaries are considered specular ($d=1$). The initial cell temperatures are taken equal to 10 K. It is well known that under these conditions, the Knudsen number is much larger than 10; therefore, the phonon transport is ballistic and is governed by the Stefan–Boltzman law [4,21]. As a result, there are temperature slips at boundaries, and the cell temperatures are constant and are given by

$$T_j = \left[\frac{T_{b,C}^4 + T_{b,H}^4}{2} \right]^{1/4} = 17.075 \text{ K}, \quad j = 1 \text{ to } N_{\text{cell}} \quad (32)$$

Figure 7 compares the current Monte Carlo results with the analytical solution (Eq. (32)) and the results reported in the literature [11]. We can tell that the current scheme reproduces well the exact solution because the maximum relative deviation remains smaller than 1% compared to 2% obtained from the transient Monte Carlo algorithm of Mazumder and Majumdar [11].

3.4.2 Diffusion Regime. The second limit corresponds to the diffusion regime during which most phonons undergo collisions before reaching a boundary. This is the case when the mean free path of phonons is much shorter than the material dimensions. Let us consider that heat conduction across thick silicon films ($Z=6$ μm) submits to a large temperature gradient. The same configuration as in the ballistic regime test is considered, except that the hot and cold boundary temperatures are maintained equal to 500 K and 250 K, respectively. The initial cell temperatures are

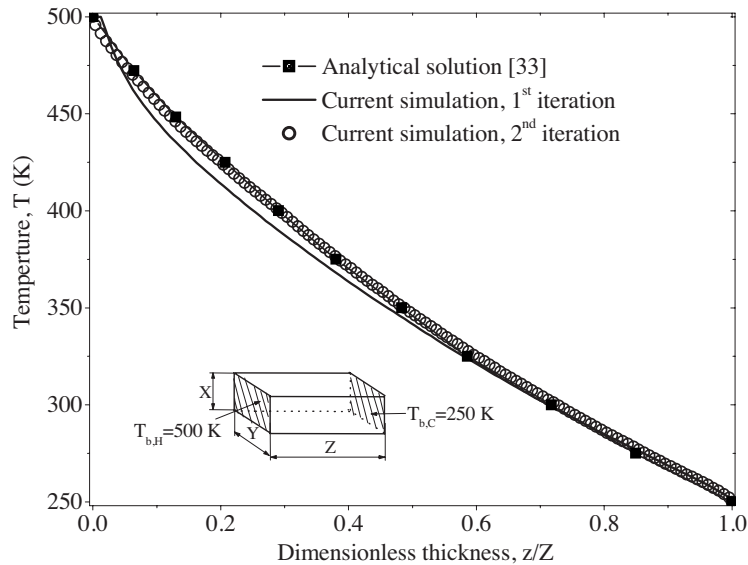


Fig. 8 Temperature profiles across silicon films of thickness $6 \mu\text{m}$ submitted to a large temperature gradient

taken equal to 250 K. Under these conditions, $\text{Kn} < 0.03$; thus, the diffusion regime prevails and there is no temperature slips at boundaries anymore. In addition, the analytical solution of the phonon transport can be known as reported in Ref. [33]. The comparison between the simulation results issued from the first two iterations and the analytical solution is shown in Fig. 8. We can see again that only very few iterations are required to obtain convergence. Moreover, the simulated temperature profile agrees well with the exact solution. Note that the nonlinear behavior of the temperature profile is due to the large temperature gradient, and, in this case, the thermal conductivity across the film is temperature dependent [33].

3.4.3 Impurity and Boundary Scattering. After an examination of the two limiting regimes, we investigate the capability of the current scheme to model the impurity and boundary scattering mechanisms. In the next, we are satisfied with performing only a

qualitative analysis. First, the impurity scattering effect on the phonon transport is investigated. We consider the phonon transport across silicon film of thickness equal to $Z = 500 \text{ nm}$. The ends of the film at abscissas $z = 0$ and $z = Z$ are maintained at $T_{b,H} = 40 \text{ K}$ and $T_{b,C} = 30 \text{ K}$, respectively, and the other four surfaces are assumed specular. The mechanism of scattering by impurities governing Eqs. (23) and (24) is activated. In these relations, the constant β and the radius r are taken arbitrarily equal to 1 and $2.71 \times 10^{-10} \text{ m}$, respectively. Four values of impurity density are considered, such as $\delta = 0$ (undoped film), $\delta = 10^{+24} \text{ m}^{-3}$, $\delta = 10^{+25} \text{ m}^{-3}$, and $\delta = 10^{+27} \text{ m}^{-3}$. The simulated temperature profiles across the film are shown in Fig. 9. We can note that when the impurity density increases, the temperature slips at boundaries decrease; i.e., the phonon transport tends to the diffusion regime. In fact, the scattering by impurities, that alter the phonon direc-

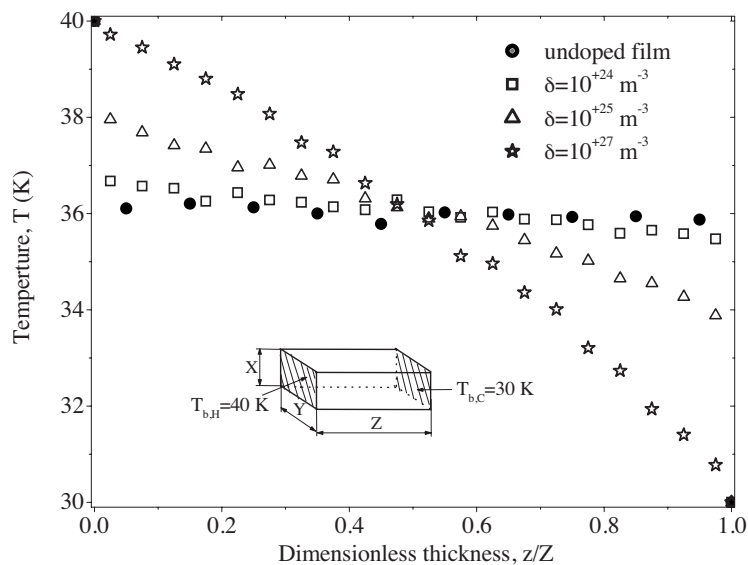


Fig. 9 Influence of scattering by impurities on the heat conduction across silicon films of thickness 500 nm at very low temperatures

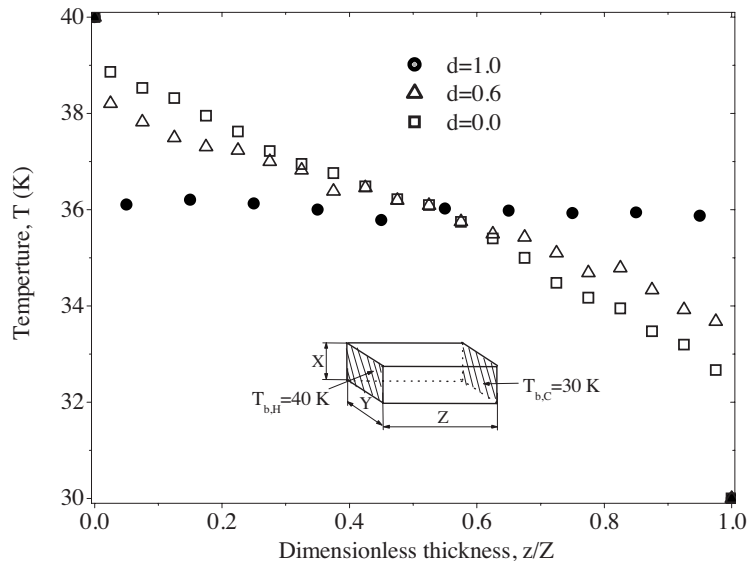


Fig. 10 Influence of scattering by boundaries on the heat conduction across silicon films of thickness 500 nm at very low temperatures.

tion, increase the phonon path between the two ends of film thus indirectly increase the phonon-phonon scattering events main responsible of the diffusion regime.

Next, we consider the same test as before by deactivating the impurity scattering form and activating the boundary scattering mechanism. The specular probability d of the top and bottom walls, which are 100 nm distant from each other, are varied between 0 and 1. Figure 10 illustrates the studied configuration and depicts the temperature fields corresponding to $d=0$, $d=0.6$, and $d=1$. It is shown that decreasing the specular probability increases the temperature gradient across the film because the scattering by the top and bottom walls and, indirectly, the phonon-phonon scattering events are increased. These results are consistent with the prior conclusion of Mazumder and Majumdar [11]. These exercises show that the current numerical scheme is well suitable for analyzing steady-state heat conduction in micro- and nanostructures. In the next section, the method is applied to predict the thermal conductivity of silicon structures, which have attracted much attention these past years.

3.5 Thermal Conductivity Prediction Along Silicon Thin Films and Silicon Nanowires. This past decade, the thermal conductivity study along silicon thin films and nanowires has attracted great interest due to their crucial role in the development of micro- and nanodevices [12,15–18,23]. Extensive measurements and modeling of thermal conductivity along silicon thin films of different thicknesses have been performed by Asheghi et al. [15] and Liu and Asheghi [16]. Experimental data are obtained from a Joule heating and electrical-resistance thermometry experiment, while modeling results are issued from famous Holland’s model of bulk thermal conductivity [24] in which the effective relaxation time of bulk materials is scaled by Sondheimer’s factor [34] aiming to account for phonon scattering by boundaries. The current Monte Carlo scheme is applied to determine thermal conductivity along silicon thin films of thickness equal to 20 nm, 100 nm, and 420 nm in the temperature range of 40–300 K. The following relation is used to deduce the thermal conductivity from the simulation statistics:

$$k = \frac{1}{A} \left| \frac{Q}{dT/dz} \right| \quad (33)$$

where Q is the net heat flux transmitted along the film according to Eq. (30). dT/dz is the temperature gradient along the film cal-

culated using the cell temperatures. A is the cross section of the simulation box, normal to the direction of the heat flux. In the simulation, all scattering mechanisms described previously are taken into account. The thin film is modeled, as illustrated in Fig. 11, where the associated dimensions are summarized in Table 2. The temperatures of the left ($T_{b,H}$) and right walls ($T_{b,C}$) are fixed with a constant temperature difference equal to 20 K. The top and

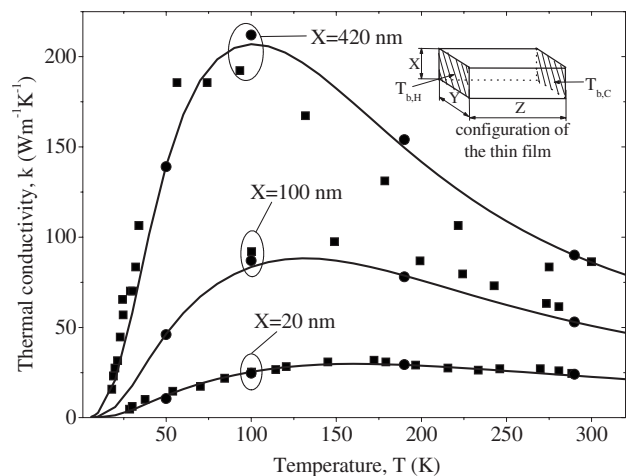


Fig. 11 Thermal conductivity along silicon thin films (lines: prediction from Refs. [15,16]; square symbols: experimental data from Refs. [15,16]; circle symbols: Monte Carlo simulation)

Table 2 Dimensions and boundary condition of studied silicon thin films

	Thin film dimensions		
	X (nm)	Y (μm)	Z (μm)
Sample (20 nm)	20	1	10
Sample (100 nm)	100	1	50
Sample (420 nm)	420	1	100
Boundary condition	Diffuse	Specular	Absorbing

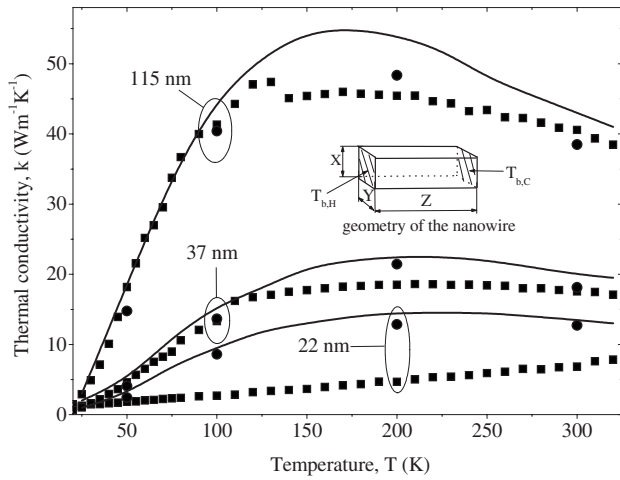


Fig. 12 Thermal conductivity along silicon nanowires (lines: Monte Carlo simulation from Ref. [12]; square symbols: experimental data from Ref. [17]; circle symbols: current Monte Carlo simulation)

bottom walls are considered diffuse ($d=0$), as in Liu and Asheghi [16]. The two remaining surfaces are considered specular. The relaxation time parameters of impurity and three-phonon scattering summarized in Table 1 are used. The average temperature of the film associated with the computed thermal conductivity is evaluated from Eq. (32) if the ballistic regime prevails, else, from an arithmetic mean of the boundary temperatures. Figure 11 compares the current simulation results with experimental data and predictions of Asheghi and co-workers [15,16]. We can see that:

- (i) The thermal conductivity along the film decreases with decreasing the film thickness because the scattering by boundaries, which contribute to the increasing of thermal resistance, are stronger for thinner than thicker films.
- (ii) The simulation results agree well with prior modeling and measurement data. The slight difference observed between both prediction methods can be attributed to the statistical errors of the Monte Carlo method, estimated about 5%.

The thermal conductivity of silicon nanowires has been measured by Li et al. [17] using analogous device as developed by Asheghi and co-workers [15,16]. The measurements were performed over a temperature range from 20 K to 320 K. Different nanowire sizes between 22 nm and 115 nm were analyzed. Recently, Chen et al. [12] and Chantrenne et al. [18] reported thermal conductivity predictions for the same silicon nanostructures. Chen et al. [12] used a Monte Carlo simulation based on Mazumder and Majumdar's algorithm [11], while Chantrenne et al. [18] used a similar analytical model as that developed by Asheghi et al. [15]. Using the current method, the thermal conductivity along silicon nanowires of widths equal to 22 nm, 37 nm, and 115 nm and over a temperature range of 40–300 K is simulated. The geometry used in the simulation is illustrated in Fig. 12, while its dimensions are reported in Table 3. According to the Mingo remark [23], diffuse boundary conditions ($d=0$) are applied along the nanowire surfaces. The simulation results, the Monte Carlo prediction of Chen et al. [12], and the available measurement of Li et al. [17] are compared in Fig. 12. We can note the following.

- (i) The current simulation predicts well the experimental data for nanowires having sizes greater than 22 nm. The deviation observed between both Monte Carlo results is mainly due to the difference in the value of the boundary scattering parameter d . In fact, Chen et al. [12] considered partially diffuse boundaries with $d=0.6$, while we

Table 3 Dimensions and boundary condition of studied silicon nanowires

	Nanowire dimensions $X=Y$ (nm)	Z (μm)
Sample (22 nm)	22	5
Sample (37 nm)	37	10
Sample (115 nm)	115	20
Boundary condition	Diffuse	Absorbing

have considered totally diffuse boundaries, i.e., $d=0$. It can be shown that partially diffuse boundaries lead to greater thermal conductivity than totally diffuse boundaries. Note that the current results are always smaller than that of Chen et al. [12], but the discrepancy is more noticeable for the biggest wire, i.e., 115 nm.

- (ii) The discrepancy between simulation results and experimental data for 22 nm nanowire width is not yet well understood. Different groups around the world have tried to explain this discrepancy and are continuing but unsuccessfully. Phonon confinement has been evoked as one of the sources of this disagreement [12,23]. In fact, it is suggested that the confinement of phonons and the corresponding change in phonon dispersion curves and, therefore, the group velocity may lead to increase in phonon scattering rates and, thus, drastic reduction in thermal conductivity [35–37] for silicon nanowire of thickness on the order of 10–20 nm. However, there could be other reasons, such as the presence of a large number of defects. To improve our simulation results, the phonon dispersion curves and relaxation rates associated with the 22 nm nanowire should be used instead of that of bulk silicon to account for the confinement. As the current paper is focused on the description and the validation of the new method; this improvement is not done here.

4 Conclusion

A Monte Carlo method enabling one to model correctly the steady-state phonon transport was presented. A novel algorithm to track phonons one by one and to treat phonon-phonon scattering, which accounts for the transition between the polarization modes and the nongray treatment of phonon lifetimes, has been introduced. First, the capability of the algorithm to capture the different phonon transport regimes and to model each scattering mechanism independent of others was examined. Then, it was applied to predict thermal conductivity along silicon thin films and silicon nanowires of different sizes and over a temperature range between 40 K and 300 K. The following conclusions can be drawn.

- (i) The comparison of the simulation results with exact solutions, prior predictions, and experimental data proves the capability of the proposed method of modeling the phonon transport in realistic micro- and nanostructures.
- (ii) The proposed algorithm has been revealed to be less memory demanding than transient Monte Carlo schemes. Then, it will be more suitable for modeling of phonon transport through complex materials such as materials, containing nanoparticles and/or nanopores.
- (iii) It was shown that this algorithm required only a few iterations to reach convergence. To reveal how much improvement the new algorithm can make in terms of convergence speed over conventional transient Monte Carlo algorithms, a benchmark will be conducted.
- (iv) To better simulate energy transport in materials having characteristic dimensions of several nanometers, future

work will focus on the implementation of the phonon dispersion curves and relaxation rates corresponding to the nanostructure.

Nomenclature

A	= boundary surface, m^2
a	= lattice parameter, m
B	= phonon relaxation time parameter
$\mathcal{D}, \dot{\mathcal{D}}$	= density of states, density of states per unit volume, s, $s\ m^{-3}$
d	= specular probability of boundary scattering
F	= cumulative probability distribution function
G	= phonon energy emitted/absorbed per unit time from/at a volume element
I^0	= phonon intensity at equilibrium, $J\ rad^{-1}\ m^{-2}\ sr^{-1}$
\hbar	= Planck constant divided by 2π , $1.054 \times 10^{-34}\ J\ s$
k	= thermal conductivity, $W\ m^{-1}\ K^{-1}$
k_B	= Boltzmann constant, $1.38 \times 10^{-23}\ J\ K^{-1}$
Kn	= Knudsen number
ℓ	= effective mean free path of phonon, m
LA	= longitudinal acoustic polarization
m_p	= number of frequency bands of polarization mode p
M	= number of phonons emitted per unit time from a volume element, phonons/s
N	= number of phonons emitted per unit time from a boundary, phonons/s
n	= phonon distribution function
$\langle n \rangle$	= Bose–Einstein (or equilibrium) phonon distribution function
N_{bw}	= number of black boundaries
N_{cell}	= number of cells
p	= polarization mode
$P(p)$	= probability for phonons to have a polarization mode p
Q	= phonon flux or energy emitted/absorbed per unit time from/at a boundary, W
r	= atomic radius of impurity (or defect radius), m
s	= phonon position vector, m
T	= temperature, K
t	= time, s
TA, TA1, TA2	= transverse acoustic phonon modes
u	= energy per unit volume, $J\ m^{-3}$
U	= energy, J
\mathbf{v}_g	= phonon group velocity vector, $s^{-1}\ m$
\mathbf{v}_p	= phonon phase velocity vector, $s^{-1}\ m$
V	= volume of a cell, m^3
X	= material dimension along the x axis of a Cartesian reference, m
Y	= material dimension along the y axis of Cartesian reference, m
z	= axis of a Cartesian reference oriented in the direction of the heat flux
Z	= material dimension along the z axis, m

Greek Symbols

β	= constant in the impurity relaxation time
χ	= defect size parameter
Δ	= wave vector direction
Δt	= time step, m
$\Delta\omega$	= width of angular frequency band, $s^{-1}\ rad$
δ	= defects or impurity density, atoms/ m^3
φ	= azimuth angle, rad
κ	= phonon wave vector, m^{-1}

λ	= phonon wavelength, m
λ	= distance between the phonon and the next scattering point, m
θ	= polar angle, rad
σ	= relative standard deviation
τ	= phonon relaxation time, s
ϖ	= defect and impurity scattering probability
ω	= phonon angular frequency, $s^{-1}\ rad$
$\omega_m(p)$	= cutoff angular frequency associated with the polarization mode p , $s^{-1}\ rad$
Ω	= solid angle, sr
ξ	= random numbers between zero and unity

Subscripts

b	= refers to boundary temperature
bd	= refers to scattering by boundary
C	= refers to cold boundary
coll	= refers to collision or scattering
eff	= refers to effective phonon relaxation time
H	= refers to hot boundary
I	= refers to scattering by impurities and defects
m	= refers to the wave number or frequency value at the boundary of the first Brillouin zone
N	= refers to the normal process
new	= refers to the position vector at the interaction point
p	= refers to the polarization mode
Q	= refers to the standard deviation on the net flux
S	= refers to the simulated phonon number
T	= refers to the standard deviation on the temperature
U	= refers to the Umklapp process
vol	= refers to volume scattering
ω	= refers to spectral quantity
1/2	= refers to the frequency of the transverse mode corresponding to the reduced wave number $\kappa^* = 0.5$
3ph	= refers to three-phonon scattering

Superscripts

+	= refers to phonon emitted from an element
−	= refers to phonon absorbed at an element
*	= refers to reduced wave vector κ^*

References

- [1] Majumdar, A., 1998, *Microscale Energy Transport*, C. L. Tien, A. Majumdar, and F. M. Gerner, eds., Taylor & Francis, Washington, DC.
- [2] Ziman, J. M., 2001, *Electrons and Phonons*, 2nd ed., Cambridge University Press, London.
- [3] McConnell, A. D., and Goodson, K. E., 2005, "Thermal Conduction in Silicon Micro- and Nanostructures," *Annu. Rev. Heat Transfer*, **14**, pp. 129–168.
- [4] Majumdar, A., 1993, "Microscale Heat Conduction in Dielectric Thin Films," *ASME J. Heat Transfer*, **115**, pp. 7–16.
- [5] Chung, J. D., and Kaviany, M., 2000, "Effects of Phonon Pore Scattering and Pore Randomness on Effective Conductivity of Porous silicon," *Int. J. Heat Mass Transfer*, **43**, pp. 521–538.
- [6] Sverdrup, P. G., Ju, Y. S., and Goodson, K. E., 2001, "Sub-Continuum Simulations of Heat Conduction in Silicon-on-Insulator Transistors," *ASME J. Heat Transfer* **123**, pp. 130–137.
- [7] Narumanchi, S. V. J., Murthy, J. Y., and Amon, C. H., 2004, "Submicron Heat Transport Model in Silicon Accounting for Phonon Dispersion and Polarization," *ASME J. Heat Transfer*, **126**, pp. 946–955.
- [8] Murthy, J. Y., and Mathur, S. R., 2002, "Computation of Sub-Micron Thermal Transport Using an Unstructured Finite Volume Method," *ASME J. Heat Transfer*, **124**, pp. 1176–1181.
- [9] Pilon, L., and Katika, K. M., 2004, "Modified Method of Characteristics for Simulating Microscale Energy Transport," *ASME J. Heat Transfer*, **126**, pp. 35–743.
- [10] Peterson, R. B., 1994, "Direct Simulation of Phonon-Mediate Heat Transfer in a Debye Crystal," *ASME J. Heat Transfer*, **116**, pp. 815–822.
- [11] Mazumder, S., and Majumdar, A., 2001, "Monte Carlo Study of Phonon

- Transport in Solid Thin Films Including Dispersion and Polarization," ASME J. Heat Transfer, **123**, pp. 749–759.
- [12] Chen, Y., Li, D., Lukes, J. R., and Majumdar, A., 2005, "Monte Carlo Simulation of Silicon Nanowire Thermal Conductivity," ASME J. Heat Transfer, **127**, pp. 1129–1137.
- [13] Sinha, S., Pop, E., Dutton, R. W., and Goodson, K. E., 2006, "Non-Equilibrium Phonon Distributions in Sub-100 nm Silicon Transistors," ASME J. Heat Transfer, **128**(7), pp. 638–647.
- [14] Murthy, J. Y., Narumanchi, S. V. J., Pascual-Gutierrez, J. A., Wang, T., Ni, C., and Mathur, S. R., 2005, "Review of Multiscale Simulation in Submicron Heat Transfer," Int. J. Multiscale Comp. Eng., **3**, pp. 5–32.
- [15] Asheghi, M., Touzelbaev, M. N., Goodson, K. E., Leung, Y. K., and Wong, S. S., 1998, "Temperature Dependent Thermal Conductivity of Single-Crystal Silicon Layers in SOI Substrates," ASME J. Heat Transfer, **120**, pp. 30–36.
- [16] Liu, W., and Asheghi, M., 2006, "Thermal Conductivity of Ultra-Thin Single Crystal Silicon Layers," ASME J. Heat Transfer, **128**, pp. 75–83.
- [17] Li, D., Wu, Y., Kim, P., Shi, L., Yang, P., and Majumdar, A., 2003, "Thermal Conductivity of Individual Silicon Nanowires," Appl. Phys. Lett., **83**, pp. 2934–2936.
- [18] Chantrenne, P., Barrat, J. L., Blasé, X., and Gale, J. D., 2005, "An Analytical Model for the Thermal Conductivity of Silicon Nanostructures," J. Appl. Phys., **97**, p. 104318.
- [19] Kittel, C., 1986, *Introduction to Solid State Physics*, 6th ed., Wiley, New York.
- [20] Chung, J. D., Mc Gaughey, A. J. H., and Kaviani, M., 2004, "Role of Phonon Dispersion in Lattice Thermal Conductivity Modeling," ASME J. Heat Transfer, **126**, pp. 376–380.
- [21] Modest, M. F., 1993, *Radiative Heat Transfer*, McGraw-Hill, New York.
- [22] Brockhouse, B. N., 1959, "Lattice Vibrations in Silicon and Germanium," Phys. Rev. Lett., **2**, pp. 256–258.
- [23] Mingo, N., 2003, "Calculation of Si Nanowire Thermal Conductivity Using Complete Phonon Dispersion Relations," Phys. Rev. B, **68**, p. 113308.
- [24] Chen, G., 2000, "Phonon Heat Conduction in Nanostructures," Int. J. Therm. Sci., **39**, pp. 471–480.
- [25] Brewster, M. Q., 1992, *Thermal Radiative Transfer and Properties*, Wiley, New York.
- [26] Vincenti, W. G., and Kruger, C. H., 1965, *Introduction to Physical Gas Dynamics*, Wiley, New York.
- [27] Bohren, C. F., and Huffman, D. R., 1983, *Absorption and Scattering of Light by Small Particles*, Wiley, New York.
- [28] Holland, M. G., 1963, "Analysis of Lattice Thermal Conductivity," Phys. Rev., **132**, pp. 2461–2471.
- [29] Han, Y. J., and Klemens, P. G., 1993, "Anharmonic Thermal Resistivity of Dielectric Crystal at Low Temperatures," Phys. Rev. B, **48**, pp. 6033–6042.
- [30] Tamura, S., 1985, "Spontaneous Decay Rates of LA Phonons in Quasi-Isotropic Solids," Phys. Rev. B, **31**, pp. 2574–2598.
- [31] Tamura, S., and Maris, H. J., 1995, "Temperature Dependence of Phonon Lifetime in Dielectric Crystal," Phys. Rev. B, **51**, pp. 2857–2863.
- [32] Waugh, J. L., and Dolling, G., 1963, "Crystal Dynamics of Gallium Arsenide," Phys. Rev., **132**, pp. 2410–2412.
- [33] Lacroix, D., Joulain, K., and Lemonnier, D., 2005, "Monte Carlo Transient Phonon Transport in Silicon and Germanium at Nanoscales," Phys. Rev. B, **72**, p. 064305.
- [34] Sondheimer, E. H., 2001, "The Mean Free Path of Electrons in Metals," Adv. Phys., **50**(6), pp. 499–537.
- [35] Nishiguchi, N., 1996, "Electron Scattering Due to Confined and Extended Acoustic Phonons in a Quantum Wire," Phys. Rev. B, **54**, pp. 1494–1497.
- [36] Bannov, N., Aristov, V., and Mitin, V., 1995, "Electron Relaxation Times Due to the Deformation-Potential Interaction of Electrons With Confined Acoustic Phonons in a Free-Standing Quantum Well," Phys. Rev. B, **51**, pp. 9930–9942.
- [37] Zou, J., and Balandin, A., 2001, "Phonon Heat Conduction in a Semiconductor Nanowire," J. Appl. Phys., **89**, pp. 2932–2938.

Numerical Experiments in Turbulent Natural Convection Using Two-Equation Eddy-Viscosity Models

X. Albets-Chico

A. Oliva¹

C. D. Pérez-Segarra

Centre Tecnològic de Transferència de Calor,
Universitat Politècnica de Catalunya (UPC),
ETSEIAT, C/ Colom 11,
08222 Terrassa, Catalunya, Spain

This work is focused on the simulation and prediction of turbulent natural convection flows by means of two-equation eddy-viscosity models. In order to show the generality, precision, and numerical issues related to these models under natural convection, three different buoyancy-driven cavities have been simulated: a tall cavity with a 30:1 aspect ratio, a cavity with a 5:1 aspect ratio, and, finally, a 4:1 aspect ratio cavity. All cases are solved under moderate and/or transitional Rayleigh numbers (2.43×10^{10} , 5×10^{10} , and 1×10^{10} , respectively) and all simulations are compared to experimental and/or direct numerical simulation data available in literature. These different situations allow to check the applicability of two-equation eddy-viscosity models in buoyancy-driven flows, giving criteria on computational effort/precision and their physical behavior.
[DOI: 10.1115/1.2907432]

Keywords: turbulence, buoyancy, natural convection, two equation, $k-\epsilon$, $k-\omega$

1 Introduction

Turbulent flows, driven or affected by buoyancy, are an important type of flows that arise in many engineering applications, such as heating, ventilating, and air conditioning (HVAC), ventilated facades, electronic equipment, solar energy collectors, cooling of nuclear reactors, material processing, etc. Heat transfer and fluid flow related to these cases are strongly affected by the transition point from laminar to turbulent flow and by the Rayleigh number.

Direct CFD solution of the Navier–Stokes equations demands high CPU-time requirements due to the unsteadiness and three-dimensional nature of turbulent situations. Consequently, direct numerical simulations (DNS) [1] are only available, at the moment, in low-Rayleigh number and simple geometry cases. For more general situations, it is necessary to use other kinds of tools to obtain numerical solutions in turbulent flows with a much lower CPU-time effort.

Among other types of models [1], Reynolds averaged Navier–Stokes (RANS) techniques have been chosen in this work. RANS techniques are based on a time-averaged filtering of the governing equations. Historically, these models have been designed and fitted under turbulent forced convection situations. Because of this, different researchers (Davidson [2,3], Hanjalić [4–6], Ince and Launder [7], etc.) have carried out an additional effort to enable these models to solve turbulent natural convection cases with a relative precision and low computational cost.

Since there are a lot of industrial situations where information on turbulent natural convection is required, the main objective of this work is to show the possibilities of RANS two-equation eddy-viscosity models as a tool to describe them. To achieve this task in a moderately high-Rayleigh number situations, different $k-\epsilon$ and $k-\omega$ models have been used.

These models allow to obtain numerical solutions in a relative short CPU time, with reasonably accurate results on different tur-

bulent buoyancy-driven differentially heated cavities with different aspect ratios (30:1, 5:1, and 4:1) at different Rayleigh numbers, as shown henceforth.

The first cavity (also called tall cavity because of its high height/width relation) presents a characteristic structure. This flow is completely developed, i.e., hot and cold thermal boundary layers interact and show a turbulent core and laminar sublayers near the walls. The influence of the corners is negligible, and the temperature field is strongly affected by convection. The second case exhibits a different behavior. Because of the lower aspect ratio, two different thermal boundary layers are developed, and the lower part of the hot wall and the upper of the cold, e.g., the core of the cavity, remain laminar. In this situation, the ability of different models to describe the transition point will be an important aspect to achieve credible predictions. This aspect is also related to different problems, which affect the convergence and asymptotic behavior of the results, as has been indicated in literature [2,8]. Finally, the third cavity, because of the even smaller aspect ratio and the lower Rayleigh number, amplifies previous perspective and brings clarity to the limiting skills and drawbacks of RANS models to predict turbulent natural convection.

2 Mathematical Models

Different two-equation eddy-viscosity models have been tested to predict fluid flow and heat transfer in turbulent natural convection cavities. As it is well known, such kind of models are designed over a time-averaged Navier–Stokes set of equations (RANS). The models use the “eddy” viscosity as an intermediate variable to model turbulent flow stresses and heat transfer. This “intermediate” variable is obtained using two different turbulent quantities: turbulent kinetic energy and a variable related to its dissipation. Both variables are obtained from the resolution of their own transport equation.

2.1 Governing Equations. The time-averaged governing equations (continuity, momentum and energy) of the fluid flow assuming fluid Newtonian behavior, constant thermophysical properties, nonparticipant radiant medium and negligible heat friction, and influence of pressure on temperature are written in tensor notation as

¹Corresponding author.

Contributed by the Heat Transfer Division of ASME for publication in the JOURNAL OF HEAT TRANSFER. Manuscript received March 5, 2007; final manuscript received October 17, 2007; published online May 19, 2008. Review conducted by Gautam Biswas.

Table 1 Terms in turbulence models used in this work

Term	IL model	GPC model	WX88 model	WX93 model	PDH+D model
π_k	$\rho(\bar{\epsilon}+D)$	$\rho\epsilon$	$C_\mu\rho\omega k$	$C_\mu f_k\rho\omega k$	$C_\mu f_k\rho\omega k$
S_k	G_k	G_k	G_k	G_k	G_k
P_z	$c_1 P_k(\bar{\epsilon}/k)$	$c_1 f_1 P_k(\epsilon/k)$	$c_1 P_k(\omega/k)$	$c_1 f_1 P_k(\omega/k)$	$c_1 f_1 P_k(\omega/k)$
π_z	$c_2 f_2 \rho(\bar{\epsilon}^2/k)$	$c_2 f_1 \rho(\epsilon^2/k)$	$c_2 \rho\omega^2$	$c_2 \rho\omega^2$	$c_2 \rho\omega^2$
S_z	$c_1 c_3 G_k(\bar{\epsilon}/k)+E+YAP$	$c_1 c_3 f_1 G_k(\epsilon/k)+f_1 YAP$	—	—	C_ω

$$\frac{\partial \bar{u}_i}{\partial x_i} = 0 \quad (1)$$

$$\rho \frac{\partial \bar{u}_i}{\partial t} + \rho \bar{u}_j \frac{\partial \bar{u}_i}{\partial x_j} = -\frac{\partial \bar{p}}{\partial x_i} + \frac{\partial \tau_{ij}}{\partial x_j} - \rho \beta (\bar{T} - T_0) g_i \quad (2)$$

$$\rho \frac{\partial \bar{T}}{\partial t} + \rho \bar{u}_i \frac{\partial \bar{T}}{\partial x_i} = -\frac{1}{c_p} \frac{\partial \dot{q}_i}{\partial x_i} \quad (3)$$

where

$$\tau_{ij} = \mu \left(\frac{\partial \bar{u}_i}{\partial x_j} + \frac{\partial \bar{u}_j}{\partial x_i} \right) - \overline{\rho u'_i u'_j} \text{ and } q_i = -\lambda \frac{\partial \bar{T}}{\partial x_i} + c_p \overline{\rho u'_i T'}$$

As previously mentioned, as a consequence of the time-averaging process of the Navier–Stokes equations, new terms have appeared in momentum and energy equations. They are the Reynolds stress tensor ($\overline{\rho u'_i u'_j}$) and turbulent heat flux ($\overline{\rho u'_i T'}$). Using eddy-viscosity models, these terms are modeled by analogy with the Stokes viscosity law and the Fourier heat conduction through the eddy viscosity (μ_t):

$$\overline{\rho u'_i u'_j} = -\mu_t \left(\frac{\partial \bar{u}_i}{\partial x_j} + \frac{\partial \bar{u}_j}{\partial x_i} \right) + \frac{2}{3} \rho k \delta_{ij} \quad (4)$$

$$\overline{\rho u'_i T'} = -\frac{\mu_t}{\sigma_T} \frac{\partial \bar{T}}{\partial x_i} \quad (5)$$

2.2 Turbulence Models. Two-equation eddy-viscosity models are based on the resolution of the turbulent viscosity (μ_t) by means of two different turbulent quantities: the turbulent kinetic energy (k) and another quantity related to its dissipation (e.g., the dissipation rate of turbulent kinetic energy (ϵ), the specific turbulent kinetic energy dissipation (ω), the characteristic time of turbulent kinetic energy dissipation (τ), etc.). In this paper, k - ϵ and k - ω models are employed. Both turbulent quantities are obtained from the resolution of their own transport equations: Eq. (6) for the turbulent kinetic energy (k) and Eq. (7) for its dissipation rate ($z = \epsilon$ or $z = \omega$). Hence, the additional set of equations that closes the problem is

$$\rho \frac{\partial k}{\partial t} + \rho \bar{u}_i \frac{\partial k}{\partial x_i} = \frac{\partial}{\partial x_i} \left[\left(\mu + \frac{\mu_\tau}{\sigma_k} \right) \frac{\partial k}{\partial x_i} \right] + P_k - \pi_k + S_k \quad (6)$$

$$\rho \frac{\partial z}{\partial t} + \rho \bar{u}_i \frac{\partial z}{\partial x_i} = \frac{\partial}{\partial x_i} \left[\left(\mu + \frac{\mu_t}{\sigma_z} \right) \frac{\partial z}{\partial x_i} \right] + P_z - \pi_z + S_z \quad (7)$$

$$\mu_t = C_\mu f_\mu \rho k^{1/2} l \quad (8)$$

where $P_k = -\overline{\rho u'_i u'_j} (\partial \bar{u}_i / \partial x_j)$, being the generation of turbulent kinetic energy due to the shear stress, which plays an important role in combination with the generation/destruction of turbulent kinetic energy due to the buoyancy effects (G_k), as explained in this paper.

As exposed, the turbulent or eddy viscosity is directly propor-

tional to both the square root of the turbulent kinetic energy ($k^{1/2}$) and the turbulent length scale (l), which is given by $l = k^{3/2} / \epsilon$ for k - ϵ models and by $l = k^{1/2} / \omega$ for k - ω models.

The high- and low-Reynolds number k - ω models by Wilcox (WX88 [9], WX93 [10]) and by Peng–Davidson–Holmberg (PDH+D) with G_k corrections [2] have been used in this work. Among k - ϵ models, the Ince–Launder (IL) model [7] and the Goldberg–Perroomian–Chakravarthy (GPC) model [11] have been employed. A summary of the terms used by these models is presented in Table 1.

The generic dissipative variable (z) adopts three different forms depending on the model. GPC model [11] uses the standard dissipation rate (ϵ), while the IL model [7] uses the “corrected” dissipation rate ($\bar{\epsilon}$). On the other hand, WX88 [9], WX93 [10], and PDH+D [2] models employ the specific dissipation rate (ω). The corrected dissipation rate ($\bar{\epsilon}$) is a numerical correction needed to achieve a zero dissipation value at the wall ($\bar{\epsilon}_w = 0$). Consequently, a D term in k -equation has to be added, which is the asymptotic value of ϵ at wall: $D = 2\nu \partial k^{1/2} / \partial x_j$. Hence, for the IL model ϵ at wall is set to 0 while for the GPC model is set to $\epsilon_w = 2\nu k_p / y_p^2$ (being k_p the turbulent kinetic energy of the first inner node and y_p the distance to the wall). Finally, for the k - ω models, $\omega = 6\nu / \beta y_p^2$ has been prescribed at the first inner node, as the value at the wall is theoretically infinity (being y_p the distance to the wall).

Models constants and damping functions have not been here included for brevity. They are clearly stated in original references: Ref. [11] for the GPC model, Ref. [7] for the IL model, Ref. [9] for the WX88 model, Ref. [10] for the WX93 model, and, finally, Ref. [2] for the PDH+D model.

2.3 Buoyancy Effects. The treatment of the buoyancy term in the turbulent transport equations needs to be especially observed, since the behavior of turbulence models in natural convection is strongly affected by this term. Table 2 indicates the different G_k terms adopted for the models. Simple gradient diffusion hypothesis (SGDH) has been adopted for GPC, WX88, and WX93 models in this work. Since these models were designed under forced convection cases, present adaptation to natural convection flows has been carried out using the simplest method. On the contrary, IL and PDH+D models show specific treatments for buoyancy term, while IL model uses the generalized gradient diffusion hypothesis (GGDH).

Table 2 G_k term for all models

	G_k
IL model	$-g_j \beta \rho \left(-\frac{3}{2} \frac{C_\mu f_\mu}{\sigma_T} k l \epsilon \overline{u'_i u'_k} \frac{\partial T}{\partial x_k} \right)$ (GGDH)
GPC/ WX88/ WX93 model	$-g_j \beta \rho \left(-\frac{\mu_t}{\sigma_T} \frac{\partial T}{\partial x_j} \right)$ (SGDH)
PDH+D model	$-g_j \beta \rho \left(\frac{\mu_t}{\sigma_T} \frac{\partial T}{\partial x_j} \right) \left[\left(1 - \exp \left[\left(\frac{R_i}{12} \right)^3 \right] \right) \left(1 + \frac{10}{R_i^{3.25}} \right) \right]$ (SGDH+Damp. f.)

Table 3 Cavity 1 ($A=30$, $Ra_H=2.43 \times 10^{10}$). WX93 convergence-estimators using five meshes: $m1$, $m2$, $m3$, $m4$, $m5$ (10×10 CV, 20×20 CV, 40×40 CV, 80×80 CV, 160×160 CV). Acceptable converged solution (p between 1 and 2, high percentage of *Richardson nodes*).

Grid $n_3/n_2/n_1$	$v^* = \bar{v}/u_{ref}$			$T^* = \bar{T}/\Delta T_{ref}$			$k^* = k/u_{ref}^2$		
	Rn (%)	p	GCI* (%)	Rn (%)	p	GCI* (%)	Rn (%)	p	GCI* (%)
$m1\ m2\ m3$	83	1.6	$2.4E-01$	88	0.5	$3.2E+00$	70	1.1	$7.2E-03$
$m2\ m3\ m4$	93	1.7	$7.2E-02$	90	1.0	$5.7E-01$	87	1.0	$3.6E-03$
$m3\ m4\ m5$	91	1.4	$3.6E-02$	95	1.0	$3.0E-01$	94	1.2	$1.4E-03$

prothesis (GGDH) to account for temperature gradients, which are orthogonal to the gravity vector. PDH+D applies the usual SGDHD adding a damping function, which improves numerical behavior and model accuracy in transitional natural induced flows. See details in Refs. [2,7].

As it can be inferred from general formulation, current $k-\omega$ models do not present any specific buoyancy term for ω -equation. In fact, this is in agreement with different authors, e.g., Markatos et al. [12,13] (who stated there was evidence that buoyancy effect should be reflected only in the k -equation), Heindel [14] (who detected a negligible effect of constant c_3), or Peng and Davidson [2] (who directly fixed $c_3=0$ for PDH+D model). Additionally, different computations have been carried out by present work and a negligible effect of the c_3 constant has been obtained for $k-\omega$ models. On the contrary, for IL and GPC models, the use of $c_3 = \tanh|u/v|$ has been maintained, following suggestions made by Henkes [17] in order to achieve Rodi's reasonings [18] (c_3 should be close to unity in the vertical boundary layer and close to 0 in the horizontal boundary layer) [2].

3 Numerical Aspects

3.1 Numerical Procedure. The set of governing partial differential equations (Eqs. (1)–(3) and Eqs. (6) and (7)) have been solved using finite volume techniques. Two different structured grids have been employed: staggered meshes (where velocities are calculated on the control volume faces) and collocated meshes (where velocities are calculated on the control volume nodal points using the Rhie–Chow interpolation method). Fully implicit time integration has been applied and a pressure based method of the Semi-implicit method for pressure-linked equations [19] (SIMPLE) family is used to solve the velocity-pressure field coupling. Central differences are employed for the evaluation of diffusion terms and convective terms are discretized by means of UPWIND and/or SMART schemes for all test cases. A multigrid iterative solver is used to solve the algebraic linear system of equations. For k and $\epsilon/\bar{\epsilon}$ or ω equations, source terms have been linearized in the usual form [19] to adding unconditional positive values avoiding numerical instabilities. All simulations have been carried out using a pseudotransient iterative algorithm, applying the highest time step, which has ensured convergence, which, generally, depends on the case and on the model. The coarsest grid of 10×10 CV volumes has been used, doubling number of CV as grid refinement is applied, and the finest mesh of 160×160 CV has been chosen.

In order to correctly reproduce the rapid gradients, which take place near walls, the adopted meshes have been designed using a hyperbolic tangent stretching (detailed in Ref. [8]) close to the isothermal and adiabatic boundaries. For all presented cavity flows, a factor of 3.0 has been applied for the vertical isothermal walls, and a factor of 2.5 for the horizontal adiabatic ones.

3.2 Numerical Solution Verification. Numerical solutions are verified using a postprocessing procedure based on the generalized Richardson extrapolation for h -refinement studies and on

the grid convergence index (GCI) proposed by Roache [20,21].

This technique is useful to establish criteria on the sensitivity of the simulation to the computational model parameters, which account for the discretization: the mesh spacing and the order of accuracy of the numerical solutions (observed order of accuracy p). The error band, where the independent grid solution is expected to be contained (uncertainty due to discretization, GCI), and criteria on the credibility of these estimations are also achieved by this process. Local estimators of the GCI and p are calculated at the grid nodes where their evaluation is possible. These grid nodes are called *Richardson nodes*. Global values of GCI and p are obtained by means of volumetric averaging. An estimation is considered credible when the global observed order of accuracy p approaches its theoretical value, and when the percentage of Richardson nodes is high enough.

More concretely, present work has generally employed a series of five meshes ($m1, \dots, m5$). The order of accuracy p , the percentage of Richardson nodes, and the normalized error estimation have been checked for each group of three consecutive meshes. This is to say, three consecutive meshes define a monotonic numerical convergence behavior. Consequently, an estimation for the final solution can be obtained if the percentage of Richardson nodes is high enough and the reached order of accuracy is close to its theoretical value (which depends, essentially, on the discretization for the convective and the diffusive terms). The finest mesh solution (for each group of meshes) is compared to the respective estimated independent grid solution. This difference is normalized by a reference value and presented in Tables 3 and 5–7 as a percentage.

As seen, this technique is able to detect nonmonotonic numerical convergence (when the percentage of Richardson nodes is low, or when the order of accuracy (p) is far from the expected value). On the other hand, when both parameters are placed between acceptable values, a credible error band where the independent grid solution is expected to be contained (uncertainty due to discretization, GCI) is reliable. If the error band is relatively small, the final solution is acceptable. Otherwise, one can continue the h -refinement until the error band is between acceptable limits. As shown afterwards, nonmonotonic numerical convergence could reveal numerical problems, which do not allow the model to converge toward an independent grid solution.

Present work has encountered all these situations. This numerical tool has been very effective to corroborate numerical problems, which were already pointed in diverse precedent publications (i.e., Refs. [2,8]) and very helpful to ensure the numerical accuracy of present final solutions. See Refs. [20–22] for details.

4 Test Cases and Results

Results computed with previously exposed turbulence models are presented in this section. They are discussed through comparison with experimental and/or DNS data. Various cavity configurations have been used in several experimental and numerical works available in literature. Three different test cases have been chosen in order to investigate the behavior of different models

when solving the turbulent natural convection. The differentially heated cavities of aspect ratios 30:1, 5:1, and 4:1, in combination with their based-on-height Rayleigh numbers ($Ra_H=2.43 \times 10^{10}$, 5×10^{10} , and 1×10^{10} , respectively) have been selected as they present different turbulent natural convection phenomena, which is interesting in order to test turbulence models' abilities and limitations. For all cases, the vertical walls are isotherms (at different temperatures) while the top and bottom walls are adiabatic. As shown, major problems take place when sudden relaminarization occurs in the core of the 4:1 and 5:1 cavities, and when turbulence regime is moderate or low. Hence, cavities of aspect ratios 5:1 and 4:1 present the most difficult aspects for turbulence models as detailed in this study.

4.1 Natural Turbulent Convection in a 30:1 Heated Cavity. This case corresponds to a differentially heated tall cavity with an aspect ratio of 30 (H/W) and a Rayleigh number based-on-height cavity H ($Ra_H=g\beta\Delta T_{ref}H^3Pr/\nu^2$) of 2.43×10^{10} . This is a natural convection cavity flow generated with two isothermal walls (east and west), and two adiabatic walls (north and south). The work of Daffa'alla and Betts [15] presents experimental results, which are used to check accuracy of the models.

This case has been solved for all models using a collocated discretization (able to solve complex geometries) and UPWIND as a numerical scheme for the convective terms. The influence of the spatial discretization and the numerical scheme for convective terms have been tested through comparison with two additional simulations: First, IL model over a staggered grid and, second, SMART for convective terms. Based on a mesh of 160×160 control volumes, the first comparison (collocated versus staggered) shows that the maximum relative difference (using nondimensional velocities, temperatures, and lengths) [8] are of 0.1% for \bar{u} , 0.7% for \bar{v} , and 0.4% for \bar{T} , while the relative differences in turbulent quantities are even smaller. The second comparison (UPWIND versus SMART) has shown maximum differences of 0.4% for \bar{u} , 4.0% for \bar{v} , and 4.5% for \bar{T} and once again smaller differences for the turbulent quantities, which was expected. Since the differences are relatively small and the flow is buoyancy affected, UPWIND scheme seems to be good enough to study the behavior of turbulence models to predict turbulent natural convection in the present case.

The influence of grid refinement is tested in the evolution of global parameters as \overline{Nu} . Moreover, the results of the local estimators p and GCI on the convergence show that the numerical results are credible using 160×160 CV for all models, spatial discretizations, and numerical schemes. As an example, the results of the verification process for WX93 model using UPWIND scheme over a collocated grid are shown in Table 3 for v^* , T^* , and k^* .

As shown in Table 3, the order of accuracy (p) has the expected value when using UPWIND scheme (approximately 1), the GCI values are low enough in last mesh, and the percentage of Richardson nodes is high enough. All these estimators conclude that 160×160 CV are sufficient to obtain a credible numerical solution. The convergence behavior of the other simulations have been similar. PDH+D model has passed the verification process only with four meshes, since it has not been possible to reach convergence with the coarsest mesh (10×10 CV), as this model uses a cross-diffusion term in ω -equation, which implies the need of a finer initial grid. A comparison of different turbulence models and the experimental results reported by Daffa'Alla and Betts [15] is presented in Table 4.

The heat transfer rate (mean Nusselt number) is underpredicted for all models, except IL and PDH+D. IL is the model that presents better behavior, as its results are relatively close to the experimental ones (see Fig. 1(b)). Its special treatment of the G_k term (GGDH) improve predictions. It is interesting to say that the PDH+D model notoriously enhances accuracy showed by the other $k-\omega$ models (WX88 and WX93), which present poorer

Table 4 Cavity 1 ($A=30$, $Ra_H=2.43 \times 10^{10}$). The difference (in percentage) with respect to the experimental data [15] ($\overline{Nu}=149$, μ_t^* at center=30.4).

Turbulence model	\overline{Nu}	μ_t^* at center
IL model	150.65(1%)	27.11(-12%)
GPC model	131.31(-12%)	22.56(-25%)
WX88 model	135.87(-9%)	24.33(-20%)
WX93 model	133.67(-10%)	21.83(-28%)
PDH+D model	152.75(2.5%)	24.69(-19%)

agreement with the experimental data. This was expected as they are models designed for forced convection cases. The PHD+D model provides these improvements by redesigning model constants, adding a cross-diffusion term for ω -equation and a damping function in G_k calculus.

However, all models have reasonably given accurate results. The reason could be probably found in the geometry of the case. More concretely, the tending-to-infinity cavity aspect ratio ensures, as has been previously introduced, the collapse of both turbulent boundary layers (from hot and cold walls), showing a complete turbulent core of the cavity. As two-equation turbulent models have been deeply suited to forced convection cases, typical transition from laminar to turbulent flow due to the wall-damping effects (i.e., the resolution of viscous sublayer and the normal-to-wall increasing turbulence intensity) has been qualitatively well captured for all low-Reynolds number models, as well as for the $k-\omega$ WX88 model, which in spite of its high-Reynolds number model condition is able to provide both viscous and inertial layer solutions, thanks to the use of ω as dissipation quantity.

Next cases, however, will show different geometries and, consequently, different flow structures. Two-equation turbulence models will be checked under relaminarization produced by the geometry, as now shown.

4.2 Natural Turbulent Convection in a 5:1 Heated Cavity.

This case corresponds to a differentially heated rectangular cavity with an aspect ratio of 5 (H/W) and a Rayleigh number based-on-height cavity H (being $Ra_H=g\beta\Delta T_{ref}H^3Pr/\nu^2$) of 5×10^{10} . The boundary conditions of the case follows the same pattern than presented for 30:1 cavity: Two vertical isothermal walls and adiabatic top and bottom walls. With reference to accuracy of the models, the experimental data from Cheesewright et al. [16] have been used to analyze turbulence models' predictions.

In order to test the influence of the numerical scheme, another comparison (UPWIND versus SMART) has been done, this time using WX93 model. Higher differences (2% for \bar{u} , 6.75% for \bar{v} , and 4.6% for \bar{T}) than the first cavity problem (30:1 aspect ratio) have been obtained, probably due to the recirculating effects. In spite of this, UPWIND has been the numerical scheme used in all simulations. Their results are acceptable to predict asymptotic transition point while this scheme allows faster and more stable numerical convergence because of its dissipative essence [23].

Historically, this case has reported different numerical problems when using low-Reynolds number turbulence models. Some researchers like Peng and Davidson [2], Pérez-Segarra et al. [8], etc., found that two-equation eddy-viscosity models were incapable to reproduce this case with realistic behavior, due to the encounter of numerical problems.

More concretely, Peng and Davidson [2] detected and corrected a grid degradation of buoyancy effects (G_k). In fact, as grid is refined, SGD approach is related to an increasing overestimation of G_k , which (since this case presents a stable stratification in the core of the cavity) becomes a sink term (gravity vector and temperature gradient vector have the same direction and sign). Therefore, the increasing G_k sink term provokes the creeping evolution to a laminar solution as the grid is refined, which obviously dis-

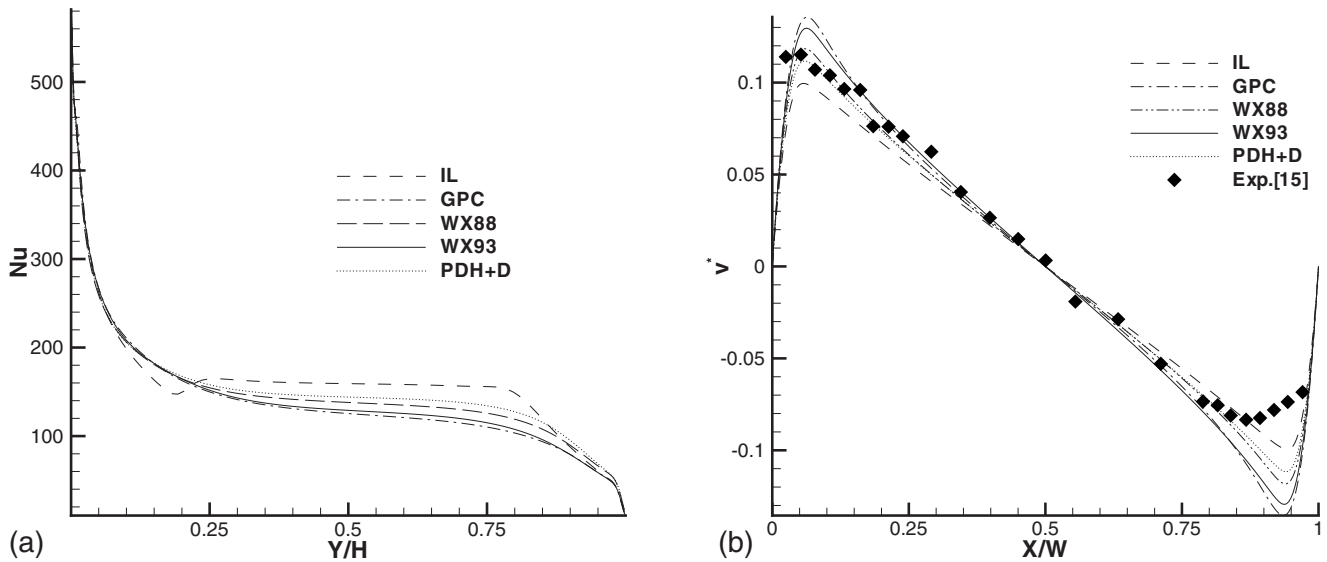


Fig. 1 Cavity 1 ($A=30$, $Ra_H=2.43 \times 10^{10}$). \bar{Nu} prediction (a) and \bar{v} at $y=H/2$ prediction (b) for all the models.

torts accuracy and disables computation credibility. This effect can be checked in Fig. 2, where the WX93 model with SGD and the PDH+D model (which uses SGD with a damping function f_g) are compared. As it is visible, normalized buoyancy effect (i.e., $N_{kb}=G_k/C_\mu k\omega$) obtained using SGD becomes degraded when refining. However, when using f_g damping function asymptotic buoyancy effects are obtained, and a final turbulent prediction is achieved. It is interesting to note that the WX88 model does not present this grid degradation, and its verification estimators are placed in the desired range. Hence, SGD grid sensitivity seems to be closely related to damping functions (which are applied on WX93 and GPC models), and do not appear in the WX88 model. This is in agreement with the work of Peng and Davidson [2], who encountered the same problem using another low-Reynolds number model (PDH). However, and despite the relative advantage of the WX88 model, its design for high-Reynolds number phenomena disables it to correctly predict the transition, as has been said, and it is not an acceptable model to

predict such natural convection cavity.

Unfortunately, there are some other problems related to this case. Another “numerical” laminarization (turbulence intensity suppression due to numerical effects) takes place when using different low-Reynolds number $k-\epsilon$ models. Despite the fact that other researchers have reported interesting results for such models when solving 5:1 cavity (see Refs. [7,14,25,26]), this present work has encountered critical numerical problems trying to solve the mentioned cavity with Ince–Launder model [7] (besides other low Reynolds $k-\epsilon$ models not reported here, as the Launder–Sharma model [27]). There are some differences between this numerical problem and the previous SGD grid-sensitivity drawback. First, this laminarization process presents a complete turbulence reduction ($\mu_t=0$). Second, it affects all the cavity ($\mu_t=0 \forall x, y$). Third it abruptly appears while convergence process is running. After different damping attempts, computations have shown that by removing damping part of dissipation from $\tilde{\epsilon}$ -equation (f_2 function), conver-

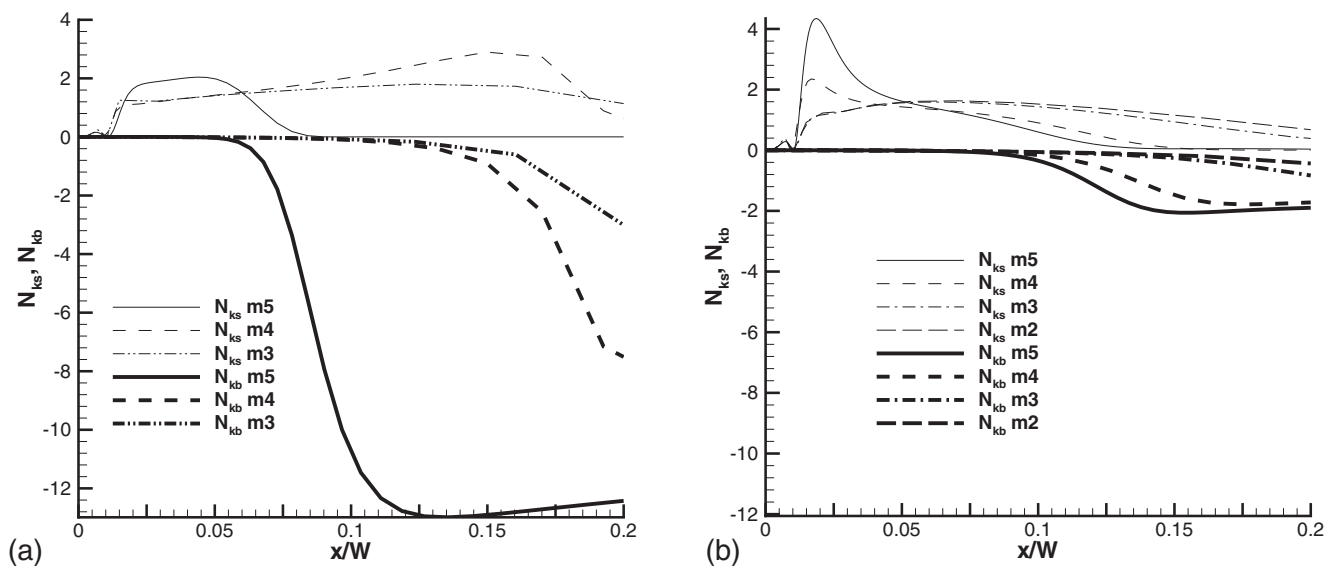


Fig. 2 Cavity 2 ($A=5$, $Ra_H=5 \times 10^{10}$). Comparison of the normalized buoyancy and shear production effects for WX93 and PDH+D model. While for WX93 model, N_{kb} increases as grid is refined (giving an asymptotic laminar cavity) (a): PDH+D model is able to give an asymptotic prediction, thanks to the stable N_{kb} prediction for $m5$ mesh (b).

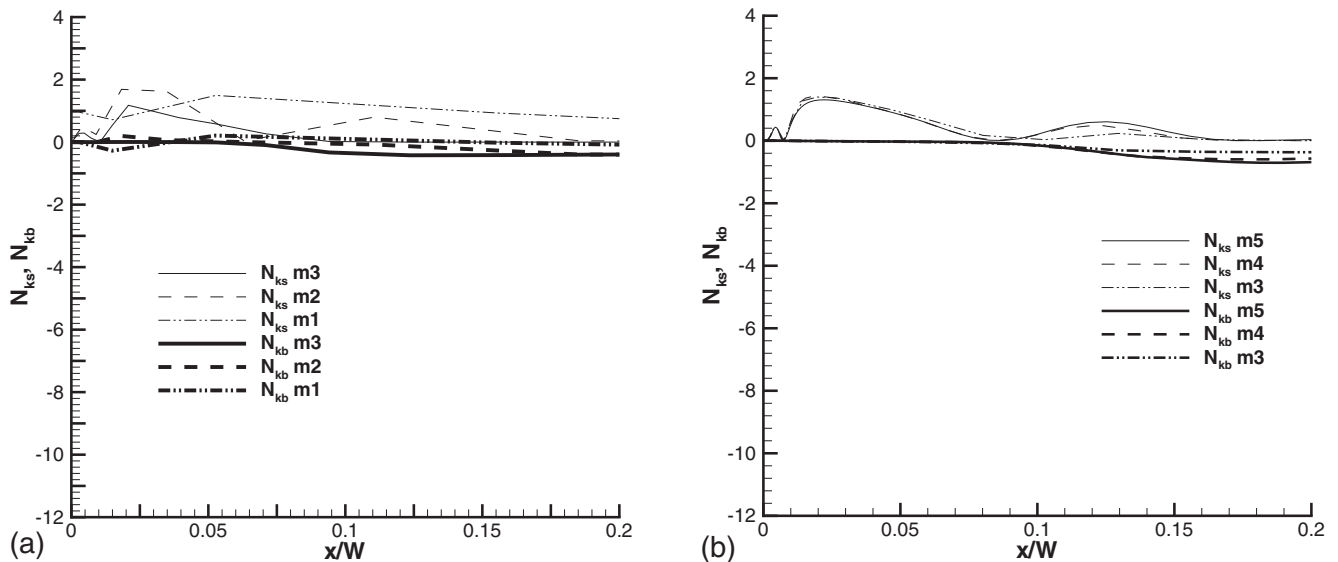


Fig. 3 (a) N_{ks} , N_{kb} prediction for $m1$, $m2$, and $m3$ meshes for IL model under Cavity 2 ($A=5$, $Ra_H=5 \times 10^{10}$). (b) N_{ks} , N_{kb} prediction for $m5$, $m4$, and $m3$ meshes for GPC model under Cavity 3 ($A=4$, $Ra_H=1 \times 10^{10}$).

gence has been possible and a turbulent solution has been achieved, obviously presenting a distorted prediction. Therefore, it seems plausible to think that (because of the relaminarization, which takes place in the core of the cavity) dissipation of $\tilde{\epsilon}$ is affected by low Re_t numbers and $c_{\tilde{\epsilon}2}$ is changed from 1.92 to 1.344 (70% of high-Reynolds number version) in this region. Since production of $\tilde{\epsilon}$ is not dampened ($P_{\tilde{\epsilon}}=c_{\epsilon1}\tilde{\epsilon}/kP_k$), an increasing sink effect on k -equation is produced through an increasing $\tilde{\epsilon}$ prediction. As the grid is refined, this effect is intensified and, finally, it returns to a sudden and unstable convergence point, which “switches off” all turbulent variables.

With reference to the present work, three initial meshes have been converged for the IL model (i.e., 10×10 , 20×20 , and 40×40 CVs), while for the fourth mesh (80×80 CV), it has not been possible to obtain convergence with nontrivial turbulent values, which was also pointed out in Ref. [8]. As to the grid-sensitivity problem, Fig. 3(a) (made with $m1$, $m2$, and $m3$ meshes) shows how the grid-sensitivity problem is not based on G_k prediction (there is no degradation of N_{kb} with grid refinement), as the IL model is using the GGDH, which is not related to the SGDH grid-sensitivity problem, as has been explained in Refs. [2,7]. Present IL G_k evolution ratifies this aspect. Additionally, detailed effect of f_2 damping function is in agreement with suggestions made by Davidson in Ref. [3], where a correction on f_2 damping function is proposed in order to modify the decay of dissipation in transitional regions.

Hence, taking into account the grid degradation of the SGDH for buoyancy effects and the sudden laminarization of some k - ϵ turbulence models due to grid refinement, this work has not been able to present converged solutions for the IL model. For other models (GPC, WX88, WX93, PDH+D), converged solutions have been obtained. As exposed, they are in agreement with numerical experiments carried out by other authors [2]. In fact, GPC and WX93 models return turbulent solutions but present nonasymptotic behavior due to the SGDH grid-sensitivity problem. The WX88 model provides an asymptotic and completely turbulent cavity and, therefore, is not capable to predict transition. On the contrary, the PDH+D model is able to solve this problem due to the damping function incorporated in G_k source term. This is the only model that gives required asymptotic numerical solutions. The model offers a reasonably accurate solution and acceptable numerical behavior.

In fact, mentioned damping function (f_g) constrains the turbu-

lence destruction due to the buoyancy and suppresses the turbulence energy diffusion from the boundary layer to the neighboring outer region, avoiding delayed prediction of transition onset, as aforementioned [2]. Additionally, this damping function corrects the asymptotic behavior for G_k near the vertical wall [2], since $G_k \propto x^2$ as $x \rightarrow 0$ [28].

In Fig. 4, differences between WX93 and PDH+D model are shown. As to this point, obtained convergence estimators have to be commented: As to the results presented for 30:1 cavity (where all the models returned expected and verified convergence estimators), for 5:1 cavity, only the PDH+D model shows acceptable results. This is shown in Tables 5 and 6. Thus, this fact shows that the nonasymptotic turbulent prediction is ratified by the convergence estimators for WX93 and GPC models. The estimators for PDH+D model have the expected values, which is in agreement with its stable transition point prediction. The PDH+D model shows a good experimental agreement in this case. It is shown in Fig. 4(b), where the experimental Nu from Cheesewright et al. [16] is plotted.

4.3 Natural Turbulent Convection in a 4:1 Heated Cavity.

Finally, an analysis of a 4:1 cavity at moderate Rayleigh number based-on-height cavity H ($Ra_H=g\beta\Delta T_{ref}H^3Pr/\nu^2=1 \cdot 10^{10}$) has been carried out. This case could be so-called “moderate” since first observed chaotic behavior is visible at $Ra_H=2.3 \times 10^8$ [29]. The DNS results from Trias et al. detailed in Ref. [24] have been used to check abilities and accuracy of present models, as well as to understand limitations of turbulent natural convection modeling by means of RANS eddy-viscosity techniques.

On the one hand, with reference to relaminarization and geometry aspect, this case presents, a priori similar phenomena to the 5:1 cavity, which could be interesting in order to ratify and/or refine comments on previously observed grid-sensitivity behavior. On the other hand, the moderate Rayleigh number applied to this geometry will bring clarity to the abilities of the models and their relationship with turbulence intensity (and, consequently, will give information on the range of Ra_H where these kinds of models can become accurate tools).

In fact, with reference to numerical problems (grid-sensitivity and numerical laminarization), this case has presented similar difficulties than previously treated 5:1 cavity. The IL model has reported the same laminarization problem trying to solve even using a coarser mesh (40×40 CV), presumably due to the lower turbu-

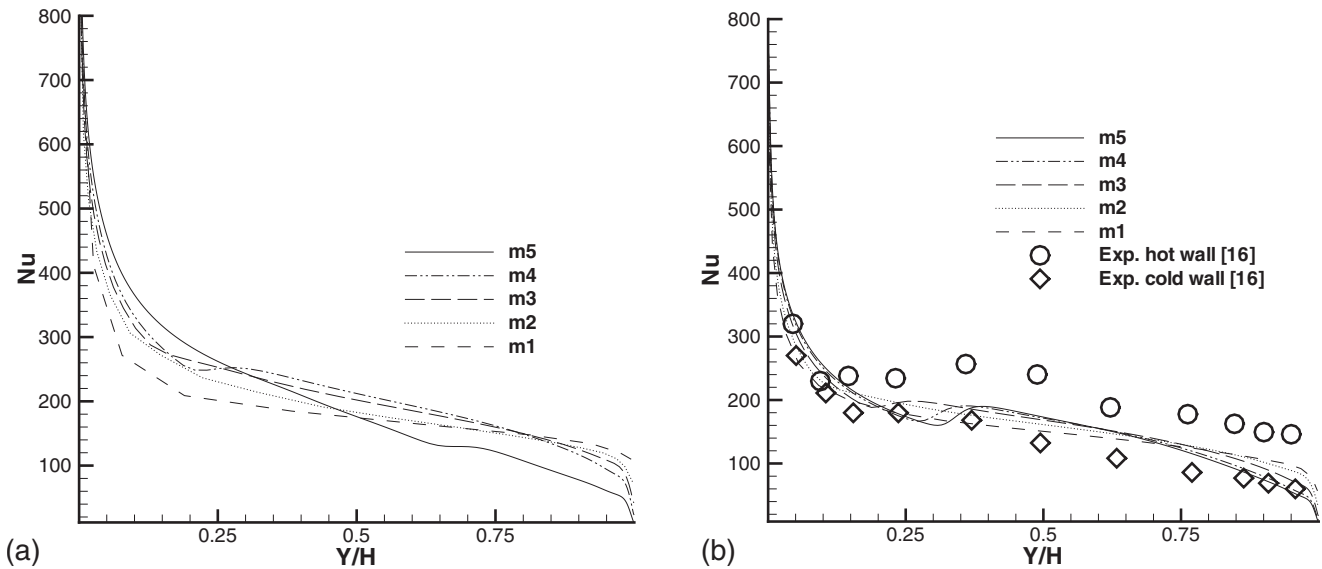


Fig. 4 Cavity 2 ($A=5$, $Ra_H=5 \times 10^{10}$). Comparison of the Nu evolution for WX93 and PDH+D model. On the one hand, it is shown that the WX93 model is not capable of giving asymptotic behavior in the prediction of transition point when refining the mesh (a). On the other, the PDH+D model is able to give an asymptotic transition point prediction (b).

lence intensity. Again, a turbulent solution has been achieved by blocking damping effects on dissipation of $\tilde{\epsilon}$. This fact reinforces suggestions made for 5:1 cavity with reference to the mathematical problem of the damping on $\tilde{\epsilon}$ -equation in IL model. Furthermore, SGDH grid-sensitivity drawback has been encountered when using WX93 model, and a progressive degradation of the turbulent prediction has been observed. Regarding WX88 model, the grid-sensitivity problems have been avoided, but accuracy and prediction of transition point from laminar to turbulent flow has not been achieved due to the model limitations.

Unlike 5:1 cavity, the GPC model has returned a turbulent prediction showing acceptable verification estimators. In this case, the GPC model has avoided a degradation of the G_k term when grid refinement has been applied, as shown in Fig. 3(b). It seems that the coupling between damping functions and SGDH depends on the turbulence intensity and on Ra_H number, and it becomes

stable at lower turbulence intensity. It is interesting to note that this effect has not been observed using the WX93 model, which is paradigmatic of the very sensitive relationship between SGDH and damping functions of the model.

The PDH+D model has presented the most interesting numerical behavior, returning a turbulent solution and a laminar-to-turbulent transition, which is in agreement with related verification estimators. These estimators have revealed acceptable orders of numerical accuracy (p) and high percentages of Richardson nodes for all variables, as shown in Table 7. In fact, this is in agreement with previous conclusions observed in 5:1 cavity.

Hence, only the GPC and PDH+D models have revealed acceptable numerical solutions under used grids and applied pseudotransient numerical algorithm. The other models (IL, WX88, and WX93) are related to different numerical and/or design problems, which do not allow them to solve this case.

Table 5 Cavity 2 ($A=5$, $Ra_H=5 \times 10^{10}$). PDH+D convergence estimators using five meshes: $m1$, $m2$, $m3$, $m4$, $m5$ (20×20 CV, 40×40 CV, 80×80 CV, 160×160 CV, 320×320 CV). Acceptable converged solution (p between 1 and 2, high percentage of Richardson nodes).

Grid $n_3/n_2/n_1$	$v^* = \bar{v}/u_{ref}$			$T^* = \bar{T}/\Delta T_{ref}$			$k^* = k/u_{ref}^2$		
	Rn (%)	p	GCI* (%)	Rn (%)	p	GCI* (%)	Rn (%)	p	GCI* (%)
m1 m2 m3	81	0.3	2.2E+00	94	-0.1	3.3E+01	88	1.4	5.7E-03
m2 m3 m4	82	0.8	9.4E-01	95	0.2	1.5E+01	95	1.2	7.8E-03
m3 m4 m5	86	1.4	1.8E-01	98	1.3	8.1E-01	92	2.1	1.3E-03

Table 6 Cavity 2 ($A=5$, $Ra_H=5 \times 10^{10}$). WX93 convergence estimators using five meshes: $m1$, $m2$, $m3$, $m4$, $m5$ (10×10 CV, 20×20 CV, 40×40 CV, 80×80 CV, 160×160 CV). The converged solution has not passed the verification process (p is not between 1 and 2, small percentage of the Richardson nodes).

Grid $n_3/n_2/n_1$	$v^* = \bar{v}/u_{ref}$			$T^* = \bar{T}/\Delta T_{ref}$			$k^* = k/u_{ref}^2$		
	Rn (%)	p	GCI* (%)	Rn (%)	p	GCI* (%)	Rn (%)	p	GCI* (%)
m1 m2 m3	66	0.3	7.8E+00	86	0.0	1.2E+03	83	1.2	9.5E-03
m2 m3 m4	72	1.6	2.3E-01	95	0.6	4.6E+00	90	2.4	1.4E-03
m3 m4 m5	65	0.1	2.0E+01	89	-1.4	1.6E+01	64	1.4	8.8E-03

Table 7 Cavity 3 ($A=4$, $Ra_H=1 \times 10^{10}$). PDH-D convergence estimators using five meshes: $m1$, $m2$, $m3$, $m4$, $m5$ (10×10 CV, 20×20 CV, 40×40 CV, 80×80 CV, 160×160 CV). Acceptable converged solution (p between 1 and 2, high percentage of *Richardson* nodes).

Grid $n_3/n_2/n_1$	$v^* = \bar{v}/u_{ref}$			$T^* = \bar{T}/\Delta T_{ref}$			$k^* = k/u_{ref}^2$		
	Rn (%)	p	GCI* (%)	Rn (%)	p	GCI* (%)	Rn (%)	p	GCI* (%)
$m1\ m2\ m3$	79	0.4	$1.1E+00$	96	0.3	$1.0E+01$	89	1.2	$5.1E-03$
$m2\ m3\ m4$	82	0.0	$2.0E+02$	94	-0.3	$1.6E+01$	94	0.5	$2.2E-02$
$m3\ m4\ m5$	86	1.7	$7.2E-02$	98	1.6	$5.1E-01$	93	2.4	$6.8E-04$

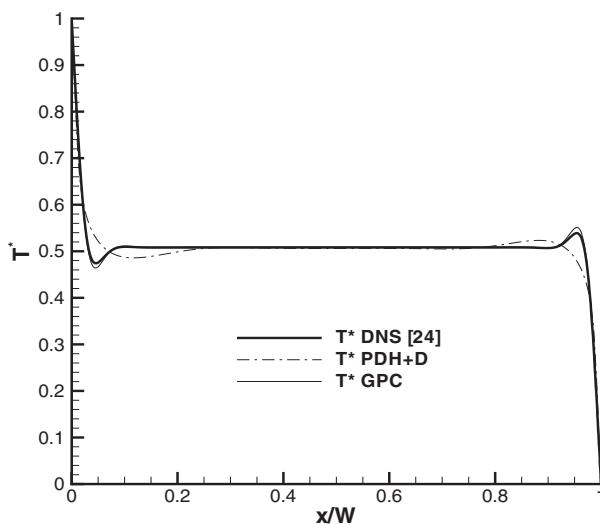
With reference to accuracy, several grades can be commented thanks to the detailed information provided by the DNS data: first, averaged values (Nu); second, velocity and temperature fields; third, turbulent statistics as k and ϵ or $C_\mu \omega k$. As was expected, the deeper the grade, the higher the differences. As far as the Nusselt number is concerned, Fig. 5(b) shows the results for GPC and PDH+D models in comparison to DNS data. While the PDH+D model was well suited for previous cavities (5:1 cavity at $Ra_H=5 \times 10^{10}$ and 30:1 cavity at $Ra_H=2.43 \times 10^{10}$), this 4:1 cavity at $Ra_H=1 \times 10^{10}$ seems to be too “transitional” (or too low turbulent) to be well predicted by this model. In fact, it is easily observed how transition from laminar to turbulent flow is moved to an extremely lower height. On the other hand, GPC model (which reported acceptable accurate predictions for 30:1 cavity, and which presented numerical problems due to SGDH grid-sensitivity problems when solving 5:1 cavity) has shown a reasonably accurate behavior solving this 4:1 cavity, obtaining a Nu prediction relatively close to the DNS data. Transition point is slightly underpredicted. It is interesting to note that the GPC prediction is very close to the Nu obtained from a previous DNS 2D data carried out by Trias et al. [24], which could reveal three-dimensional effects, which are impossible to be observed by RANS-EVM models.

Related to the second grade of comparison, Figs. 5–7 present the GPC and PDH+D performances in comparison to DNS data [24] for temperature and velocities at $y=H/2$ and $y=15H/16$ planes. In agreement with which was observed for Nu prediction, GPC model offers interesting predictions (very close to DNS data), especially for $y=H/2$ where there is a very small turbulence

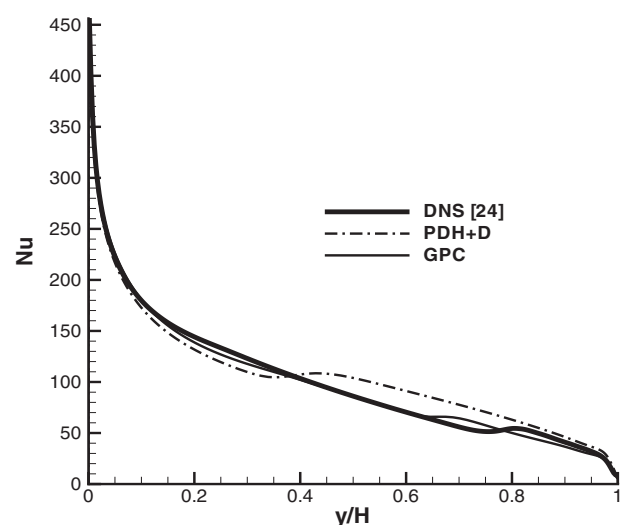
intensity. With reference to $y=15H/16$ plane, turbulence intensity is larger and differences are higher. Performance is admissibly accurate. On the other hand, PDH+D model offers worse predictions due to an overprediction of turbulence intensity. The results for $y=H/2$ were especially distorted.

Finally, and as to turbulence statistics, two aspects have to be addressed. On the one hand, turbulent kinetic energy (k) predictions can be observed in Fig. 8. As shown, both GPC and PDH+D models quantitatively present results comparable to the DNS data. As to their quality, GPC model offers a transition point quite close to DNS predictions, while PDH+D predicts a very early transition point and presents a strongly larger turbulent boundary layer. As can be observed in Fig. 8(a), it implies a strong overprediction in $y=H/2$ plane. This explains the distorted predictions for Nu, and specifically, for u^* , v^* , and T^* in $y=H/2$ plane. However, both models relatively present acceptable turbulent boundary-layer normal-to-wall height predictions. On the other hand, with reference to ϵ predictions, both models provide inaccurate predictions (as can be seen in Fig. 9), which was expected due to the limitations of ϵ/ω -equation. GPC model offers a qualitatively good behavior for both $y=H/2$ and $y=15H/16$ planes, while PDH+D model suffers a strong overprediction for both planes once again. See Fig. 9.

Hence, an accurate resolution of k has an immediate effect on both temperature and velocity fields. This allows to obtain acceptable transition point prediction, which is of great interest for engineering purposes.



(a)



(b)

Fig. 5 Cavity 3 ($A=4$, $Ra_H=1 \times 10^{10}$). (a) Dimensionless temperature profiles: $y=H/2$. (b) Nu number prediction for GPC and PDH+D models. Sudden rising of Nu number indicates transition from laminar to turbulent flow.

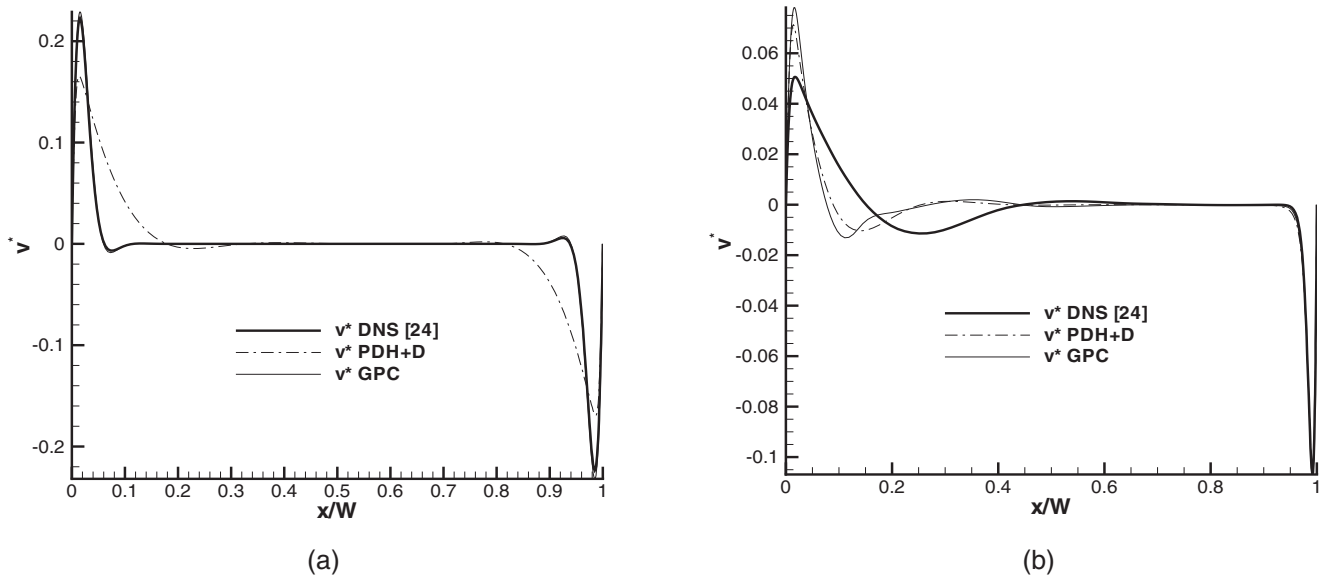


Fig. 6 Cavity 3 ($A=4$, $Ra_H=1 \times 10^{10}$). Dimensionless v profiles: (a) $y=H/2$; (b) $y=15H/16$.

5 Concluding Remarks

Abilities and drawbacks related to two-equation eddy-viscosity models have been analyzed under turbulent natural convection cases. A detailed formulation based on $k-\epsilon$ and $k-\omega$ models has been presented and different rectangular cavities have been addressed with exposed models, offering several numerical and physical aspects. Treated cavities expose different phenomena due to their diverse aspect ratio and turbulence intensity. In order to quantify model accuracy, experimental and DNS data extracted from literature have been used.

As a result from computations, this work has basically revealed two different subjects. First, numerical problems related to prediction of turbulent natural convection. Second, skills and abilities of such models to accurately predict heat transfer and fluid flow for the studied cases.

Related to the first item, low-Reynolds number two-equation models seem to work reasonably well when solving turbulent boundary layers under increasing turbulence intensity from wall to cavity core. In fact, even high-Reynolds number WX88 model has

shown an acceptable behavior when solving 30:1 cavity. All buoyancy models (SGDH, GGDH, and GGDH+ f_g) have presented correct numerical behaviors. This fact seems to be in agreement with the original design of two-equation turbulence models, which are mainly devised to predict laminarization produced due to the presence of walls under forced convection. On the contrary, solving 5:1 and 4:1 cavities, diverse numerical problems have appeared. Currently, these cases present an additional laminarization phenomenon, which is generated by cavity aspect ratio (in combination with moderate turbulent intensity), instead of wall-damping effect (which is the only laminarization process in 30:1 cavity). This phenomena lead to two different numerical problems: On the one hand, the IL model suffers a sudden laminarization presumably due to a damping effect on dissipation of $\tilde{\epsilon}$ -equation, which collapses all turbulent variables while refining the mesh. On the other hand, SGDH presents a numerical degradation with grid refinement in combination with damping functions, which was also highlighted by Peng et al. [2]. This fact does not allow to obtain an asymptotic prediction. Both effects are

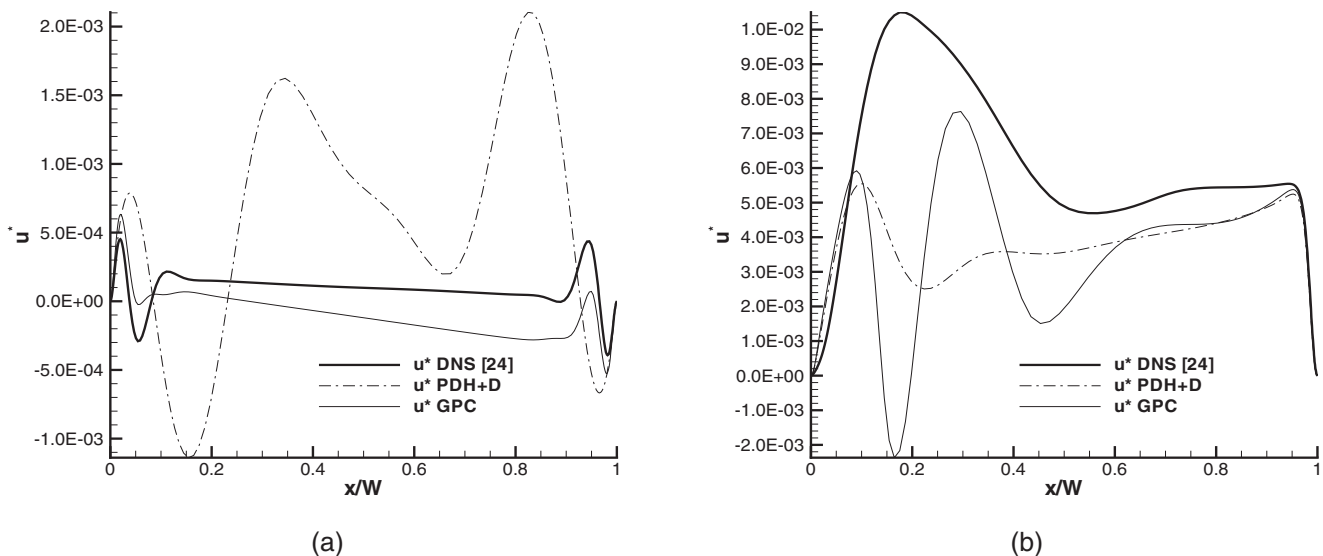


Fig. 7 Cavity 3 ($A=4$, $Ra_H=1 \times 10^{10}$). Dimensionless u profiles: (a) $y=H/2$; (b) $y=15H/16$.

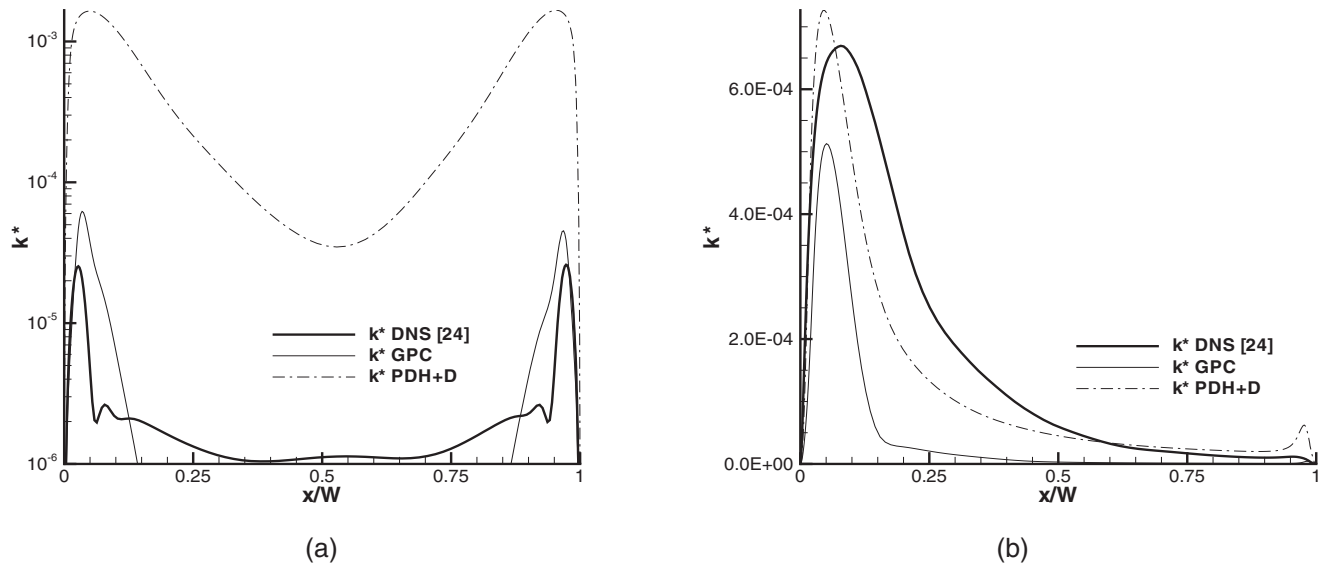


Fig. 8 Cavity 3 ($A=4$, $Ra_H=1 \times 10^{10}$). Dimensionless k profiles: (a) $y=H/2$; (b) $y=15H/16$.

related to the models' inability to capture the laminarization produced in the core of the cavity. Hence, only the PDH+D and GPC models have returned verified numerical computations for 4:1 cavity while solely PDH+D model has achieved an acceptable numerical behavior for 5:1 cavity.

Related to the second subject, accuracy is clearly related to the flow structure of the case. For 30:1 cavity, all models have shown an interesting behavior to predict Nu , and also vertical velocity v^* , despite an important underprediction of turbulent viscosity in the core of the cavity. On the other hand, regarding the 5:1 cavity Nu number and transition point, they are well captured by the PDH+D model, as well as k distribution along the cavity. Finally, with reference to the 4:1 cavity, the GPC model has reported very interesting results, relatively close to the DNS data regarding diverse fields. While on the contrary, the PDH+D model has not been able to reproduce this lower turbulent case and has strongly over predicted turbulent variables.

Hence, turbulent natural convection prediction by means of two-equation turbulence models is associated with physical and

numerical limitations of the models. However, they are generally acceptable tools for different Rayleigh numbers and aspect ratio cavities, taking into account that, depending on the case, specific models should be used.

Acknowledgment

This work has been financially supported by the Ministerio de Educación y Ciencia, Secretaría de Estado de Universidades e Investigación, Spain (ref. ENE2006-14247/ALT and ENE2007-67185).

Nomenclature

- A = aspect ratio ($A=H/W$)
- $C_\mu, c_1, c_2, c_3, c_{rw}$ = turbulent model constants
- c_p = specific heat at constant pressure
- CV = control volume
- f_1, f_2, f_k, f_μ = damping functions of low-Reynolds number models

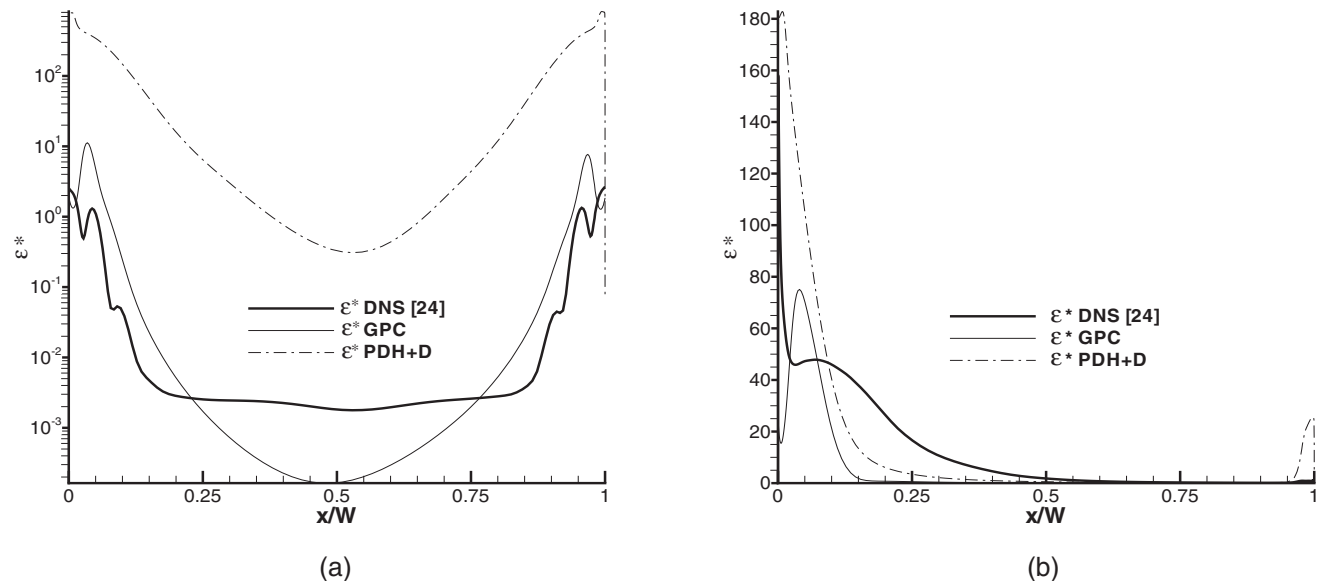


Fig. 9 Cavity 3 ($A=4$, $Ra_H=1 \times 10^{10}$). Dimensionless ϵ profiles: (a) $y=H/2$; (b) $y=15H/16$.

H = cavity height
 k = turbulent kinetic energy
 k^* = dimensionless turbulent kinetic energy
 (k/u_{ref}^2)
 l_{ref} = reference length ($l_{ref}=H$)
 l = turbulent length scale ($l=k^{3/2}/\epsilon$ for $k-\epsilon$ models) and ($l=k^{1/2}/\omega$ for $k-\omega$ models)
 N_{ks} = normalized shear stress production of k
 $(N_{ks}=P_k/\rho C_\mu k\omega$ or $P_k/\rho\epsilon)$
 N_{kb} = normalized buoyancy production of k (N_{kb}
 $=G_k/\rho C_\mu k\omega$ or $G_k/\rho\epsilon)$
 Nu = Nusselt number
 P_k = production of k due to shear stresses
 G_k = production of k due to buoyancy effects
 Pr = Prandtl number ($Pr=\mu c_p/\lambda$)
 \bar{p} = the mean pressure
 Ra_H = Rayleigh number based-on-height length
 $(Ra_H=g\beta\Delta T_{ref}H^3Pr/\nu^2)$
 Re_t = turbulent Reynolds number ($Re_t=k/\nu\omega$ or
 $k^2/\nu\epsilon)$
 \bar{S}_{ij} = mean rate of strain tensor
 \bar{T} = mean temperature
 T' = turbulent fluctuating temperature
 T_{ref} = reference temperature ($T_{ref}=T_{cold}$)
 T^* = dimensionless temperature
 $(T^*=\bar{T}-T_{ref}/\Delta T_{ref})$
 ΔT_{ref} = reference temperature ($\Delta T_{ref}=T_{hot}-T_{cold}$)
 t = time
 t_{ref} = reference time ($t_{ref}=l_{ref}/u_{ref}$)
 u_i = mean velocity in the i -direction
 u'_i = turbulent fluctuating velocity in the
 x_i -direction
 $\overline{u'_i T'}$ = turbulent heat flux
 u_{ref} = reference velocity for 30:1 and 5:1 cavities
 $(u_{ref}=\sqrt{g\beta\Delta T_{ref}L_{ref}})$
 u_{ref} = reference velocity for 4:1 cavity
 $(u_{ref}=\alpha\sqrt{Ra_H}/H)$
 u^* = dimensionless velocity (\bar{u}/u_{ref})
 v^* = dimensionless velocity (\bar{v}/u_{ref})
 u_τ = friction velocity ($u_\tau=\sqrt{\tau_w/\rho}$)
 W = cavity width
 x_i = Cartesian coordinate in the i -direction
 y^+ = dimensionless distance to the nearest wall
 $(y^+=y u_\tau/\nu)$

Greek Symbols

α = thermal diffusivity ($\alpha=\nu/Pr$)
 δ_{ij} = Kronecker delta
 ϵ = dissipation rate of k
 ϵ^* = dimensionless dissipation rate
 $(\epsilon^*=\epsilon/(\nu t_{ref}^2))$
 λ = thermal conductivity
 μ = dynamic viscosity
 μ_t = eddy or turbulent viscosity
 μ_t^* = dimensionless eddy or turbulent viscosity
 $(\mu_t^*=\mu_t/\mu)$
 ν = kinematic viscosity ($\nu=\mu/\rho$)
 ρ = density
 σ_T = turbulent Prandtl number
 $\sigma_k, \sigma_\epsilon$ = model constants
 τ = turbulent time scale
 ω = specific dissipation rate of k
 ω^*

= dimensionless specific dissipation rate (ω^*
 $=\omega H^2/\nu$)

References

- [1] Pope, S., 2000, *Turbulent Flows*, Cambridge University Press, Cambridge.
- [2] Peng, S., and Davidson, L., 1999, "Computation of Turbulent Buoyant Flows in Enclosures With Low-Reynolds Number $k-\omega$ Models," *Int. J. Heat Fluid Flow*, **20**, pp. 172–184.
- [3] Davidson, L., 1990, "Calculation of the Turbulent Buoyancy-Driven Flow in a Rectangular Cavity Using an Efficient Solver and Two Different Low Reynolds Number $k-\epsilon$ Models," *Numer. Heat Transfer, Part A*, **18**, pp. 129–147.
- [4] Hanjalić, K., and Vasić, S., 1993, "Computation of Turbulent Natural-Convection in Rectangular Enclosures With an Algebraic Flux Model," *Int. J. Heat Mass Transfer*, **36**, pp. 3603–3624.
- [5] Hanjalić, K., Kenjereš, S., and Durst, F., 1995, "Natural Convection in Partitioned Two-Dimensional Enclosures at Higher Rayleigh Numbers," *Int. J. Heat Mass Transfer*, **39**(7), pp. 1407–1427.
- [6] Kenjereš, S., Gunarjo, S. B., and Hanjalić, K., 2005, "Contribution to Elliptic Relaxation Modelling of Turbulent Natural and Mixed Convection," *Int. J. Heat Fluid Flow*, **26**(7), pp. 569–586.
- [7] Ince, N., and Launder, B., 1989, "Computation of Buoyancy-Driven Turbulent Flows in Rectangular Enclosures," *Int. J. Heat Fluid Flow*, **10**(1), pp. 110–117.
- [8] Pérez-Segarra, C. D., Oliva, A., Costa, M., and Escanes, F., 1995, "Numerical Experiments in Turbulent Natural and Mixed Convection in Internal Flows," *Int. J. Numer. Methods Heat Fluid Flow*, **5**(1), pp. 13–33.
- [9] Wilcox, D. C., 1988, "Reassessment of the Scale-Determining Equation for Advanced Turbulence Models," *AIAA J.*, **26**, pp. 1299–1310.
- [10] Wilcox, D. C., 1994, "Simulation of Transition With a Two-Equation Turbulence Model," *AIAA J.*, **32**, pp. 247–255.
- [11] Goldberg, U., Peroomian, O., and Chakravarthy, S., 1998, "A Wall-Distance-Free $k-\epsilon$ Model With Enhanced Near-Wall Treatment," *ASME J. Fluids Eng.*, **120**, pp. 457–462.
- [12] Markatos, N., Malin, M., and Cox, G., 1982, "Mathematic Modelling of Buoyancy-Induced Smoke Flow in Enclosures," *Int. J. Heat Mass Transfer*, **25**, pp. 63–75.
- [13] Markatos, N., and Pericleous, K., 1984, "Laminar and Turbulent Natural Convection in an Enclosed Cavity," *Int. J. Heat Mass Transfer*, **27**, pp. 755–772.
- [14] Heindel, T., Ramadhyani, S., and Incropera, F., 1994, "Assessment of Turbulence Models for Natural Convection in an Enclosure," *Numer. Heat Transfer, Part B*, **26**, pp. 147–172.
- [15] Dafa'alla, A., and Betts, P., 1996, "Experimental Study of Turbulent Natural Convection in a Tall Air Cavity," *Exp. Heat Transfer*, **9**, pp. 165–194.
- [16] Cheeswright, R., King, K., and Ziai, S., 1986, "Experimental Data for the Validation of Computer Codes for the Prediction of Two-Dimensional Buoyant Cavity Flows," *Proceedings of Significant Questions in Buoyancy Affected Enclosure or Cavity Flows*, pp. 75–81.
- [17] Henkes, R., van Der Vlugt, F., and Hoogendoorn, C., 1991, "Natural Convection Flow in a Square Cavity Calculated With Low Reynolds-Number Turbulence Models," *Int. J. Heat Mass Transfer*, **34**, pp. 377–388.
- [18] Rodi, W., 1984, "Turbulence Models and Their Application in Hydraulics: A State-of-the-Art Review," University of Karlsruhe, Germany.
- [19] Patankar, S. V., 1980, *Numerical Heat Transfer and Fluid Flow*, Hemisphere, Washington, DC.
- [20] Cadafalch, J., Pérez-Segarra, C. D., Cónsul, R., and Oliva, A., 2002, "Verification of Finite Volume Computations on Steady State Fluid Flow and Heat Transfer," *ASME J. Fluids Eng.*, **124**, pp. 11–21.
- [21] Roache, P., 1997, "Quantification of Uncertainty in Computational Fluid Dynamics," *Annu. Rev. Fluid Mech.*, **29**, pp. 123–160.
- [22] Roache, P., 1998, *Verification and Validation in Computational Science and Engineering*, Hermosa, Albuquerque, NM.
- [23] Roache, P., 1972, "On Artificial Viscosity," *J. Comput. Phys.*, **10**, pp. 169–184.
- [24] Trias, F. X., Soria, M., Oliva, A., and Pérez-Segarra, C. D., 2007, "Direct Numerical Simulation of Two and Three-Dimensional Turbulent Natural Convection Flows in a Differentially Heated Cavity of Aspect Ratio 4," *J. Fluid Mech.*, **586**, pp. 259–293.
- [25] Murakami, S., Kato, S., Chiakamoto, T., and Laurence, D., 1996, "New Low-Reynolds-Number $k-\epsilon$ Model Including Damping Effect due to Buoyancy in a Stratified Flow Field," *Int. J. Heat Mass Transfer*, **39**(16), pp. 3483–3496.
- [26] Liu, F., and Wen, J., 1999, "Development and Validation of an Advanced Turbulence Model for Buoyancy Driven Flows in Enclosures," *Int. J. Heat Mass Transfer*, **42**, pp. 3967–3981.
- [27] Launder, B., and Sharma, B., 1974, "Application of the Energy Dissipation Model of Turbulence to the Calculation of Flow Near a Spinning Disc," *Lett. Heat Mass Transfer*, **1**(2), pp. 131–138.
- [28] So, R., and Sommer, T., 1994, "A Near-wall Eddy Conductivity Model for Fluids With Different Prandtl Numbers," *ASME J. Fluids Eng.*, **116**, pp. 844–854.
- [29] Xin, S., and Quere, P., 1995, "Direct Numerical Simulations of Two-Dimensional Chaotic Natural Convection in a Differentially Heated Cavity of Aspect Ratio 4," *J. Fluid Mech.*, **304**, pp. 87–118.

Performance of the Various S_n Approximations of DOM in a 3D Combustion Chamber

Manosh C. Paul
Department of Mechanical Engineering,
University of Glasgow,
Glasgow G12 8QQ, UK
e-mail: m.paul@mech.gla.ac.uk

We have carried out a three-dimensional numerical study to investigate the radiative heat transfer in a model gas turbine combustor. The combustion chamber is a representative of the Rolls-Royce Tay engine combustor. The discrete ordinate method (S_n) in general body-fitted coordinate system is developed and then applied to solve the filtered radiative transfer equation for the radiation modeling, and this has been combined with a large eddy simulation of the flow, temperature, and composition fields within the combustion chamber. Various approximations of S_n have been considered and their performances in the investigation of the radiative heat transfer are presented in the paper. The radiation considered in this work is due only to the hot combustion gases, notably carbon dioxide (CO_2) and water vapor (H_2O) also known as nonluminous radiation. The instantaneous results of the radiation properties such as the incident radiation and the radiative energy source or sink as the divergence of the radiative heat fluxes are computed inside the combustion chamber and presented graphically. Effects of the wall emissivity on the incident radiation inside the combustion chamber have been examined, and it has been found that the radiative energy is enhanced with the increment of the wall emissivity.
[DOI: 10.1115/1.2897924]

Keywords: discrete ordinate method, large eddy simulation, radiative heat transfer, turbulent combustion

1 Introduction

A large part of the total heat transfer in a combustion chamber, whether it is a gas turbine engine, a car engine, or a furnace, occurs by radiation from the flame. This radiation has two components: (i) the “nonluminous,” which emanates from the combustion gases notably carbon dioxide (CO_2) and water vapor (H_2O), and (ii) the “luminous,” which is mainly due to the soot formed in the flame.

The prediction of wall temperatures is an important aspect in the design of practical engine combustors, and this clearly requires that the radiative heat fluxes be predicted accurately. An inability to predict the wall temperatures may lead to an excessive amount of the combustor airflow being used for cooling the liner wall, and this is likely to lead to a reduced combustion efficiency and an increased emission of the pollutants such as carbon monoxide (CO), NO_x formations, and unburned hydrocarbons (UHCs). In addition, excessive combustor wall temperatures have a deleterious impact on combustor “life.”

To meet the world environmental regulations and for safer environment, one of the main objectives in designing of the practical combustion devices is to reduce the pollutant emissions. The numerical study becomes a vital tool to predict the radiative heat transfer inside high-temperature combustion devices, and nowadays, it is also used to replace very costly and time-consuming experimental test procedures of any devices.

The discrete ordinate method (DOM) was first proposed by Chandrasekhar [1] in his work on one-dimensional stellar and atmospheric radiation. Subsequently, Carlson and Lathrop [2] developed the DOM for multidimensional radiation problems employing the finite volume approach. More recently, the DOM has been widely used on various different problems [3–5], where the

major emphasis has been on solving only the radiative transfer equation (RTE), which is the steady state representation of the radiative transfer. However, the radiative transfer in high-temperature combustion devices requires a simultaneous solution of the RTE and the governing flow equations such as the Navier–Stokes, enthalpy and species concentration conservation equations, etc. [6–8].

Among the other different numerical methods such as the discrete transfer method, the finite volume method, the finite element method, etc., found in the literature, the DOM becomes a popular numerical method for radiations although it suffers by the ray effect in an optically thin medium [9]. The DOM has some obvious advantages such as the simplicity of concepts, the control volume approaches, etc.

With respect to combining the RTE with the large eddy simulation (LES), to the author’s knowledge, only a small amount of work has been done to date. Desjardin and Frankel [7] studied soot formation in the near field of a strongly radiating turbulent jet flame involving LES, and a simplified two-dimensional treatment of radiation involving gray and nonscattering medium was considered. Recently, Jones and Paul [8] have investigated the radiative heat transfer in a three-dimensional model of a gas turbine combustor, where only the S_4 approximation of the DOM was applied in conjunction with LES.

In this paper, we have extended the DOM including its various lower and higher order approaches, i.e., S_2, S_6, S_8 , and applied into the model Tay gas turbine combustion chamber for further investigation of the radiative heat transfer and to see how the radiation results are affected with the various orders of approximations of the DOM. To the best of our knowledge, there has been no other attempt that combines the three-dimensional DOM with the LES for computing the turbulent flame radiation in a gas turbine combustor.

2 Governing Equations

The main feature of the model gas turbine combustor is shown in Fig. 1, which is representative of the Rolls-Royce Tay gas

Contributed by the Heat Transfer Division of ASME for publication in the JOURNAL OF HEAT TRANSFER. Manuscript received February 8, 2007; final manuscript received September 18, 2007; published online May 20, 2008. Review conducted by Walter W. Yuen.

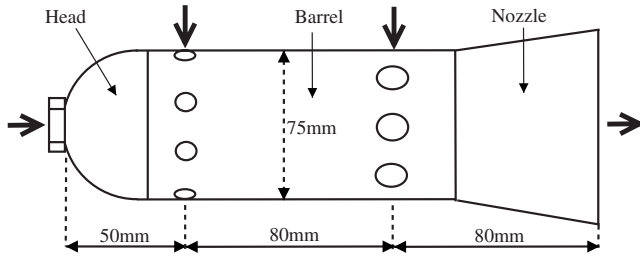


Fig. 1 The feature of a model Tay gas turbine combustor

turbine [10]. The combustor walls are made of transply, a laminated porous material. The geometry of the combustor includes a relatively small swirler at the head of the combustor in the center of which the fuel injector is located and a hemispherical head section attached to a circular barrel of 75 mm diameter. This barrel contains a set of six primary ports/holes of 10 mm diameter each at the front and another set of six dilution ports/holes of 20 mm diameter each at 80 mm downstream of the first set. A circular-to-rectangular nozzle is attached to the end of the barrel. High purity gaseous fuel comprising over 95% propane (C_3H_8) was injected into the combustion chamber through the center of the swirler.

The equations of motion in LES are obtained after applying a spatial filter [11] and a density weighted Favre filter [12] to the continuity, the Navier–Stokes, and the mixture fraction equations. In DOM, the discrete ordinate representation of the RTE is filtered using the spatial filter. Finally, these equations take the following forms [8]:

$$\frac{\partial \bar{\rho}}{\partial t} + \frac{\partial \bar{\rho} \bar{u}_j}{\partial x_j} = 0 \quad (1)$$

$$\frac{\partial \bar{\rho} \bar{u}_i}{\partial t} + \frac{\partial \bar{\rho} \bar{u}_i \bar{u}_j}{\partial x_j} = - \frac{\partial \bar{p}}{\partial x_i} + \frac{\partial}{\partial x_j} \left(2\mu \bar{S}_{ij} - \frac{2}{3} \mu \bar{S}_{kk} \delta_{ij} \right) - \frac{\partial \tau_{ij}}{\partial x_j} \quad (2)$$

$$\frac{\partial \bar{\rho} \bar{f}}{\partial t} + \frac{\partial \bar{\rho} \bar{u}_j \bar{f}}{\partial x_j} = \frac{\partial}{\partial x_j} \left(\frac{\mu}{Sc} \frac{\partial \bar{f}}{\partial x_j} \right) - \frac{\partial J_j}{\partial x_j} \quad (3)$$

$$\alpha_m \frac{\partial \bar{I}_m}{\partial x} + \beta_m \frac{\partial \bar{I}_m}{\partial y} + \gamma_m \frac{\partial \bar{I}_m}{\partial z} + \bar{\kappa} I_m = \bar{\kappa} I_b \quad (4)$$

where ρ is the mixture density, t is the time, $x_j=(x,y,z)$ is the coordinate vector, u_j is the velocity vector, p is the dynamic pressure, μ is the coefficient of viscosity, S_{ij} is the strain rate defined as $S_{ij}=1/2((\partial u_i/\partial x_j)+(\partial u_j/\partial x_i))$, δ_{ij} is the Kronecker delta, f is the mixture function, and Sc is the Schmidt/Prandtl number. In Eqs. (1)–(4), the variables with overbar represent the spatial filtered variables, while the Favre filter variables are with tilde.

In Eq. (4), I_m represents the radiative intensity along the angular direction, where $m=1,2,\dots,M$ (see Refs. [13,8] for a detailed angular representation); thus, the equation represents a set of total M different directional radiative intensities from a computational grid node. In a three-dimensional enclosure, the total number of the different discrete directions M to be considered at each computational node is again related to the order of the S_n approximation and is defined as $M=n(n+2)$ [13,2]. For example, in the S_4 approximation of the DOM, the radiative intensities in a total of $M=24$ discrete directions are calculated from each computational node point, in the case of S_6 total number of directions is $M=48$, while for S_8 , it is $M=80$.

The terms α_m , β_m , and γ_m in Eq. (4) represent the direction cosines of an angular direction along the coordinates and I_b is the

blackbody intensity at the temperature of the medium, which is defined as $\sigma \tilde{T}^4/\pi$, where σ is the Stefan–Boltzmann constant and \tilde{T} is the flame temperature.

In a high-temperature combustion process, the spectral bands from H_2O and CO_2 are the most dominant feature in a nonluminous radiation compared to the other species such as CO and H_2 , see Ref. [14]. Therefore, the absorption coefficient κ is based on a mixture of H_2O and CO_2 , which is expressed as [6,15]

$$\bar{\kappa} = 0.1(\tilde{Y}_{H_2O} + \tilde{Y}_{CO_2}) \quad (m^{-1}) \quad (5)$$

where \tilde{Y}_{H_2O} and \tilde{Y}_{CO_2} correspond to the Favre filtered mole fractions of H_2O and CO_2 , respectively.

In the radiation modeling, we have assumed that the enclosure contains an absorbing-emitting, nonscattering, and radiatively gray medium. In Eqs. (2) and (3), the sub-grid-scale stresses, τ_{ij} , and the sub-grid-scale scalar fluxes, J_j , are modeled using the standard Smagorinsky model [16] and a gradient model [17], respectively.

The unknown terms, $\bar{\kappa} \bar{I}_m$ and $\bar{\kappa} \bar{I}_b$, in Eq. (4), which are the nonlinear correlations between turbulence and radiation, are simply expressed as $\bar{\kappa} \bar{I}_m$ and $\bar{\kappa} \bar{I}_b$, respectively, ignoring the sub-grid-scale turbulence interaction with radiation. A future study is required to incorporate these interactions and to investigate their effects in the radiative heat transfer predictions in a turbulent flame.

The detailed boundary conditions for solving the filtered equations (Eqs. (1)–(3)) are presented in Ref. [18], and while for the filtered RTE (4), these are given in Ref. [8], which will not be repeated here.

3 Numerical Procedures

The filtered equations (1)–(4) are rewritten in general boundary/body-fitted coordinate system using the approach introduced by Thompson et al. [19], where the governing differential equations in the Cartesian coordinates are transformed into the curvilinear coordinate system. The details of the numerical procedures in the LES approach to solve Eqs. (1)–(3) have already been presented in Refs. [20,18] and will not be repeated here. The numerical procedures in DOM to solve the RTE (4) can be found in Ref. [8]. Also, a benchmark problem was considered in Ref. [8] to assess accuracy of the numerical results of the DOM code in the general body-fitted coordinate system, and a very good agreement was obtained compared to the results available in literature; for further details, the readers are referred to Ref. [8].

4 Results and Discussion

In the present computation, we have employed a total of about 10^5 control volumes with $40 \times 60 \times 40$ grid nodes along the x , y , and z directions, respectively. A variable time step is used in the simulation based on the consideration of the maximum Courant number, which never exceeded 0.1 throughout the computations. The average time step in the simulation is about $dt=5.5 \times 10^{-7}$ s. Overall, the LES code is second order accurate in both space and time domains and for the DOM, we used the step scheme described in Ref. [8]. The results presented in Figs. 2–6 are at the time iteration of 6.5×10^5 , which is at the real clock time of $t \approx 0.036$ s.

Instantaneous results of the flame temperatures, the absorption coefficient, and the total radiative intensity, $\bar{I}=\sum_{m=1}^M \bar{I}_m$, at various horizontal locations of the combustion chamber are presented in Fig. 2. The radiation results shown in this figure are obtained by applying the highest order approximation of the DOM, S_8 , and the emissivity of walls was kept at 0.5.

We note that the results of temperature and absorption coefficients are initially obtained without considering any radiation effects. These results are then fed into the radiation solver, DOM, to

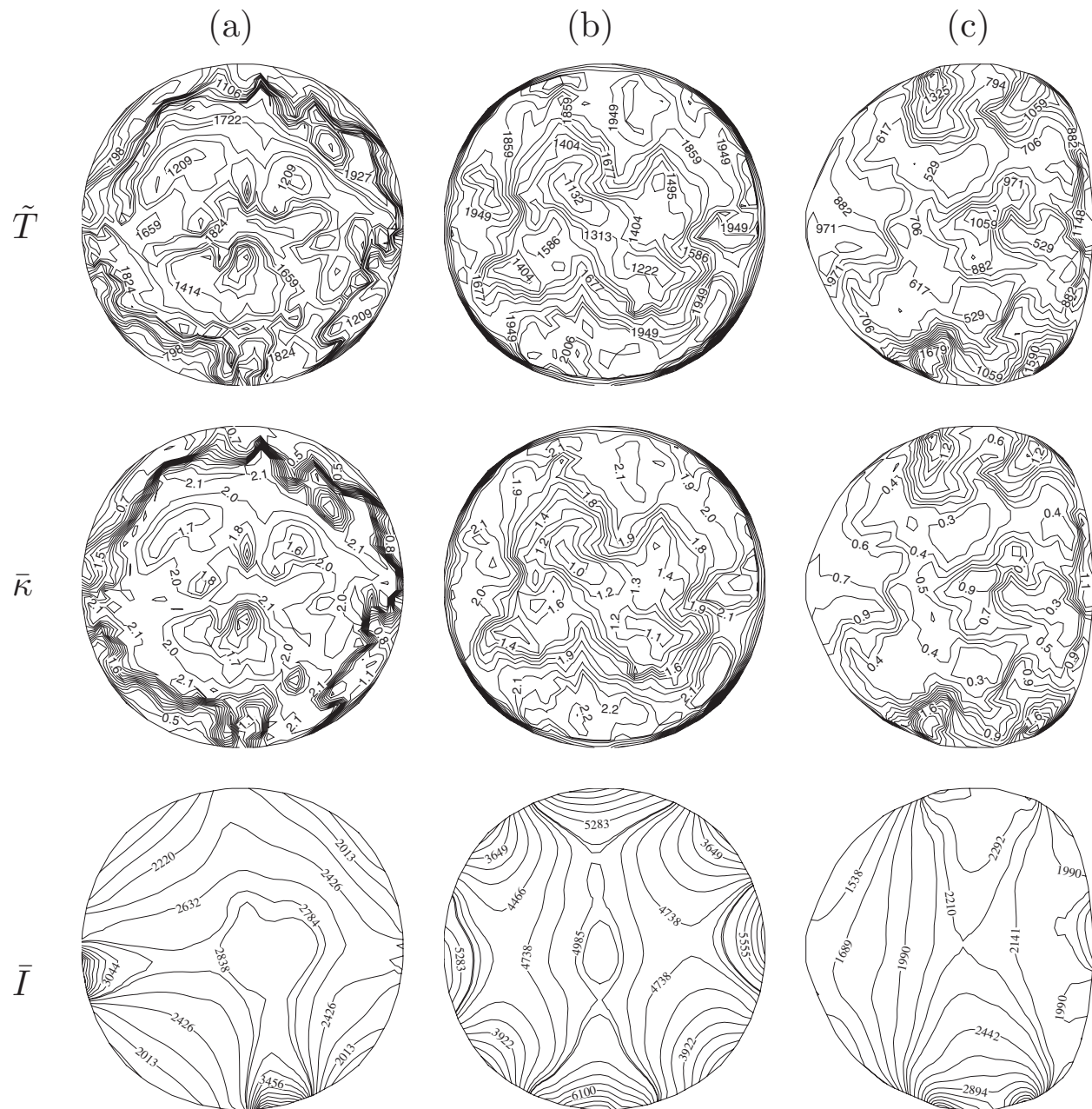


Fig. 2 Instantaneous contour plots of \tilde{T} (K), $\tilde{\kappa}$ (cm^{-1}), and \tilde{I} (kW m^{-2}) at (a) $y=20$ mm, (b) $y=95$ mm, and (c) $y=165$ mm

solve the RTE (4). These are required, as the sources of radiation, e.g., the blackbody intensity (\tilde{I}_b), depend on the flame temperature, and the absorption coefficient $\tilde{\kappa}$, which is considered to be a function of the mole fractions of H_2O and CO_2 . A good agreement was achieved when di Mare et al. [18] compared the computational results of \tilde{T} , $\tilde{Y}_{\text{H}_2\text{O}}$, and \tilde{Y}_{CO_2} against the experimental measurements done by Bicen et al. [10], which again will not be repeated here.

In this figure, we can also see that the total radiative intensity attains a maximum at the region where both the temperature and the absorption coefficient are maximum. Thus, it provides a clear evidence that the medium is highly dominated by the hot H_2O and CO_2 gases. The radiative heat flux distributions, not shown in the figure, also become maximum at the position where the radiative intensities are predicted maximum.

Figure 3 shows the net loss or gain of the radiative energy as a divergence of the radiative heat fluxes, $\nabla \cdot \bar{\mathbf{q}}$, which have been calculated using the following relation:

$$\nabla \cdot \bar{\mathbf{q}} = 4\pi\bar{\kappa}\tilde{I}_b - \int_{4\pi} \bar{\kappa}\tilde{I}d\Omega \quad (6)$$

In this figure, the dashed lines represent the negative contours, while the solid lines are the positive contours. These results were also obtained using the highest order approximation of DOM (S_8), and the wall emissivity remains the same, i.e., $\epsilon_w=0.5$.

In Eq. (6), the first term on the right hand side represents the emitted/outgoing radiation from a computational control volume, while the second term represents the total incident radiation into that control volume. Thus, $\nabla \cdot \bar{\mathbf{q}}$ gives the rate of generation of

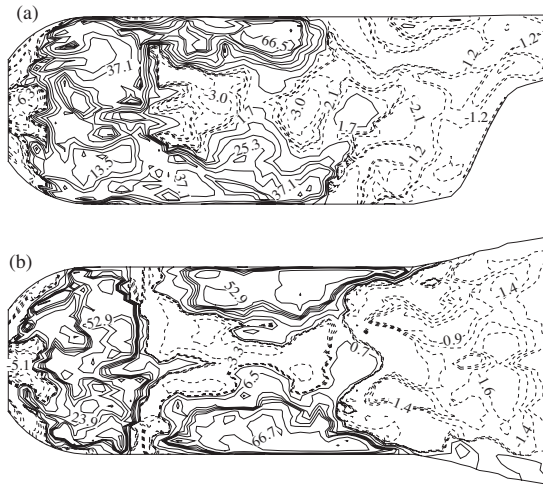


Fig. 3 Contours of the divergence of the radiative heat fluxes on (a) the midvertical and (b) the midhorizontal planes of the combustor

energy by radiation, and this must be coupled in the overall energy conservation, which turns to be an improved temperature

prediction inside the combustion chamber. Further work is required to investigate this effect on the flame temperature and combustion species. However, this would require a substantial increase in computer resources as, at every time step, the radiation intensities would have to be calculated by the radiation solver for updating the radiative heat fluxes and finally obtaining a new temperature for the next time step.

In Fig. 4, we show some results of the incident radiation, G , at various positions on the horizontal plane of the gas turbine combustor. To judge the performance and accuracy of the various orders of approximation of the DOM (S_n), the results of the incident radiation are plotted for S_2 , S_4 , S_6 , and S_8 . The wall emissivity in this plot still remain unchanged. It is interesting to mention here that the incident radiation is an important radiation property related to the radiative energy density, by which the total radiation energy is stored in each computational node, so each frame in this figure shows a distinct variation of the energy storage inside the combustion chamber. Prediction of the incident radiation is also an essential task, which allows the radiative energy transfer to be coupled with the global energy conservation (for example, see Eq. (6)). The incident radiation is calculated using the following relation;

$$G = \int_{4\pi} \bar{I} d\Omega \approx \sum_{m=1}^M \omega_m \bar{I}_m \quad (7)$$

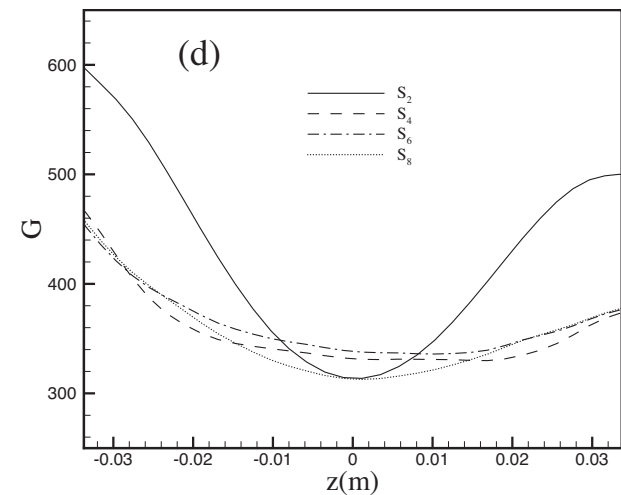
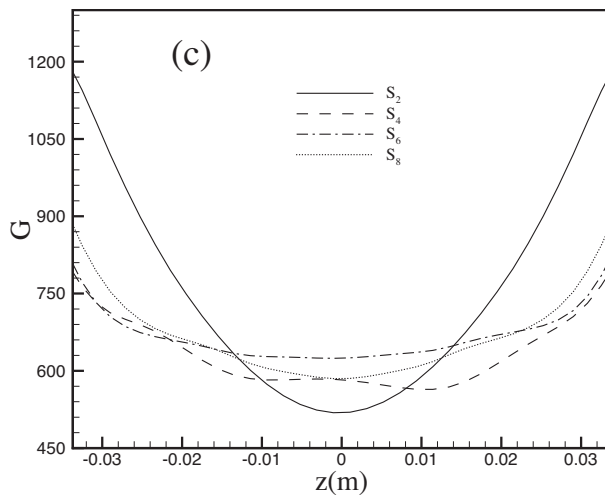
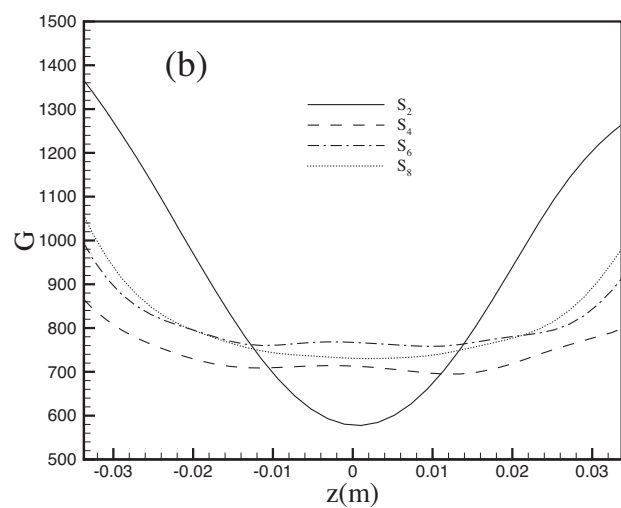
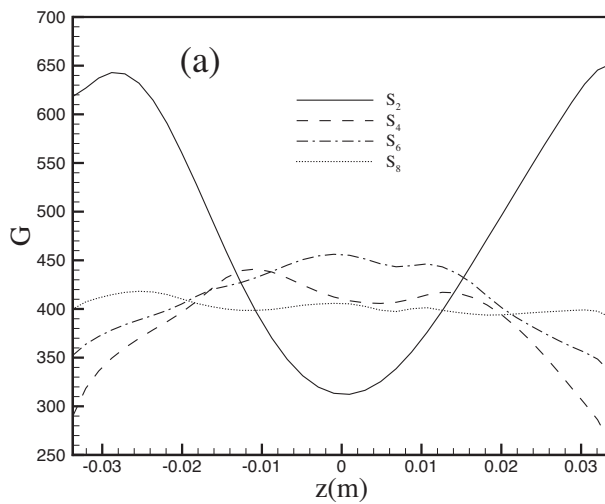


Fig. 4 Radial profiles of the incident radiation, G (kW m^{-2}), at (a) $y=20$ mm, (b) $y=95$ mm, (c) $y=130$ mm, and (d) $y=165$ mm on the midhorizontal plane of the combustor

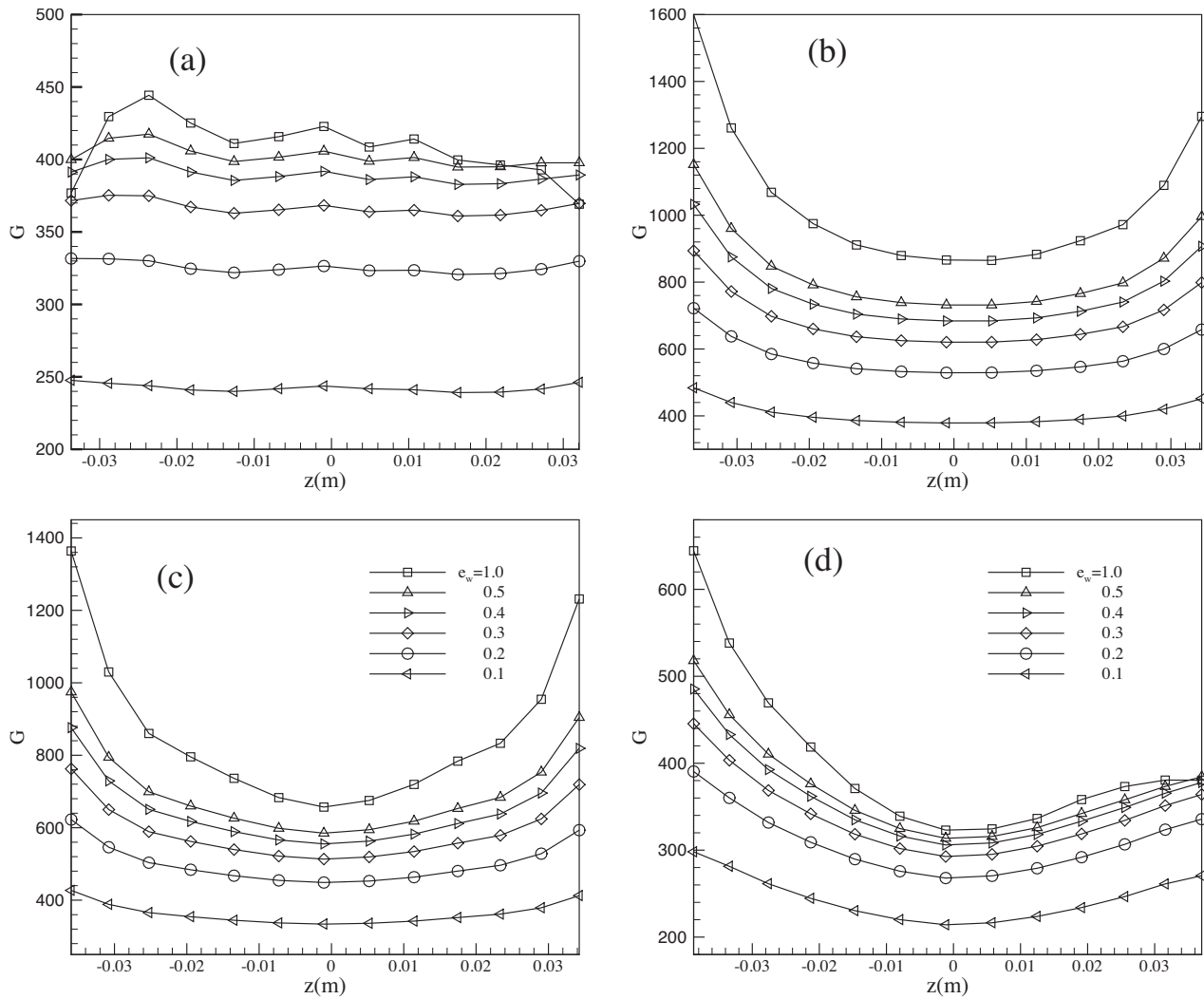


Fig. 5 Effects of the wall emissivity on the incident radiation, G , plotted at (a) $y=20$ mm, (b) $y=95$ mm, (c) $y=130$ mm, and (d) $y=165$ mm on the midhorizontal plane of the combustor

In Fig. 4, we can see how the results obtained using the most lower order approximation, S_2 , of the DOM divert from those with the higher orders. However, the higher order S_n (S_4 , S_6 , and S_8) results appear to converge together at a level of G .

In frame (a), G is calculated in a position of the combustor head, and it is found to be lower compared to those shown in the other frames. This is expected, as the radiative intensity, the absorption-emission rate, and the flame temperature in the combustor head region are all predicted lower (see Fig. 2). However, in the combustor barrel (at $y=95$ mm, frame (b)), G is predicted to be maximum, because this part of the combustor houses the extremely hot gases. At the dilution ports (at $y=130$ mm, frame (c)), the effect of the large amount of cooling air on the prediction of the incident radiation is clear, and at the downstream (at $y=165$ mm, frame (d)), G decreases again because of the effect of the cooling air through the dilution ports, and no combustion occurs downstream of these ports and the temperature drops.

The effects of the wall emissivity ϵ_w on the prediction of the incident radiation are now shown in Fig. 5. The four horizontal locations along the combustion chamber are chosen at (a) $y=20$ mm, (b) $y=95$ mm, (c) $y=130$ mm, and (d) $y=165$ mm, which are the same frame locations we took to present the results of G already shown in Fig. 4. Our intention here is to see how the radiation results are influenced by the choice of the wall emissivity. In this figure, only the S_8 results of the DOM are presented.

When $\epsilon_w=1.0$, the results at all frames in Fig. 5 show that the prediction of the incident radiation is maximum. For the other values of ϵ_w less than 1.0, the results of the incident radiation decrease. These predictions are quite practical and expected. Because the wall emissivity of $\epsilon_w=1.0$ represents the walls of the combustion chamber that are completely black, and the rate of the outgoing radiative intensities from the walls is maximum, which is the same rate as the blackbody intensity, no surface irradiation occurred in this situation. For the other cases, as we decrease ϵ_w from 1.0, the rate of the wall outgoing radiative intensities decreases; hence, the results of G in all frames decrease gradually.

In Fig. 6, a comparison of the rate of convergence of the various approximations of S_n against the wall emissivity is given. It is clear that the DOM order S_4 converges quicker for all selected wall emissivities than the other two higher orders, S_6 and S_8 , and the lower order, S_2 , do. As we increase the order of approximations from S_4 , the number of iteration to satisfy the following convergent condition

$$\max_{1 \leq m \leq M} |\bar{I}_m^{P(i+1)} - \bar{I}_m^{P(i)}| \leq 10^{-5} \quad (8)$$

increases. This is reasonable given the fact that the total number of discrete directions M depends on the order of approximations and increases with their orders. For S_2 , it is expected that the DOM code converges faster than all other cases, but surprisingly,

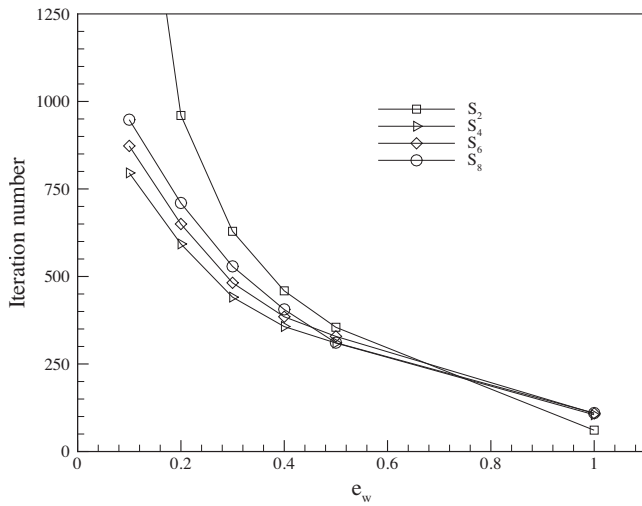


Fig. 6 Rate of convergence with various S_n and e_w

the computational cost for this order is highest. The S_2 approximation was also tested considering a relatively smaller wall emissivity, less than $\epsilon_w=0.1$, and a very poor convergence rate was achieved in the radiation solver due to the very oscillatory nature of the radiative intensity solutions. In relation (8), i is the number of iteration and P represent a computational node point.

5 Conclusions

The DOM has been implemented to investigate the radiative heat transfer inside a 3D model gas turbine combustor. Performances of the various higher and lower order approximations of the DOM have been examined in the prediction of the radiative transfer, and we have found that the results of the higher orders agree well with each other. The DOM code has been combined with a LES of the flow, temperature, and composition fields within the combustion chamber. In the radiation model, a gray-gas and nonscattering approximation to the RTE has been assumed, and the absorption coefficient for both H_2O and CO_2 gases is calculated.

The instantaneous results of the radiative heat fluxes, incident radiation, and divergence of radiative heat fluxes have been presented. A coupling of the radiative heat flux gain/loss is likely to yield accurate prediction of the wall temperature and this will aid combustor design by allowing an optimum amount of air to be used for wall cooling. The beneficial effects will be a reduction in the emission of pollutant gases by maximizing the combustion efficiency and a longer liner life.

A detailed presentation of the effects of the wall emissivity in the prediction of the incident radiation has been given, and we found that the incident radiation inside the combustion chamber is enhanced by increasing the value of the wall emissivity and it is maximum when the wall emissivity is equal to 1, which is the same characteristic value for a black wall.

In the present investigation, the effects of the soot particles on the radiative heat transfer have been excluded. Soot is likely to enhance the radiation field, and ultimately the coupling of soot formation and consumption to heat radiation is an important requirement. The soot concentrations are required, and this in turn requires the solution of the appropriate conservation equations for the soot properties. Research is currently underway on this.

Nomenclature

Roman Characters

- G = incident radiation
 J_j = subgrid scale scalar fluxes

- I = radiative intensity
 Sc = Schmidt number
 M = total number of the discrete directions
 p = dynamic pressure
 q = radiative heat fluxes
 t = time
 T = temperature
 u_j = velocity components along the Cartesian coordinates
 x_j = Cartesian coordinates (x, y, z)
 Y_α = mole fraction of species α

Greek Symbols

- α, β, γ = direction cosines
 δ = Kronecker delta
 ϵ = emissivity
 κ = absorption coefficient
 μ = coefficient of viscosity
 ρ = fluid density
 σ = Stefan–Boltzmann constant
 τ_{ij} = subgrid scale stresses
 f = mixture fraction

Subscripts

- b = blackbody
 m = angular discrete direction
 n = approximation of S_n
 w = wall

Superscripts

- $\bar{\cdot}$ = spatial filtered quantities
 $\tilde{\cdot}$ = Favre filtered quantities

Abbreviation

- SGS = subgrid scale

References

- Chandrasekhar, S., 1960, *Radiative Transfer*, Dover, New York.
- Carlson, B. G., and Lathrop, K. D., 1968, "Transport Theory: The Method of Discrete Ordinates," *Computing Methods in Reactor Physics*, Gordon and Breach, New York, pp. 165–266.
- Jamaluddin, A. S., and Smith, P. J., 1988, "Predicting Radiative Transfer in Rectangular Enclosures Using the Discrete Ordinates Method," *Combust. Sci. Technol.*, **59**, pp. 321–340.
- Liu, J., Shang, H. M., Chen, Y. S., and Wang, T. S., 1997, "Prediction of Radiative Transfer in General Body-Fitted Coordinates," *Numer. Heat Transfer, Part B*, **31**, pp. 423–439.
- Kayakol, N., Selcuk, N., Campbell, I., and Gulder, O. L., 2000, "Performance of Discrete Ordinates Method in a Gas Turbine Combustor Simulator," *Exp. Therm. Fluid Sci.*, **21**, pp. 134–141.
- Kaplan, C. R., Back, S. W., Oran, E. S., and Ellzey, J. L., 1994, "Dynamics of a Strongly Radiating Unsteady Ethylene Jet Diffusion Flame," *Combust. Flame*, **96**, pp. 1–21.
- Desjardin, P. E., and Frankel, S. H., 1999, "Two-Dimensional Large Eddy Simulation of Soot Formation in the Near-Field of a Strongly Radiating Non-premixed Acetylene-Air Turbulent Jet Flame," *Combust. Flame*, **119**, pp. 121–132.
- Jones, W. P., and Paul, M. C., 2005, "Combination of DOM With LES in a Gas Turbine Combustor," *Int. J. Eng. Sci.*, **43**, pp. 379–397.
- Chai, J. C., Lee, H. S., and Patankar, S. V., 1993, "Ray Effect and False Scattering in the Discrete Ordinates Method," *Numer. Heat Transfer, Part B*, **24**, pp. 373–389.
- Biceu, A. F., Tse, D. G. N., and Whitelaw, J. H., 1987, "Combustion Characteristics of a Model Can-Type Combustor," Imperial College London, Technical Report No. fs/87/28.
- Leonard, A., 1974, "Energy Cascade in Large-Eddy Simulations of Turbulent Fluid Flows," *Adv. Geophys.*, **18A**, pp. 237–248.
- Favre, A., 1968, "Statistical Equations of Turbulent Cases in Problems of Hydrodynamics and Continuum Mechanics," Society of Industrial and Applied Mathematics, Technical Report.
- Modest, M. F., 2003, *Radiative Heat Transfer*, 2nd ed., Academic, New York.
- Lefebvre, A. H., 1984, "Flame Radiation in Gas Turbine Combustion Chambers," *Int. J. Heat Mass Transfer*, **27**(9), pp. 1493–1510.
- Magnussen, B. F., and Hjertager, B. H., 1976, "On Mathematical Modelling of Turbulent Combustion With Special Emphasis on Soot Formation and Combustion," *16th Symposium (International) on Combustion*, The Combustion Institute, pp. 719–729.
- Smagorinsky, J., 1963, "General Circulation Experiments With the Primitive

- Equations. I. The Basic Experiment," *Mon. Weather Rev.*, **91**, pp. 99–164.
- [17] Schmidt, H., and Schumann, U., 1989, "Coherent Structure of the Convective Boundary Layer Derived From Large Eddy Simulation," *J. Fluid Mech.*, **200**, pp. 511–562.
- [18] di Mare, F., Jones, W. P., and Menzies, K., 2004, "Large Eddy Simulation of a Model Gas Turbine Combustor," *Combust. Flame*, **137**, pp. 278–294.
- [19] Thompson, J. F., Thames, F., and Mastin, C., 1974, "Automatic Numerical Generation of Body-Fitted Curvilinear Coordinates System for Field Containing Any Number of Arbitrary Two-Dimensional Bodies," *J. Comput. Phys.*, **15**, pp. 299–319.
- [20] Branley, N., and Jones, W. P., 2001, "Large Eddy Simulation of a Turbulent Nonpremixed Flame," *Combust. Flame*, **127**, pp. 1913–1934.

Experimental and Analytical Studies of Reciprocating-Mechanism Driven Heat Loops (RMDHLs)

Yiding Cao
Mingcong Gao

Department of Mechanical Engineering,
Florida International University,
Miami, FL 33199

This paper conducts experimental and analytical studies of a novel heat-transfer device, reciprocating-mechanism driven heat loop (RMDHL) that facilitates two-phase heat transfer while eliminating the so-called cavitation problem commonly encountered by a conventional pump. A RMDHL normally includes a hollow loop having an interior flow passage, an amount of working fluid filled within the loop, and a reciprocating driver. The hollow loop has an evaporator section, a condenser section, and a liquid reservoir. The reciprocating driver is integrated with the liquid reservoir and facilitates a reciprocating flow of the working fluid within the loop, so that liquid is supplied from the condenser section to the evaporator section under a substantially saturated condition and the so-called cavitation problem associated with a conventional pump is avoided. The reciprocating driver could be a solenoid-operated reciprocating driver for electronics cooling applications and a bellows-type reciprocating driver for high-temperature applications. Experimental study has been undertaken for a solenoid-operated heat loop in connection with high heat flux thermal management applications. Experimental results show that the heat loop worked very effectively and a heat flux as high as 300 W/cm^2 in the evaporator section could be handled. A working criterion has also been derived, which could provide a guidance for the design of a RMDHL. [DOI: 10.1115/1.2909078]

Keywords: two-phase heat transfer, two-phase reciprocating flow, high heat flux, solenoid driver

Introduction

A heat-transfer device utilizing a two-phase heat-transfer mode is very effective in terms of the rate of heat transfer and temperature uniformity. Such a heat-transfer device typically includes an evaporator section where vaporization of the working fluid hermetically sealed within the device occurs through the heat transfer from an external heat source into the heat-transfer device, and a condenser section where the vapor generated in the evaporator is condensed into liquid through the heat transfer out of the heat-transfer device to an external heat sink. The heat-transfer device requires a driving mechanism for returning the liquid back to the evaporator from the condenser. Since the liquid within the two-phase heat-transfer device is substantially saturated, a conventional pump would encounter the so-called cavitation problem, which would prevent the pump from creating a pressure head for circulating the liquid within the heat-transfer device [1]. Subsequently, the utilization of a conventional pump in a two-phase heat-transfer device is rare unless the size of the heat-transfer device is sufficiently large and a sufficient subcooling of the liquid at the inlet of the pump can be maintained.

Because of the cavitation problem associated with an actively pumped two-phase heat-transfer system, a passive heat-transfer device is usually considered for two-phase heat-transfer purposes. Since the invention of the heat pipe by Grover in 1963 Grover [2], the heat pipe has been successfully developed as a passive two-phase heat-transfer device [3–5]. Although the heat pipe originally invented by Grover employs the capillary action of a wick structure as the driving force for returning the condensate from the

condenser to the evaporator, several other driving forces were also employed. These driving forces that have found significant applications include centrifugal forces (rotating heat pipes) and gravitational force (gravity-assisted heat pipes). In addition, the capillary pumped loop or capillary pumped heat pipe which requires a capillary-wick structure only in the evaporator section, has also been developed [6–8]. Recent variations of passive two-phase heat transfer devices include pulsating heat pipes by Akachi [9] and network heat pipes or thermal spreaders by Cao and Gao [10]. The capillary-wick based heat pipe has found substantial applications especially in aerospace undertakings such as satellite isothermization and consumer electronics cooling for computers, and the gravity-assisted heat pipe has found significant terrestrial applications such as those in heat recovery units. However, the magnitude of the capillary pumping action is relatively small and is limited by the pressure difference across the menisci in the capillaries. As a result, the heat pipe would have difficulty handling applications involving a very high heat flux and power input. Furthermore, the gravity-assisted heat pipe is limited to the terrestrial applications where the gravitational head is available.

Cao and Wang [11] developed a reciprocating heat pipe, which has a heat-transfer mechanism different from those of traditional heat pipes. The reciprocating heat pipe is attached to an axially reciprocating mechanism, such as a slider-crank mechanism of an internal combustion engine. During the operation, the heat pipe experiences the same reciprocating motion as that of the reciprocating mechanism, which creates a reciprocating motion of the liquid within the heat pipe relative to the heat pipe container. This reciprocating motion of the liquid inside the heat pipe effectively returns the liquid condensate from the condenser section to the evaporator section. The collision of the liquid with the heat pipe interior wall and the rapid mixing of the working fluid in the heat pipe also significantly enhance the heat transfer within the heat

Contributed by the Heat Transfer Division of ASME for publication in the JOURNAL OF HEAT TRANSFER. Manuscript received April 16, 2007; final manuscript received August 23, 2007; published online May 16, 2008. Review conducted by Giulio Lorenzini.

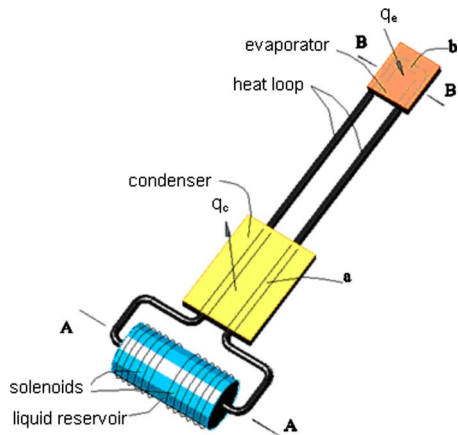


Fig. 1 Schematic of a RMDHL

pipe. The reciprocating heat pipe substantially eliminates many heat-transfer limitations associated with the heat pipe and produces a substantially uniform temperature distribution along the heat pipe length even under a high heat loading condition. The application of the reciprocating heat pipe, however, is substantially limited to the heat transfer in a reciprocating element. Since most heat-transfer applications involve nonreciprocating elements, the applicability of the reciprocating heat pipe concept may be limited.

Reciprocating-Mechanism Driven Heat Loops (RMDHLs)

Cao and Gao [12] conceived a heat-transfer device, which attains a reciprocating flow of the working fluid inside the heat-transfer device without requiring a reciprocating motion of the entire heat-transfer device, so that the application of the heat-transfer device will not be limited to reciprocating elements. The concept also provides a novel fluid pumping mechanism for heat-transfer purposes. Such a heat-transfer device is schematically illustrated in Fig. 1. The heat-transfer device, the reciprocating-mechanism driven heat loop (RMDHL) or the reciprocating-flow heat loop, includes a hollow loop having an interior flow passage, an amount of working fluid filled within the loop, and a reciprocating driver. The heat loop has an evaporator section, a condenser section, and a liquid reservoir. The reciprocating driver is integrated with the liquid reservoir and facilitates a reciprocating flow of the working fluid within the heat loop, so that liquid is supplied from the condenser section to the evaporator section and a high heat-transfer rate from the evaporator section to the condenser section is achieved. A substantial temperature uniformity is also attained when the air is evacuated from the loop and the working fluid hermetically sealed within the loop is under a substantially saturated condition. As a result, many of the heat-transfer limitations associated with a heat pipe or capillary pumped loop may be eliminated.

In a conventional pump, a unidirectional pressure difference between the pump outlet and inlet is needed to produce a pressure head for the circulation of the working fluid. When the working fluid is a two-phase condition, however, it has a tendency thermodynamically to reach a pressure and temperature equilibrium in the system. Therefore, some liquid in the pump inlet would flash into vapor due to a lower pressure there, which raises the pressure at the inlet and eliminates the pump pressure head. This phenomenon is called cavitation [1]. In the present RMDHL, however, this unidirectional pressure head is not necessary. In fact, the pressure at a given location of the loop would oscillate around a certain value. The working fluid in the loop is driven from the con-

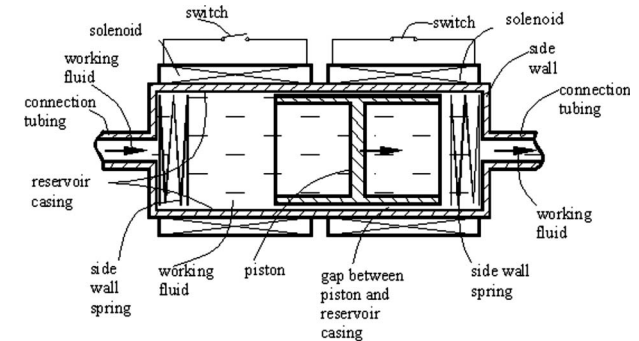


Fig. 2 Schematic of a solenoid driver integrated with the liquid reservoir

denser section to the evaporator section reciprocatingly through the displacement of the piston. As a result, the cavitation problem associated with a conventional pump is avoided.

The reciprocating driver, as shown in Fig. 1, can be a solenoid-operated electromagnetic driver and is schematically illustrated in Fig. 2, which is a sectional view taken on Line A-A in Fig. 1. The electromagnetic driver includes a pair of solenoids, which are disposed outside of the casing of the liquid reservoir in an axial direction of the reservoir, and a piston of magnetic metal disposed movably inside the reservoir. In the case shown in Fig. 2, the circuit of the right-hand solenoid is closed through a switch while the circuit of the left-hand solenoid is opened through a switch associated with it. As a result, the piston is being attracted toward the right through the magnetic field generated by the solenoid, and a counterclockwise flow of the working fluid within the loop is produced. When the piston approaches the right end of the liquid reservoir, the switch of the left-hand solenoid is closed while the switch of the right-hand solenoid is opened. As a result, the piston stops being attracted by right-hand solenoid and is attracted by left-hand solenoid toward the left, and a clockwise flow of the working fluid within the loop is produced (not shown here). With the circuits of the two solenoids being opened and closed alternately opposite to each other, a reciprocating motion of the piston is induced, which in turn produces a reciprocating flow of the working fluid within the heat loop. Because the liquid reservoir has a substantially larger inner diameter than that of the loop tubing (or the volume of the reservoir is large compared to the remainder of the interior volume of the loop) and a sufficient fraction of the interior volume of the loop is occupied by liquid, with a sufficiently large piston stroke, liquid is effectively supplied to the evaporator section from the condenser section.

When the working temperature of the heat loop is high, a bellows-type reciprocating heat loop employing an external reciprocating mechanism could be used (Fig. 3). As shown in the figure, through a connecting rod, the bellows is coupled with a reciprocating mechanism, which could produce a reciprocating motion with a sufficiently large reciprocating stroke. A detailed description of the aforementioned bellows-type driver is schematically illustrated in Fig. 4. In this case, part of or substantially entire circumferential casing of the liquid reservoir is a bellows. A partition is disposed near the midsection of the bellows. The partition is coupled with an external reciprocating mechanism through a connecting rod. The external reciprocating mechanism can be a solenoid-operated electromagnetic driver or a mechanical reciprocating mechanism driven by an electric motor. When the external reciprocating mechanism is in operation, a reciprocating motion of the partition is produced through the coupling with the reciprocating mechanism, which in turn produces a reciprocating flow of the heat-carrying fluid enclosed within the loop. Since the bellows-type reciprocating heat loop does not contain any contacting surfaces having a relative motion in the high-temperature region, it could work at a much higher temperature. Additionally,

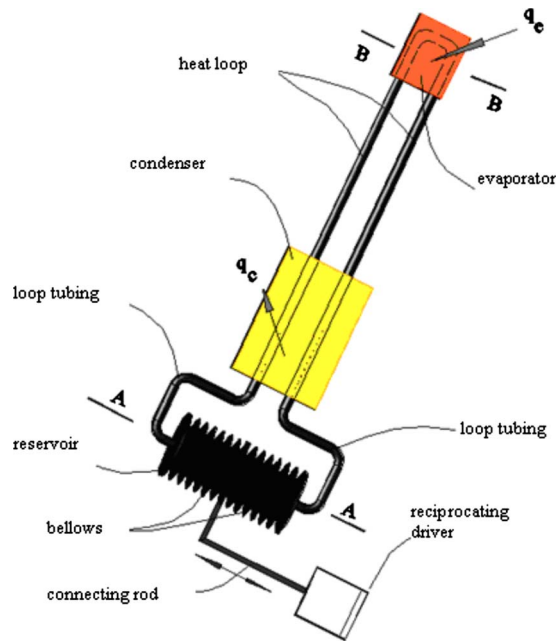


Fig. 3 Schematic of a bellows-type RMDHL

during the operation of the bellows-type driver, the outer surface of the bellows can be adequately cooled so that the bellows can be maintained at a sufficiently low temperature for its reliability. Additionally, a noncondensable gas can be filled within the bellows to further reduce the bellows temperature.

Experimental Study of a Solenoid-Operated Heat Loop

In this study, two solenoid-operated reciprocating loops similar to that shown in Fig. 1 were fabricated and studied experimentally. Figure 5 shows a photograph of one of the heat loops fabricated and tested. The experimental setup for this study is shown in Fig. 6, which includes an electric heater for supplying heat to the

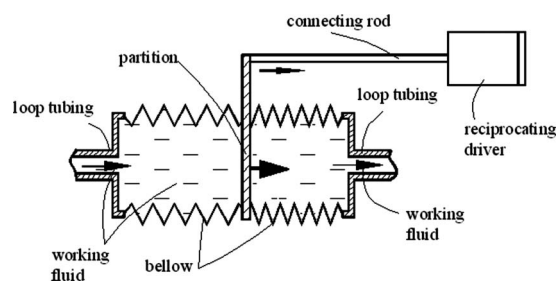


Fig. 4 Schematic axial cross-sectional view of a bellows-type reciprocating driver

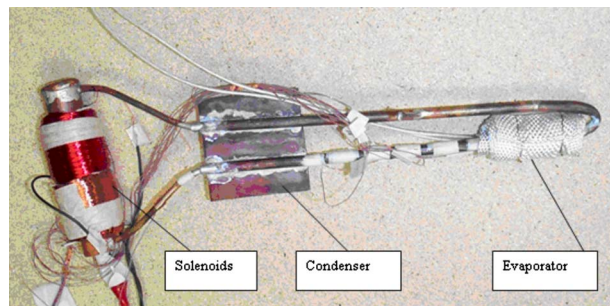


Fig. 5 A photograph of the fabricated RMDHL

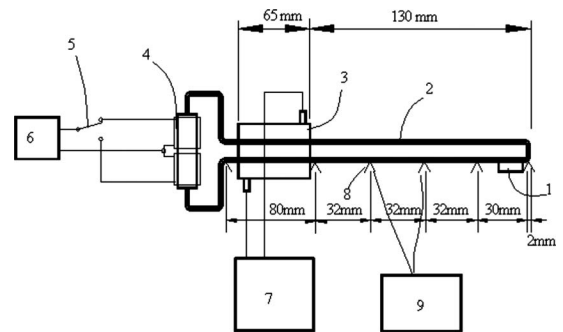


Fig. 6 Experimental setup: (1) heater, (2) heat loop, (3) cooling jacket, (4) solenoids, (5) switch, (6) power supply, (7) constant temperature circulator, (8) thermocouples, and (9) data acquisition system

evaporator of the heat loop, a power supply to the solenoid driver, a constant temperature circulator to maintain a constant coolant inlet temperature, a data acquisition system, and the heat loop to be studied. The portion of the heat loop from the evaporator section to the condenser section was placed in a horizontal position to eliminate the influence of gravity on the performance of the heat loop. The heat loop is made of copper tubing having an outer diameter of 0.25 in. and a wall thickness of 0.035 in.. The reservoir has an inner diameter of 0.75 in. and a length of about 104 mm. The heater is a small cartridge heater for providing a high heat flux heat input to the evaporator. The heater was welded onto the outside surface of the heat loop at the right end of the heat loop, as shown in Fig. 6. The contact surface area between the heater and the heat loop was approximately 0.56 cm². This small contact surface area was deliberately set for providing a high heat flux to the evaporator. After the heater was welded to the heat loop, it was insulated from the ambient using a fiber glass tape to eliminate the heat loss from the heater to the ambient. Six thermocouples were placed on the outer surface of a branch of the heat loop with the first thermocouple being close to the heater to measure the axial temperature distribution. A liquid circulator is used to adjust and maintain a constant liquid inlet temperature at the cooling jacket so that the heat loop could operate at different working temperatures. The distance between the right end of the heat loop and the cooling jacket and the length of the cooling jacket are also indicated in Fig. 6. A control circuit board was used to control the reciprocating frequency of the solenoid driver. Water is used as working fluid for the study and it occupied approximately 70% of the interior volume of the heat loop. The magnetic material of the reciprocating driver is carbon steel coated with copper in order to be compatible with water.

To qualify the performance of the RMDHL, the temperature distribution due to pure heat conduction along the loop wall was measured and plotted in Fig. 7. In this case, the solenoid driver was turned off and a small amount of heat was added at evaporator until the temperature distribution reached the steady condition (a higher heat input would burn the heater). Then, the solenoid driver was turned on. The temperature spike at the evaporator quickly disappeared and the temperature uniformity was attained along the heat loop. The corresponding temperature distribution is also shown in Fig. 7. After the performance of the heat loop was qualified, the heat loop was tested at different working temperatures through the control of the cooling jacket inlet temperature. Figure 8 shows the temperature distributions along the heat loop at different heat inputs to the evaporator when the cooling water temperature at the inlet of the cooling jacket was maintained at 50°C. The maximum attained heat input to the evaporator was about 171 W and the corresponding heat flux at the evaporator was approximately 306 W/cm². The power consumption of the solenoid driver was approximately 16 W. The stroke of the driver

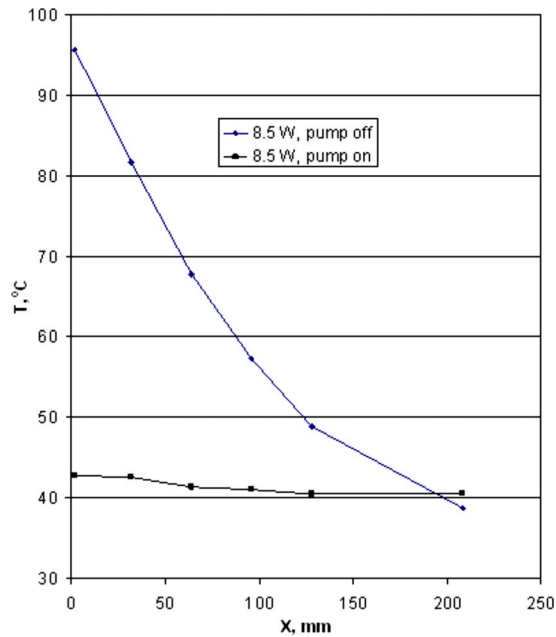


Fig. 7 Comparison of temperature distributions with pump on and off

was about 40 mm, and the magnitude of the reciprocating frequency was 1 Hz. The sources of the experimental uncertainty were only the instruments themselves. The scanning thermocouple thermometer has an accuracy of $\pm 0.1\%$ of reading $\pm 0.4^\circ\text{C}$. The power meter has an accuracy of $\pm (1\% \text{ reading} + 5 \text{ digits})$, so the maximum uncertainty for the temperature and heating power measurement would be 1.0% and 2%, respectively.

To quantify the performance of the heat loop, the so-called effective heat conductance, which was commonly employed to evaluate the performance of a heat pipe, was calculated by using the following relation:

$$k_{\text{eff}} = \frac{qL}{A\Delta T}$$

For the maximum heat input in Fig. 8, $q=171 \text{ W}$, $L=0.206 \text{ m}$, and $\Delta T=12.0^\circ\text{C}$. The cross-sectional area A should be the total cross-sectional area of the loop at a given location and should be

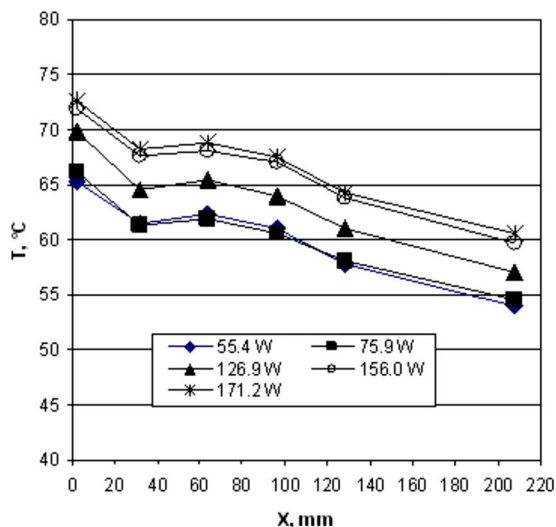


Fig. 8 Axial temperature distributions ($T_c=50^\circ\text{C}$)

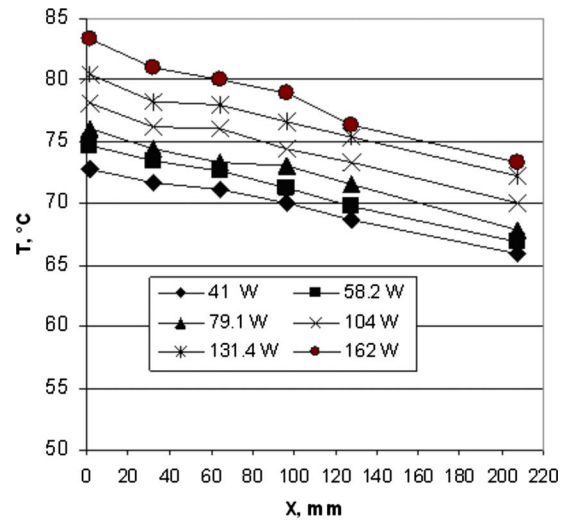


Fig. 9 Axial temperature distributions ($T_c=65^\circ\text{C}$)

evaluated based on the outer diameter of the loop tubing. Since two tubings exist at a given axial location, a factor of 2 should be multiplied. Therefore,

$$A = 2 \left(\frac{\pi}{4} d^2 \right) = 2 \left(\frac{\pi}{4} 0.00635^2 \right) \approx 6.33 \times 10^{-5} \text{ m}^2$$

The effective thermal conductance of the heat loop can then be calculated as follows:

$$k_{\text{eff}} = \frac{(171)(0.206)}{(6.33 \times 10^{-5})(12)} = 46,374.0 \text{ W/mK}$$

If the thermal conductivity of copper is taken to be 400 W/m K , then

$$\frac{k_{\text{eff}}}{k_{\text{Cu}}} = \frac{46,374}{400} = 116.0$$

It can be seen from the calculation that the RMDHL is a very effective heat-transfer device; it could achieve an effective thermal conductance more than 100 times that of copper at a heat flux more than 300 W/cm^2 . It should be mentioned that the maximum heat flux can be further increased by providing heat-transfer enhancement surfaces at the inner surface of the evaporator. These heat-transfer surfaces include inserts, grooves, and porous structures. The heat-transfer enhancement surfaces could increase the critical heat flux at the evaporator, reduce the temperature difference between the inner surface of the evaporator and the working fluid, and provide a liquid retain mechanism to reduce power consumption of the solenoid driver. Figures 9 and 10 show the temperature distributions at different power inputs to the evaporator at cooling water inlet temperatures of 65°C and 40°C , respectively. As can be seen, the performance at cooling water temperature of 40°C deteriorated somewhat. It should be pointed out that this deterioration was due to the reattachment of the heater to the evaporator. During the previous runs of the experiment, the cartridge heater welded to the evaporator was burnt out. The burnt-out heater was thus removed and a new heater was welded to the heat loop. During these removal and attachment, the evaporator of the heat loop was subject to a high temperature during a relatively long period of time. As a result, oxidation could have occurred at the inner surface of the evaporator and the liquid wetting condition at the evaporator could have deteriorated, which would have adversely affected the boiling heat transfer at the inner surface of the evaporator.

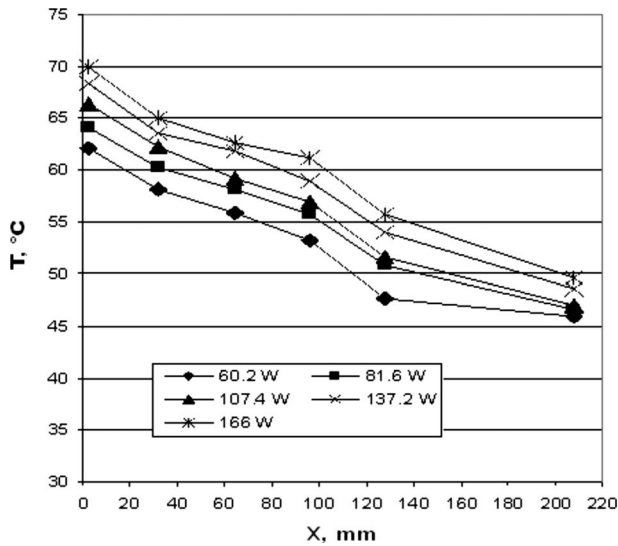


Fig. 10 Axial temperature distributions ($T_c=40^\circ\text{C}$)

Critical Displacement of the Reciprocating Driver

For a given RMDHL, the volume displacement of the reciprocating driver must be sufficiently large so that the liquid can be supplied from the condenser section to the evaporator section. We wish to find a relation that could describe this critical requirement for the operation of the heat loop. Consider a RMDHL under a two-phase working condition (liquid and vapor coexist) similar to that shown in Fig. 1. The heat loop is assumed to have a condenser section on each side of the reciprocating driver, and the loop is symmetric about the line connecting the midpoints of the evaporator and reservoir. Because of this geometric symmetry, we would like to concentrate on the right half of the loop, as shown in Fig. 11. The length and average interior cross-sectional area of the evaporator are denoted by L_e and A_e , respectively, the length and average interior cross-sectional area of the connection tubing between the evaporator and the condenser are L_i and A_i , the length and interior cross-sectional area of each condenser section are L_c and A_c , the interior volume of the section between the end of the condenser and the piston right dead center is $V_d/2$, and the piston cross-sectional area and reciprocating stroke are A_p and S , respectively. We consider initially that the circuits of both solenoids are open and the piston is stationed in the midsection of the liquid reservoir, and the vapor generated in the evaporator section pushes the liquid toward the condenser section with a liquid-vapor interface as indicated in the figure. Although there could be thin liquid films at the interior surface of the evaporator, the amount of liquid associated is neglected in the current analysis. In the derivation of the critical liquid displacement, the critical working condition is assumed to be reached when the liquid at the center of condenser, denoted by A , can just reach the midsection of the evaporator when the right-hand solenoid is turned on and the piston reaches the right dead center in the reservoir. This condition means that the liquid initially at the condenser center would move to or pass the center of the evaporator, as indicated in Fig. 12, if the RMDHL would work properly. A liquid balance between these two states would give the following relation:

$$A_p \frac{S}{2} + \frac{V_d}{2} + A_c L_c + A_i L_i \geq \frac{V_d}{2} + A_c L_c + A_i L_i + \frac{1}{2} A_e L_e + \frac{1}{2} A_c L_c + A_i L_i \quad (1)$$

Canceling out the common terms on both sides of the equation and multiplying the resulting equation by 2, we have

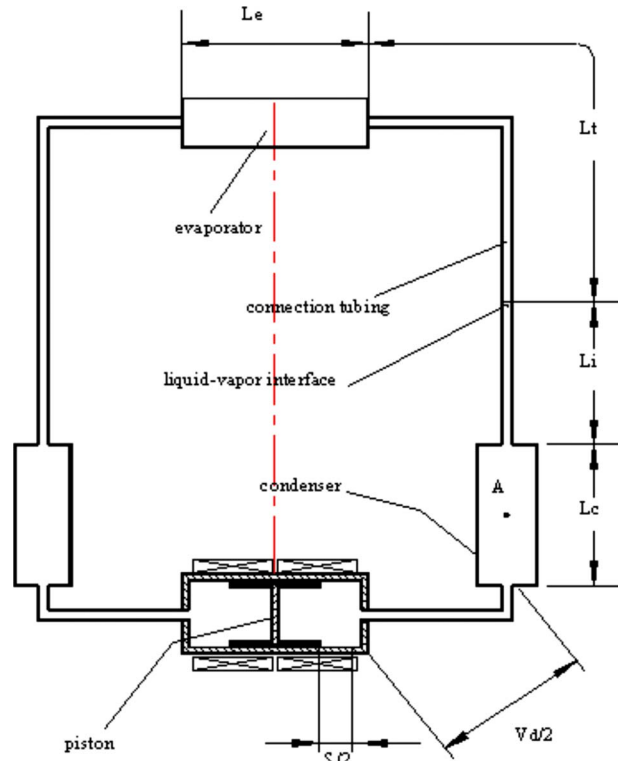


Fig. 11 The initial state of the heat loop for the derivation of the working criterion

$$A_p S \geq A_c L_c + 2A_i L_i + A_e L_e \quad (2)$$

The above equation can be rewritten as

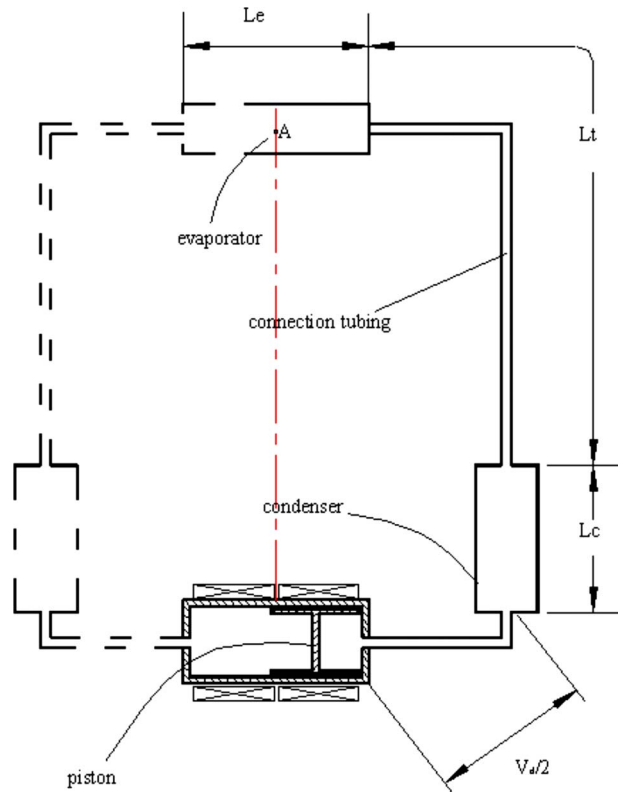


Fig. 12 The final state of the heat loop for the derivation of the working criterion

$$A_p S \geq 2 \left(\frac{1}{2} A_c L_c + A_t L_t + \frac{1}{2} A_e L_e \right) \quad (3)$$

The terms in the parentheses on the right-hand side of the above equation are the interior volume from the center of the condenser to the center of the evaporator on each side of the heat loop, which reflects one of the essential geometric characteristics of the heat loop in connection with the heat-transfer distance and fluid displacement volume. If an effective displacement volume is defined for the entire heat loop,

$$V_{\text{eff}} = 2 \left(\frac{1}{2} A_c L_c + A_t L_t + \frac{1}{2} A_e L_e \right) \quad (4)$$

Equation (3) can be written as

$$A_p S \geq V_{\text{eff}} \quad (5)$$

Equation (5) indicates that the liquid displacement volume of the piston as represented by $A_p S$ must be equal to or greater than the effective displacement volume of the heat loop if the heat loop is to work properly. Equation (5), however, is true only for a single-phase heat-transfer mode. For a two-phase heat-transfer mode, the criterion as represented by Eq. (4) or Eq. (5) is too conservative due to several reasons. Since the cross-sectional area of the reservoir is usually much greater than that of the rest of the heat loop, the liquid velocity exiting the liquid reservoir should be relatively high. Even if after the piston has reached the dead center in the reservoir, the liquid would continue to move toward the evaporator until the kinetic energy associated with it is exhausted. Additionally, once the liquid enters the evaporator section, some liquid will be evaporated into vapor. The evaporation will drastically change the volume of the flow stream and the liquid/vapor two-phase mixture will expand vigorously into the evaporator section. As a result, the section between the piston right dead center and the center of the evaporator in Fig. 12 would be filled with both liquid and vapor and the flow is in a two-phase flow condition. It is understood that the liquid fraction would change substantially along the loop. For the derivation of a more concise relation, an effective liquid fraction, ϕ , is used. By taking into account the two-phase flow condition, the liquid balance as represented by Eq. (1) should be modified as follows:

$$A_p \frac{S}{2} + \frac{V_d}{2} + \phi A_c L_c + \phi A_t L_t \geq \frac{V_d}{2} + \phi \left(A_c L_c + A_t L_t + \frac{1}{2} A_e L_e + \frac{1}{2} A_c L_c + A_t L_t \right) \quad (6)$$

Following the same deriving procedure, the following relation is obtained:

$$A_p S \geq 2 \left(\frac{1}{2} A_c L_c + A_t L_t + \frac{1}{2} A_e L_e \right) \phi \quad (7)$$

or

$$A_p S \geq \phi V_{\text{eff}} \quad (8)$$

The value of ϕ , by definition, is greater than zero and less than unity. An actual value of ϕ , however, has to be determined experimentally for most practical applications due to the complex heat-transfer process in the heat loop. Still, Eq. (3) or Eq. (7) provides a concise criterion that could be used for the design of a heat loop. It should be pointed out that during the derivation of the above relations, the liquid reservoir is assumed to contain pure liquid and the back flow through the gap between the outer surface of the piston and the inner surface of the reservoir casing is neglected. If the reservoir would deal with a two-phase liquid-vapor mixture

and the back flow effect is taken into account, the term $A_p S$ in the above equations may need to be multiplied by a driver efficiency η that is less than unity as follows:

$$\eta A_p S \geq 2 \phi \left(\frac{1}{2} A_c L_c + A_t L_t + \frac{1}{2} A_e L_e \right) \quad (9)$$

Conclusions

Two solenoid-operated RMDHLs have been fabricated and tested experimentally. Experimental results indicated that the heat loop worked very well and could handle a heat flux of more than 300 W/cm² in the evaporator section. In addition, a criterion that reveals the working mechanism of the heat loop was derived. The working criterion provides a concise guidance for the design of a heat loop. A reciprocating heat loop based on bellows-type reciprocating driver is also described for high-temperature applications. Some typical applications of the heat loop would include thermal management of high-power electronics, cooling the leading edges/nose caps of supersonic/hypersonic cruise vehicles, removing the waste heat for directed energy based new weapon systems, and cooling advanced gas turbines. However, as the RMDHL is further developed, many other important applications may be identified.

Nomenclature

A	= cross-sectional area, m ²
k	= thermal conductivity, W/m K
L	= length, m
q	= heat-transfer rate, W
S	= stroke, m
V	= volume, m ³
ϕ	= liquid fraction
η	= efficiency
ΔT	= temperature difference

Subscripts

e	= evaporation
t	= tubing
c	= condenser
p	= piston
eff	= effective

References

- [1] Fox, R. W., and McDonald, A. T., 1998, *Introduction to Fluid Mechanics*, 5th ed., Wiley, New York.
- [2] Grover, G., 1966, "Evaporation-Condensation Heat Transfer Devices," U.S. Patent No. 3229759.
- [3] Faghri, A., 1995, *Heat Pipe Science and Technology*, Taylor and Francis, Washington, D.C.
- [4] Peterson, G. P., 1994, *An Introduction to Heat Pipes: Modeling, Testing and Applications*, Wiley, New York.
- [5] Dunn, P. D., and Reay, D. A., 1982, *Heat Pipes*, 3rd ed., Pergamon, New York.
- [6] Ku, J., Kroliczek, E. J., and McIntosh, R., 1987, "Capillary Pumped Loop Technology Development," Proceedings of the Sixth International Heat Pipe Conference, France.
- [7] Maidanik, Y., Vershinin, S., Kholodov, V., and Dolgirev, J., 1985, "Heat Transfer Apparatus," U.S. Patent No. 4515209.
- [8] Hoang, T., O'Connell, T. A., Ku, J., Butler, C. D., and Swanson, T. D., 2003, "Miniature Loop Heat Pipes for Electronic Cooling," InterPack 2003, Paper No. 35245.
- [9] Akachi, H., 1990, "Structure of a Heat Pipe," U.S. Patent No. 4921041.
- [10] Cao, Y., and Gao, M., 2002, "Wickless Network Heat Pipes for High Heat Flux Spreading Applications," *Int. J. Heat Mass Transfer*, **45**, pp. 2539–2547.
- [11] Cao, Y., and Wang, Q., 1996, "Engine Piston," U.S. Patent No. 5454351.
- [12] Cao, Y., and Gao, M., 2003, "Reciprocating-Mechanism Driven Heat Loops and Their Applications," ASME Paper No. HT03-47195.

Analysis of the Thermal Behavior of a Multilayer Slab With Imperfect Contact Using the Dual-Phase-Lag Heat Conduction Model

K. Ramadan

Department of Mechanical Engineering,
Mu'tah University,
P.O. Box 7,
Karak 61710, Jordan
e-mail: rkhalid@mutah.edu.jo

M. A. Al-Nimr

Department of Mechanical Engineering,
Jordan University of Science and Technology,
P.O. Box 3030,
Irbid 22110, Jordan
e-mail: malnimr@just.edu.jo

The thermal behavior of a multilayered slab in imperfect contact using the dual-phase-lag heat conduction model is numerically analyzed, considering a range of heat flux-phase lag, temperature gradient-phase lag, and thermal contact resistance. Wave reflections from both insulated boundaries and contact surfaces take place when the phase lag of the temperature gradient is less than the phase lag of the heat flux. Due to the wave nature of energy transport in composite slabs having much less temperature gradient-phase lag than heat flux-phase lag and with a low thermal contact resistance, an initially low-temperature layer can attain a higher temperature than that of the initially high-temperature layer. For composite slabs with temperature gradient-phase lag higher than the heat flux-phase lag and due to the absence of the wave nature of energy transport and the enhancement of heat diffusion, a thermal disturbance is more quickly felt in the whole domain when the temperature gradient-phase lag increases, although in terms of the interfacial temperature difference, the contact surface shows lower response with increasing temperature gradient-phase lag during early stages of the transient energy transport. [DOI: 10.1115/1.2909074]

Keywords: dual phase lag, imperfect contact, thermal contact resistance

1 Introduction

The classical heat diffusion theory assumes thermal disturbances to propagate at an infinite speed in a medium; consequently, the heat flux vector and the temperature gradient simultaneously occur as postulated by Fourier's law of heat conduction:

$$\mathbf{q}(\mathbf{r}, t) = -k \nabla T(\mathbf{r}, t) \quad (1)$$

Fourier's law breaks down in applications with high heat flux intensities, very short times, and cryogenic temperatures. To account for the finite speeds of thermal disturbances, a phase-lag time between the temperature gradient and the heat flux is introduced into Fourier's law [1]:

$$\mathbf{q}(\mathbf{r}, t + \tilde{\tau}_q) = -k \nabla T(\mathbf{r}, t) \quad (2)$$

where $\tilde{\tau}_q$ is the lag time of the heat flux after the temperature gradient has been applied to the medium and is related to thermal wave speed and thermal diffusivity by

$$\tilde{\tau}_q = \alpha / C^2 \quad (3)$$

The first order approximation of Eq. (2) using Taylor series expansion gives the Cattaneo–Vernotte (CV) thermal wave model [1]:

$$\mathbf{q}(\mathbf{r}, t) + \tilde{\tau}_q \frac{\partial \mathbf{q}}{\partial t}(\mathbf{r}, t) \cong -k \nabla T(\mathbf{r}, t) \quad (4)$$

The precedence of the temperature gradient over the heat flux vector in the CV thermal wave model makes the temperature gradient as the cause for energy transport and the heat flux as the effect. Incorporating Eq. (4) in the energy equation leads to the hyperbolic heat conduction equation (HHCE) that resolves the finite speed of thermal wave propagation and describes the wave nature of energy transport. The HHCE, however, produces some anomalies and physically unacceptable results [2–4]. To remove the assumption of the temperature gradient precedence over the heat flux vector in the CV model, Tzou [1] proposed the dual-phase-lag (DPL) model:

$$\mathbf{q}(\mathbf{r}, t + \tilde{\tau}_q) = -k \nabla T(\mathbf{r}, t + \tilde{\tau}_T) \quad (5)$$

where $\tilde{\tau}_q$ is the phase lag of the heat flux and $\tilde{\tau}_T$ is the phase lag of the temperature gradient. In the DPL model with $\tilde{\tau}_q > \tilde{\tau}_T$, the temperature gradient within the medium induces the heat flux; hence, the temperature gradient is the cause for energy transport and the heat flux is the effect, while for $\tilde{\tau}_q < \tilde{\tau}_T$, the heat flux is the cause for energy transport and the temperature gradient is the effect. For $\tilde{\tau}_q = \tilde{\tau}_T$ with homogeneous initial temperature, the DPL model reduces to classical Fourier's law [1].

The DPL model has attracted much attention since it has been experimentally verified [5], and intensive research has been conducted on the thermal behavior of single and multilayer slabs by using the DPL model [6–13]. The thermal behaviors of a single-layer thin slab under different operating and thermal boundary conditions are investigated in Refs. [6–9] by using analytical solution methods, and comparisons between the DPL, hyperbolic, and the classical heat diffusion models are presented.

The thermal behavior of a multilayer slab within the DPL model framework has also been investigated by many researchers [10–13]. Al-Huniti and Al-Nimr [10] investigated the thermoelastic behavior of a composite slab in perfect contact with different material properties of the slab layers. A study of the thermal behavior of a perfect contact composite slab carrying periodic signals was conducted by Al-Nimr et al. [11]. The deviations among the predictions of the DPL, hyperbolic, and classical heat diffusion models are also investigated. Ho et al. [12] studied heat transfer in multilayered structure in perfect thermal contact subject to a pulsed volumetric heat source. They also investigated the effect of the temperature gradient-phase lag on the thermal wave transmission and reflection phenomena at the perfect interface. Recently, Lee and Tsai [13] studied the thermal behavior of a two-layered semi-infinite material with interfacial contact conductance subject to ultrafast pulse-laser heating by using the Laplace transform semianalytical method. A simple temperature jump was assumed at the interface due to the finite interfacial conductance. The hyperbolic heat conduction model was used by Khadrawi et al. [14] to study the thermal behavior of perfect and imperfect contact composite slabs and Lor and Chu [15] to investigate the effect of the interface thermal contact resistance on heat transfer in a composite medium.

As is clear from the above survey, the thermal behavior of finite multilayer slabs with imperfect contact within the framework of the DPL heat conduction model has not been investigated yet. This motivates us to conduct the present study.

Contributed by the Heat Transfer Division of ASME for publication in the JOURNAL OF HEAT TRANSFER. Manuscript received March 20, 2007; final manuscript received August 9, 2007; published online May 16, 2008. Review conducted by Jamal Seyed-Yagoobi.

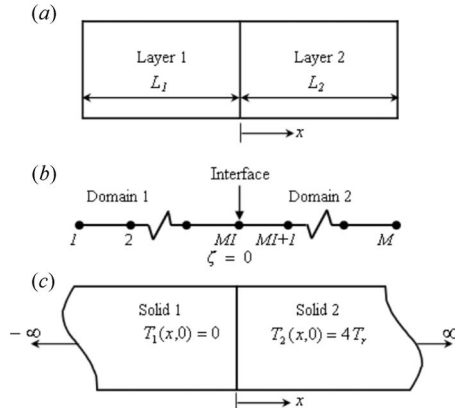


Fig. 1 Illustration of problem geometry (a), grid numbering in the computational domain (b), and two semi-infinite solids in perfect contact (c)

2 Mathematical Formulation

The dimensionless form of the governing equations and boundary conditions for transient heat conduction in a two-layer slab (Fig. 1(a)) is given as below:

$$\frac{\partial \theta_1}{\partial \eta} + \frac{\partial Q_1}{\partial \zeta} = 0 \quad (6)$$

$$Q_1 + \tau_{q1} \frac{\partial Q_1}{\partial \eta} + \frac{\partial \theta_1}{\partial \zeta} + \tau_{T1} \frac{\partial^2 \theta_1}{\partial \eta \partial \zeta} = 0 \quad (7)$$

$$\frac{\partial \theta_2}{\partial \eta} + \frac{\alpha_r \partial Q_2}{k_r \partial \zeta} = 0 \quad (8)$$

$$Q_2 + \tau_{q2} \frac{\partial Q_2}{\partial \eta} + \frac{\partial \theta_2}{\partial \zeta} + \tau_{T2} \frac{\partial^2 \theta_2}{\partial \eta \partial \zeta} = 0 \quad (9)$$

$$\theta_1(\zeta, 0) = 1, \quad -1 \leq \zeta \leq 0 \quad (10)$$

$$\theta_2(\zeta, 0) = 2, \quad 0 \leq \zeta \leq L_r \quad (11)$$

$$Q_1(\zeta, 0) = Q_2(\zeta, 0) = 0 \quad (12)$$

$$Q_1(-1, \eta) = Q_2(L_r, \eta) = 0 \quad (13)$$

The heat flux continuity and the temperature jump due to the thermal contact resistance at the contact interface are given by

$$\begin{aligned} Q_1(0, \eta) = Q_2(0, \eta) &= \frac{L_1/k_1}{\tilde{R}_c} [\theta_1(0, \eta) - \theta_2(0, \eta)] \\ &= \frac{1}{R_c} [\theta_1(0, \eta) - \theta_2(0, \eta)] \end{aligned} \quad (14)$$

The dimensionless parameters are given by

$$\eta = \frac{\alpha_1 t}{L_1^2}, \quad \zeta = \frac{x}{L_1}, \quad \tau_{q1} = \frac{\alpha_1 \tilde{\tau}_q}{L_1^2}, \quad \tau_{T1} = \frac{\alpha_1 \tilde{\tau}_T}{L_1^2}, \quad \theta = \frac{T}{T_r}, \quad Q = \frac{q L_1}{k_1 T_r} \quad (15)$$

$$\alpha_r = \frac{\alpha_2}{\alpha_1}, \quad k_r = \frac{k_2}{k_1}, \quad L_r = \frac{L_2}{L_1}, \quad R_c = \frac{\tilde{R}_c}{L_1/k_1} = \frac{\tilde{R}_c}{R_1}$$

Next, Eqs. (6) and (8) are used to eliminate the mixed-derivative terms in Eqs. (7) and (9):

$$\tau_{T1} \frac{\partial^2 Q_1}{\partial \zeta^2} - Q_1 = \tau_{q1} \frac{\partial Q_1}{\partial \eta} + \frac{\partial \theta_1}{\partial \zeta} \quad (16)$$

$$\tau_{T2} \alpha_r \frac{\partial^2 Q_2}{\partial \zeta^2} - Q_2 = \tau_{q2} \frac{\partial Q_2}{\partial \eta} + k_r \frac{\partial \theta_2}{\partial \zeta} \quad (17)$$

3 Numerical Solution Method

The finite difference forms of Eqs. (16) and (6) for Layer 1 and Eqs. (17) and (8) for Layer 2 are given below, where second-order-accurate difference formulas are used for the spatial derivatives and first-order-accurate difference formulas for the time derivatives. An illustration of the grid numbering system is shown in Fig. 1(b), where the computational domain is divided into \$M-1\$ computational cells with equal spacing between grid points.

$$S_1 Q_{1,i+1}^{n+1} - [2S_1 + \tau_{q1} + \Delta \eta] Q_{1,i}^{n+1} + S_1 Q_{1,i-1}^{n+1} = -\tau_{q1} Q_{1,i}^n + S_2 \delta \theta_{1,i}^n \quad (18)$$

$$\theta_{1,i}^{n+1} = \theta_{1,i}^n - S_2 \delta Q_{1,i}^{n+1} \quad (19)$$

$$Z_1 Q_{2,i+1}^{n+1} - [2Z_1 + \tau_{q2} + \Delta \eta] Q_{2,i}^{n+1} + Z_1 Q_{2,i-1}^{n+1} = -\tau_{q2} Q_{2,i}^n + Z_2 \delta \theta_{2,i}^n \quad (20)$$

$$\theta_{2,i}^{n+1} = \theta_{2,i}^n - Z_3 \delta Q_{2,i}^{n+1} \quad (21)$$

$$S_1 = \frac{\tau_{T1} \Delta \eta}{\Delta \zeta^2}, \quad S_2 = \frac{\Delta \eta}{2 \Delta \zeta}, \quad Z_1 = \frac{\tau_{T2} \alpha_r \Delta \eta}{\Delta \zeta^2}, \quad Z_2 = \frac{k_r \Delta \eta}{2 \Delta \zeta} \quad (22)$$

$$Z_3 = \frac{\alpha_r \Delta \eta}{2 \Delta \zeta k_r}$$

$$\delta \phi_{1,i} = \begin{cases} -3\phi_{1,i} + 4\phi_{1,i+1} - \phi_{1,i+2}, & i=1 \\ \phi_{1,i+1} - \phi_{1,i-1}, & 1 < i < MI \\ 3\phi_{1,i} - 4\phi_{1,i-1} + \phi_{1,i-2}, & i=MI \end{cases} \quad (23)$$

$$\delta \phi_{2,i} = \begin{cases} -3\phi_{2,i} + 4\phi_{2,i+1} - \phi_{2,i+2}, & i=MI \\ \phi_{2,i+1} - \phi_{2,i-1}, & MI < i < M \\ 3\phi_{2,i} - 4\phi_{2,i-1} + \phi_{2,i-2}, & i=M \end{cases}$$

where \$\delta \phi_{1,i}\$ in Eq. (23) stands for \$\delta \theta_{1,i}^n\$ and \$\delta Q_{1,i}^{n+1}\$ in Eqs. (18) and (19), and \$\delta \phi_{2,i}\$ stands for \$\delta \theta_{2,i}^n\$ and \$\delta Q_{2,i}^{n+1}\$ in Eqs. (20) and (21).

The iterative solution procedure over one time step is summarized below:

1. Assume \$\theta_{1,i}^p, \theta_{2,i}^p\$ and solve Eqs. (18) and (20) for \$Q_{1,i}^{n+1}, Q_{2,i}^{n+1}\$.
2. Solve Eqs. (19) and (21) for \$\theta_{1,i}^{n+1}, \theta_{2,i}^{n+1}\$.
3. If \$|\theta_{1,i}^{n+1} - \theta_{1,i}^p| < \epsilon\$ and \$|\theta_{2,i}^{n+1} - \theta_{2,i}^p| < \epsilon\$, solution has converged.
4. If \$|\theta_{1,i}^{n+1} - \theta_{1,i}^p| \geq \epsilon\$ or \$|\theta_{2,i}^{n+1} - \theta_{2,i}^p| \geq \epsilon\$, set \$\theta_{1,i}^p = \theta_{1,i}^{n+1}, \theta_{2,i}^p = \theta_{2,i}^{n+1}\$ and go to Step 2.

The convergence criterion is taken as \$\epsilon = 10^{-10}\$ for all the results shown in this article.

4 Results and Discussion

A computer program utilizing the numerical solution method detailed in the previous section is developed, and the numerical solution is verified by using the exact solution of the heat diffusion equation in a two semi-infinite solids initially at different temperatures and brought together at time=0, as illustrated in Fig. 1(c). The temperature distribution in the two semi-infinite solids in thermally perfect contact with the initial conditions \$\theta_1(\zeta, 0) = 0, \theta_2(\zeta, 0) = \theta_0\$ is given by [16]

$$\theta_1(\zeta, \eta) = \frac{\theta_0}{1 + \sqrt{\alpha_r/k_r}} [1 - \text{erf}(|\zeta|/\sqrt{4\eta})] \quad (24)$$

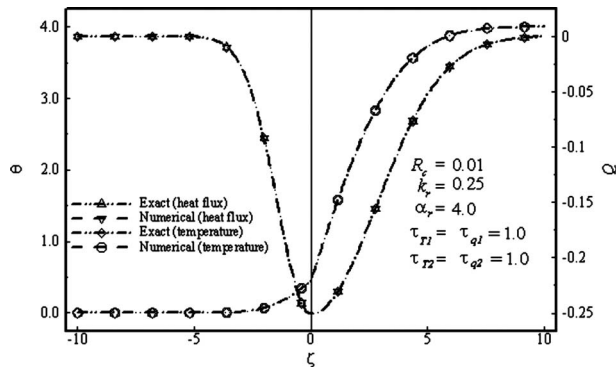


Fig. 2 Temperature and heat flux distribution at time=1 in two semi-infinite bodies: A comparison between the exact solution and the DPL model

$$\theta_2(\zeta, \eta) = \frac{\theta_0}{1 + \sqrt{\alpha_r/k_r}} [1 + (\sqrt{\alpha_r/k_r}) \operatorname{erf}(\zeta/\sqrt{4\alpha_r\eta})] \quad (25)$$

In addition, the corresponding heat fluxes in the two semi-infinite solids are given by

$$Q_1(\zeta, \eta) = - \frac{\theta_0}{[1 + \sqrt{\alpha_r/k_r}] \sqrt{\pi\eta}} \exp\left(-\frac{\zeta^2}{4\eta}\right) \quad (26)$$

$$Q_2(\zeta, \eta) = - \frac{\theta_0}{[1 + \sqrt{\alpha_r/k_r}] \sqrt{\pi\eta}} \exp\left(-\frac{\zeta^2}{4\alpha_r\eta}\right) \quad (27)$$

To compare the numerical results with the exact solution, the phase lags of the temperature gradient and heat flux are set as $\tau_{T1} = \tau_{T2} = \tau_{q1} = \tau_{q2} = 1$, and the thermal contact resistance is assigned a small value, $R_c = 0.01$. In the limit when $R_c \rightarrow 0$, the contact surface approaches the thermally perfect conditions with $Q_1(0, \eta) = Q_2(0, \eta)$ and $T_1(0, \eta) = T_2(0, \eta)$. With these parameters, the DPL model necessarily reduces to the classical heat diffusion problem. Figure 2 shows both the exact solutions as given by Eqs. (24)–(27) and the numerical solutions at time $\eta = 1$ for the initial condition $\theta_1(\zeta, 0) = 0$, $\theta_2(\zeta, 0) = \theta_0 = 4$. As is clear from Fig. 2, the agreement between the exact and the numerical solutions is very well in terms of both the heat flux and temperature distributions in the two layers.

Next, the effect of the grid size on the numerical solution accuracy is assessed. Figure 3 shows the temperature and heat flux distributions in the composite slab for different grid sizes. The parameters are shown in Fig. 3 with $\tau_q = 100\tau_T$, forcing the DPL model to be more of a hyperbolic nature. This choice of the phase

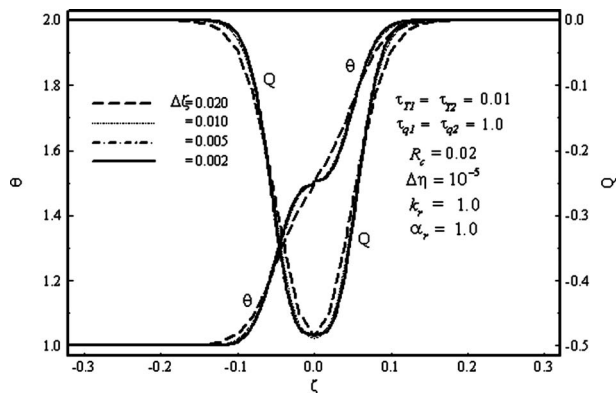


Fig. 3 Temperature and heat flux distributions at time=0.05 calculated with different grid sizes

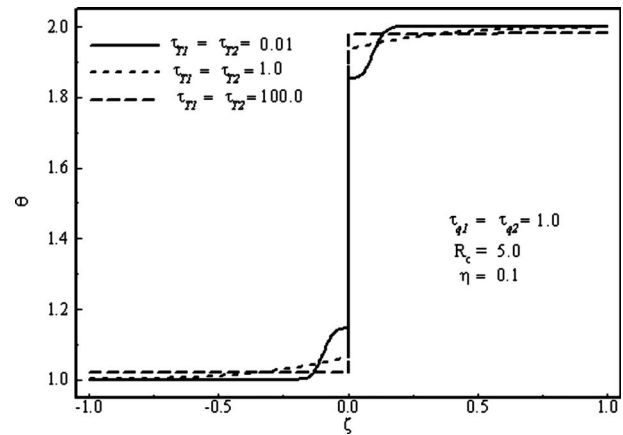


Fig. 4 Temperature distribution with different values of the temperature gradient-phase lag

lags imposes the most stringent resolution requirement in this study, and thus the grid size that gives a grid-independent solution with $\tau_q = 100\tau_T$ is adequate for any case with $\tau_q < 100\tau_T$. The numerical solutions clearly coincide for $\Delta\zeta < 0.01$. A grid size of $\Delta\zeta = 0.004$ is used in the remainder of the analysis to ensure having grid-independent solutions for all the choices of the parameters considered in this work. The time step chosen is $\Delta\eta = 10^{-5}$, while thermal conductivity and thermal diffusivity ratios are set as $k_r = \alpha_r = 1$ and domain lengths are taken as $L_1 = L_2$.

Figure 4 shows the temperature distribution in the composite slab at an early time ($\eta = 0.1$) for different values of the temperature gradient-phase lag and with heat flux-phase lag $\tau_q = 1$. With $\tau_T = 100\tau_q$, the thermal disturbance generated at the interface is felt by the whole domain and the composite slab more quickly responds than the other cases considered. The case with $\tau_T = \tau_q$ reduces the DPL model to the classical heat diffusion model. Thus, the DPL model with $\tau_T > \tau_q$ results in heat diffusion enhancement, which is attributed to the additional diffusion mechanism in the model. For the case with $\tau_T \ll \tau_q$, Fig. 4 clearly shows that the thermal disturbance generated at the interface is not felt by much of the two slabs during the time considered with the lowest interfacial temperature difference among the cases considered. This is due to the domination of the wave nature of energy transport over the heat diffusion mechanism. Although the response of the composite slab to a thermal disturbance becomes faster with increasing temperature gradient-phase lag, Fig. 4 shows that the interfacial temperature difference increases with increasing temperature gradient-phase lag, i.e., the interfacial temperature difference is the highest with $\tau_T = 100\tau_q$ at the time considered. The variation with time of the interfacial temperature difference is shown in Fig. 5 for different values of τ_T . Increasing the value of τ_T results in an increase in the temperature difference at the contact surface, as is clearly shown at early times $\eta < 1$. This means that for $\tau_T > \tau_q$, a thermal disturbance is more quickly felt in the whole domain when τ_T increases, although the imperfect contact surface shows the lowest response during the early stage of the transient energy transport. For $\tau_q \gg \tau_T$, the wave structure of the DPL model is clearly shown in Fig. 5, and the temperature difference almost instantaneously drops to around 0.72, where left- and right-running thermal waves are generated at the interface. This is more clearly shown in Fig. 6 where the thermal waves continue propagating and dying out due to heat diffusion, eventually reach the left- and right-insulated boundaries, causing the temperature to decrease at the right boundary and to increase at the left boundary. The waves then reflect back from the left and right boundaries, continue dying out, meet at the interface at time $\eta = 2$, and reflect again toward the left and right boundaries. This explains the second relatively sharp drop of the interfacial tem-

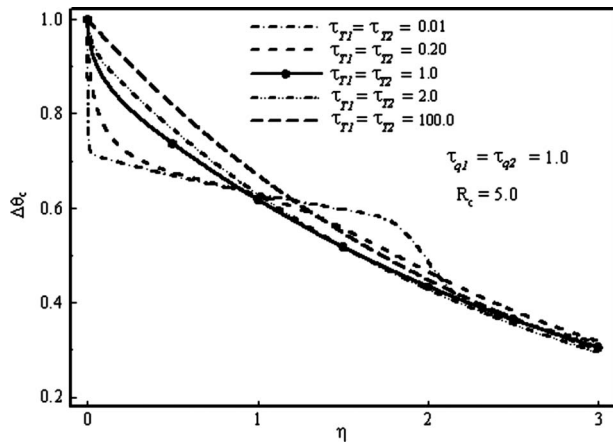


Fig. 5 Variation of the interfacial temperature difference with time for different values of the temperature gradient- and heat flux-phase lags

perature difference in Fig. 5 with $\tau_q = 100\tau_T$. A more clear picture of wave propagation and reflection phenomena in the two-layer slab is demonstrated in Fig. 7 for a low thermal contact resistance ($R_c = 0.01$). The temperature difference at the interface in this case almost instantaneously drops to around zero with the temperature at the interface being around $[\theta_1(0, \eta) + \theta_2(0, \eta)]/2$. It can be noticed from Fig. 7 that after the first wave reflection from the left

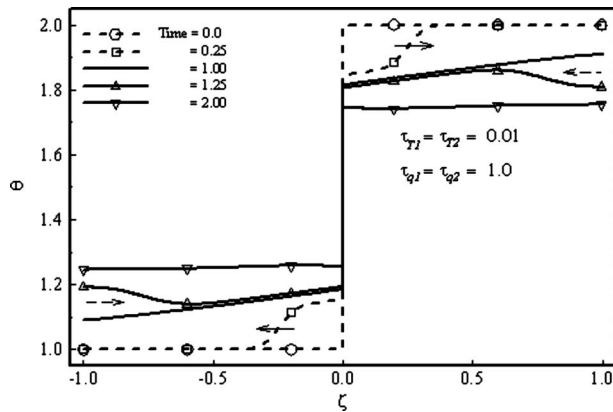


Fig. 6 Temperature distribution at different times with $R_c = 5.0$ and $\tau_q = 100\tau_T$

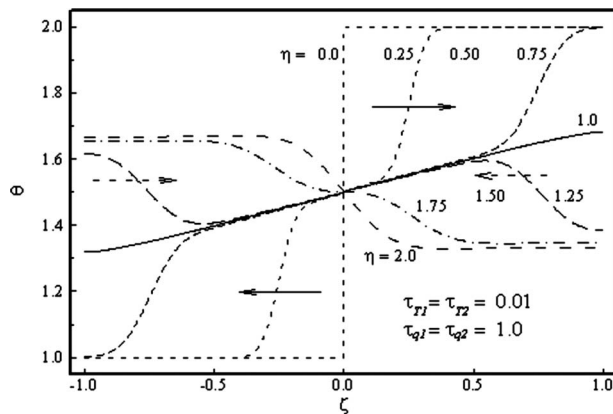


Fig. 7 Temperature distribution at different times with $R_c = 0.01$ and $\tau_q = 100\tau_T$

and right boundaries, the left layer attains a higher temperature than its initial temperature, while the temperature of the right layer drops to below its initial temperature, and for $\eta \geq 1.75$, the left layer is at a higher temperature than the right layer. The waves then meet at the interface at time $\eta = 2$ and start reflecting toward the boundaries.

5 Conclusions

The thermal behavior of a two-layer slab in imperfect contact within the DPL model framework is analyzed by using an iterative implicit finite difference method. The mixed-derivative term appearing in the DPL heat conduction model is eliminated utilizing the energy equation, and the discretization of the governing equations results in a tridiagonal system of algebraic equations that can be efficiently solved using a tridiagonal system solver. The results show that wave propagation and reflection from both the insulated surfaces and the contact surface are experienced by the DPL model with $\tau_T \ll \tau_q$. Also, with $\tau_T \ll \tau_q$ and due to the domination of the wave nature of energy transport over heat diffusion, the temperature of the initially low-temperature layer can be higher than that of the initially high-temperature layer during the transient process of energy transport. With $\tau_T > \tau_q$, the DPL model experiences an additional mechanism of heat diffusion with no wave form of energy transport. Also, as the temperature gradient-phase lag increases, heat more quickly diffuses in the composite slab when subject to a thermal disturbance, although the interfacial temperature difference remains the highest during the early times in the transient process of energy transport.

Nomenclature

- C = thermal wave speed, m/s
- k = thermal conductivity, W/m K
- k_r = thermal conductivity ratio, k_1/k_2
- L_i = length of domain i , m
- L_r = length ratio, L_1/L_2
- \mathbf{q} = heat flux vector, W/m²
- Q = dimensionless heat flux
- \mathbf{r} = position vector
- \tilde{R}_c = thermal contact resistance per unit surface area, m² K/W
- R_c = dimensionless thermal contact resistance
- t = time, s
- T = temperature, K
- T_r = reference temperature
- x = x -coordinate
- α = thermal diffusivity, m²/s
- α_r = thermal diffusivity ratio, α_1/α_2
- $\Delta\theta_c$ = temperature difference at the contact surface
- ε = convergence criterion
- ζ = dimensionless distance
- η = dimensionless time, $\alpha_1 t/L_1^2$
- θ = dimensionless temperature, T/T_r
- $\tilde{\tau}_q$ = phase lag of the heat flux, s
- τ_q = dimensionless phase lag of the heat flux, $\alpha_1 \tau_q/L_1^2$
- $\tilde{\tau}_T$ = phase lag of the temperature gradient, s
- τ_T = dimensionless phase lag of the temperature gradient, $\alpha_1 \tau_T/L_1^2$

Subscripts

- 1 = Domain 1
- 2 = Domain 2

Superscripts

- p = previous iteration
- n = previous time level
- $n+1$ = current time level

References

- [1] Tzou, D. Y., 1997, *Macro- to Microscale Heat Transfer: The Lagging Behavior*, Taylor & Francis, New York, pp. 25–50.
- [2] Haji-Sheikh, A., Minkowycz, W. J., and Sparrow, E. M., 2002, “Certain Anomalies in the Analysis of Hyperbolic Heat Conduction,” *ASME J. Heat Transfer*, **124**, pp. 307–319.
- [3] Korner, C., and Bergmann, H. W., 1998, “The Physical Defects of the Hyperbolic Heat Conduction Equation,” *Appl. Phys. A: Mater. Sci. Process.*, **67**, pp. 397–401.
- [4] Bai, C., and Lavine, A. S., 1995, “On the Hyperbolic Heat Conduction and the Second Law of Thermodynamics,” *ASME J. Heat Transfer*, **117**, pp. 256–263.
- [5] Tzou, D. Y., 1995, “Experimental Support for the Lagging Response in Heat Propagation,” *J. Thermophys. Heat Transfer*, **9**, pp. 686–693.
- [6] Hader, M., and Al-Nimr, M. A., 2002, “Thermal Behavior of a Thin Layer Carrying Pulsating Signals in the Dual-Phase-Lag Model,” *Heat Transfer Eng.*, **23**(3), pp. 35–41.
- [7] Hader, M., Al-Nimr, M. A., and Abu Nabah, B., 2002, “The Dual-Phase-Lag Heat Conduction Model in Thin Slabs Under Fluctuating Volumetric Thermal Disturbance,” *Int. J. Thermophys.*, **23**(6), pp. 1669–1680.
- [8] Abdel-Jabbar, N. M., and Al-Nimr, M. A., 2003, “The Dual-Phase-Lag Heat Conduction Model in Thin Slab Under Fluctuating Thermal Disturbance,” *Heat Transfer Eng.*, **24**(5), pp. 47–54.
- [9] Khadrawi, A. F., Al-Nimr, M. A., and Tahat, M., 2004, “Dual-Phase-Lag Heat Conduction Model in Thin Slab Under the Effect of a Moving Heating Source,” *Int. Commun. Heat Mass Transfer*, **31**(7), pp. 1015–1026.
- [10] Al-Huniti, N. S., and Al-Nimr, M. A., 2004, “Thermo Elastic Behavior of a Composite Slab Under a Rapid Dual-Phase-Lag Heating,” *J. Therm. Stresses*, **27**, pp. 607–623.
- [11] Al-Nimr, M. A., Naji, M., and Abdallah, R. I., 2004, “Thermal Behavior of a Multi-Layered Thin Slab Carrying Periodic Signals Under the Effect of the Dual-Phase-Lag Heat Conduction Model,” *Int. J. Thermophys.*, **25**(3), pp. 949–966.
- [12] Ho, J.-R., Kuo, C.-P., and Jiang, W.-S., 2003, “Study of Heat Transfer in Multilayered Structure Within the Framework of Dual-Phase-Lag Heat Conduction Model Using Lattice Boltzmann Method,” *Int. J. Heat Mass Transfer*, **46**, pp. 55–69.
- [13] Lee, Y.-M., and Tsai, T.-W., 2007, “Ultra-Fast Pulse Laser Heating on a Two-Layered Semi-Infinite Material with Interfacial Contact Conductance,” *Int. Commun. Heat Mass Transfer*, **34**, pp. 45–51.
- [14] Khadrawi, A. F., Al-Nimr, M. A., and Hammad, M. M., 2002, “Thermal Behavior of Perfect and Imperfect Contact Composite Slab Under the Effect of the Hyperbolic Heat Conduction Model,” *Int. J. Thermophys.*, **23**(2), pp. 581–598.
- [15] Lor, W.-B., and Chu, H.-S., 2000, “Effect of Interface Thermal Resistance on Heat Transfer in a Composite Medium Using the Thermal Wave Model,” *Int. J. Heat Mass Transfer*, **43**, pp. 653–663.
- [16] Eckert, E. R. G., and Drake, Jr., R. M., 1972, *Analysis of Heat and Mass Transfer*, McGraw-Hill, New York, pp. 165–166.

Two-Phase Convective Heat Transfer in Miniature Pipes Under Normal and Microgravity Conditions

Chidambaram Narayanan

Djamel Lakehal¹

e-mail: lakehal@ascomp.ch

ASCOMP GmbH,
Technoparkstrasse 1,
8005 Zurich, Switzerland

Detailed numerical simulations have been performed to study the effect of flow orientation with respect to gravity on two-phase flow heat transfer (without phase change) in small diameter pipes. The Nusselt number distribution shows that the bubbly, slug, and slug-train regimes transport as much as three to four times more heat from the tube wall to the bulk flow than pure water flow. The flow blockage effect of the inclusions results in a circulating liquid flow superimposed on the mean flow. For upflow, the breakup into bubbles/slugs occurs earlier and at a higher frequency. The average Nusselt numbers are not significantly affected by the flow orientation with respect to gravity. A mechanistic heat transfer model based on frequency and length scale of inclusions is also presented. [DOI: 10.1115/1.2909076]

Keywords: two phase, heat transfer, miniature pipes

1 Introduction

Experimental research on thermal flow in miniature pipes has so far centered on three issues: (i) flow regime map and transition, (ii) confinement effects, and (iii) characterization of heat transfer in the presence of phase change. Convective two-phase flow heat transfer without phase change has surprisingly been absent from the list of priorities. The experiment of Monde and Mitsutake [1] is one of the rare exceptions. Computational studies are rarer, except the recent contribution of Ua-Arayaporn et al. [2], who investigated convective two-phase flow heat transfer in small tubes in a small periodic box rather than in an elongated tube, as done in the companion paper by the current authors [3]. Together with our earlier study [3], the present communication sets up a debate on the following question: Is it practically meaningful to resort to convective two-phase flow heat transfer without phase change as an alternative for select microcooling applications?

In this contribution, we compare new simulation results for two-phase flow subject to gravity (upflow and downflow) to the earlier data obtained at zero gravity [3]. The focus here is on the role played by flow regimes and associated blockage/confinement effects in controlling heat transfer.

2 Modeling and Simulation

The incompressible Navier–Stokes equations within the one-fluid formalism are used in this study. The level set method is used for interface tracking. Temperature was treated as a passive scalar,

such that it is merely transported by the flow. The CMFD code TransAT[®] developed at ASCOMP is a finite-volume multiblock structured-mesh code solving the one-fluid Navier–Stokes equations. Details of the equations and numerical methods used are available in Ref. [3].

3 Two-Phase Flow Regimes and Heat Transport

3.1 Numerical Setup. The data used as reference are from the experiments by Chen et al. [4]. In their experiments, air-water flow was pumped at various flow rates in a closed loop into 1 mm and 1.5 mm diameter pipes. Five flow regimes were investigated in horizontal pipes: Bubbly, slug, slug train, churn, and annular. The simulations were performed under axisymmetric conditions for single- and two-phase flows for zero-gravity, down-flow, and up-flow configurations. The small diameter and reasonably high velocities (around 1 m/s) result in high Froude numbers of ≈ 100 , justifying the comparison between the zero-gravity simulations and horizontal flow in the experiments.

The pipe wall was set to a constant temperature $T_w=340$ K, and the inflow to $T_{in}=300$ K. The inlet flow conditions were extracted from the experiment. The phase inflow velocities and corresponding void fractions α are listed in Table 1; the void fractions were set by adjusting the inlet area.

For typical values of velocity=1.11 m/s, liquid viscosity = 10^{-3} kg/m s, surface tension coefficient=0.072 N/m, and liquid density=1000 kg/m³, one obtains a Capillary number ≈ 0.0154 , a Weber number ≈ 17 , and a Reynolds number ≈ 1110 . This suggests that the resulting flow will be dominated by the interplay between inertia and surface tension.

Grid and domain size sensitivity studies revealed that a domain extension of at least 40 diameters is necessary for the two-phase flows to establish a periodic pattern around the inclusions. Grid independence required the domain to be covered by 900×30 cells (half the diameter). Note that the slug-train case is not described in detail here.

3.2 Flow Regimes. Figure 1(a) compares the zero-gravity (central panel) bubbly flow patterns to down-(upper panel) and up-flow (lower panel) conditions. The gas jet breaks at $x/D=4$ when surface tension effects exceed the inertia. Individual bubbles are then periodically released. Gravity has an impact on the breakup time/length, with breakup happening the earliest for the up-flow case, followed by zero gravity and downflow (see Table 2). This is because the effect of gravity counters inertia when the flow is against gravity, thus making surface tension more dominant.

As discussed by the authors before [3], the breakup into slugs (Fig. 1(b)) takes place further downstream as compared to the bubbly flow because of the higher void fraction requiring a larger amplitude of the instability wave to develop before breakup. The effect of gravity is stronger for slug flow as compared to bubbly flow. The slug breakup happens slightly earlier for upflow, which results in a higher breakup frequency. Figure 1(b) also reveals the strong interaction between the slug and the wall, the proximity shown later to be responsible for substantial heat transport down to the core-flow region.

3.3 Nusselt Number. In order to quantify the increase in heat transfer in two-phase flow, the Nusselt number (see Ref. [3] for details) variation along the wall is presented in Figs. 2(a) and 2(b) for bubbly and slug flows, respectively, and compared to their equivalent single-phase flow distributions. The comparison reveals a substantial increase in the heat transfer rate with increasing inclusion length scale, denoted in Table 2 as L_{GB} . For the bubbly flow, an average Nusselt number of ≈ 10.7 is obtained for all the three cases with different orientations relative to gravity. For the slug flow, an average Nusselt number of ≈ 15 is obtained. In this case, a discernible trend is present with respect to gravity orientation. The down-flow case has a 4% higher Nu_{avg} as compared to

¹Corresponding author.

Contributed by the Heat Transfer Division of ASME for publication in the JOURNAL OF HEAT TRANSFER. Manuscript received April 2, 2007; final manuscript received October 3, 2007; published online May 16, 2008. Review conducted by Louis C. Chow.

Table 1 Inflow velocity and void fraction conditions

Case study	α	U_G (m/s)	U_L (m/s)	Domain size
Water	0.0	0	1.11	$1 \times 70 D$
Bubbly	0.205	0.66	1.11	$1 \times 40 D$
Slug	0.376	0.66	1.11	$1 \times 40 D$
Slug-train	0.480	1.57	1.11	$1 \times 40 D$

the zero-gravity case (which in turn has a 1% higher value than upflow). For the slug-train flows (not presented here), average Nusselt numbers of ≈ 15.6 and 17 were obtained. These numbers imply an overall enhancement in heat transfer by a factor between 3 and 4 compared to single-phase flow. This purely hydrodynamic effect should be taken into consideration in conditions where phase change results in similar two-phase flow regimes [5].

A closer view of the Nusselt number variation (Fig. 3) reveals that it has a very coherent variation around each inclusion. For the bubbly flow, the Nusselt number smoothly goes through a maximum at the center of the bubble where the liquid layer is squeezed. For the slug flow, the maximum value of the Nusselt number occurs at the rear end of the slug where the gap between the interface and the wall is very small (see Fig. 4(c)). Values as high as 32 can be observed. Orientation with respect to gravity plays a role in shifting the location of breakup upstream for the up-flow case, which results in a larger breakup frequency. The Nusselt numbers obtained are of similar magnitudes to those obtained by others [2,1].

3.4 Defect-Flow Analysis. In order to clarify the mechanism enhancing heat transfer, the flow field has been decomposed into

Table 2 Average Nusselt numbers, time, and length scales

Case	Nu_{mean}	Freq. (Hz)	L_{GB}/D	Re_{LS}
Water (single phase)	3.67	0.0	0.0	—
Bubbly (downflow)	10.76	632	0.8	505.6
Bubbly (zero gravity)	10.69	669	0.8	535.2
Bubbly (upflow)	10.72	727	0.8	581.6
Slug (downflow)	15.44	391	1.8	703.8
Slug (zero gravity)	14.81	414	1.8	745.2
Slug (upflow)	14.72	439	1.8	790.2
Slug-train 1	15.61	519	2.7	1401
Slug-train 2	17.20	350	5.14	1799

the sum of the single-phase flow and a perturbation flow superimposed on top of it (induced by the presence of inclusions), i.e., $U = U_{sp} + U_p$. Results of this flow decomposition are presented below in Fig. 4 for bubbly and slug flows; the snapshots are taken at approximately 26 diameters from the inlet in a periodic cell around an inclusion. For each flow regime, the top figures show the total velocity vectors at four stations in the periodic cell and the bottom figures show the perturbation flow components. The perturbation flow field is of a circulating nature around the inclusion such that near the wall, the shear is increased as compared to a single-phase profile. This additional shear created by the perturbation flow field is responsible for increasing the heat transfer rate in two-phase flow.

4 Mechanistic Heat Transfer Modeling

For practical applications, it is desirable to have a simple mechanistic model for the heat transfer coefficient. A simple anal-

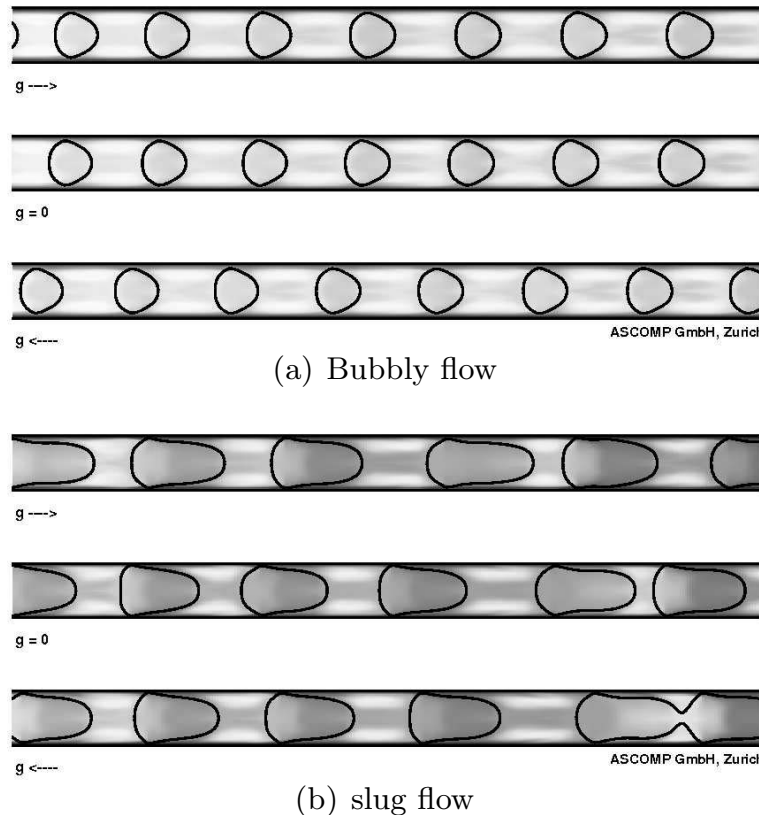
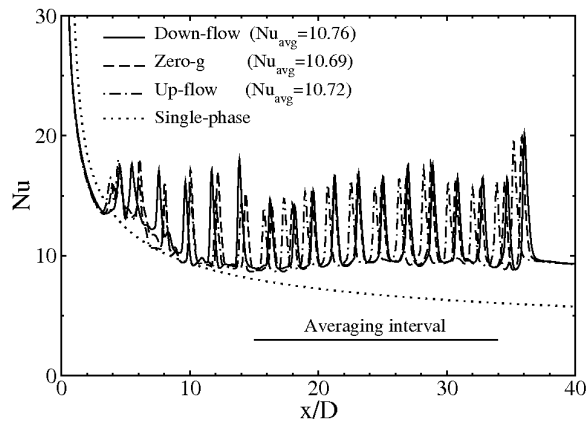
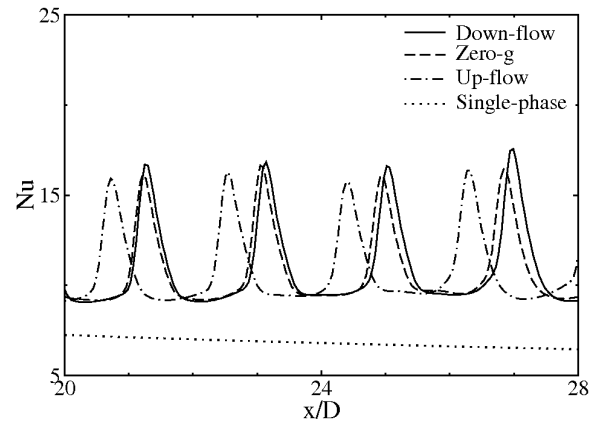


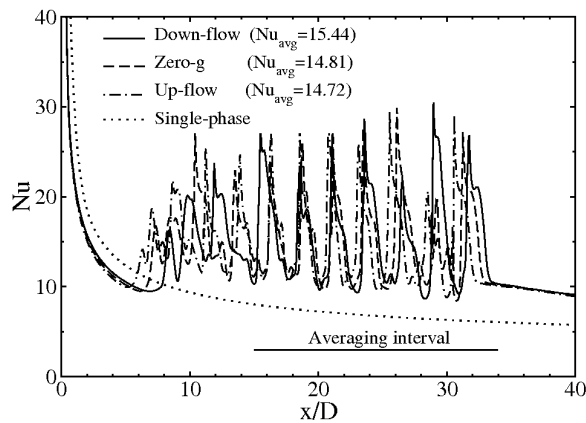
Fig. 1 Flow evolution under normal- and microgravity conditions. Domain: 18–32 D . Scale: Higher temperature corresponds to darker shade.



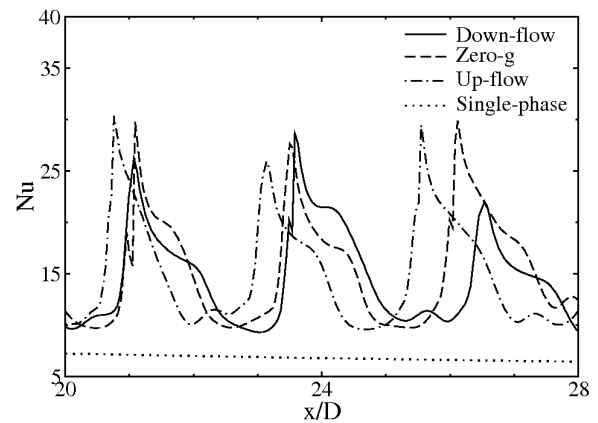
(a) Bubbly flow



(a) Bubbly flow



(b) Slug flow



(b) Slug flow

Fig. 2 Nusselt number distribution along the axis under normal- and microgravity conditions

Fig. 3 Detailed view of Nusselt number distribution under normal- and microgravity conditions

ogy with turbulent flow has been successfully proposed [3], where it was postulated that the passage of individual bubbles and slugs may act as fluid structures or eddies washing out the wall-adjacent layer, thereby increasing the temperature gradient at the wall. This is the spirit of surface renewal theory of Higbie [6].

Using the Dittus–Boelter [7] expression for heat transfer in turbulent pipe flows, the Nusselt number may be expressed as follows:

$$Nu \approx Nu_w + C Pr_L^{0.4} Re_{LS}^{4/5} \quad (1)$$

where Nu_w is the value for fully developed single-phase flow (equal to 3.67 for constant wall temperature and 4.36 for constant wall heat flux), C is a model constant, and Re_{LS} is the liquid slug Reynolds number defined based on the pipe diameter D and the velocity scale of the inclusions V_{GB} . Therefore, $Re_{LS} = DV_{GB}/\nu L$, where $V_{GB} = L_{GB}/\tau$ and τ is the time scale of bubble/slug passage.

The frequency of bubble/slug detachment together with the inclusion characteristic length scale L_{GB} is reported in Table 2. These would be better estimates of the flow time and length scales, rather than simply the superficial inflow velocities and void fraction. Bubbles detach at a higher frequency as compared to the slug and slug train, but have a smaller streamwise length. This dichotomy should be taken into account in the mechanistic modeling of heat transfer.

The best fit to the computational data is obtained for a model constant $C=0.022$, as shown in Fig. 5, which is of the same order of magnitude as the original Dittus–Boelter correlation ($C=0.023$). The frequency of breakup and passage of inclusions is

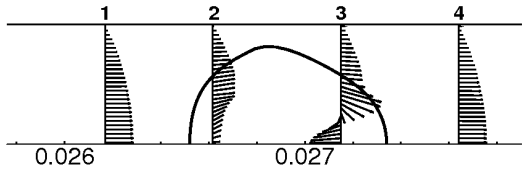
systematically affected by the orientation of the flow with respect to gravity. Up-flow case has a higher frequency as compared to zero gravity, which in turn has a higher frequency than the down-flow case. Since the inclusion length scales L_{GB} are not affected by gravity, the above correlation holds for both down- and up-flow cases.

This model can be used to determine the Nusselt number in similar situations involving well defined gas inclusions such as bubbles, and slugs evolving in microfluidic devices, where $L > 1$ mm, and for $Pr > 1$ liquids. As shown in Fig. 5, the proposed model fits remarkably well the simulated Nusselt number data for the range of flow topologies. This is a new valuable result for practical applications.

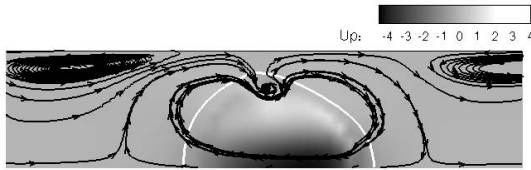
5 Pressure Drop

The effect of gravity on the pressure drop is intuitive. Pressure drop is higher in the case of upflow as compared to zero-gravity and down-flow cases in that order. Interestingly, it is observed that while the bubbly flow (Fig. 6(a)) has a lower pressure drop than the single-phase water flow (except the up-flow case), the slug flow (Fig. 6(b)) has a 14–15% larger pressure drop than the single-phase flow.

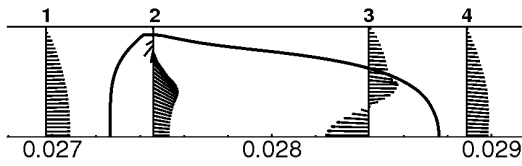
The factors affecting pressure drop are the mass flow rates, which reduce with increasing void fraction, and the inclusion-induced wall shear, which increases with void fraction. In the bubbly flow regime, the reduction in the mass flow rate has a higher impact than the bubble-induced increase in the shear, resulting in a lower pressure drop. In the slug flow (and the slug-



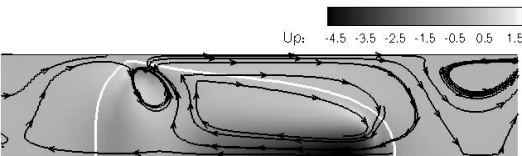
(a) Flow over bubble and stations



(b) Defect flow over bubble



(c) Flow over slug and stations



(d) Defect flow over slug

Fig. 4 Total and defect flow fields

train flow), the mass flow rate is even lower but the shear stress is significantly larger in proportion, which explains the increase in pressure drop. Thus, an optimum condition could exist, which enhances heat transfer by a factor of 4 with no increase in pressure drop.

Note that in Fig. 6(b), the axial pressure profile for the down-flow case has a large downward shift. This particular instance has been chosen to show the effect of the breakup phenomenon, as shown in Fig. 7. During the process of necking, a large pressure

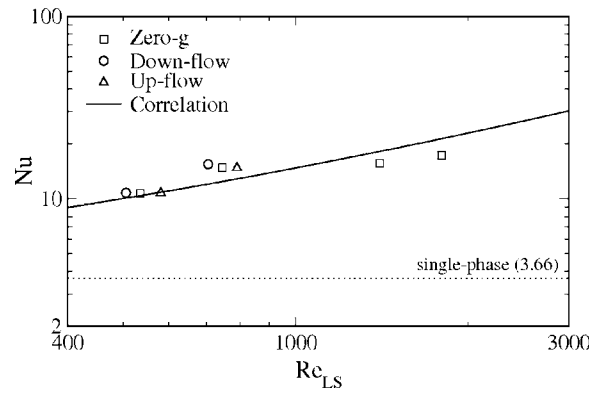
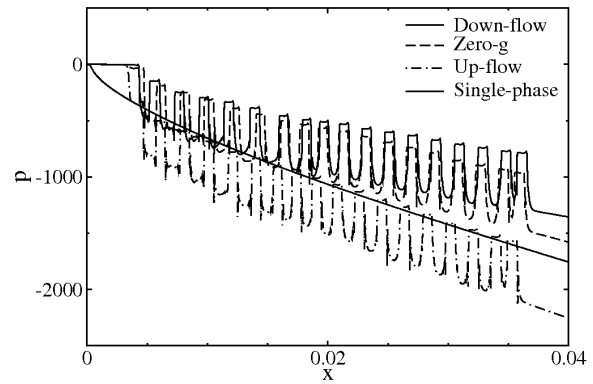
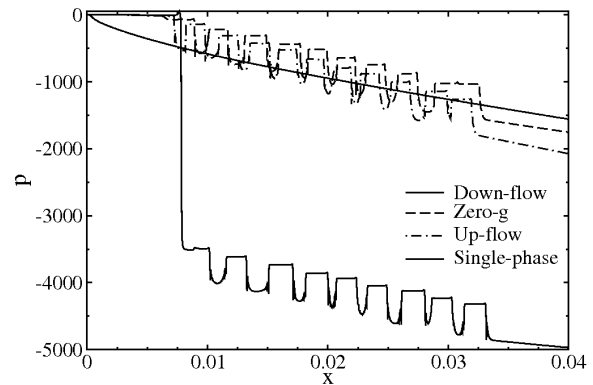


Fig. 5 Nusselt number correlation as a function of Reynolds number

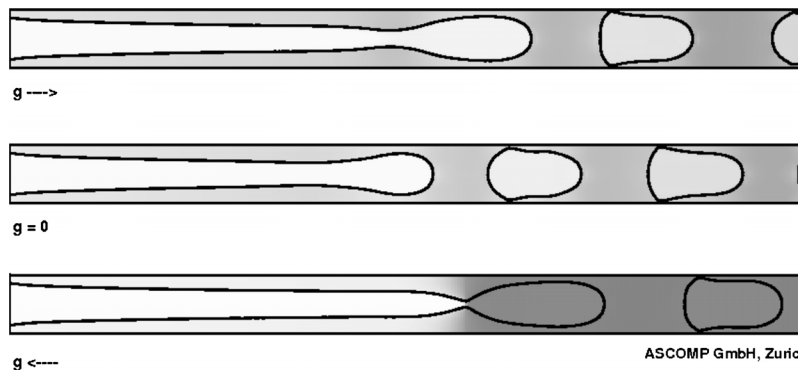


(a) Bubbly flow



(b) Slug flow

Fig. 6 Pressure variation along the pipe for normal- and microgravity conditions



ASCOMP GmbH, Zurich

Fig. 7 Slug breakup under normal- and microgravity conditions

drop is created across the neck due to gas flow acceleration, which produces this downward shift in pressure. The relevant point here is that in designing a two-phase system, these pressure pulses will have to be taken into account, even though the average pressure drop would be similar to single-phase flow.

6 Conclusions

Overall, the heat removal rate in two-phase flow is significantly higher than in single phase. The additional circulating flow induced by the presence of bubbles and slugs is shown to substantially increase the wall shear and in turn heat transfer. The average Nusselt number distribution shows that the bubbly and slug patterns transport three to four times more heat from the tube wall to the bulk flow than the single-phase water flow. The heat transfer results are only marginally affected by gravity, even though there is a noticeable effect on the breakup frequency. From an engineering standpoint, the present results may be helpful in designing intelligent flow control systems. The simple correlation proposed is meant to be used as a guideline for design purposes.

Acknowledgment

This work has been granted by the European Space Agency (ESA) through the MAP research program MAP AO-1999-045.

The authors are thankful to the Coordinators, Olivier Minster (ESA) and Professor Lounes Tadrist (University of Marseille) for their valuable comments.

References

- [1] Monde, M., and Mitsutake, Y., 1995, "Enhancement of Heat Transfer Due to Bubble Passing Through a Narrow Vertical Rectangular Channel," *Heat Mass Transfer*, **31**, pp. 77–82.
- [2] Ua-Arayaporn, P., Fugakata, K., Kasagi, N., and Himeno, T., 2005, "Numerical Simulation of Gas-Liquid Two-Phase Convective Heat Transfer in a Microtube," *Proceedings of the ECI International Conference on Heat Transfer and Fluid Flow in Microscale*, Castelvechio Pascoli, Italy, Sept. 25–30.
- [3] Lakehal, D., Larrignon, G., and Narayanan, C., 2007, "Computational Heat Transfer and Two-Phase Flow Topology in Miniature Tube," *Microfluid. Nanofluid.*, **4**, pp. 261–271.
- [4] Chen, W. L., Twu, M. C., and Pan, C., 2002, "Gas-Liquid Two-Phase Flow in Microchannels," *Int. J. Multiphase Flow*, **28**, pp. 1235–1247.
- [5] Thome, J. R., Dupont, V., and Jacobi, A. M., 2004, "Heat Transfer Model for Evaporation in Microchannels, Part I: Presentation of the Model," *Int. J. Heat Mass Transfer*, **47**, pp. 3375–3385.
- [6] Higbie, R., 1935, "The Rate of Absorption of Pure Gas Into a Still Liquid During Short Period of Exposure," *Trans. Am. Inst. Chem. Eng.*, **31**, pp. 365–388.
- [7] Dittus, F. W., and Boelter, L. M. K., 1930, "Heat Transfer in Automobile Radiators of the Tubular Type," *Univ. Calif. Publ. Eng.*, **2**(13), pp. 443–461.

Heat Transfer Analysis Through Solar and Rooted Fins

A.-R. A. Khaled¹

Thermal Engineering and Desalination
Technology Department,
King Abdul Aziz University,
P.O. Box 80204,
Jeddah 21589, Saudi Arabia
e-mail: akhaled@kau.edu.sa

Heat transfer through solar fins and rooted fins is analyzed theoretically in this work. The terminology of "solar fin" is used to refer to fins that are subject to external irradiations while the terminology "rooted fin" is used to refer to fins partially embedded in the base wall. One-dimensional heat transfer analysis is conducted and heat transfer rate through the fin, fin efficiency, as well as other performance indicators are obtained. It is found that the fin efficiency of the solar fins is maximized at certain fin indices and that rooted fins are preferable over ordinary fins for a wide range of fin indices. This range of fin indices is summarized in a correlation for insulated walls or insulated fin roots. Moreover, the minimum fin length that maximizes fin heat transfer is found to increase as solar irradiation intensity increases for solar fins subjected partially to solar irradiations. Finally, this work provides new passive methods for enhancing heat transfer in thermal systems. [DOI: 10.1115/1.2897927]

Keywords: fins, irradiation, heat transfer, extended surfaces, enhancement

1 Introduction

Heat transfer through extending surfaces was studied extensively in the literature [1,2]. In this work, heat transfer through new families of fins is analyzed analytically, which receives less attention in the literature. These fins are (a) solar fins, which are fins subjected to external irradiation, and (b) rooted fins, which are fins partially embedded in the wall. One-dimensional heat transfer analysis is conducted, and heat transfer rate through the fin, fin efficiency, as well as other performance indicators are obtained. The main controlling parameters are identified, and their role on the thermal performance of the analyzed fins is explored.

2 Problem Formulation

2.1 Solar Fin

2.1.1 Solar Fin Fully Subject to Solar Irradiation. Consider a fin having a length L and a uniform cross-sectional area A_C and a uniform perimeter P extending from a wall that is kept at a base temperature T_b . Let the fin absorb a uniform heat flux q_r'' at its outer surface, which is subject to convection with free stream temperature T_∞ and convection coefficient h shown in Fig. 1(a). Note that the absorbed heat flux q_r'' is equal to the irradiation G on the fin surface times the fin solar absorptivity α_S times area factor Ar (ratio of irradiated area to the total fin area), $q_r'' = (\alpha_S G) Ar$. The x -axis is taken along the length of the fin starting from the base. The one-dimensional energy equation for the fin [1] is

$$\frac{d^2 T}{dx^2} - m^2(T - T_\infty) = -\frac{q_r'' P}{kA_C} \quad (1)$$

where m is equal to

$$m = \sqrt{\frac{hP}{kA_C}} \quad (2)$$

2.1.1.1 Infinite fin (Case A). The solution to Eq. (1) is the following when L approaches infinity:

$$\frac{T(x) - T_\infty}{T_b - T_\infty} = e^{-mx} + \frac{q_r''}{h(T_b - T_\infty)}(1 - e^{-mx}) \quad (3)$$

The ratio of the fin heat transfer when $q_r'' \neq 0$ to that when $q_r'' = 0$ is equal to

$$\gamma = \frac{q_f}{q_f|_{q_r''=0}} = -\frac{(kA_C dT/dx|_{x=0})}{\{-(kA_C dT/dx|_{x=0})\}|_{q_r''=0}} = 1 - \frac{q_r''}{h(T_b - T_\infty)} \quad (4)$$

2.1.1.2 Insulated tip fin (Case B). For this case, the solution to Eq. (3) is

$$\frac{T(x) - T_\infty}{T_b - T_\infty} = \left(1 - \frac{q_r''}{h(T_b - T_\infty)}\right) \frac{\cosh[m(L-x)]}{\cosh(mL)} + \frac{q_r''}{h(T_b - T_\infty)} \quad (5)$$

The fin efficiency η_f for this case is

$$\eta_f = \frac{-kA_C dT/dx|_{x=0}}{hPL(T_b - T_\infty)} = \frac{\sqrt{hPkA_C} \left[(T_b - T_\infty) - \frac{q_r''}{h} \right] \tanh(mL)}{hPL(T_b - T_\infty)} = (\eta_f)_{q_r''=0} \left[1 - \frac{1}{(mL)^2} R_m \right] \quad (6)$$

where the dimensionless parameters $(\eta_f)_{q_r''=0}$ and R_m are equal to

$$(\eta_f)_{q_r''=0} = \frac{\tanh(mL)}{(mL)}, \quad R_m = \frac{q_r'' L^2 P}{kA_C (T_b - T_\infty)} \quad (7)$$

2.1.2 Solar Fin Subject Partially to Solar Irradiation. Consider a fin having a length H and a uniform cross-sectional area A_C and a uniform perimeter P extending from a wall that is kept at a base temperature T_b . A fin portion starting from a distance L from the base is subject to a uniform heat flux q_r'' at its outer surface. The fin is subject to convection with free stream temperature T_∞ and convection coefficient h , as shown in Fig. 1(b). The x -axis is taken along the length of the fin starting from the base. The one-dimensional energy equations for the fin [1] are

$$\frac{d^2 T_1}{dx^2} - m^2(T_1 - T_\infty) = 0 \quad (8)$$

$$\frac{d^2 T_2}{dx^2} - m^2(T_2 - T_\infty) = -\frac{q_r'' P}{kA_C} \quad (9)$$

where m is defined in Eq. (2). T_1 and T_2 are the temperature fields for the portion free from solar irradiation and that subject to solar irradiation, respectively.

The boundary conditions are

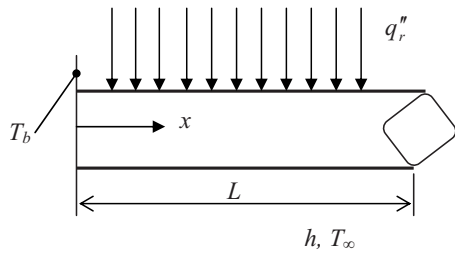
$$T_1(x=0) = T_b \quad (10a)$$

$$\left. \frac{dT_2}{dx} \right|_{x=H} = 0 \quad (10b)$$

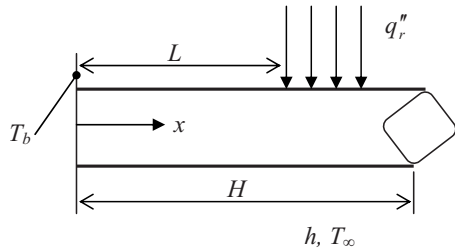
$$T_1(x=L) = T_2(x=L) \quad (11a)$$

¹Corresponding author.

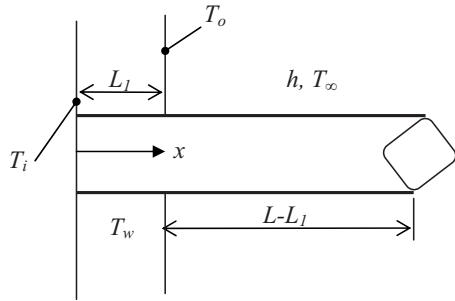
Contributed by the Heat Transfer Division of ASME for publication in the JOURNAL OF HEAT TRANSFER. Manuscript received February 15, 2007; final manuscript received June 28, 2007; published online May 20, 2008. Review conducted by Peter Vadasz.



Case A



Case B



Case C

Fig. 1 (a) Solar fin fully subject to solar irradiation. (b) Solar fin partially subject to solar irradiation. (c) Rooted fin.

$$\left. \frac{dT_1}{dx} \right|_{x=L} = \left. \frac{dT_2}{dx} \right|_{x=L} \quad (11b)$$

The fin heat transfer rate q_f is equal to

$$q_f = -kA_C \left. \frac{dT_1}{dx} \right|_{x=0} \quad (12)$$

Solving Eqs. (8) and (9) results in the following formula for the fin heat transfer rate:

$$q_f = \sqrt{hPkA_C} \left([T_b - T_\infty] - \frac{q_r''}{h} \cosh[mL] \right) \tanh(mH) + \sqrt{hPkA_C} \frac{q_r''}{h} \sinh[mL] \quad (13)$$

As such, the fin efficiency η_f and the performance indicator γ are equal to

$$\eta_f = \frac{q_f}{hPH(T_b - T_\infty)} = \left\{ 1 - \frac{R_m \cosh(mL)}{(mL)^2} \right\} \left(\frac{\tanh(mH)}{mH} \right) + R_m \left\{ \frac{\sinh(mL)}{(mL)^3} \left(\frac{L}{H} \right) \right\} \quad (14)$$

$$\gamma = \frac{q_f}{q_f|_{q_r''=0}} = \left\{ 1 - \frac{q_r''}{h(T_b - T_\infty)} \cosh(mL) \right\} \tanh(mH) + \frac{q_r''}{h(T_b - T_\infty)} \sinh(mL) \quad (15)$$

The performance indicator γ is greater than 0.99 when $L > L_\infty$, where L_∞ is equal to

$$L_\infty = \frac{4.65}{m} + \frac{1}{m} \ln \left(\frac{q_r''}{h[T_b - T_\infty]} \right) \quad (16)$$

2.2 Rooted Fins. Consider a fin having a length L and a uniform cross-sectional area A_C extending from the interior surface of a wall having a thickness L_1 , ($L_1 < L$), as shown in Fig. 1(c). The temperature of the interior surface is T_i , while it is equal to T_o for the exterior surface. The thermal conductivity of the wall and the fin are k_w and k_f , respectively. The fin portion facing the outside fluid stream is subject to convection with free stream temperature equal to T_∞ and a convection coefficient of h_f . It is assumed that h_f does not vary with position and that the variation of the fin temperature in the transverse direction is negligible. As such, the heat transferred through the fin at the interface q_{int} is

$$q_{\text{int}} = \eta_o h_f P (L - L_1) [T_{\text{int}} - T_\infty] \quad (17)$$

where T_{int} , P , and η_o are the fin temperature at $x=L_1$, the perimeter of the fin, and the efficiency of the fin portion facing the outside stream, respectively. The x -axis is directed along the fin centerline starting from the interior surface of the wall (Fig. 1(c)).

The heat diffusion equation for the fin portion embedded in the wall is

$$\frac{d^2 T_f}{dx^2} - n^2 (T_f - T_w) = 0 \quad (18)$$

where n is equal to

$$n = \sqrt{\frac{k_w S P}{k_f A_C}} \quad (19)$$

where T_f , S , and T_w are the fin temperature, shape factor, and wall temperature, respectively. The unit of S is the reciprocal of the length unit. For example, if the wall temperature reaches its one-dimensional temperature field at an average distance t from the surface of the fin, then $S=1/t$. The boundary conditions for this equation are

$$T_f(x=0) = T_i \quad (20a)$$

$$T_f(x=L_1) = T_{\text{int}} \quad (20b)$$

$$-k_f A_C \left. \frac{dT_f}{dx} \right|_{x=L_1} = \eta_o h_f A_f (T_{\text{int}} - T_\infty) \quad (20c)$$

The temperature distribution through the wall is

$$T_w = (T_o - T_i) \left(\frac{x}{L_1} \right) + T_i \quad (21)$$

The solution of Eq. (18) with boundary conditions (Eqs. (20a)–(20c)) is

$$\frac{T_f(x) - T_i}{T_o - T_i} = \frac{x}{L_1} + \left\{ \frac{\eta_o (mL_1)^2 (L/L_1 - 1) \left[\left(\frac{T_i - T_\infty}{T_i - T_o} \right) - 1 \right] - 1}{\eta_o (mL_1)^2 (L/L_1 - 1) + \frac{nL_1}{\tanh(nL_1)}} \right\} \times \frac{\sinh(nx)}{\sinh(nL_1)} \quad (22)$$

where m is the fin index of the fin portion facing the fluid stream. It is equal to

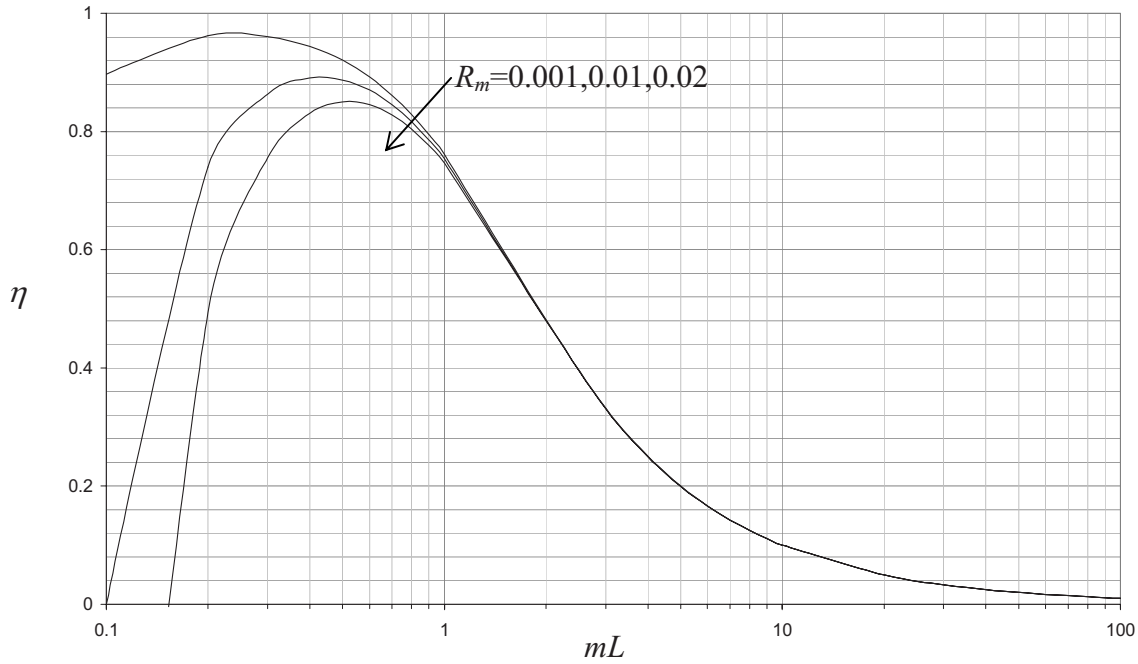


Fig. 2 Effects of mL and the solar irradiation parameter R_m on the fin efficiency η for the solar fin fully subject to solar irradiations for an insulated tip fin

$$m = \sqrt{\frac{h_f P}{k_f A_C}} \quad (23)$$

As such, the fin heat transfer rate is

$$q_f = -k_f A_C \left. \frac{dT_f}{dx} \right|_{x=0} = -\frac{k_f A_C}{L_1} \theta_o \left\{ 1 + \frac{\left[\eta_o (mL_1)^2 (L/L_1 - 1) \left[\left(\frac{T_i - T_\infty}{T_i - T_o} \right) - 1 \right] - 1 \right] \left(\frac{nL_1}{\sinh(nL_1)} \right)}{\eta_o (mL_1)^2 (L/L_1 - 1) + \frac{nL_1}{\tanh(nL_1)}} \right\} \quad (24)$$

where $\theta_o = T_o - T_i$. Define the performance indicator γ as follows:

$$\gamma = \frac{q_f}{(q_f)_{\text{very long}|L_1=0}} = \frac{q_f}{\sqrt{k_f A_C h_f P} (T_o - T_\infty)} \quad (25)$$

It is equal to

$$\gamma = \frac{1}{mL_1} \left\{ \left[\left(\frac{T_i - T_\infty}{T_i - T_o} \right) - 1 \right]^{-1} + \frac{\left[\eta_o (mL_1)^2 (L/L_1 - 1) - \left[\left(\frac{T_i - T_\infty}{T_i - T_o} \right) - 1 \right]^{-1} \right] \left(\frac{nL_1}{\sinh(nL_1)} \right)}{\eta_o (mL_1)^2 (L/L_1 - 1) + \frac{nL_1}{\tanh(nL_1)}} \right\} \quad (26)$$

Special case. When $n=0$, as when $S=0$, or when $k_w \ll k_f$, the fin performance indicator is equal to

$$\gamma = \frac{1}{mL_1} \left\{ \left[\left(\frac{T_i - T_\infty}{T_i - T_o} \right) - 1 \right]^{-1} + \frac{\left[\eta_o (mL_1)^2 (L/L_1 - 1) - \left[\left(\frac{T_i - T_\infty}{T_i - T_o} \right) - 1 \right]^{-1} \right]}{\eta_o (mL_1)^2 (L/L_1 - 1) + 1} \right\} \quad (27)$$

For a very long fin, the fin efficiency η_o is equal to

$$\eta_o = \frac{1}{m(L - L_1)} = \frac{1}{mL_1(L/L_1 - 1)} \quad (28)$$

As such, the performance indicator γ is equal to

$$\gamma = \frac{1}{mL_1} \left\{ \left[\left(\frac{T_i - T_\infty}{T_i - T_o} \right) - 1 \right]^{-1} + \frac{\left[mL_1 - \left[\left(\frac{T_i - T_\infty}{T_i - T_o} \right) - 1 \right]^{-1} \right]}{mL_1 + 1} \right\} \quad (29)$$

3 Discussion of the Results

Figure 2 illustrates the effects of the absorbed irradiation R_m and the fin index m parameters on the fin efficiency η for an insulated tip fin. As can be seen, the fin efficiency is maximized at certain values of m , indicating that solar fins are preferred to have

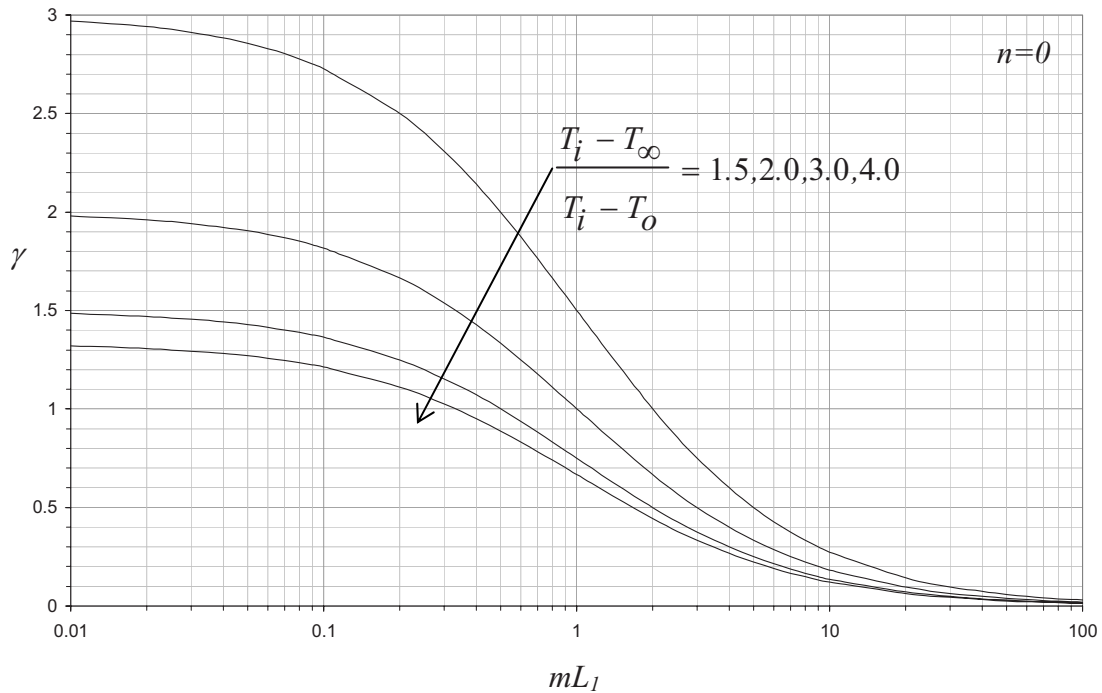


Fig. 3 Effects of mL_1 and the temperature ratio on the performance indicator γ for a very long rooted fin

specific fin indices. To eliminate the reduction in fin heat transfer, the solar fin is recommended to be partially shaded in the region closer to the base with a shaded length greater than L_∞ (Eq. (16)).

Figure 3 illustrates the effects of the fin index m , the length of the fin root L_1 , and the temperature ratio $(T_i - T_\infty)/(T_i - T_o)$ on the performance indicator γ . As can be seen from the figure, the very long rooted fin is recommended over the very long fin for small values of m , L_1 , and $(T_i - T_\infty)/(T_i - T_o)$ when $n=0$. It can be concluded from this figure that when the following inequality is satisfied:

$$mL_1 < -0.0693 \left(\frac{T_i - T_\infty}{T_i - T_o} \right)^3 + 0.784 \left(\frac{T_i - T_\infty}{T_i - T_o} \right)^2 + 3.1027 \left(\frac{T_i - T_\infty}{T_i - T_o} \right) + 4.624 \quad (30)$$

the very long rooted fin is recommended over the very long fin.

4 Conclusions

Heat transfer through solar fins and rooted fins was analyzed theoretically in this work. A one-dimensional heat transfer analysis is conducted, and heat transfer rate through the fin, fin efficiency, as well as other performance indicators are obtained. It was found that the fin efficiency of solar fins is maximized at certain fin indices. Moreover, the minimum fin length that maximizes fin heat transfer is found to increase as solar irradiation intensity increases for solar fins subjected partially to solar irradiations. Rooted fins were found to be preferable over ordinary fins for a wide range of fin indices. This range of fin indices is summarized in a correlation for insulated walls or insulated fin roots. Finally, this work provides new passive methods for enhancing heat transfer in thermal systems.

Nomenclature

A_r = area factor
 G = solar irradiation
 h_f = convection coefficient
 H = fin length for the solar fin partially subject to irradiations
 k_f = thermal conductivity for the fin
 k_w = thermal conductivity for the wall
 L = fin length
 L_1 = length of the fin root
 m = fin index
 n = fin index of the fin root
 P = perimeter
 q_f = heat transfer through the fin
 T_b = base temperature
 T_f = fin temperature
 T_i = inside wall temperature
 T_o = outside wall temperature
 T_w = wall temperature
 T_∞ = free stream temperature

Greek Symbols

γ = fin performance ratio
 η = fin efficiency

References

- [1] Lienhard, J. H., IV, and Lienhard, J. H., V, 2004, *A Heat Transfer Textbook*, Phlogiston, Cambridge, MA.
- [2] Gardner, K. A., 1945, "Efficiency of Extended Surfaces," *Trans. ASME* **67**, pp. 621–631.